The Dissertation Committee for Nicolas Patrick Roussel Certifies that this is the approved version of the following dissertation:

STRESS REORIENTATION IN LOW PERMEABILITY RESERVOIRS

Committee:

Mukul M. Sharma, Supervisor

Matthew T. Balhoff

Steven L. Bryant

Eric P. Fahrenthold

Jon E. Olson

STRESS REORIENTATION IN LOW PERMEABILITY RESERVOIRS

by

Nicolas Patrick Roussel, Diplôme d'Ingénieur; M.S.M.E.

Dissertation

Presented to the Faculty of the Graduate School of

The University of Texas at Austin

in Partial Fulfillment

of the Requirements

for the Degree of

Doctor of Philosophy

The University of Texas at Austin

August 2011

Dedication

I dedicate this dissertation to my wonderful mother Eliane Roussel. The true courage and abnegation she has demonstrated throughout difficult times is my strongest inspiration.

Acknowledgements

I would like to thank all those who participated in making this dissertation possible.

I am especially grateful to my advisor, Dr. Mukul Sharma for his guidance throughout the project. Despite his busy schedule, he has always been keen on sharing his experience and suggesting ever more fascinating ideas and concepts to work on. I am particularly thankful for the collaborative atmosphere, and the numerous opportunities he gave me to present this work to industry partners and sponsors. I must thank also the members of my dissertation committee for their sound advice during the completion of this work.

The multiple challenges of graduate school were greatly facilitated thanks to the day-to-day contributions of Glen Baum and Jin Lee, whose dedication to the success of students is remarkable.

I am indebted to many of my friends and colleagues who through their suggestions and fruitful discussions shaped this dissertation in so many ways. In particular I would like to thank Kaveh Ahmadi, Guillaume Rannou and Lionel Ribeiro, whose moral support has been crucial in the last stretch of the dissertation, as well as Patrick Louis, Sahil Malhotra, Ripudaman Manchanda, Philippe Marouby, Somnath Mondal, Antoine Montaut, Divya Ramaswamy, David Torres, and many others whom I did not cite explicitly.

STRESS REORIENTATION IN LOW PERMEABILITY RESERVOIRS

Publication No._____

Nicolas Patrick Roussel, Ph.D.

The University of Texas at Austin, 2011

Supervisor: Mukul M. Sharma

The acknowledgement of the existence of stress changes in the reservoir due to production from a propped-open fracture has resulted in the development of a new concept: oriented or altered-stress refracturing. By initiating a secondary fracture perpendicular to the initial fracture, refracturing makes it possible to access higher pressurized regions of the reservoir, thus improving the productivity of the well.

The redistribution of stresses around a fractured vertical well has two sources: (a) opening of propped fracture (mechanical effects) and (b) production or injection of fluids in the reservoir (poroelastic effects). The coupling of both phenomena is numerically modeled to quantify the extent and timing of stress reorientation around fractured production wells. Guidelines and type-curves are established that allow an operator to choose the timing of the refracture operation in the life of the well, and evaluate the potential increase in well production after refracturing.

The selection of candidate wells for refracturing is often very difficult based on the information available at the surface. We propose a systematic methodology, based on dimensionless groups, that allows a field engineer to evaluate a well's potential for refracturing from an analysis of field production data and other reservoir data commonly available. This analysis confirms the crucial role played by stress reorientation in the success of refracturing operations.

Another topic of interest is the multi-stage fracturing of horizontal wells. The opening of a propped transverse fracture causes a reorientation of stresses in its neighborhood, which in turn affects the direction of propagation of subsequent fractures. This phenomenon, often referred to as stress shadowing, can negatively impact the efficiency of each fracturing stage. By calculating the trajectory of multiple transverse fractures, we offer some insight on the completion designs that will (a) minimize fracture spacing without compromising the efficiency of each fracturing stage and (b) effectively stimulate natural fractures in the vicinity of the created fracture. In addition, a novel detection method of mechanical interference between multiple transverse fractures is established, based on net fracturing pressure data measured in the field, to calculate the optimum fracture spacing for a specific well.

Table of Contents

List of Tables

List of Figures

CHAPTER 1: INTRODUCTION

The dissertation reports on research that has been conducted on stress reorientation around fractured wells in low-permeability reservoirs. This stress reorientation can be caused by (a) opening of a propped fracture (mechanical effects) and (b) production or injection of fluids in the reservoir (poroelastic effects). The findings on the extent and timing of stress reorientation were applied to two important stimulation techniques: refracturing of vertical wells and the multi-stage fracturing of horizontal wells.

1. CONTEXT OF THE STUDY: UNCONVENTIONAL GAS RESOURCES

The recent development of shale gas resources has profoundly modified the characteristics of the natural gas market in the United States. Shale gas production has increased from 0.39 trillion cubic feet (TCF) in 2000 to 4.87 TCF in 2010 and now constitutes 23% of the total natural gas production. By 2035, the U.S. Energy Information Administration (2011) predicts that shale gas may account for almost half of U.S. natural gas production. Unconventional oil production from shales and ultra-low permeability dolomites (unconventional oil) has had a significant impact on domestic US production of oil. It is expected that over 1 million barrels of oil per day will be produced from unconventional resources by 2013.

A recent investigation of 48 shale gas basins in 32 countries concludes that the shale gas is far from being confined to the U.S. (**Fig. 1.1**). An initial assessment of the extent of the international shale gas resource base, which is probably conservative because of limited available data, reports an estimated 6,622 TCF of technically

recoverable resources (including 862 TCF in the U.S.). The distribution of shale gas resources over the 32 countries analyzed is detailed in **Table 1.1**.

Shales have been known to contain significant hydrocarbon resources for a long time but sizeable production from shale gas dates back to only the mid-nineties. At that time, the successful implementation of hydraulic fracturing in a horizontal well by Mitchell Energy in the Barnett shale convinced many other companies to enter that play, making it the largest contributor to the domestic production of natural gas today. Since then, novel technologies such as slick-water fracturing (Britt et al. 2006; Gadde et al. 2004; Liu et al. 2007; Palisch et al. 2008; Sharma et al. 2004), multi-stage fracturing combined to horizontal drilling (Cipolla et al. 2009; Daneshy 2011; McDaniel 2010), multi-lateral completions (Lolon et al. 2009; Mutalik and Gibson 2008; Waters et al. 2009) and microseismic fracture diagnostics (Fisher et al. 2004; Le Calvez et al. 2007; Maxwell et al. 2002; Waters et al. 2009), have resulted in an increase in the projected gas recovery from a couple percent to as much as 50% (King 2010). Many shale formations other than the Barnett such as the Eagle Ford, Fayetteville, Haynesville, Marcellus and Woodford shales are now being actively pursued.

Still, the potential for improving production and rates of recovery in shale-specific well completions is significant. Issues such as stress shadowing (Cheng 2009; Fisher et al. 2004; Ketter et al. 2008; Olson 2008), fracture network propagation (King et al. 2008; Mayerhofer et al. 2010; Maxwell et al. 2009; Warpinski et al. 2008; Weng et al. 2011), the propping of natural fractures (Cipolla 2009; Olsen et al. 2009; Soliman et al. 2010), and water consumption still need to be addressed. The present study focuses on the impact of stress reorientation from hydraulically fracturing low-permeability rocks and introduces novel strategies that may help to improve gas and oil production rates and ultimate recovery.

If there is one lesson that can be learned from past experience in shale gas production over the last thirty years, it is that "no two shales are alike" (King 2010). Consequently, there is not a single completion strategy that will be optimum for all wells, or even most of them, and a careful analysis of the shale characteristics will be required to achieve the next level of performance enhancement.

Another unconventional gas resource has been increasingly developed, specifically in the U.S., in the past 40 years: tight gas sands. They are typically low-permeability reservoirs and require the wells to be stimulated by a large fracture treatment in order to be produced at economic flow rates. According to Holditch (2006), because natural resources are distributed log normally in nature, the resource base in low-permeability reservoirs such as tight gas or shale gas that require improved technologies and higher gas prices to be economical, should be much larger than conventional (high-permeability) natural gas resources (**Fig 1.2**). In 2009, 6.59 TCF were produced from tight gas reservoirs in the U.S., accounting for more than 30% of the domestic natural gas production. The supply from tight gas reservoirs is predicted to stabilize over the next 25 years (U.S. EIA 2011).

Restimulation operations have been instrumental in extending the life of tight gas sand reservoirs and restoring well production to near original or even higher rates. While vertical wells have been refractured from as early as the 1970s, it is undergoing a revival as a result of the current low natural gas prices. Also, in a context where access to new resources is often limited, increasing production, even in small proportions, in existing wells may lead to significant incremental reserve volumes (Dozier et al. 2003).

Disappointing results in initial refracturing campaigns, often due to poor candidate well selection, have discouraged many operators to refracture their wells. However, the Gas Technology Institute (GTI) (1996) demonstrated the potential of

refracturing treatments to yield incremental reserves at a much lower cost than required to find and develop new gas resources, provided the top candidate wells are correctly identified.

2. OBJECTIVES

The main objective of this dissertation is to better understand stress reorientation around wellbores and to propose novel strategies to improve the performance of multi-stage horizontal completions in gas / oil shales, tight gas sands and vertical well re-stimulation treatments. This overall objective is met by addressing the following:

- Extent of stress reversal and stress reorientation from poroelastic and mechanical effects
- Timing of the stress reversal region
- Candidate well selection for refracturing
- Superposition of mechanical stress reorientation for multiple transverse fractures, multiple laterals, and different fracture sequences in horizontal wells
- Trajectory and net closure stress of multiple transverse fractures initiated from a horizontal wellbore

3. STRUCTURE OF THE DISSERTATION

The core of the dissertation is divided into five chapters. The first two feature a comprehensive study of the extent and timing of stress reorientation from poroelastic and mechanical effects. The following chapter is an application of our findings regarding stress reorientation around a vertical fracture to the refracturing of vertical wells. In an effort to facilitate the selection of candidate wells for refracturing, we introduce a novel

method using well completion and production data and based on dimensionless quantities. Finally, stress reorientation effects from multiple transverse fractures are quantified in Chapter 6. New completion strategies are proposed that minimize the negative impacts of stress reorientation on the efficiency of multi-stage fracturing treatments.

3.1. Chapter 2: Poroelastic Stress Reorientation around a Vertical Fracture

The production or injection of fluids in reservoirs results in a redistribution of stresses. In this chapter, the extent of stress reorientation has been calculated for fractured production and injection wells and the results have been analyzed for their impact on refracturing operations. The final result demonstrates the potential of the stress reversal region to increase the reservoir sweep in unconventional reservoirs, for which the optimum time-window for refracturing is of the order of months to years.

3.2. Chapter 3: Mechanical Stress Reorientation around a Vertical Fracture

The opening of a propped fracture results in the redistribution of local earth stresses. In this chapter, the extent of stress reversal and reorientation has been calculated around a vertical fracture using a three-dimensional numerical model of the stress interference induced by the opening of one propped fracture. The results can be applied to the refracturing of vertical wells and the multi-stage fracturing of horizontal wells.

3.3. Chapter 4: Role of Stress Reorientation in the Refracturing of Vertical Wells

In this chapter, the coupling of mechanical and poroelastic effects has been numerically modeled to quantify the extent of stress reorientation around fractured

production wells. It is shown that the combined effects of porelasticity and mechanical stresses are not simply additive. The stress reversal region drives the refracture to propagate orthogonally to the initial fracture, making it possible to access zones of the reservoirs that are less depleted, thus increasing well production and allowing access to additional reserves.

Guidelines are drawn that allow an operator to (a) select candidate wells, (b) choose the timing of the refracture operation in the life of the well, and (c) evaluate the potential increase in well production after refracturing.

3.4. Chapter 5: Candidate Well Selection for Refracturing

The selection of candidate wells for refracturing is often very difficult based on the information available at the surface. We propose a systematic methodology to allow a field engineer to evaluate a well's potential for refracturing from an analysis of field production data and other reservoir data that is commonly available. We successfully tested our method for a case study in the Wattenberg field using data from 300 Codell tight gas wells.

After identifying the physical phenomena that are thought to impact the performance of refracturing operations, five dimensionless groups have been developed to quantify them. Guidelines for the selection of refracturing candidates were expressed in terms of the potential for stress reorientation, the quality of the initial completion, the initial production decline and the reservoir depletion around the well of interest.

3.5. Chapter 6: Strategies for the Multi-Stage Fracturing of Horizontal Wells

It is shown that stress interference, or reorientation, caused by the opening of a propped fracture increases with the number of fractures created and also depends on the sequence of fracturing. Three fracturing sequences are investigated for a typical field case in the Barnett shale: (a) consecutive fracturing, (b) alternate fracturing and (c) simultaneous fracturing of adjacent wells.

Using a numerical model allowing non-transverse fractures (those that deviate from the orthogonal path), we show that some induced fractures propagate into previously stimulated areas during the consecutive fracturing of a Barnett shale well, thus decreasing the reservoir drainage efficiency of the frac treatment.

The alternate sequencing of transverse fractures as well as multi-lateral completions were recognized to be effective ways to (a) minimize induced fracture spacing without compromising the efficiency of each frac stage and (b) enhance natural fracture stimulation, by allowing fracture stages to experience a smaller stress contrast during propagation. More importantly, it is shown that net fracturing pressure data measured in the field can be used to detect mechanical interference between multiple transverse fractures and optimize fracture spacing for a specific well.

	2009 Natural Gas Market[1] (trillion cubic feet, dry basis)			Proved Natural Gas Reserves[2] (trillion cubic feet)	Technically Recoverable Shale Gas Resources (trillion cubic feet)
	Production	Consump-tion	Imports (Exports)		
Europe					
France	0.03	1.73	98%	0.2	180
Germany	0.51	3.27	84%	6.2	8
Netherlands	2.79	1.72	(62%)	49.0	17
Norway	3.65	0.16	(2,156%)	72.0	83
U.K.	2.09	3.11	33%	9.0	20
Denmark	0.30	0.16	(91%)	2.1	23
Sweden	-	0.04	100%		41
Poland	0.21	0.58	64%	5.8	187
Turkey	0.03	1.24	98%	0.2	15
Ukraine	0.72	1.56	54%	39.0	42
Lithuania	-	0.10	100%		4
Others[3]	0.48	0.95	50%	2.71	19
North America					
United States[4]	20.6	22.8	10%	272.5	862
Canada	5.63	3.01	(87%)	62.0	388
Mexico	1.77	2.15	18%	12.0	681
Asia					
China	2.93	3.08	5%	107.0	1,275
India	1.43	1.87	24%	37.9	63
Pakistan	1.36	1.36	-	29.7	51
Australia	1.67	1.09	(52%)	110.0	396
Africa					
South Africa	0.07	0.19	63%	-	485
Libya	0.56	0.21	(165%)	54.7	290
Tunisia	0.13	0.17	26%	2.3	18
Algeria	2.88	1.02	(183%)	159.0	231
Morocco	0.00	0.02	90%	0.1	11
Western Sahara	-	-		-	7
Mauritania	-	-		1.0	0
South America					
Venezuela	0.65	0.71	9%	178.9	11
Colombia	0.37	0.31	(21%)	4.0	19
Argentina	1.46	1.52	4%	13.4	774
Brazil	0.36	0.66	45%	12.9	226
Chile	0.05	0.10	52%	3.5	64
Uruguay	-	0.00	100%		21
Paraguay	-	-			62
Bolivia	0.45	0.10	(346%)	26.5	48
Total of above areas	**53.1**	**55.0**	**(3%)**	**1,001**	**6,622**
Total world	**106.5**	**106.7**	**0%**	**6,609**	

Sources:
[1]Dry production and consumption: EIA, International Energy Statistics, as of March 8, 2011.
[2] Proved gas reserves: *Oil and Gas Journal*, Dec., 6, 2010, P. 46-49.
[3]Romania, Hungary, Bulgaria.
[4] U.S. data are from various EIA sources.

Table 1.1 – Estimated shale gas technically recoverable resources for select basins in 32 countries, compared to existing reported reserves, production and consumption during 2009 (U.S. EIA 2011)

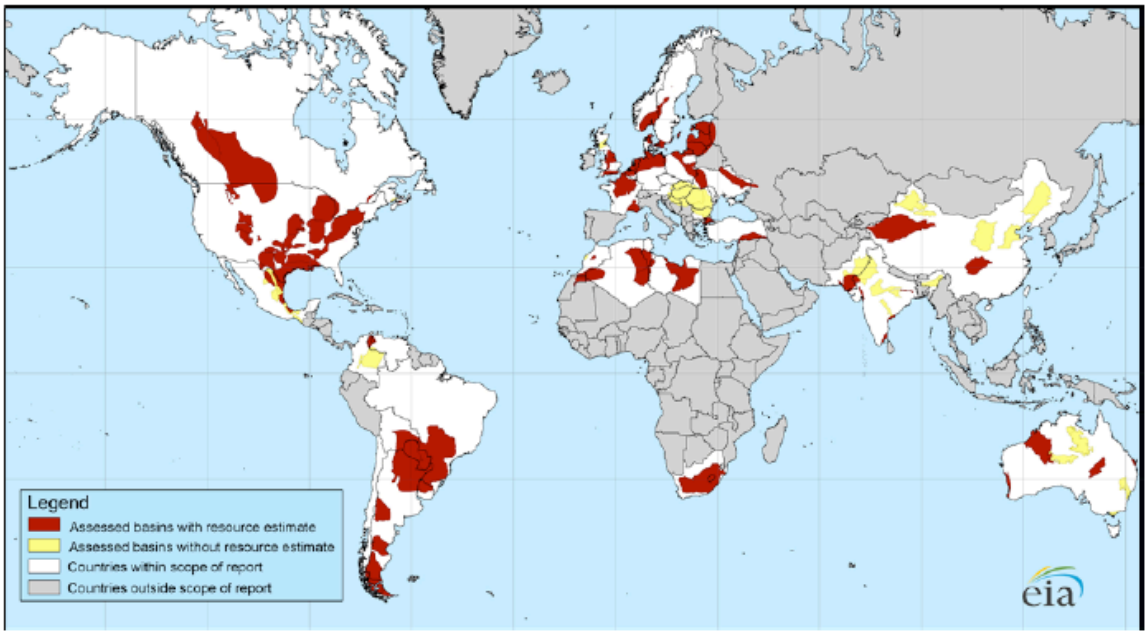

Fig. 1.1 – Map of 48 major shale gas basins in 32 countries (U.S. EIA 2011)

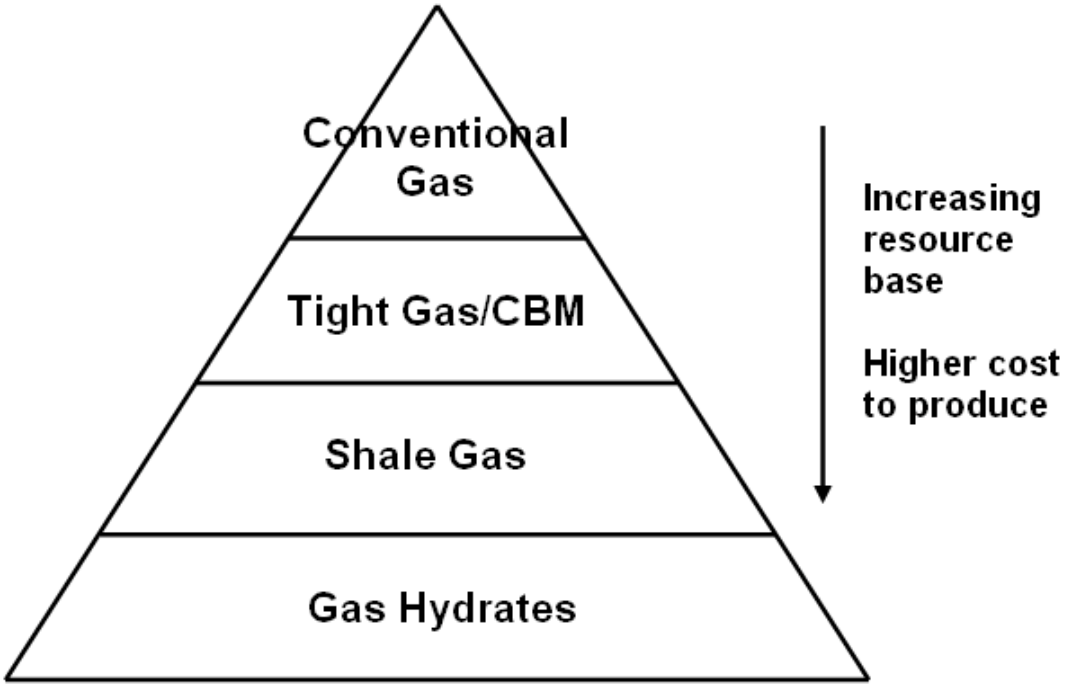

Fig. 1.2 – Resource triangle for natural gas

CHAPTER 2: POROELASTIC STRESS REORIENTATION AROUND A VERTICAL FRACTURE

The production or injection of fluids in reservoirs results in a redistribution of stresses. In this chapter, the extent of stress reorientation has been calculated for fractured production and injection wells and the results have been analyzed for their impact on refracturing operations. Rules of thumb and charts are provided to help candidate-well selection for refracturing based on the study.

For previously fractured wells, it is possible to create a secondary fracture that is perpendicular to the first. The secondary orthogonal fracture can be created only within a certain time-window that, in turn, depends on the reservoir properties. Conditions leading to orthogonal secondary fractures in different kinds of reservoirs (oil, gas and tight gas reservoirs) have been analyzed to establish some rules of thumb. The effects of the layers bounding the pay zone and of permeability heterogeneity and anisotropy on stress reorientation are also discussed.

Our results allow us to quantify the phenomenon of orthogonal secondary fracturing around fractured production wells by calculating the extent of the poroelastic stress-reversal region as a function of time. The results of our model are shown to agree qualitatively with field observations obtained from microseismic measurements. The model presented in the study helps to clarify the concept of refracturing and provides a quantitative estimate of the time-window for refracturing as a function of dimensionless parameters. The final result demonstrates the potential of the model to increase the reservoir sweep in unconventional reservoirs for which the optimum time-window for refracturing is of the order of months to years. The conclusions of this study are useful for the design of refracturing operations and candidate-well selection.

1. INTRODUCTION

Refracture treatments are applied in wells that have been fractured previously. The performance of these treatments has been observed to be highly variable with some wells underperforming while others are restored to initial production rates. A procedure for the selection of candidate wells that will improve the odds of a successful treatment is needed. This chapter presents guidelines based on a poroelastic model that allow an operator to (a) select candidate wells, (b) choose the timing of the refracture operation in the life of the well, and (c) suggest a design for the refracture treatment that will result in the best chance of success.

The varying stress state has a central role in many petroleum-engineering problems, such as borehole stability, formation-sand control, wellbore-casing damage, reservoir compaction, and subsidence.

In this chapter, we investigate stress and hydraulic-fracture reorientation for fractured wells. Hydraulic-fracture orientation is critical to both primary and secondary oil recovery from low-permeability reservoirs. In primary recovery, common production problems caused by hydraulic-fracture reorientation often result in overlapping drainage patterns, poor choice of well patterns, and poor location of new wells. In secondary recovery, poor sweep and premature breakthrough of water and steam can result from fracture propagation and reorientation.

The acknowledgement of the existence of stress changes in the reservoir because of production or injection from a previous fracture has resulted in the development of a new concept: oriented or altered-stress refracturing. Refracturing makes it possible to complete new intervals and improve the productivity of previously unstimulated or understimulated zones. The quantitative evaluation of these effects is crucial in the design of the refracturing of vertical wells.

2. LITERATURE REVIEW

In the vicinity of fractured and unfractured wells, the in-situ stresses are altered because of poroelastic stresses generated by pressure gradients in the reservoir. As a result, the orientation of the maximum and minimum horizontal stresses may change and, consequently, affect the fracture-propagation direction. The injection/production rate and pore pressure in the reservoir, among other factors, primarily determine the magnitude of stress reorientation (Zhai and Sharma 2007; Singh et al. 2008).

Warpinski and Branagan (1989) first proposed taking advantage of stress reorientation in the region of influence to create a favorable fracture orientation. The process is referred to as altered-stress fracturing. Palmer (1993) elaborated on the process of altered-stress fracturing with an emphasis on its application to coalbed-methane reservoirs.

Elbel and Mack (1993) presented a fracture-reorientation theory and applied the theory to tight gas wells. Initially, the direction of maximum horizontal stress is aligned with the initial vertical fracture. During production, the maximum horizontal stress decreases faster than the minimum horizontal stress, causing stress reversal to occur in the vicinity of the fracture. As a result, the second fracture may propagate orthogonal to the initial fracture (**Fig. 2.1**). Past the isotropic point (L_f'), the maximum principal stress switches back to its original direction, causing the fracture to reorient gradually and become parallel to the initial fracture. More recently, a 3D numerical model was used (Siebrits and Elbel 1998) to investigate the effect of the layers bounding the reservoir in the development of the stress-reversal region. These authors showed that the stiffer the bounding layers were, the smaller the stress reorientation around the fracture was.

Numerous field measurements have been published validating the existing theories. Wright and Conant (1995) first reported field evidence of fracture reorientation.

Tiltmeter fracture mapping performed on five refracture treatments shows that refracture treatments propagate at an angle of 30–60° to the initial fracture, while an infill hydraulic fracture in a secondary recovery project was shown to start and propagate at an angle greater than 60° to the original fracture orientation. Fracture dip and strike both were shown to be affected by the fluid pressure gradients.

Flow-induced stress reorientation does not always occur in the field (Li and Song 2006). Indeed, a low stress contrast and a high-enough pressure drawdown are needed. Wright and Conant (1995) establish a distinct relationship between reservoir subsidence and fracture reorientation using tiltmeter mapping, and they develop strategies for both enhancing primary recovery and mitigating some common problems with secondary recovery. Laboratory tests conducted on rock samples by Liu et al. (2008) simulate a 3D stress field during a hydraulic-fracturing process and show a change in the direction of refracture treatments.

The analysis of the pressure response of two field cases from the Barnett shale (Weng and Siebrits 2007) shows that during refracturing, as the second fracture propagates, the pressure increases to greater than the closure stress of the initial fracture because of the fracture penetrating into the higher-stress region. As a result, the initial fracture reopens and consumes most of the injected fluid until it reaches the tip. Thereafter, both the initial and secondary fractures continue their propagation.

3. MODEL FORMULATION

3.1. Mechanical Description of a Poroelastic Material

Biot's poroelasticity equations describing the mechanical behavior of a fluid-filled porous material (**Fig. 2.2**) are based on conceptual model of a solid skeleton and a

freely moving pore fluid, each phase being fully connected (Detournay and Cheng 1993). The two kinematic quantities (a) u_i, the displacement vector of the solid frame and (b) q_i, the specific discharge vector track the movement of the porous solid and the fluid, respectively. Two strain quantities are introduced to describe the deformation of the solid matrix and the variation of fluid volume per unit volume of porous material, respectively the strain tensor ε_{ij} and the variation of fluid content ζ, which is a scalar. The relationships between the strain quantities and the kinematic quantities are the compatibility equations Eq. (2.1) and the fluid mass balance (continuity equation) Eq. (2.2). Einstein notations are used in subsequent equations. A comma followed by subscript indicates differentiation with respect to spatial coordinates (i.e. $u_{i,j}$); repeated indices means summation over the range of indices (ε_{kk}). Finally, Kronecker's delta δ_{ij} takes the value 1 when i = j, and 0 otherwise.

$$\varepsilon_{ij} = \frac{1}{2}\left(u_{i,j} + u_{j,i}\right) \tag{2.1}$$

$$\frac{\partial \varsigma}{\partial t} + q_{i,i} = q_{\mathrm{v}} \tag{2.2}$$

With q_v the rate of injected fluid per unit volume (source density).

Two stress quantities are conjugate to the strain tensor ε_{ij} and variation of fluid content ζ: the total stress tensor σ_{ij}, and the pore pressure p. The work increment in the fluid-filled porous material can be divided in a mechanical and a fluid contribution (Eq. (2.3)):

$$dW = \underbrace{\sigma_{ij}\, d\varepsilon_{ij}}_{mechanical} + \underbrace{p}_{f\ luid}\, d\zeta \tag{2.3}$$

3.2. Governing Equations

The coupled fluid-flow/mechanical isothermal response of a linear isotropic poroelastic material is governed by differential equations that relate pore pressure p, flux vector q_i, stress tensor σ_{ij}, strain tensor ε_{ij} and the increment of fluid content ζ introduced by Biot (1955). Temperature is assumed constant in all simulations, thus thermoelastic effects are not modeled. In the numerical formulation, space and time derivatives are approximated using finite-difference schemes (FLAC3D 2011).

3.2.1. Poroelastic Parameters

Fluid effects only the volumetric response which can be described by three independent mechanical parameters (i.e. α, K and K_u). K is the drained bulk modulus, meaning the bulk modulus of a porous material where fluid escapes without resistance (p = 0). On the other hand, the undrained modulus K_u corresponds to a zero flux material, in which fluid cannot escape as a volumetric force is applied.

In Biot's poroelastic formulation, the material's shear behavior is not influenced by the presence of fluid, and is thus described by the shear modulus G of the solid matrix.

3.2.2. Constitutive Laws

In the literature, there are numerous formulations of the volumetric response of a poroelastic material. The chosen approach here is a continuum formulation where the fluid-filled porous material is treated as a whole (Detournay and Cheng 1993). The constitutive equations of the poroelastic material relate the strain (ε_{ij}, ζ) and stress quantities (σ_{ij}, p) (Eqs. (2.4) and (2.5)):

$$\sigma_{ij} = 2G\varepsilon_{ij} + \left(K - \frac{2}{3}G \right)\varepsilon_{kk}\delta_{ij} - \alpha\delta_{ij}p \tag{2.4}$$

$$\zeta = \alpha\varepsilon_{kk} + \frac{p}{M} \tag{2.5}$$

with $\frac{1}{M} = \frac{\alpha - \phi}{K_s} + \frac{\phi}{K_f}$ and $\alpha = 1 - \frac{K}{K_s}$

The constitutive equations contain two poroelastic quantities expressed in function of porosity ϕ and bulk moduli K, K_s and K_f: Biot coefficient α and Biot modulus M.

Biot's coefficient α compares the material's deformation from the solid matrix and from the grains that compose it. In the special case of incompressible solid constituents ($K_s >> K$), Biot's coefficient takes the value 1. The inverse of the Biot modulus M is defined as the change in the rock's fluid content resulting from a change in pore pressure, for a contant volumetric strain (Eq. (2.6)).

$$\frac{1}{M} = \left.\frac{\partial\zeta}{\partial p}\right|_{\varepsilon_{kk}} \tag{2.6}$$

3.2.3. Transport Law

The fluid transport is modeled by Darcy's law of the fluid discharge in a porous material, derived from Navier-Stokes equations (Eq. (2.7)):

$$q_i = -\frac{k}{\mu}\left(p_{,i} - \rho_f g_i\right) \tag{2.7}$$

with k the isotropic permeability and ϱ_f is the constant fluid density

3.2.4. Balance Laws

The fluid mass balance takes into account the changes in the variation of the fluid content ζ is given in Eq. (2.2).

Assuming that the equilibrium state is established at all times, the balance of local stresses in the fluid-filled porous material takes the form (Eq. (2.8)):

$$\sigma_{ij,j} + \rho g_i = 0 \qquad (2.8)$$

where $\rho = (1-\phi)\rho_s + \phi\rho_f$

with ϱ_s and ϱ_f, the densities of the solid and the fluid phase, respectively

When incorporating Eq. (2.4) into Eq. (2.8), we can highlight the contributions of mechanical strains and pore-pressure gradients in the poroelastic equilibrium equations solved at each grid-block of the numerical model (Eq. (2.9)):

$$\underbrace{2G\varepsilon_{ij,j} + \left(K - \frac{2}{3}G\right)\varepsilon_{kk,j}\delta_{ij}}_{stresses\ from\ mechanical\ strains} - \underbrace{\alpha\delta_{ij}p_{,j}}_{pore-pressure\ gradients} + \underbrace{\rho g_i}_{volumetric\ stresses} = 0 \qquad (2.9)$$

Where p_j are the gradients in pore pressure along x_j

3.3. Geometry and Boundary Conditions

The geometry of the simulated fractured well is shown in **Figs. 2.3 through 2.5**. The study is limited to the situation where the fracture and pay-zone heights are equal. The geometry of interest is modeled using a commercial code, FLAC3D (Fig. 2.2). Using a finite-difference and explicit-numerical scheme, the software couples fluid flow and the stress state in the reservoir. The poroelastic coupling is based on Biot's theory (Eq. (2.5)). The reservoir is homogeneous, isotropic, purely elastic, and is bounded by layers with a different value of shear modulus. Flow only occurs within the reservoir and does not leak into the bounding layers.

The far-field no-flow boundaries are located at a distance (from the fracture) equal to at least three times the fracture half-length L_f. Their effect on the computed stress reorientation is shown in section 4.1. The model boundary conditions are detailed below:

- Uniform fluid pressure in the fracture: $p = p_f$ at $-L_f < x < L_f$, $y = 0$, $-h_f < z < h_f$
- Constant stress applied at outside boundaries: $\sigma_{zz} = -\sigma_v$, $\sigma_{xx} = -\sigma_{hmax}$ and $\sigma_{yy} = -\sigma_{hmin}$
- No-flow reservoir boundaries at $x = \pm x_r$, $y = \pm y_r$ and $z = \pm z_r$

3.4. Dimensionless Numbers

It is evident that the extent of the region over which stress reversal occurs will depend on many different parameters, such as the reservoir and wellbore pressure, the stress contrast, the mechanical properties of the sand, and the bounding layers. To minimize the number of independent parameters, we follow Berchenko and Detournay (1997) to define two dimensionless quantities: Π, the ratio of the initial deviatoric stress to the difference between initial reservoir pressure and well pressure; and τ, a dimensionless time:

- Dimensionless time:

$$\tau = \frac{4ct}{L_{xf}^2} = 4\frac{\kappa}{S}\frac{t}{L_{xf}^2} = \frac{4kt}{\mu L_{xf}^2\left(c_f\phi + \dfrac{\alpha(1+\nu)(1-2\nu)}{(1-\nu)E}\right)} \tag{2.10}$$

- Dimensionless stress deviator:

$$\Pi = \frac{S_0}{\sigma_*} = \frac{S_0}{\eta p_*} = \frac{\sigma_{h\max} - \sigma_{h\min}}{\dfrac{\alpha(1-2\nu)}{1-\nu}\left|p_{R_i} - p_{wf}\right|} \tag{2.11}$$

where $S = \frac{1}{M} + \frac{\alpha}{K + \frac{4}{3}G_r}$, $K_r = \frac{E}{3(1-2\nu)}$, $G_r = \frac{E}{2(1+\nu)}$

Siebrits and Elbel (1998) showed numerically that the layers bounding the reservoir affect stress reorientation. Two additional parameters take into account the effects of the reservoir height and of the mechanical characteristics of the bounding layers:

Dimensionless fracture height ratio is

$$\gamma = \frac{h}{L_f} \tag{2.12}$$

and dimensionless shear modulus ratio is

$$\beta = \frac{G_b}{G_r} \tag{2.13}$$

The effect of the bulk modulus K of the bounding layers can be neglected. If it, indeed, affects the values of the vertical stress in the reservoir, it does not alter the stresses in the plane orthogonal to the fracture controlling stress reorientation.

4. RESULTS AND DISCUSSION

The results presented here are organized to highlight the important conclusions that we can arrive at on the basis of the simulations. The validity of numerical simulations is verified through a study of the influence of boundary conditions and their location. The profile of stress reorientation around fractured production and injection wells is also described. Reservoir and fluid parameters (τ), stress contrast and pressure drawdown (Π), bounding layers (β, γ), and permeability heterogeneity and anisotropy

affect the spatial extent of the stress-reversal region. Their effects are discussed in the following subsections.

4.1. Boundary Effects

Two pore-pressure boundary conditions are typically used: no flux and constant pressure. A no-flow boundary condition should be applied to depleting reservoirs with no fluid influx. The constant-pressure boundaries are more suitable for reservoirs experiencing active water influx. With constant-pressure boundaries, the extent of stress reversal (represented by L_f', the distance of the isotropic point to the well) decreases more slowly at late times (**Fig. 2.6**). This is because the pressure gradients do not decrease and instead reach a steady-state profile. In depleting reservoirs, the decrease in pressure gradients over time will cause the stress reorientation to increase (as the pressure propagates into the reservoir) and then decrease with time.

It is very important to note that the magnitude and timing of the maximum distance to the isotropic point L_f' are not altered by the location of far-field boundaries. These boundary effects start to become significant when the boundaries are located at only one L_f from the fracture. The validation of the numerical model was conducted on only a few examples. We assume that conclusions we arrived at regarding boundary effects in the example of Fig. 2.6 are valid for the rest of the study. In summary, the location and nature of the pressure at the drainage boundary affects the pressure distribution in the reservoir and this, in turn, has a significant impact on the stress reorientation around the well.

4.2. Poroelastic Coupling

A change in the pore-pressure distribution affects the mechanical stresses in the reservoir. Varying mechanical stresses, in turn, affect the volume of the pores and, consequently, the fluid pressure inside them. The equations governing the poroelastic coupling are shown in Eq. (2.9). In a fully-coupled model, the change in the mechanical stresses from pore-pressure changes is calculated at every time step.

This coupling is unfortunately very time intensive. In order to simulate decades of field production, the computation time can reach over several days. To speed up numerical calculations, we tried to partially decouple the problem by calculating the new mechanical stresses each time data is saved instead of at each time-step. So for most time steps, only the single-phase fluid flow problem (Eq. (2.7)) is solved, while the stresses in the poroelastic material remain unchanged, in effect neglecting the impact of mechanical stresses on pore-pressure and vice-versa. The poroelastic equilibrium (Eq. (2.9)) is solved for a limited number of time-steps.

The computation time was reduced to less than a day, without the calculation of the extent and timing of the stress-reversal region to be affected (**Fig. 2.7**). The partial-poroelastic coupling approach is chosen for all calculations and is assumed not to impact the calculated values of the maximum extent of stress reversal and the corresponding optimum time-window, in the subsequent numerical simulations.

4.3. Fractured Production vs. Injection Wells

The pressure decreases in the vicinity of a producing fractured vertical well. As a result, the stresses decrease but not uniformly. It is illustrated in **Fig. 2.8** that, within an elliptical region around the fracture, the stresses parallel to the fracture decrease faster than in the orthogonal direction, as a result of non-isotropic reservoir depletion. Indeed,

the reservoir is depleted more along the fracture than parallel to it. Differences in pressure gradients in the reservoir during depletion are responsible for the fact that the maximum horizontal stress decreases faster than the minimum horizontal stress.

If the stress contrast is small, a stress reversal may occur in the vicinity of the fracture, meaning that the directions of maximum and minimum horizontal stress are switched 90°. Outside the stress-reversal region, the direction of minimum horizontal stress orients toward the producing fractured well. This region will be referred to as the reoriented-stress region. Far from the fracture, the direction of maximum stress is unaffected by production. Initially, it is aligned with the first fracture, as it is the direction that requires the least amount of energy for fracture propagation.

Fig. 2.9 shows results for the corresponding fractured-injection-well case. Stress reversal does not take place around the fracture. Using the same logic as for the producing well, this phenomenon can be explained physically. As the pressure increases around the fracture, the stresses increase faster in the direction parallel to the fracture than perpendicular to it (because of pressure gradients), thus increasing the stress contrast close to the fracture. Results may be applied to predict hydraulic-fracture reorientation during water injection.

Another way to look at stress reorientation is to plot the contours of the reorientation angle (**Figs. 2.10 and 2.11**). These results present a better perspective of the extent of stress reorientation in the altered-stress region (for both the production and injection cases). Clearly, the orientation of the maximum horizontal stress is tilted away from production wells and toward injection wells. This is consistent with earlier field observations and poroelastic calculations (Wright and Conant 1995; Singh et al. 2008).

The magnitude of the stress reorientation for a producing well is maximum immediately around the fracture. In the stress-reversal region and in a region immediately

ahead of the fracture tip, the reorientation angle is 90°. Away from the fracture, reorientation angles of 20 to 30° are computed for distances up to L_f from the wellbore. In injection wells, the maximum stress orientation is 45° and occurs at some distance away from the fractured wellbore. The pressure gradients around the fracture reinforce the stress contrast. Away from the fracture, the pressure gradients are oriented at an angle to the principal-stress directions. This results in the maximum stress reorientation occurring at a 45° angle to the fracture.

4.4. Spatial Extent of the Stress-Reversal Region (Position of the Isotropic Point L_f')

As stated previously, the objective of the study is to compute the extent of the stress-reversal region as a function of the relevant physical parameters. At a given time, the maximum distance of stress reversal along the y coordinate is the isotropic point L_f'. Its position is monitored as a function of the dimensionless time τ. Its value is directly proportional to the fracture length.

The dimensionless quantity $\lambda = L_f'/L_f$ reaches a maximum λ_{max} at some dimensionless time τ_{max}. This time, at which the region of stress reorientation will be a maximum, will also be function of Π, β and γ.

It is seen that, for the specific range of parameters chosen, the dimensions of the area of stress reversal are approximately 20% of the original fracture length (the area of stress reorientation is much larger). For typical fracture dimensions this clearly implies a region that is large enough to provide additional drainage area for incremental oil/gas recovery, particularly in low permeability or heterogeneous formations.

4.5. Effect of the Dimensionless Stress Deviator Π

A smaller value of the dimensionless stress deviator implies a smaller initial stress contrast or a larger drawdown in a production well. We expect the second fracture to propagate orthogonally to the initial fracture, farther into the reservoir for small values of the stress deviator. **Fig. 2.12** confirms the fact that λ_{max} increases as Π decreases. The stress-reversal region is largest when Π = 0 (i.e. when the initial stress state is isotropic). In this particular case, λ_{max} is equal to 0.58, confirming previous results by Siebrits and Elbel (1998).

We also show that the value of the optimum time for refracturing τ_{max} increases as the dimensionless stress deviator decreases. This has significant economic implications, since the reservoirs that have small stress contrasts (small values of Π) show the largest time windows for refracturing. The time between consecutive refracturing treatments in these reservoirs is also the longest, making them good candidates for refracturing.

4.6. Effect of the Dimensionless Shear Modulus Ratio β

The value of the shear modulus in the bounding layers significantly affects the stress reorientation around the fracture. During production, the pay-zone stresses in the plane orthogonal to the fracture decrease. A discontinuity forms between the horizontal stresses within the reservoir and the bounding layers, because of the no-flow boundary condition, resulting in a shear stress at the pay zone boundaries (**Fig. 2.13**). Depending on the value of the dimensionless shear modulus, the shear stress will differ. When the bounding layers are stiff, the shear stress at the reservoir boundary becomes high, thus constraining stress reorientation.

The sensitivity study on the dimensionless shear modulus β confirms our physical intuition showing that stress reorientation increases as β decreases (**Fig. 2.14).** Reservoirs

with low shear modulus (such as weak sandstones) bounded by shales with high shear modulus (high β) will be less susceptible to stress reorientation (Fig. 2.14). On the other hand, gas shales bounded by softer sediments or shales (low β) will be much more susceptible to stress reorientation later in the producing life of the field (larger τ) and will be good refracturing candidates. The difference is substantial, as can be seen in Fig. 2.14.

4.7. Effect of the Dimensionless Fracture Height Ratio γ

The parameter γ is the ratio of the height of the pay zone, also equal to the fracture height, to the fracture half-length. The shear stress at the boundary identified in the preceding subsection increases as the reservoir boundaries get closer to each other relative to the fracture length (**Fig. 2.15**). This results in a decrease in the magnitude of λ_{max} and τ_{max}. In practice, the thicker the pay zone is, the larger the area of stress reversal is and the longer the optimum time for refracturing is.

As shown in **Figs. 2.16 and 2.17**, the sensitivity to fracture-height ratio is dependent on the shear-modulus ratio. As the value of β increases, the sensitivity of stress reorientation to the variation of the value of the fracture-height ratio γ increases.

4.8. Effect of Permeability Heterogeneity

Stress reorientation is computed as a function of time for two reservoir models having layers of different permeability (**Figs. 2.18 and 2.19**). To be able to compare these simple models of heterogeneous reservoirs to a homogeneous one, we need to evaluate their permeability in order to compute the dimensionless time τ. Since the reservoir layers are parallel to the direction of flow, the average permeability for the two models is taken to be equal to $(k_1+k_2)/2$ and $(2k_1+k_2+2k_3)/5$ (arithmetic average), respectively.

Fig. 2.19 shows that both the magnitude and timing of the maximum stress reversal in the heterogeneous reservoir are equal to the values obtained in a homogeneous reservoir, with the permeability suitably averaged according to Eq. (2.14):

$$k_{avg} = \frac{\sum_{i=1}^{n} k_{iy} \cdot h_i}{\sum_{i=1}^{n} h_i} \tag{2.14}$$

with k_{iy} the value of permeability of the layer i, in the direction orthogonal to the fracture face, and h_i the layer thickness.

On the other hand, the transient growth of the stress reversal region is affected by the nature of heterogeneity. It is clear from this result that the model can be applied reliably to layered reservoirs.

4.9. Effect of Permeability Anisotropy

Stress reorientation is computed for two different cases in which the permeability in the x direction is different from that in the y direction (**Fig. 2.20**). It was shown that the areal extent of the stress-reversal region, from early times to the time it reaches a maximum, strictly depends on the value of permeability in the direction orthogonal to the fracture k_y. At late times, the pressure gradients decrease in the reservoir causing the area of stress reversal to retract. Fig. 2.20 illustrates that this phenomenon depends on the value of the horizontal anisotropy ratio k_x/k_y (in the dimensionless analysis).

When the permeability in the direction parallel to the fracture is smaller than in the orthogonal direction, it is observed that stress reversal decreases faster. It must be noted that the permeability in the vertical direction does not affect stress reorientation at

any time. Similar to heterogeneity effects, permeability anisotropy does not affect the extent and dimensionless timing of the maximum stress reversal region.

4.10. Type Curves for Stress Reorientation

The effect of dimensionless parameters on λ_{max} and τ_{max} are summarized in **Figs. 2.21 through 2.23**. Knowing the values for the parameters Π, β and γ, it is possible to estimate the value of the maximum reorientation and of the optimum dimensionless time for refracturing. It is clearly seen that λ_{max} and τ_{max} decrease with Π and β and increase with γ. These curves represent type curves that can be used to estimate the timing and extent of stress reorientation under a wide range of reservoir conditions. Some example cases are discussed subsequently.

5. Application of the Model to Typical Reservoir Types

The results of our model can be applied to computing the optimum time for refracturing for five different types of reservoirs: shale gas, tight gas, conventional oil and gas sandstone, and heavy oil (**Figs. 2.24 and 2.25**). The parameter values are listed in **Table 2.1**. As seen in Fig. 2.24, the optimum time window for refracturing for gas shales is on the order of months to years. This implies that shale gas wells are good candidates for refracturing and should be carefully evaluated for the time window for refracturing. The type curves provided in this chapter allow us to do this systematically.

For typical values of the petrophysical parameters, the time window for tight gas sands is on the order of months. Heavy-oil wells are also potential candidates for refracturing (Fig. 2.25). As shown by Wright et al. (1994, 1995), fractures initiated several months or years after the initial fractures show a strike and dip that are different

from those of the original fractures. These low-mobility fluids require additional wellbore access to drain large portions of the reservoir effectively.

For most conventional oil and gas reservoirs, the time window for refracturing may be too early (days or weeks) for refracturing to be a practical and economic solution. In addition to the early stress reorientation, the ability to access additional reserves with fractures in these high-permeability reservoirs is limited and does not justify refracturing.

The optimum time for refracturing is mostly sensitive to permeability, hydrocarbon viscosity, and fracture length.

6. CONCLUSIONS

A comprehensive and quantitative study of stress reorientation around fractured vertical wells has been presented. It is possible to estimate both the magnitude of the stress-reversal region and the optimum time for refracturing for any reservoir using the dimensionless parameters presented in this study. The proposed model is able to take into account successfully the effect of different reservoir boundary conditions, the mechanical properties of the target sand and the bounding layers, fluid properties, in-situ stresses, and permeability heterogeneity and anisotropy.

It is shown that stress reversal can occur in fractured production wells but not injection wells. The region of stress reorientation is significantly larger than the region of stress reversal and occurs immediately around the fracture in production wells. In injection wells, stress reorientation occurs at an angle (45°) to the direction of the original fracture. The magnitude (λ_{max}) and timing (τ_{max}) of the stress reversal depend on the stress deviator (Π), the thickness of the reservoir (γ) and the shear modulus of the reservoir and the bounding layers (β). In addition, the fluid-drainage (pore-pressure) boundary

conditions also have a significant effect. It is clearly shown that λ_{max} and τ_{max} decrease with Π and β and increase with γ.

It was proved numerically that permeability heterogeneity and anisotropy do not affect the magnitude and timing of maximum stress reversal and that the value of permeability for a layered reservoir should be chosen equal to $k_{avg} = \sum k_{iy} \cdot h_i / \sum h_i$ in the dimensionless variable τ. Reservoirs having a small stress contrast, a large pressure drawdown, relatively weak bounding layers and a thick pay zone experience a large stress reorientation and, thus, are primary targets for refracturing.

The conclusions of this study are useful for improving the recovery efficiency after refracturing a vertical well, in particular in low permeability reservoirs. The time window for refracturing was shown to significantly depend on the nature of the reservoir. For unconventional resources such as tight gas, shale gas or heavy oil, the optimum time for refracturing is usually on the order of months to years. Fractured production wells in these reservoirs constitute ideal candidates for the use of the proposed charts to estimate the optimum time window for refracturing.

	Shale gas	Tight gas	Sandstone (gas)	Sandstone (oil)	Heavy oil
Permeability k (md)	10^{-4}	10^{-2}	1	10	1000
Viscosity μ (cp)	0.02	0.02	0.02	10	10^{6}
Mobility k/μ (md/cp)	0.005	0.5	50	1	0.1
Young's modulus E (psi)	$5x10^{6}$	$3x10^{6}$	$1x10^{6}$	$1x10^{6}$	$3x10^{5}$
Poisson's ratio ν	0.3	0.3	0.3	0.3	0.3
Biot's coefficient α	0.7	0.7	0.7	0.7	0.7
Porosity ϕ	0.05	0.1	0.2	0.3	0.3
Compressibility (1/psi)	$2x10^{-4}$	$2x10^{-4}$	$2x10^{-4}$	$5x10^{-6}$	$5x10^{-6}$
Fracture half-length L_f (ft)	500	500	500	500	500
Reservoir pressure p_R (psi)	4000	4000	4000	4000	4000
Wellbore pressure p_{wf} (psi)	1000	1000	1000	1000	1000
Vertical stress σ_v (psi)	7000	7000	7000	7000	7000
Max. horizontal stress σ_{hmax} (psi)	4600	4600	4600	4600	4600
Min. horizontal stress σ_{hmin} (psi)	4500	4500	4500	4500	4500

Table 2.1 – Reservoir parameters for five oil or gas reservoir types

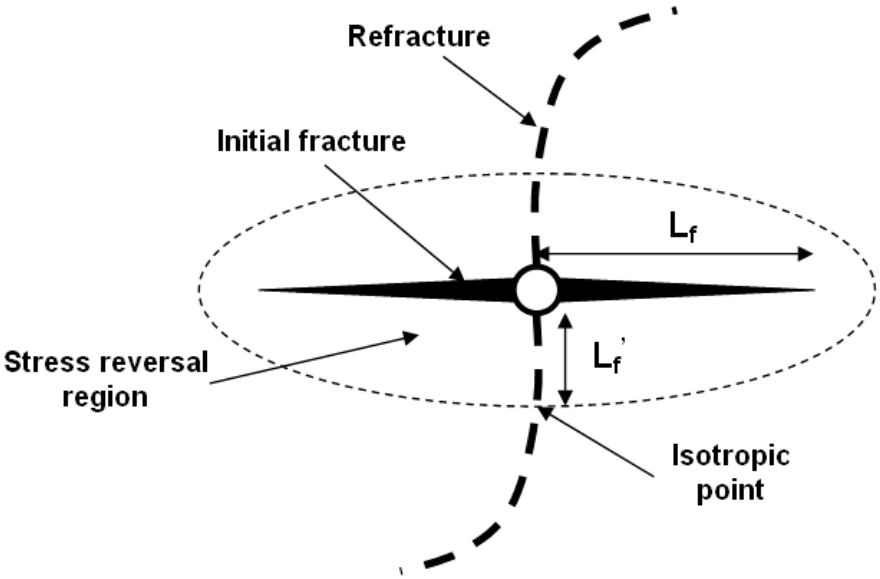

Fig. 2.1 – Flow-induced stress reversal and refracture direction

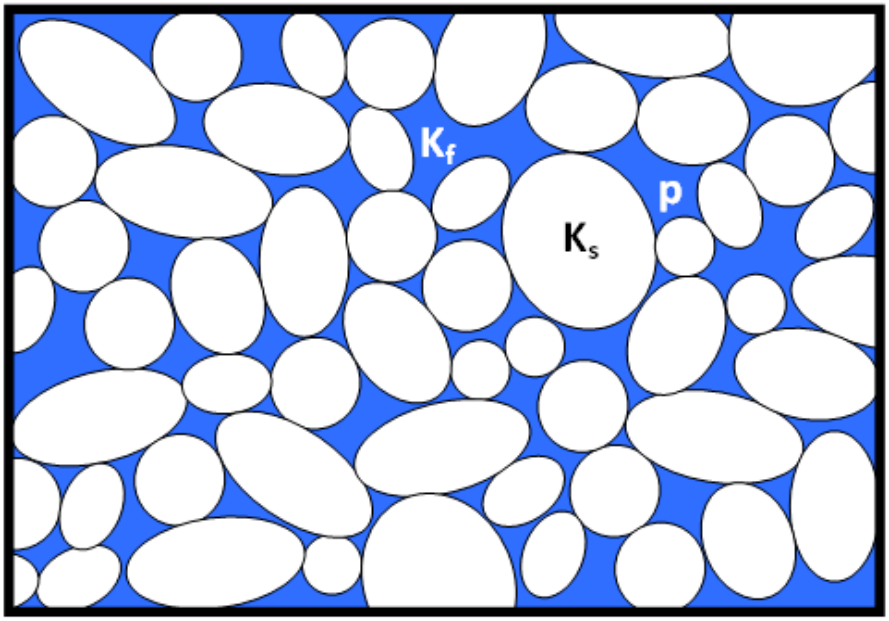

Fig. 2.2 – Representation of a fluid-filled porous material

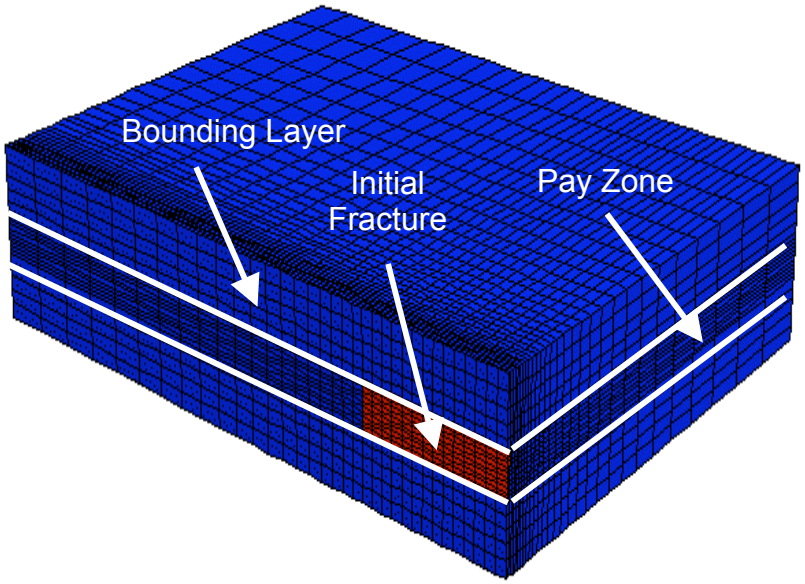

Fig. 2.3 – Numerical mesh around a fractured well in a bounded reservoir (FLAC3D)

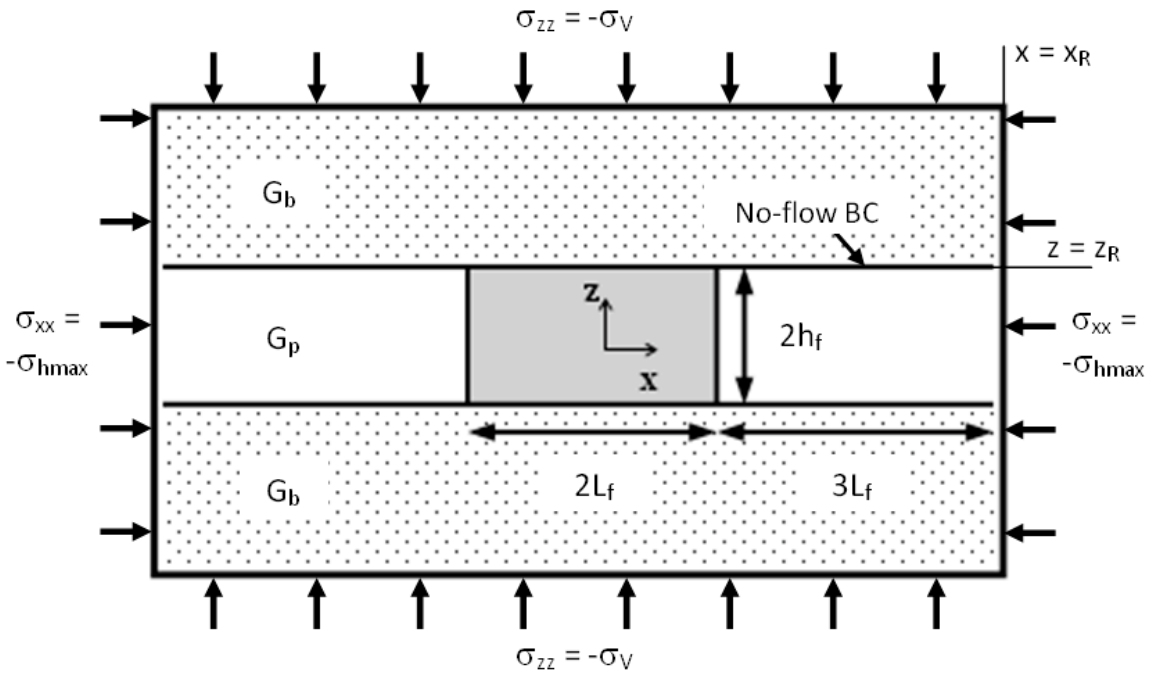

Fig. 2.4 – Geometry of a vertical fracture in a layered rock (xz-plane)

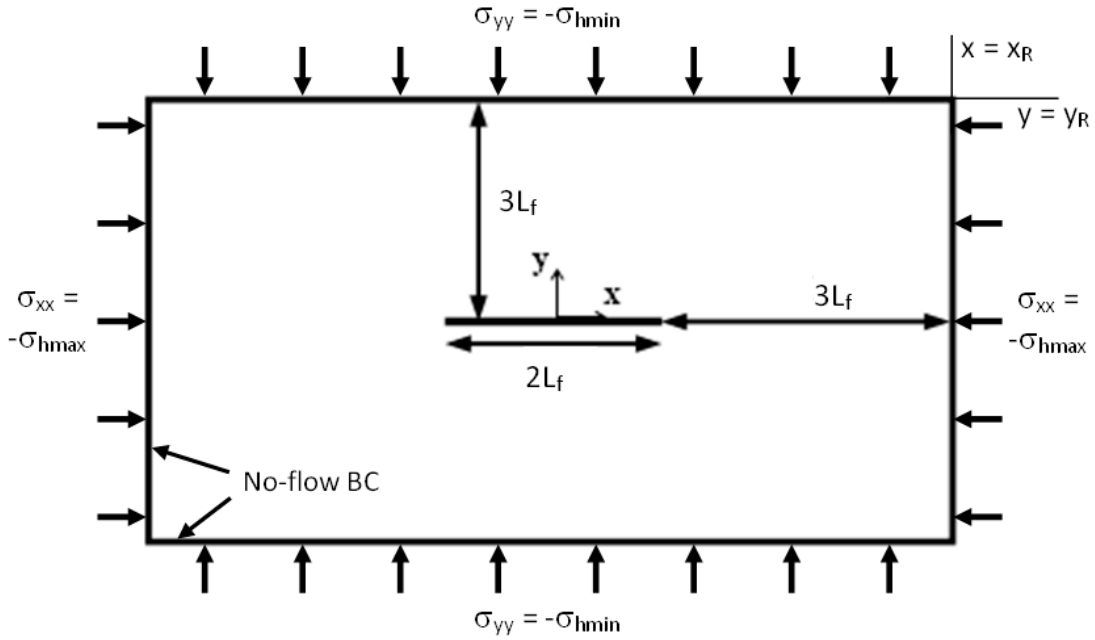

Fig. 2.5 – Modeled geometry in the horizontal, xy-plane

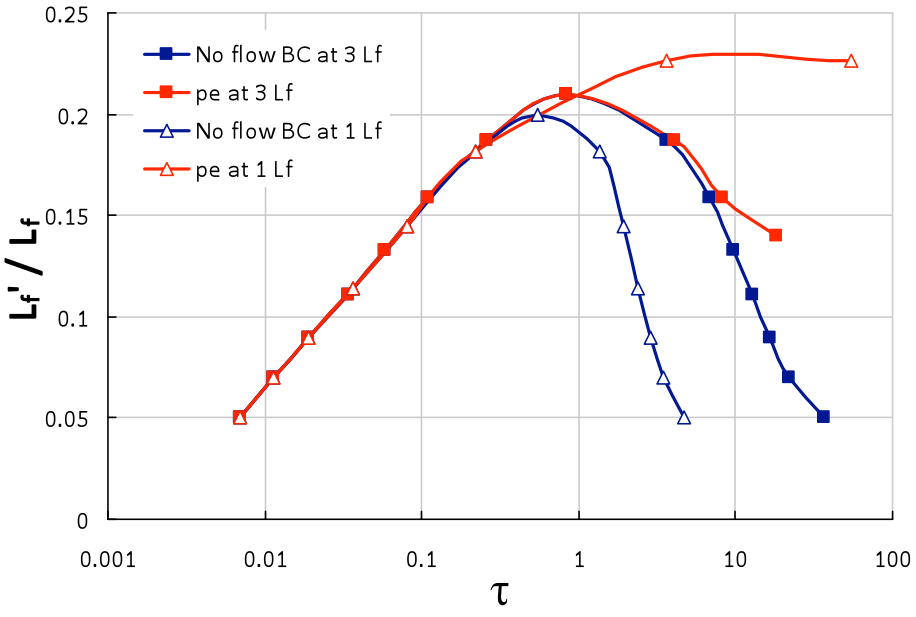

Fig. 2.6 – Effect of far-field boundary conditions (no flow or constant pressure) and their location on the evolution of the extent of stress reversal ($\Pi = 0.0583$, $\gamma = 0.2$ and $\beta = 1$)

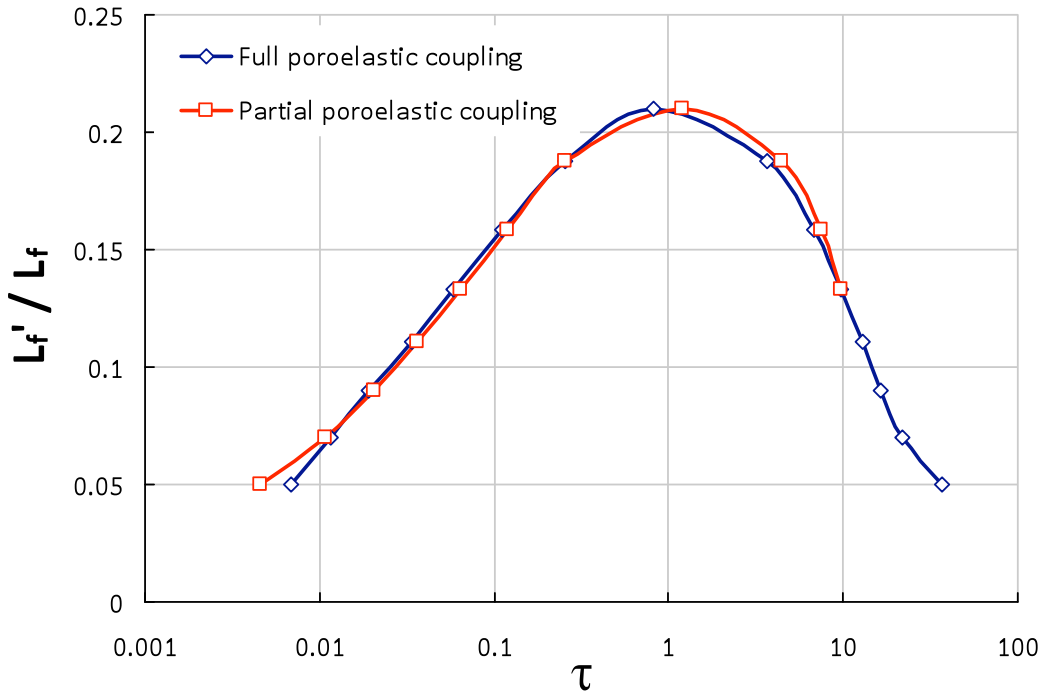

Fig. 2.7 – Effect of poroelastic coupling on the evolution of the extent of stress reversal ($\Pi = 0.0583$, $\gamma = 0.2$ and $\beta = 1$)

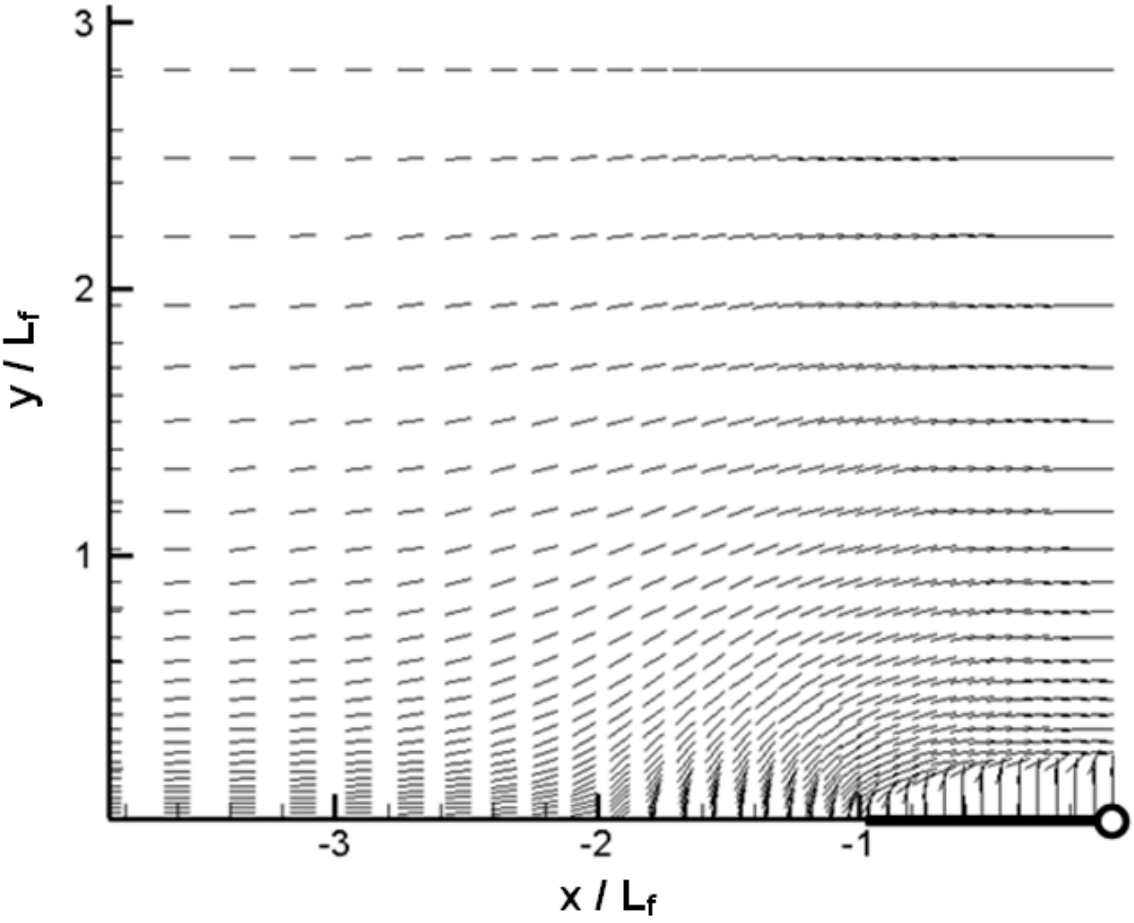

Fig. 2.8 – Direction of maximum horizontal stress around a production well for $\tau = 0.917$, $\Pi = 0.0583$, $\gamma = 0.2$ and $\beta = 1$

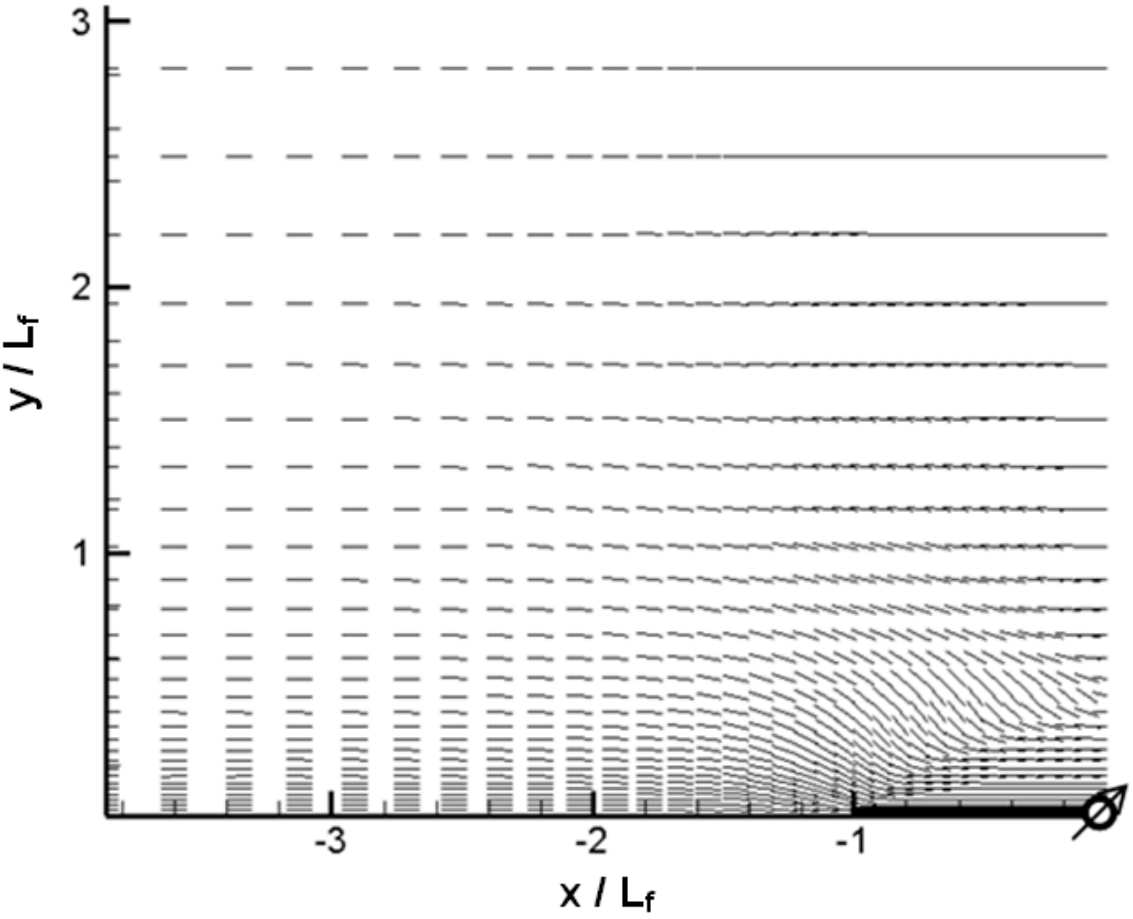

Fig. 2.9 – Direction of maximum horizontal stress around an injection well for $\tau = 0.917$, $\Pi = 0.0583$, $\gamma = 0.2$ and $\beta = 1$

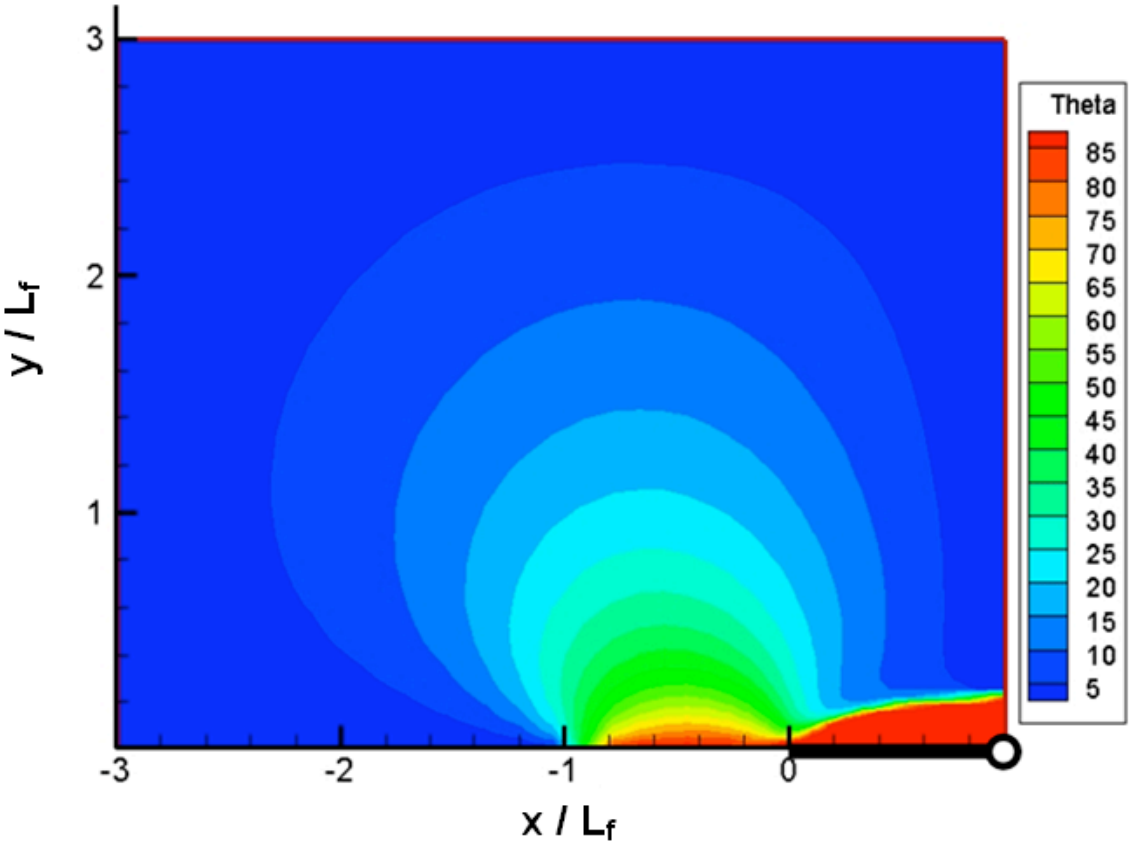

Fig. 2.10 – Angle of stress reorientation θ around a production well for $\tau = 0.917$, $\Pi = 0.0583$, $\gamma = 0.2$ and $\beta = 1$

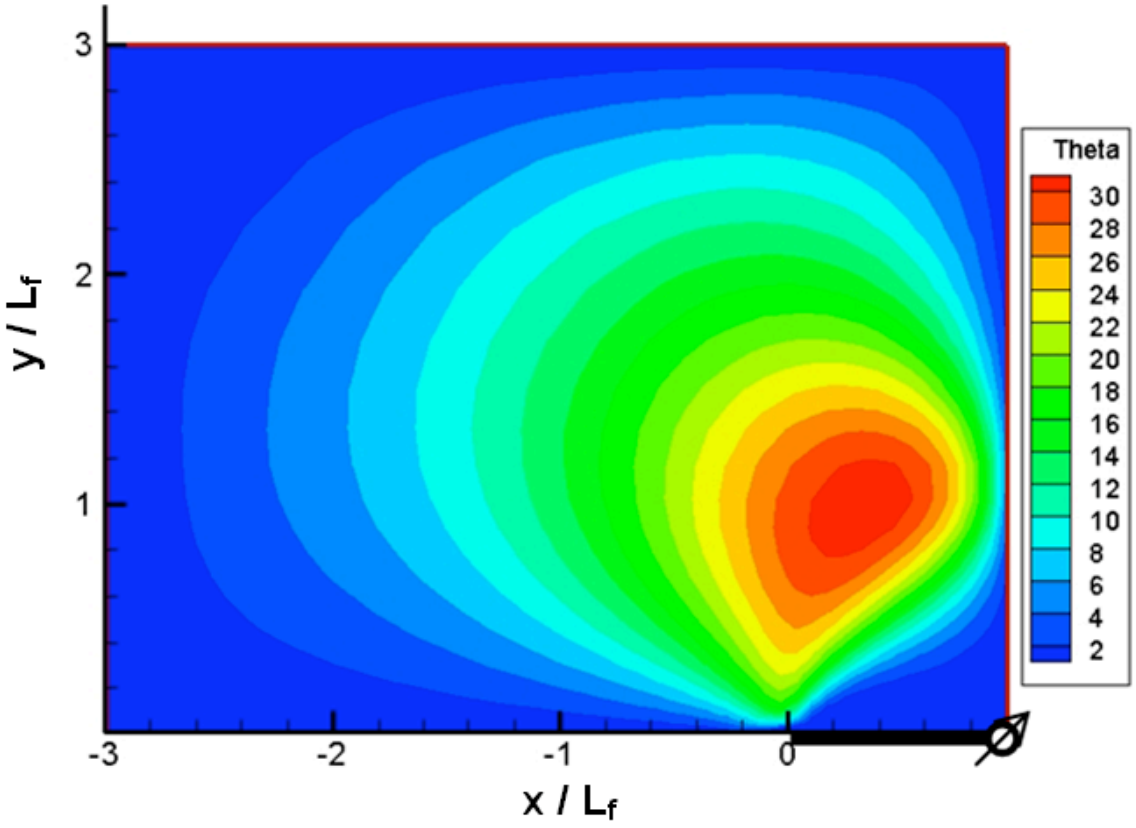

Fig. 2.11 – Angle of stress reorientation θ around an injection well for $\tau = 0.917$, $\Pi = 0.0583$, $\gamma = 0.2$ and $\beta = 1$

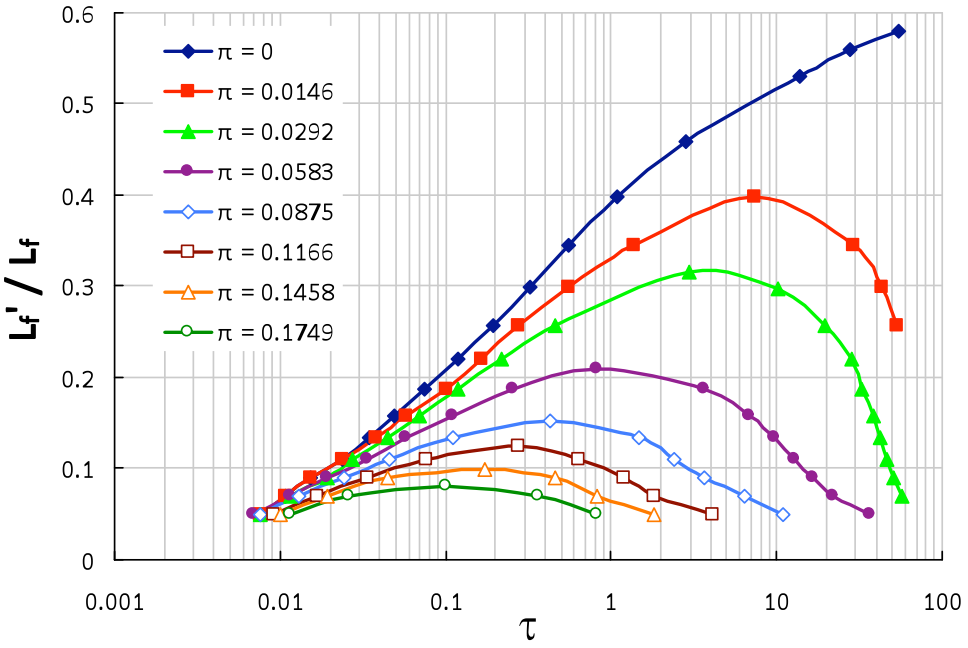

Fig. 2.12 – $\lambda = L_f'/L_f$ versus the dimensionless time τ for different values of Π, with $\beta = 1$ and $\gamma = 0.2$

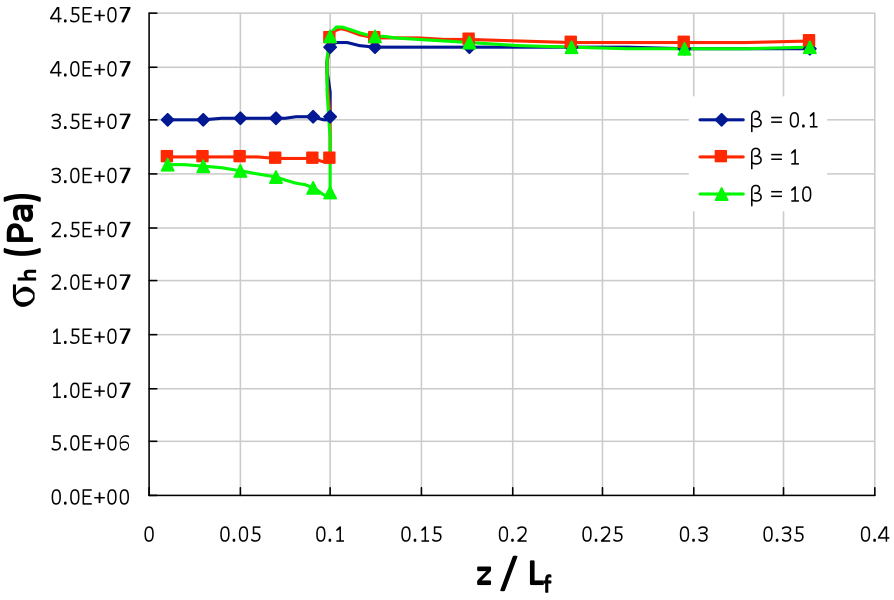

Fig. 2.13 – Effect of β on the shear stress at the pay zone boundaries for $\gamma = 1$

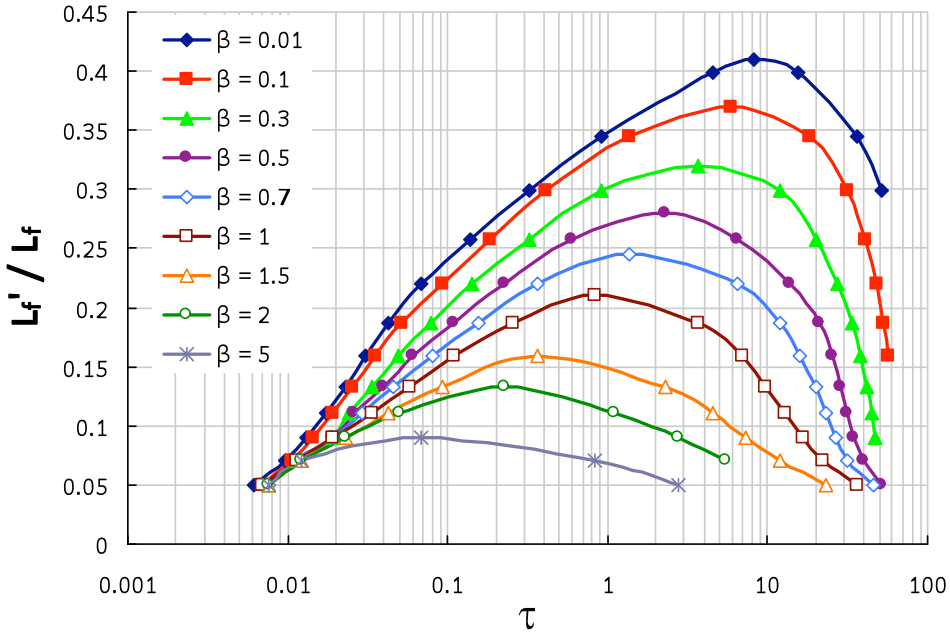

Fig. 2.14 – $\lambda = L_f'/L_f$ versus the dimensionless time τ for different values of β, with $\Pi = 0.0583$ and $\gamma = 0.2$

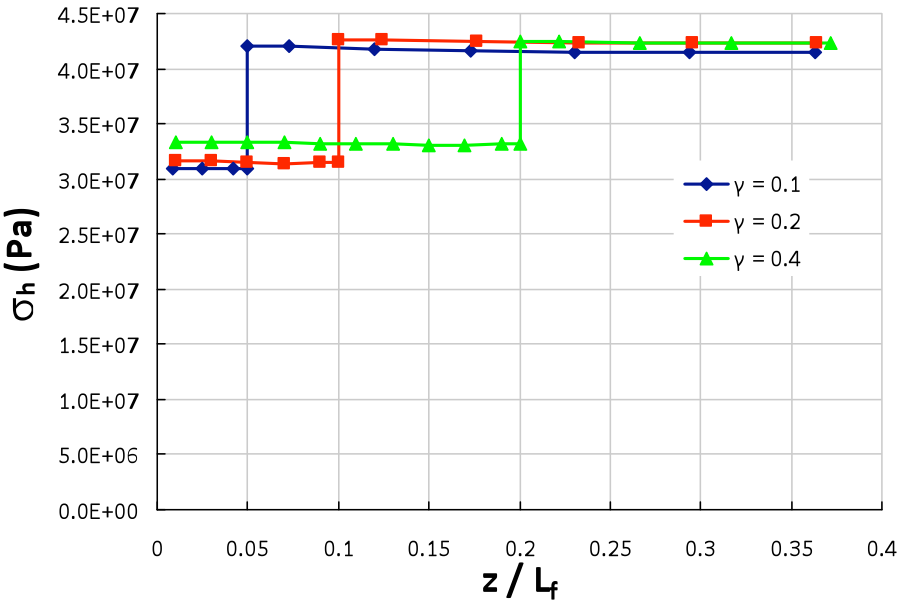

Fig. 2.15 – Effect of γ on the shear stress at the pay zone boundaries for $\beta = 1$

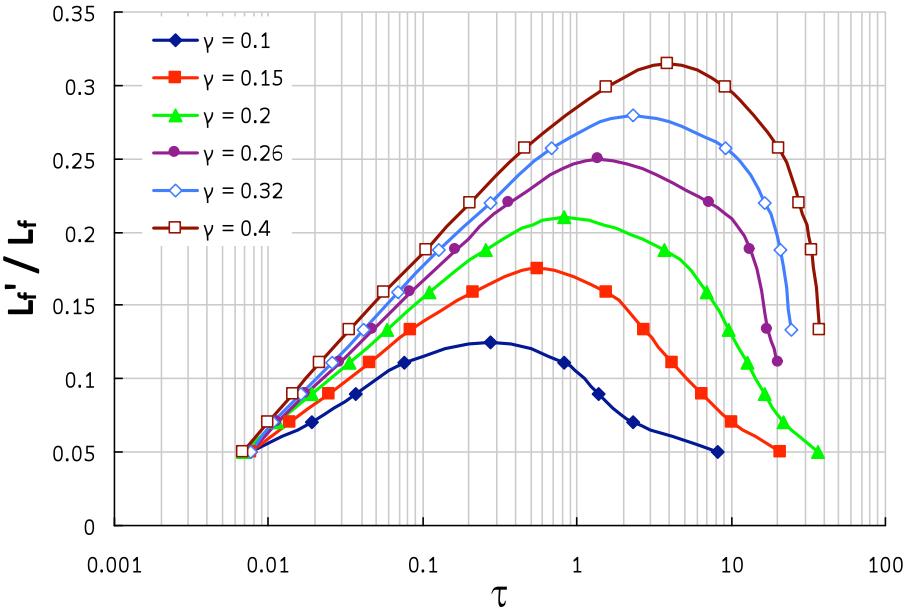

Fig. 2.16 – $\lambda = L_f'/L_f$ versus the dimensionless time τ for different values of γ, with $\Pi = 0.0583$ and $\beta = 1$

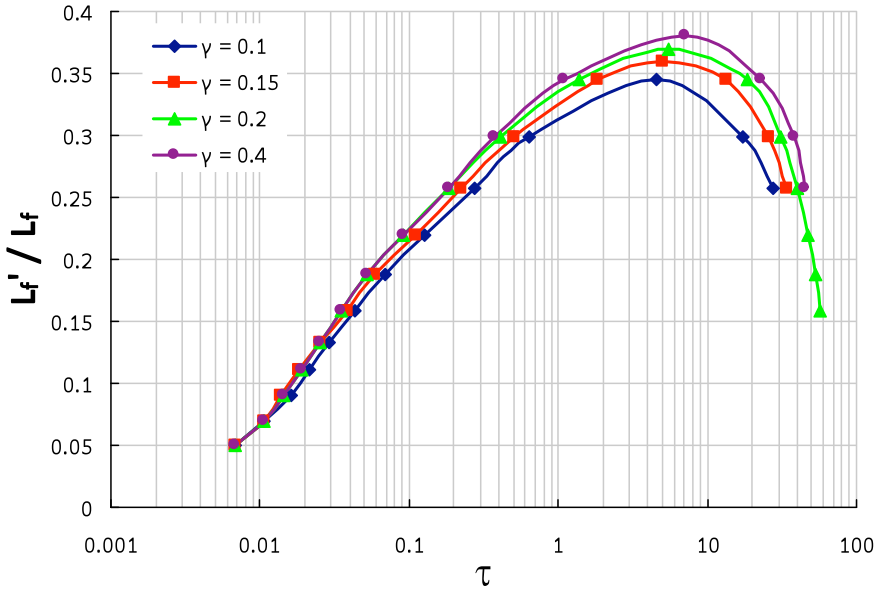

Fig. 2.17 – $\lambda = L_f'/L_f$ versus the dimensionless time τ for different values of γ, with $\Pi = 0.0583$ and $\beta = 0.1$

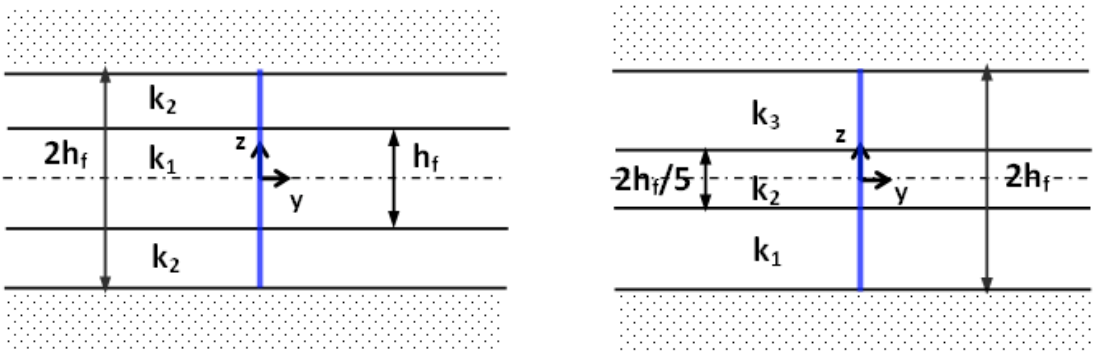

Fig. 2.18 – Geometry of two modeled layered reservoirs of average permeability (a) $k_{avg} = (k_1+k_2)/2$ and (b) $k_{avg} = (2k_1+k_2+2k_3)/5$

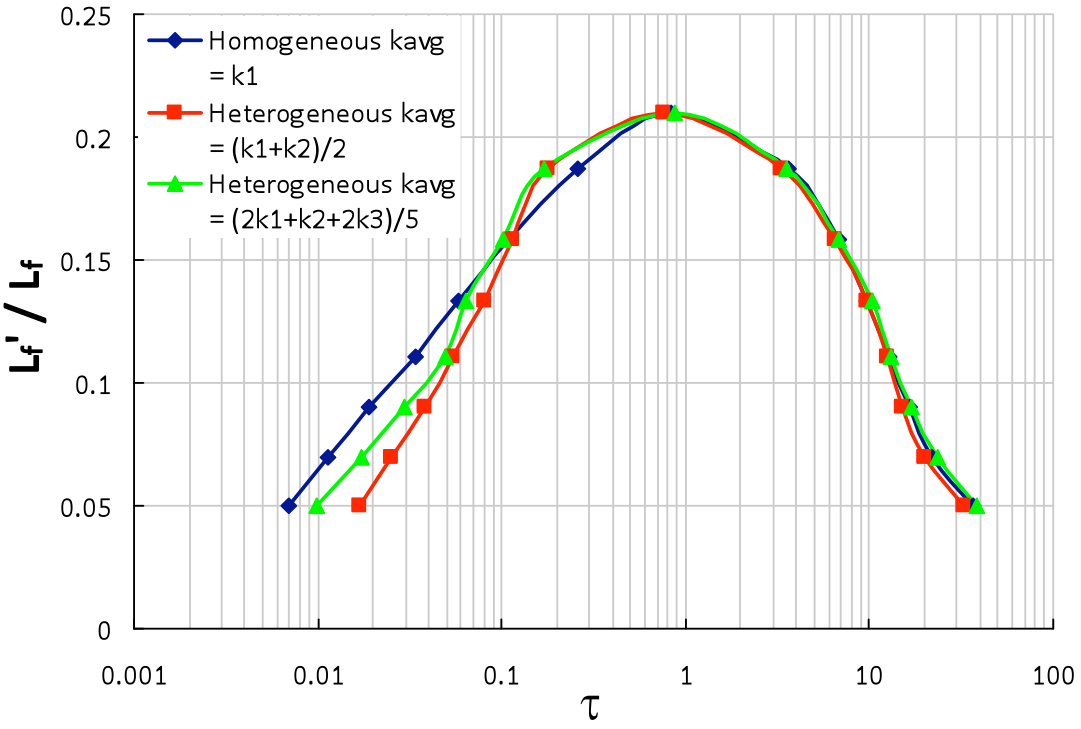

Fig. 2.19 – $\lambda = L_f'/L_f$ versus τ for one homogeneous and two heterogeneous reservoirs, with $\Pi = 0.0583$, $\beta = 1$ and $\gamma = 0.2$

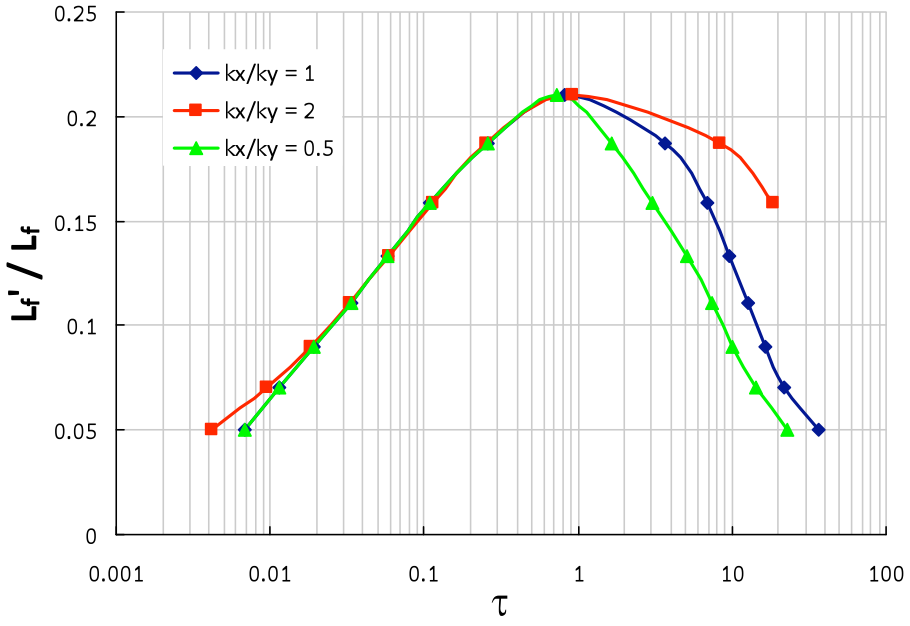

Fig. 2.20 – $\lambda = L_f'/L_f$ versus τ (defined using k_y) for different values of the ratio k_x/k_y, with $\Pi = 0.0583$, $\beta = 1$ and $\gamma = 0.2$

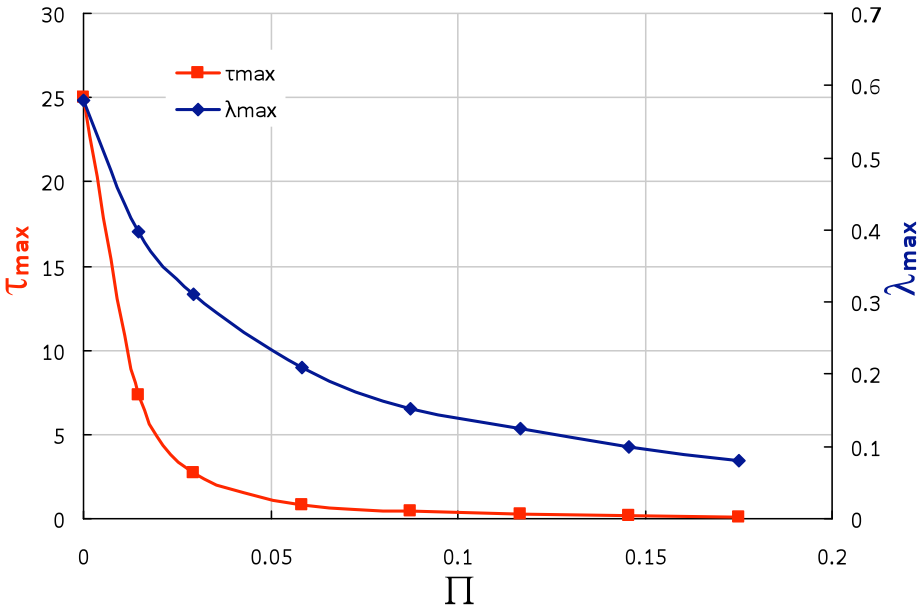

Fig. 2.21 – λ_{max} and τ_{max} versus Π, with $\beta = 1$ and $\gamma = 0.2$

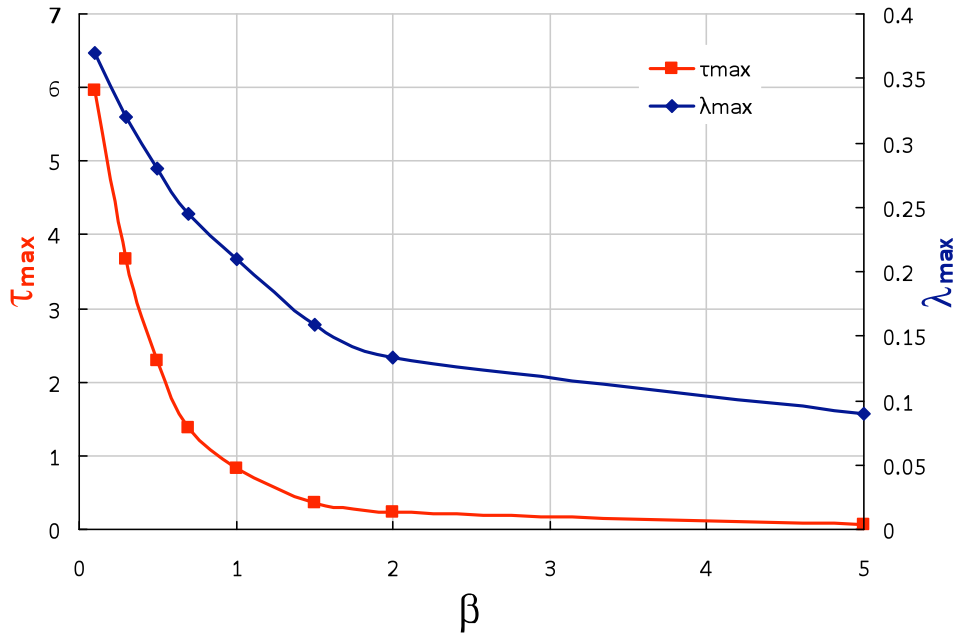

Fig. 2.22 – λ_{max} and τ_{max} versus β, with $\Pi = 0.0583$ and $\gamma = 0.2$

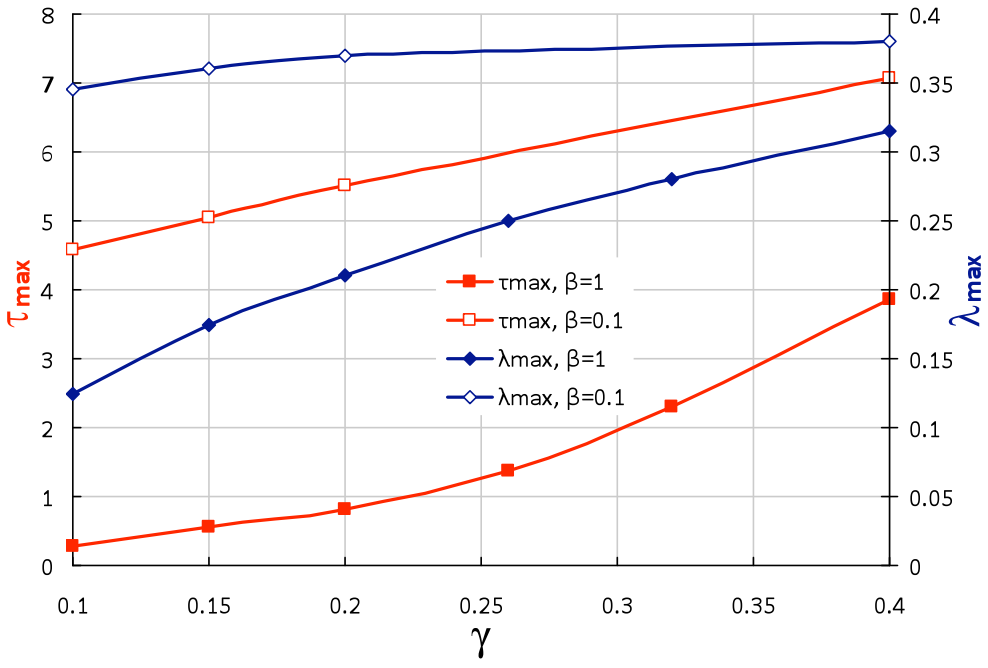

Fig. 2.23 – λ_{max} and τ_{max} versus γ, with $\Pi = 0.0583$ and $\beta = 0.1$ and 1

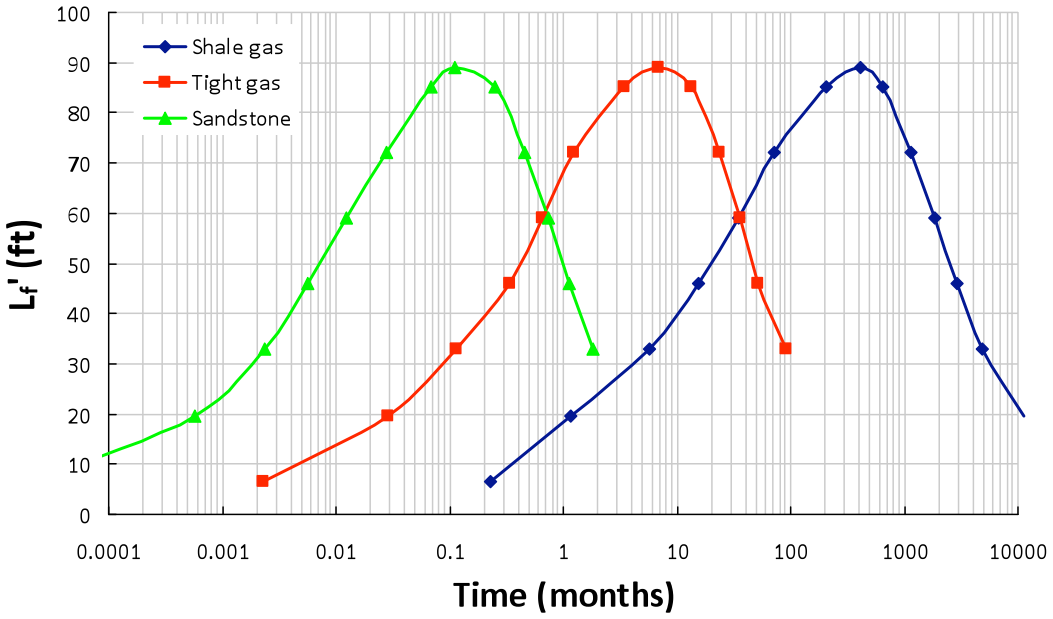

Fig. 2.24 – Extent of the stress reversal region L_f' as a function of production time for the 3 gas reservoir types listed in Table 2.1

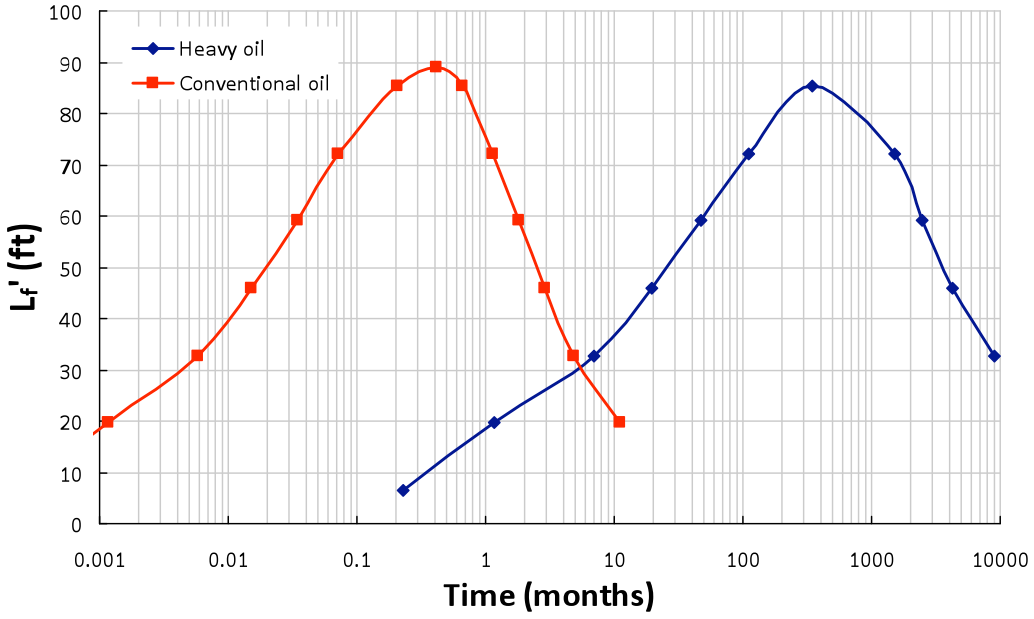

Fig. 2.25 – Extent of the stress reversal region L_f' as a function of production time for the 2 oil reservoir types listed in Table 2.1

CHAPTER 3: MECHANICAL STRESS REORIENTATION AROUND A VERTICAL FRACTURE

The opening of a propped fracture results in the redistribution of local earth stresses. In this chapter, the extent of stress reversal and reorientation has been calculated around a vertical fracture using a three-dimensional numerical model of the stress interference induced by the opening of one propped fracture. The results will be analyzed in following chapters for their impact on the refracturing of vertical wells and the multiple fracturing of horizontal wells.

The effect of the reservoir's mechanical properties on the spatial extent of stress reorientation caused by an opened crack has been quantified. The model takes into account the presence of layers that bound the pay zone, which may have different mechanical properties from the pay zone. The impact of fracture vertical growth into the bounding layers on the shape of the fracture, and the resulting stress interference, is also examined.

1. INTRODUCTION

Warpinski and Branagan (1989) first proved using field tests that mechanical interference from a propped-open fracture may generate stress reversal in its vicinity. So far, mechanical stress interference (Soliman et al. 2004) and poroelastic stress interference (Siebrits and Elbel 1998) have been analyzed separately for their impact on the refracturing of vertical wells. Analytical solutions exist that describe the stress field around an elliptical crack (Sneddon et al. 1946) for two specific geometries: (a) an infinitely long 2D crack (plane strain) and (b) a penny-shaped crack ($L_f = h_f$). All

solutions may be used to calculate mechanical stress interference assuming a homogeneous, isotropic, elastic rock.

Previous studies in the literature on fracture-induced stress interference mostly focus on the effect of a single fracture. But the recent development of multiple fracturing in horizontal wells brought about the question of the mechanical interference generated by multiple transverse fractures. Using analytical solutions, Soliman et al. (2004) calculated the effect of multiple fractures on the expected net pressure and the stress contrast. Both quantities increase substantially with the number of sequential fractures and a smaller fracture spacing.

Microseismic measurements have demonstrated the existence of mechanical stress interference between multiple transverse fractures. This is sometimes referred to as the stress shadow effect (Fisher et al. 2004). When multiple fractures are propagated simultaneously, the stress shadow can restrict growth in the middle section of the wellbore, while favoring growth at the heel or at the toe. Numerical calculations based on displacement discontinuity method for 3 and 5 transverse fractures experiencing the same net pressure, show that the center fractures, subject to most stress interference, exhibit a decrease in their width and conductivity (Cheng 2009). Field experience has demonstrated that the optimal cluster spacing to limit fracture interference must be at least 1.5 to 2 times the fracture height (Ketter et al. 2008).

2. MODEL FORMULATION

The validity of numerical simulations is verified through comparison with existing analytical models (Sneddon et al. 1946) for simple fracture geometries. The important addition to existing models consists in the evaluation of the impact of the

layers bounding the pay zone on the width of the fracture, which eventually affects the stress interference caused by a propped fracture. The identified dimensionless parameters are the fracture aspect ratio (h_f/L_f), the Poisson's ratio of the pay zone (ν_p), the fracture containment (h_p/h_f), and the ratio of Young's moduli (E_b/E_p). Their effects on the stress contrast generated by the propped fracture, and consequently the spatial extent of the stress reversal region, are discussed in the following sections.

2.1. Governing Equations

The geometry of the simulated fracture is shown in **Fig. 3.1**. The model includes the presence of layers bounding the reservoir and cases where the fracture is not fully contained ($h_f>h_p$), are accounted for. The layers bounding the pay zone may have mechanical properties (E_b, ν_b) differing from the pay zone (E_p, ν_p).

The mechanical behavior of the continuous three-dimensional medium is described mathematically by the equations of equilibrium Eq. (3.1), the definition of strain Eq. (3.2) and the constitutive equations Eq. (3.3). The system of 15 equations for 15 unknowns (6 components of stress tensor σ_{ij} and strain tensor ε_{ij}, plus the 3 components of the displacement vector u_i) is solved at each node using an explicit, finite difference numerical scheme. The Einstein summation conventions apply.

$$\sigma_{ij,j} + \rho g_i = \rho \frac{\partial^2 u_i}{\partial t^2} \tag{3.1}$$

$$\varepsilon_{ij} = \frac{1}{2}\left(u_{i,j} + u_{j,i}\right) \tag{3.2}$$

The pay zone is homogeneous, isotropic, and purely elastic. Hooke's law relates the components of the strain and stress tensors (constitutive equation):

$$\sigma_{ij} = 2G\varepsilon_{ij} + \left(K - \frac{2}{3}G \right)\varepsilon_{kk}\delta_{ij} \tag{3.3}$$

$$\text{Where, } K = \frac{3}{2(1-2\nu)},\ G = \frac{E}{2(1+\nu)}$$

2.2. Boundary Conditions

Displacement is allowed along the faces of the fracture where a constant stress, equal to the net pressure, p_{net}, plus the minimum in-situ horizontal stress σ_{hmin}, is imposed (**Fig. 3.2**). At the end of the fracturing process, the fracture closes down on the proppant, which keeps the fracture open. The width of the propped-open fracture will depend on the fractured length and the amount of sand pumped during the fracturing job. The uniform stress boundary condition applied on the fracture face is equal to the pressure required for the proppant to maintain an opening of maximum width w_0. This pressure value is smaller than the pressure required to propagate a hydraulic fracture in the same rock. To avoid an impact on the stress distribution around the hydraulic fracture, the far-field boundaries are placed at a distance from the fracture equal to at least three times the fracture half-length L_f (see Figs. 2.2 and 2.3). A constant stress boundary condition normal to the "block" faces is applied at outside boundaries. In-situ stresses are initialized prior to the opening of the fracture:

$$\begin{cases} \sigma_{xx} = -\sigma_{h\max} \\ \sigma_{yy} = -\sigma_{h\min} \\ \sigma_{zz} = -\sigma_{V} \end{cases} \tag{3.4}$$

2.3. Model Validation

Sneddon et al. (1946) derived analytical expressions of the additional normal and shear stresses versus the distance normal to the fracture for two geometries: semi-infinite (**Fig. 3.3**) and penny-shaped fractures (**Fig. 3.4**).

The results of the three-dimensional numerical model were compared to analytical solutions by plotting the additional stress in the direction parallel ($\Delta\sigma_{xx}$) and perpendicular ($\Delta\sigma_{yy}$) to the fracture as a function of the net closure stress (p_{net}). The net closure stress is the stress remaining as the fracture closes on the proppant minus the minimum horizontal stress (σ_{hmin}). In the present study, net pressure is assumed to be constant along the fracture (uniform proppant distribution). Stress distributions are plotted versus the distance normal to the fracture face (y) normalized by the fracture half-height (h_f).

Figs. 3.3 and 3.4 show that the additional stress in the horizontal plane is always higher in the direction perpendicular to the fracture than parallel to the fracture. As is true initially, the direction of maximum horizontal stress is parallel to the crack, and the stresses are reoriented in the vicinity of the fracture. The numerical results agree well with the analytical solution indicating that the numerical results are correct for this simple case.

The additional stress normal to the fracture ($\Delta\sigma_{yy}$) decreases monotonically with distance away from the fracture. For the case of the penny-shaped fracture (Fig. 3.3), $\Delta\sigma_{xx}$ becomes negative at some distance normal to the fracture and then passes through a minimum.

3. SENSITIVITY STUDY

3.1. Effect of Fracture Dimensions

The additional stresses in the normal and parallel directions are plotted versus the dimensionless distance y/h_f normal to the fracture respectively in **Figs. 3.5 and 3.6**. Both components increase as the fracture length increases compared to its height. The quantity of practical interest, though, is the difference between the additional stress in the direction perpendicular to and in the direction parallel to the fracture (**Fig. 3.7**). This difference represents the stress contrast that is generated by the opening of the fracture:

$$Generated\ Stress\ Contrast\ (GSC) = \Delta\sigma_{\perp} - \Delta\sigma_{//} = \Delta\sigma_{yy} - \Delta\sigma_{xx} \qquad (3.5)$$

In most situations the creation of the fracture generates large additional stresses perpendicular to the fracture face. This alters the stress contrast and may cause the direction of maximum stress to rotate 90° in the vicinity of the fracture. The stress contrast generated by the open crack decreases as the distance from the fracture increases (Fig. 3.7). At some distance from the fracture, it becomes smaller than the in-situ stress contrast and the direction of maximum stress is oriented as initially.

The areal extent of the stress reversal region is directly proportional to the fracture height, as the distance to the fracture is normalized by the fracture half-height in our analysis. Fig. 3.7 also shows that as the fracture length increases, the GSC is higher. For instance, assuming the in-situ stress contrast is equal to 0.2 p_{net}, the maximum distance of stress reversal L_f' is increased by 36% for a semi-infinite fracture compared to a penny-shaped fracture.

3.2. Effect of Poisson's Ratio in the Pay Zone

The effect of the Poisson's ratio in the pay zone on the stress reorientation around the fracture depends on the fracture geometry. In the limiting case of a penny-shaped fracture ($h_f = L_f$), stresses are independent of the Poisson's ratio (Sneddon et al. 1946), and so is the generated stress contrast. In the more general case where the fracture length differs from the fracture height, Poisson's ratio will play a role.

It is shown in **Fig. 3.8** that an opened crack generates more stress contrast in a rock with a low Poisson's ratio. A low Poisson's ratio implies that the deformation in the direction parallel to the fracture is small compared to the deformation along the normal to the fracture. When $\nu_p = 0$, all the deformation occurs along the in-situ direction of minimum horizontal stress ($\varepsilon_{yy} = 0$), thus maximizing the stress contrast generated.

3.3. Effect of the Bounding Layers' Mechanical Properties

Models of stress interference available in the literature (Sneddon et al. 1946; Cheng 2009) assume homogeneous mechanical properties and do not accurately model layered rocks. The rocks bounding gas reservoirs often have different mechanical properties than the reservoir and can play an important role in stress reorientation. **Fig. 3.9** shows that, for a fixed fracture penetration factor h_p/h_f equal to 0.75, the GSC decreases if the Young's modulus of the bounding layers is higher than in the pay zone.

The width of an opened crack is proportional to the Young's modulus. The relationship between maximum fracture width w_0 (at the center of the fracture) and net pressure for a semi-infinite fracture is given in Eq. (3.6) (Palmer 1993). If the fracture penetrates into a weaker bounding layer (E_b/E_p smaller than 1), the fracture width is positively affected (**Fig. 3.10**). Thus, a larger stress contrast is generated by the fracture (Fig. 3.8).

$$w_0 = \frac{4\left(1-\nu^2\right)}{E} p_{net} h_f \tag{3.6}$$

3.4. Effect of Fracture Containment

The bounding layers' mechanical properties do not affect the extent of stress reorientation if the fracture is fully contained. In the Barnett shale, fractures are generally well contained in the pay zone even though "out-of-zone" growth has been measured in the field (Maxwell et al. 2002). From the relationship between fracture width and Young's modulus in Eq. (3.6), it can be deduced that the further the fracture penetrates into the bounding layers, the more the stress reorientation will be affected by their mechanical properties. For instance, in the case where the Young's modulus is higher in the layers bounding the pay zone, the maximum width of the crack, and consequently the generated stress contrast, decreases as the fracture height increases (**Figs. 3.11 through 3.14**). For both a semi-infinite and a penny-shaped fracture, similar conclusions can be made when the Young's modulus ratio is higher than 1 ($E_b/E_p = 1.67$) where the fracture width and the generated stress contrast decrease as the fracture height increases (**Figs. 3.15 through 3.18**).

The effect of the Poisson's ratio in the bounding layers was also analyzed (**Figs. 3.19 through 3.22**). It is shown that the GSC is independent of this value, and rather depends only on the Poisson's ratio inside the pay zone.

4. MECHANICAL STRESS REORIENTATION AROUND A SINGLE FRACTURE

4.1. Application to the Barnett Shale

We calculated the additional stress generated by a propped single fracture, in the case of a Barnett shale gas well (**Fig. 3.23**). Commonly accepted values for the propped fracture width (Palisch et al. 2008) and the horizontal stress contrast (Weng and Siebrits 2007) in the Barnett shale are 4 mm and 100 psi respectively (**Table 3.1**).

The isotropic point is located at a distance from the fracture equal to 150 ft, where the curves of σ_{xx} and σ_{yy} cross (**Fig. 3.24**). Between the fracture and the isotropic point, the stresses in the direction perpendicular to the fracture become superior to the stresses parallel to the fracture (Fig. 3.24). As a result, the direction of maximum horizontal stress is switched 90° in an elliptical zone called the stress reversal region (**Fig. 3.25**). The stress interference around a propped open-fracture may also be represented by plotting the angle of stress reorientation (**Fig. 3.26**). The red zone represents the region of 90° stress reorientation which extends up to 150 ft from the fracture. Outside the stress reversal region, in a region called the reoriented-stress region, the angle of stress reorientation gradually decreases and finally becomes smaller than 5° at a distance from the fracture equal to 450 ft.

4.2. Effect of Fracture Width and In-Situ Stress Contrast

In **Fig. 3.27**, the distance between the fracture and the isotropic point (L_f') is plotted against the maximum fracture width (w_0) for different values of the in-situ stress contrast.

As the fracture width increases, the stress contrast generated by a propped-open fracture increases. Thus, depending on the horizontal contrast present in-situ and the

fracture design, the stress interference caused by the opening of a propped fracture will be affected.

When the in-situ horizontal stress contrast is large, stress reversal may never occur in the field as a result of mechanical stress interference. For a deviatoric stress equal to 500 psi, the minimum value of the propped fracture width required to generate stress reversal (in a rock having similar mechanical characteristics as the Barnett shale) is 1.5 cm, which is high (Fig. 3.27).

On the other hand, when the in-situ stress contrast is small, the areal extent of the stress reversal region becomes very sensitive to the fracture width. If the deviatoric stress is equal to 50 psi, the extent of the stress reversal region is calculated to grow from 147 ft to 284 ft (almost double), as the fracture width goes from 2 mm to 4 mm.

5. CONCLUSIONS

A comprehensive and quantitative study of stress reorientation around fractured horizontal wells has been presented. A three-dimensional numerical model was used to take into account the presence of layers bounding the pay zone as well as fracture containment. It was shown that the stress contrast generated by the opening of a propped fracture is a function of the fracture dimensions (w_0, h_f, L_f), the Poisson's ratio in the pay zone (ν_p), the ratio of Young's moduli of the reservoir and bounding layers (E_b/E_p) and the fracture penetration into the bounding layers (h_p/h_f). The results of the sensitivity study may be summarized as follows:

- The extent of the stress reversal region (L_f') is directly proportional to the fracture height.
- The generated stress contrast increases with the fracture length.

- Fracture penetration into rock layers bounding the reservoir increases stress reorientation if bounding layers are weaker than the pay zone.
- The Poisson's ratio of only the pay zone plays a role on stress reorientation.
- Stress reversal is unlikely to occur in reservoirs having a high horizontal stress contrast.
- Stress reversal is very sensitive to fracture width when the deviatoric stress is low.

Understanding mechanical stress reorientation is of practical interest as it plays a significant role in the refracturing of vertical wells (Chapter 4) and the multiple fracturing of horizontal wells (Chapter 6).

	Barnett shale gas
Pay zone Young's Modulus E_p (psi)	7.3×10^6
Bounding layer Young's Modulus E_b (psi)	3.0×10^6
Poisson's Ratio ν	0.2
σ_{hmax} (psi)	6400
σ_{hmin} (psi)	6300
Depth (ft)	7000
Pay zone half-thickness h_p (ft)	150
Fracture half-height h_f (ft)	150
Fracture half-length L_f (ft)	500
Fracture maximum width w_0 (mm)	4

Table 3.1 – Reservoir parameters for Barnett shale gas (Weng and Siebrits 2007)

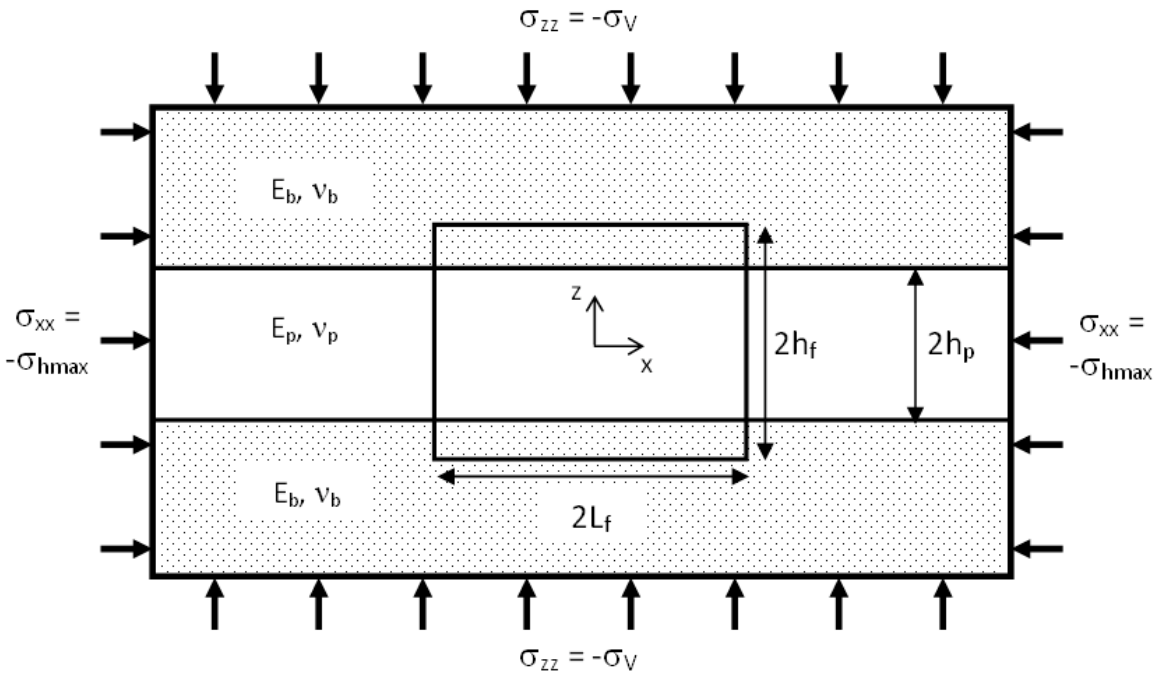

Fig. 3.1 – Geometry of a vertical fracture in a layered rock (xz-plane)

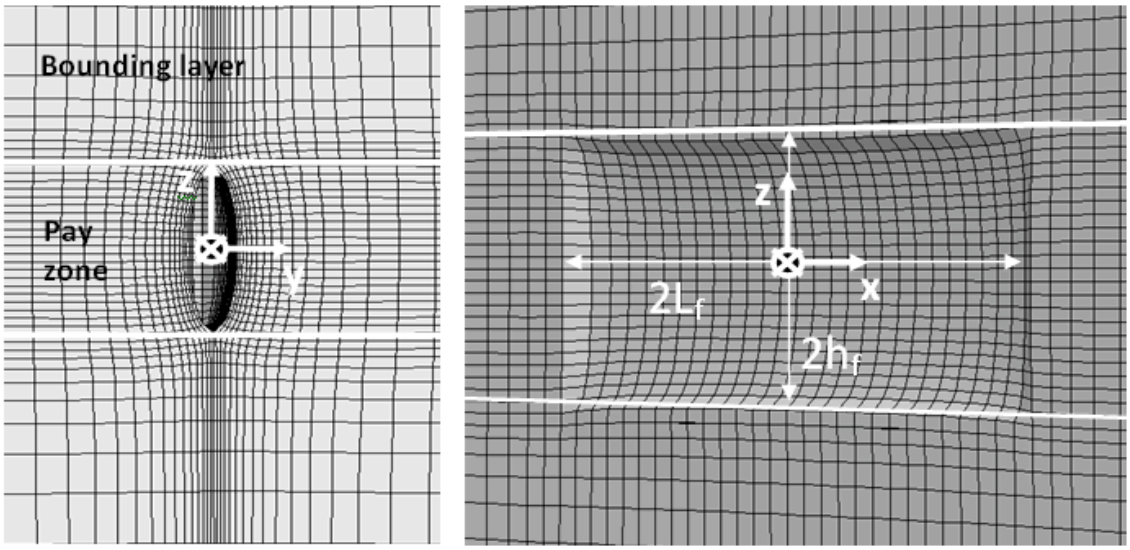

Fig. 3.2 – Elliptical deformation profile resulting from uniform pressure boundary condition at the fracture face

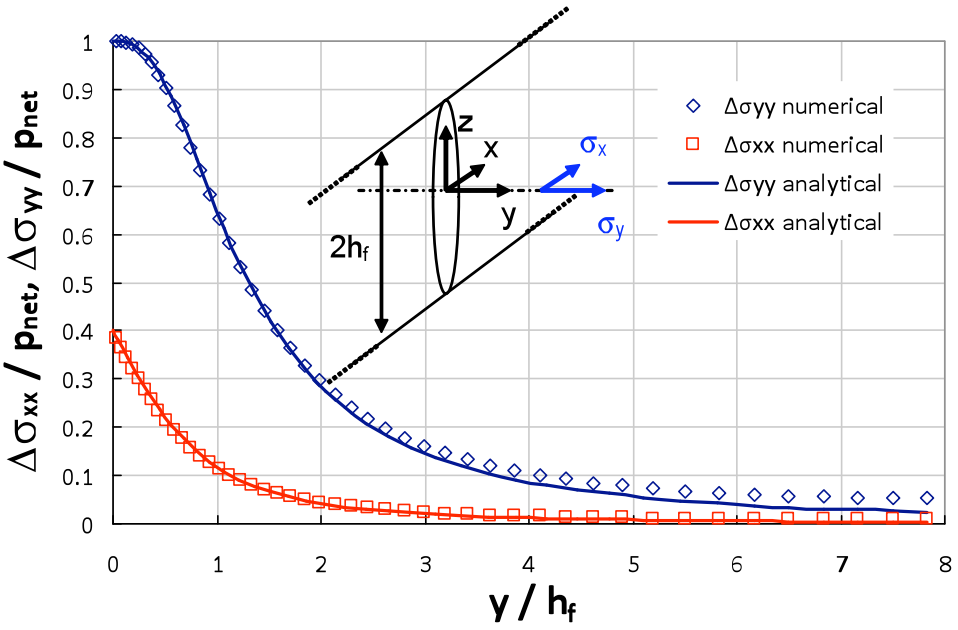

Fig. 3.3 – Comparisons of analytical (Sneddon et al. 1946) and numerical additional stresses along a normal (y=z=0) to a semi-infinite fracture (ν = 0.2)

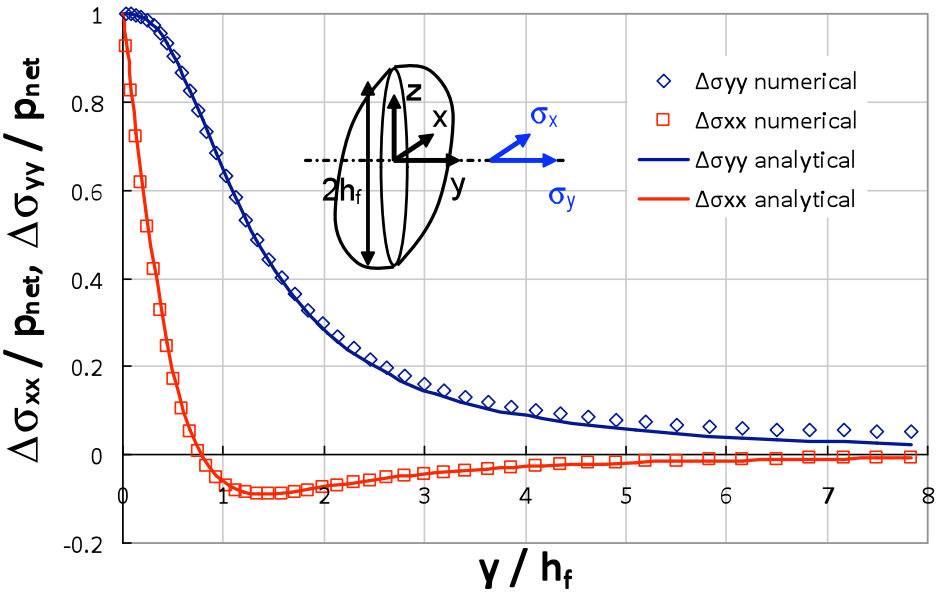

Fig. 3.4 – Comparisons of analytical (Sneddon et al. 1946) and numerical additional stresses along a normal (y=z=0) to a penny-shaped fracture

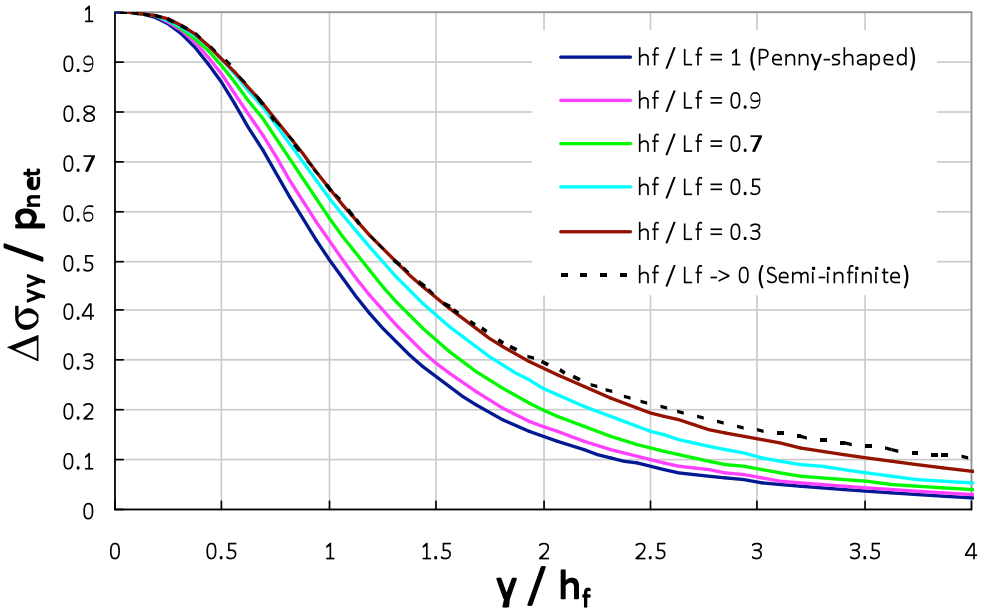

Fig. 3.5 – Effect of fracture aspect ratio (h_f/L_f) on the additional stress in the direction perpendicular to the fracture face

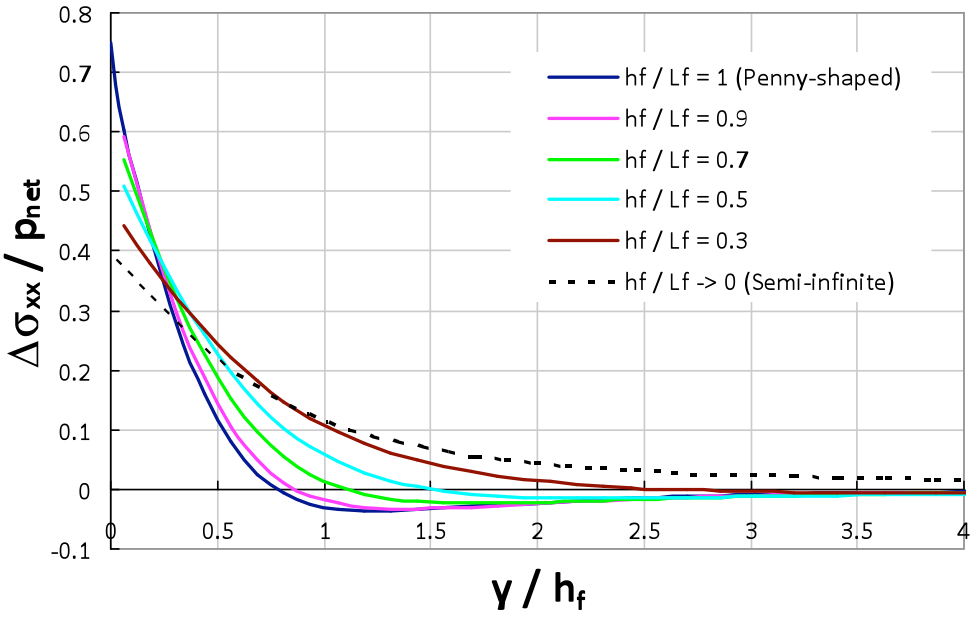

Fig. 3.6 – Effect of fracture aspect ratio (h_f/L_f) on the additional stress in the direction parallel to the fracture face

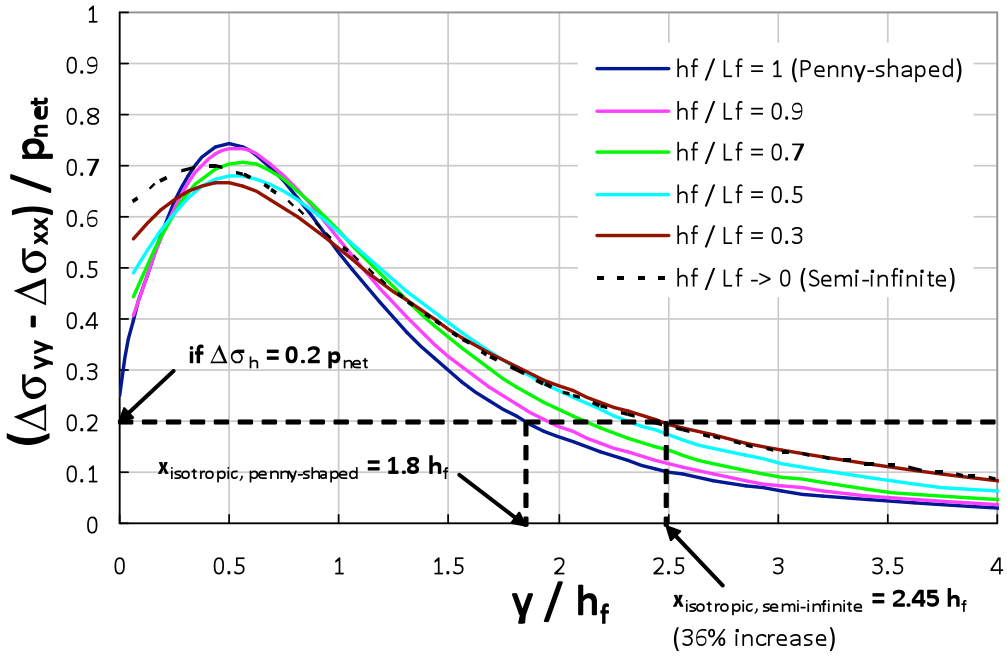

Fig. 3.7 – Effect of fracture aspect ratio (h_f/L_f) on the generated stress contrast

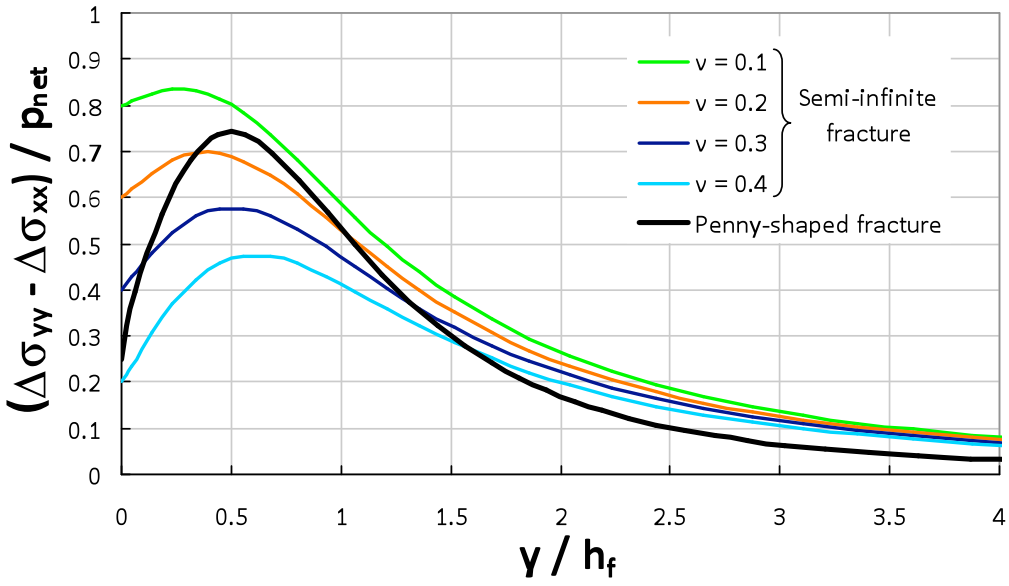

Fig. 3.8 – Effect of Poisson's ratio in the pay zone on the generated stress contrast for semi-infinite and penny-shaped fractures

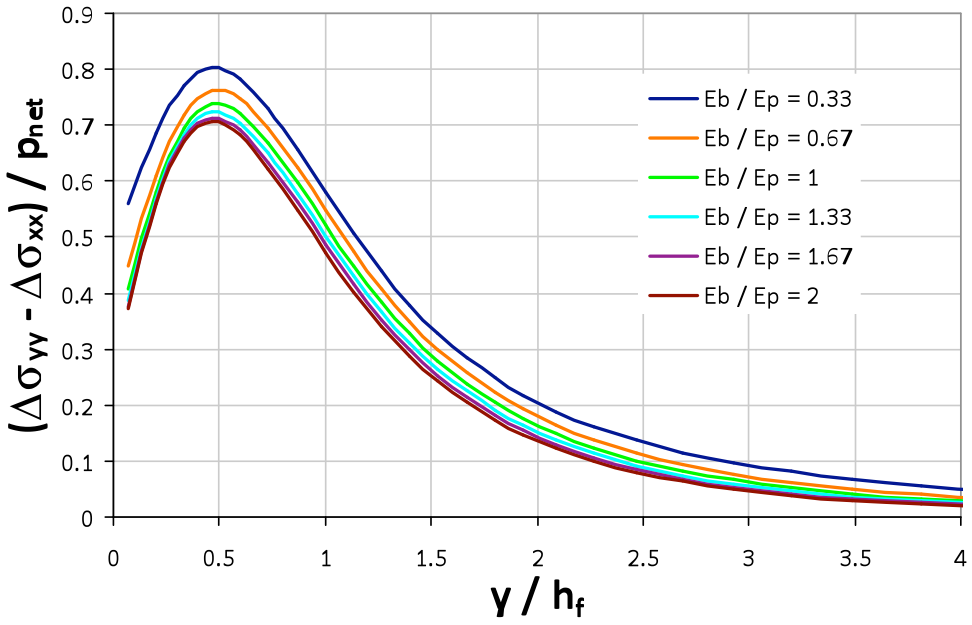

Fig. 3.9 – Effect of Young's modulus of the bounding layers on the generated stress contrast for a penny-shaped fracture and a fracture penetration ratio h_p/h_f = 0.75

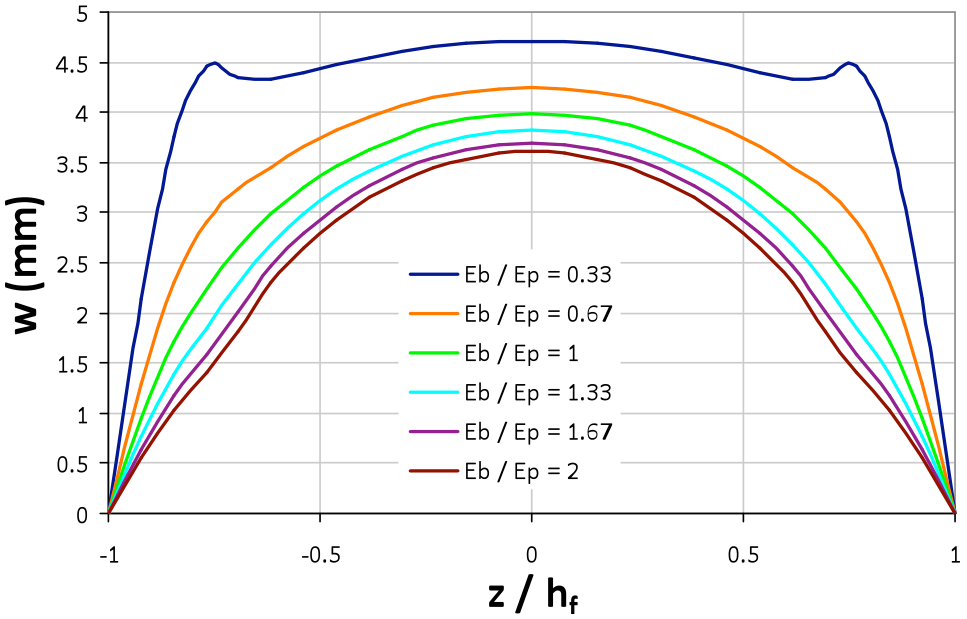

Fig. 3.10 – Effect of Young's modulus of the bounding layers on fracture width for a penny-shaped fracture and a fracture penetration ratio $h_p/h_f = 0.75$

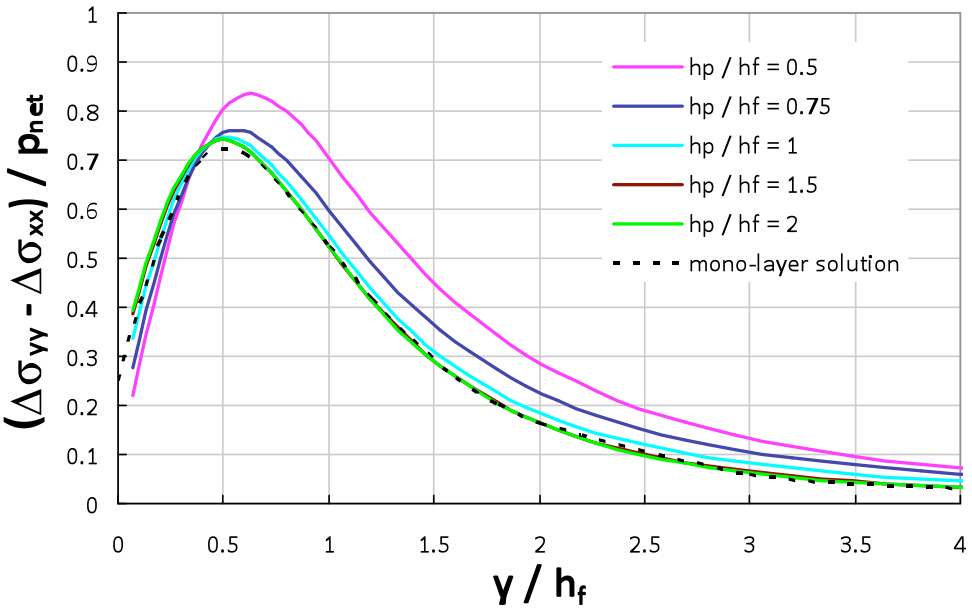

Fig. 3.11 – Effect of fracture penetration on the generated stress contrast for a penny-shaped fracture ($h_f/L_f = 1$) and $E_b/E_p = 0.33$

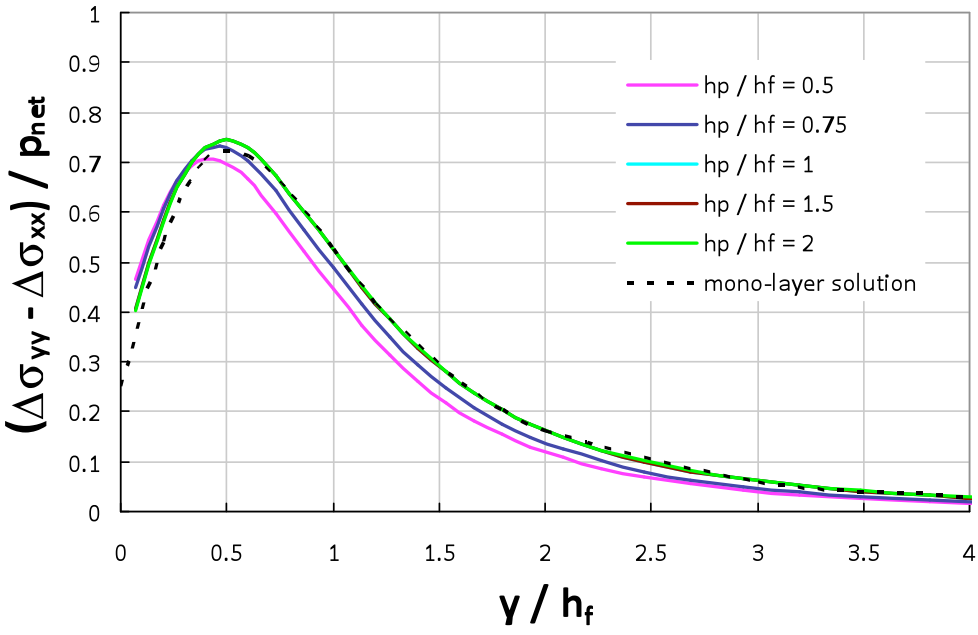

Fig. 3.12 – Effect of fracture penetration on the generated stress contrast for a penny-shaped fracture ($h_f/L_f = 1$) and $E_b/E_p = 1.67$

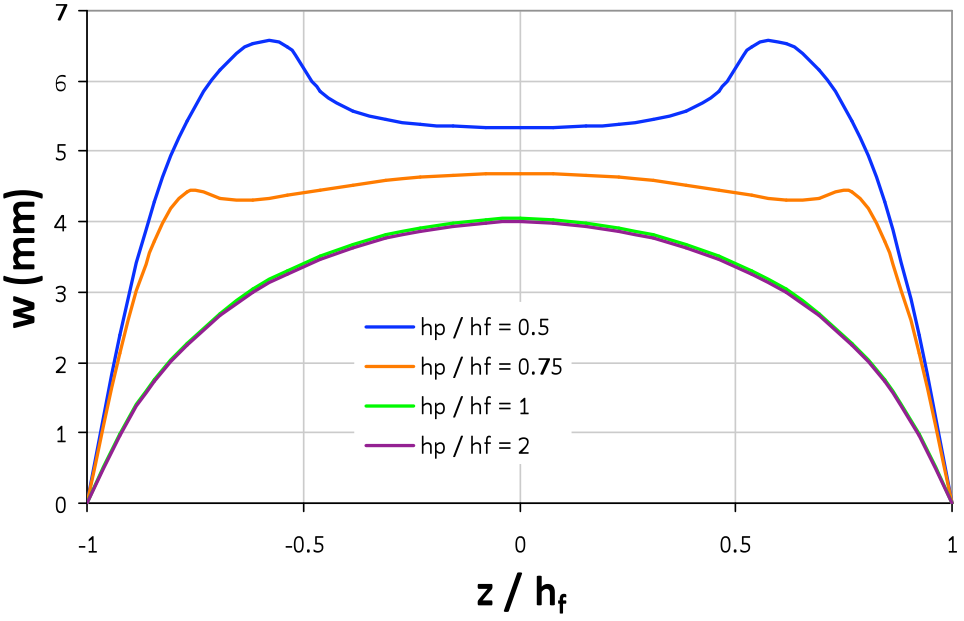

Fig. 3.13 – Effect of fracture penetration on fracture width for a penny-shaped fracture ($h_f/L_f = 1$) and $E_b/E_p = 0.33$

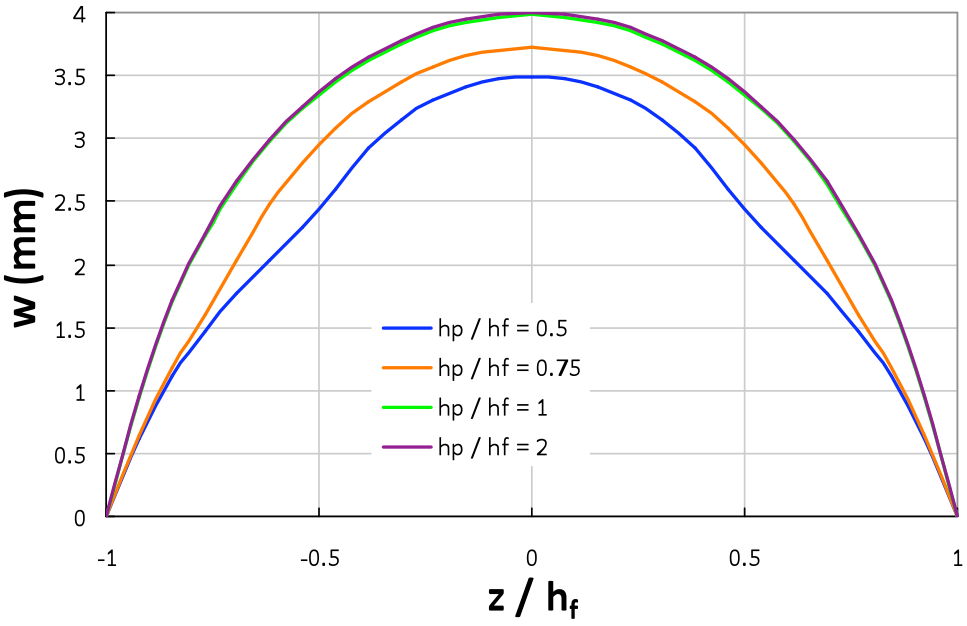

Fig. 3.14 – Effect of fracture penetration on fracture width for a penny-shaped fracture ($h_f/L_f = 1$) and $E_b/E_p = 1.67$

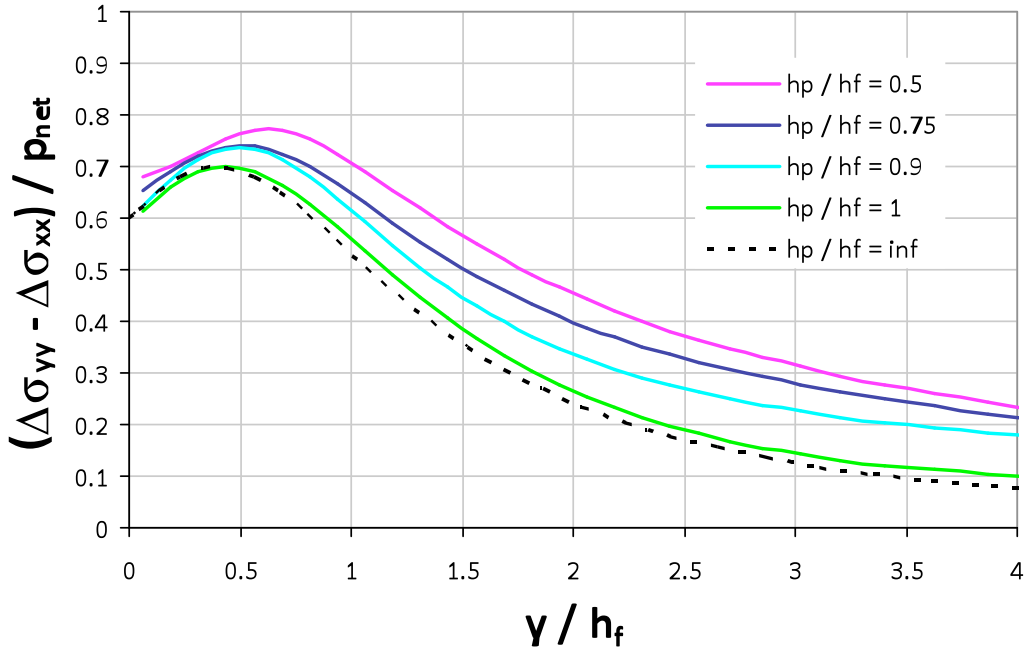

Fig. 3.15 – Effect of fracture penetration on the generated stress contrast for a semi-infinite fracture ($h_f/L_f = 1$) and $E_p/E_b = 0.33$

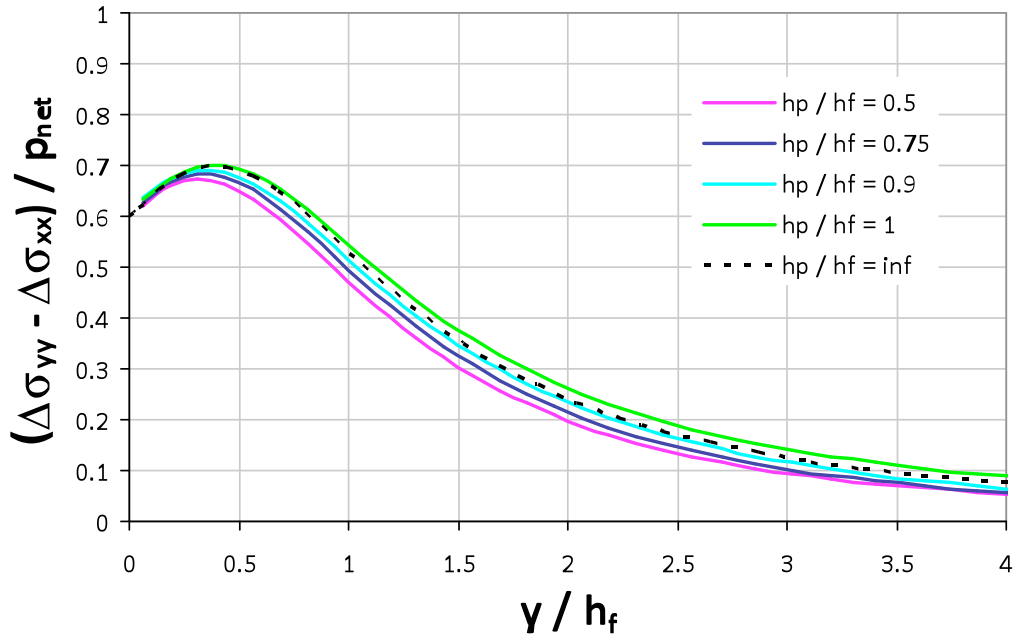

Fig. 3.16 – Effect of fracture penetration on the generated stress contrast for a semi-infinite fracture ($h_f/L_f = 1$) and $E_b/E_p = 1.67$

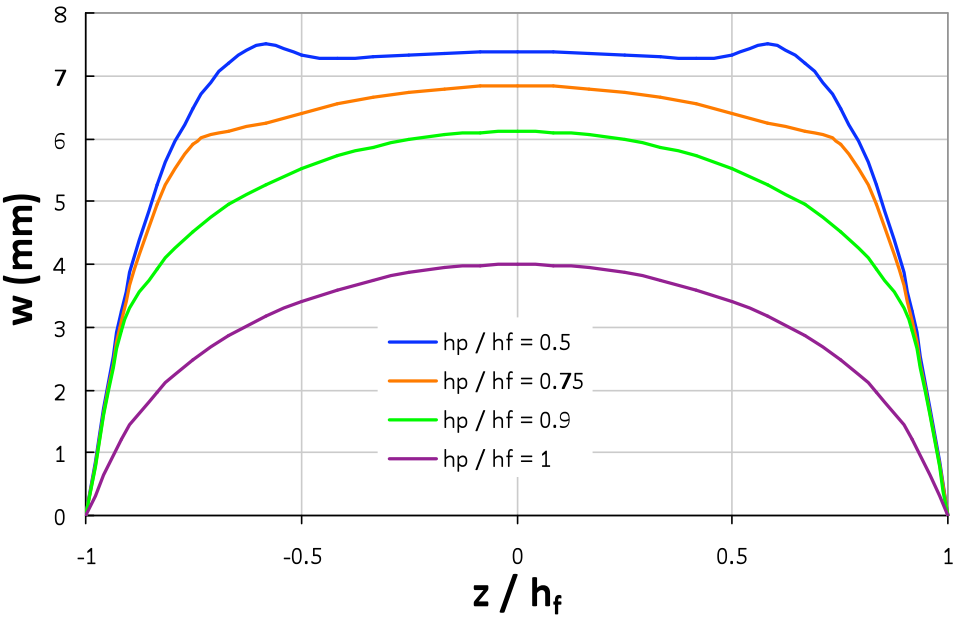

Fig. 3.17 – Effect of fracture penetration on fracture width for a semi-infinite fracture ($h_f/L_f = 1$) and $E_b/E_p = 0.33$

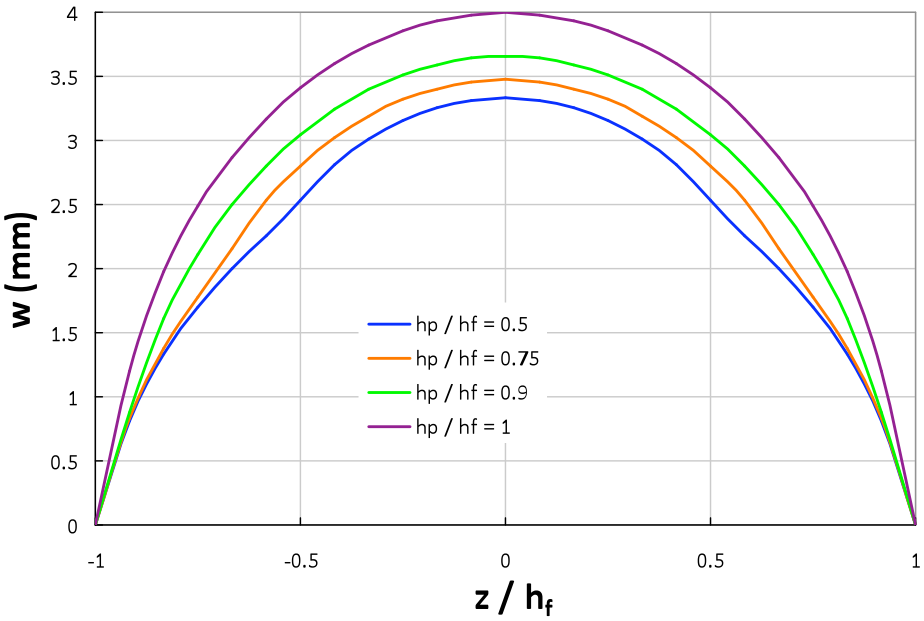

Fig. 3.18 – Effect of fracture penetration on fracture width for a semi-infinite fracture ($h_f/L_f = 1$) and $E_b/E_p = 1.67$

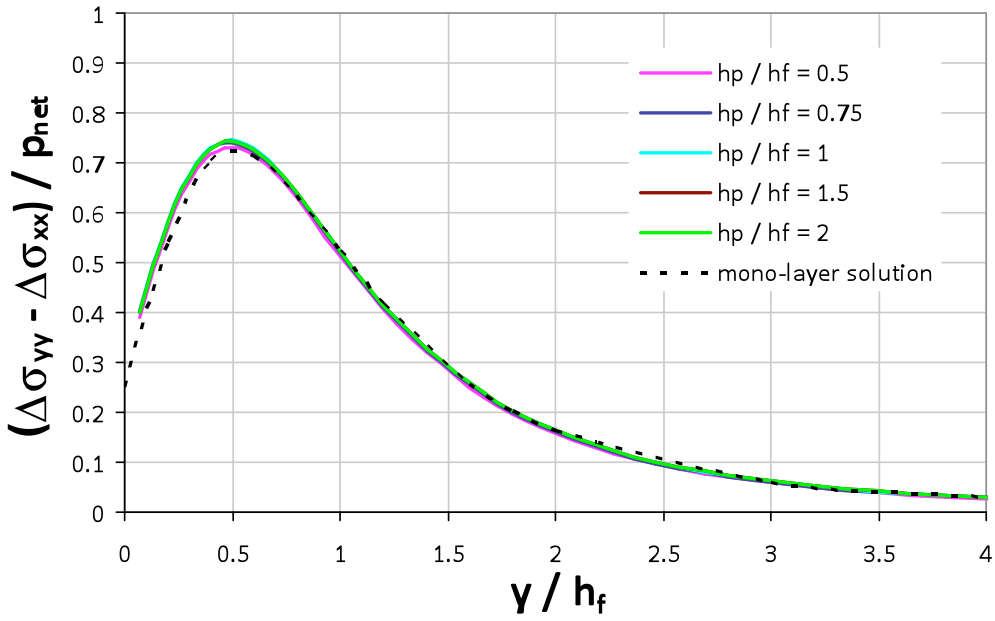

Fig. 3.19 – Effect of fracture penetration on the generated stress contrast for a penny-shaped fracture ($h_f/L_f = 1$) and $\nu_b/\nu_p = 2$

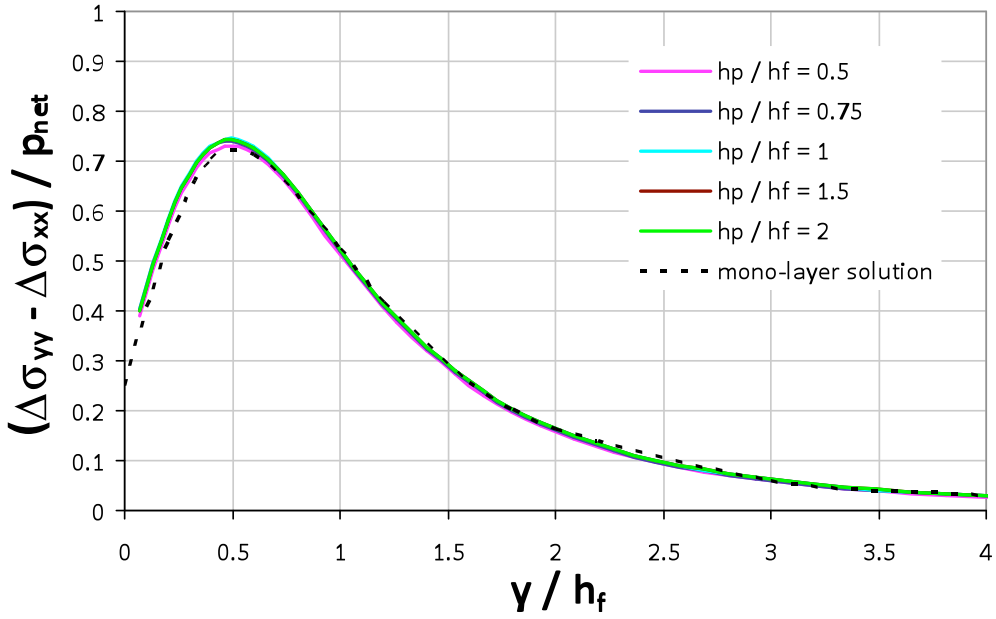

Fig. 3.20 – Effect of fracture penetration on the generated stress contrast for a penny-shaped fracture ($h_f/L_f = 1$) and $\nu_b/\nu_p = 0.67$

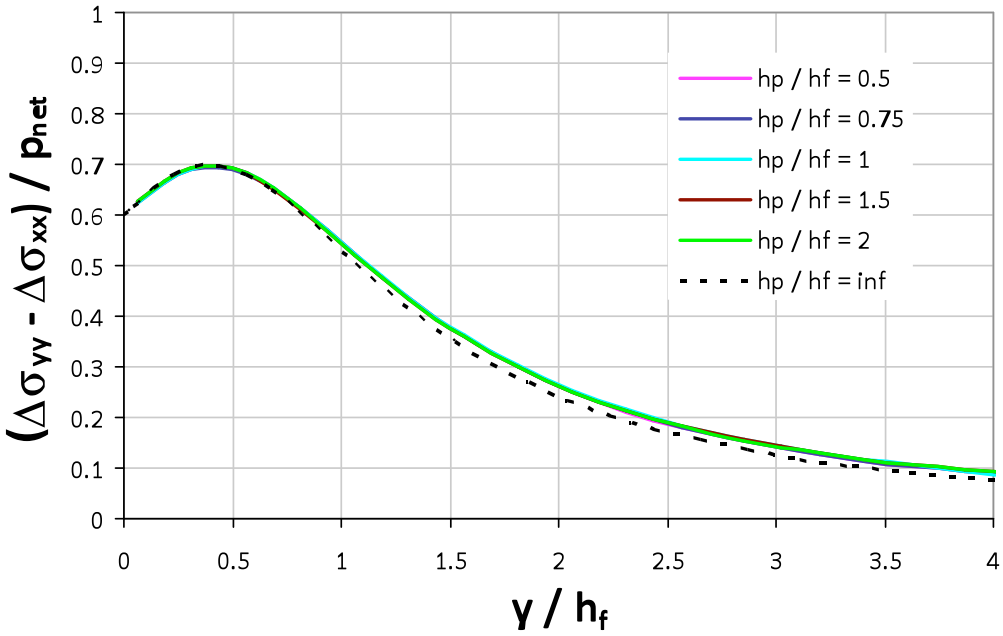

Fig. 3.21 – Effect of fracture penetration on the generated stress contrast for a semi-infinite fracture ($h_f/L_f = 1$) and $\nu_b/\nu_p = 2$

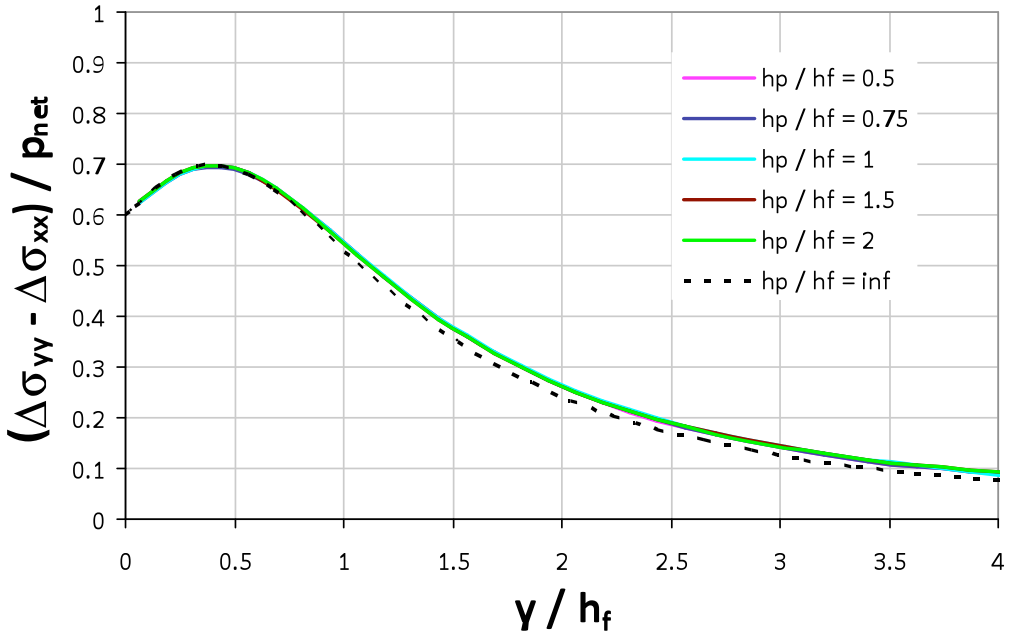

Fig. 3.22 – Effect of fracture penetration on the generated stress contrast for a semi-infinite fracture ($h_f/L_f = 1$) and $\nu_b/\nu_p = 0.67$

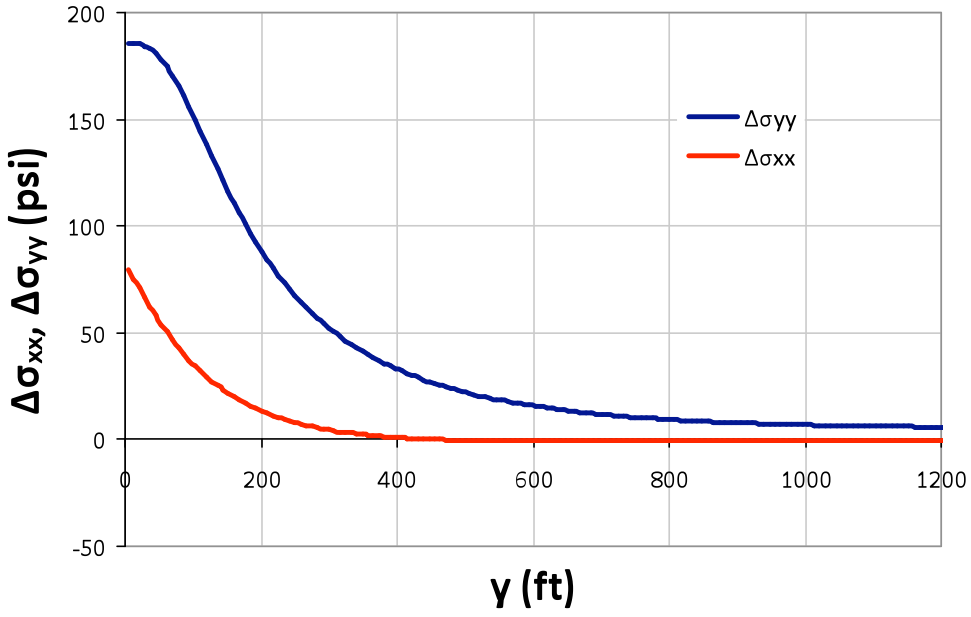

Fig. 3.23 – Additional stresses generated by a typical propped-open fracture in the Barnett shale

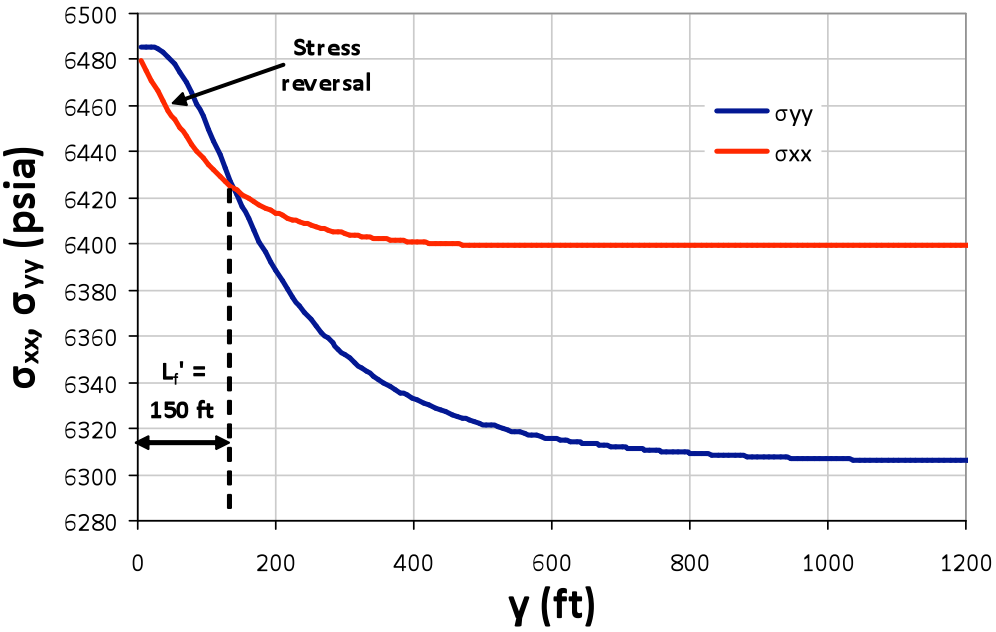

Fig. 3.24 – Stresses in the direction parallel and perpendicular to the fracture face for a typical propped-open fracture in the Barnett shale

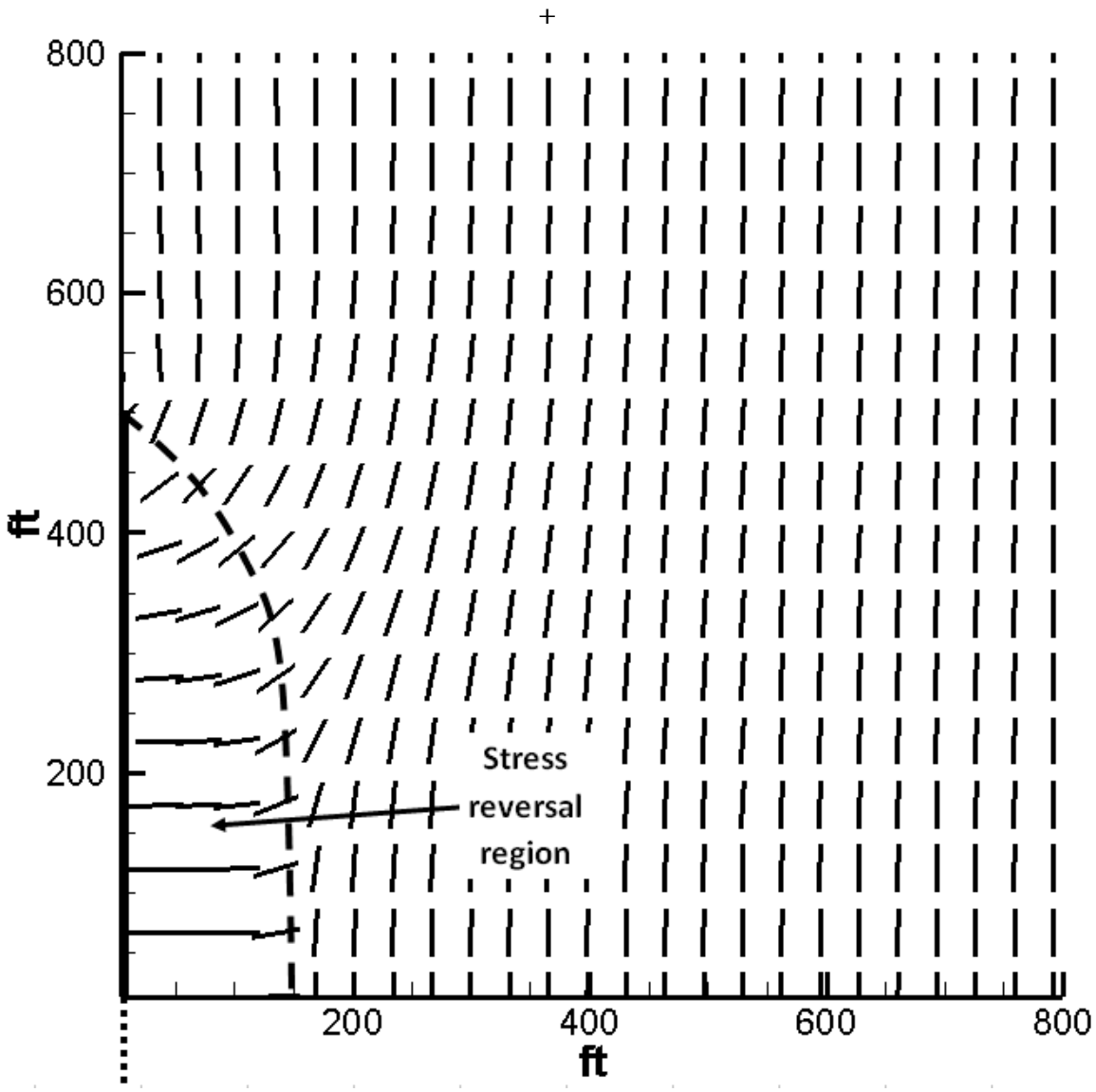

Fig. 3.25 – Direction of maximum horizontal stress around a single propped-open fracture in the Barnett shale

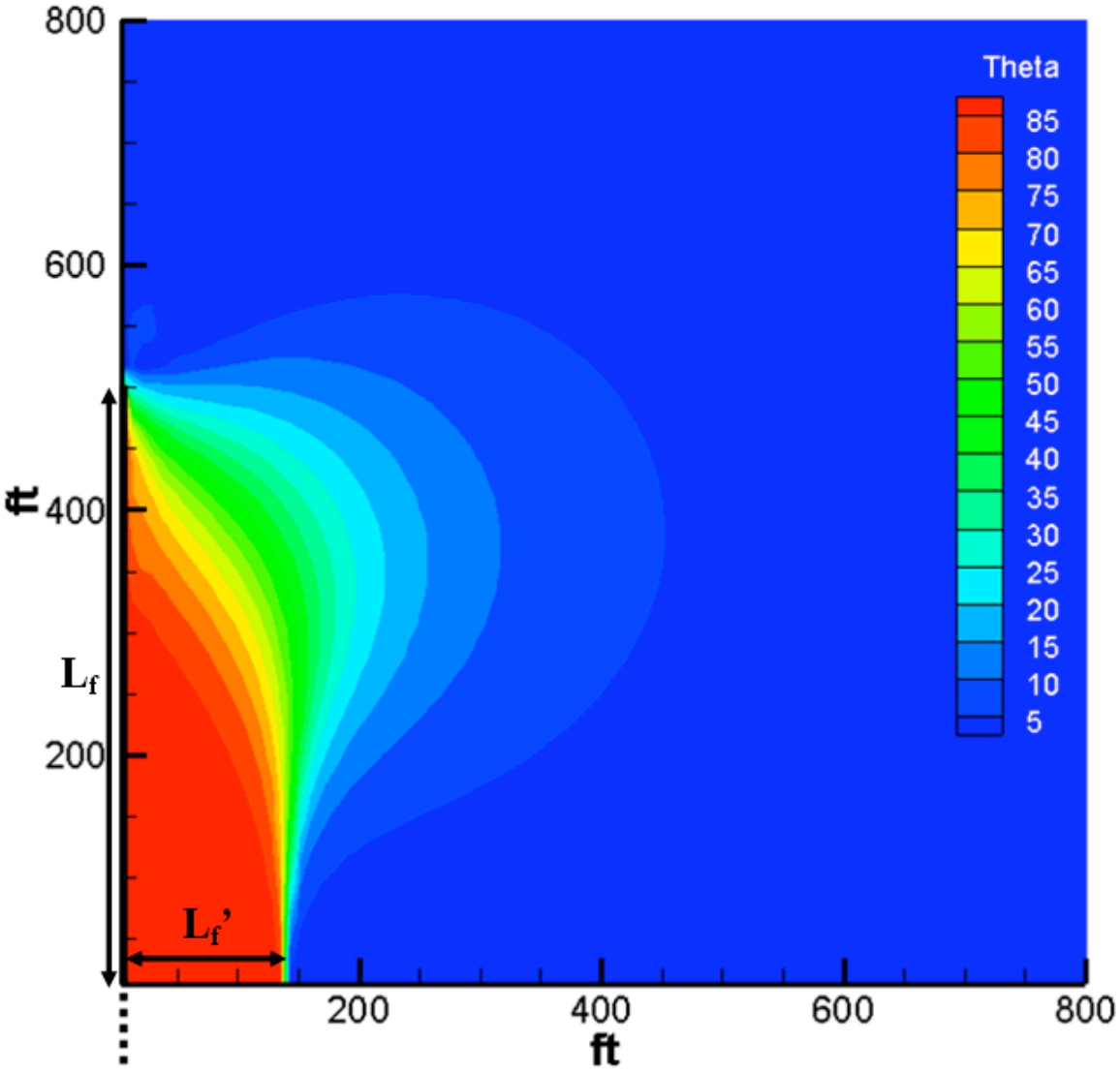

Fig. 3.26 – Angle of stress reorientation (θ) around a single propped-open fracture in the Barnett shale

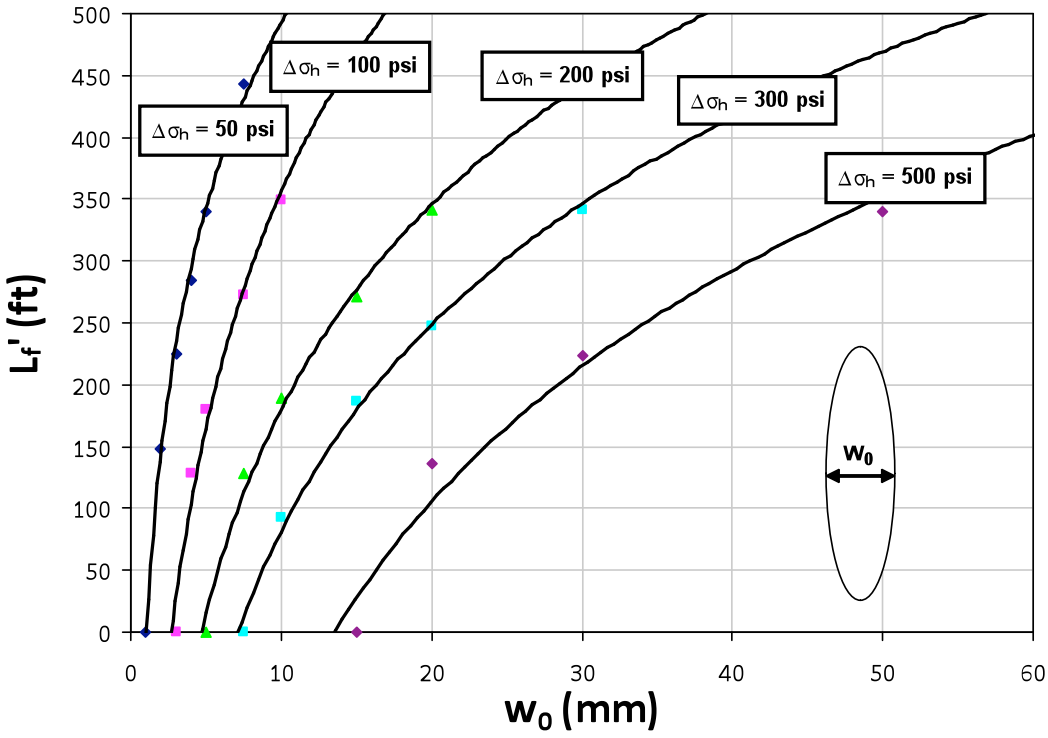

Fig. 3.27 – Extent of the stress reversal region (L_f') versus the maximum fracture width for different values of the horizontal stress contrast

CHAPTER 4: ROLE OF STRESS REORIENTATION IN THE REFRACTURING OF VERTICAL WELLS

The redistribution of stresses around a fractured vertical well has two sources: (a) opening of propped fracture (mechanical effects) and (b) production or injection of fluids in the reservoir (poroelastic effects). In this chapter, the coupling of both phenomena was numerically modeled to quantify the extent of stress reorientation around fractured production wells. It was shown that poroelastic and mechanical effects are not simply additive but show a complex dependence on each other. The results have been analyzed for their impact on refracturing operations.

For previously fractured wells, a secondary fracture may be initiated perpendicular to the first fracture if a stress reversal region is present. The size of the stress reversal region may be increased through better initial fracture design (longer fracs) and appropriate timing of the refracture. A study of the impact of the production from neighbor wells also reveals the possibility to create a favorable stress orientation outside the stress reversal region through improved field design and production schedule.

Altered-stress refracturing makes it possible to access zones of the reservoirs that are less depleted, thus increasing well production and allowing access to additional reserves.

We numerically investigated the potential of the orthogonal refracture to increase production in the Barnett shale and the Codell tight gas formations. Mechanical and poroelastic contributions to stress reversal have been shown to differ in these two formations suggesting that reservoirs may be more prone to one source of stress reorientation or the other depending on their properties.

Finally, guidelines are drawn that allow an operator to (a) select candidate wells, (b) choose the timing of the refracture operation in the life of the well, and (c) evaluate the potential increase in well production after refracturing.

1. INTRODUCTION

Refracturing has long been recognized as a successful way to restore production rates, particularly in low-permeability gas wells. It makes it possible to complete new intervals and improve the productivity of previously un-stimulated or under-stimulated zones. By propagating a second fracture orthogonal to the initial one, restimulation may also help decrease the number of drilled wells while preserving reservoir drainage. The quantitative evaluation of the physical mechanisms responsible for stress reorientation is crucial in the design of successful refracturing treatments for vertical wells.

The stresses around fractured production wells are reoriented because of non-uniform depletion of the reservoir. Initially, the direction of maximum horizontal stress is aligned with the initial vertical fracture. During production, the maximum horizontal stress decreases faster than the minimum horizontal stress because of higher depletion in the fracture direction, causing stress reversal to occur in the vicinity of the fracture (Elbel and Mack 1993). As a result, the second fracture may propagate orthogonally to the initial fracture (**Fig. 4.1**). Past the isotropic point, the maximum principal stress switches back to its original direction, causing the refracture to gradually reorient parallel to the initial fracture. The distance between the well and the isotropic point (which limits the stress reversal region) is called L_f'. It is a good indication of the potential of refracturing operations. The stress reversal region grows at early production times before reaching a maximum extent (Siebrits and Elbel 1998; Singh et al. 2008). If refracturing is

implemented at this time (optimum time for refracturing t_{max}), incremental production should be maximized.

Stress reorientation is controlled by multiple reservoir and fracture parameters, and by the properties of the layers bounding the reservoir (Siebrits and Elbel 1998). Berchenko and Detournay (1997) developed dimensionless parameters that minimize the number of independent parameters and simplify the construction of type-curves applicable to any reservoir properties and fracture geometries.

In addition to production-induced pore pressure gradients, the deformation of the rock volume around the fracture caused by the presence of the fracture opening has long been identified as a source of stress reorientation (Warpinski and Branagan 1989). At the end of a fracturing job, the fluid pressure in the fracture decreases and the fracture walls close down on the injected proppant. The additional stresses are higher in the direction normal to the fracture (along the direction of in-situ minimum horizontal stress) than parallel to the fracture face. When the stress contrast generated by the propped-open fracture ($=\Delta\sigma_{perp} - \Delta\sigma_{//}$) exceeds the in-situ stress contrast ($\Delta\sigma_h$), then stress reversal occurs in the vicinity of the fracture.

There is limited field evidence for the modified propagation direction of refractures in the literature. Wright et al. (1994, 1995) first reported field evidence of fracture reorientation. Tiltmeter fracture mapping performed on five refracture treatments shows that refracture treatments propagate at an angle of 30–60° to the initial fracture, while an infill hydraulic fracture in a secondary recovery project was shown to start and propagate at an angle greater than 60° to the original fracture orientation. Both the fracture dip and strike were shown to be affected by the fluid pressure gradients. Laboratory tests conducted on rock samples by Liu et al. (2008) also showed a change in the direction of the refracture after producing from the initial fracture.

It is clear from the discussion above that the effects of poroelastic stresses and mechanical opening of the fracture on the in-situ stress field have not been considered together. The following sections offer some insight on the interactions between poroelastic and mechanical stress reorientation.

Refracturing has long been used to increase production in poorly fractured wells. Siebrits et al. (2000), provide field evidence of increased production due to refracturing tight gas wells having deeply penetrating initial fractures. Another example of successful refracturing in a low-permeability reservoir is reported for the Codell formation in the Wattenberg field (Wolhart et al. 2007). The performance of the refracturing treatments has been observed to be highly variable though with some wells underperforming while others are restored to initial production rates. When fracturing in shale reservoirs, the presence of natural fractures tends to generate networks of parallel fractures, increasing the reservoir sweep (Fisher et al. 2002; Maxwell et al. 2002). Fracturing in naturally fractured shales (such as parts of the Barnett shale) indicates that fractures in these types of rocks follow very complicated pathways and are unlikely to be planar and bi-wing. Fractures in this instance tend to follow the path of pre-existing fractures or planes of weakness that are more susceptible to fracturing (Li 2008).

2. MODEL FORMULATION

The geometry of the simulated fractured vertical well is set up in FLAC3D (Figs. 2.2 through 2.4). Layers bounding the reservoir are modeled but the study is limited to the situation where the fracture and pay zone heights are equal. The layers bounding the pay zone may have mechanical properties (E_b, ν_b) differing from the pay zone (E_p, ν_p).

All layers are assumed to have homogeneous, isotropic properties and to deform elastically. Flow occurs only within the reservoir and not in the bounding layers.

The poroelastic stresses are calculated using an explicitly coupled formulation in which the stresses are solved using the equations of mechanical equilibrium. The fluid flow is solved using Darcy's law and the mass conservation equation. Pore pressure gradients generate volumetric strains that in turn affect the pore pressure field. The flow calculation is performed independently of the stress calculation (explicitly) between each saved simulation time. The new stress distribution is subsequently calculated based on Biot's theory of poroelasticity and Hooke's constitutive law for elastic media (see Chapter 2).

The boundary conditions chosen for the numerical model are presented below:

- Constant fluid pressure in the fracture: for $-L_f < x < L_f$ and $-h_f < z < h_f$, $p = p_{wf}$
- No-displacement of fracture faces: for $-L_f < x < L_f$ and $-h_f < z < h_f$
- Constant stress applied at outside boundaries: $\sigma_{zz} = -\sigma_v$, $\sigma_{xx} = -\sigma_{hmax}$ and $\sigma_{yy} = -\sigma_{hmin}$.
- No-flow reservoir boundaries at $x = \pm x_r$, $y = \pm y_r$ and $z = \pm z_r$

The far-field no-flow boundaries are located at a distance from the fracture equal to at least three times the fracture half-length L_f. At this distance, far-field boundaries do not impact the extent of the stress reversal region before it reaches its maximum value, which is of practical interest (see Chapter 2). Constant stress boundary conditions are applied at outside boundaries, equal to the in-situ stresses.

The fracture is created by applying a uniform stress p_c (equal to $p_{net} + \sigma_{hmin}$) on its faces. Before production starts, the mechanical boundary condition on the fracture face is

changed to no displacement. The width of the proppant-filled fracture is therefore assumed to remain constant during production.

3. SENSITIVITY STUDY

The effects of relevant reservoir, fluid and fracture parameters on the size of the stress reversal region generated by a producing propped-open fracture, and on the relative importance of poroelastic and mechanical stress reorientation, are discussed in the following sections. The final results are summarized in **Table 4.1**.

3.1. Comparison of Stress Reorientation Profiles Caused by Poroelastic and Mechanical Effects

The structure of stress reorientation around a single fracture due to poroelastic effects has been well described in the literature (Siebrits et al. 1998, 2000; Singh et al. 2008). In the vicinity of the fracture, the direction of maximum horizontal stress is rotated 90° from its in-situ direction (for producing wells). Stress reorientation is not limited to the stress reversal region. The stress distribution resulting from the mechanical opening of a fracture differs from the one due to poroelastic stresses. It was shown that outside the stress reversal region, the direction of maximum horizontal stress points toward the fracture (radial orientation), while it is oriented in the orthoradial direction in the case of poroelastic effects (**Fig. 4.2**).

The extent of the stress reversal region (L_f') is not limited to 0.58 L_f, which has numerically been shown by Siebrits and Elbel (1998) to be the highest possible value of L_f' due to poroelastic effects. The stress reversal region may even extend to a distance larger than the fracture half-length (L_f). How far it extends in the reservoir depends

mainly on fracture width and height, and on the Young's modulus in the pay zone. The reoriented stress region (outside the stress reversal region) is confined to the vicinity of the fracture, contrary to poroelastic stress reorientation, which can be observed far inside the reservoir.

3.2. Stress Reorientation around a Producing Propped-open Hydraulic Fracture

The evolution of the extent of the stress reversal region was computed during production, for the reservoir and fracture parameters listed in **Table 4.2**. In the first calculation, only poroelastic effects are calculated. The distance of the isotropic point from the induced fracture reaches a maximum value after 2.2 months of production (**Fig. 4.3**). In reality, stresses are reoriented even before production starts as a consequence of the opening of a propped hydraulic fracture. At t = 0, principal stresses are reversed up to 33 ft from the fracture. When the additional contribution of pressure gradients to stress reorientation is calculated, L_f' reaches a maximum value of 75 ft, almost 50% higher than when mechanical effects were not taken into account. Maximum stress reversal also occurs at a later production time equal to 4.4 months.

It may seem surprising at first that the extent of the stress reversal region significantly decreases at early production times. This phenomenon can be explained by the difference in the stress orientation between poroelastic and mechanical stress reorientation outside the stress reversal region (Fig. 4.2). Immediately after production is started, the direction of maximum stress reorients in the zone just outside the stress reversal region, causing the stress reversal region to shrink (**Fig. 4.4**). It only takes a few hours of production for the direction of maximum stress to fully reorient. Subsequently, the stress reversal region grows back. The partial uncoupling of the flow and stress

calculation exaggerates the shrinkage of the stress reversal region. At late production times, poroelastic stress reorientation decreases, causing the extent of the stress reversal to decrease toward its initial value.

3.3. Effect of the Mobility k/μ

A change in the rock matrix permeability and fluid viscosity only affects the timing of poroelastic effects. This finding is in accordance with the dimensionless formulation of Berchenko and Detournay (1997), where k and μ appear strictly in the expression for the dimensionless time. **Fig. 4.5** shows that the evolution of the extent of the stress reversal region is translated along the time axis when the value of permeability is modified (the opposite trend exists for the viscosity). Poroelastic stress reorientation will be at its maximum at late production times in unconventional gas reservoirs, which are characterized by low mobility values.

3.4. Effect of the Horizontal Stress Contrast and Pressure Drawdown

As **Fig. 4.6** demonstrates, stress reorientation is extremely sensitive to changes in the difference between the in-situ maximum and minimum horizontal stresses. For a stress contrast of 100 psi, the stress reversal region extends up to almost 120 ft away from the wellbore, providing favorable conditions for a successful refracture. Conversely, for stress contrasts higher than 300 psi, the orthogonal propagation of the refracture will be limited to a close vicinity of the wellbore (<60 ft). As it affects both mechanical and poroelastic stress reorientation, the in-situ stress contrast is one of the most important parameters in the evaluation of the extent of stress reversal, and consequently of the potential of refracturing operations in a given field (or given horizontal layer).

Unfortunately, measurements of the deviatoric stress are not common because of their complexity. While the minimum horizontal stress can be routinely measured through a mini-frac test, the maximum horizontal stress is tougher to estimate.

On the other hand, the pressure drawdown affects only production-induced stress reorientation (poroelastic stresses). The sensitivity of the extent of stress reversal to this parameter is thus smaller compared to the stress contrast (**Fig. 4.7**). This is true especially for the base case, for which the contribution of mechanical effects to the stress reversal is close to that of poroelastic effects (respectively L_f'=33 ft against 50 ft, see Fig. 4.3).

3.5. Effect of Mechanical Properties in the Pay Zone

The pay zone's mechanical properties primarily affect stress reorientation induced by the opening of a propped fracture. It is shown in **Fig. 4.8** that more stress contrast is generated in a rock having a low Poisson's ratio. A low Poisson's ratio implies that the deformation in the direction parallel to the fracture is small compared to the deformation along the normal to the fracture. When $\nu_p = 0$, all the deformation occurs along the in-situ direction of minimum horizontal stress, thus maximizing the stress contrast generated.

The net stress applied by the open fracture on the formation is proportional to the Young's modulus. The relationship between Young's modulus and net pressure for a semi-infinite fracture is given in Eq. (4.1) (Palmer 1993). Thus, the stress contrast generated by the fracture increases with the Young's modulus in the pay zone (**Fig. 4.9**).

$$w_0 = \frac{4\left(1-\nu^2\right)}{E} p_{net} h_f \text{ with } p_{net} = p_c - \sigma_{h\min} \tag{4.1}$$

3.6. Effect of Fracture Properties

As can be inferred from Eq. (4.1), the net pressure in the fracture affects stress reorientation in a manner that is similar to the Young's modulus for a semi-infinite fracture. This trend is verified for a finite fracture in **Fig. 4.10**. Contrary to Young's modulus though, fracture width is a controllable parameter. Its positive impact on stress reorientation should be considered in the design of the initial fracture, meaning a fatter fracture could extend stress reversal.

Fracture length is also favorable for generating stress reversal (**Fig. 4.11**). When only poroelastic effects are taken into account, the distance of the isotropic point to the well (L_f') is directly proportional to the fracture length (Siebrits and Elbel 1998). On the other hand, mechanical stress reorientation is much less sensitive to the fracture length. The stress contrast generated by a propped-open fracture is primarily affected by its height (smallest dimension), the fracture aspect ratio L_f/h being a second-order parameter.

Based on **Fig. 4.12**, stress reorientation seems to be higher when the fracture is taller. But when looking separately at mechanical and poroelastic effects, opposite trends are observed. While stress reorientation induced by pressure gradients is increased by the fracture height (Weng and Siebrits 2007), a taller fracture leads to a lower mechanical net pressure (see Eq. (4.1)) and consequently less stress reversal from mechanical effects (see dashed lines in Fig. 4.12). The evolution of stress reorientation with fracture height therefore depends on the relative importance of its mechanical and poroelastic components.

4. PRODUCTION FROM NEIGHBORING WELLS

The impact of the well pattern on the direction of the refracture has been studied previously by Minner et al. (2002) and Singh et al. (2008). An injector is known to attract far-field fractures from neighboring wells, while a producer is known to reorient them away from the producing well.

To analyze the effect of the production of neighboring wells on the stress reorientation profile around a well scheduled for refracturing, we modeled five well configurations shown in **Fig. 4.13**. Depending on the case, some or all of the four wells surrounding the well of interest have a history of prior production. In Section 3.1, we have identified two regions of stress reorientation (a) the stress reversal region and (b) the reoriented stress region. The effect of neighboring well interference on each region is studied below.

4.1. Effect of Well Interference on the Stress Reversal Region

The maximum extent of the stress reversal region and the corresponding optimum time-window for refracturing have been calculated for all cases described in Fig. 4.13 for times of prior neighbor well production equal to 1, 3 and 10 years.

The value of λ_{max} at t = 0 (0.15) corresponds to the base case value of a single producing well (**Fig. 4.14**). The maximum extent of stress reversal decreases as the time of production from neighboring wells increases. This trend is consistent with the sensitivity study in Section 3, which shows that stress reversal decreases when the pressure drawdown decreases. The difference in the areal extent of the stress reversal region is small among all the simulated cases (Fig. 4.14).

Two cases stand out when looking at the impact of non-uniform field depletion on the timing of the refracture (**Fig 4.15**). Cases 3 and 5 display a later time window for

refracturing as a result of field depletion being more pronounced in the direction parallel to the initial fracture than perpendicular to it.

4.2. Effect of Well Interference on the Reoriented Stress Region

So far, the focus has been on quantifying the impacts of reservoir and well properties on the size of the stress reversal region. The current paradigm in refracture reorientation is that the larger the stress reversal region is, the larger the region where the refracture propagates orthogonal to the direction of the original fracture. The location of neighboring wells and production history may impact the direction of propagation outside the stress reversal region as demonstrated in Cases 3, 4 and 5 (**Figs. 4.16 through 4.25**).

The stress distribution in Case 1, with wells producing at the four corners of the reservoir, is similar to the stresses seen around a single producing well (Figs. 4.16 and 4.17). Case 2, in which only the top two wells are producing, also displays a direction of maximum horizontal stress oriented slightly toward the initial fracture (Fig. 4.18). This example seems to indicate that a non-uniform depletion in the direction perpendicular to the initial fracture has little effect on the profile of the direction of maximum horizontal stress.

In Cases 3 to 5, where depletion is non-uniform in the direction parallel to the initial fracture, the direction of maximum horizontal stress is oriented slightly away from the initial fracture. This orientation is more favorable for propagation of the refracture toward less-depleted regions of the reservoir (**Figs. 4.26 and 4.27**).

Thus to enhance the orthogonal propagation of the refracture, it is crucial to (a) maximize the size of the stress reversal region through initial fracture design (fracture length) and timing of the refracture, and (b) create a favorable stress orientation outside

the stress reversal region (which we call reoriented stress region) through improved well placement and fracture design.

5. Incremental Recovery from Refracturing in the Barnett Shale and the Codell Tight Gas Formations

5.1. Evolution of the Stress Reversal Region

The extent and timing of the stress-reversal region were calculated for typical parameters of the Barnett shale and Codell tight gas formations (**Table 4.2**). The numerical simulation of the superposition of mechanical and poroelastic effects is compared to calculations of the poroelastic stress reorientation only (Chapter 2). It must be noted that only single phase gas flow is modeled, and as a result the impact of water produced on stress reorientation (which may be significant in some shales) is not represented.

In the Barnett shale (Weng and Siebrits 2007), stress reversal extends up to 174 feet from the well after 42 months of production (**Fig. 4.28**). Taking into account mechanical effects, the maximum extent of the stress reversal region grows to 213 ft, while the optimum time-window for refracturing is pushed to 58 months. The extent of stress reversal from poroelastic effects is much smaller for the Codell gas well (Wolhart et al. 2007), mainly because of a thinner pay zone (**Fig. 4.29**). Stress reorientation is maximum after little more than a month of production. Clearly, it is impractical to refracture the well after such a short time. However, when superposing mechanical effects to the poroelastic effects, the optimum time window for refracturing is increased to almost 5 months. Also, stress reversal extends over 50 ft from the initial fracture until 60 months of production.

5.2. Geometry of the Refracture

The trajectory of the refracture is simplified to facilitate the modeling of the production from a refractured well (**Fig. 4.30**). The trajectory is split into two main directions of propagation, orthogonal to the initial fracture and parallel to it. As a result, the geometry of the refracture can be described by only two variables. The first variable is the total refrac half-length, which is assumed to be equal to the initial fracture half-length (L_f). The later one is the distance of orthogonal propagation of the refracture. If the refracture was following exactly the direction of maximum horizontal stress, this distance would be equal to the extent of the stress reversal region (L_f'). But as Weng and Siebrits (2007) noted, the fracture only gradually reorients in the direction parallel to the initial fracture when it exits the stress reversal region, as a function of the fracture toughness factor. So in order to take into account the gradual turning of the refracture, an additional portion of orthogonal propagation (equal to 0.5 L_f') is represented.

5.3. Production of a Well Refractured at the Optimum Time

Production from the two field cases (Barnett shale gas and Codell tight gas) was numerically simulated assuming the wells are refractured at the optimum time for refracturing (**Figs. 4.31 and 4.32**). For simplicity, we did not model the presence of proppant in the fracture and refracture, and consequently its impact on the extent of the stress reorientation region. Available field data of the production of a Barnett shale gas well corresponding to the reservoir and fracture properties described in Table 4.2 (Siebrits et al. 2000) fit well the numerically modeled well production (Fig. 4.30). Pore-pressure profiles were calculated just after refracturing, and 1 and 10 years following refracturing (**Figs. 4.33 through 4.38**). By propagating farther orthogonally to the initial fracture, the refracture is in contact with higher pressured rocks in the case of the Barnett

shale compared to the Codell, which will lead to a larger increase in production rates following refracturing (Figs. 4.33 and 4.36). After 10 years of production from both the initial fracture and refracture, it can be seen that the pressure front extends further into the Barnett shale than into the Codell formation (Figs. 4.35 and 4.38), thus adding more reserves.

5.4. Additional Ultimate Recovery from Refracturing

The cumulative production from the refractured wells is compared to what would have been produced by just the initial fracture. In the case of the Codell well, the additional production from refracturing is limited as shown in **Fig. 4.39**. The incremental recovery goes through a maximum a few days after refracturing and quickly goes to zero (**Fig. 4.40**). This is the consequence of a relatively high permeability and a low potential for poroelastic stress reversal. On the other hand, the low matrix permeability of the Barnett shale leads to a slow depletion of the reservoir around the fracture. By propagating the refracture far into less depleted parts of the reservoir, significant production gains are obtained (**Fig. 4.41**). The incremental recovery from refracturing increases with time and even surpasses 50% after 14 years (**Fig. 4.42**).

This final result demonstrates the potential of poroelastic stress reorientation to improve production and reserves, in particular in low permeability reservoirs like shales. It also demonstrates the importance of quantifying poroelastic effects since they may not be so important under some conditions (such as in the Codell formation). It must be noted that pore pressure gradients (poroelastic effects) may not be the main factor responsible for the success of the refracture treatments. Other factors such as a reduction in the conductivity of the original fracture because of solid or liquid buildup may significantly

reduce the effectiveness of the original fracture and lead to the need for a refracture treatment. Mechanical stresses (due to opening of the propped fracture) can also lead to stress reorientation, and have been shown in section 3 to be predominant in the Codell. Taking into account the mechanical effects would lead to much higher values of the incremental recovery in the Codell. The numerical simulations present only a partial picture as they consider only poroelastic stress reorientation and do not consider other potential benefits of refracturing.

6. CONCLUSIONS

A new model to calculate the extent of stress reversal around a producing well has been presented taking into account both the mechanical effects associated with the opening of the initial fracture and the poroelastic effects associated with fluid production. It was shown that in unconventional gas reservoirs (tight or shale gas), both mechanical and poroelastic effects contribute significantly to stress reorientation. The addition of the stress contribution from rock deformation due to fracture creation changed the predicted value of both the extent of stress reversal and the optimum time for refracturing.

The net effect of production-induced and deformation-induced stress reorientation may differ significantly from one field to another. Typically, mechanical effects will be predominant in reservoirs having a thin pay zone, high Young's modulus and low pressure drawdown. Mechanical stress reorientation can be enhanced by increasing the width of the initial fracture. Conversely, poroelastic stress reorientation will be important in reservoirs featuring a high pressure drawdown and a tall pay zone. Finally, a low in-situ stress contrast and a long initial fracture will favor both poroelastic and mechanical stress reorientation.

Production from neighboring wells may also impact the stress reorientation profile around a well of interest. If the stress reversal region is mostly not affected, the reoriented stress region located outside the stress reversal region will direct the refracture away from the initial fracture when the field is more depleted in the direction parallel to the first fracture than perpendicular to it.

Thus, the propagation of the refracture away from the initial fracture can be improved by (a) maximizing the size of the stress reversal region through initial fracture design (fracture length) and timing of the refracture, and (b) creating a favorable stress orientation outside in the reoriented stress region through improved field design and production schedule.

The proposed numerical model can also be used to estimate incremental production from refracturing. The potential of the refracturing technique to add production and reserves was demonstrated in very-low-permeability reservoirs such as shales. Incremental recoveries of more than 50% may be achieved, only taking into consideration poroelastic stress reorientation.

	Poroelastic stress reorientation	Mechanical stress reorientation
Permeability k	Timing only	None
Viscosity μ	Timing only	None
Pay zone Young's Modulus E_p	+	++
Pay zone Poisson's Ratio ν_p	-	--
Porosity ϕ	None	None
Wellbore pressure p_{wf}	--	None
Reservoir pressure p_R	++	None
Deviatoric stress $\sigma_{hmax} - \sigma_{hmin}$	++	++
Fracture half-height h_f	+++	---
Fracture half-length L_f	+++	++
Maximum fracture width w_0	None	+++

A "+" sign means that stress reorientation increases when the parameter's value is increased.

Table 4.1 – Effects of fracture and reservoir parameters on poroelastic and mechanical effects

	Base case tight gas	Codell tight gas (Wolhart et al. 2007)	Barnett shale gas (Weng et al. 2007)
Permeability k (md)	0.01	0.05	0.0034
Pay zone Young's Modulus E_p (psi)	$4x10^6$	$4x10^6$	$7.3x10^6$
Bounding layer Young's Modulus E_b (psi)	$4x10^6$	$3x10^6$	$3x10^6$
Poisson's Ratio ν	0.25	0.2	0.2
Porosity ϕ	0.1	0.14	0.05
Compressibility (1/psi)	$2x10^{-4}$	$3x10^{-4}$	$3x10^{-4}$
Viscosity μ (cp)	0.0`2	0.02	0.02
Wellbore pressure p_{wf} (psi)	1000	500	500
Reservoir pressure p_R (psi)	4000	4500	3500
σ_{hmax} (psi)	4600	6000	6400
σ_{hmin} (psi)	4500	5900	6300
Depth (ft)	8000	7500	7000
Fracture half-height h_f (ft)	50	10	142
Fracture half-length L_f (ft)	500	500	600

Table 4.2 – Reservoir and fracture parameters for the base case of the sensitivity study, a Codell tight gas well in the Wattenberg field, and a Barnett shale gas well

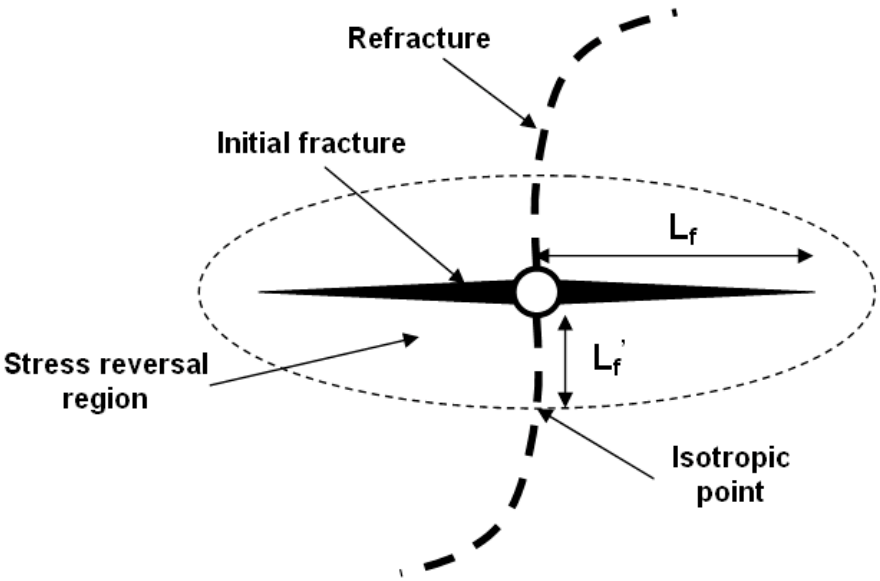

Fig. 4.1 – Flow-induced stress reversal and refracture direction

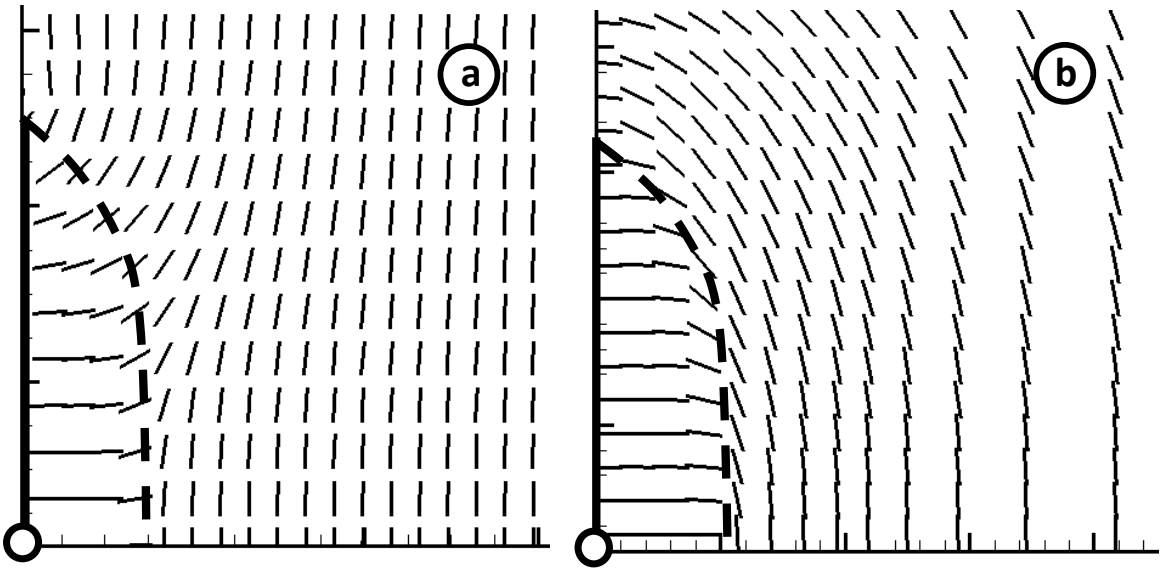

Fig. 4.2 – Profile of the direction of maximum horizontal stress around a vertical fracture from (a) mechanical effects and (b) poroelastic effects

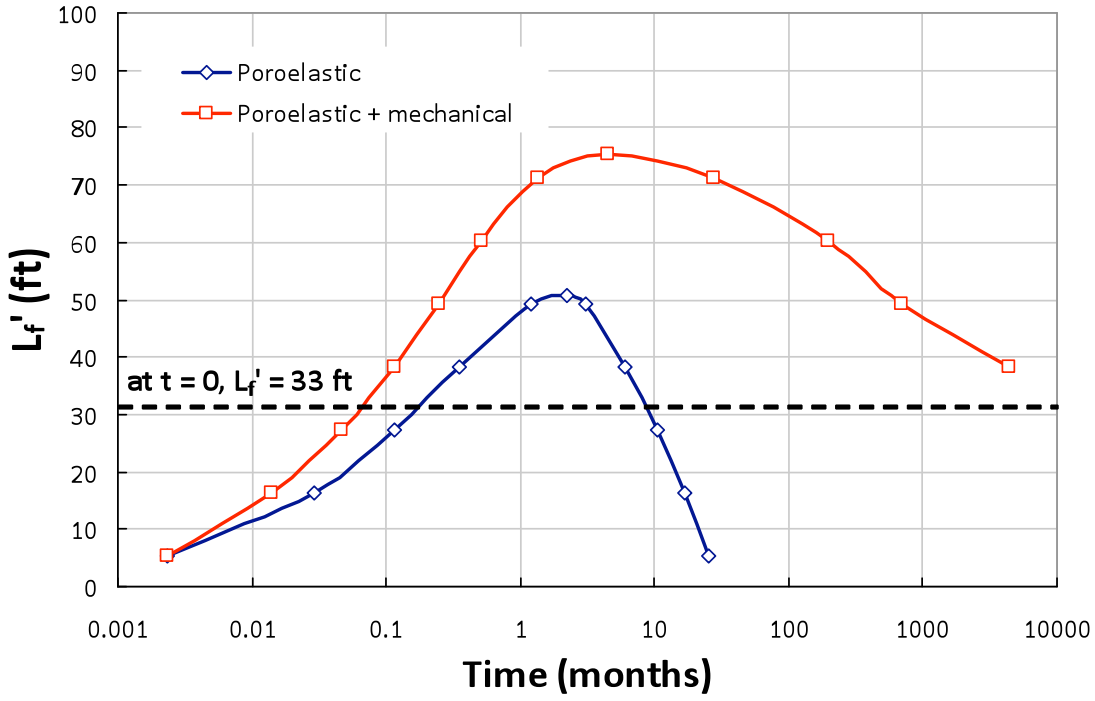

Fig. 4.3 – Extent of stress reversal (L_f') versus production time for the base case

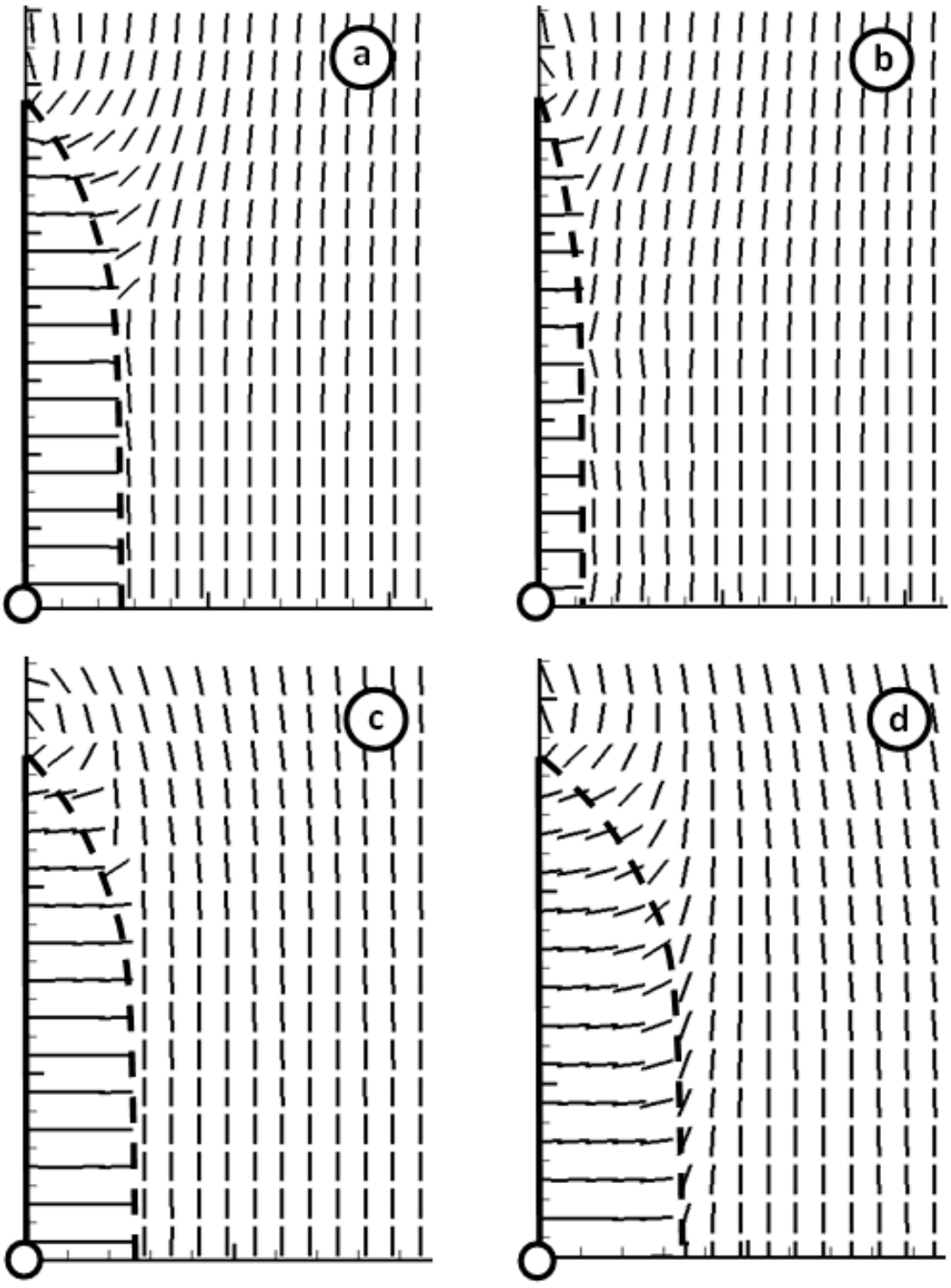

Fig. 4.4 – Evolution of the direction of maximum horizontal stress at early production times (a) t = 0, (b) t = 1 day, (c) t = 21 days and (d) t = 3.5 months

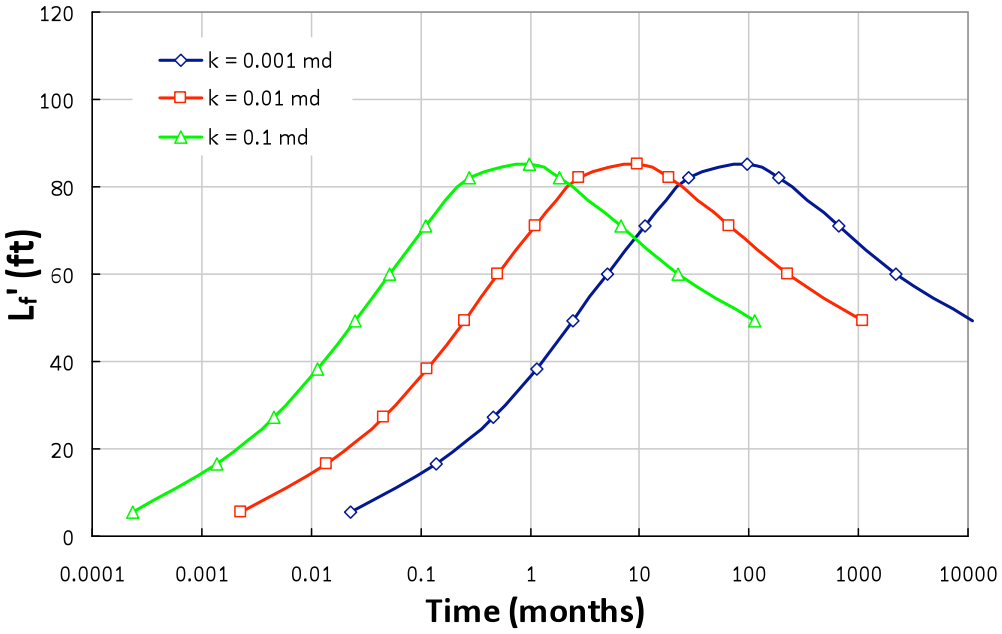

Fig. 4.5 – Effect of the permeability of the rock matrix on the extent of stress reversal (L_f') versus production time

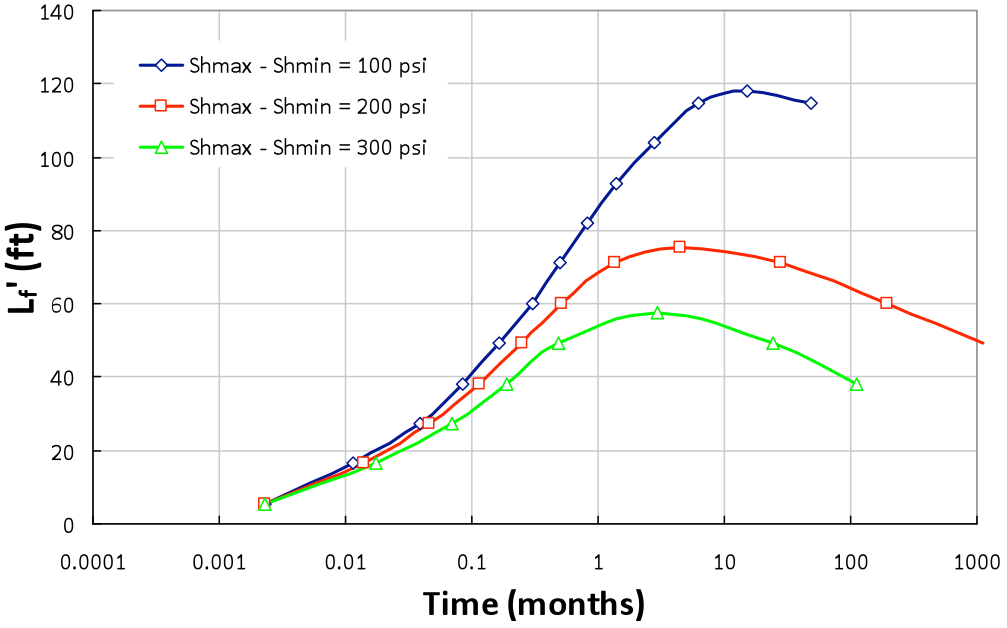

Fig. 4.6 – Effect of the deviatoric stress on the extent of stress reversal (L_f') versus production time

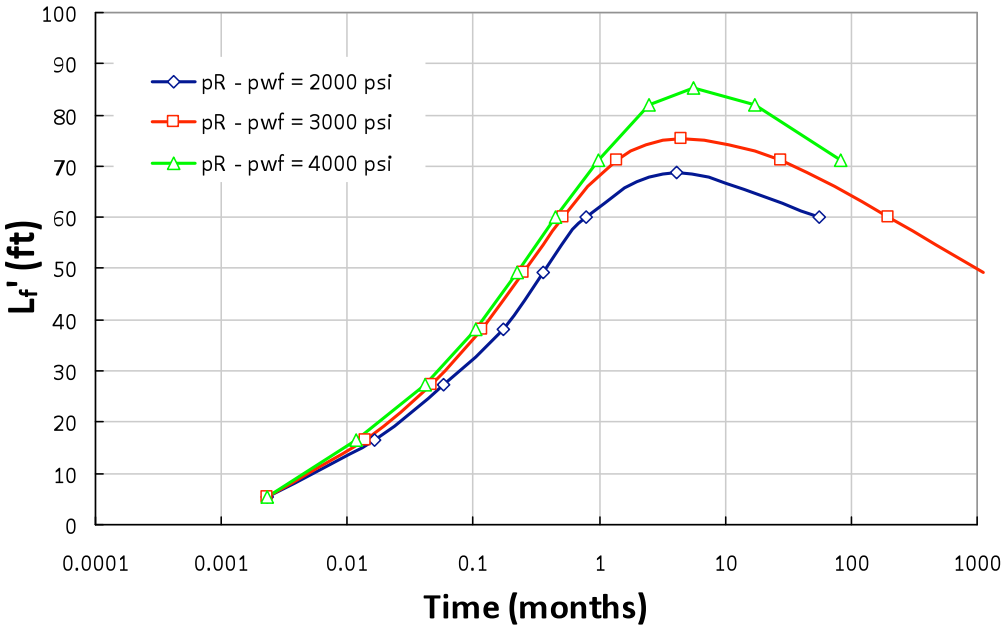

Fig. 4.7 – Effect of the pressure drawdown on the extent of stress reversal (L_f') versus production time

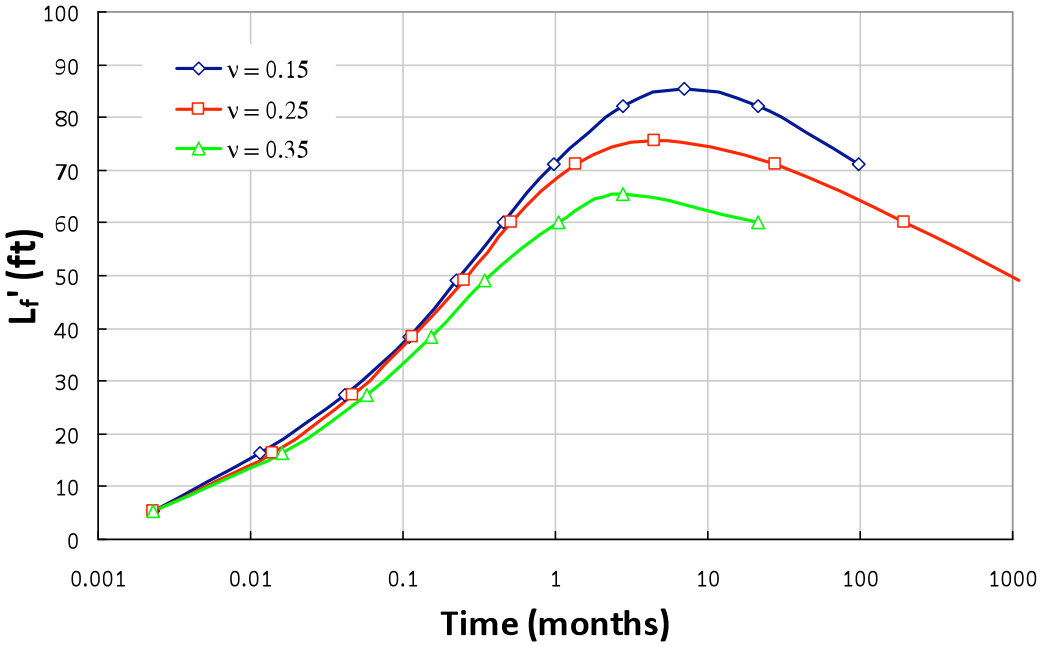

Fig. 4.8 – Effect of the rock's Poisson's ratio on the extent of stress reversal (L_f') versus production time

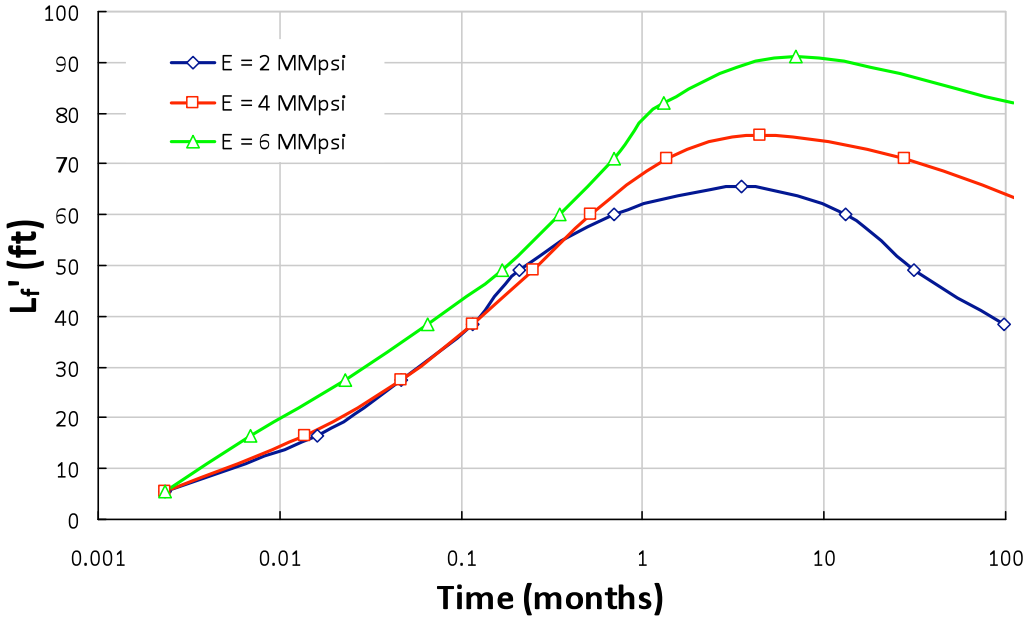

Fig. 4.9 – Effect of the rock's Young's modulus on the extent of stress reversal (L_f') versus production time

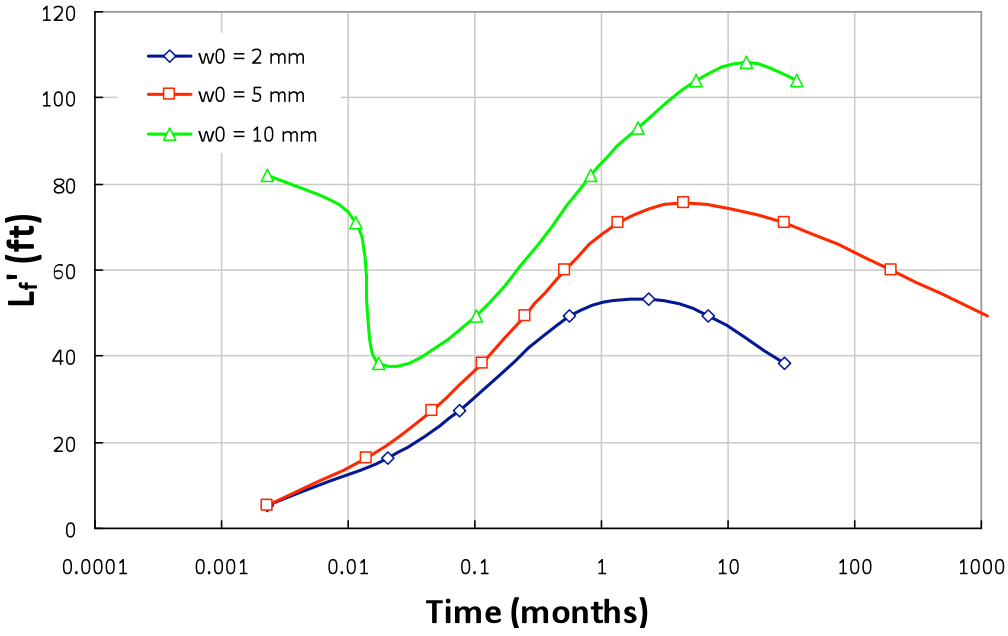

Fig. 4.10 – Effect of the maximum fracture width w_0 on the extent of stress reversal (L_f') versus production time

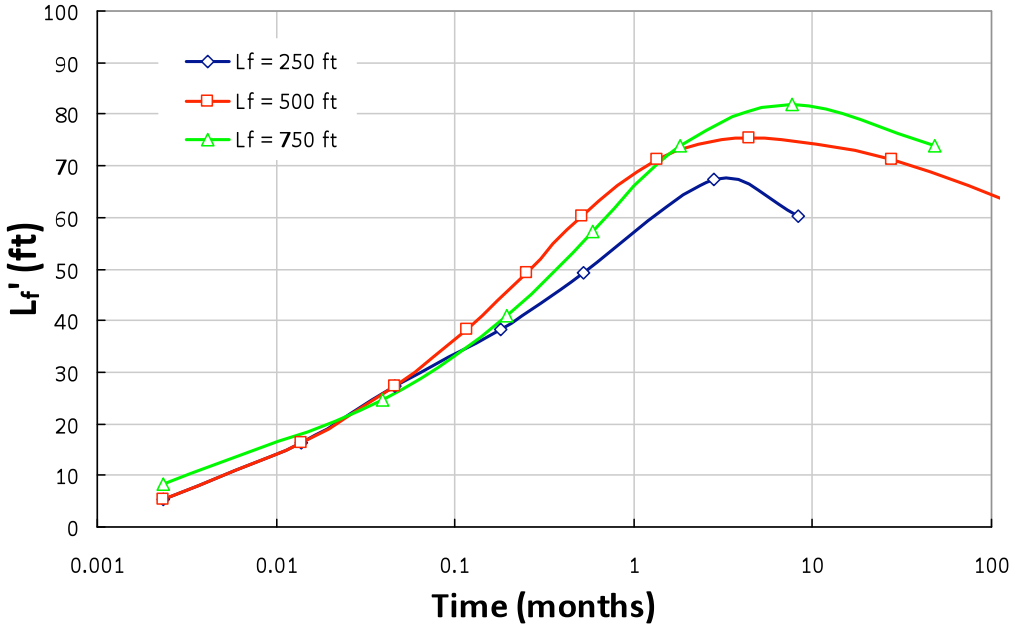

Fig. 4.11 – Effect of the fracture length L_f on the extent of stress reversal (L_f') versus production time

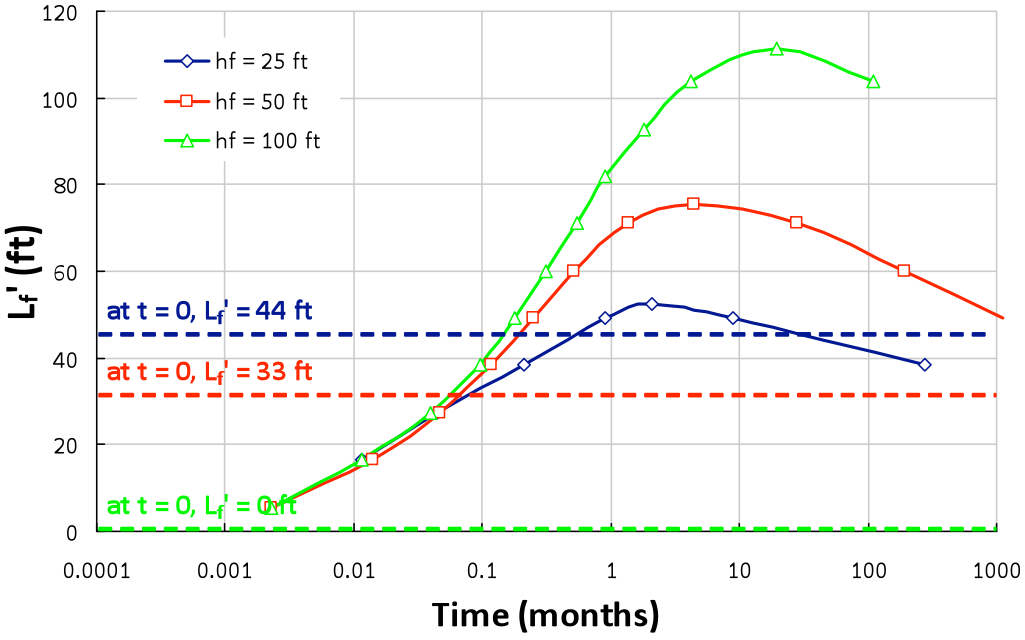

Fig. 4.12 – Effect of the fracture half-height h_f on the extent of stress reversal (L_f') versus production time

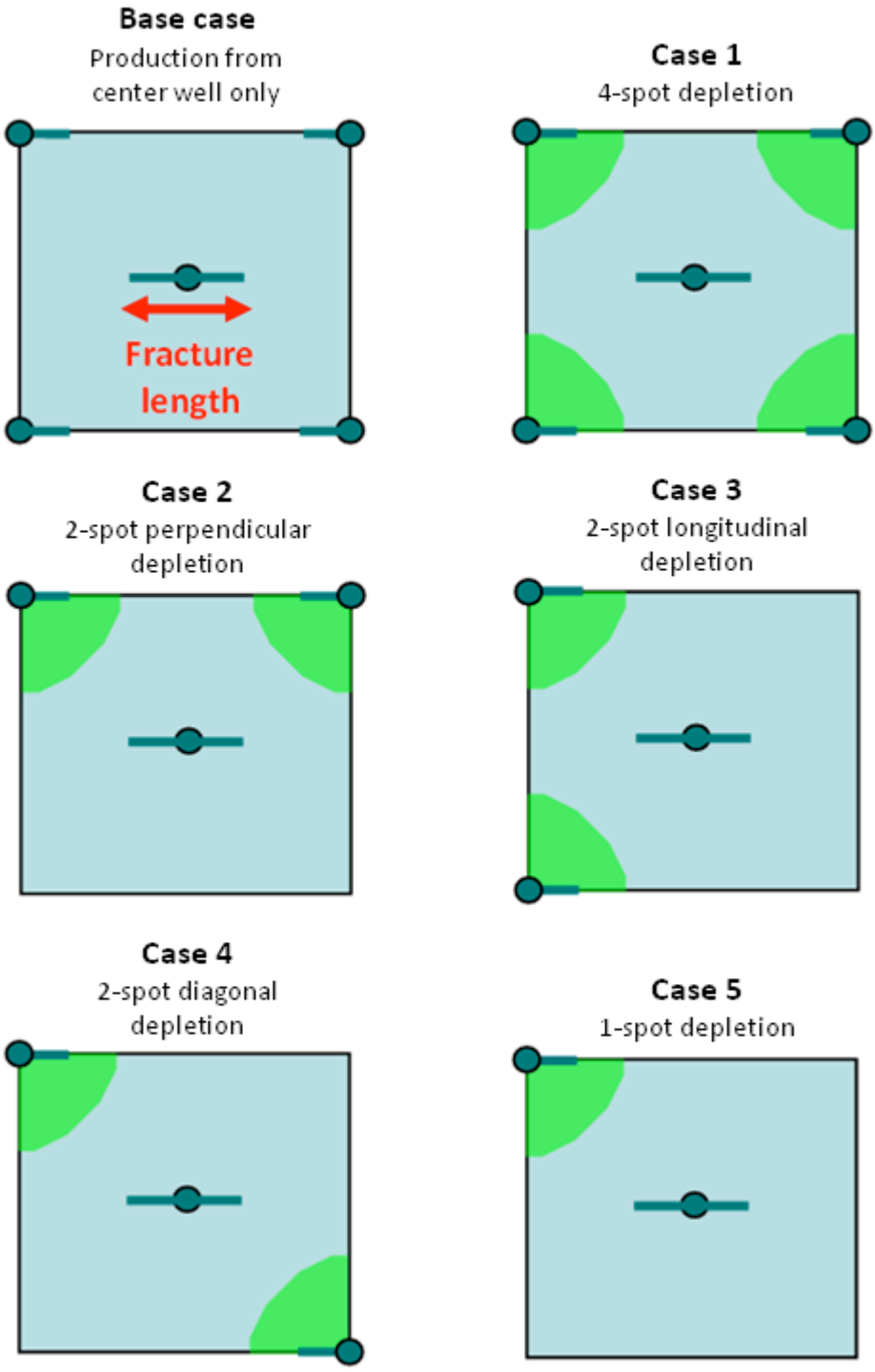

Fig. 4.13 – Well configurations modeled in the study of the effect of production from neighboring wells on stress reorientation

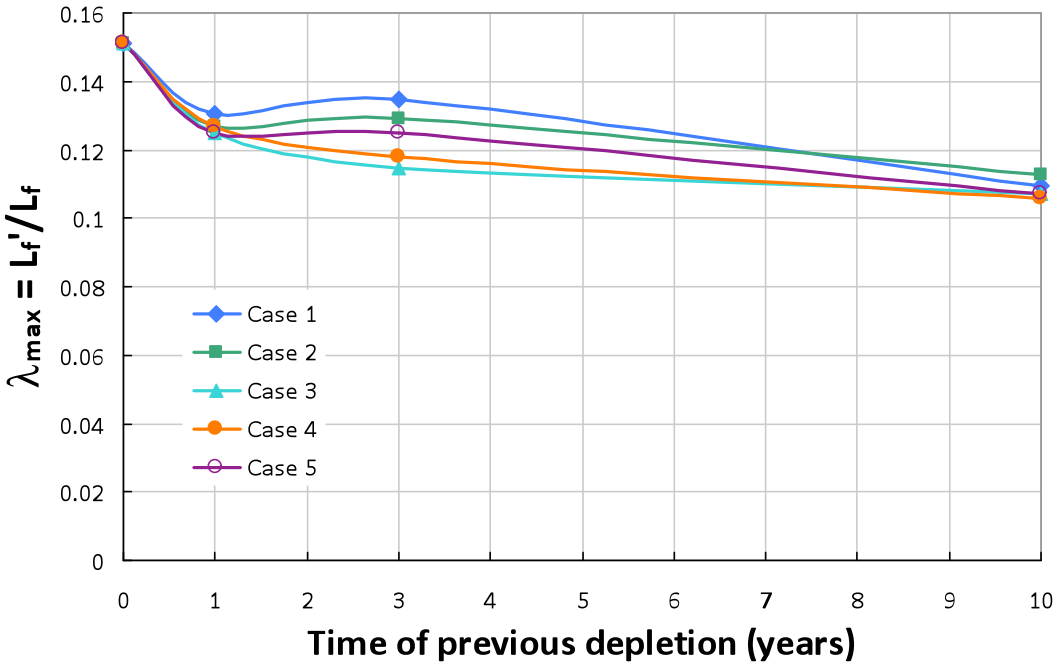

Fig. 4.14 – Effect of well interference on the extent of the stress reversal region

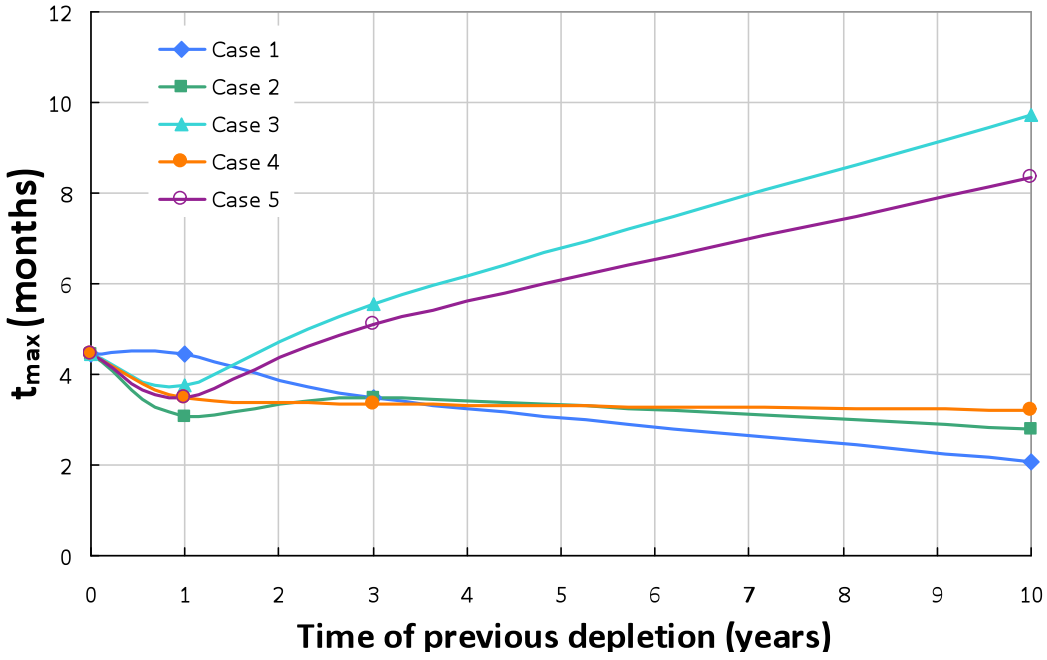

Fig. 4.15 – Effect of well interference on the timing of the stress reversal region

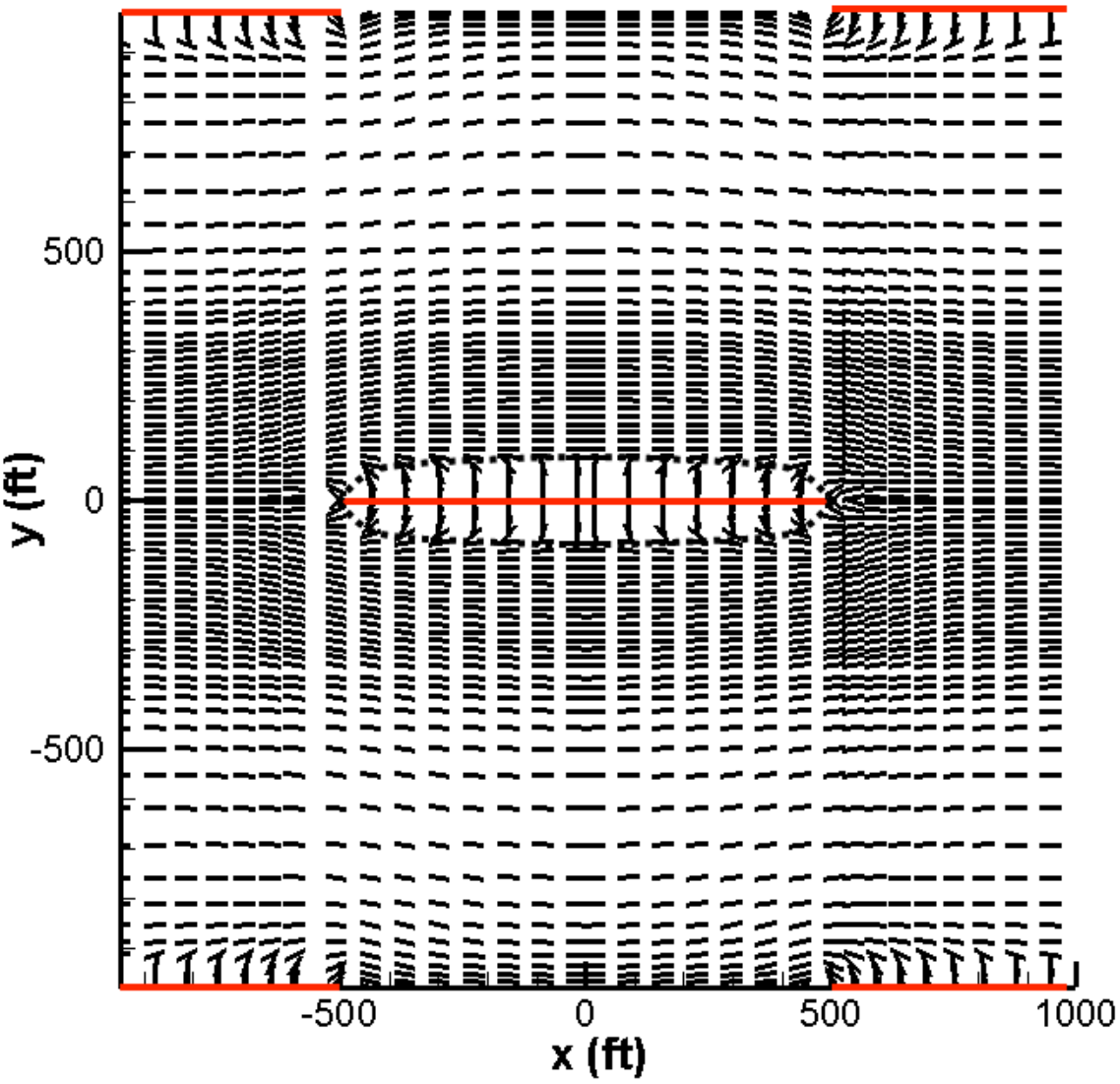

Fig. 4.16 – Direction of maximum horizontal stress at the optimum time for refracturing (Case 1, 3 years of previous depletion)

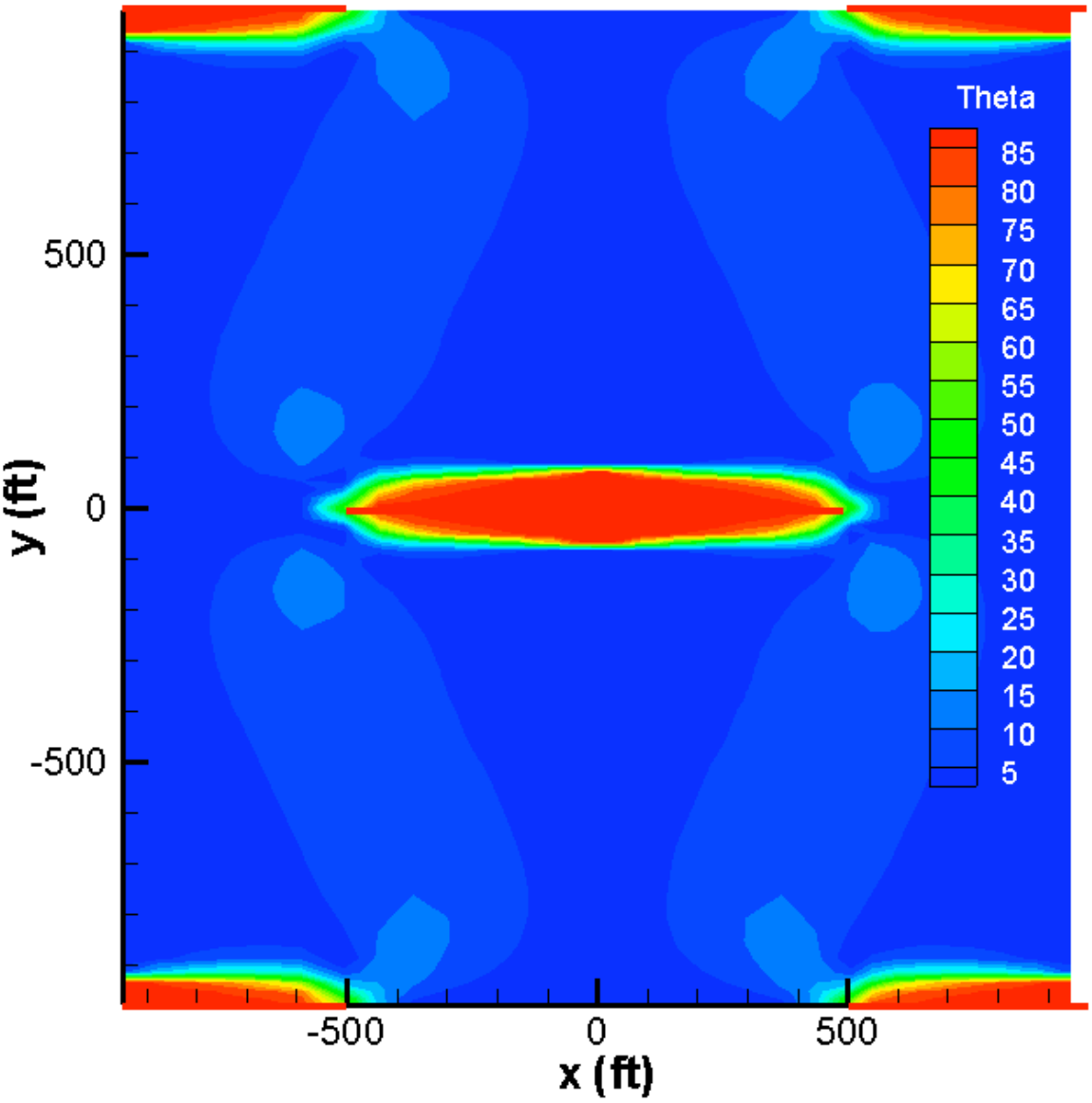

Fig. 4.17 – Angle of stress reorientation at the optimum time for refracturing (Case 1, 3 years of previous depletion)

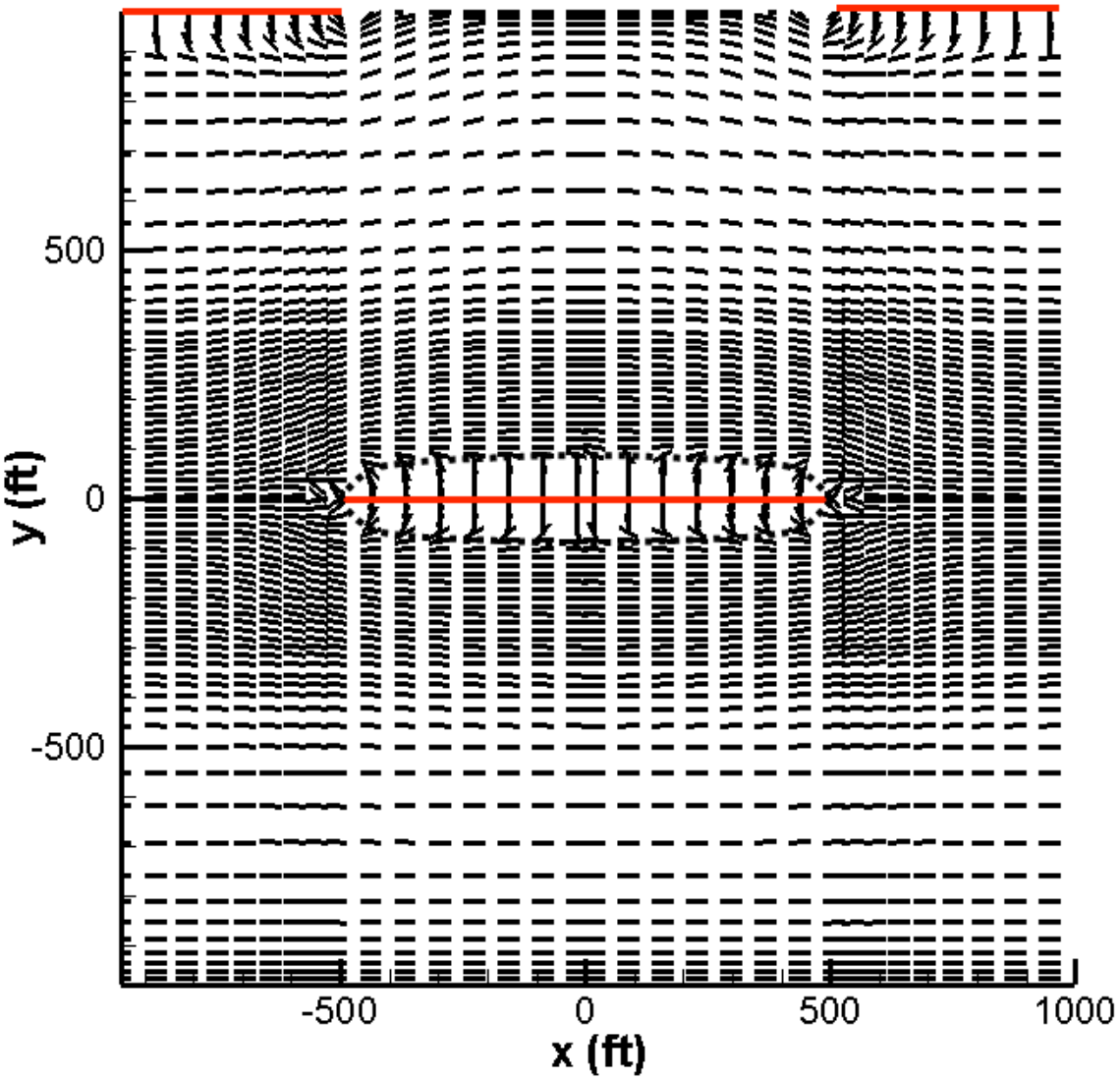

Fig. 4.18 – Direction of maximum horizontal stress at the optimum time for refracturing (Case 2, 3 years of previous depletion)

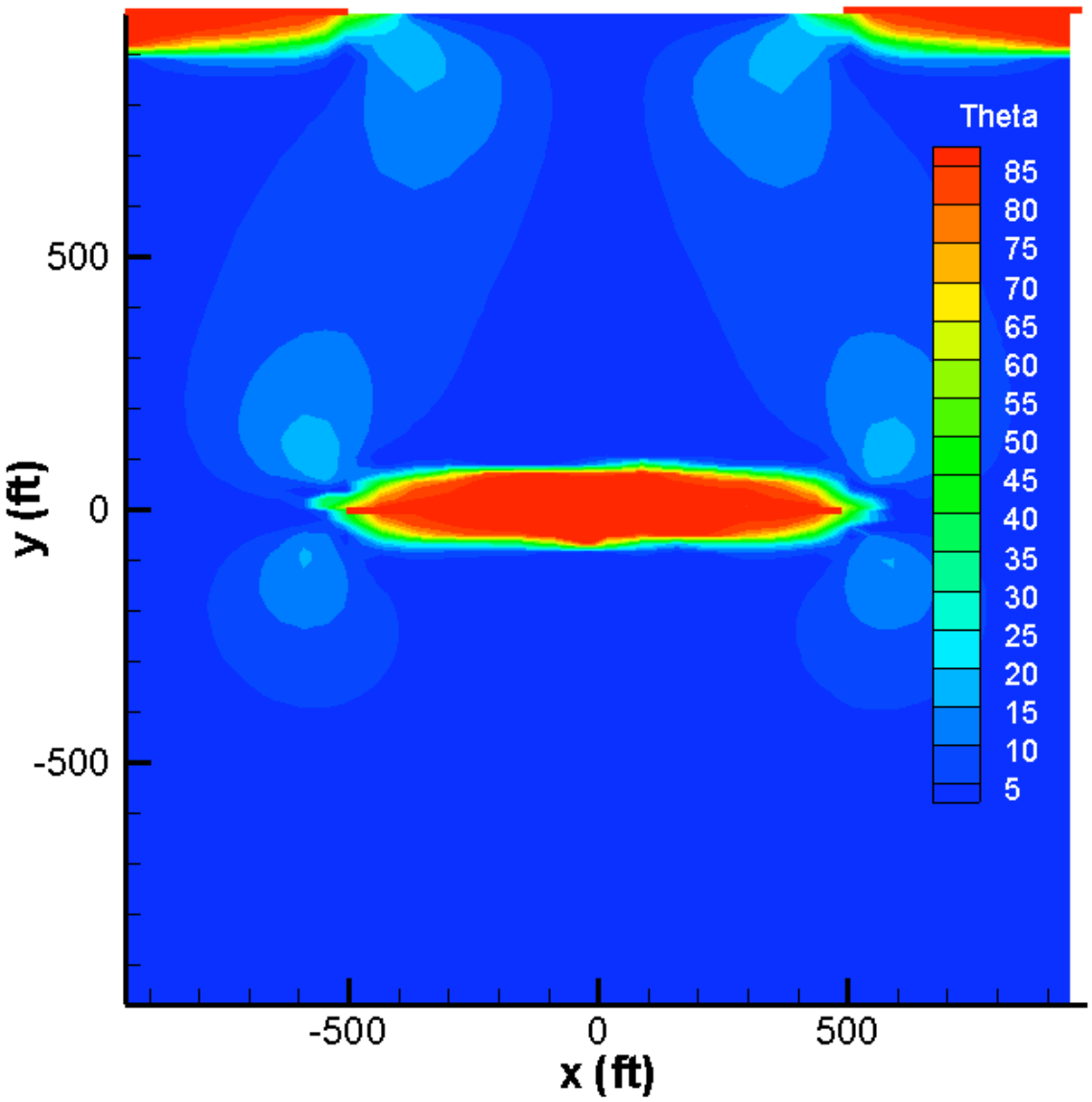

Fig. 4.19 – Angle of stress reorientation at the optimum time for refracturing (Case 2, 3 years of previous depletion)

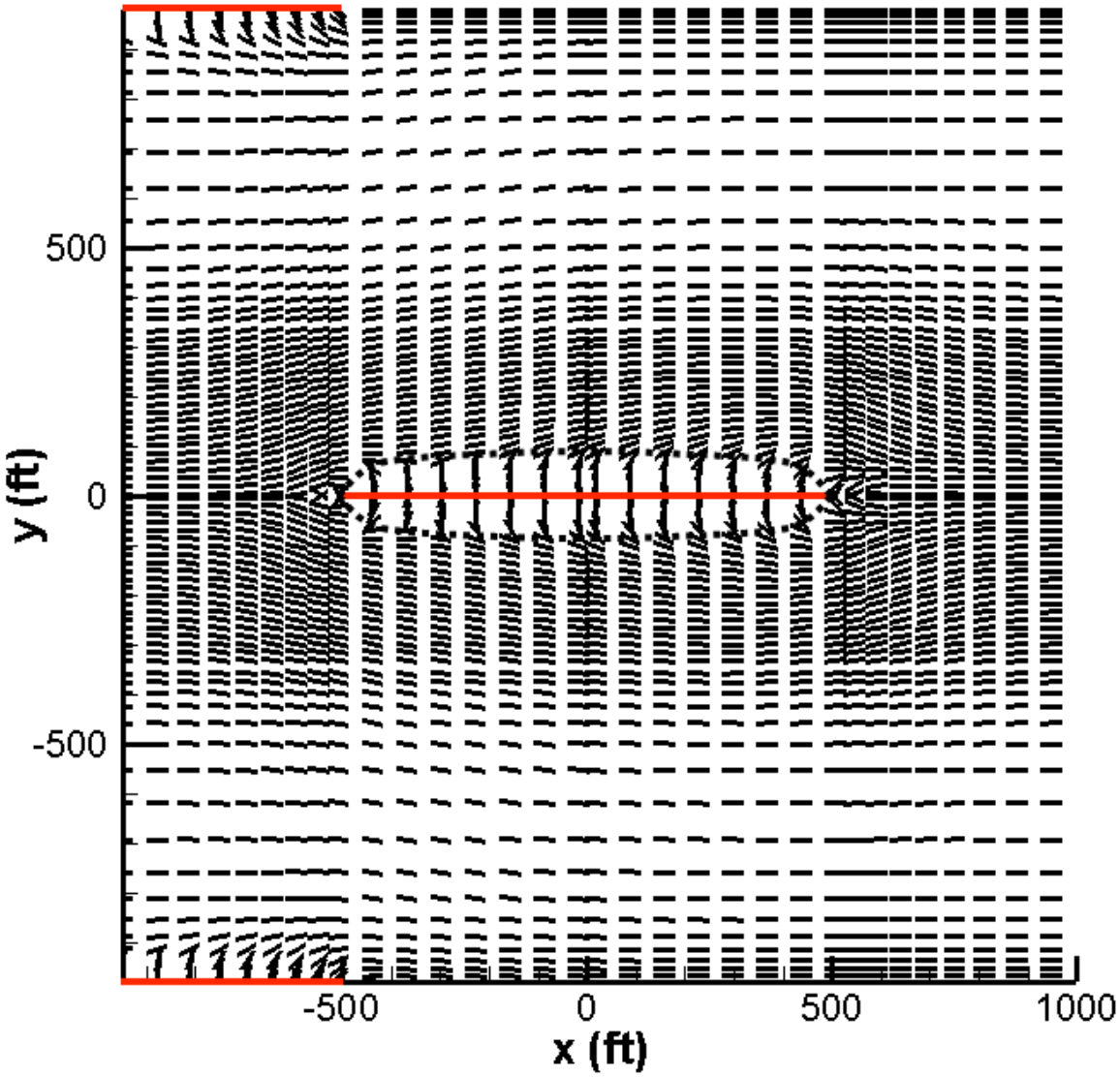

Fig. 4.20 – Direction of maximum horizontal stress at the optimum time for refracturing (Case 3, 3 years of previous depletion)

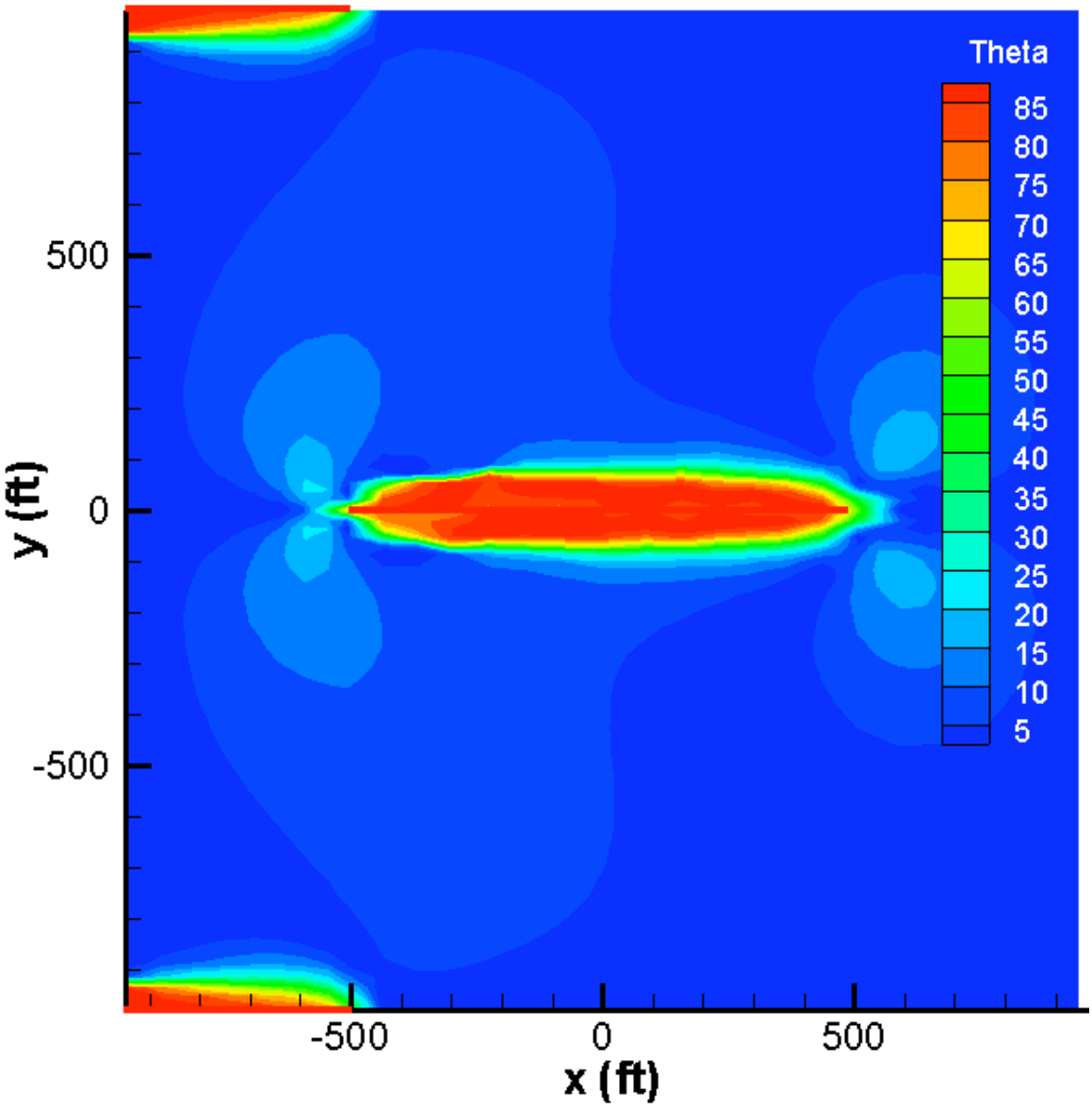

Fig. 4.21 – Angle of stress reorientation at the optimum time for refracturing (Case 3, 3 years of previous depletion)

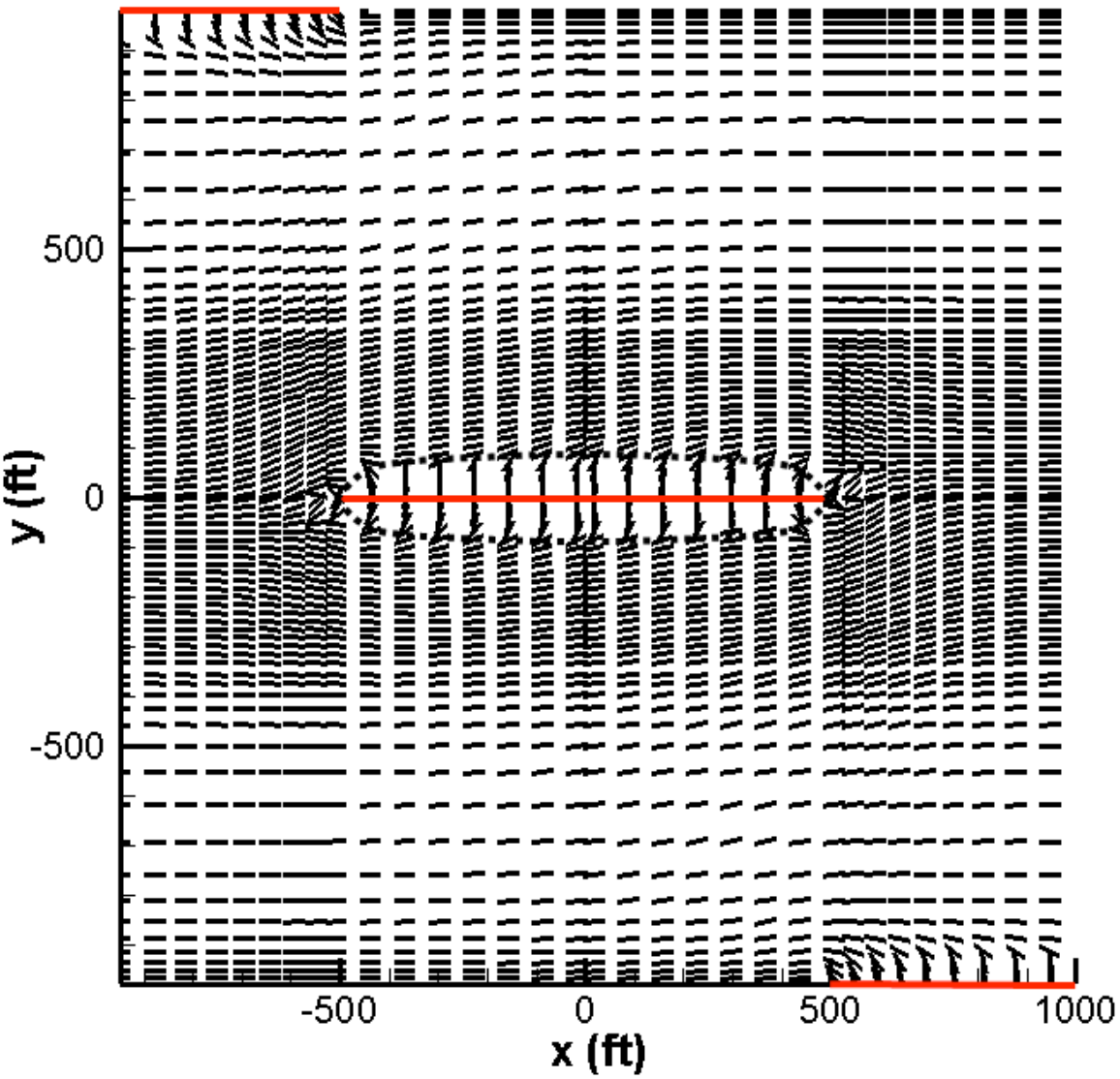

Fig. 4.22 – Direction of maximum horizontal stress at the optimum time for refracturing (Case 4, 3 years of previous depletion)

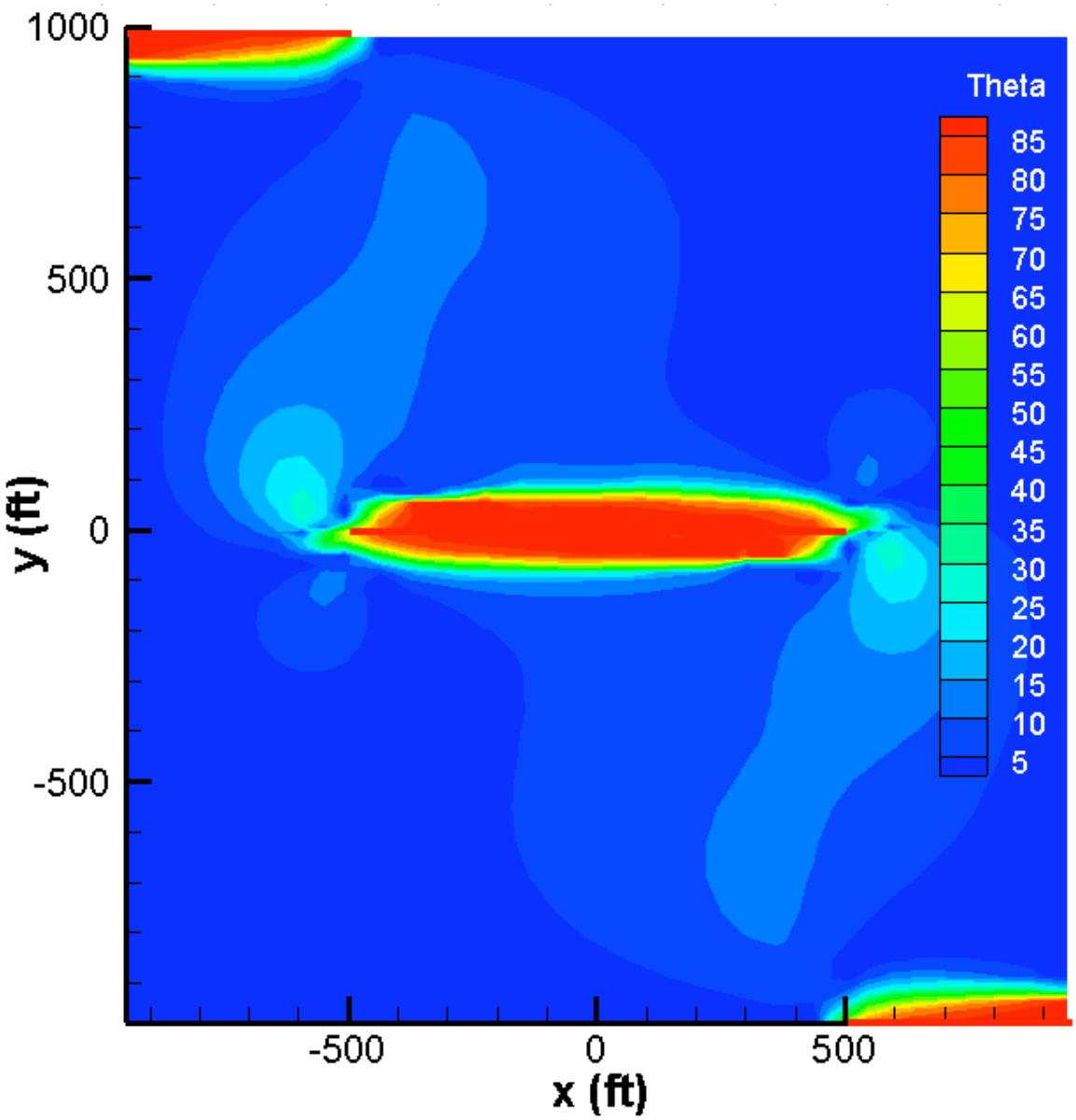

Fig. 4.23 – Angle of stress reorientation at the optimum time for refracturing (Case 4, 3 years of previous depletion)

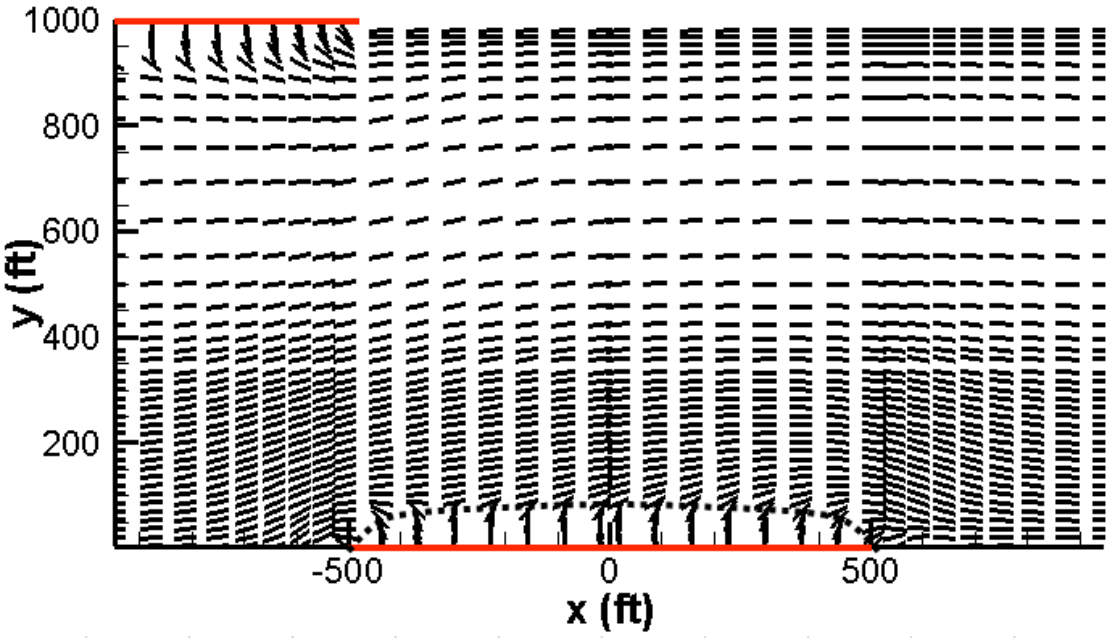

Fig. 4.24 – Direction of maximum horizontal stress at the optimum time for refracturing (Case 5, 3 years of previous depletion)

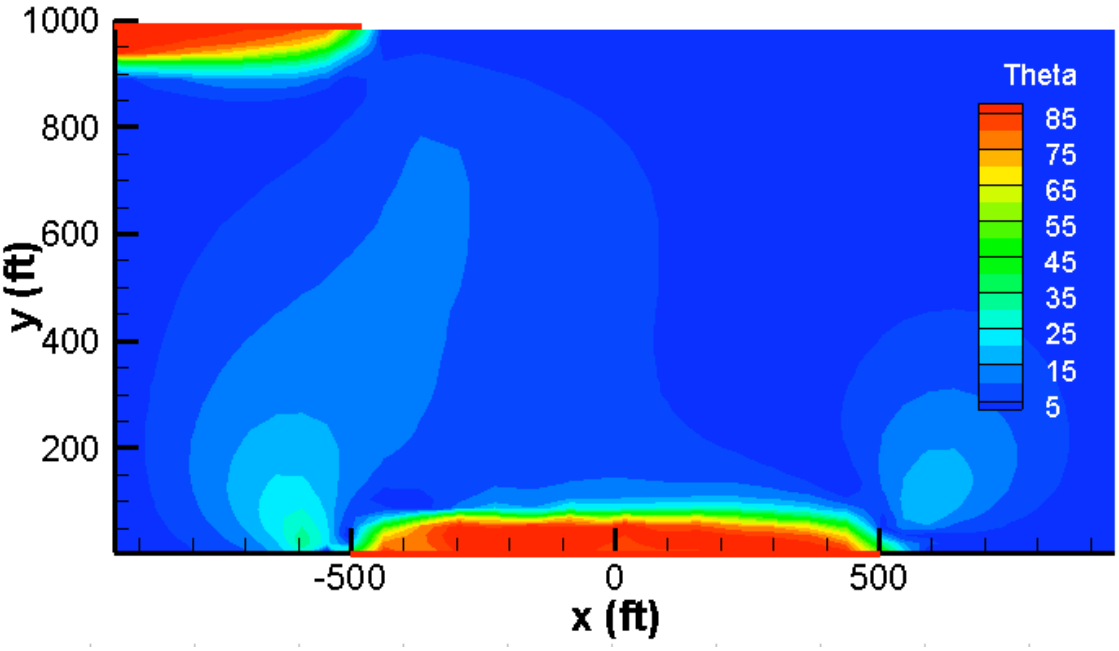

Fig. 4.25 – Angle of stress reorientation at the optimum time for refracturing (Case 5, 3 years of previous depletion)

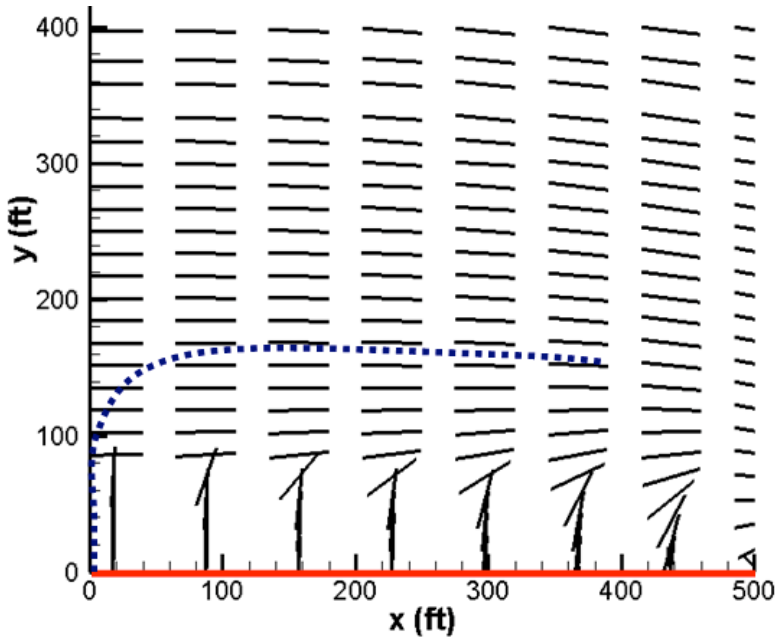

Fig. 4.26 – Impact of the reoriented stress region on the propagation direction of a refracture (Case 1)

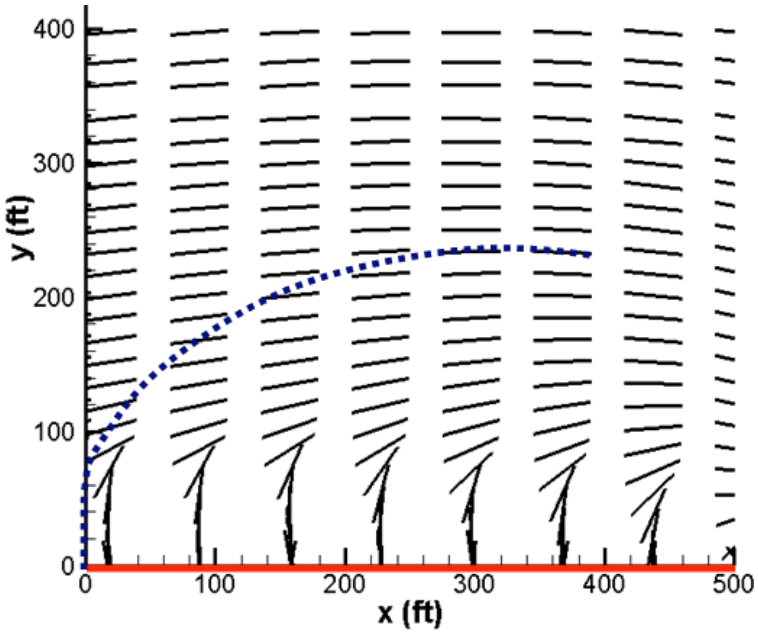

Fig. 4.27 – Impact of the reoriented stress region on the propagation direction of a refracture (Case 3)

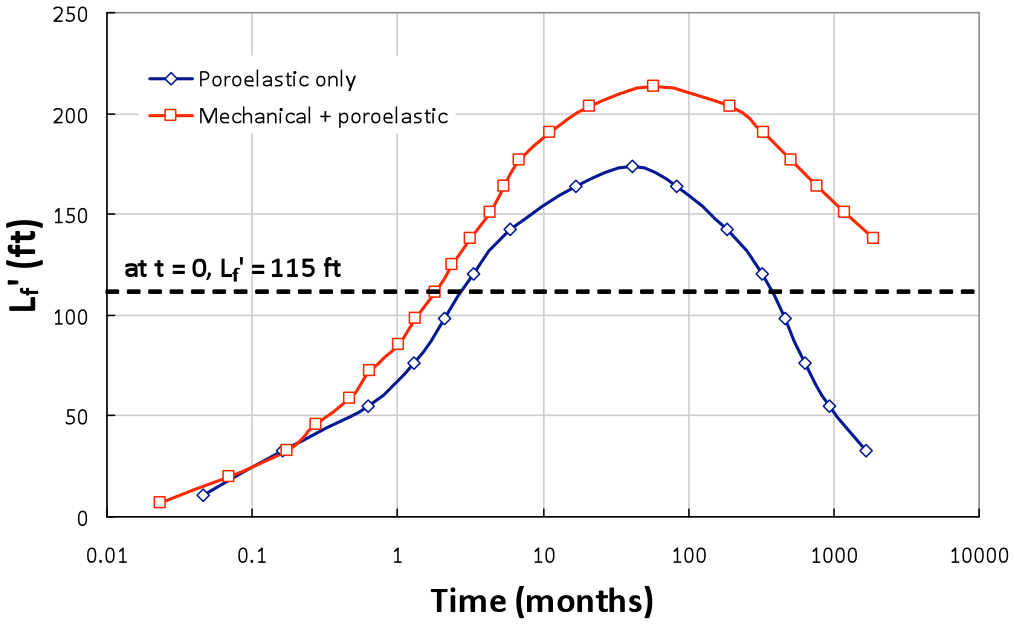

Fig. 4.28 – Extent of stress reversal (L_f') versus production time for a Barnett shale gas well

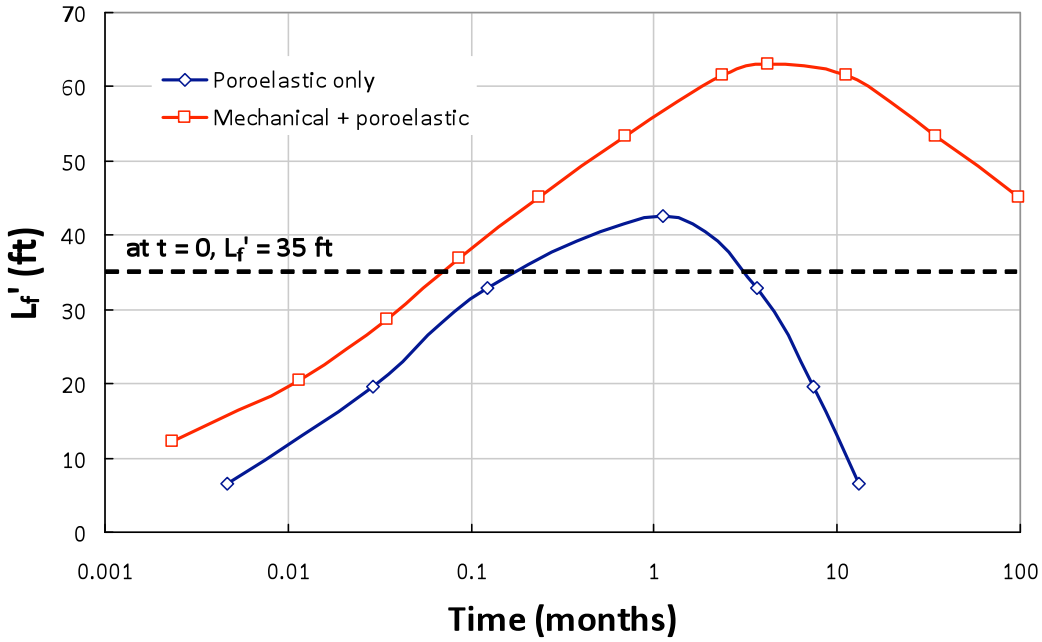

Fig. 4.29 – Extent of stress reversal (L_f') versus production time for a Codell tight gas well in the Wattenberg field

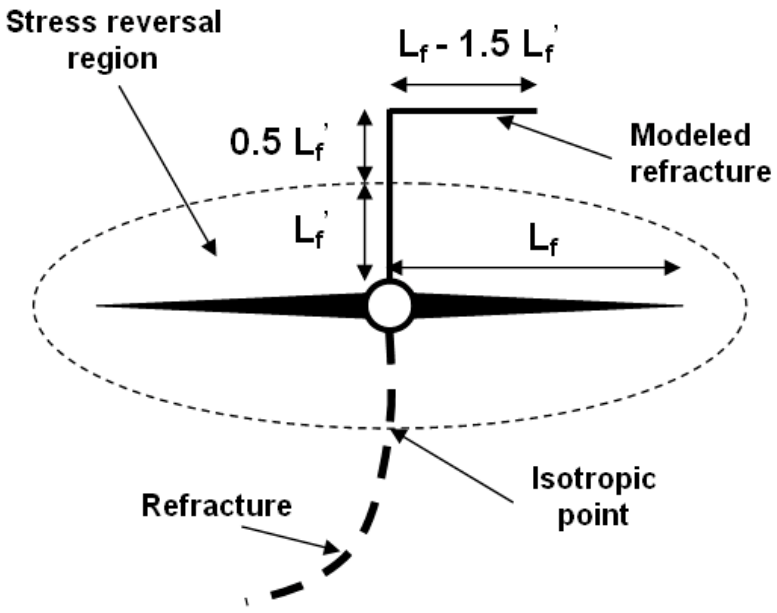

Fig. 4.30 – Refracture model based on the size of the stress reversal region

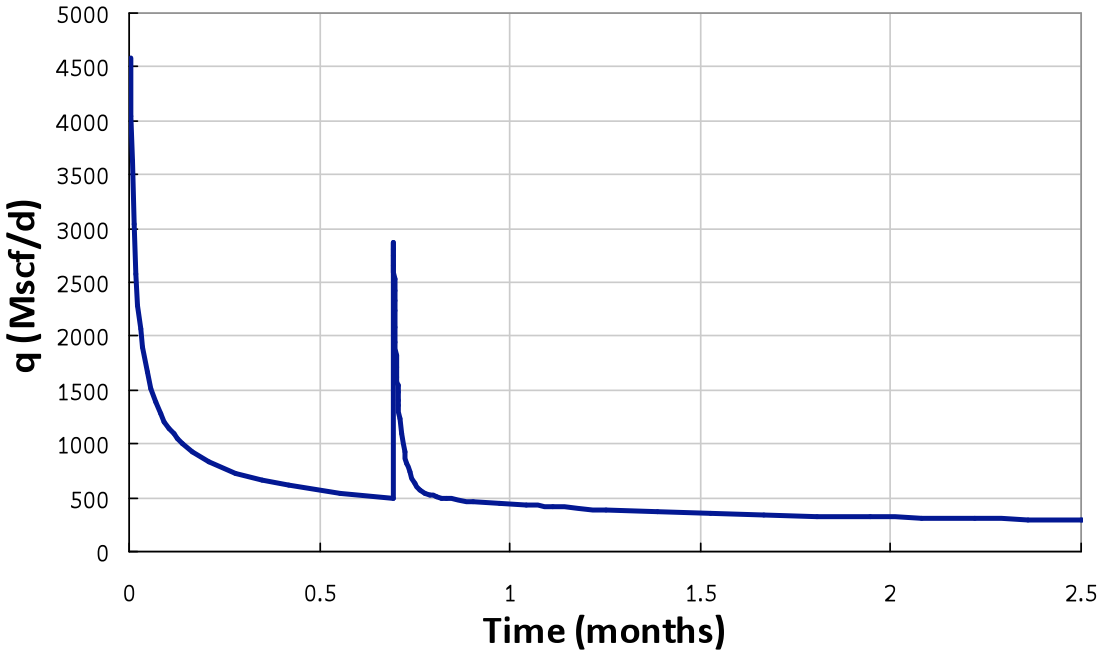

Fig. 4.31 – Simulated production for a Codell tight gas well refractured at optimum time

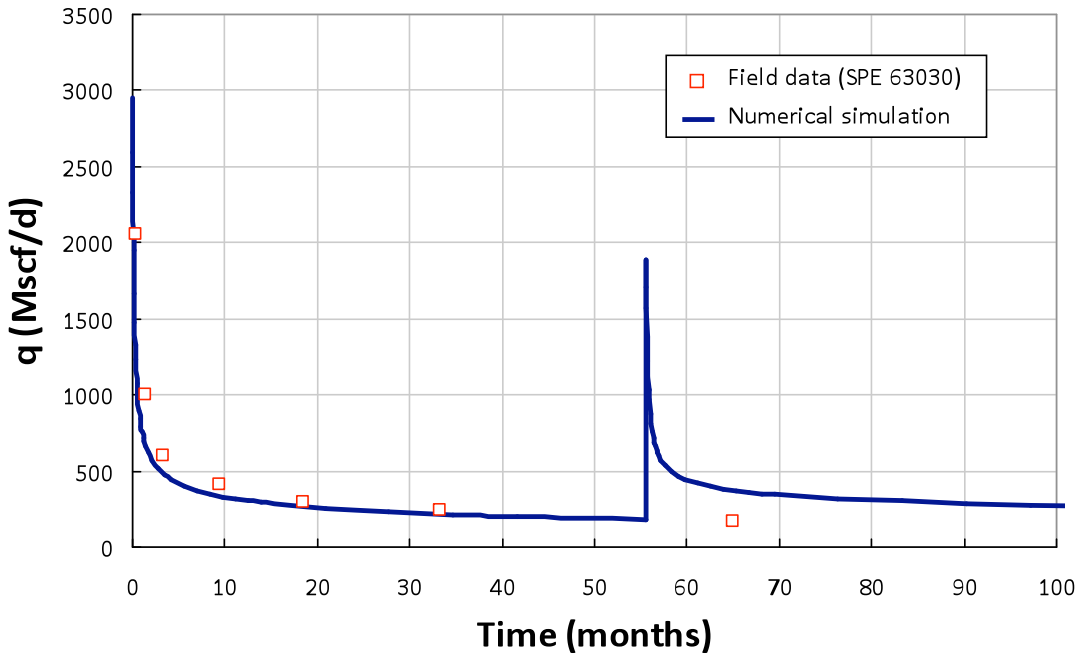

Fig. 4.32 – Simulated production for a Barnett shale gas well refractured at optimum time

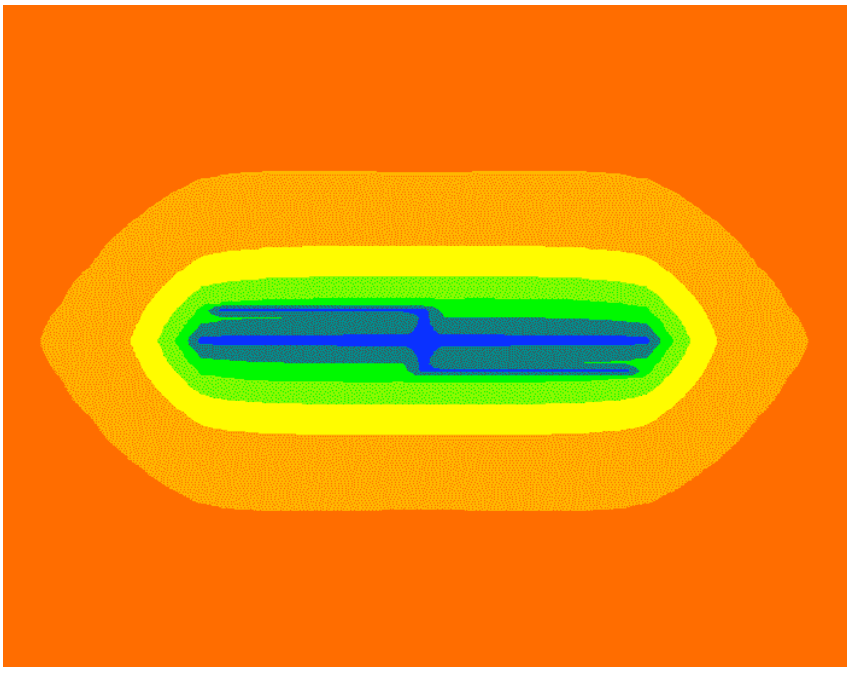

Fig. 4.33 – Pore pressure distribution around a Codell tight gas well after refracturing

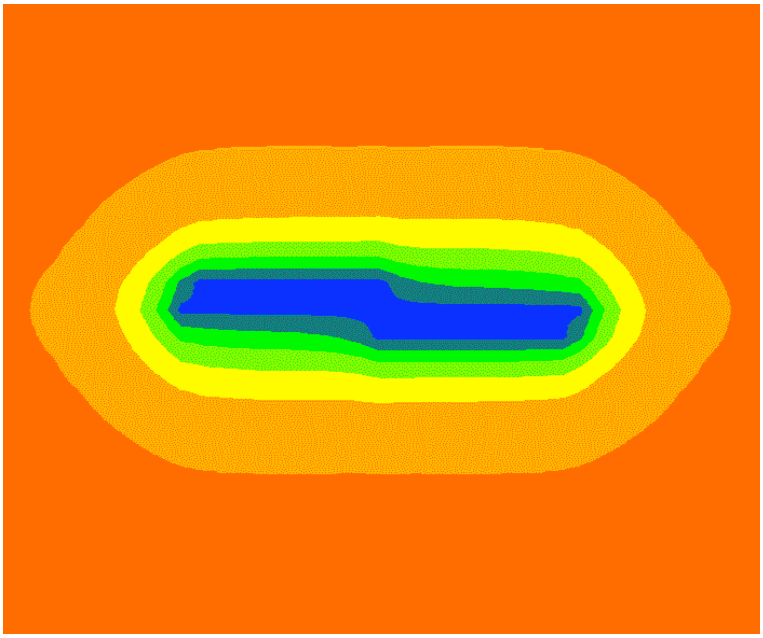

Fig. 4.34 – Pore pressure distribution around a Codell tight gas well 1 year after refracturing

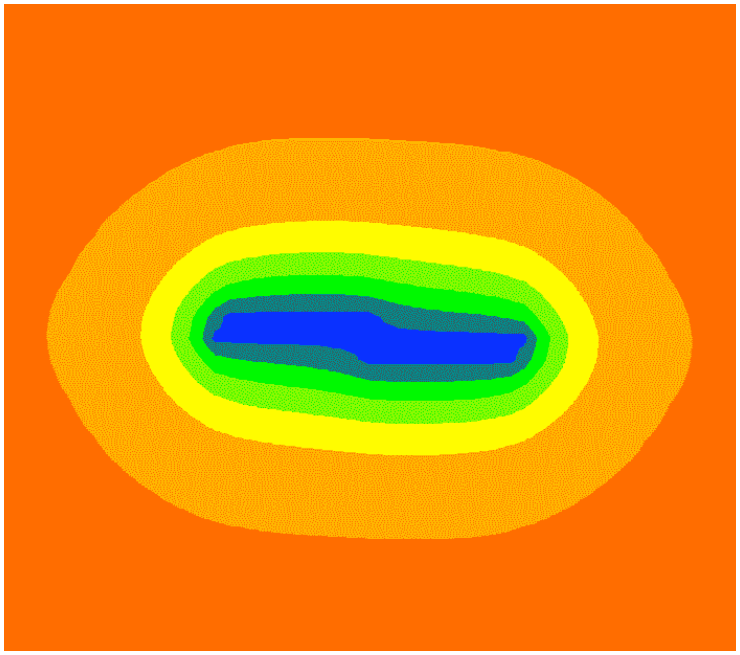

Fig. 4.35 – Pore pressure distribution around a Codell tight gas well 10 years after refracturing

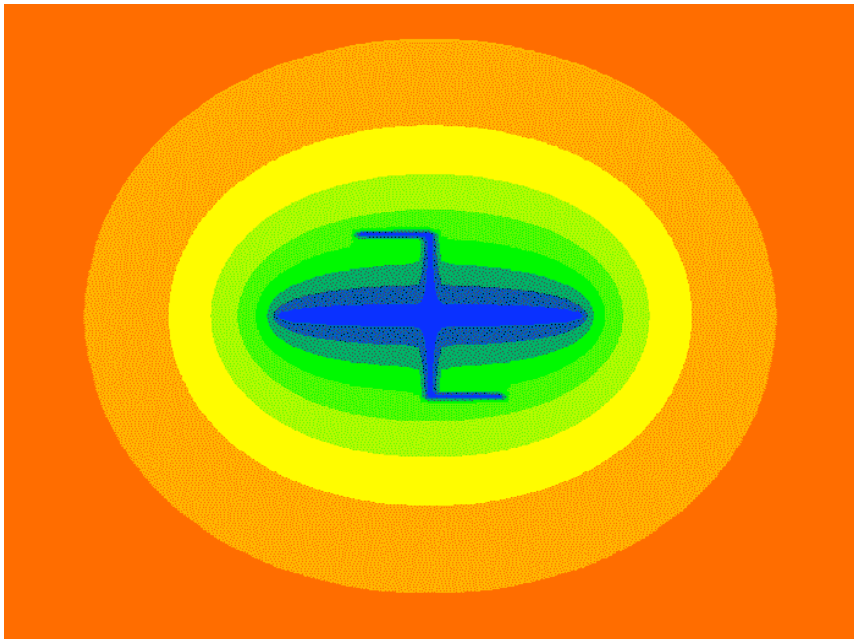

Fig. 4.36 – Pore pressure distribution around a Barnett shale gas well after refracturing

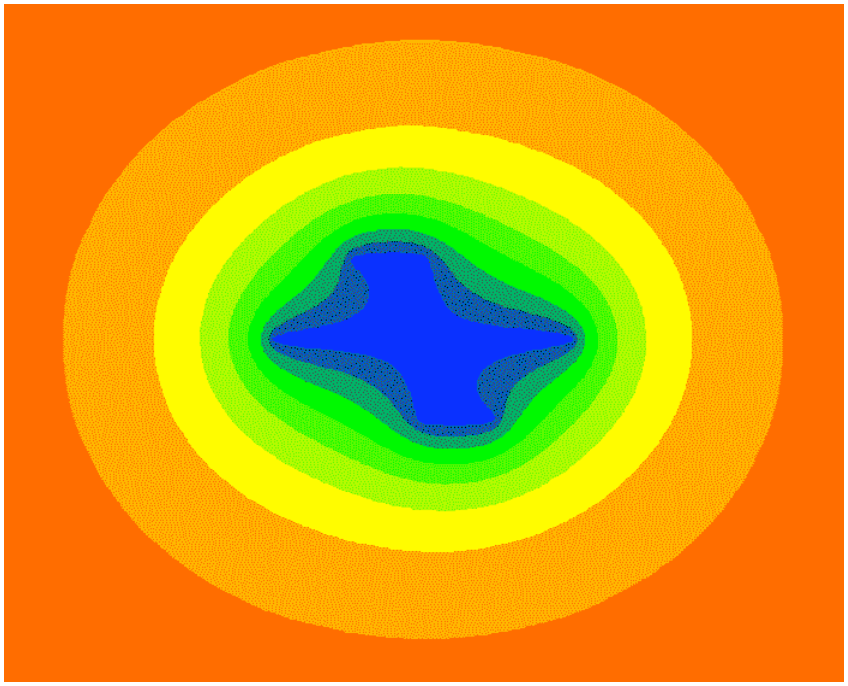

Fig. 4.37 – Pore pressure distribution around a Barnett shale gas well 1 year after refracturing

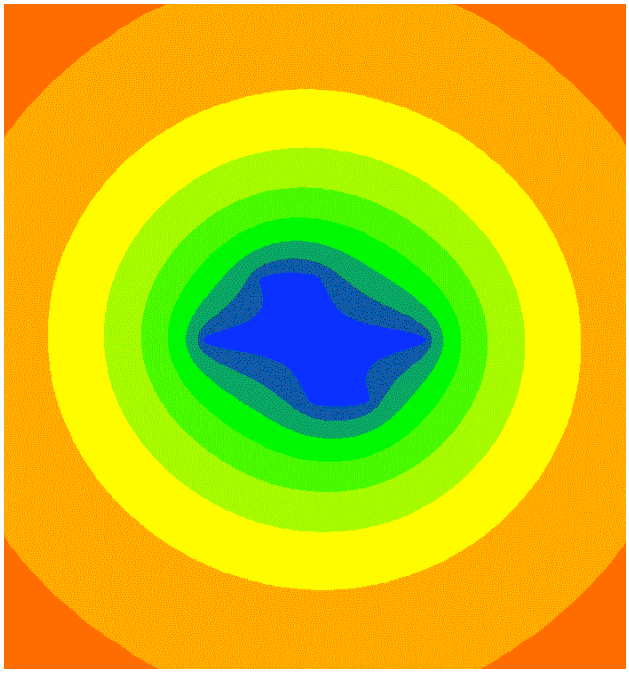

Fig. 4.38 – Pore pressure distribution around a Barnett shale gas well 10 years after refracturing

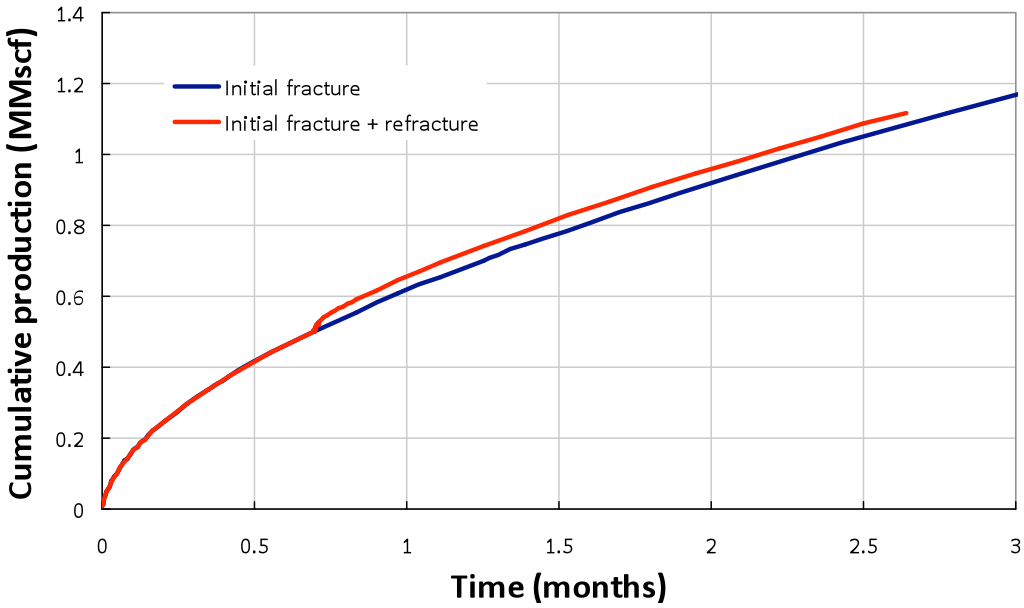

Fig. 4.39 – Cumulative production from the initial fracture and refracture in a Codell tight gas well

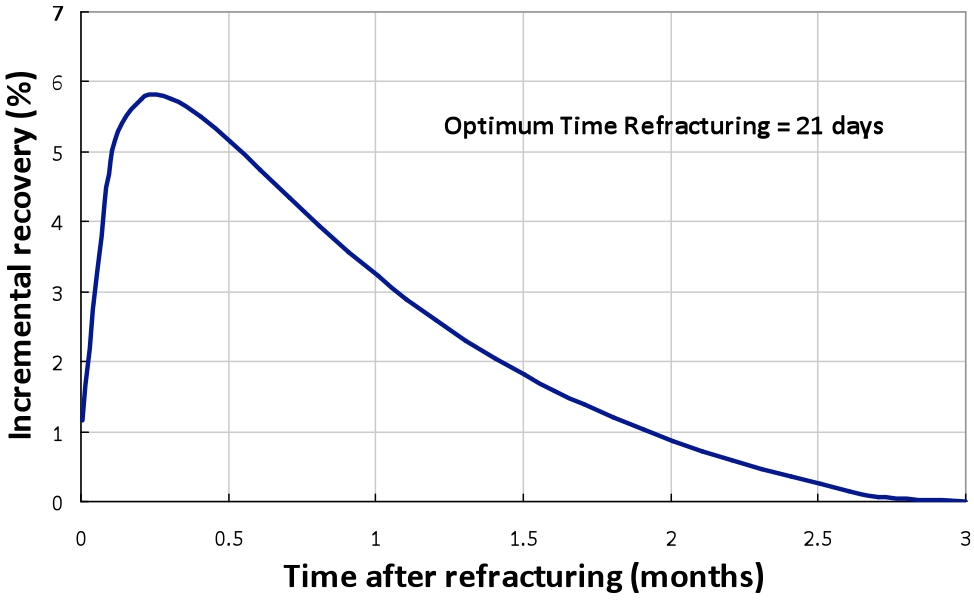

Fig. 4.40 – Incremental gas recovery (%) from refracturing wells in a Codell tight gas well

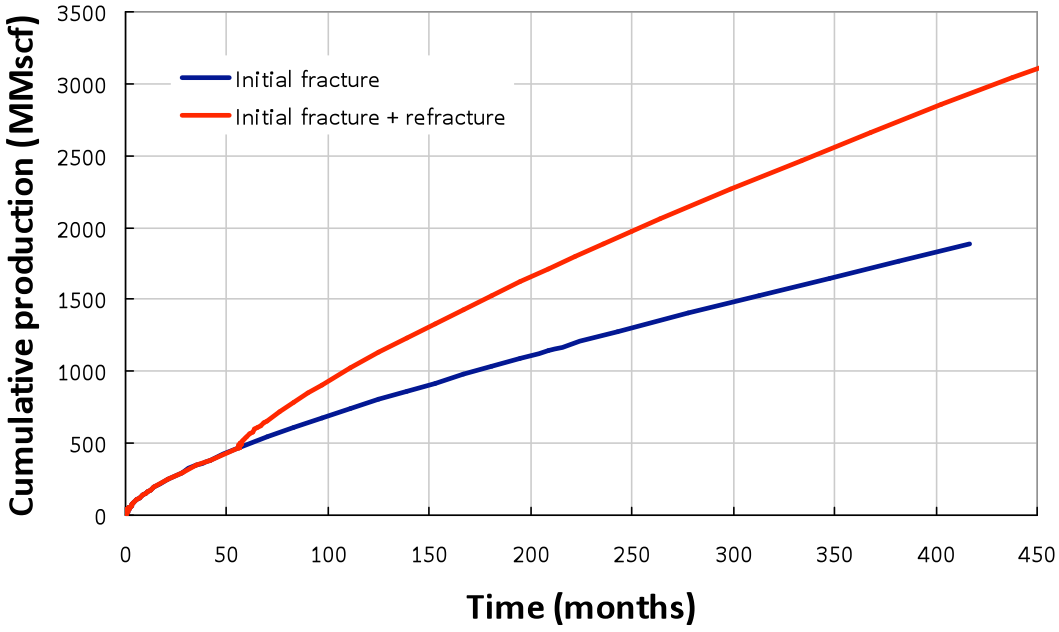

Fig. 4.41 – Cumulative production from the initial fracture and refracture in a Barnett shale gas well

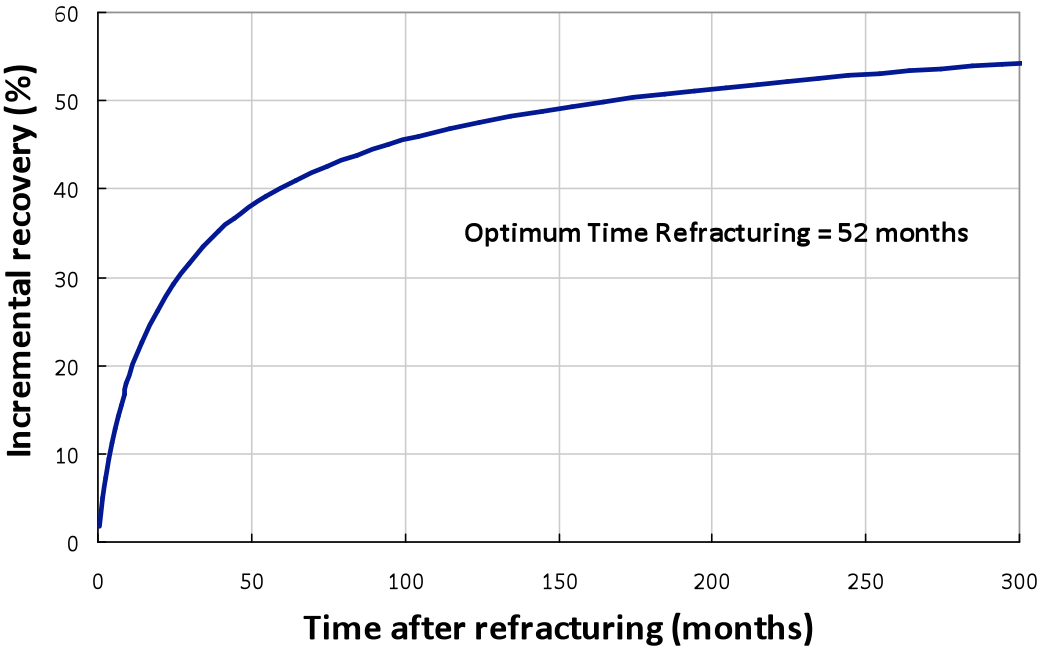

Fig. 4.42 – Incremental gas recovery (%) from refracturing wells in a Barnett shale gas well

CHAPTER 5: CANDIDATE WELL SELECTION FOR REFRACTURING

The selection of candidate wells for refracturing is often very difficult based on the information available at the surface. We propose a systematic methodology to allow a field engineer to evaluate a well's potential for refracturing from an analysis of field production data and other reservoir data that is commonly available. We successfully confronted our method to a case study in the Wattenberg field using data from 300 Codell tight gas wells.

The performance of refracturing treatments has been observed to be highly variable in the Wattenberg field (Colorado) with some wells underperforming while others are restored to initial or even higher production rates. Historically, multiple approaches have been taken to select the best candidate wells, including heuristic guidelines, field correlations, and neural networks.

After identifying the physical phenomena that are thought to impact the performance of refracturing operations, we developed five dimensionless groups to quantify them. By choosing a dimensionless approach, we establish refracturing criteria that may be applied to any oil or gas field. One potential motivation for refracturing is the stress reorientation occurring around a fractured well causing the refracture to propagate orthogonally to the initial fracture in under-depleted sections of the reservoir. Numerical simulations of the areal extent of the stress reversal region as well as tiltmeter measurements confirmed the existence of refracture reorientation in the Codell formation. Guidelines for the selection of refracturing candidates were expressed in terms of the potential for stress reorientation, the quality of the initial completion, the initial production decline and the reservoir depletion around the well of interest. Two groups of

wells showed the most promise for refracturing: (a) ineffective initial completions with a small initial production decline and (b) long initial fractures in under-depleted reservoirs. The dimensionless groups help us identify such wells and provide quantitative criteria for selection of wells that may be good candidates for refracturing.

1. INTRODUCTION

The potential of restimulation to enhance production in tight gas formations has been the subject of a comprehensive study from the Gas Research Institute (GRI) (Reeves 2001). A case study in the Rocky Mountains revealed that significant opportunities exist to increase incremental recovery from refracturing, but that most of the restimulation potential (85%) tends to be confined to a minority (15%) of the wells (Reeves et al. 1999). As a result, identification methods are greatly needed to improve the economics of refracturing.

Common candidate selection techniques are production statistics, type-curves and virtual intelligence. The latter consists in training neural networks (Mohaghegh and Reeves 2000; Oberwinkler et al. 2004). As they become more and more skilled in detecting trends involving multiple variables, they can be very useful in fields having extensive records of past refracturing treatments. But since they look more for statistical patterns rather than identifying the physics behind refracturing success, the experience built into a neural network in a given field does not easily translate to other fields. Another issue with artificial neural nets is the amount and quality of data that are required for the analysis to be meaningful. Any missing piece of data can either eliminate a well or a parameter (for all wells) from the analysis (Reeves et al. 1999).

Experience is also a valuable tool in detecting the common traits of good refracturing candidates. In a comprehensive review of the numerous publications on refracturing, Vincent (2010) listed major factors contributing to successful refracs. Refracturing has been shown to restore the conductivity of the refracture that can decline during production because of the degradation of the proppant, condensate blocking, and fines plugging. In addition, improved stimulation practices (fracturing fluids, proppant concentrations, injection rates, etc.) can lead to additional vertical and longitudinal extension of the initial fracture and thus improve reservoir contact.

The objective of the study is to link production data to the performance of a refracture treatment. This data being readily available to field engineers should allow them to select candidate wells for refracturing without extensive modeling (Barba 2009). Statistical production data analysis attempting to correlate refrac performance with a group of field variables has often not been successful in selecting the best candidate wells for refracturing. Such an approach, even if it were successful, would be applicable only to the field in question, and would have to be re-evaluated for another field. Another reason for the poor performance of initial restimulation programs was their focus on underperforming wells. It was shown later that far from being ideal, this strategy results in poorer refracs than if refracturing candidate wells were randomly selected (Moore and Ramakrishnan 2006). Some authors have claimed that the best wells often make the best refrac candidates (Vincent 2010).

It is evident from the literature that many factors control the success of refracs. This is precisely the reason why it is not possible to correlate successful refrac treatments with one or more well properties. In the discussion below we present a set of dimensionless groups that capture different aspects of well performance and reservoir depletion that we show correlate with the success of refracs. The dimensionless

formulation should allow the experience built on the physical parameters that impact refrac success to be at least partially transferred from one field to another. This approach is similar to production type-curve matching which can identify properties affecting the performance of individual wells such as permeability, skin and drainage area. But the noise inherent to field production data as well as the typical heterogeneity of tight sands can complicate the identification of a unique solution using type curves, making it labor-intensive and subject to some interpretation bias (Reeves et al. 2000).

2. DIMENSIONLESS CRITERIA

The extent of stress reorientation from poroelastic effects and mechanical effects is the basis of the first criterion that is indicative of success in a refrac treatment. This criterion can be calculated to quantify the potential for the propagation of orthogonal refractures in a given field (Roussel and Sharma 2010). The next three criteria are specific to a given well. The production at early times can be compared to the theoretically predicted value for the well to quantify the quality of the completion (F_{Co}). Production data from adjacent wells may be used to quantify the extent of depletion around the well of interest (R_{Dep}). Finally, the production decline at early times is an indication of reservoir quality and fracture design (D_{iD}). For each criterion, a dimensionless number has been defined. The expressions of the five dimensionless numbers are summarized in **Table 5.1**.

2.1. Stress Reorientation Numbers, Π_{poro} and Π_{mech}

There are two known contributors to stress reorientation around induced fractures: mechanical and poroelastic effects (**Fig. 5.1**) (Warpinski and Branagan 1989).

Mechanical stress reorientation results from the opening of a propped fracture. The stresses increase more in the direction perpendicular to the fracture than parallel to it. Initially, the maximum horizontal stress is parallel to the first fracture. If the stress contrast is small, the direction of maximum horizontal stress may be switched 90º in the vicinity of the fracture: this region is called the stress reversal region. Mechanical stress interference, often referred to as stress shadow, can play a very important role in the multi-stage fracturing of horizontal wells (Roussel and Sharma 2011). Similarly, pore pressure gradients may cause stress reorientation and even stress reversal. The reservoir is more depleted in the direction parallel to the fracture than perpendicular to it, causing the maximum horizontal stress to decrease faster than the minimum stress (Roussel and Sharma 2010; Singh et al. 2008; Weng and Siebrits 2007).

Because the main stresses are switched in the vicinity of the fracture, the refracture will propagate orthogonally to the initial fracture until it reaches the isotropic point, after which it will gradually reorient parallel to the initial fracture (**Fig. 5.2**) (Siebrits and Elbel 1998). This allows the refracture to contact pressurized regions of the reservoir (Elbel and Mack 1993). Laboratory experiments (Liu et al. 2008) and field tiltmeter and microseismic measurements (Minner et al. 2002; Wright and Conant 1995) have demonstrated that the altered stress field around fractured wells causes the refracture to propagate in a different direction.

The extent of the stress reversal region (L_f') increases as Π_{poro} and Π_{mech} decrease. Practically, it means that the smaller the stress reorientation number, the more the refracture will propagate in under-depleted regions of the reservoir, which means a better production rate and access to additional reserves. The potential for poroelastic stress reorientation is quantified by the ratio of the in-situ stress contrast and the stress contrast generated by pore pressure gradients (Eq. (5.1)). A field having a low value of the stress

contrast and a high value of the pressure drawdown will be susceptible to stress reorientation. This expression was adopted from the work of Berchenko and Detournay (1997):

$$\Pi_{poro} = \frac{\sigma_{h\max} - \sigma_{h\min}}{\sigma_*} = \frac{\Delta\sigma_h}{\frac{\alpha(1-2\nu)}{1-\nu}\left(p_{R_i} - p_{wf}\right)} \tag{5.1}$$

Similarly, to quantify the potential for mechanical stress reorientation Π_{mech}, we define the ratio of the in-situ stress contrast and the net closing pressure of a propped fracture (Eq. (5.2)) as a dimensionless group. The net pressure can be expressed analytically for a 2D semi-infinite fracture (Sneddon 1946):

$$\Pi_{mech} = \frac{\sigma_{h\max} - \sigma_{h\min}}{p_c - \sigma_{h\min}} = \frac{\Delta\sigma_h}{p_{net}} = \frac{2\Delta\sigma_h\left(1-\nu^2\right)h}{Ew_f} \tag{5.2}$$

Similarly to the poroelastic stress reorientation number, the field's potential for mechanical stress reorientation increases as Π_{mech} decreases. Eq. (5.2) is expressed as a function of the propped fracture width, which is not a typical input parameter. Assuming that the proppant is uniformly distributed inside a fracture of constant width, the fracture width can be substituted by the sand weight pumped during a frac job using Eq. (5.3):

$$m_s = 2\pi w_f L_f h\left(1-\phi_f\right)\rho_s \tag{5.3}$$

The final expression of Π_{mech} is function of the size of the fracturing treatment, the rock mechanical properties and the dimensions of the designed fracture (Eq. (5.4)). Among the factors that favor mechanical stress reorientation are a small stress contrast, a narrow pay zone, a stiff rock and large proppant volumes.

$$\Pi_{mech} = \frac{4\Delta\sigma_h\left(1-\nu^2\right)\left(1-\phi_f\right)\rho_s L_f h^2}{Em_s} \tag{5.4}$$

2.2. Well Completion Number, F_{Co}

The production of a well is reported on a daily or monthly basis. Its initial value, the first-month cumulative production, is a good indication of the quality of the initial completion. This quantity may be compared to a value calculated from existing analytical expressions for the designed fracturing job, in a given field. As a result, F_{Co} should be confined between 0 and 1, the latter representing an ideal completion.

According to Guppy et al. (1981), the early-time behavior of a fractured vertical gas well producing at constant pressure may be calculated analytically by a linear flow approximation in the case of high conductivity fractures (Eq. (5.5)), or by a bilinear flow approximation for low conductivity fractures (Eq. (5.6)):

$$q_D = \frac{2}{\sqrt{\pi^3 t_{D_{L_f}}}} \text{ for } F_{CD} = \frac{k_f w_f}{kL_f} \geq 100\pi \tag{5.5}$$

$$\frac{1}{q_D} = \frac{\pi\,\Gamma(3/4)}{\sqrt{2F_{CD}}} t_{D_{L_f}}^{1/4} \text{ for } F_{CD} = \frac{k_f w_f}{kL_f} < 100\pi \tag{5.6}$$

$$\text{with } \frac{1}{q_D} = \frac{kh\left[m(p_R) - m(p_{wf})\right]}{1424T} \cdot \frac{1}{q_{sc}} \text{ and } t_{D_{Lf}} = \frac{0.0002637kt}{\phi(\mu c_t)_i L_f^{\,2}}$$

After integrating the analytical expression of the early-time flow rate of a producing fracture over the first month of production, we obtain the expressions of the fracture completion number for the high-conductivity (Eq. (5.7)) and low-conductivity (Eq. (5.8)) fracture approximations with variables expressed in oil field units. The details of the derivation of the dimensionless fracture completion numbers can be found in Appendix B:

$$F_{Co} = \left(\frac{Q_{field}}{Q_{theory}}\right)_{1month} = 28.793 \frac{Q_{1month} ZT}{\left(p_R^2 - p_{wf}^2\right) L_f h} \sqrt{\frac{\mu}{\phi k c_t}} = \frac{(L_f)_{actual}}{(L_f)_{ideal}} \tag{5.7}$$

$$F_{Co} = \left(\frac{Q_{field}}{Q_{theory}} \right)_{1month} = 63.9825 \frac{Q_{1month} \mu^{3/4} ZT}{h\sqrt{k_f w_f}\left(p_R^2 - p_{wf}^2\right)\left(k\phi c_t\right)^{1/4}} \tag{5.8}$$

$$= \sqrt{\frac{\left(k_f w_f\right)_{actual}}{\left(k_f w_f\right)_{ideal}}}$$

Since the first-month cumulative production is a function of reservoir properties, F_{Co} in high-conductivity fractures (Eq. (5.7)) is the physical representation of the real propped fracture length resulting from the completion over the designed length of the fracture (**Fig. 5.3**). On the other hand, the effect of fracture length on the cumulative production is negligible for low-conductivity fractures (Eq. (5.8)). Thus, the fracture completion number is a measure of how the conductivity of the propped fracture in a given well differs from its ideal value (**Fig. 5.4**).

2.3. Reservoir Depletion Number, R_{Dep}

Production data from neighboring wells can be used to quantify the extent of depletion around a given well (**Fig. 5.5**). The extent of reservoir depletion in the vicinity of a well is a function of the reservoir parameters, the distance separating the well of interest from its neighbors and their cumulative production. We propose the following expression for the depletion number (Eq. (5.9)). The derivation of the reservoir depletion number is given in Appendix B:

$$R_{Dep}(t) = \frac{\overline{B_g}}{2\phi h\left(1 - S_w\right)} \max_n \left(\frac{1}{n} \sum_{i=1}^{n} \frac{G_{p_i}(t)}{r_i^2} \right) \tag{5.9}$$

The reservoir depletion number is bounded between 0 and 1. Proximity and efficient production of the neighboring wells should lead to a high value of R_{Dep}. The

potential for the refracture to gain access to higher pressurized rock should be higher when the reservoir depletion number is low.

2.4. Production Decline Number, D_{iD}

The last criterion is the initial production decline in the well with the initial fracture. The production decline number reflects the extent and quality of the reservoir. Smaller decline rates indicate larger reservoir drainage volumes and / or better quality rock. The slope of production decline at the time when the well is put to production is calculated (**Fig. 5.6**). The decline rate has dimensions of inverse of time (Eq. (5.10)):

$$D_i = -\left(\frac{1}{q_{sc}} \frac{dq_{sc}}{dt} \right)_{t=0} \tag{5.10}$$

The initial production decline is calculated through a graphical method. Assuming that production during the first 12 months can be modeled by a hyperbolic production decline model (Eq. (5.11)), the inverse of the decline rate is inversely proportional to time (Eq. (5.12); Walsh and Lake 2003). The initial production decline is the intercept of the plot of 1/D versus production time with the axis t=0 (**Fig. 5.7**).

$$q(t) = \frac{q_i}{(1 + bD_i t)^{1/b}} \tag{5.11}$$

$$D = -\frac{1}{q(t)} \frac{dq(t)}{dt} = \frac{D_i}{1 + bD_i t} \Rightarrow \frac{1}{D} = \frac{1}{D_i} + bt \tag{5.12}$$

The dimensionless decline is defined as the product of the initial production decline rate and the production time from the well with the initial fracture (Eq. (5.13)).

$$D_{iD} = D_i \cdot t_{IF} \tag{5.13}$$

3. SELECTION OF CANDIDATE WELLS FOR REFRACTURING IN THE WATTENBERG FIELD

Activity in the Wattenberg field, located in the Denver-Julesburg basin, has occurred mostly in the J-Sand, Codell and Niobrara formations. The Codell formation is a low-permeability and clay-rich sandstone. It is fairly thin (between 10 and 20 feet thick) and produces gas and condensate, with little to no water (Wolhart et al. 2007). Production and stimulation data from the Codell tight gas formation were analyzed using the dimensionless numbers defined in the previous section. After cleaning up, production data from 300 wells was selected, including 170 refractured wells.

We plotted the additional ultimate recovery in barrels equivalent as a function of the amount of proppant and water pumped during the refracturing treatment (**Figs. 5.8 and 5.9**). No obvious trend was identified. These plots demonstrate the difficulty in correlating refrac performance to individual parameters of the refracturing treatment, and also suggest that not just the completion but also reservoir parameters may influence the success of refracturing.

3.1. Wattenberg's Field Potential for Stress Reorientation

To quantify the potential of the Wattenberg field for stress reorientation, Π_{poro} and Π_{mech} are calculated. Both quantities are below 0.1, which is a value above which stress reorientation is unlikely to happen. For instance, if the pressure drawdown is equal to 3000 psi, a Π_{poro} of 0.1 would correspond to a stress contrast of approximately 300 psi, which is a moderately high value of stress contrast.

$$\begin{cases} \Pi_{poro} = 0.0476 \\ \Pi_{mech} = 0.0127 \end{cases}$$

The lower value of Π_{mech} is an indication that mechanical stress reorientation should predominate over poroelastic effects. This is confirmed by a calculation of the

extent of the stress reversal region around a typical Codell tight gas well in the Wattenberg field described in **Table 5.2** (**Fig 5.10**). The numerical model including the contributions of both the displacement of the fracture walls and pressure gradients is used to calculate stress reorientation in the Codell tight gas formation in the Wattenberg field. The distance separating the isotropic point from the initial fracture (L_f') is higher because of mechanical effects than it is from poroelastic effects.

As shown earlier in Chapter 4, a thin pay zone tends to favor mechanical stress reorientation. In the particular case of the Codell formation, height is generally confined between 15 and 25 ft (Wolhart et al. 2007). The other two reservoir parameters controlling the balance between mechanical and poroelastic effects are the reservoir pressure and the Young's modulus.

Quantifying the potential for stress reorientation, which can vary significantly from one field to another, may be useful not only for candidate well selection but also to determine well spacing during field design. If the spacing between wells is too large, hydrocarbons may be left undrained. Conversely, if wells are spaced too close to each other, the incremental production from refracturing may be negatively affected. Careful consideration of the potential extent of stress reversal when designing the well pattern and spacing, may improve the recovery efficiency after refracturing and minimize initial field development costs.

3.2. Refracture Reorientation in the Wattenberg Field: Validation of the Numerical Model of the Extent of Stress Reversal

Tiltmeter measurements conducted during the refracturing of five Codell tight gas wells in the Wattenberg field confirm that the direction of refractures differ from the one of the initial fracture treatment (**Fig. 5.11**). The measured values of the fracture

reorientation (from the in-situ direction of maximum stress, which is N66°E) are indicated in **Table 5.3**. The average change in azimuth was measured to be slightly over 20º.

Using the numerical model of the extent of stress reversal around a fractured vertical well, it is possible to calculate the trajectory of the refracture and compare its angle of deviation from direction of the initial fracture to the values measured in the Wattenberg field. Since we do not explicitly model fracture propagation in this study, the present calculation is only meant to be a first-order estimation.

The trajectory of the refracture is modeled according to assumptions that are detailed in the section 5.2 of Chapter 4. These assumptions are summarized below:

- The length of the refracture is assumed to be equal to the fracture length ($2L_f$).
- The refracture propagates orthogonally to the initial fracture inside the stress reversal region of extent L_f'.
- In order to take into account the gradual turning of the refracture as it exist the stress reversal region, an additional portion of orthogonal propagation (equal to 0.5 L_f') is represented.

Fig. 5.10 shows that the stress reversal region may extend up to 65 ft from the initial fracture when both poroelastic and mechanical effects are modeled. Following the assumptions expressed above, the refracture may propagate orthogonally to the initial fracture for a distance equal to 1.5 times the extent of the stress reversal region. The refracture then is assumed to propagate parallel to the initial fracture during the remaining length (L_f - 1.5L_f'). The calculation of the angle of fracture reorientation, based on the results of our numerical model and the assumptions made previously, is shown in Eq. (5.14) and illustrated in **Fig. 5.12**.

$$\arctan\left(\frac{L_f'(1+0.5)}{L_f - L_f'(1+0.5)}\right) = \arctan\left(\frac{65(1+0.5)}{500-65(1+0.5)}\right) = 14^\circ \qquad (5.14)$$

The final result (14°) is close to the field measured value but still inferior. If mechanical effects are neglected (L_f'= 42 ft), the prediction of the angle of refracture reorientation is reduced to as low as 8°. It is, therefore, important to consider both effects when calculating the angle of stress reorientation.

The combined use of simple assumptions on the geometry of the refracture and of the numerical model of coupled poroelastic and mechanical stress reorientation, may provide a good approximation of the degree of refracture reorientation to be expected in a given field.

3.3. Optimum Time-Window for Refracturing

The timing of the stress reorientation should also be considered in the planning of refracturing operations. As illustrated in Fig. 5.10, taking into account both mechanical and poroelastic effects, makes a significant impact on the optimum time for refracturing (6 months instead of 21 days). Even more important is the evolution of the stress reversal region after the optimum time for refracturing. When only poroelastic effects are considered, stress reversal goes back to 0 after less than a year of production. Conversely when mechanical effects are added, the extent of stress reversal may still be higher than 50 ft after five years of production, and higher than 43 ft after ten years of production.

Thus, significant opportunities for refracturing may still exist long past the optimum time for refracturing, which is equal to 6 months in the present case. But

planning refracturing treatments closer to the optimum time-window may provide a higher incremental recovery.

3.4. Impact of the Well Completion (F_{Co}) and Production Decline Numbers (D_{iD}) and the Reservoir Depletion Number (R_{Dep}) on Refrac Performance

The dimensionless fracture conductivity is computed to be 13.1 for the Codell formation and the designed fracture (Table 5.1). Because F_{CD} is lower than 100π, the gas flow at early production times can be estimated by assuming bilinear flow (**Fig. 5.13**). The fracture completion number (F_{Co}) is the ratio of the field measured value of the cumulative production after the first month and the predicted theoretical value of the designed fracture, which is calculated using Eq. (5.8) and equal to 36,190 MSCF.

After verifying that the field has potential to propagate a secondary fracture orthogonal to the initial fracture, we applied the defined dimensionless numbers to detect trends in the production data. We plotted the incremental recovery from refracturing versus the completion number of the initial fracture (**Fig. 5.14**). There is no obvious correlation. However, we notice the presence of a group of successful refracs located at low completion numbers and at high completion numbers. As a result of the two distinct trends, we decided to study low completion number wells separately (F_{Co}<0.1).

For the group of wells having a completion number smaller than 0.1, we identified a correlation between the incremental recovery and the initial production decline D_i (**Fig. 5.15**). Note that this relationship does not apply to wells having a higher completion number. This trend probably captures the impact of reservoir quality on the refracturing success of failed completions.

The completion number of the refracture (RF_{Co}) looks to be influenced by the quality of the initial completion, in wells with a fracture completion number higher than

0.1 (**Fig. 5.16**). This trend supports the hypothesis that stress reorientation is primarily responsible for the success of the refracs in the Codell formation. The extent of the stress reversal region is very sensitive to the length of the initial fracture, and is even directly proportional to it in the case of poroelastic stress reorientation (Roussel and Sharma 2010). As a result, we can expect refracture reorientation to be most severe for the longest initial fractures, thus the most productive initial completions. This graph confirms that in the Codell tight gas formation, stress reorientation plays a large role in the success of refracturing operations. We expect the correlation between refrac success and initial completion performance to be most pronounced in fields for which the stress reorientation numbers Π_{poro} and Π_{mech} are low.

The trend of Fig. 5.16 can be improved when taking into account the nature of the production decline. The best correlation is obtained when the completion number of the refrac is plotted versus the initial completion over the square root of the dimensionless production decline (**Fig. 5.17**). The best candidates for refracturing correspond to the highest values of the new dimensionless quantity. More than the refrac completion number, the incremental recovery is the quantity that is of practical importance. Not surprisingly, high flow rates following refracturing generally translate to high values of the incremental recovery (**Fig. 5.18**). Not only does the quality of the refrac matter, but the amount of depletion in the vicinity of the well also influences incremental recovery (**Fig. 5.19**). We recommend that wells having high values of the reservoir depletion number (R_{Dep}>0.2) should not be refraced.

3.5. Decision Method for the Selection of Candidate Wells for Refracturing

The framework for selecting the ideal candidates for refracturing is summarized in a decision algorithm (**Fig. 5.20**). The first step is to calculate stress reorientation numbers to verify the potential for stress reorientation in the field of interest. Two groups of successful refractures were identified in the previous section, one for low values of the fracture completion number, and the other one for high values of F_{Co}. For failed completions, the wells having low values of the initial production decline ($D_i < 0.1$ month^{-1}) were shown to lead to the most successful refracturing treatments. A typical production profile of a well belonging to the first group of refrac candidates is shown in **Fig. 5.21**.

For wells having a fracture completion number higher than 0.1, $F_{Co}/\sqrt{D_{iD}}$ and R_{Dep} are calculated and the second group of successful refractures exists for low values of these dimensionless quantities (respectively 0.1 and 0.2). **Fig. 5.22** shows the production profile of a well fitting the description above.

The cut-off values of the decision algorithm will in all likelihood be field dependent. But the dimensionless framework should allow the cut-off values proposed in this study to be first-order estimates when considering refracturing for the first time in a given field. They can further be adjusted to the measured performance of the refracturing treatments. Also, it must be noted that there is no particular reason for choosing the variable group $F_{Co}/\sqrt{D_{iD}}$ except that it gave us the best correlation in the Wattenberg field. Different values of the exponent on F_{Co} and D_{iD} may work better in different fields.

The average additional recovery in wells selected by the proposed decision algorithm is 22,625 barrels of oil equivalent, which is 35% higher than the average additional recovery of all refractured wells (16,744 bble). If the decision algorithm successfully selected the best refracturing candidates, it also included under-performing

refracs. It may be because some of the wells were not restimulated according to optimal practices. Indeed, this study did not discriminate based on fracturing practices, but solely on the performance of the initial fracturing treatment and the level of depletion in the vicinity of the well of interest. Coupling the proposed decision method with a careful analysis of the best fracturing parameters for a given field and reservoir rock could further improve the performance of refracturing treatments.

4. CONCLUSIONS

A novel framework for the selection of candidate wells for refracturing has been presented, based on five dimensionless quantities. These variables are calculated from known reservoir properties and production data. They quantify the impacts of stress reorientation, of the initial completion performance, of the reservoir quality, and of the reservoir depletion by neighboring wells on the expected incremental recovery from a refracturing treatment.

The proposed well selection method was applied to a case study of refracturing of Codell tight gas wells in the Wattenberg field. The major findings are summarized below:

- Two groups of successful refractures were identified: (a) ineffective initial completions showing small initial production decline and (b) long initial fractures surrounded by under-depleted rocks.
- The strong correlation between the fracture completion number and the incremental recovery after refracturing suggests the central role played by stress reorientation in the success of refracs.
- The performance of the wells selected by the decision algorithm is 35% higher than a random selection.

Because of the dimensionless formulation, the model may be used in any reservoir and field, and may prove particularly useful in fields where refracturing experience is limited. In addition to being a selection method, it also provides quantified estimates of the incremental recovery of future refracturing treatments.

Dimensionless Number	Expression
Π_{poro}	$\dfrac{\Delta\sigma_h}{\dfrac{\alpha(1-2\nu)}{1-\nu}\left(p_{R_i}-p_{wf}\right)}$
Π_{mech}	$\dfrac{4\Delta\sigma_h\left(1-\nu^2\right)\left(1-\phi_f\right)\rho_s L_f h^2}{Em_s}$
Completion number F_{Co}	$28.793\dfrac{Q_{1month}ZT}{\left(p_R^2-p_{wf}^2\right)L_f h\sqrt{\dfrac{\mu}{\phi k c_t}}}$ for $F_{CD}\geq 100\pi$ $63.9825\dfrac{Q_{1month}\mu^{3/4}ZT}{h\sqrt{k_f w_f}\left(p_R^2-p_{wf}^2\right)\left(k\phi c_t\right)^{1/4}}$ for $F_{CD}<100\pi$
Reservoir depletion number R_{Dep}	$\dfrac{\overline{B_g}}{2\phi h\left(1-S_w\right)}\max_n\left(\dfrac{1}{n}\sum_{i=1}^{n}\dfrac{G_{p_i}(t)}{r_i^2}\right)$
Production decline number D_{iD}	$-t_{IF}\left(\dfrac{1}{q_{sc}}\dfrac{dq_{sc}}{dt}\right)_{t=0}$

Table 5.1 – List of five dimensionless numbers used in the proposed refracturing candidate well selection method

	Codell tight gas		Codell tight gas
Permeability k (md)	0.05	Wellbore pressure p_{wf} (psi)	500
Pay zone Young's Modulus E_p (psi)	4.0×10^6	Reservoir pressure p_R (psi)	4500
Bounding layer Young's Modulus E_b (psi)	3.0×10^6	σ_{hmax} (psi)	6000
Poisson's Ratio ν	0.2	σ_{hmin} (psi)	5900
Porosity ϕ	0.14	Depth (ft)	7500
Compressibility c_{fl} (1/psi)	3×10^{-4}	Pay zone height h (ft)	20
Viscosity μ (cp)	0.02	Fracture length $2L_f$ (ft)	1000

Table 5.2 – Reservoir and fracture parameters for a typical Codell tight gas well in the Wattenberg field

Well number	Fracture azimuth	Delta from initial azimuth of N68°E
C2R	N44°E	24°
C3R	N47°E, N71°E	21°
C4R	N29°E, N6°W	21°
C5R	N52°E, N32°W	21°
C6R	N2°W	70°

Table 5.3 – Tiltmeter measurements in five wells in the Wattenberg field (Wolhart et al. 2007)

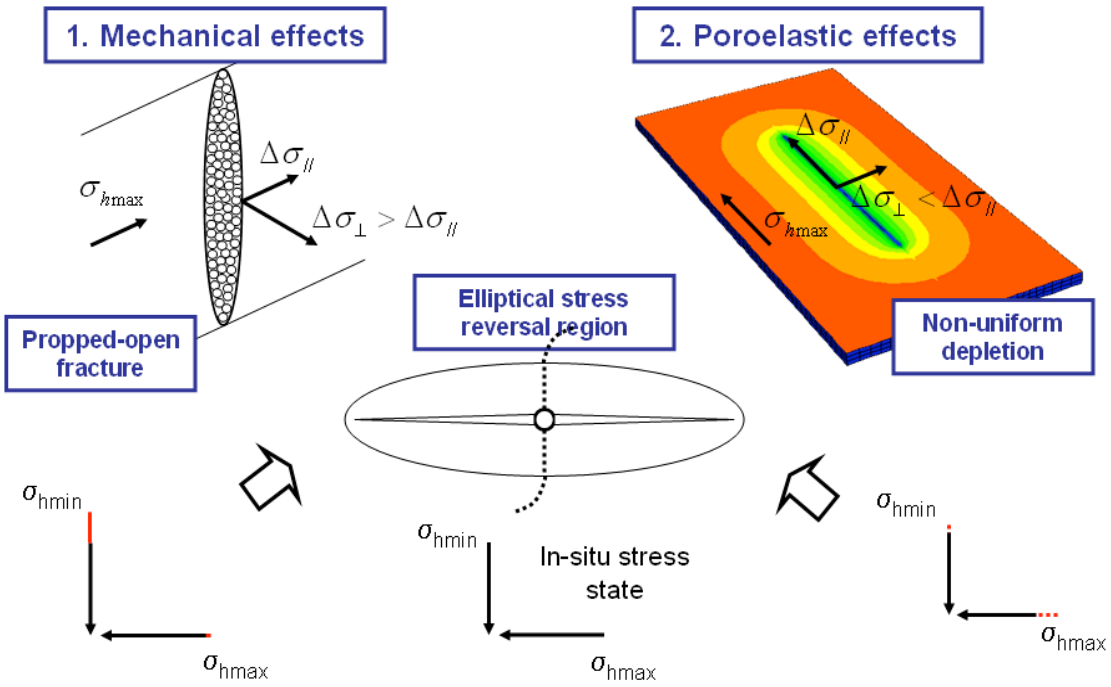

Fig. 5.1 – Stress reversal from mechanical and poroelastic effects

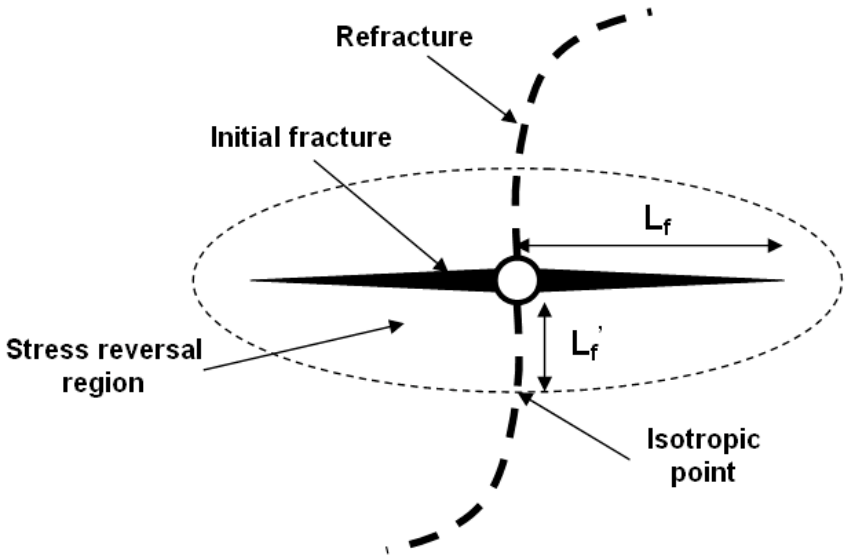

Fig. 5.2 – Geometry of the stress reversal region and refracture propagation direction

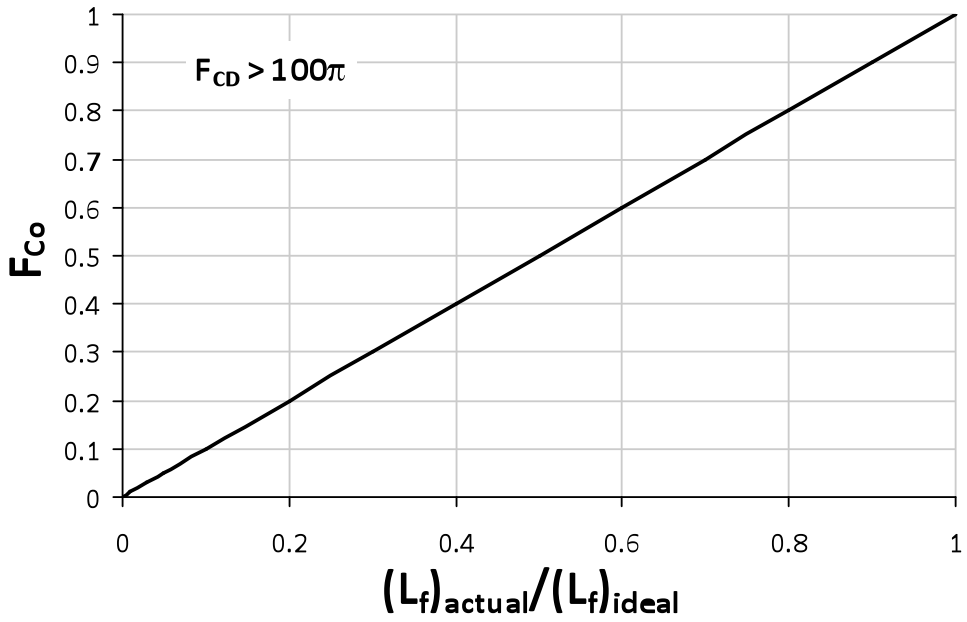

Fig. 5.3 – Impact of fracture length on the fracture completion number for high-conductivity fractures

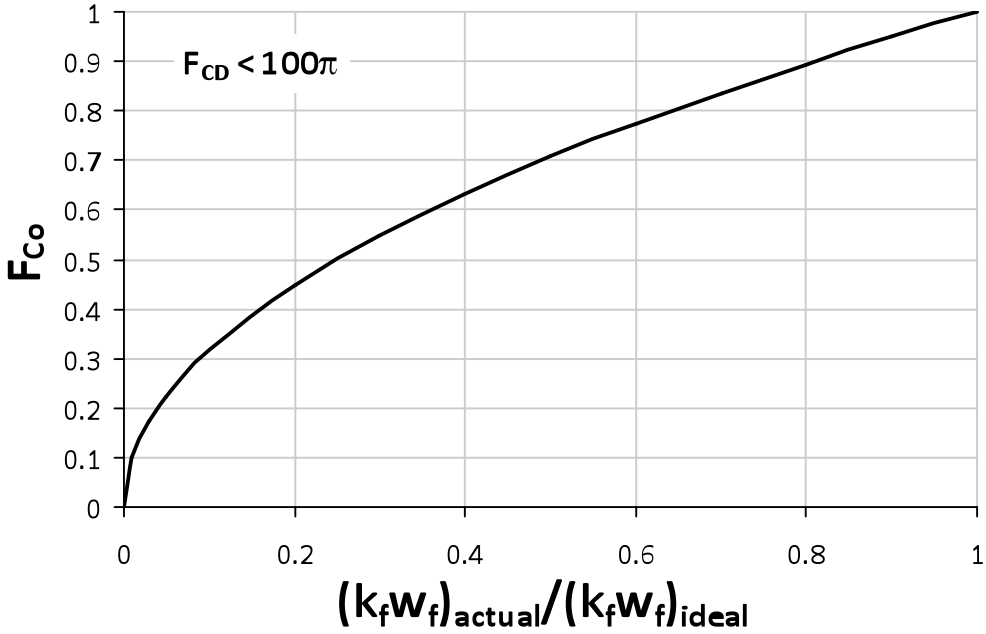

Fig. 5.4 – Impact of fracture conductivity on the fracture completion number for low-conductivity fractures

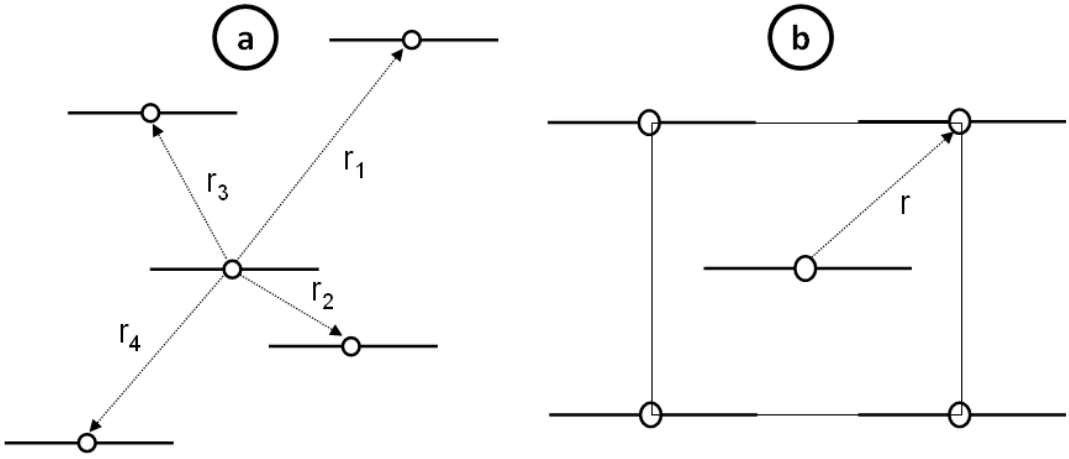

Fig. 5.5 – Geometry of neighboring wells: (a) random distribution and (b) four wells at the corners of the depletion area

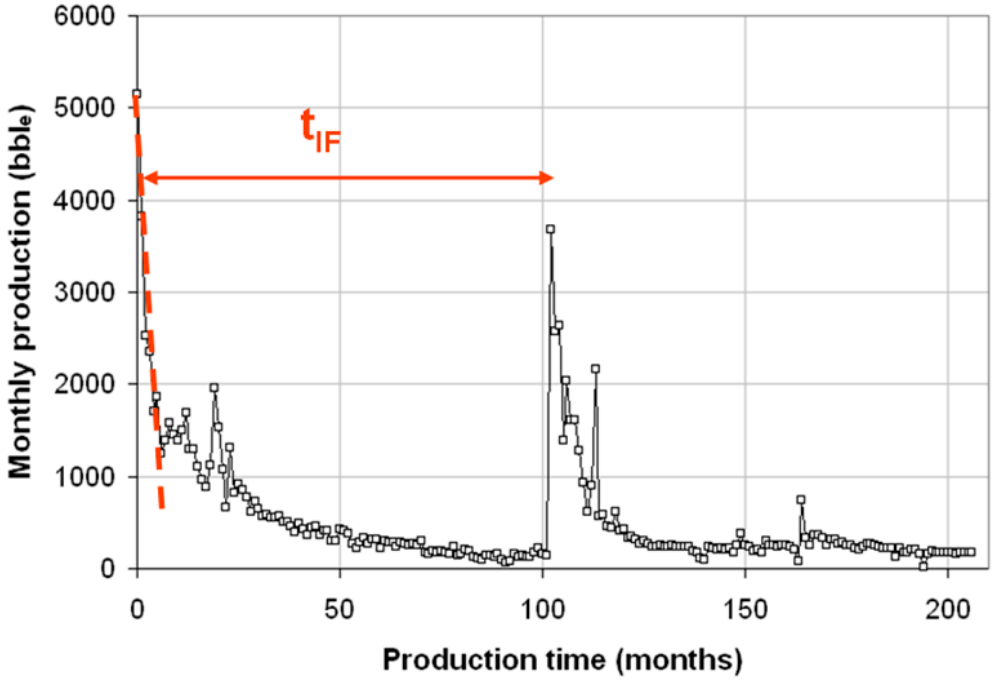

Fig. 5.6 – Definition of the dimensionless production decline number D_{iD}

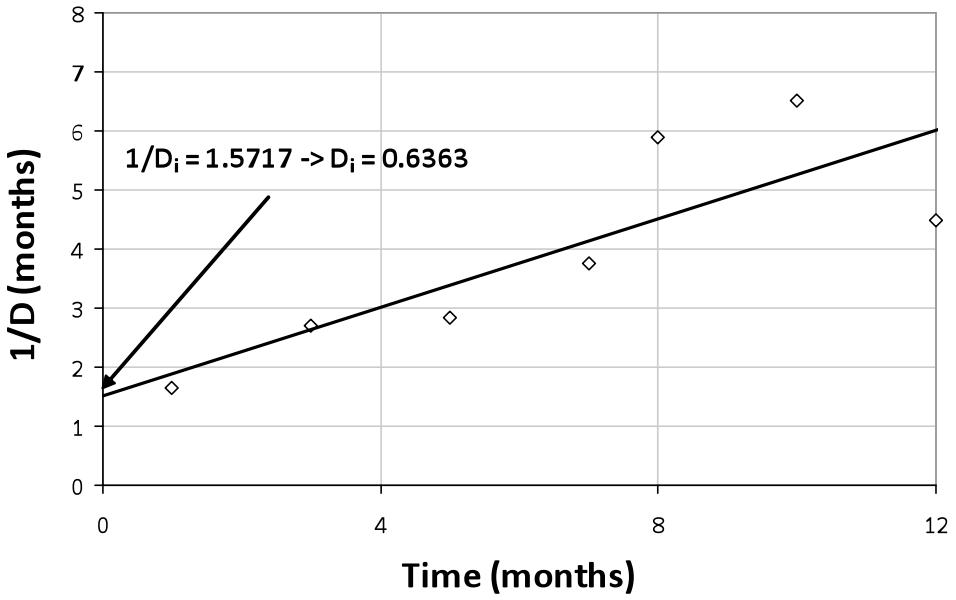

Fig. 5.7 – Calculation of the initial production decline using production data from the first 12 months

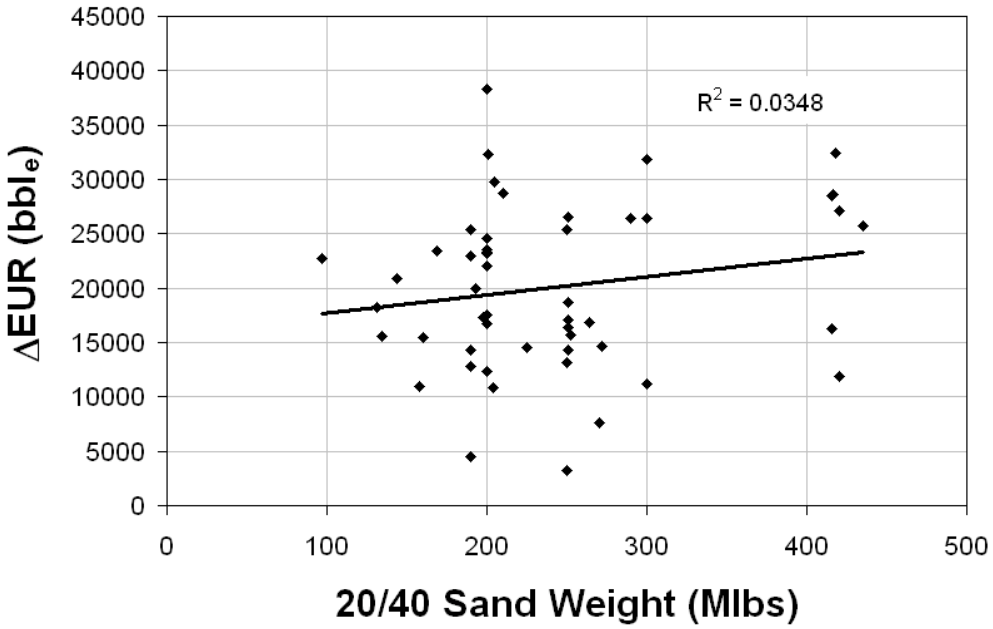

Fig. 5.8 – Additional ultimate recovery from the refracture is not correlated with the weight of proppant pumped

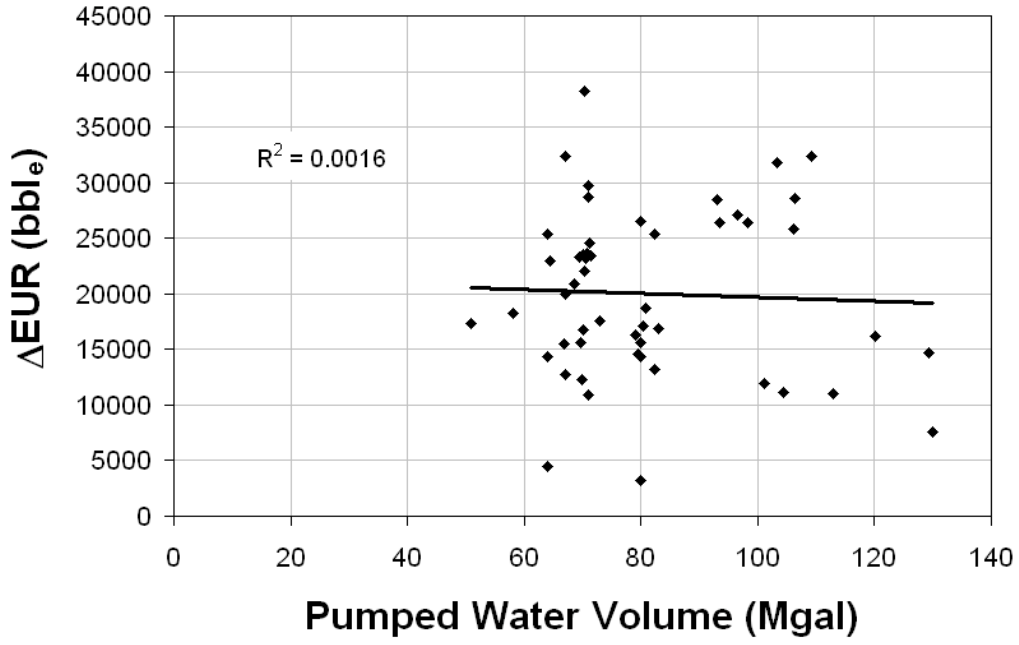

Fig. 5.9 – Additional ultimate recovery from the refracture is not correlated with pumped water volume

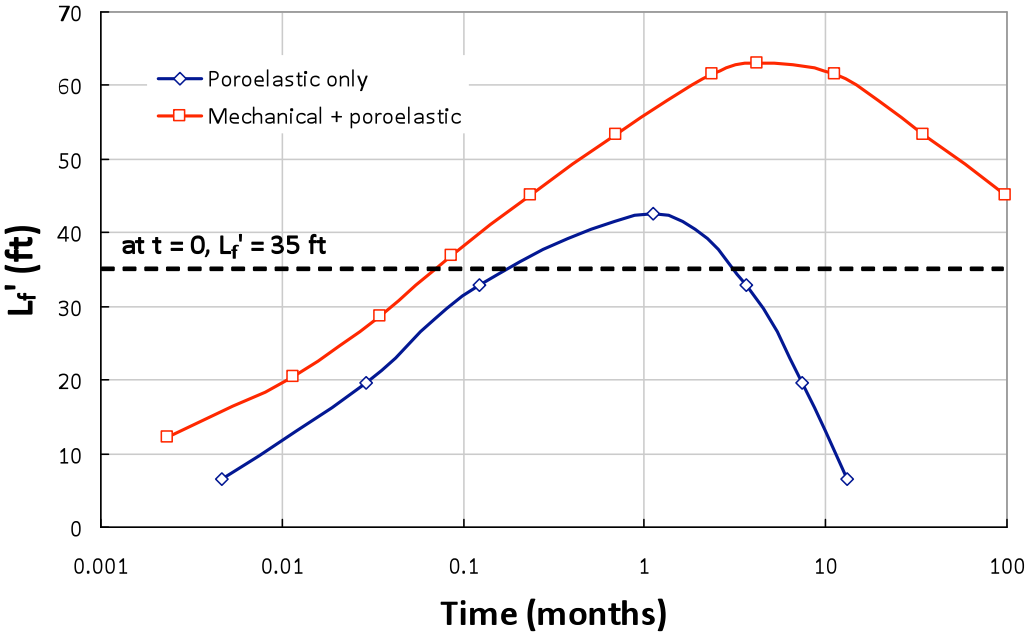

Fig. 5.10 – Extent of stress reversal (L_f') versus production time for a Codell tight gas well in the Wattenberg field

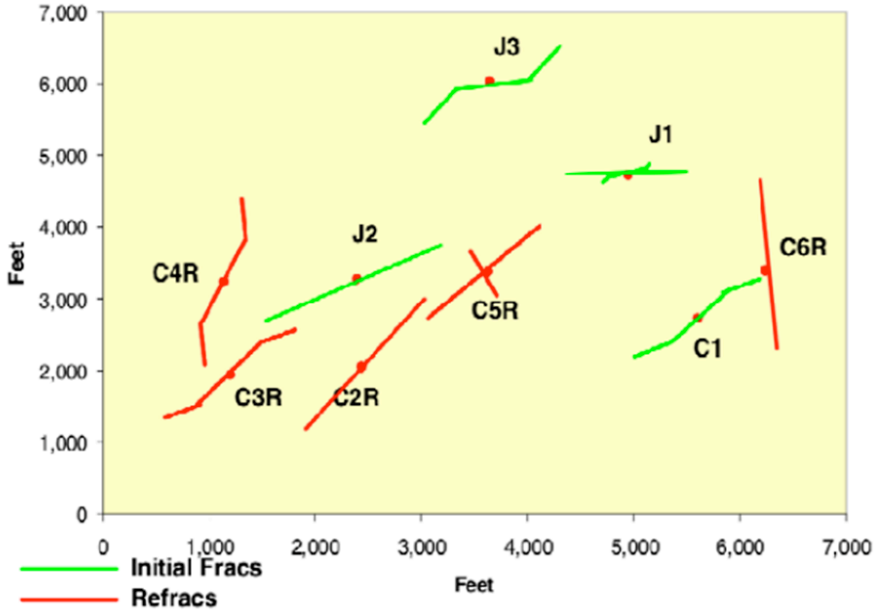

Fig. 5.11 – Direction of initial fractures and refractures in J-sand and Codell wells from tiltmeter measurements in the Wattenberg field (Wolhart et al. 2007)

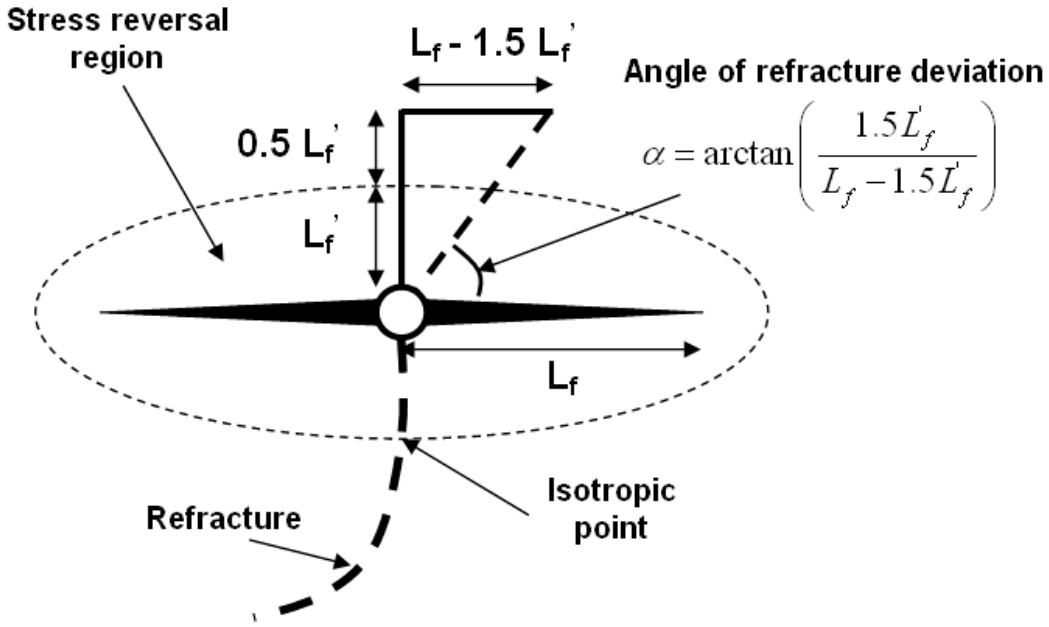

Fig. 5.12 – Calculation of the angle of deviation of the refracture from the direction of the initial fracture based on the size of the stress reversal region

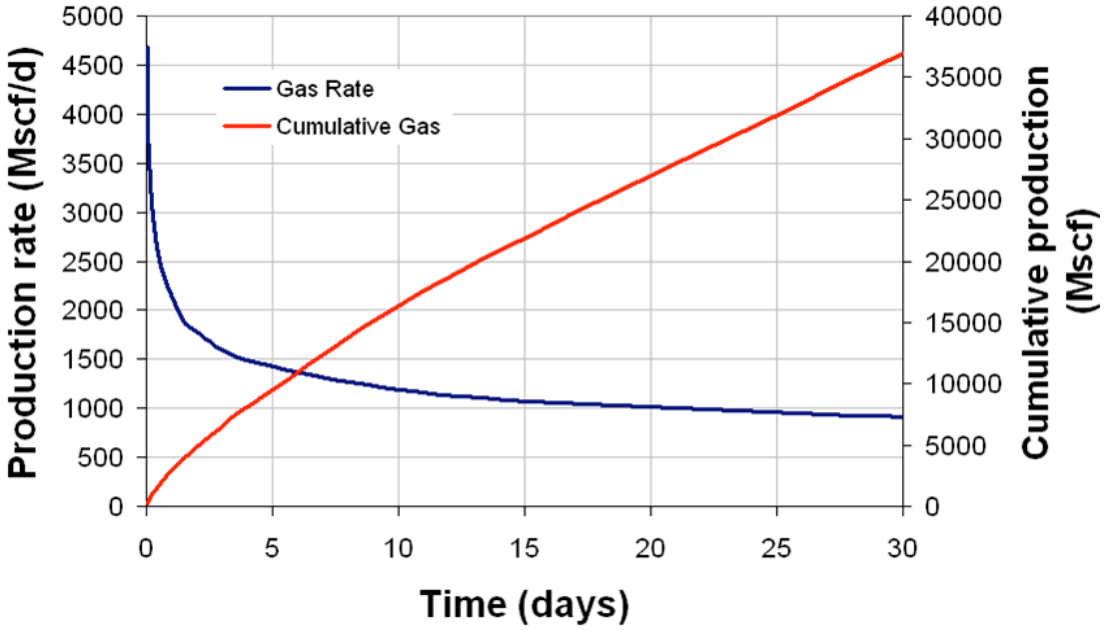

Fig. 5.13 – Estimated production rate and cumulative production of a typical fractured vertical well in the Wattenberg field (bilinear flow approximation)

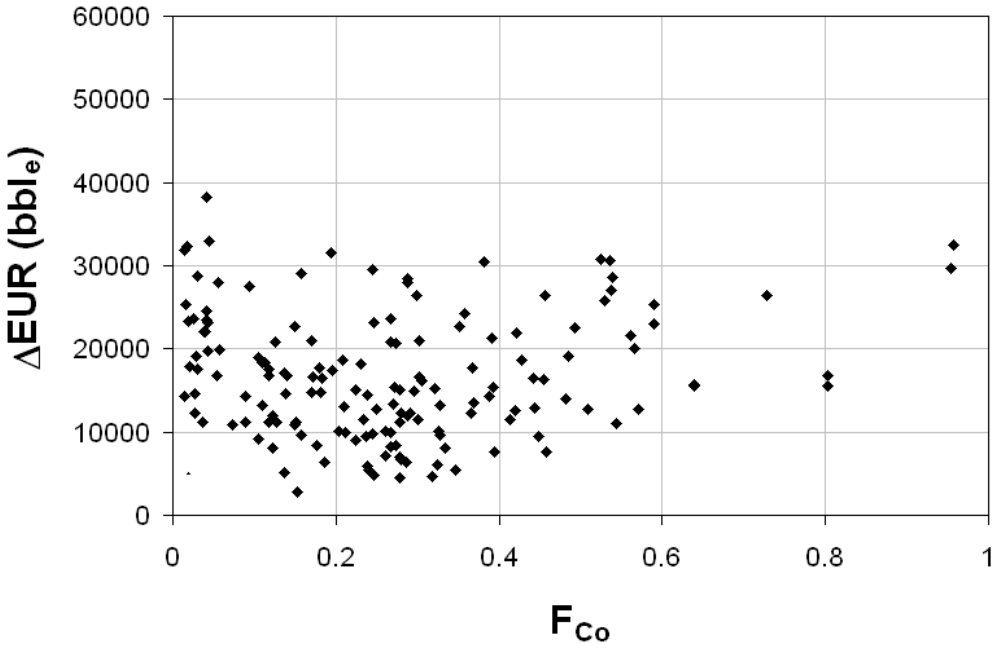

Fig. 5.14 – Additional ultimate recovery from the refracture as a function of the well completion number (F_{Co})

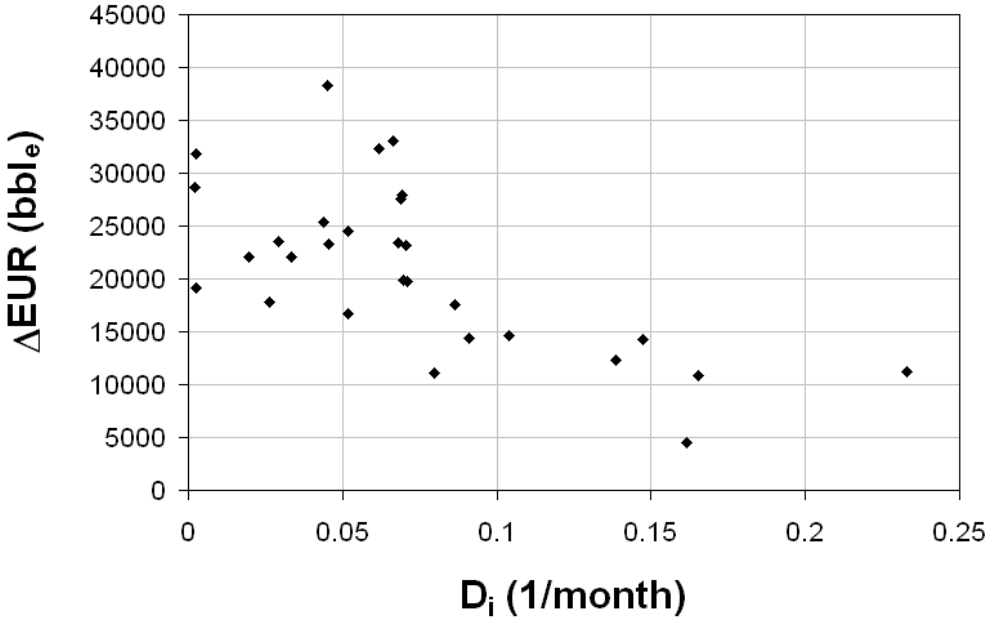

Fig. 5.15 – Additional ultimate recovery from the refracture as a function of the initial fracture decline (D_i) for small values of the well completion number ($F_{Co} < 0.1$)

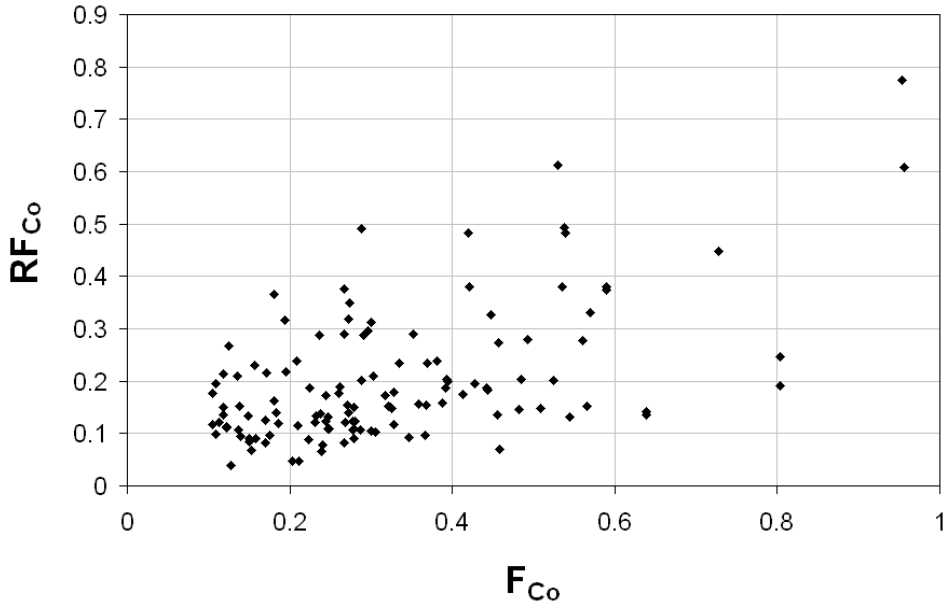

Fig. 5.16 – Refracture completion number as a function of the well completion number ($F_{Co} > 0.1$)

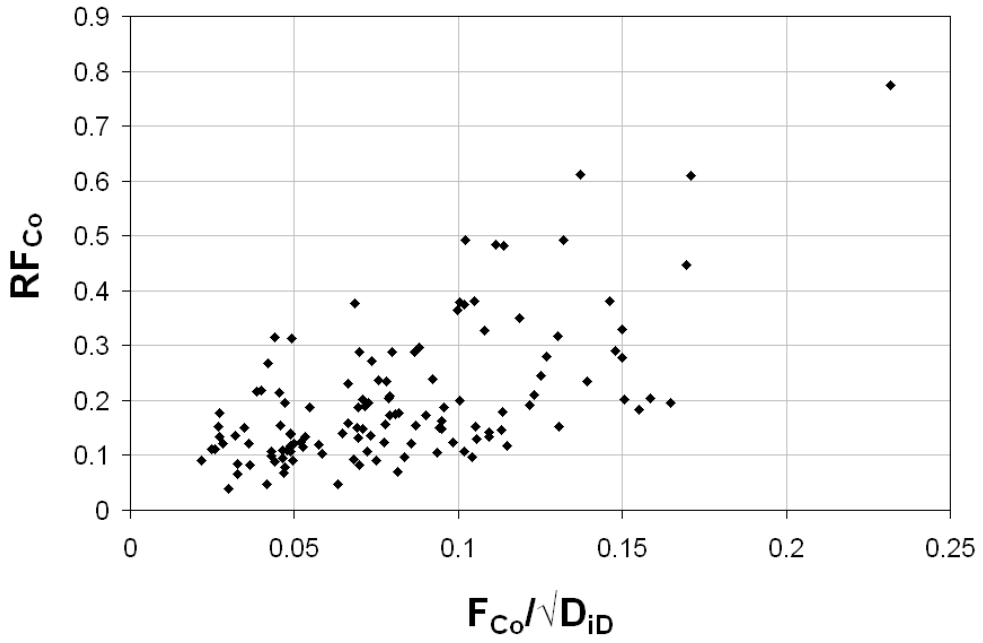

Fig. 5.17 – Refracture completion number as a function of the well completion and production decline numbers ($F_{Co}/\sqrt{D_{iD}}$)

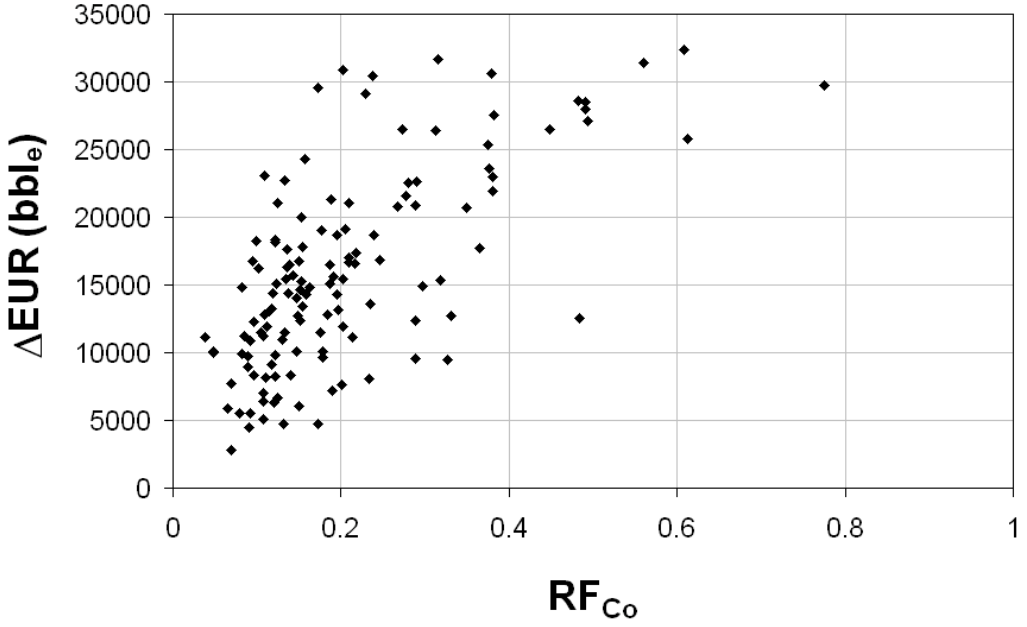

Fig. 5.18 – Additional ultimate recovery from the refracture as a function of the refracture completion number (RF_{Co})

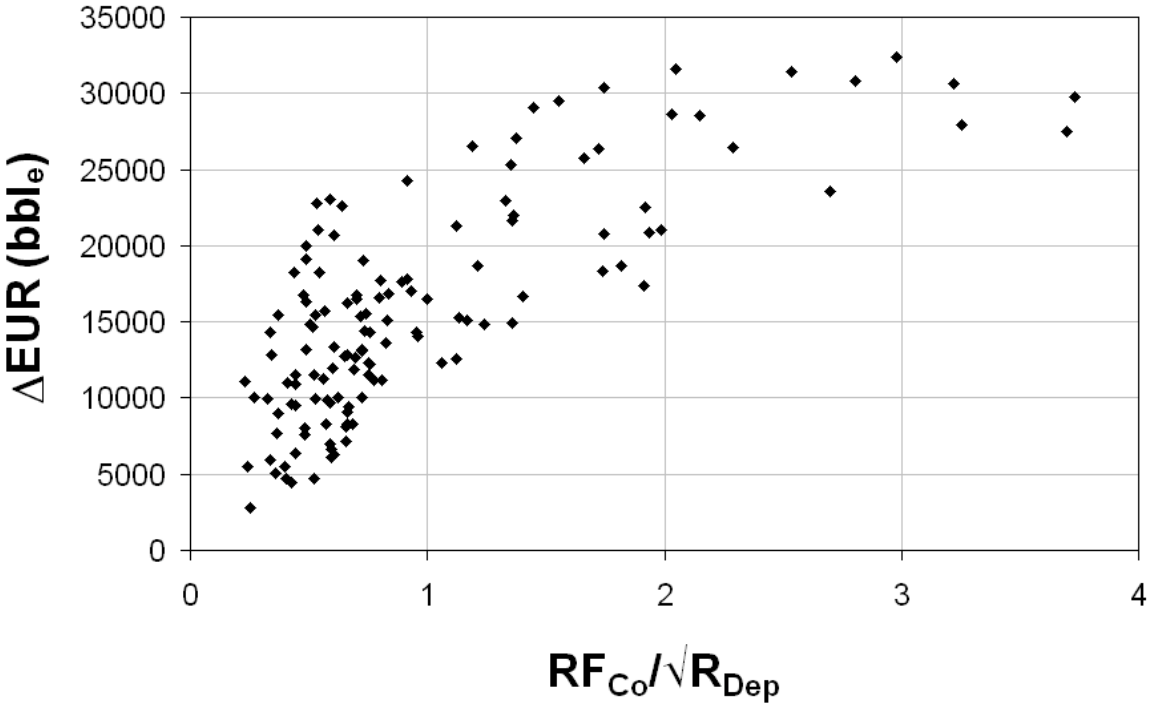

Fig. 5.19 – Additional ultimate recovery from the refracture as a function of the refracture completion number and the reservoir depletion number ($RF_{Co}/\sqrt{R_{Dep}}$)

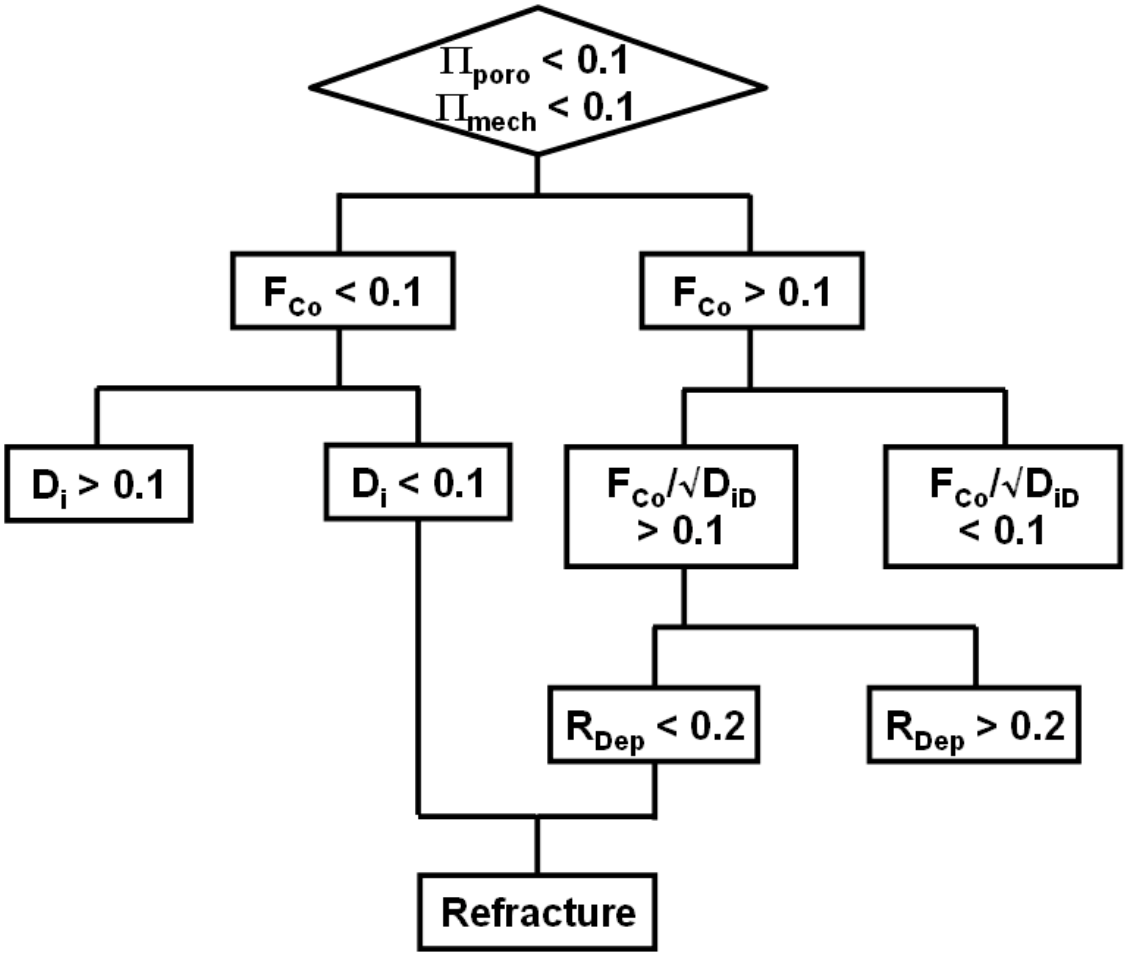

Fig. 5.20 – Decision algorithm for the selection of candidate wells for refracturing

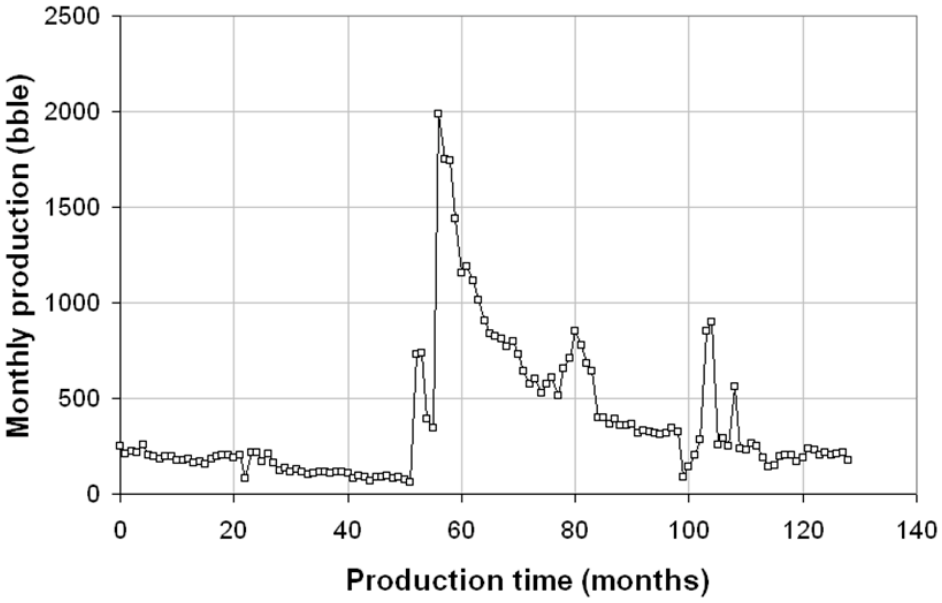

Fig. 5.21 – Typical production profile of a well selected for refracturing: $F_{Co} < 0.1$ and $D_i < 0.1$

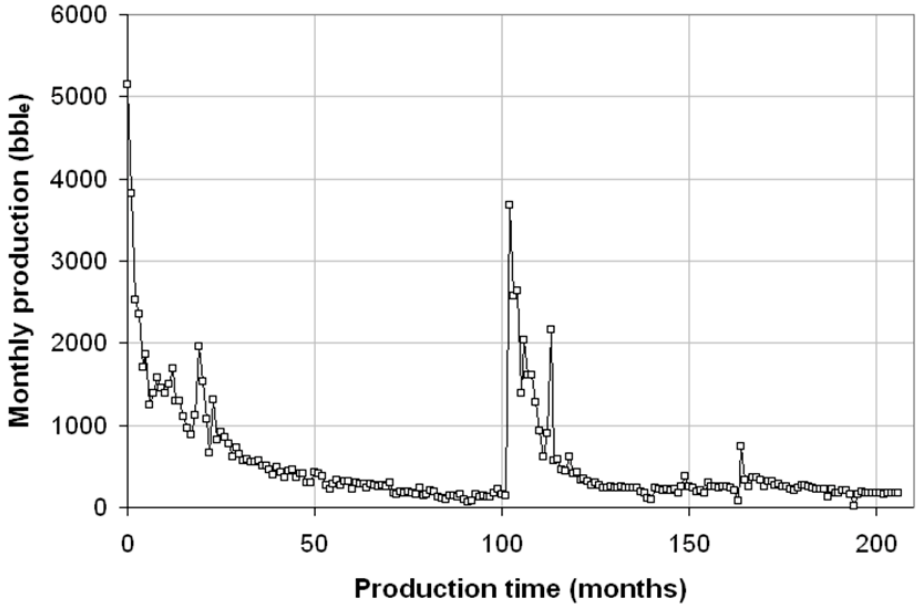

Fig. 5.22 – Typical production profile of a well selected for refracturing: $F_{Co} > 0.1$, $F_{Co}/\sqrt{D_{iD}} > 0.1$ and $R_{Dep} < 0.2$

CHAPTER 6: STRATEGIES FOR THE MULTIPLE FRACTURING OF HORIZONTAL WELLS

The opening of a propped transverse fracture in horizontal wells causes a reorientation of stresses in its neighborhood, which in turn affects the direction of propagation of subsequent fractures. This phenomenon, often referred to as stress shadowing, can negatively impact the efficiency of each frac stage. By mapping the angle of stress reorientation and the horizontal deviatoric stress in multi-fractured horizontal wells, we offer some insight on the completion designs that will (a) minimize induced fracture spacing without compromising the efficiency of each frac stage and (b) effectively stimulate natural fractures in the vicinity of the created fracture.

The understanding and quantification of the mechanical stress interference generated during the stimulation of horizontal wells is crucial toward the improvement of shale gas reservoir drainage. A 3-D geomechanical model was used to demonstrate the superiority of novel single-well and multi-lateral completion strategies.

It is shown that stress interference, or reorientation, increases with the number of fractures created and also depends on the sequence of fracturing. Three fracturing sequences are investigated for a typical field case in the Barnett shale: (a) consecutive fracturing, (b) alternate fracturing and (c) simultaneous fracturing of adjacent wells. The numerical calculation of the fracture spacing required to avoid fracture deviation during propagation, for all three fracturing techniques, demonstrate the potential advantages of alternate fracture sequencing and zipper-fracs to improve the performance of stimulation treatments in horizontal wells.

Transverse fractures initiated from a horizontal well may deviate toward or away from the previous fracture depending on the mechanical properties of the reservoir rock,

fracture spacing, and the orientation of the previous fracture. Using a numerical model allowing non-transverse fractures (those that deviate from the orthogonal path), we show that some induced fractures propagate into previously stimulated areas during the consecutive fracturing of a Barnett shale well, thus decreasing the reservoir drainage efficiency of the frac treatment. The observed net pressure trend matches field observations during fracturing and microseismic measurements.

The alternate sequencing of transverse fractures as well as multi-lateral completions were recognized to be effective ways to enhance natural fracture stimulation, by allowing fracture stages to experience a smaller stress contrast during propagation. More importantly, it is shown that net fracturing pressure data measured in the field can be used to detect mechanical interference between multiple transverse fractures and optimize fracture spacing for a specific well.

1. INTRODUCTION

The rapid development of shale gas in North America can be tied to the combination of horizontal drilling and multi-stage fracturing. The spacing between fractures and perforation clusters as well as the ability to stimulate the fractures naturally present in the rock are thought to be major factors in the success of horizontal completions in shale gas reservoirs.

In very low permeability reservoirs such as the Barnett shale, it is crucial to minimize the spacing between fractures in order to achieve commercial production rates and an optimum depletion of the reservoir (Cipolla et al. 2009). It has been observed in many fields that increasing the number of fractures (to a point) leads to higher initial production rates and presumably better drainage of the reservoir. But the mechanical

stress perturbation created by the opening of a propped-open fracture has been identified to be a limiting factor in the spacing of transverse fractures in horizontal completions (Soliman et al. 1997, 2008; Cheng 2009). Indeed, great attention should be given to avoid stress interference between transverse fractures and ensure transverse fracture growth (Bunger et al. 2011). Microseismic measurements confirm the existence of a stress shadowing effect during horizontal completions (Fisher et al. 2004; Mayerhofer et al. 2006).

One of the key questions that needs to be answered is: what is the optimum number of fractures that should be placed to maximize both the hydrocarbon rates and reservoir drainage? In this chapter we address the question posed above by showing how stress interference can lead to sub-optimal fracture placement.

For the past few years, most new wells drilled in the Barnett shale, and other shale and tight gas plays, have been horizontal wells. Slickwater fracturing is the primary technique used to hydraulically fracture these wells. The horizontal well is generally fractured multiple times, one fracture at a time, starting from the toe. More recently, new stimulation techniques have been investigated to improve the reservoir volume effectively stimulated, or SRV (Mayerhofer et al. 2010). The simultaneous fracturing of two or more parallel adjacent wells, such as simul-fracs or zipper-fracs, aim to generate a more complex fracture network in the reservoir (Mutalik and Gibson 2008; Waters et al. 2009).

2. NUMERICAL MODEL

The model geometry, governing equations, and the boundary conditions are all detailed in the section 2 of Chapter 3. The main difference in this chapter is the fact that multiple transverse fractures are sequentially opened.

2.1. Multiple Transverse Fracture Model

After the first fracture is created, its geometry is fixed (no displacement of the fracture walls is allowed). We assume that the compression of the proppant placed inside previous fractures is negligible as subsequent fractures are opened. Subsequent transverse fractures are modeled using boundary conditions similar to the first fracture (**Fig. 6.1**).

It is observed that the net pressure required to achieve a specified fracture width increases with each additional fracture. Instead of specifying a displacement boundary condition, an iterative process was used to determine, for each fracture, the net pressure corresponding to a given maximum fracture width w_0. An initial value of the net pressure applied on the fracture walls is estimated using the analytical expression of Sneddon (1946) for a semi-infinite fracture (Eq. (6.1)):

$$p_{net}^{i} = p_c - \sigma_{h\min} = \frac{w_0 E}{4\left(1-\nu^2\right)h_f} \tag{6.1}$$

Because the fracture is of finite length, the initial value of the net closure stress, calculated for a semi-infinite fracture, is an underestimate. To converge toward the value of the net closure stress corresponding to the prescribed maximum fracture width w_0^{input}, the next value of applied net closure stress is interpolated from the numerically calculated maximum fracture width (w_0^{model}) according to Eq. (6.2):

$$p_{net}^{k+1} = \sigma_{h\min} + p_{net}^{k} - \sigma_{h\min} \frac{w_0^{input}}{w_0^{model}} \tag{6.2}$$

with k, the step number.

When the calculated value of maximum fracture width (w_0^{model}) approaches the input value (w_0^{input}) within a certain error range, convergence is achieved. The evolution of the net closure stress in the sequential fracturing of a horizontal well is described in more details in the section 5 of this chapter.

3. Application of the Model to Multiple Hydraulic Fractures in Horizontal Wells

The quantification of the extent of the stress reversal region around a propped-open fracture is critical in the design of multiple hydraulic fractures in horizontal wells. In low permeability reservoirs such as shales in which the slow depletion allows for short spacing between sequential fractures, great attention should be given to avoid stress interference between transverse fractures. The model of mechanical stress reorientation from multiple transverse fractures is applied to the case of the Barnett shale. Values of the reservoir and fracture parameters are provided in **Table 6.1**. The dimensions of the opened cracks (height, length and width) are similar for all fractures.

Poroelastic effects due to the leak-off of the fracturing fluid into the reservoir are neglected in this study, due to the very low permeability of the shale and the small amount of fluid leak-off during fracturing.

3.1. Definition of the Minimum Fracture Spacing

As can be seen in **Figs. 6.2 and 6.3**, a stress reorientation of 90° occurs in the vicinity of the transverse fracture. This region is called the stress reversal region. The

minimum fracture spacing can be defined as the distance between the fracture and the end of the stress reversal region, also known as the isotropic point. This is shown as s_{90}^{o} in Fig. 6.3. No refracturing should be done within s_{90}^{o}. In this stress reversal region, the direction of maximum horizontal stress is parallel to the horizontal well, which would lead the refracture to either grow longitudinal to the well, or screen out as the change in fracture orientation is very rapid. The gain in production and new reserves will be very limited.

Even when refracturing is done past s_{90}^{o}, refracture propagation is affected by previous fractures. If a fracture is initiated just outside of the stress reversal region, it will propagate away from the previous fracture, following the direction of maximum horizontal stress. This fracture reorientation decreases as fracture spacing increases. The distances between subsequent fractures needed to limit fracture deviations from the orthogonal plane to less than 5^{o} and 10^{o} are respectively defined as s_{5}^{o} and s_{10}^{o} (Fig. 6.3). Note that the presence of natural fractures, and their effect on fracture propagation, is not modeled. In the situation where the natural fractures are mainly oriented perpendicular to the direction of maximum horizontal stress (as in the Barnett shale), the direction of propagation of hydraulic fractures may significantly deviate from the preferential direction, in particular when stress anisotropy is low (Olson and Dahi-Taleghani 2009).

In very low permeability reservoirs such as the Barnett shale, it is desirable to minimize fracture spacing while at the same time ensuring transverse fracture growth, to efficiently access gas in the reservoir. This implies that the optimal fracture spacing should be just beyond the s_{5}^{o} contour.

3.2. Impact of Fracture Sequence on Fracture Spacing

The stress interference caused by one transverse fracture is shown in Figs. 6.2 and 6.3. Horizontal wells are, however, fractured multiple times. Thus, the values for the minimum fracture spacing provided in Fig. 6.3 are under-estimates (s_{90^o}=140 ft, s_{10^o}=320 ft, and s_{5^o}=450 ft). The stress perturbation caused by each fracture is cumulative with the effect of all prior fractures. Therefore, stress interference (or reorientation) increases with the number of fractures and also depends on the sequence of fracturing. In this section, we will investigate and compare three fracturing sequences: (a) a conventional consecutive fracturing from toe to heel (**Fig. 6.4**), (b) sequencing the fractures alternately (**Fig. 6.5**), and (c) simultaneously fracturing two adjacent wells.

3.2.1. Consecutive Fracturing (1-2-3-4-5…)

When a horizontal well is consecutively fractured, the stress perturbation ahead of the latest fracture increases with each additional fracture (Soliman et al. 2008) until it reaches a maximum. This maximum state of stress reorientation in turn depends on the fracture spacing. The spacing between multiple transverse fractures has been adjusted so that the maximum value taken by s_{90^o} (extent of the stress reversal region) remains inferior to the fracture spacing (**Fig. 6.6**). The calculation of the stress perturbation ahead of the last fracture (n+1) of Fig. 6.6 provides a good estimate of the maximum state of stress reorientation, when taking into account the effect of multiple transverse fractures (**Figs. 6.7 and 6.8**). The spacing quantities corresponding to the maximum state of stress reorientation are summarized below:

$$\begin{cases} s_{90^o} = 230 \text{ ft} \\ s_{10^o} = 430 \text{ ft} \\ s_{5^o} = 600 \text{ ft} \end{cases}$$

In order to limit refracture deviation, the horizontal well corresponding to the values given in Table 6.1 should be refractured every 430 to 600 ft, which is equal to 1.4 to 2 fracture heights. This calculation corroborates typical values of the recommended fracture spacing from field experience (Ketter et al. 2008).

3.2.2. Alternate Fracturing Sequence (1-3-2-5-4…)

If the sequence of fracture placement was altered to conduct fractures in the sequence 1-3-2-5-4, it is shown here that the fractures could be placed closer to each other. This proximity helps to most efficiently drain the reservoir by ensuring that the fractures remain transverse. The alternate fracturing sequence is also referred to as "the Texas two-step" method in the literature (Soliman et al. 2010). We recognize that this fracturing sequence may not be possible with current downhole tools and that special tools may need to be developed. However, our goal is to demonstrate the benefits of this alternate fracturing sequence compared to the sequential fractures currently being pumped.

The new strategy consists of placing the second fracture at the location of what would traditionally be the third fracture. Perforations for the second fracture are placed at a distance greater than s_5^o. This ensures that its deviation from a transverse or perpendicular trajectory is minimal. In the first calculation (600-ft spacing, **Figs. 6.9 and 6.10**), the direction of maximum horizontal stress is reversed along the whole interval separating the fractures. When the fracture spacing is increased to 650 ft, there is an interval where the stress distribution will force the third fracture to grow along a normal path intersecting the horizontal well at the middle point between previous fractures, where the reorientation angle is exactly equal to zero (**Figs. 6.11 and 6.12**). However, the

width of the acceptable interval for the new perforations is extremely narrow (20 ft). For a 700-ft spacing, the width of the refracturing interval is considerably increased (220 ft, **Figs. 6.13 and 6.14**). If the third fracture were to be initiated in this interval, the stress reorientation would favor transverse fracture growth. The location of this third fracture does not have to be exactly at the mid-point between the previous fractures. In fact, even if the fracture is initiated at some distance from the middle, it will follow a trajectory (as seen in the stress profiles, Fig. 6.14) that will force it to grow along the mid-plane between the previous fractures.

For the last simulation, the fracture spacing is equal to 350 ft (1.17 times the fracture height) which is smaller than the recommended value for consecutive fracturing (s_5^o=600 ft). The practical advantage of this fracturing sequence, in addition to the fact that minimum fracture spacing is decreased compared to consecutive fracturing, is that stress reorientation is playing to our advantage, forcing the middle fracture to propagate in the optimum direction.

3.2.3. Simultaneous Fracturing from Adjacent Wells (Zipper-fracs)

The technique of zipper-fracs consists of simultaneously fracturing two parallel horizontal wells. In the particular case that was modeled, the spacing between adjacent wells is equal to the fracture length.

The maximum state of stress reorientation for zipper-fracs was calculated following the same procedure than for a single well, shown in **Fig. 6.15**. Compared to consecutive fracturing of a single well, the fracture spacing needed to minimize fracture deviation (s_{10}^o, s_5^o) is reduced (**Fig. 6.16**):

$$\begin{cases} s_{90^o}\text{, zipper-fracs} = 230 \text{ ft} \\ s_{10^o}\text{, zipper-fracs} = 330 \text{ ft} = 77\%\ s_{10^o}\text{, single well} \\ s_{5^o}\text{, zipper-fracs} = 400 \text{ ft} = 67\%\ s_{5^o}\text{, single well} \end{cases}$$

It is shown that the extent of stress reversal around zipper-fracs is unchanged compared to the case of the single fracture (s_{90^o}=230 ft). However, the reoriented zone outside the stress reversal region significantly shrank (s_{10^o}=330<430 ft and s_{5^o}=400<600 ft). This is due to the symmetry along the plane x =500 ft (middle plane between adjacent wells), where the reorientation angle is equal to zero.

3.3. Impact of Fracture Sequence on Fracture Complexity

Olson and Dahi-Taleghani (2009) showed that hydraulic fracture interaction with pre-existing natural fractures is a function of the relative net pressure R_n. This parameter is inversely proportional to the local deviatoric stress in which the fracture propagates (Eq. (6.3)):

$$R_n = \frac{p_f - \sigma_{h\min}}{\sigma_{h\max} - \sigma_{h\min}} \tag{6.3}$$

High values of the relative net pressure R_n favor fracture path complexity. Thus, a hydraulic fracture propagating in a region of low stress contrast is likely to create larger networks of interconnected fractures. We calculated the local stress contrast along the direction of propagation of a transverse fracture for (a) the middle fracture in an alternate fracturing sequence and (b) consecutive fracturing.

The average value of the horizontal stress contrast midway between two transverse fractures is plotted in **Fig. 6.17**. The stress contrast is lowest (18 psi) when the outside fractures are spaced 650 ft apart (s_f = 325 ft). We have shown before that a

fracture spacing less than 325 ft does not allow propagating a middle fracture in the alternate fracturing sequence. Thus, the minimum fracture spacing in the alternate fracturing sequence is also predicted to be the optimum case for creating fracture complexity.

A comparison of the local stress contrast seen by a propagating fracture along its direction of propagation, in the consecutive and alternate fracture sequence, demonstrates the superiority of the later sequence to generate fracture complexity (**Fig. 6.18**). The deviatoric stress approaches zero in the near wellbore region in the case of the optimum spacing in the alternate fracturing sequence (325 ft). Along the first half of propagation, the stress contrast remains lower than 10 psi, which is equal to 10% of the in-situ stress contrast (Fig. 6.18). It is only in the second half of the fracture propagation that the local stress contrast increases significantly. Thus, choosing the alternate fracturing sequence, we can expect high fracture complexity in the near-wellbore region as a result of the propagation of the "middle fracture". The results of this study corroborate the conclusions of Soliman et al. (2010) on the stress anisotropy between two transverse fractures.

4. MULTIPLE FRACTURING OF MULTIPLE HORIZONTAL LATERALS

The study of the impact of the fracture sequence revealed that between two transverse fractures, if the spacing is large enough, it is possible for a middle fracture to be propagated in a region of (a) low stress contrast and (b) favorable direction of maximum horizontal stress. The literature has been recently reporting an increasing number of multi-lateral horizontal completions, especially in gas shales. So, it is relevant

to wonder whether an approach similar to the single-lateral alternate fracturing sequence could be applied to horizontal wells having multiple laterals.

4.1. Fracture Sequence and Geometry in Multi-Lateral Horizontal Completions

The geometry of a multiple fractured multi-lateral horizontal well is represented in **Fig. 6.19**. It may be described by the following variables:

- Fracture dimensions L_f, h_f
- Fracture spacing s_f
- Inter-well spacing s_w

In an approach similar to the alternate fracturing sequence, the middle well (HW_2) is used to propagate a fracture between two pairs of fractures previously initiated from the outside wells (HW_1 and HW_3). The same strategy may be adopted in any horizontal completions having an uneven number of laterals (and of course more than just one lateral). Such a strategy allows us to benefit from the propagation of a "middle fracture", as in alternate fracturing completions, without the need for special downhole tools. Indeed, in each lateral, the fractures are initiated in a conventional consecutive fracturing sequence.

4.2. Stress Distribution between Fractures Propagated from the Outside Laterals

The stress distribution between two pairs of fractures propagated from the outside laterals HW_1 and HW_3 is shown in **Fig. 6.20**, for the reservoir properties and fracture geometry of Table 6.1, a fracture spacing s_f equal to 600 ft and a well spacing s_w equal to 500 ft. The direction of maximum horizontal stress is reversed everywhere along the

outside laterals. Thus, the outside fractures 1 and 2 are too closely spaced to allow propagation of a transverse fracture from the outside laterals HW_1 and HW_3, similarly to the alternate fracturing sequence.

When considering fracturing the center lateral, the direction of maximum horizontal stress still allows propagation of a transverse fracture. The distance of transverse propagation $L_{transverse}$ is maximum midway from the previous fractures and will be a function of not only the spacing between the outside fractures but also the inter-well spacing (s_w). The zone of transverse fracture propagation can also be identified when plotting the angle of stress reorientation (**Fig. 6.21**).

4.3. Optimum Fracture and Inter-Well Spacing

After identifying the possibility of propagating a transverse middle fracture from the center lateral, we recorded the value of $L_{transverse}$ for different values of the fracture and inter-well spacing (**Fig. 6.22**). It is clear that if the wells are spaced too close to each other, the opportunity to propagate a transverse middle fracture from the center lateral may not exist at all ($s_w/L_f = 0.1$). The length of transverse fracture propagation increases with inter-well spacing and reaches its maximum value when the inter-well spacing is at least equal to the fracture length ($s_w/L_f = 2$).

$L_{transverse}$ also increases with the spacing between the outside fractures (s_f). Transverse fracture propagation is not affected if the fracture spacing is at least equal to twice the minimum fracture spacing in the alternate fracturing sequence ($2s_f = 650$ ft). In this case, the stress reorientation angle is equal to zero everywhere along a line equidistant from the outside fractures.

The local stress contrast was recorded along the assumed propagation direction of the middle fracture (**Fig. 6.23**). This quantity is minimum for the minimum possible inter-well spacing ($s_w/L_f = 1$) and appears also to be more sensitive to the inter-well spacing than to the fracture spacing. Thus, the best practice for the positioning of the horizontal laterals is to place them close to each other, but not closer than a distance equal to the fracture half-height. Otherwise, the benefit of propagating long transverse fractures would be lost. Indeed, that may result in fracturing zones of the reservoir that are already stimulated.

Looking back at Fig. 6.22, the distance of transverse fracture propagation is extremely sensitive to the fracture spacing when the inter-well spacing is small. Transverse propagation length is decreased by over 50% as the fracture spacing decreases from 650 ft to 600 ft, which is only a 50-ft spacing differential. So similarly to the case of the alternate fracturing sequence in a single well, the spacing between the outside fractures should at least be equal to 650 ft (for this specific set of parameters). Finally, the optimum multi-lateral completion strategy in a typical Barnett shale gas well is summarized below:

$$\begin{cases} s_w = L_f = 500 \text{ ft} \\ s_f = 650 \text{ ft} \end{cases}$$

The predicted values of the transverse fracture propagation and average stress contrast for the middle fracture are:

$$\begin{cases} L_{transverse} = L_f = 500 \text{ ft} \\ \Delta\sigma_{hmiddlefrac} = 0.24\ \Delta\sigma_{hi} = 24 \text{ psi} \end{cases}$$

We can finally note that while a 650-ft spacing may not be practical in an alternate fracturing sequence (as the refracturing interval is only 20-ft wide), this spacing would suffice in a multi-lateral completion. In the latter case, the middle fracture is

initiated from the middle well (and not from the outside well), where the refracturing interval is wide enough to allow fracture initiation from multiple perforation clusters.

5. TRANSVERSE FRACTURES DEVIATING FROM THE ORTHOGONAL PATH

So far, we have modeled fractures perfectly orthogonal to the horizontal wells. In order to truly quantify the evolution of the direction of propagation of consecutive transverse fractures, it is imperative to allow the transverse fracture to deviate from the orthogonal path. Contrary to the previous section, we allow the fractures to deviate from the orthogonal path and propagate away and toward the previous fracture. The strategy consists in calculating the additional stress caused by a fracture at the spot of the subsequent fracture as well as the fracture trajectory.

We investigated the effect of fracture spacing on the propagation direction of multiple transverse fractures in the Barnett shale.

5.1. Validation of the Modeling Strategy

Model simplifications must be made in order to tackle this problem. As opposed to perfectly orthogonal fractures, multiple inclined fractures are challenging to model on a single numerical mesh. In a finite difference model, the geometry of all fractures must be set from the beginning, which may be very difficult, as the angle of propagation of subsequent transverse fractures may depend on the mechanical stress perturbation generated by the previous fractures. This would require a complex and time consuming re-meshing after every single fracture stage.

In a simplified approach, the net closure stress and the propagation direction are calculated in the vicinity of the previous fracture (**Fig. 6.24**). At each fracturing stage, the

stress created by the propped fracture in the direction perpendicular to it is computed at some distance from the fracture. The net closure stress in the subsequent fracture is equal to the net closure stress of a single transverse fracture (without stress shadow) plus the stresses generated by the previous fracture (Eq. (6.4)):

$$p_{net}^{n+1} = p_{net}^{1} + \sigma_{yy}^{n}\left(s_f\right) - \sigma_{h\min} \tag{6.4}$$

Based on the stress distribution around a transverse fracture, we can track the trajectory of the subsequent fracture assuming that it will follow the direction of maximum horizontal stress. The average angle of deviation from the orthogonal trajectory, $\theta_f(s_f)$, is then calculated from the coordinates of the final fracture position (Fig. 6.24).

In order to validate this approach, we calculated the increase in net fracturing pressure in a numerical model including four subsequently opened transverse fractures, each of them perfectly orthogonal to the well, for three different values of the fracture spacing (Fig. 6.1). The net pressure profile calculated in the single-fracture approximation fits the one from the more complicated, multiple-fracture model (**Fig. 6.25**). It means that to a first order, each transverse fracture "sees" the mechanical interference created by only the previous fracture. Note that this approach still allows the net fracturing pressure to build up with each new transverse fracture as the result of the opening of multiple previous fractures.

5.2. Propagation Direction of Consecutive Transverse Fractures

For a 400-ft fracture spacing, transverse fractures propagate away from the previous fracture with a small angle of deviation from the orthogonal path (less than 2°)

(**Fig. 6.26**), as expected from the stress reorientation profile shown in Figs. 6.2 and 6.3 (simulated using the same parameters). When the spacing is reduced to 300 ft, the average angle of deviation from the orthogonal path increases to a little over 5° (**Fig. 6.27**). Contrary to what may have been expected, the angle of deviation from the orthogonal path does not increase with each new transverse fracture. We note that after stage 4, the average angle of deviation converges toward a value $\theta_f = 5.7°$. A closer look at the fracture trajectory shows that after stage 5, the fracture initially propagates toward the previous fracture. Then at some distance from the wellbore, the fracture starts propagating away from the previous fracture. Plotting the stress distribution around a non-transverse fracture reveals the explanation behind this non-trivial trend (**Fig. 6.28**).

It is indeed possible to draw a zone where the subsequent fracture will be attracted by the previous fracture, and another zone where the fracture will propagate away from the previous fracture. The size of the attraction zone will be a function of the net pressure, the in-situ stress contrast and the average angle of deviation from the orthogonal path. In the present example, stage 5 is initiated within the attraction zone of the previous stage, thus fracture 5 initially propagates back toward fracture 4 until it leaves the attraction zone (Fig. 6.28).

As the fracture spacing is decreased to 250 ft the extent of fracture deviation is larger (**Fig. 6.29**). For instance, stages 2, 5 and 8 propagate away from the previous fracture at an angle $\theta_f > 5°$. But what stands out the most is the fact that under a critical value of the fracture spacing, the attraction zones associated with fractures 2, 5 and 8 cause three fracture stages (3, 5 and 9) to intersect previous fractures. The practical consequence of such intersections is a less efficient drainage of the reservoir, even though the fractures are initiated closer to each other. Additionally, it may be noted that to calculate the trajectory of fractures 4, 7 and 10, a geometry including the presence of the

two previous fractures is simulated. For instance, the direction of propagation of fracture 4 is affected by the stress distribution calculated in the vicinity of the fracture system consisting of intersecting fractures 2 and 3 (**Fig. 6.30**).

Fracture propagation maps were also calculated for a 200-ft and a 150-ft fracture spacing (**Figs. 6.31 and 6.32**). In these cases, the "unsuccessful" stages not only intersect the previous fracture but propagate longitudinally along the horizontal well. For such small values of the fracture spacing, unsuccessful fractures are initiated within the stress reversal region of the previous fracture, which is located inside the attraction zone associated with the previous fracture (Fig. 6.28). In the present example (150-ft spacing), only every other fracturing stage effectively stimulates the shale, thus leaving significant portions of the reservoir inadequately drained. Calculated trajectories of sequential transverse fractures recall propagation patterns obtained by Olson (2008) who modeled the actual propagation (simultaneous and sequential) of multiple transverse fractures using a displacement discontinuity, boundary element technique.

Fig. 6.33 illustrates the impact of fracture spacing on the angle of deviation from the orthogonal path. Below a critical value of the fracture spacing, the efficiency of fracturing stages is negatively affected as shown by the large variations in deviation angles. As a matter of fact, the gain in reservoir drainage area may be marginal compared to the additional cost represented by an increased number of fracture stages. This result suggests that because of mechanical stress interference, spacing transverse fractures ever closer to each other may not be a desirable completion strategy. Indeed the fractures need to be spaced sufficiently far away that they do not intersect each other.

5.3. Use of Net Fracturing Pressure Data to Detect Stress Shadowing and Optimize Fracture Spacing

Fig. 6.34 illustrates the impact of fracture spacing on the evolution of the net closure stress. As shown in Fig. 15, for fracture spacings of 400 ft and 300 ft, the net closure stress only increases with each new stage until reaching a plateau. However for the 250, 200 and 150 foot fracture spacings, the net pressure profile features an up-and-down trend.

We observe that counting the number of times the net fracturing pressure decreases from one stage to another indicates the number of unsuccessful fracture stages identified in the maps of fracture propagation (Figs. 6.29, 6.31 and 6.32). The decrease in the fracture closure stress (from one stage to another) is a consequence of the smaller mechanical stress interference (stress shadow) generated by the previous fracture when propagating into stimulated regions of the reservoir instead of propagating orthogonal to the well. In the extreme case of the smallest spacing, while the designed value is 150 ft, the effective spacing is only equal to 300 ft, as every other fracture is longitudinal with respect to the wellbore. This means that doubling the number of frac stages (compared to the 300-ft spacing case) may result in little improvement in well production and reservoir drainage.

When compared to previous work on the mechanical interaction of multiple transverse fractures, the new results confirm the effect of fracture spacing on the rise in net fracturing pressure as predicted by Roussel and Sharma (2010) and Vermylen and Zoback (2011). However, allowing deviation from the orthogonal path reveals new trends in the evolution of the net closure stress. Several field measurements brought to our attention show trends that are similar to those reported above. These will be the subject of a future publication. The net fracturing pressure data measured during each fracturing job

can now be used as a diagnostic tool to suggest changes in the designed fracture spacing of future completions (Roussel and Sharma 2011).

6. CONCLUSIONS

The multiple-fracture model presented in this chapter can be applied to estimate values of the minimum and optimum fracture spacing in horizontal wells for a given set of reservoir properties, well and fracture design, and fracturing sequence. Values for the recommended fracture spacing for an example case of the Barnett shale are presented in **Table 6.2** for three possible fracturing sequences: (a) consecutive fracturing, (b) alternate fracturing and (c) simultaneous fracturing of adjacent wells. The last two techniques make it possible to shrink the stress reorientation region, thus significantly reducing the fracture spacing needed to limit fracture deviation from the desired orthogonal path.

Based on the results of the simulations, we can summarize our recommendations as follows:

- To avoid longitudinal fractures, the minimum fracture spacing must be larger than s_{90^o}. The model presented here allows us to obtain reliable estimates of s_{90^o} for a given set of reservoir and fracture properties.
- To ensure transverse fractures and avoid deviation of the fracture from its orthogonal path, the fracture spacing should be larger than s_{5^o} which can be calculated from the model.
- The alternate fracturing method offers the potential to enhance fracture complexity through the propagation of a "middle fracture" in a region of low stress contrast and may decrease minimum fracture spacing.

- Alternate fracturing also presents the important advantage of forcing the "middle fracture" to propagate along the orthogonal plane midway between the previous two fractures.
- The development of technologies allowing the alternate fracturing technique to be applied in the field may prove beneficial to the performance of stimulation treatments in horizontal wells.
- Under a critical value of the spacing during consecutive fracturing, some fracture stages intersect previous fractures, thus reducing the efficiency of reservoir drainage.
- Multi-lateral completions allow benefits similar to alternate fracturing without the need for special downhole tools. Fractures initiated from the middle well propagate in a region of low stress contrast in the proposed fracture sequence.

Numerical simulations in multiple-lateral horizontal wells suggest the use of different fracturing treatments (fluids, flow rate, etc.) in the middle well as opposed to the outside wells. Indeed, the main goal when fracturing the outside laterals is to propagate long transverse fractures. On the other hand, fracture complexity is what matters most in the center well. It is still widely debated whether complex fracture networks are preferable or not to long bi-wing induced fractures. Multi-lateral completions may provide a way to implement both in the same well, at a potentially reasonable cost.

Another important conclusion lies in the newly discovered signification of the net pressure data collected during the fracturing treatment. Up-and-down variations of the net pressure from one stage to another indicate propagation of transverse fractures into previously stimulated regions of the reservoir. Fracturing pressure data can then be used

to optimize the spacing between subsequent fracture stages for a specific well and estimate the geometry of a multiple fractured horizontal well (that can be used later as an input in a reservoir drainage simulation). As opposed to the minimum horizontal stress which can easily be measured through a mini-frac test, the maximum horizontal stress is more often grossly estimated. The proposed numerical model of multiple transverse fracture interaction has the potential to quantify the local horizontal stress contrast, and thus obtain a good estimation of the maximum horizontal stress when combined with a mini-frac test.

	Barnett shale gas
Pay zone Young's Modulus E_p (psi)	7.3×10^6
Bounding layer Young's Modulus E_b (psi)	3.0×10^6
Poisson's Ratio ν	0.2
σ_{hmax} (psi)	6400
σ_{hmin} (psi)	6300
Depth (ft)	7000
Pay zone half-thickness h_p (ft)	150
Fracture half-height h_f (ft)	150
Fracture half-length L_f (ft)	500
Fracture maximum width w_0 (mm)	4

Table 6.1 – Reservoir parameters for a typical Barnett shale gas well

	Consecutive fracturing (1-2-3-4-5…)	Alternate fracturing (1-3-2-5-4…)	Simultaneous fracturing of adjacent wells (well spacing = 2 Lf)
Minimum fracture spacing (ft) (= s_{90}^o or interval for 3rd frac>0 ft)	230	325	230
Recommended fracture spacing (ft) (= s_5^o or interval for 3rd frac>100 ft)	600	340	400

Table 6.2 – Comparison of minimum and recommended fracture spacing for different fracturing techniques for a Barnett Shale field case

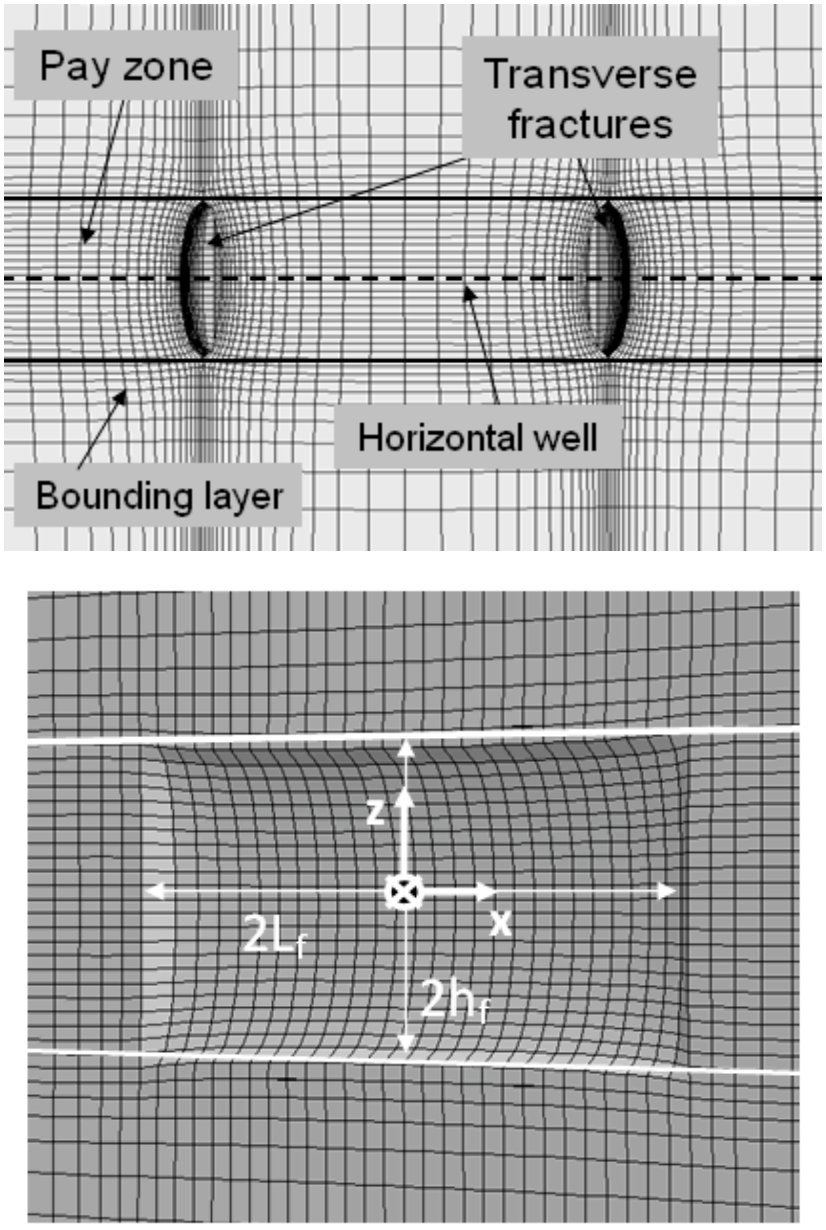

Fig. 6.1 – Three-dimensional model of multiple transverse fractures in a layered reservoir

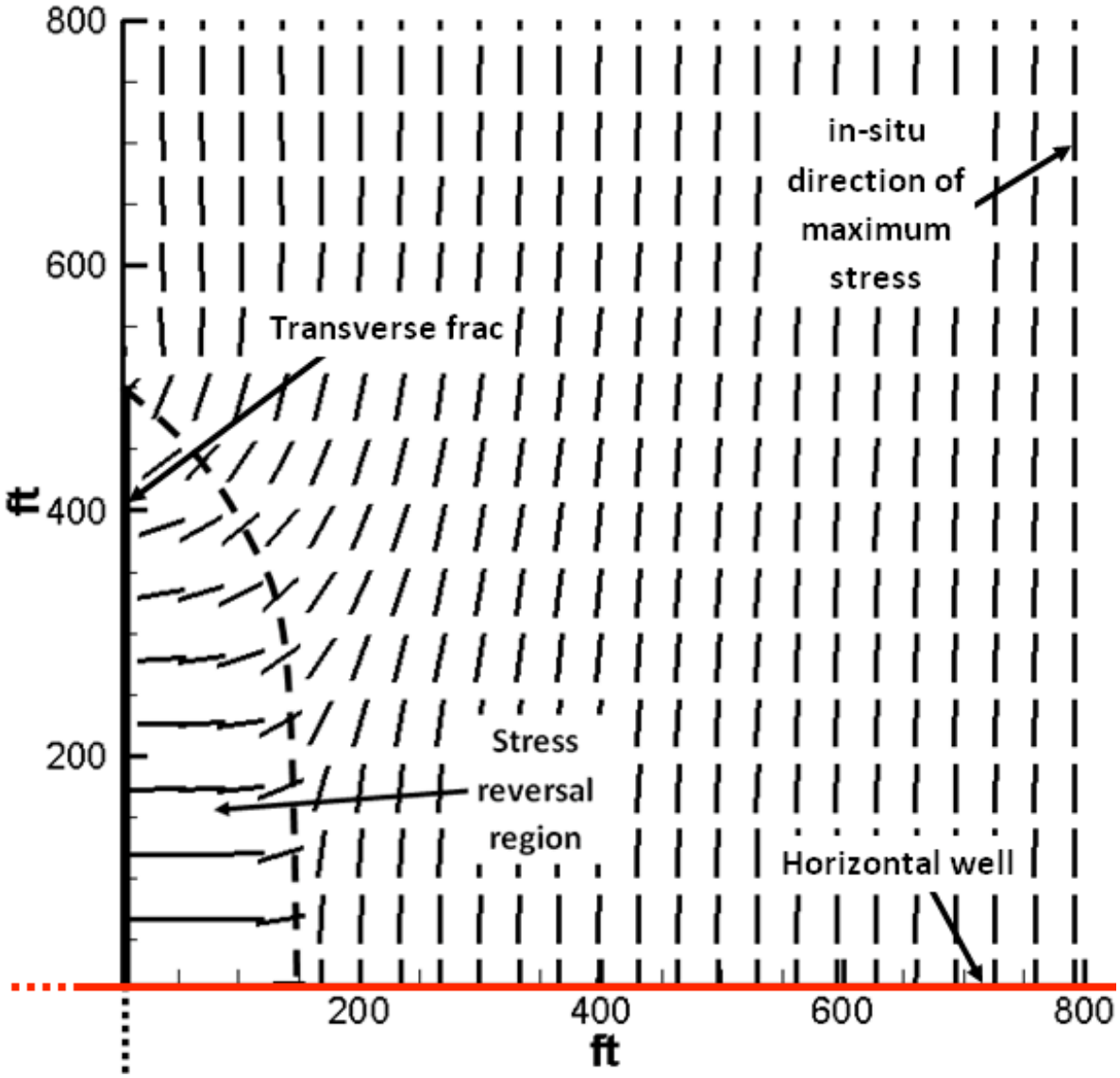

Fig. 6.2 – Direction of maximum horizontal stress around a single transverse fracture in the Barnett shale

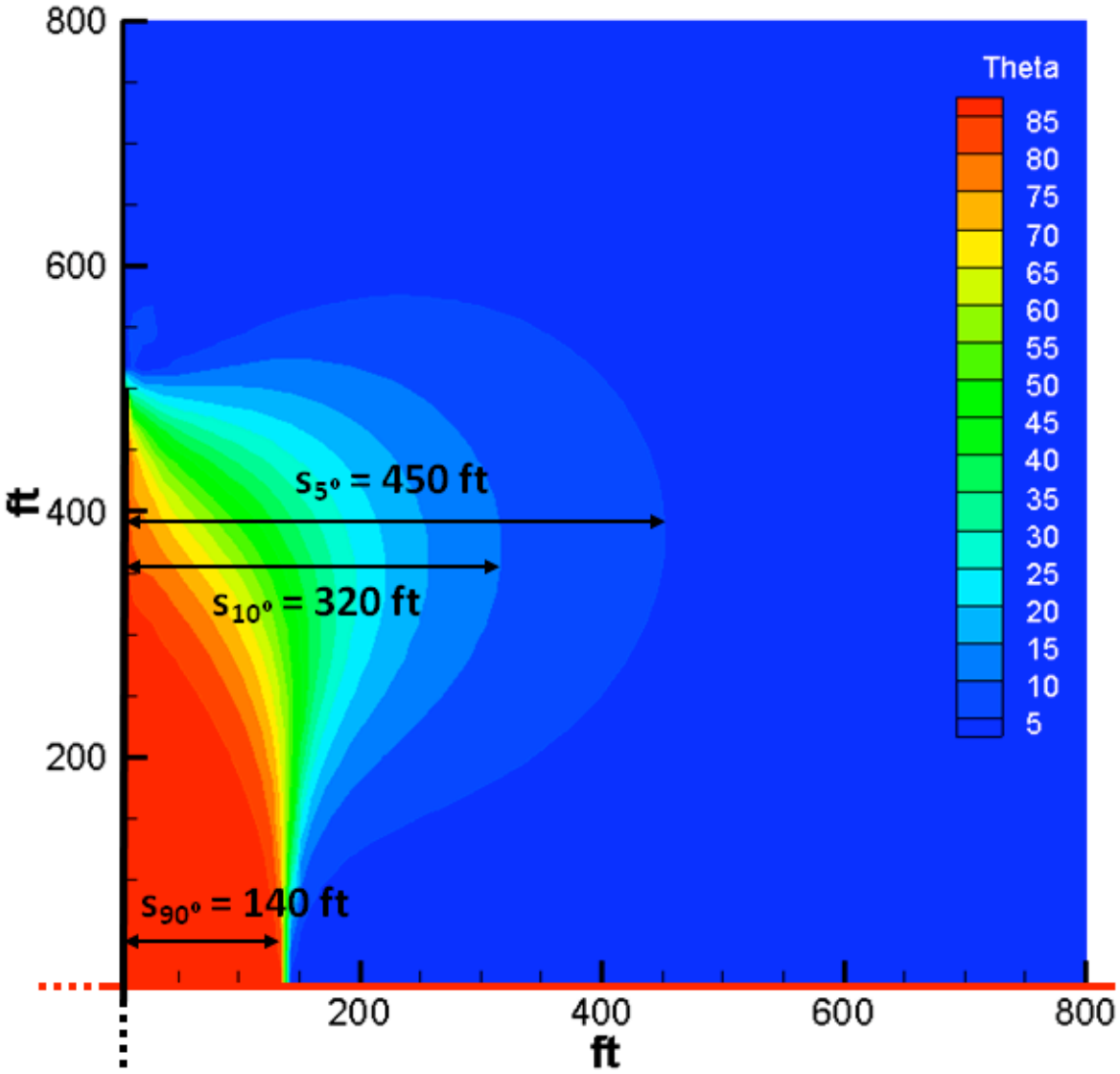

Fig. 6.3 – Angle of stress reorientation (θ) around a single propped-open fracture in the Barnett shale

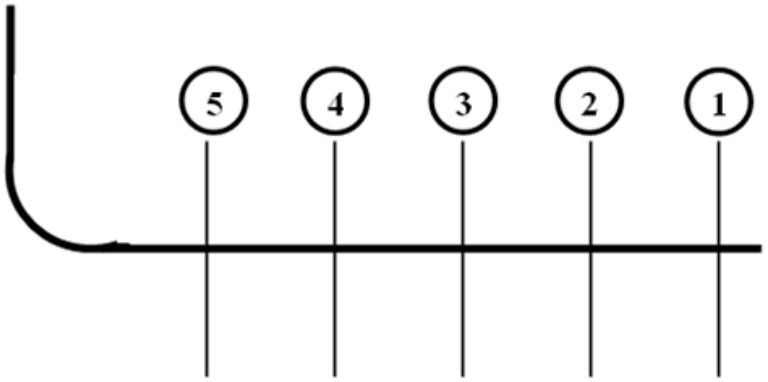

Fig. 6.4 – Consecutive fracturing sequence (1-2-3-4-5) in the multiple fracturing of a horizontal well

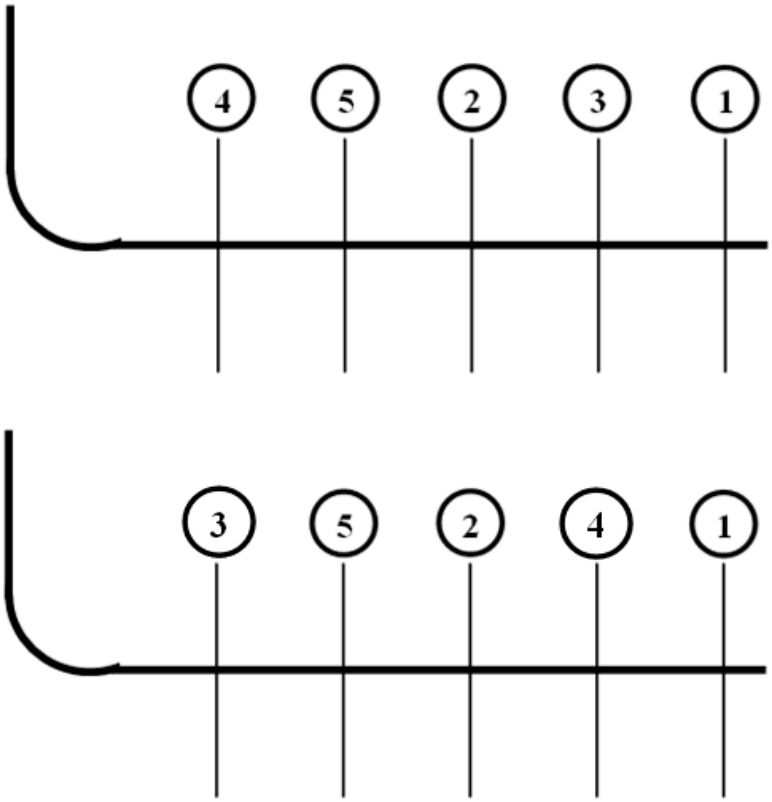

Fig. 6.5 – Two alternate fracturing sequences (a) 1-3-2-5-4 and (b) 1-4-2-5-3 in the multiple fracturing of a horizontal well

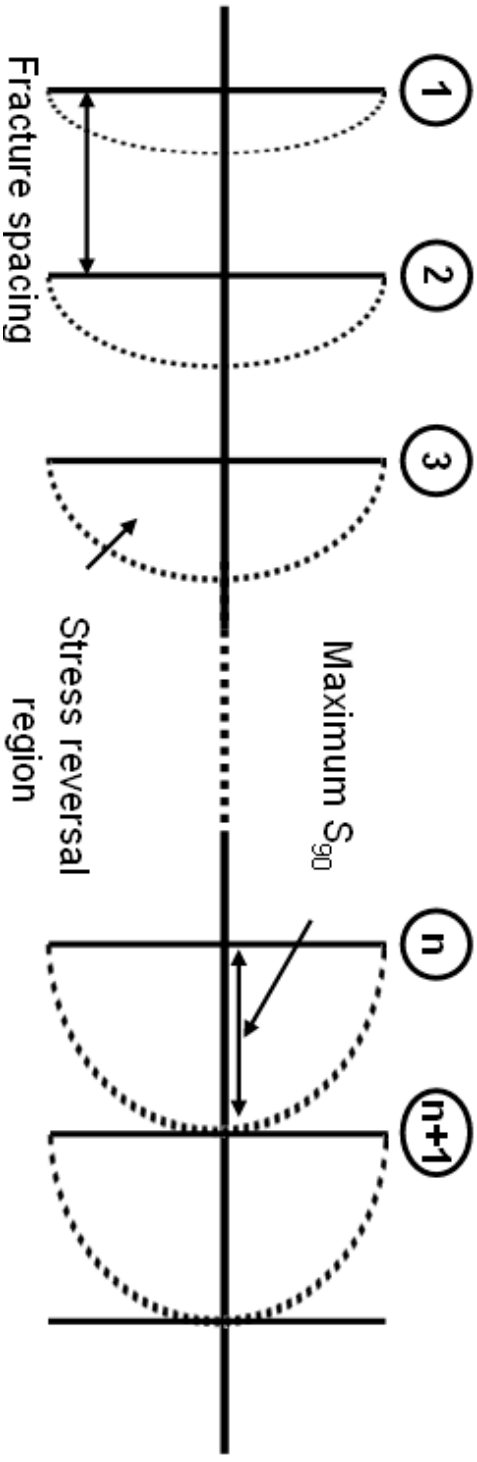

Fig. 6.6 – Modeling of maximum stress reorientation due to multiple consecutive fractures in a horizontal well

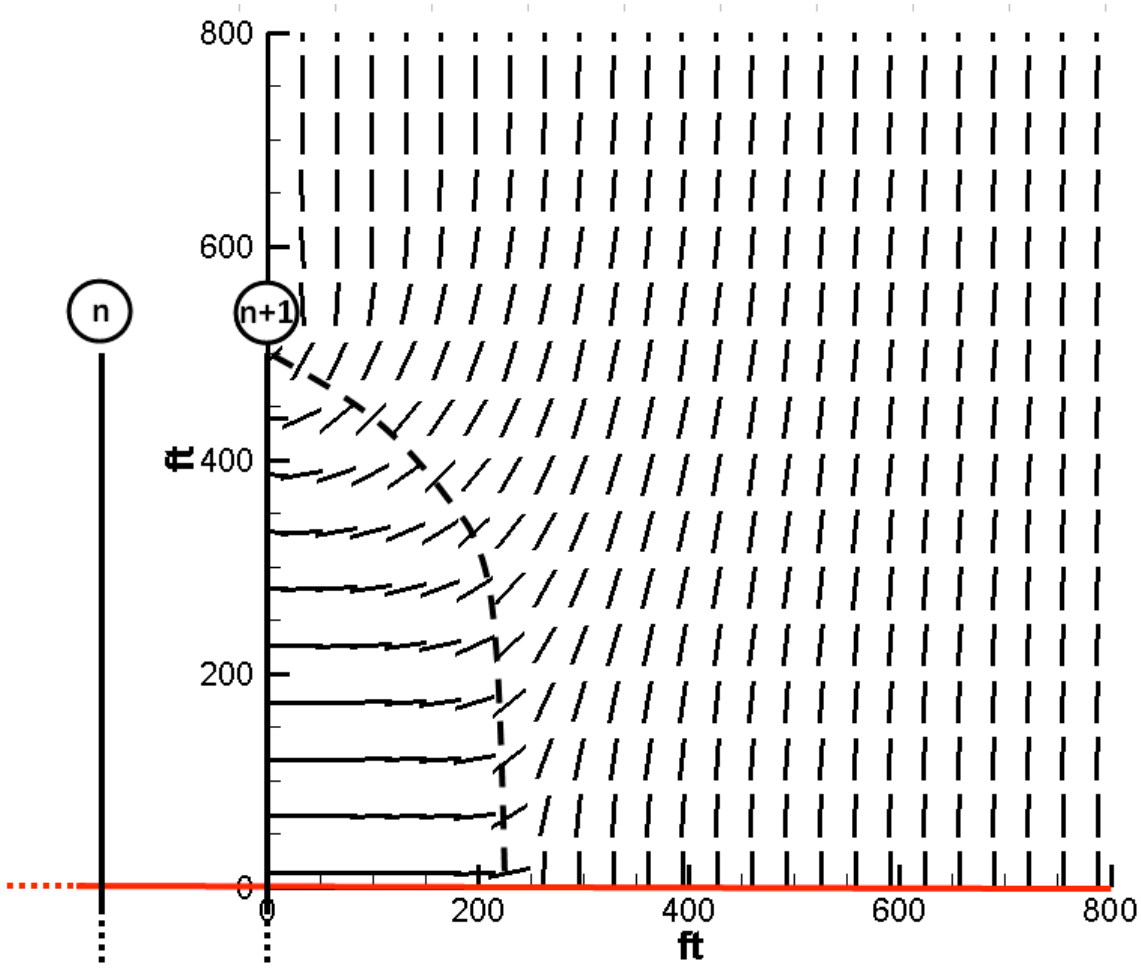

Fig. 6.7 – Direction of maximum horizontal stress around multiple consecutive transverse fracture in the Barnett shale (maximum state of stress reorientation)

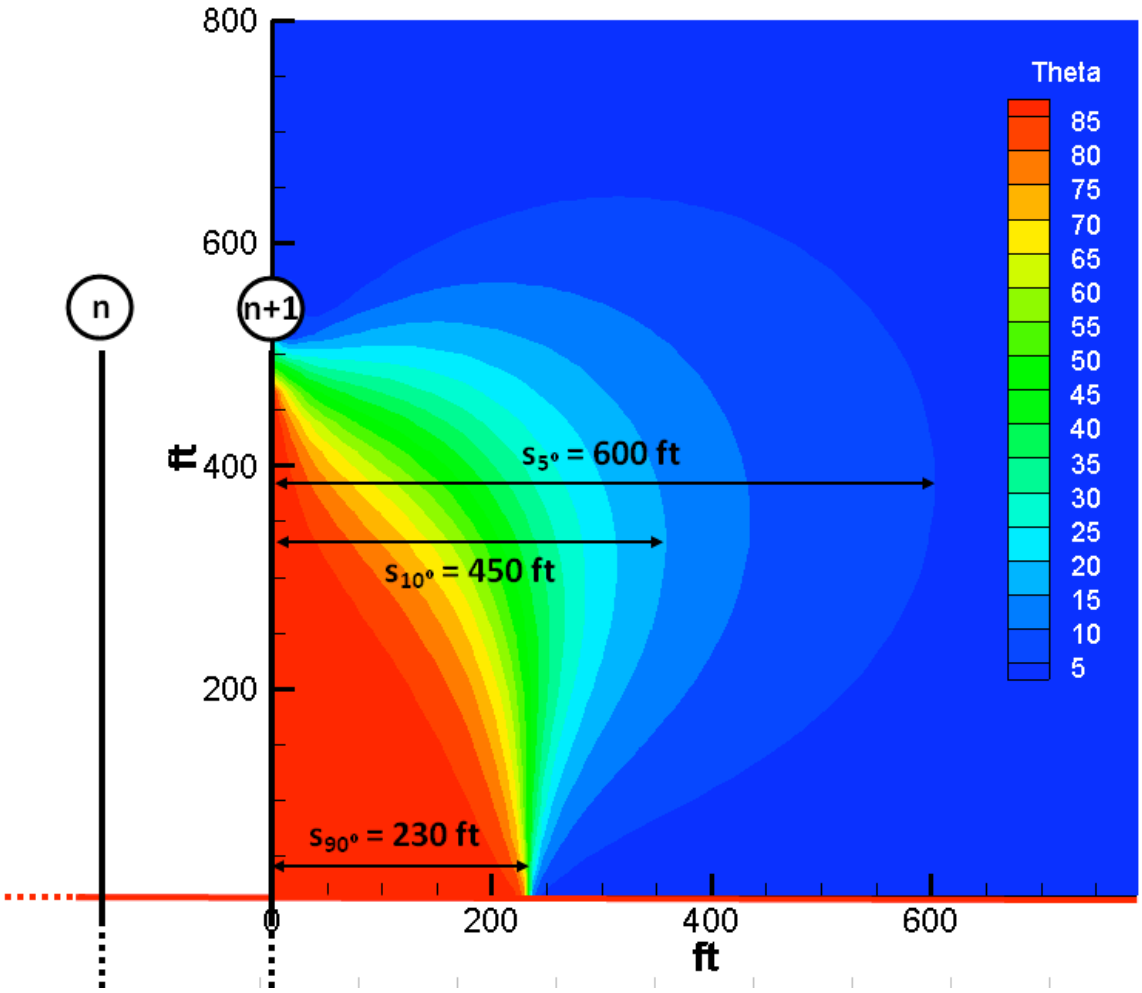

Fig. 6.8 – Angle of stress reorientation around multiple consecutive transverse fracture in the Barnett shale (maximum state of stress reorientation)

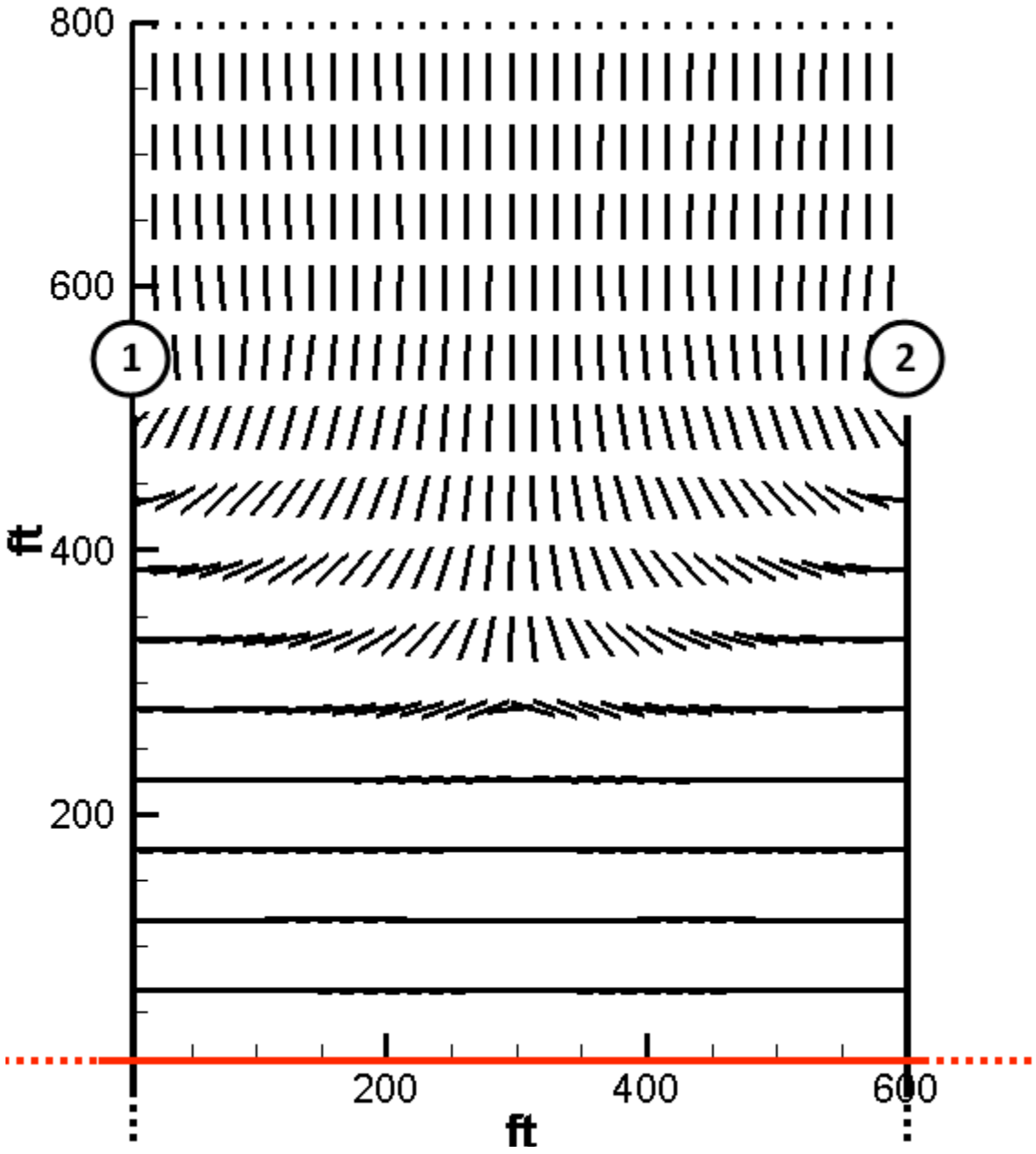

Fig. 6.9 – Direction of maximum horizontal stress between two transverse fractures spaced 600 ft apart

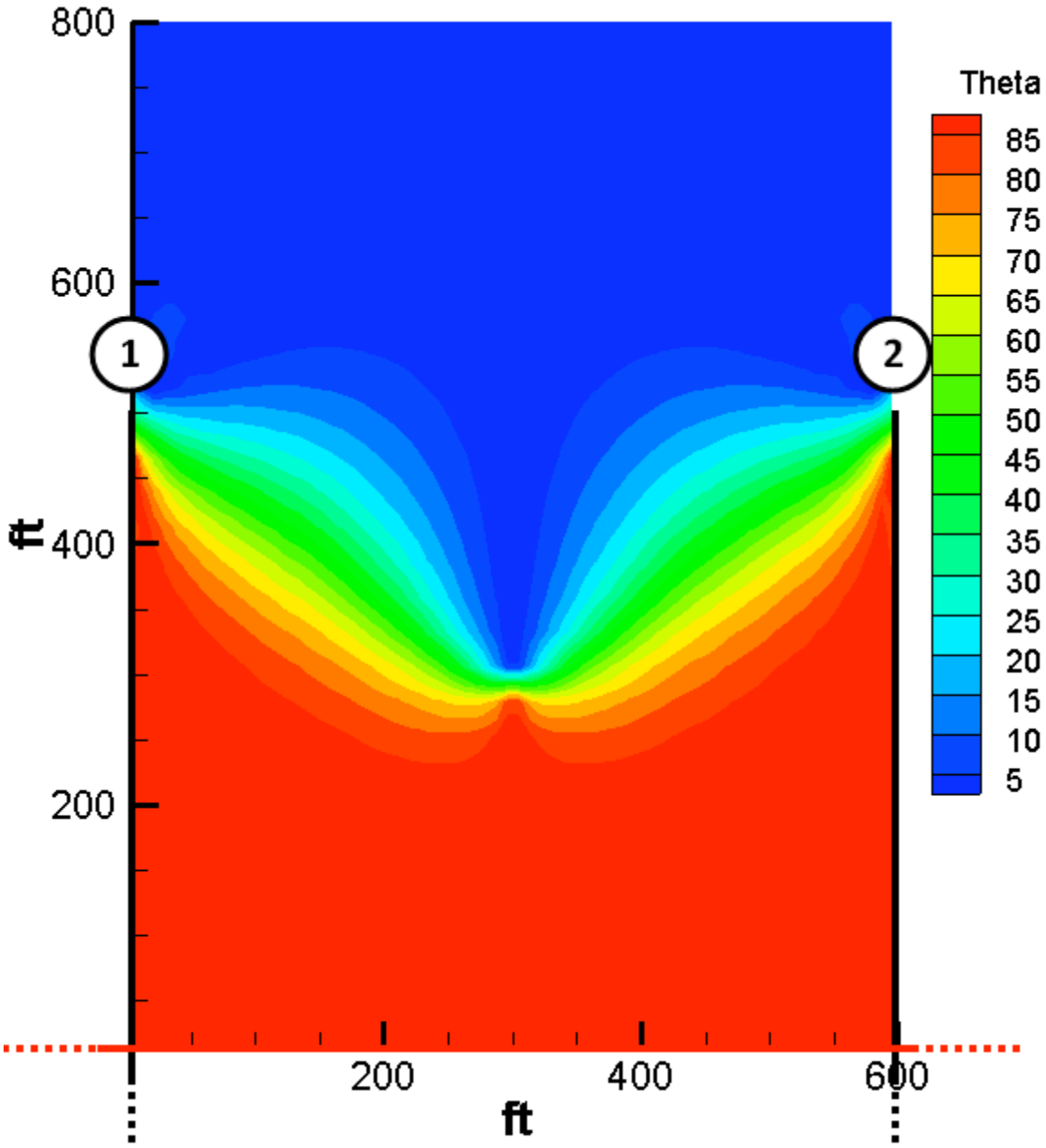

Fig. 6.10 – Angle of stress reorientation between two transverse fractures spaced 600 ft apart

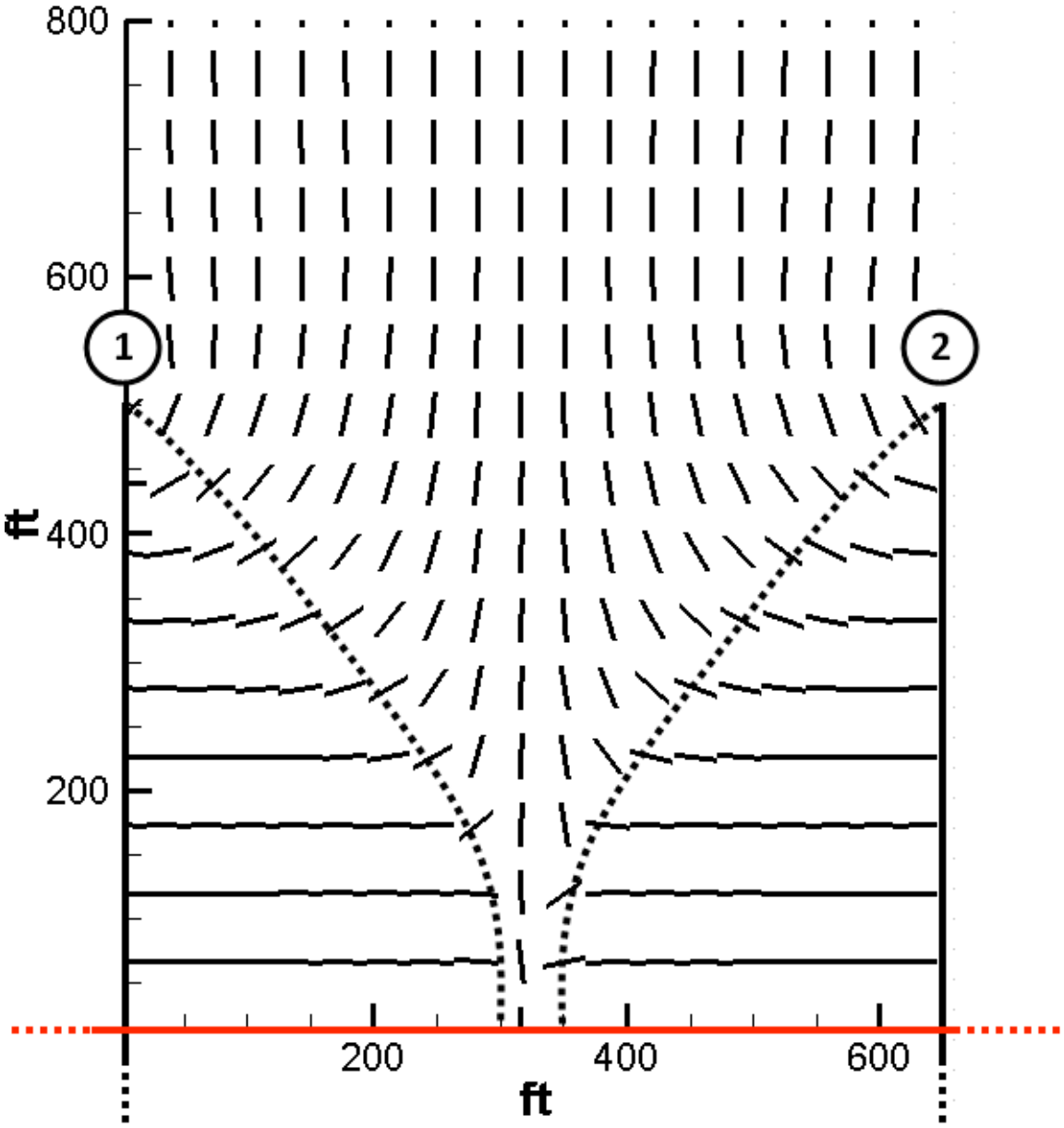

Fig. 6.11 – Direction of maximum horizontal stress between two transverse fractures spaced 650 ft apart

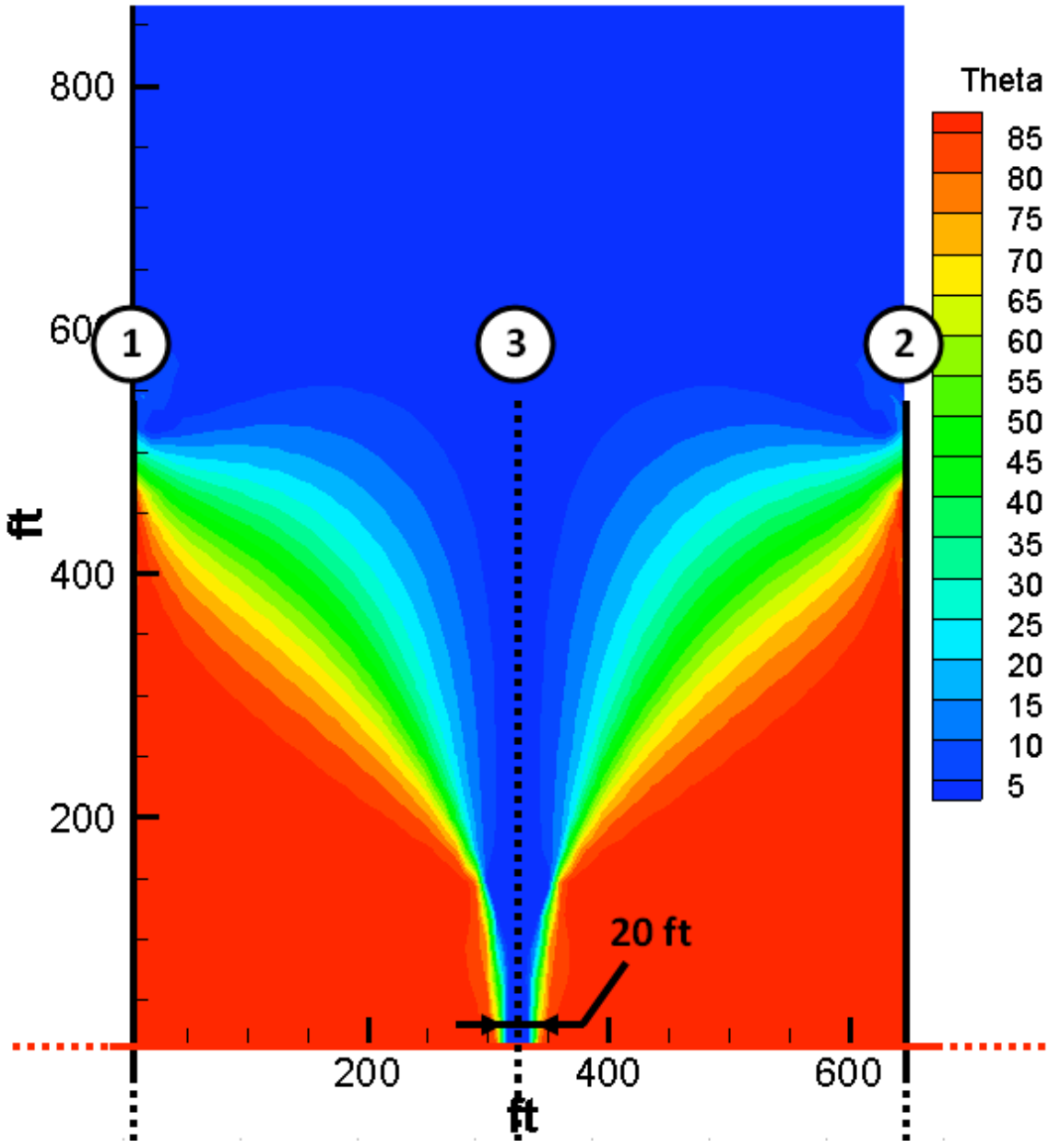

Fig. 6.12 – Angle of stress reorientation between two transverse fractures spaced 650 ft apart

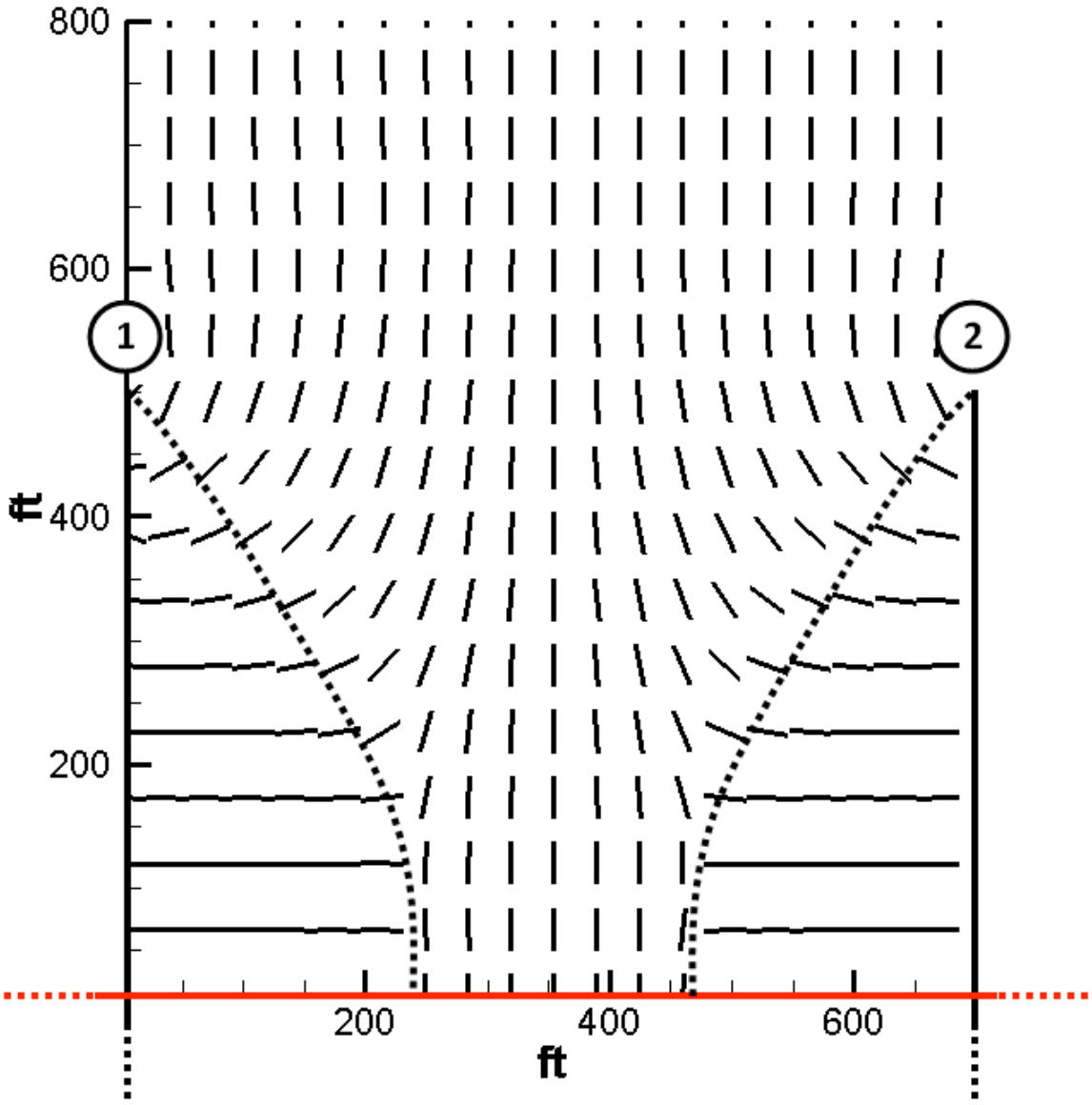

Fig. 6.13 – Direction of maximum horizontal stress between two transverse fractures spaced 700 ft apart

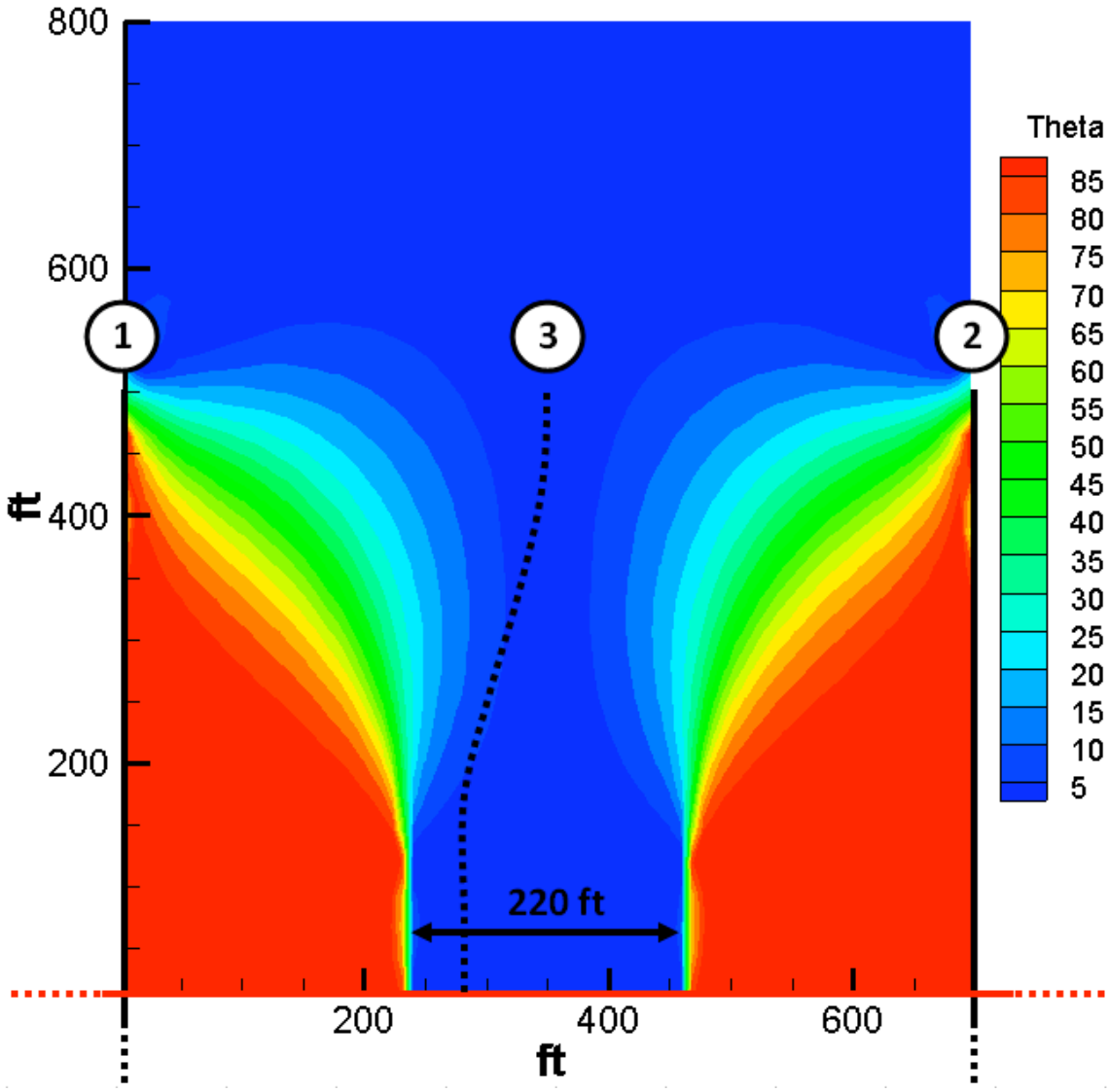

Fig. 6.14 – Angle of stress reorientation between two transverse fractures spaced 700 ft apart

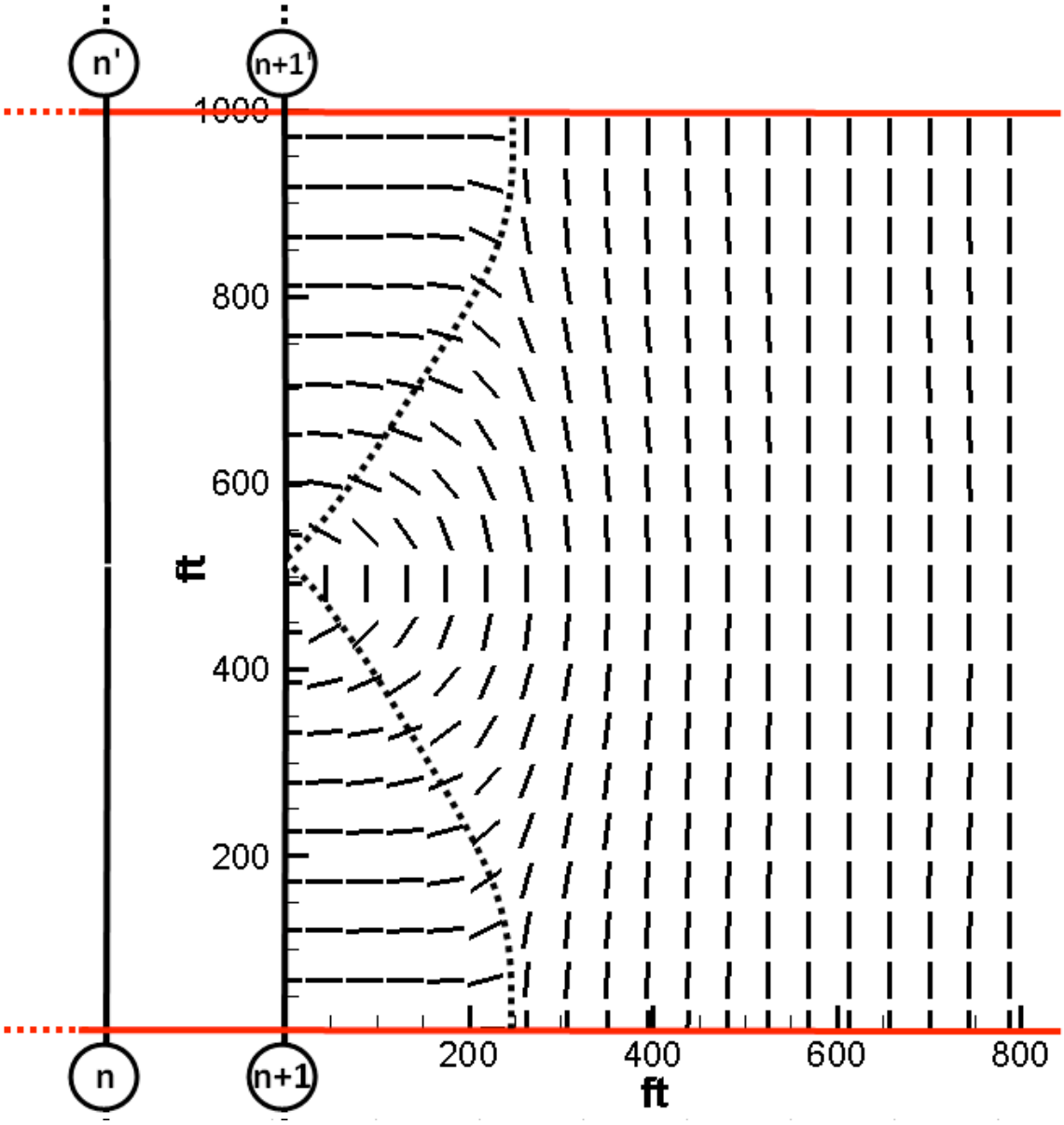

Fig. 6.15 – Direction of maximum horizontal stress around multiple pairs of transverse fractures (Maximum state of stress reorientation)

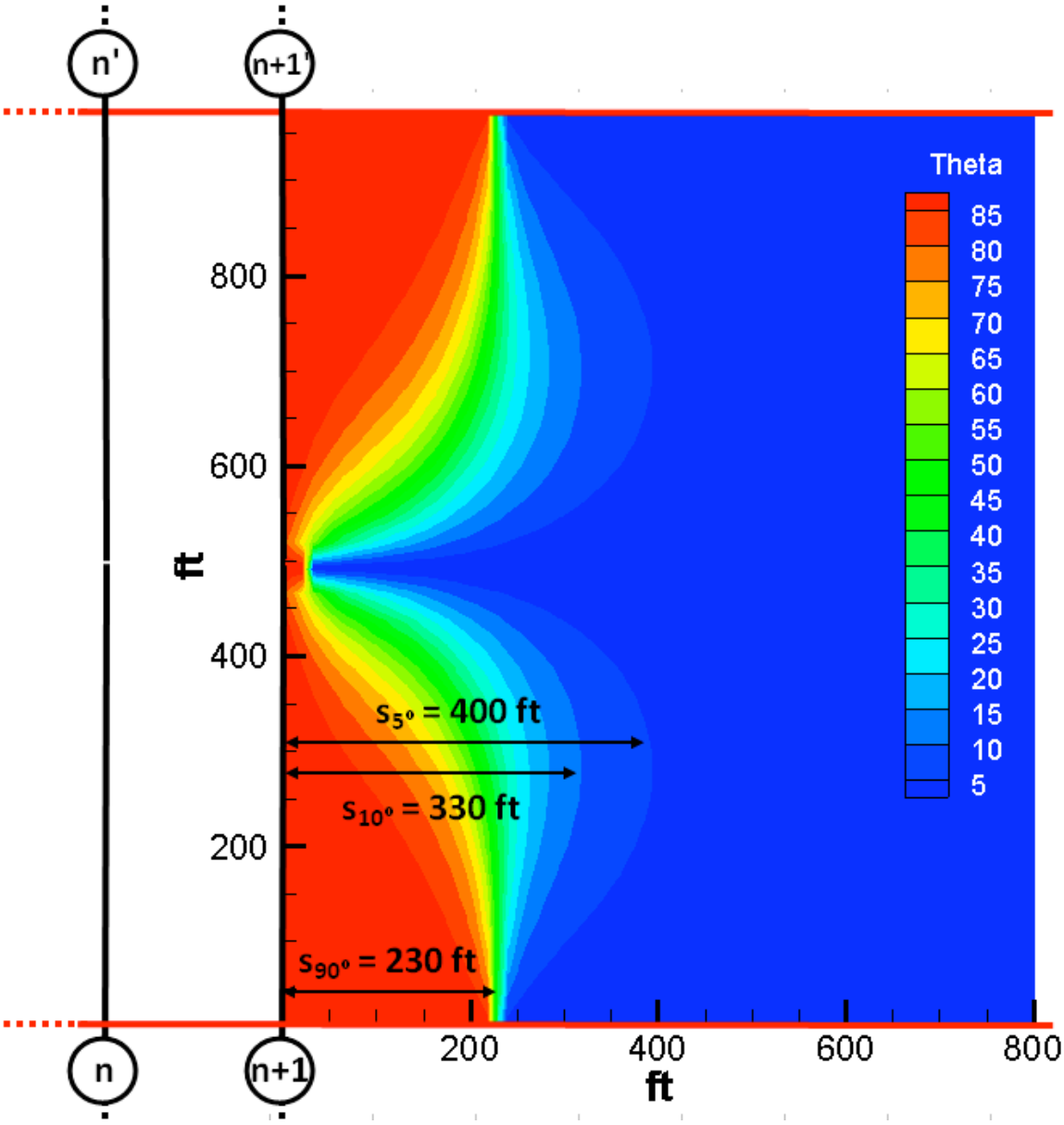

Fig. 6.16 – Angle of stress reorientation around multiple pairs of transverse fractures (Maximum state of stress reorientation)

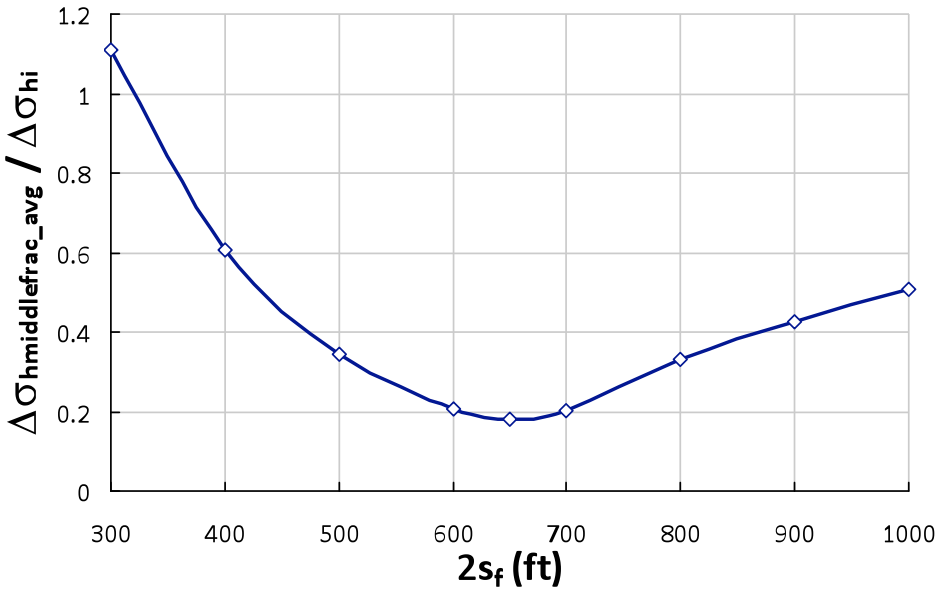

Fig. 6.17 – Average stress contrast experienced by the "middle fracture" in the alternate fracturing sequence along its total length ($2L_f$) versus the spacing between the outside fractures ($2s_f$)

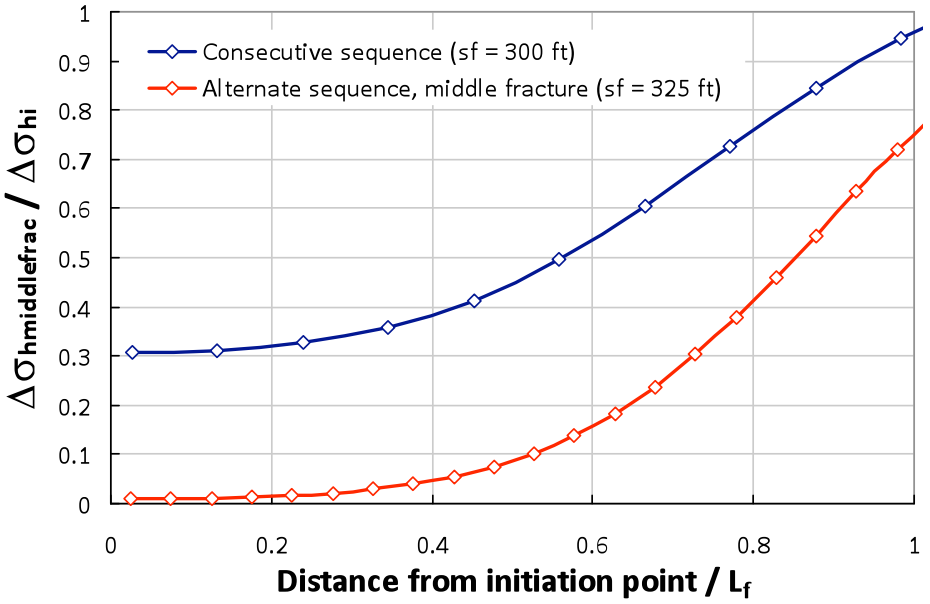

Fig. 6.18 – Local deviatoric stress experienced by the "middle fracture" in the alternate fracturing sequence as it propagates away from the wellbore and its comparison to consecutive fracturing

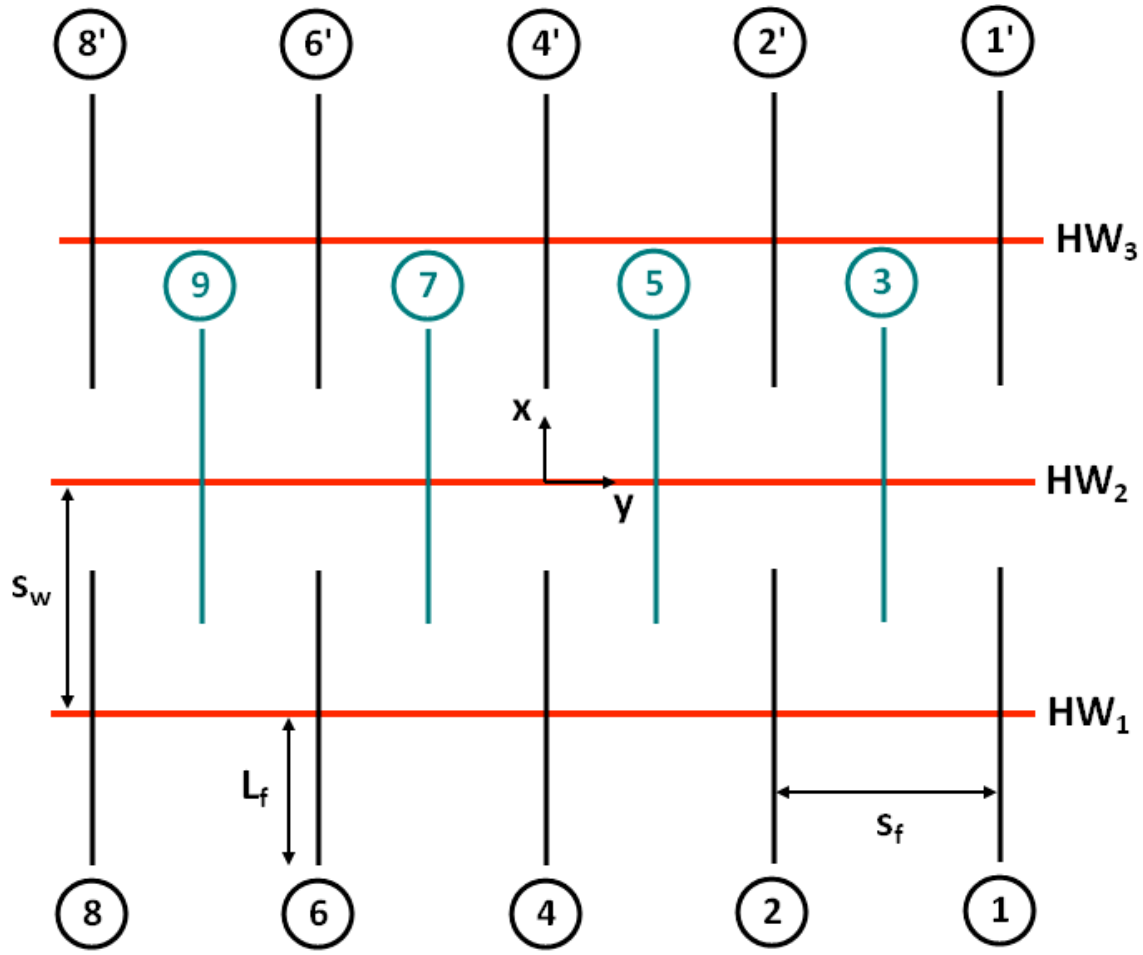

Fig. 6.19 – Proposed fracture sequence in a three-lateral multi-fractured horizontal well

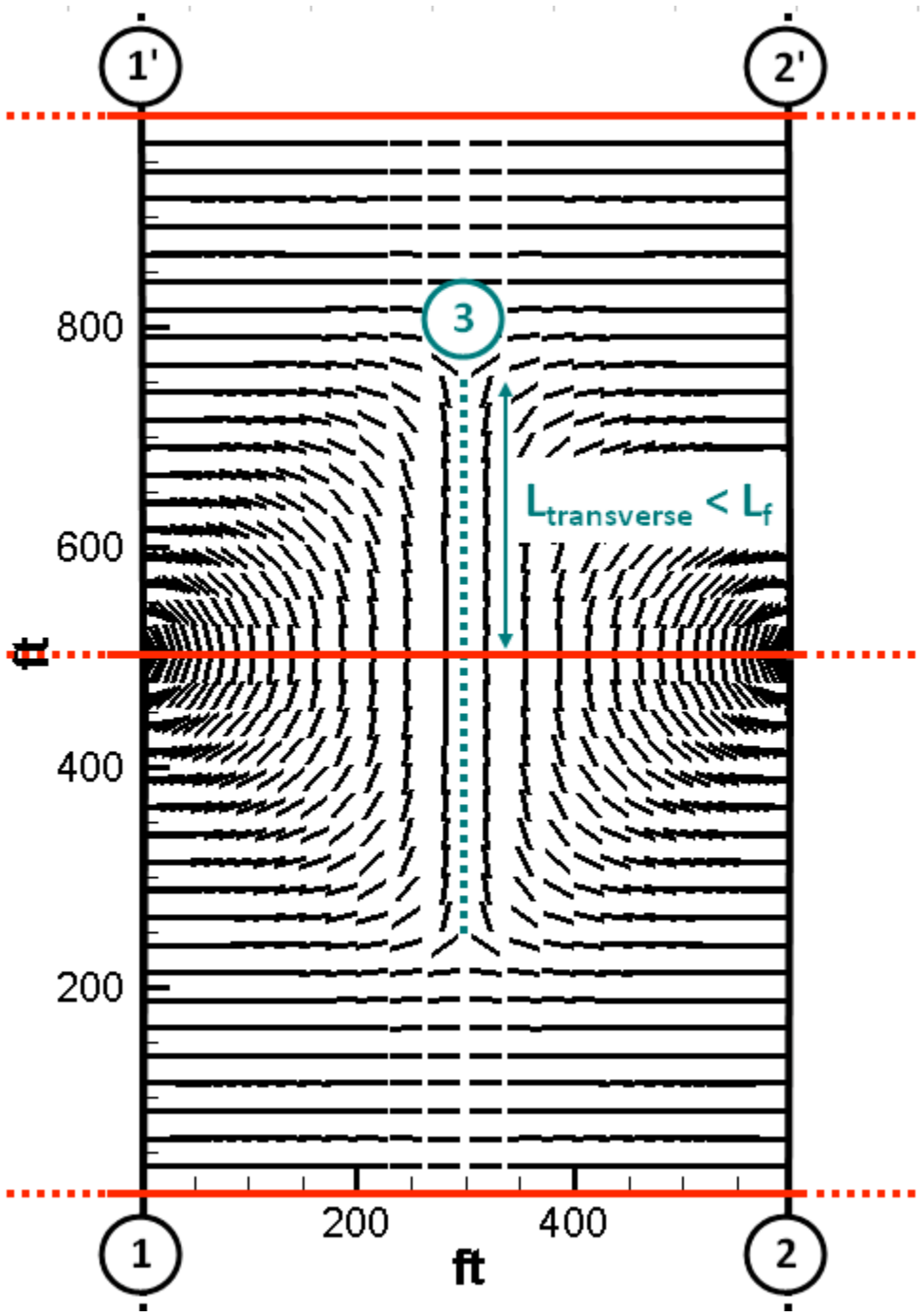

Fig. 6.20 – Direction of maximum horizontal stress between two pairs of fractures propagated from the outside wells HW_1 and HW_3

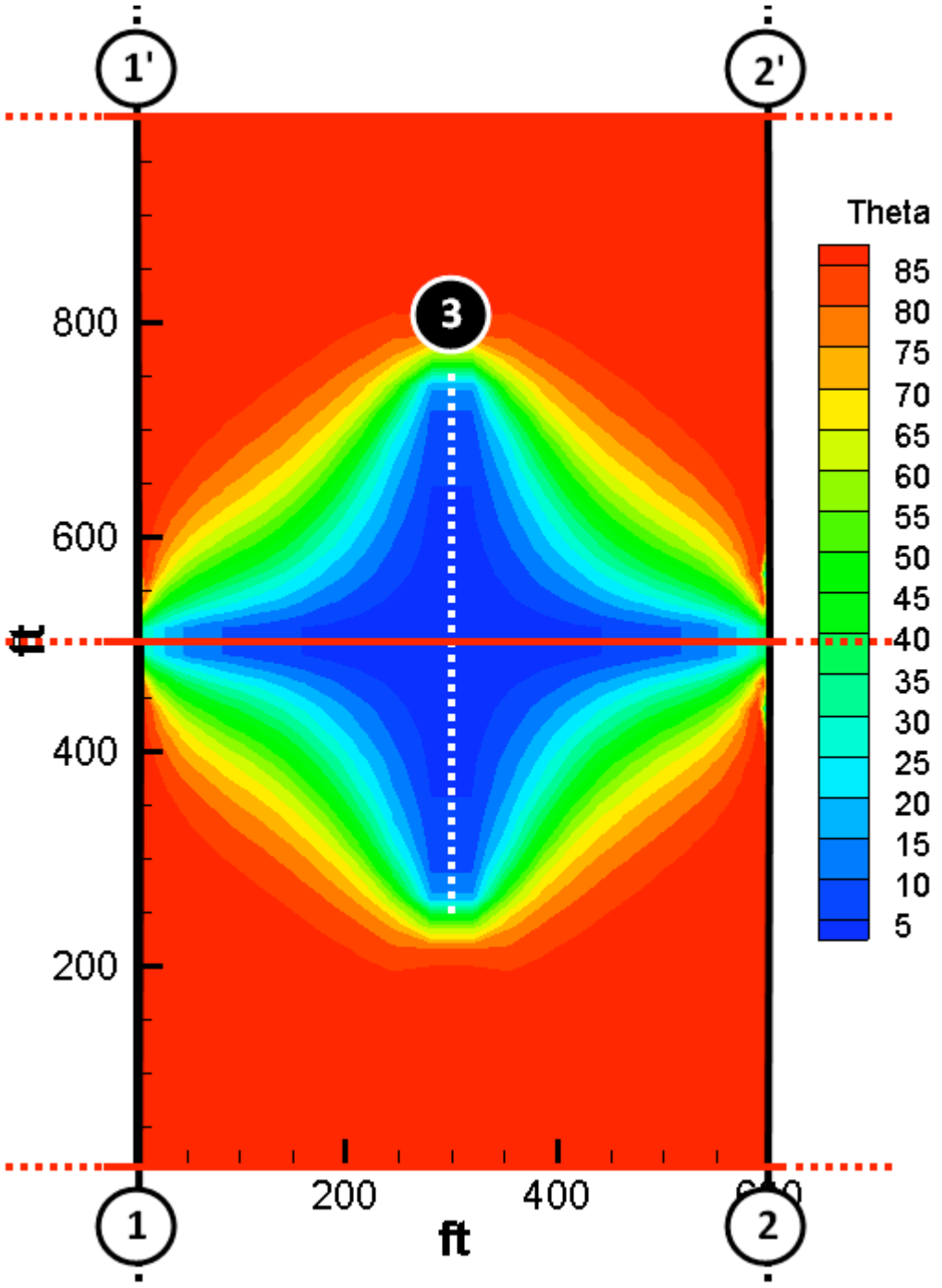

Fig. 6.21 – Angle of stress reorientation between two pairs of fractures propagated from the outside wells HW_1 and HW_3

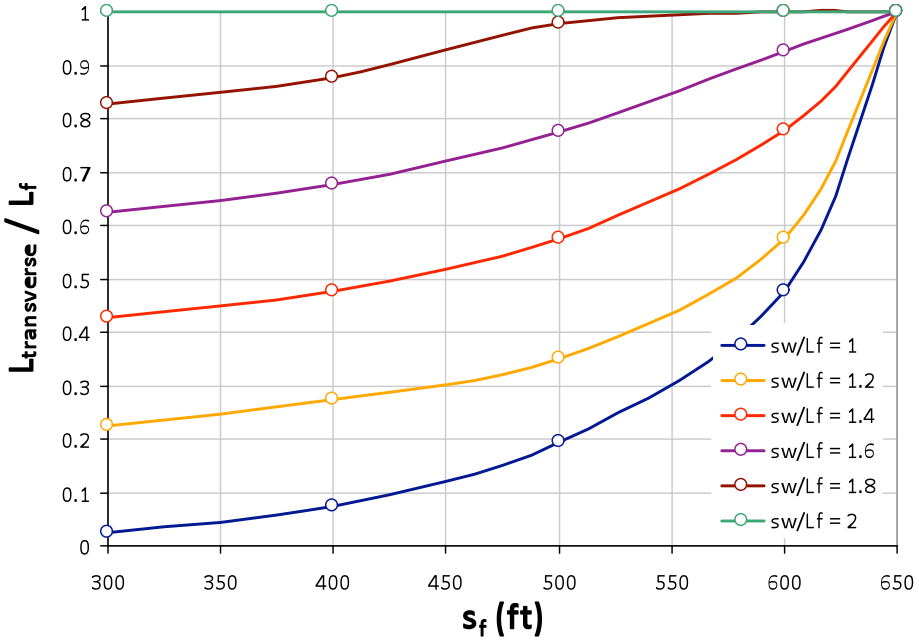

Fig. 6.22 – Distance of transverse propagation of a "middle fracture" propagated from HW_2 versus fracture spacing s_f

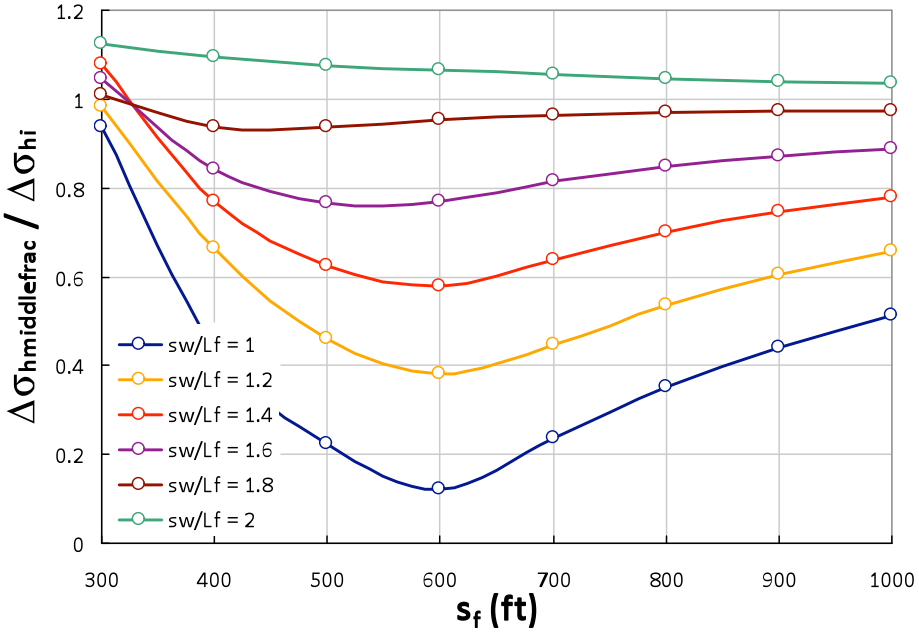

Fig. 6.23 – Average stress contrast seen by a "middle fracture" propagated from HW_2 along its total length ($2L_f$) versus fracture spacing s_f

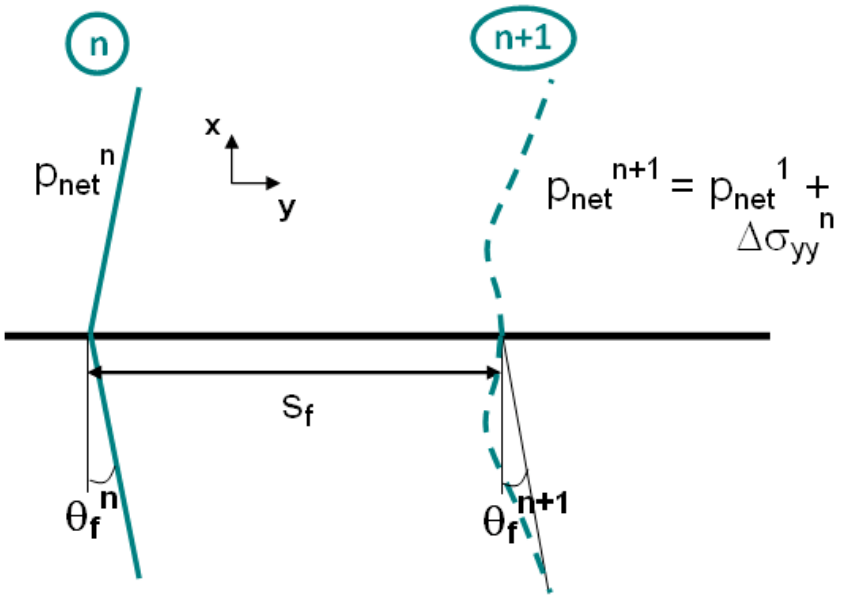

Fig. 6.24 – Method of calculation of the net closure stress and trajectory of the subsequent fracture in consecutive fracturing

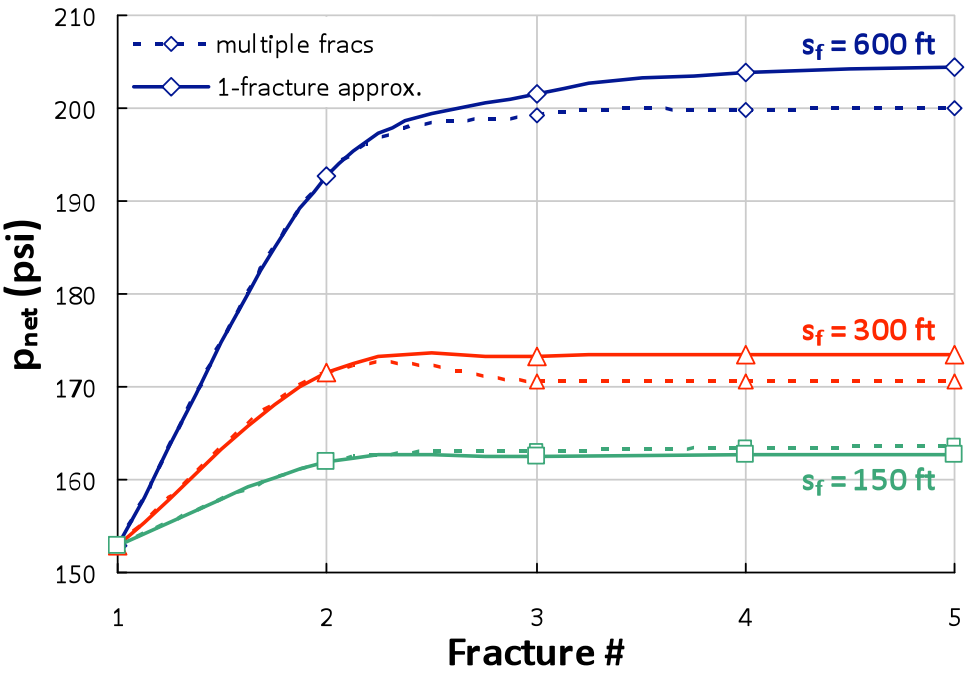

Fig. 6.25 – Evolution of the net closure stress with each additional consecutive transverse fracture in a multiple-fracture model and the single-fracture approximation

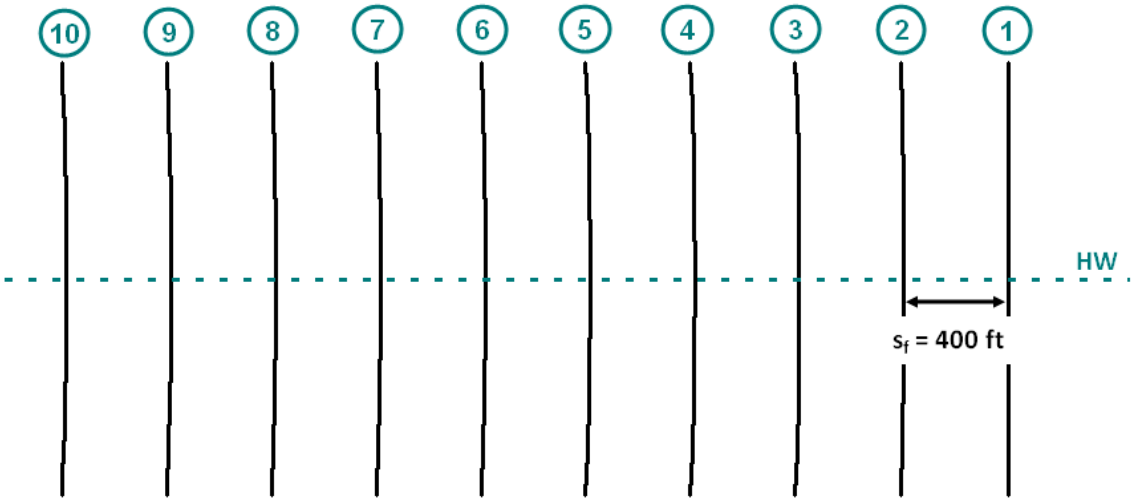

Fig. 6.26 – Trajectory of multiple consecutive transverse fractures spaced 400 ft apart

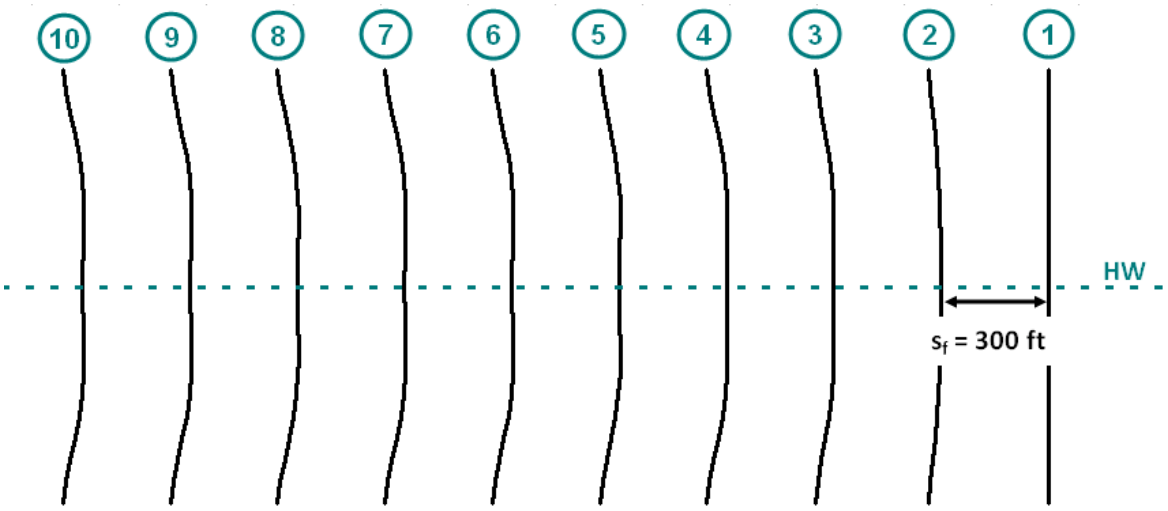

Fig. 6.27 – Trajectory of multiple consecutive transverse fractures spaced 300 ft apart

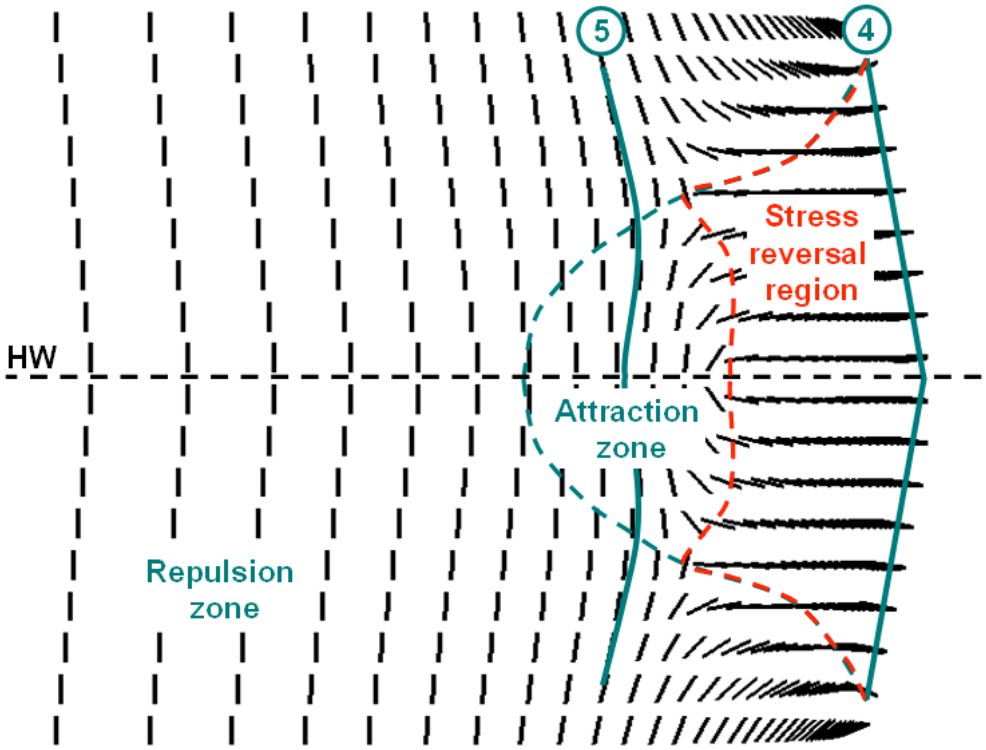

Fig. 6.28 – Direction of maximum horizontal stress in the vicinity of stage 4 (300-ft spacing)

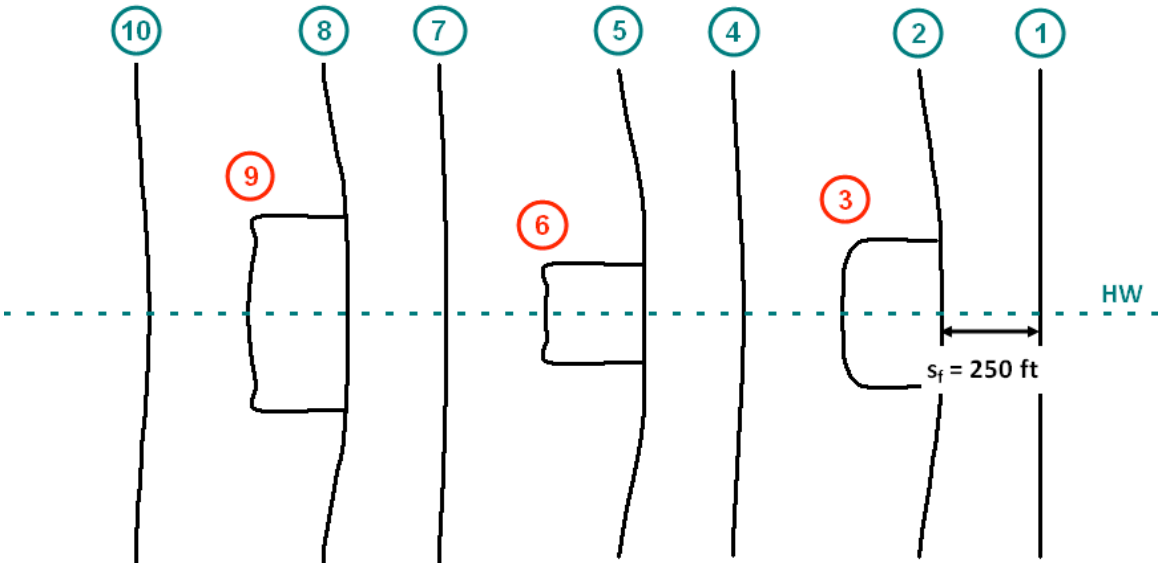

Fig. 6.29 – Trajectory of multiple consecutive transverse fractures spaced 250 ft apart

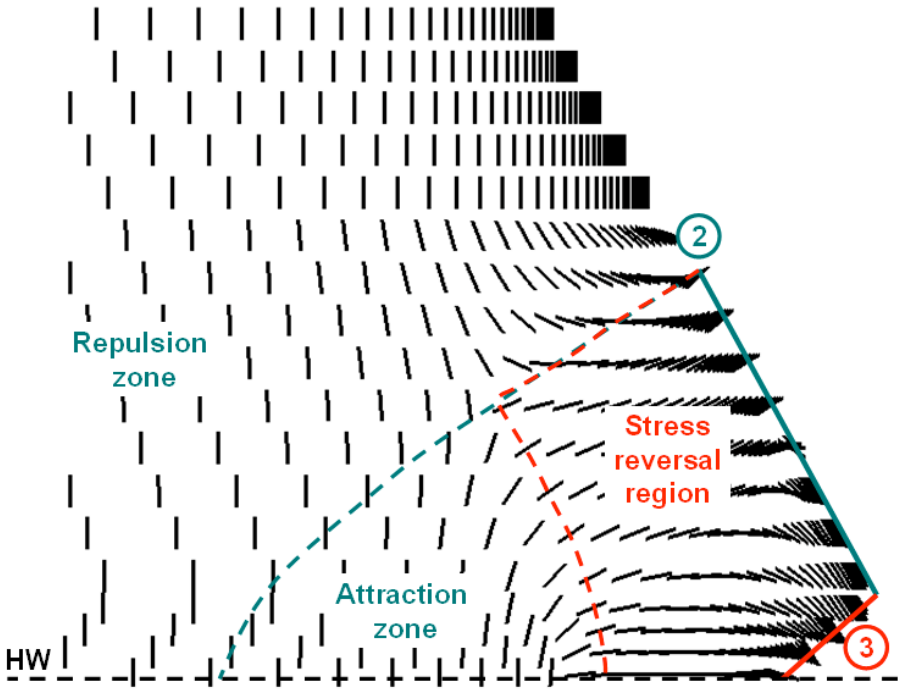

Fig. 6.30 – Direction of maximum horizontal stress around a two-fracture system (250-ft spacing)

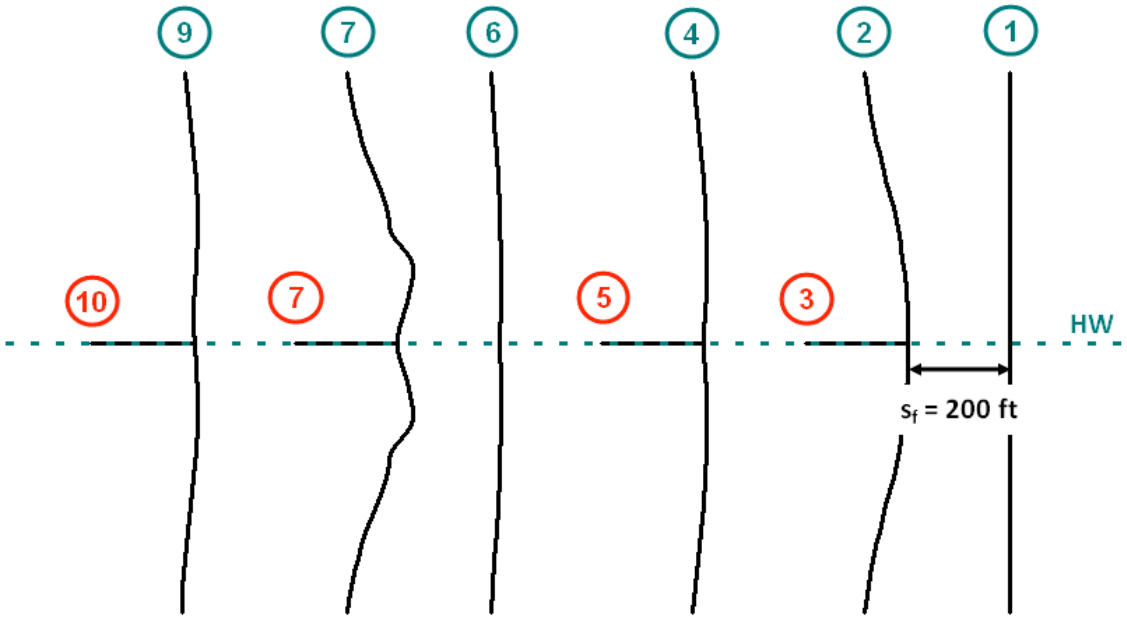

Fig. 6.31 – Trajectory of multiple consecutive transverse fractures spaced 200 ft apart

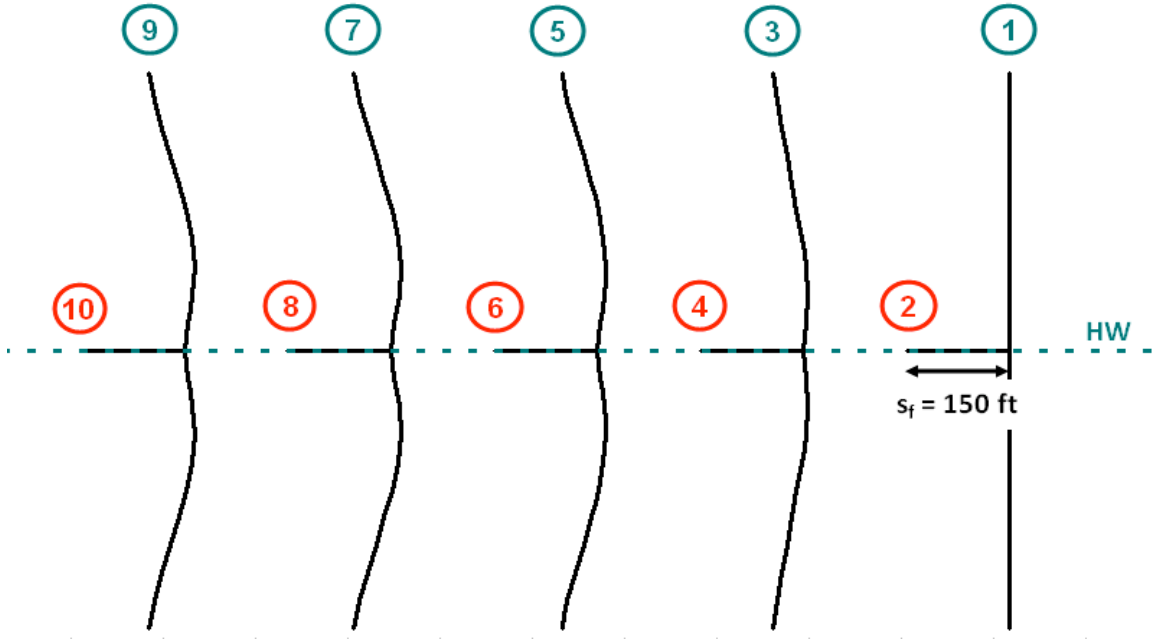

Fig. 6.32 – Trajectory of multiple consecutive transverse fractures spaced 150 ft apart

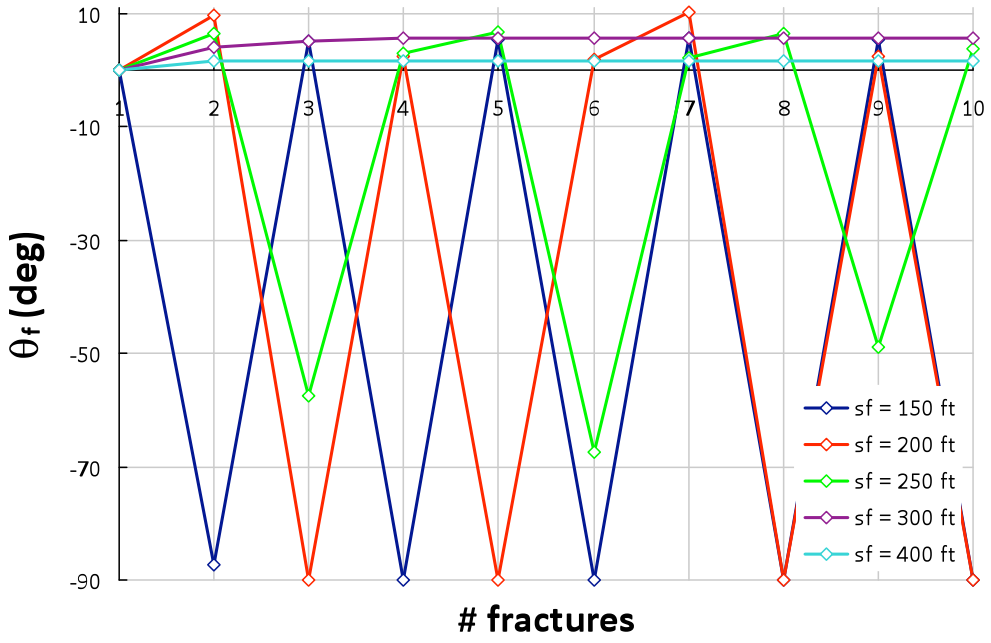

Fig. 6.33 – Evolution of the angle of deviation from the orthogonal path with each additional consecutive transverse fracture as a function of the fracture spacing s_f

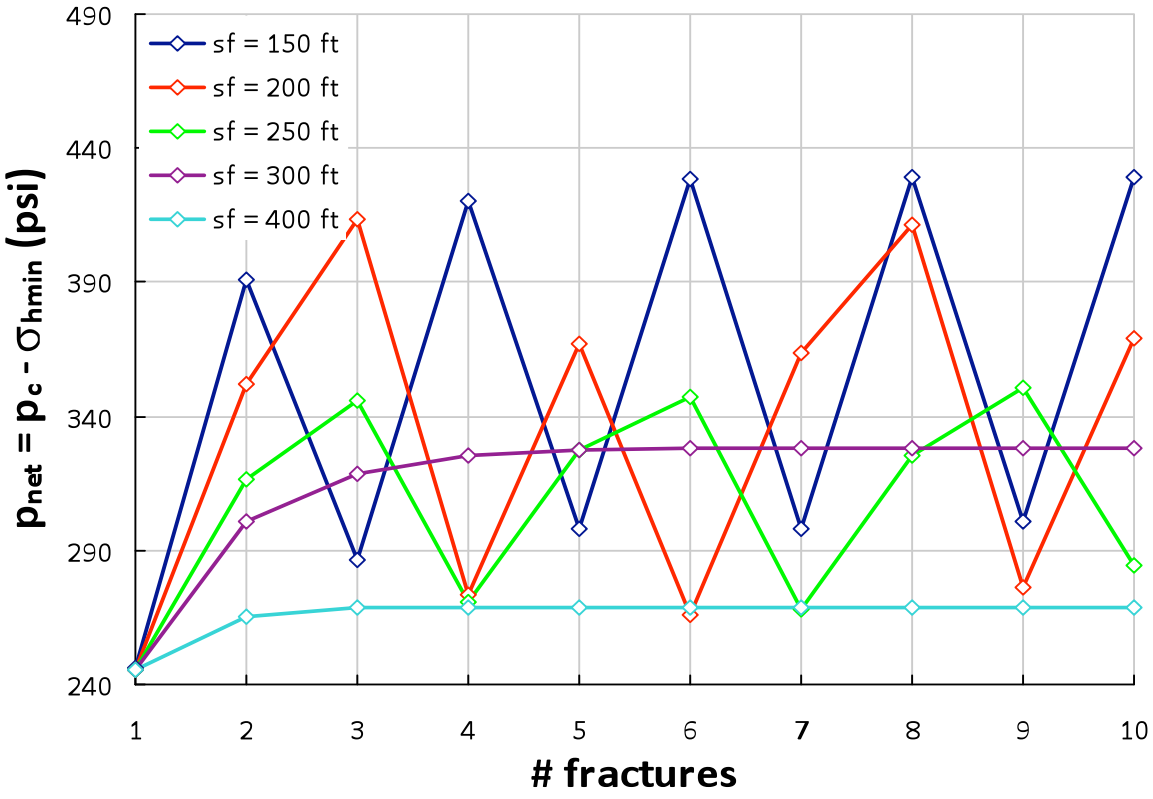

Fig. 6.34 – Evolution of the net closure stress with each additional consecutive transverse fracture as a function of the fracture spacing s_f

CHAPTER 7: CONCLUSIONS AND FUTURE WORK

The conclusions of this study and their implications for the refracturing of vertical wells and multi-stage horizontal completions are presented below. New research directions are proposed to further improve the performance of fracturing and refracturing operations.

1. CONCLUSIONS

The conclusions of the dissertation are split into four sections (a) the coupling of stress reorientation from poroelastic and mechanical effects, (b) the impact of stress reorientation on the refracturing of vertical wells, (c) refracture candidate well selection, and (d) the impact of mechanical stress interference on the multiple fracturing of horizontal wells.

1.1. Poroelastic and Mechanical Stress Reorientation

- Stress reversal occurs in production wells but not injection wells.
- To predict the extent of stress reversal and the optimum time for refracturing, both poroelastic and mechanical effects must be taken into account. The effects of both when considered together are not simply additive.
- An optimum time exists when the areal extent of the stress reversal region reaches a maximum.
- For unconventional resources such as tight gas, shale gas or heavy oil, the optimum time for refracturing is usually on the order of months to years.

- The extent (λ_{max}) and timing (τ_{max}) of the stress reversal depend on the fluid properties and permeability (τ), the stress contrast and drawdown (Π), the thickness of the reservoir (γ) and the shear modulus of the reservoir and the bounding layers (β).
- The effect of permeability heterogeneity and anisotropy on the magnitude and timing of maximum stress reversal can be incorporated into an appropriate definition of τ for layered reservoirs.
- Dimensionless type curves were developed to estimate the optimum time-window for refracturing (Appendix A).
- Poroelastic effects will be predominant in reservoirs having a large pressure drawdown, relatively weak bounding layers, and a thick pay zone.
- Mechanical effects will be predominant in reservoirs having a thin pay zone, high Young's modulus and low pressure drawdown.
- Mechanical stress reorientation can be enhanced by increasing the width of the initial fracture.
- Fracture penetration into rock layers bounding the reservoir increases stress reorientation if bounding layers are weaker than the pay zone.
- A long initial fracture and low stress contrast favor both poroelastic and mechanical stress reorientation.
- Production from neighboring wells may impact the reoriented stress region located outside the stress reversal region associated with a producing well.

1.2. Refracturing of Vertical Wells

- There is evidence in the field of refracture reorientation and of the positive impact of stress reorientation on the success of refracturing operations.
- The potential of the refracturing technique to gain access to new reserves was demonstrated in very-low-permeability reservoirs such as shales. Incremental recoveries of more than 50% may be achieved.
- The timing of the second fracture is critical for optimizing the performance of refracture treatments.
- Fractured production wells in unconventional reservoirs (tight gas, shale gas, heavy oil) with modest stress contrasts constitute ideal candidates for refracturing.
- It is crucial to take into consideration the potential extent of stress reversal when designing the well pattern and spacing, in order to maximize the recovery efficiency after refracturing and minimize initial field development costs.
- The reoriented stress region located outside the stress reversal region will direct the refracture away from the initial fracture when the field is more depleted in the direction parallel to the first fracture than perpendicular to it.
- The propagation of the refracture away from the initial fracture can be improved by (a) maximizing the size of the stress reversal region through initial fracture design (fracture length) and timing of the refracture, and (b) creating a favorable stress orientation in the reoriented stress region through improved field design and production schedule.

1.3. Selection of Candidate Wells for Refracturing

- A novel framework of the selection of candidate wells for refracturing was developed, based on five dimensionless quantities: Π_{poro}, Π_{mech}, F_{Co}, R_{Dep}, D_{iD}.
- The dimensionless numbers quantify the impacts of stress reorientation, of the initial completion performance, of the reservoir quality, and of the reservoir depletion by neighbor wells on the expected incremental recovery from a refracturing treatment.
- An algorithm based on cut-off values of the dimensionless quantities, was proposed to identify and select wells for refracture treatments.
- Analysis of 300 wells in the Codell formation showed that there were two groups of successful refractures: (a) ineffective initial completions showing small initial production decline and (b) long initial fractures surrounded by under-depleted rocks.
- The strong correlation between the fracture completion number and the incremental recovery after refracturing suggests that stress reorientation plays a key role in the success of refracs.
- The performance of the Wattenberg field wells producing from the Codell tight gas formation and selected by the decision algorithm is 35% higher than a random selection of wells.
- Because of the dimensionless formulation, the model may be used in any reservoir and field, and may prove particularly useful in fields where refracturing experience is limited.
- In addition to being a selection method, the proposed method also provides quantified estimates of the incremental recovery of future refracturing treatments.

1.4. Multi-Stage Fracturing of Horizontal Wells

- To avoid longitudinal fractures, the minimum fracture spacing must be larger than S_{90^o}.
- To ensure transverse fractures and avoid deviation of the fracture from its orthogonal path, the fracture spacing should be larger than S_{5^o}.
- A new fracturing sequence is proposed, alternate fracturing, which consists of initiating a fracture between two previous fracture stages.
- The alternate fracturing technique is shown to be a way to minimize fracture spacing.
- During alternate fracturing, the "middle fracture" is forced to propagate along the orthogonal plane midway between the previous two fractures.
- The alternate fracturing method offers the potential to enhance fracture complexity through the propagation of a "middle fracture" in a region of low stress contrast.
- Special downhole tools have been recently developed to allow the alternate fracturing sequence to be implemented in the field.
- Zipper-fracs are shown to reduce the extent of the reoriented stress region.
- Minimum fracture spacing can be estimated for any given set of reservoir, fracture properties.
- When fracture spacing is too small, the gain in reservoir drainage from additional fracture stages becomes marginal.
- A new interpretation of the net pressure data collected during fracturing has been presented.

- Up-and-down variations of the net pressure from one stage to another indicate propagation of transverse fractures into previously stimulated regions of the reservoir.
- Fracturing pressure data may be used to optimize the spacing between subsequent fracture stages for a specific well.
- Fracturing pressure data may be used to estimate the geometry of a multiple fractured horizontal well (that can be used later as an input in a reservoir drainage simulation).
- The proposed numerical model of multiple transverse fracture interaction has the potential to quantify the local horizontal stress contrast, and thus obtain a good estimate of the maximum horizontal stress when combined with a mini-frac test.
- The multiple-fracture model presented in this paper can be applied to calculate values of the optimum fracture spacing in horizontal wells for a given set of reservoir properties, well and fracture design, and fracturing sequence.
- Under a critical value of the spacing during consecutive fracturing, some fracture stages intersect previous fractures, thus reducing the efficiency of reservoir drainage.
- For a multiple-lateral completion, fractures initiated from the middle well propagate in a region of low stress contrast in the proposed fracture sequence.
- Multi-lateral completions allow benefits similar to alternate fracturing without the need for special downhole tools.
- A different type of fracturing treatment (fluids, flow rate, etc.) may be used in the middle well, aimed at enhancing fracture complexity as opposed to long bi-wing fractures (outside laterals).

2. FUTURE WORK

The numerical modeling of stress reorientation and its application to hydraulic fracturing revealed new strategies in the completion of horizontal wells and the restimulation of vertical wells. The existence of the second fracture during refracturing and the positive impact of initial fracture length on refracture reorientation has been demonstrated using field tiltmeter and production data. On the other hand, it is still unclear as to how novel completion strategies such as alternate fracturing and the fracture spacing optimization method using net fracturing pressures would work in the field.

As a result, two separate field trials are planned to be conducted to validate the concepts and methods introduced and described in this dissertation. The first test is planned in 2011-12 in the Barnett shale. It will be conducted in collaboration with Halliburton, Pioneer Resources under a Department of Energy contract.

The modeling effort may also be extended to further comprehend and quantify stress reorientation from poroelastic and mechanical effects. Below is a list of suggested directions of investigation:

- Develop type curves for the extent of stress reversal around a fractured vertical well from both mechanical and poroelastic effects.
- Validate decision algorithm and dimensionless parameters for refracturing candidate well selection in various types of reservoirs (i.e. Barnett shale, Eagle ford shale, conventional sand).
- Compare the efficiency of the proposed decision method with other available refracturing candidate well selection methods.
- Investigate poroelastic effects during horizontal fracturing. The use of hesitation fractures is something that has been observed in the field and is not completely understood.

- Investigate additional well and fracture placement strategies in multi-lateral horizontal completions.
- Use field measurements of the net fracturing pressure to optimize fracture spacing in the field (i.e. in Barnett shale).

The findings of the study may also serve as a starting point for research topics linked to horizontal completions, including but not limited to:

- Interactions of multiple fractures propagated from a horizontal wellbore.
- Near-wellbore effects of fractures initiated from closely-spaced perforation clusters.
- Interactions of a propagating transverse fracture with natural fractures.
- Impact of horizontal completion strategies on the extent of the stimulated rock volume (SRV).
- Fracturing fluid leak-off when propagating induced fractures in naturally-fractured rocks.
- Propping of natural fractures.
- Refracturing of horizontal wells.

3. MULTIFRAC

A graphic user interface is being developed to make the calculation of the optimum fracture spacing in horizontal completions more easily available (based on a pending patent from Roussel and Sharma 2011). At each fracturing stage, the propagation trajectory of the subsequent fracture is calculated assuming that the fracture follows the direction of maximum horizontal stress, and will be displayed in the user interface.

Depending on the stress profile, the subsequent fracture may propagate toward or away from the previous fracture. This will determine which one of three potential fracture geometries that will need to be simulated next: (a) single-fracture geometry (**Fig. 7.1**), (b) two-fracture system if a transverse fracture intersects the previous one (**Fig. 7.2**), and (c) 2nd longitudinal fracture (**Fig. 7.3**).

For the first fracturing stage, an algorithm has been developed to converge toward the value of the closure stress in the fracture corresponding to the designed fracture geometry (length, height and width). For the next stages, the evolution of the net closure stress is captured by measuring the additional stress perpendicular to the previous fracture at the designed point of fracture initiation (see Chapter 6).

MultiFrac may be used to optimize the design of multi-stage horizontal completions and offer solutions specific to a given well. Among the future functionalities of the MultiFrac method and user interface are:

- Value of the optimum transverse fracture spacing specific to a given well based on measured fracturing pressure data.
- Value of the optimum transverse fracture spacing based on assumed field stresses and formation and fracture properties (potentially fracture geometry as calculated by a fracturing simulator, see paragraph below).
- Map of the direction of transverse fractures to be used in horizontal well drainage simulations.
- Value of the maximum horizontal stress for a specific well using measured fracturing pressure data and the results of a mini-frac test.

The project economic evaluation of horizontal completions typically includes the use of fracturing simulator and of a reservoir simulator to determine the projected costs

and revenues of a given project. So far, the geometry of multiple horizontal fractures was assumed to be independent of the spacing between the fracture stages (**Fig. 7.4**). We recommend that MultiFrac be used as an additional tool in the decision process of a horizontal completion, as it can determine the geometry of a multi-fractured horizontal well (**Fig. 7.5**). It would interact with the both the hydraulic fracturing and the reservoir simulations. We have shown that interactions of multiple transverse fractures is influenced by the geometry a single hydraulic fracture (without interactions), which can be calculated using a fracturing simulator. The expected well production and thus ultimate recovery will in turn depend on the distribution of the multiple transverse fractures in the reservoir.

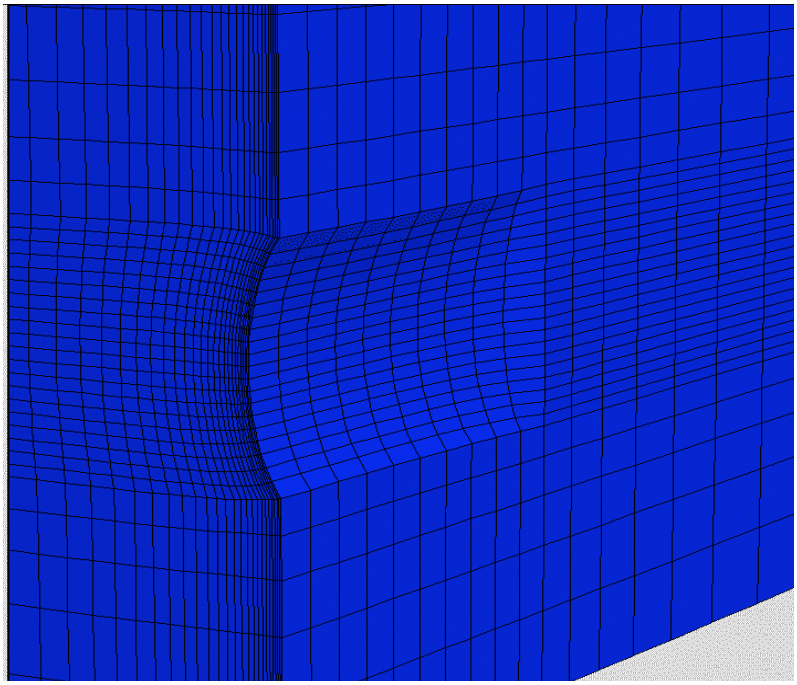

Fig. 7.1 – Numerical grid in a single-fracture geometry

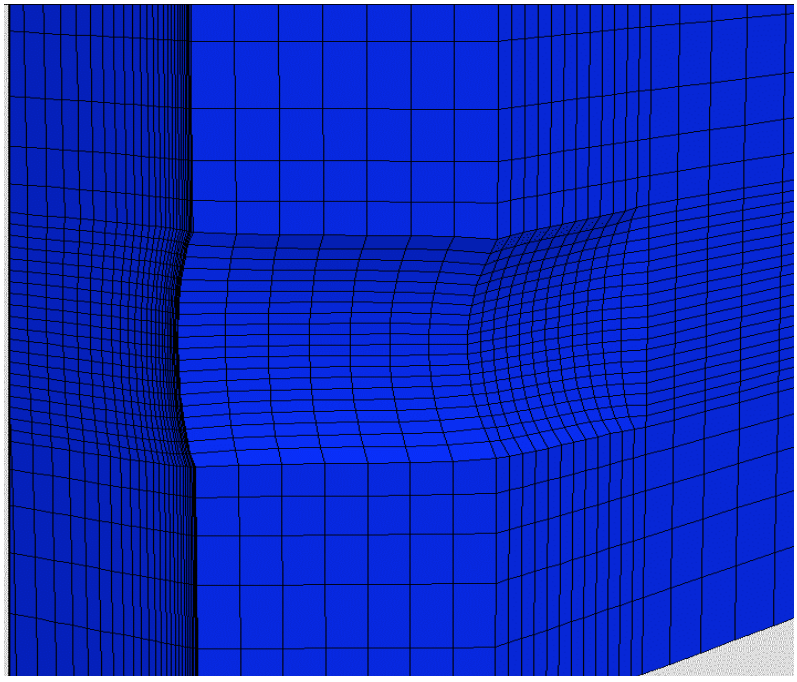

Fig. 7.2 – Numerical grid in a two-fracture geometry

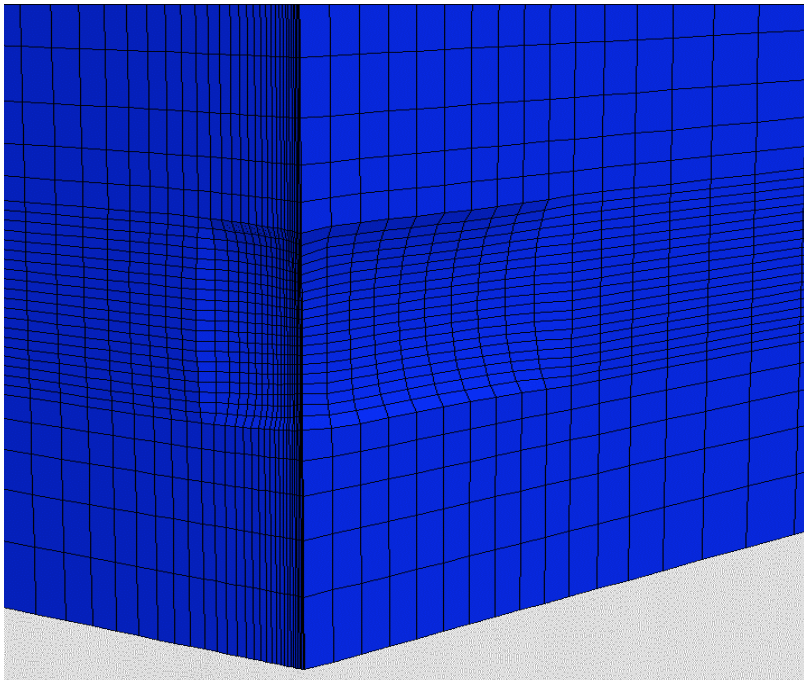

Fig. 7.3 – Numerical grid in a two-fracture geometry (with the 2nd fracture being longitudinal to the well)

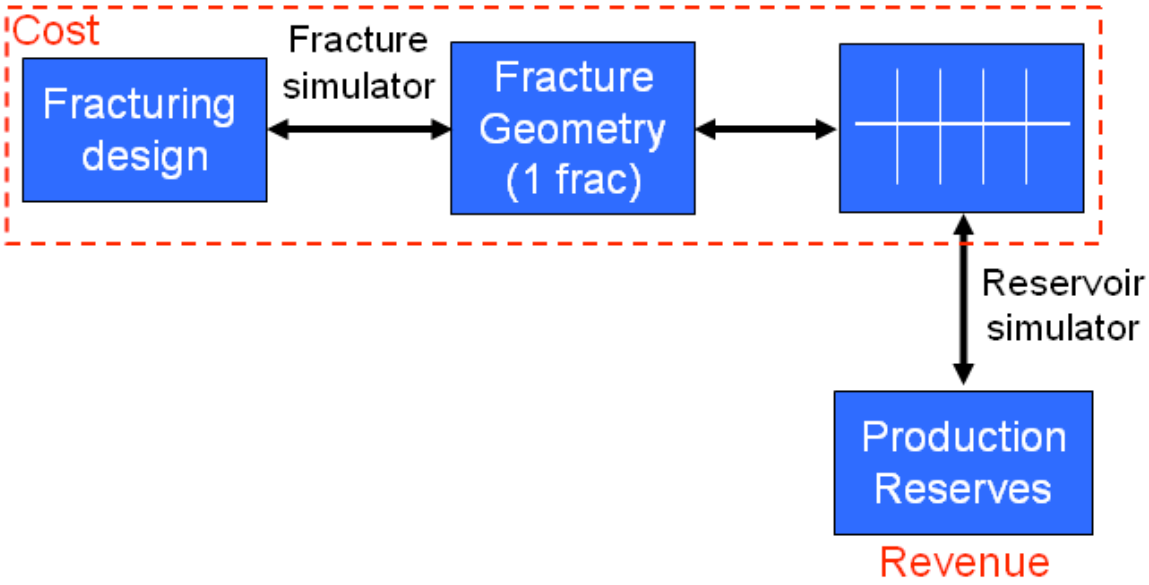

Fig. 7.4 – Typical structure of the economic evaluation of a horizontal completion assuming orthogonal transverse fracture trajectories

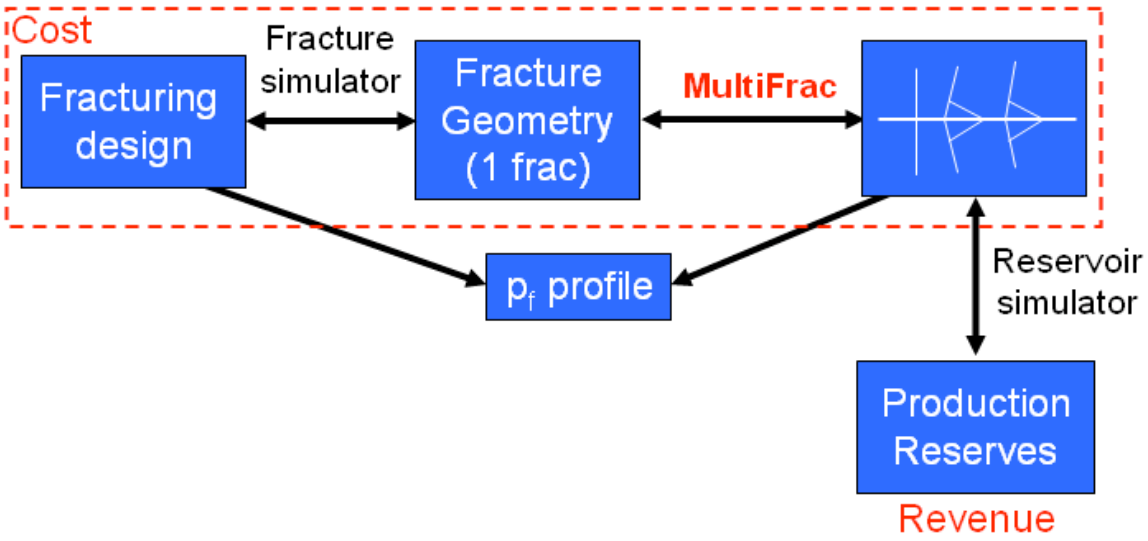

Fig. 7.5 – Proposed updated project economic evaluation using MultiFrac to calculate the geometry of multiple transverse fracture in a horizontal well

Appendix A: Type Curves of Poroelastic Elastic Stress Reorientation

Plots of Chapter 2 are included in the Appendix A and shown on a full page, to be used as type-curves for the calculation of the extent of the stress reversal region because of poroelastic stress reorientation. The plots below are:

1. $\lambda = L_f'/L_f$ versus the dimensionless time τ for different values of Π, with $\beta = 1$ and $\gamma = 0.2$ (Fig. 2.11)
2. $\lambda = L_f'/L_f$ versus the dimensionless time τ for different values of β, with $\Pi = 0.0583$ and $\gamma = 0.2$ (Fig. 2.13)
3. $\lambda = L_f'/L_f$ versus the dimensionless time τ for different values of γ, with $\Pi = 0.0583$ and $\beta = 1$ (Fig. 2.15)
4. $\lambda = L_f'/L_f$ versus the dimensionless time τ for different values of γ, with $\Pi = 0.0583$ and $\beta = 0.1$ (Fig. 2.16)

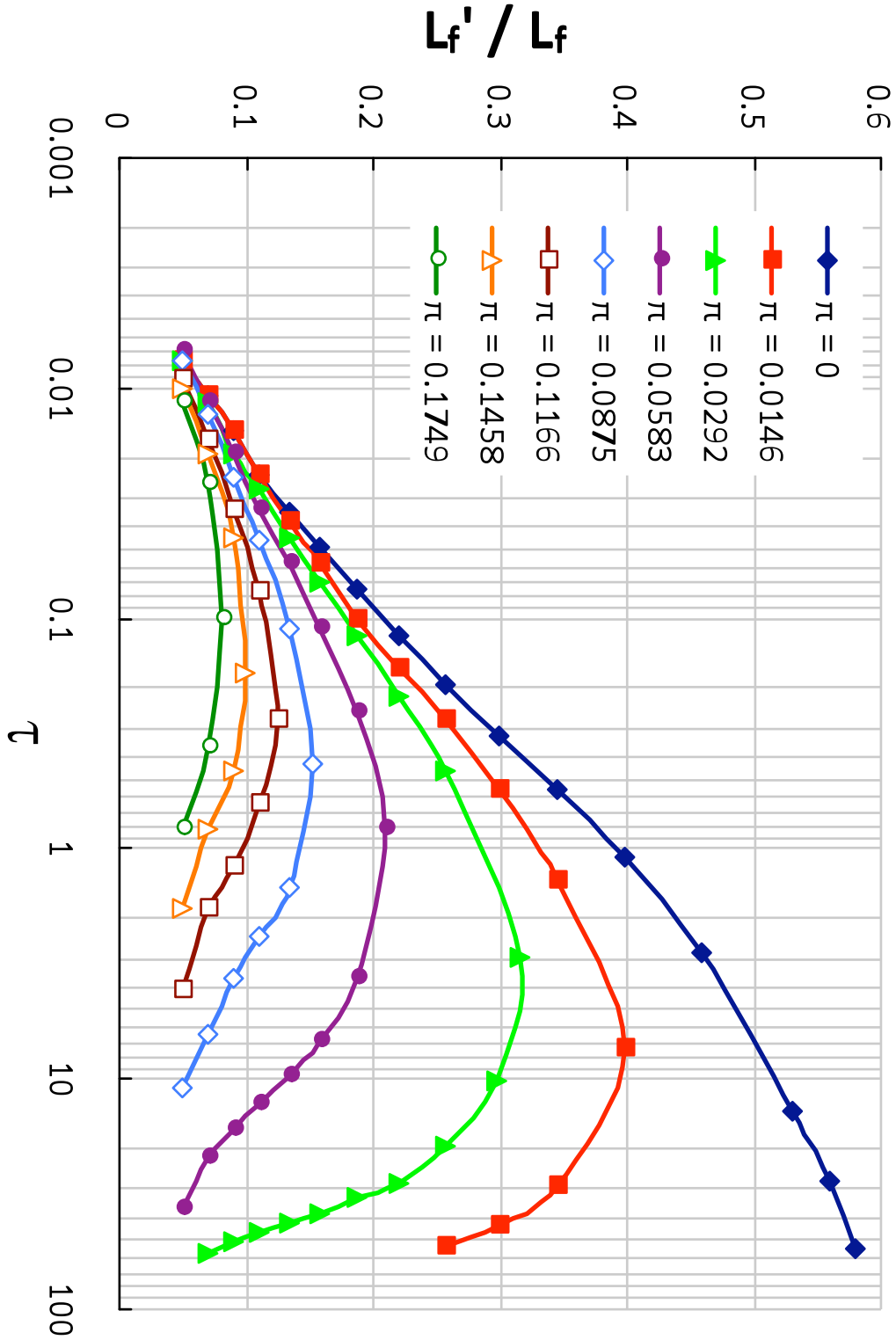
L_f' / L_f
0
0.1
0.2
0.3
0.4
0.5
0.6
τ
0.001
0.01
0.1
1
10
100
π = 0
π = 0.0146
π = 0.0292
π = 0.0583
π = 0.0875
π = 0.1166
π = 0.1458
π = 0.1749

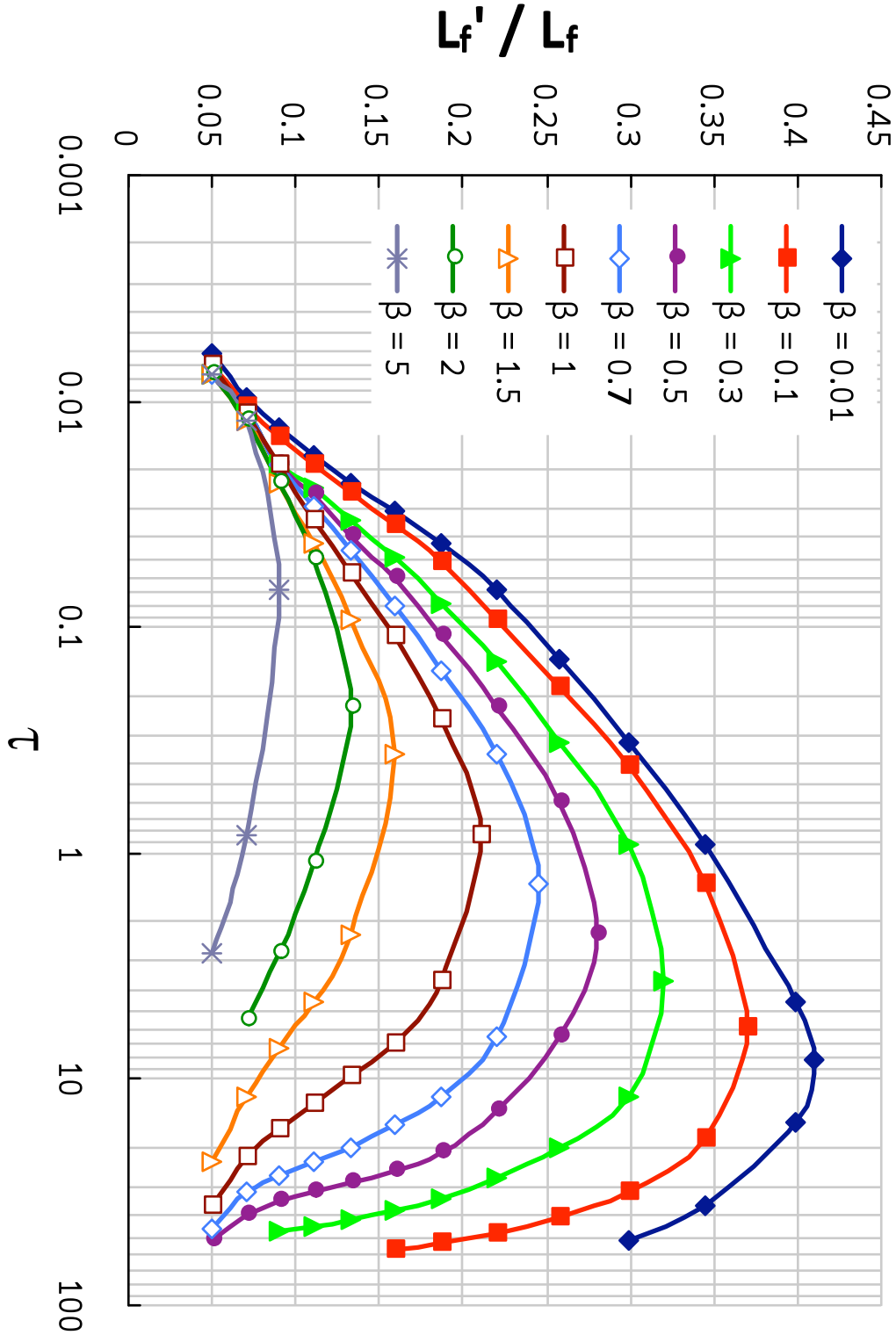
Lf' / Lf
τ
0
0.05
0.1
0.15
0.2
0.25
0.3
0.35
0.4
0.45
0.001
0.01
0.1
1
10
100
β = 0.01
β = 0.1
β = 0.3
β = 0.5
β = 0.7
β = 1
β = 1.5
β = 2
β = 5

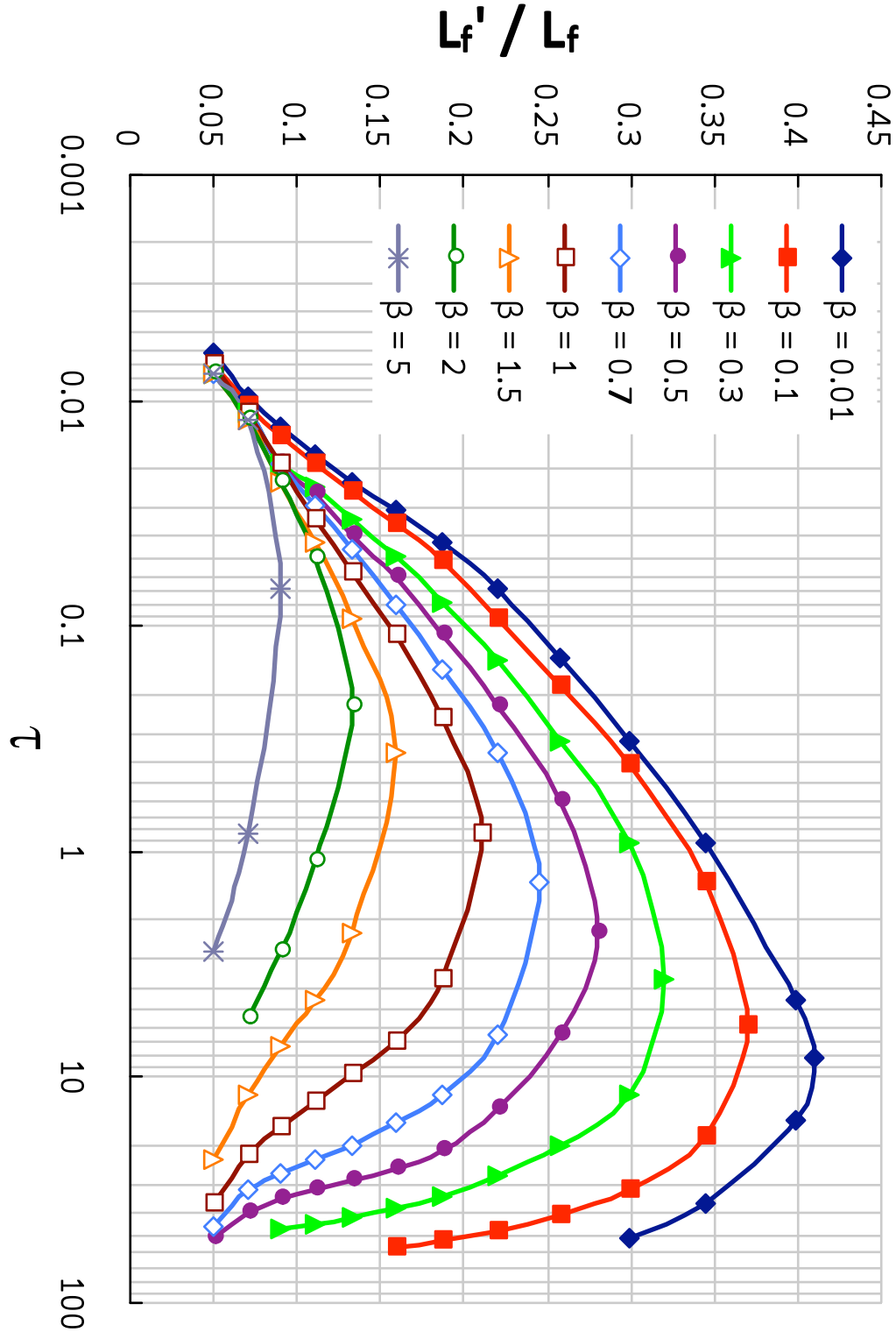
Lf' / Lf
τ
0
0.05
0.1
0.15
0.2
0.25
0.3
0.35
0.4
0.45
0.001
0.01
0.1
1
10
100
β = 0.01
β = 0.1
β = 0.3
β = 0.5
β = 0.7
β = 1
β = 1.5
β = 2
β = 5

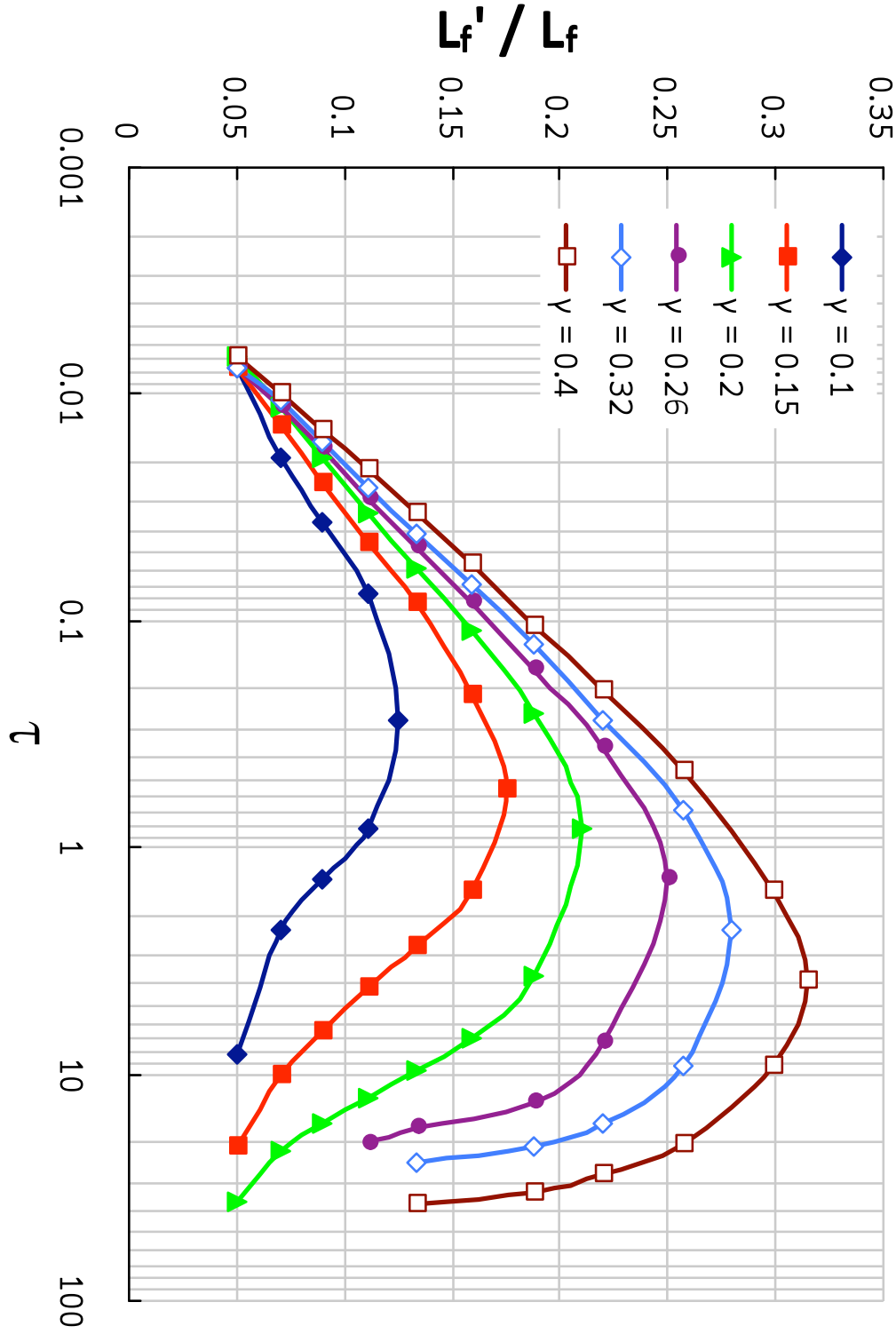
Lf' / Lf
0.35
0.3
0.25
0.2
0.15
0.1
0.05
0
τ
0.001
0.01
0.1
1
10
100
γ = 0.1
γ = 0.15
γ = 0.2
γ = 0.26
γ = 0.32
γ = 0.4

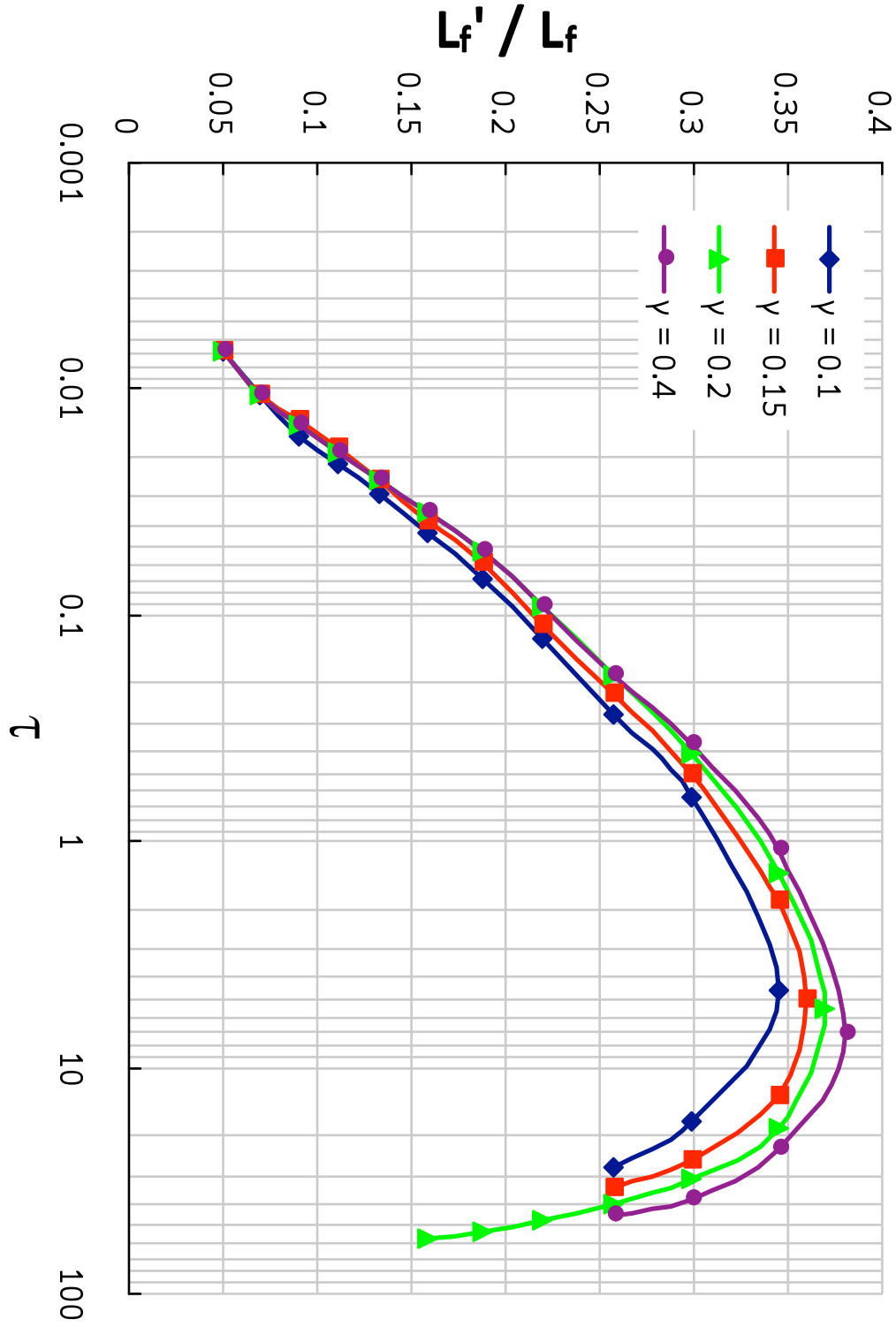
Lf' / Lf
0
0.05
0.1
0.15
0.2
0.25
0.3
0.35
0.4
τ
0.001
0.01
0.1
1
10
100
γ = 0.1
γ = 0.15
γ = 0.2
γ = 0.4

Appendix B: Derivation of the Well Completion Number F_{Co} and the Reservoir Depletion Number R_{Dep}

B.1. Well Completion Number F_{Co}

B.1.1. Case 1, linear flow approximation: $F_{CD} = \frac{k_f w_f}{k L_f} \geq 100\pi$

According to Guppy et al. (1981), the dimensionless flow rate at early production times is:

$$q_D = \frac{2}{\sqrt{\pi^3 t_{D_{L_f}}}} \text{ with } \frac{1}{q_D} = \frac{kh\left[m(p_R) - m(p_{wf})\right]}{1424T} \cdot \frac{1}{q_{sc}}$$

$$\text{and } t_{D_{L_f}} = \frac{0.0002637kt}{\phi(\mu c_t)_i L_f^{\ 2}}$$

The flow rate at standard conditions is then derived, with all variables expressed in oil field units:

$$q_{sc} = 0.015532 \frac{\Delta m(p)\sqrt{\phi\mu k c_t} L_f h}{T} t^{-\frac{1}{2}}$$

$$= 0.015532 \frac{(p_R^2 - p_{wf}^2) L_f h}{ZT} \sqrt{\frac{\phi k c_t}{\mu t}}$$

$$\text{with } m(p) = 2\int_{p_0}^{p} \frac{p}{\mu(p) Z(p)} dp$$

$$\Rightarrow \Delta m(p) = m(p_R) - m(p_{wf}) = \frac{p_R^2 - p_{wf}^2}{\mu Z} \text{ if } \mu, Z \text{ are constant}$$

We integrate the flow rate over the first month of production:

$$Q_{1month} = \frac{1}{24}\int_0^{720} 0.015532 \frac{\left(p_R^2 - p_{wf}^2\right)L_f h}{ZT}\sqrt{\frac{\phi k c_t}{\mu t}}dt$$

$$= 0.001294 \frac{\left(p_R^2 - p_{wf}^2\right)L_f h}{ZT}\sqrt{\frac{\phi k c_t}{\mu}}\left[\sqrt{t}\right]_0^{720}$$

$$= 0.034731 \frac{\left(p_R^2 - p_{wf}^2\right)L_f h}{ZT}\sqrt{\frac{\phi k c_t}{\mu}}$$

Finally,

$$F_{Co} = \left(\frac{Q_{field}}{Q_{theory}}\right)_{1month} = 28.793 \frac{Q_{1month} ZT}{\left(p_R^2 - p_{wf}^2\right)L_f h}\sqrt{\frac{\mu}{\phi k c_t}}$$

B.1.2. Case 2, bi-linear flow approximation: $F_{CD} = \frac{k_f w_f}{k L_f} < 100\pi$

According to Guppy et al. (1981), the dimensionless flow rate at early production times is:

$$\frac{1}{q_D} = \frac{\pi\,\Gamma(3/4)}{\sqrt{2F_{CD}}} t_{D_{L_f}}^{1/4} \text{ with } \frac{1}{q_D} = \frac{kh\left[m(p_R) - m(p_{wf})\right]}{1424T}\cdot\frac{1}{q_{sc}}$$

$$\text{and } t_{D_{L_f}} = \frac{0.0002637kt}{\phi(\mu c_t)_i L_f^{\,2}}$$

Then,

$$q_{sc} = 0.002024 \frac{h\sqrt{k_f w_f}\cdot\Delta m(p)\cdot(\phi k \mu c_t)^{1/4}}{T} t^{-\frac{1}{4}}$$

$$= 0.002024 \frac{h\sqrt{k_f w_f}\left(p_R^2 - p_{wf}^2\right)(k\phi c_t)^{1/4}}{\mu^{3/4} ZT} t^{-\frac{1}{4}}$$

We integrate the flow rate over the first month of production:

$$Q_{1month} = \frac{1}{24}\int_0^{720} 0.002024 \frac{h\sqrt{k_f w_f}\left(p_R^2 - p_{wf}^2\right)\left(k\phi c_t\right)^{1/4}}{\mu^{3/4} ZT} t^{-\frac{1}{4}} dt$$

$$= 0.000113 \frac{h\sqrt{k_f w_f}\left(p_R^2 - p_{wf}^2\right)\left(k\phi c_t\right)^{1/4}}{\mu^{3/4} ZT} \left[t^{\frac{3}{4}} \right]_0^{720}$$

$$= 0.01563 \frac{h\sqrt{k_f w_f}\left(p_R^2 - p_{wf}^2\right)\left(k\phi c_t\right)^{1/4}}{\mu^{3/4} ZT}$$

Finally,

$$F_{Co} = \left(\frac{Q_{field}}{Q_{theory}} \right)_{1month} = 63.9825 \frac{Q_{1month} \mu^{3/4} ZT}{h\sqrt{k_f w_f}\left(p_R^2 - p_{wf}^2\right)\left(k\phi c_t\right)^{1/4}}$$

B.2. RESERVOIR DEPLETION NUMBER R_{DEP}

$$R_{Dep}(t) = \max_n \left(\frac{1}{n} \sum_{i=1}^{n} \frac{G_{p_i}(t)}{PV_i} \right) = C \frac{\overline{B_g}}{\phi h (1 - S_w)} \max_n \left(\frac{1}{n} \sum_{i=1}^{n} \frac{G_{p_i}(t)}{r_i^2} \right)$$

The reservoir depletion number is calculated by summing the ratios of the cumulative production of a surrounding well and the squared value of the distance separating it from the well of interest (G_{pi} / r_i^2), and then dividing it by the number of wells. This expression reaches a maximum value for a certain number of wells n. The value of the constant C is chosen so that the expression of the reservoir depletion number R_{Dep} corresponds to the known expression for a reservoir depleted by four wells located at its corners (Fig. 5.2(b)). The sweep efficiency of a 4-spot depletion pattern is expressed below:

$$\frac{\overline{B_g}}{\phi h (1 - S_w)} \cdot \frac{G_p(t)}{4} \cdot \frac{1}{\left(r/\sqrt{2}\right)^2} = \frac{\overline{B_g} G_p(t)}{2\phi h (1 - S_w) r^2}$$

Applying the expression of the reservoir depletion number to the geometry of Fig. 5.2(b), we find that the constant C should be equal to 0.5:

$$R_{Dep}(t) = C\frac{\overline{B_g}}{\phi h(1-S_w)}\left(\frac{1}{4}\frac{4G_p(t)}{r^2}\right) = C\frac{\overline{B_g}G_p(t)}{\phi h(1-S_w)r^2} \Rightarrow C = 1/2$$

Appendix C: Production and Completion Data in the Wattenberg Field

C.1. Production History of Wells Used in the Data Analysis

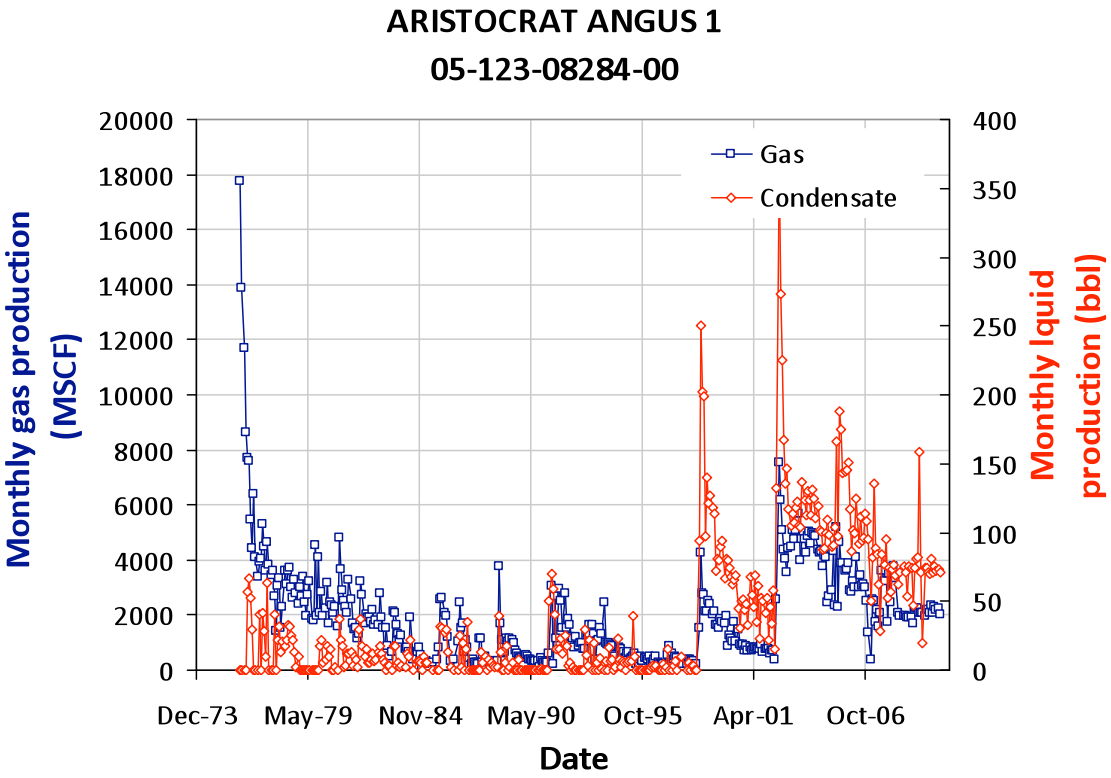

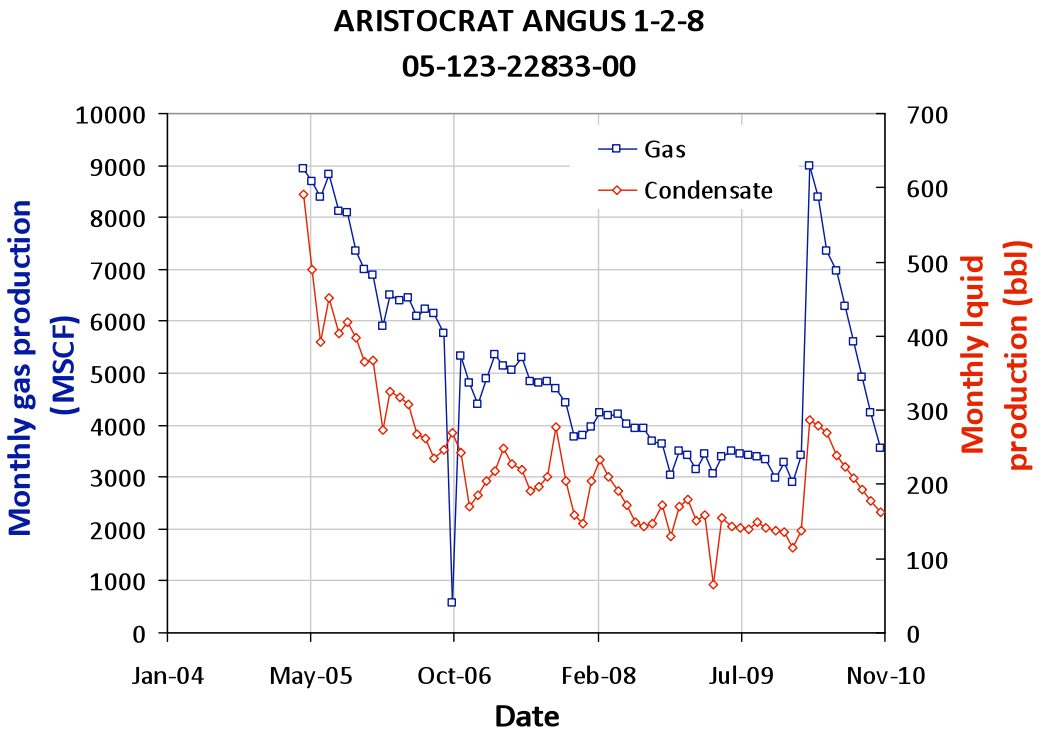
ARISTOCRAT ANGUS 1-2-8
05-123-22833-00
Gas
Condensate
Monthly gas production (MSCF)
Monthly lquid production (bbl)
Date
Jan-04
May-05
Oct-06
Feb-08
Jul-09
Nov-10
0
1000
2000
3000
4000
5000
6000
7000
8000
9000
10000
100
200
300
400
500
600
700

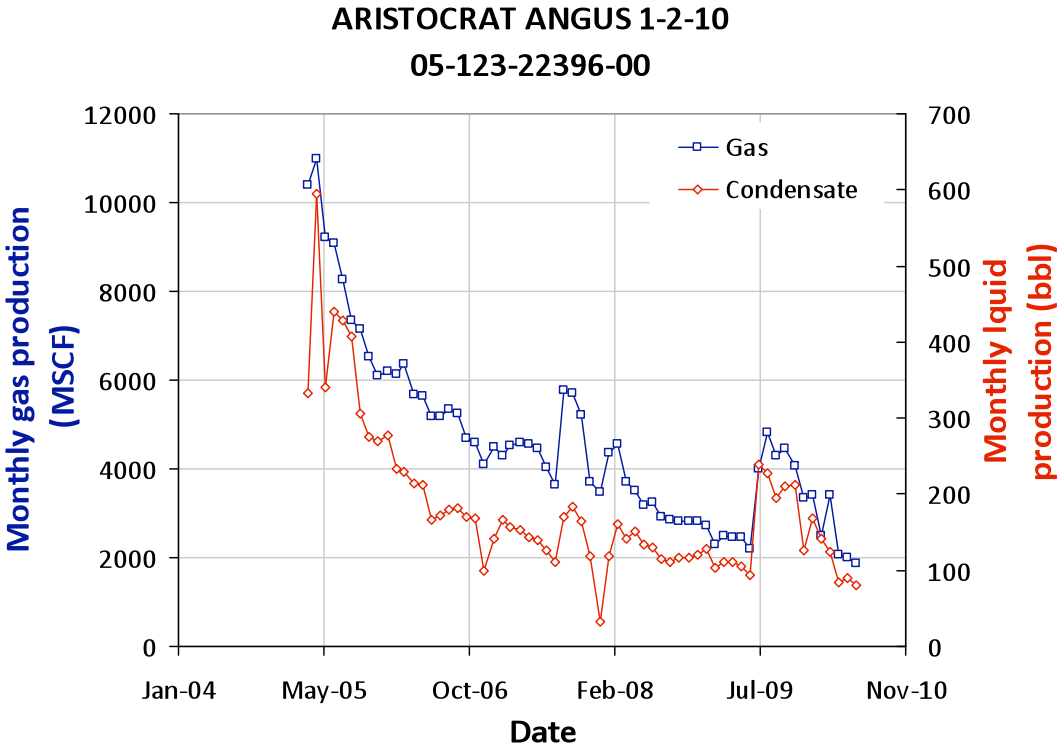
ARISTOCRAT ANGUS 1-2-10
05-123-22396-00
Gas
Condensate
Monthly gas production (MSCF)
Monthly lquid production (bbl)
Date
Jan-04
May-05
Oct-06
Feb-08
Jul-09
Nov-10
0
2000
4000
6000
8000
10000
12000
100
200
300
400
500
600
700

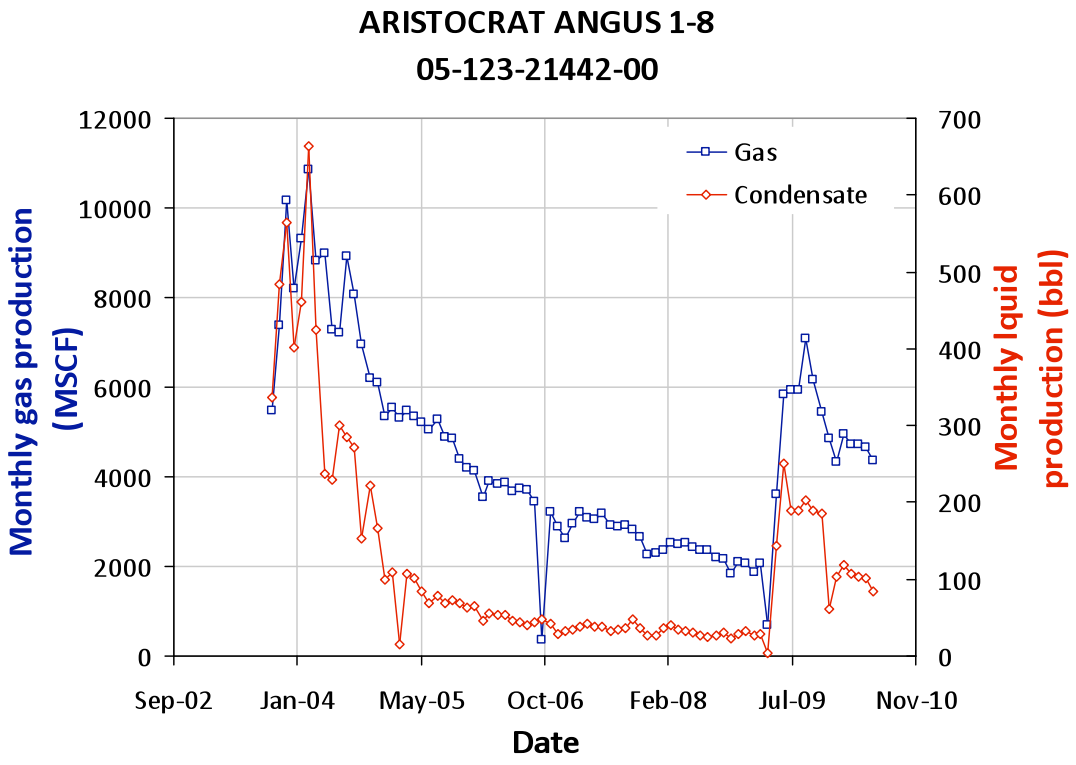
ARISTOCRAT ANGUS 1-8
05-123-21442-00
Monthly gas production (MSCF)
Monthly lquid production (bbl)
Gas
Condensate
12000
10000
8000
6000
4000
2000
0
700
600
500
400
300
200
100
0
Sep-02
Jan-04
May-05
Oct-06
Feb-08
Jul-09
Nov-10
Date

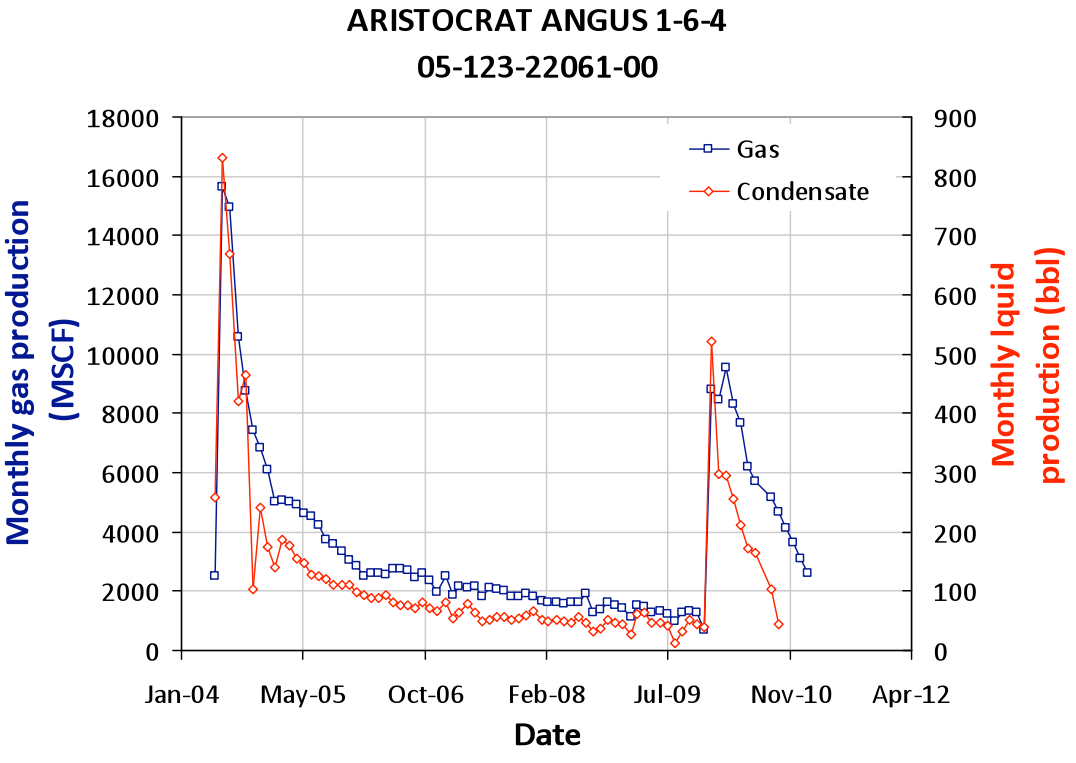
ARISTOCRAT ANGUS 1-6-4
05-123-22061-00
Monthly gas production (MSCF)
Monthly lquid production (bbl)
Gas
Condensate
18000
16000
14000
12000
10000
8000
6000
4000
2000
0
900
800
700
600
500
400
300
200
100
0
Jan-04
May-05
Oct-06
Feb-08
Jul-09
Nov-10
Apr-12
Date

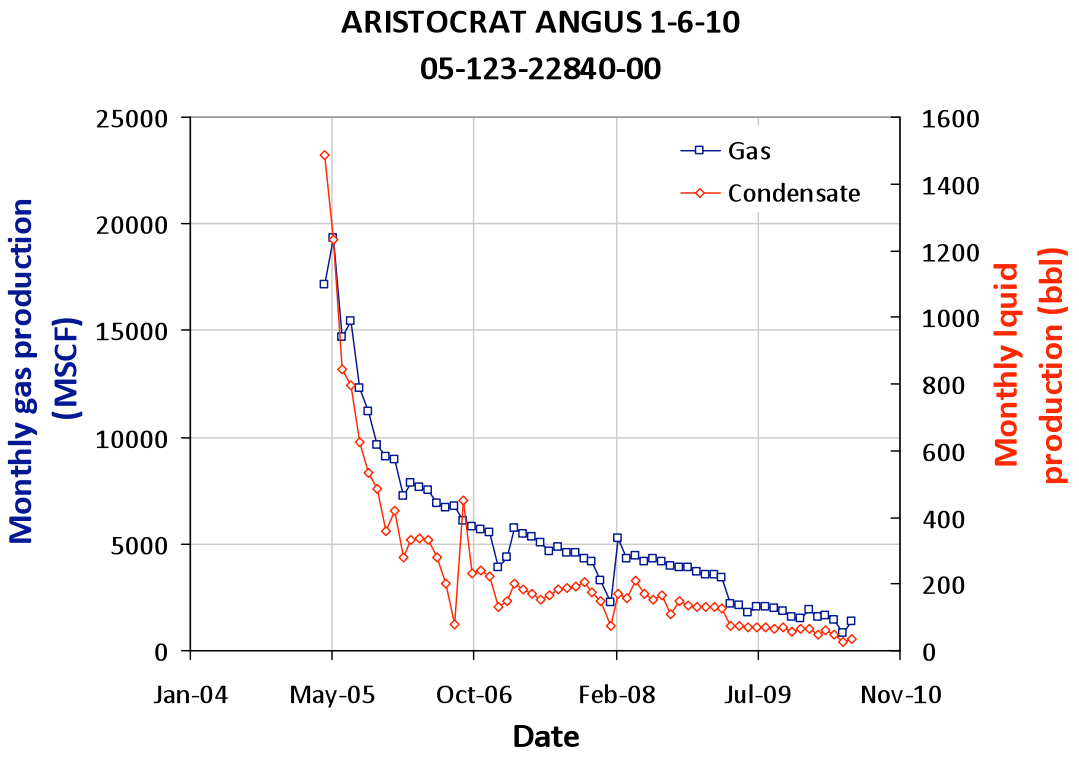
ARISTOCRAT ANGUS 1-6-10
05-123-22840-00
Monthly gas production (MSCF)
Monthly liquid production (bbl)
Gas
Condensate
25000
20000
15000
10000
5000
0
1600
1400
1200
1000
800
600
400
200
0
Jan-04
May-05
Oct-06
Feb-08
Jul-09
Nov-10
Date

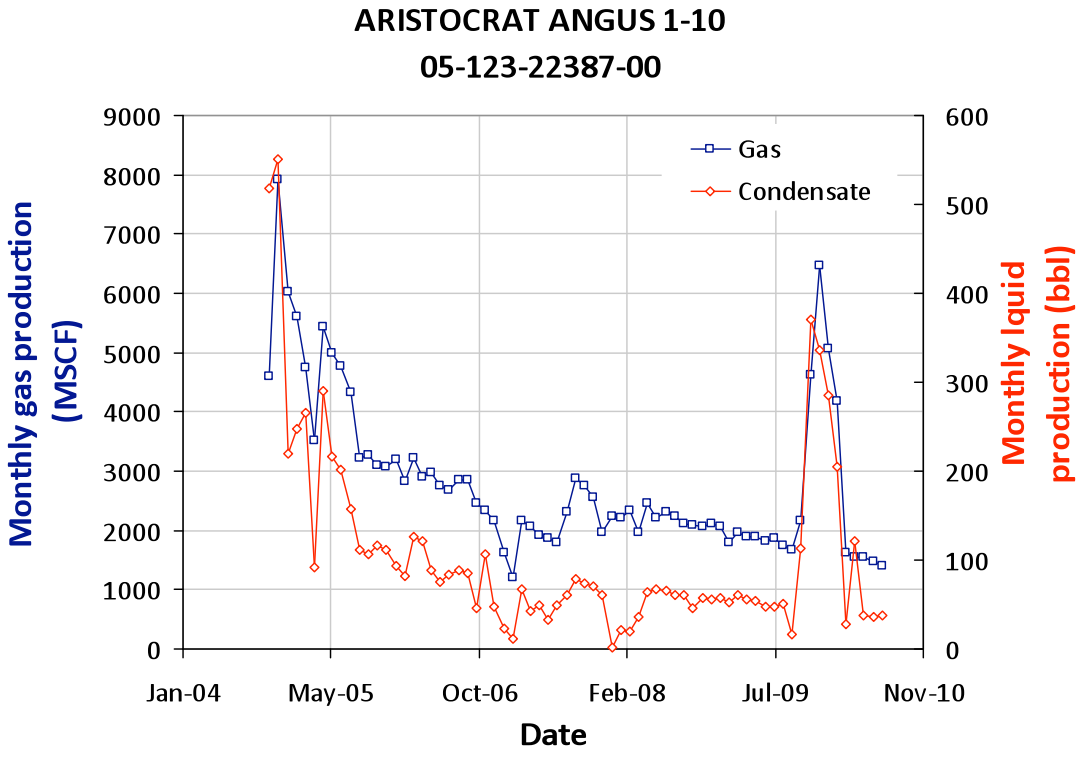
ARISTOCRAT ANGUS 1-10
05-123-22387-00
Monthly gas production (MSCF)
Monthly liquid production (bbl)
Gas
Condensate
9000
8000
7000
6000
5000
4000
3000
2000
1000
0
600
500
400
300
200
100
0
Jan-04
May-05
Oct-06
Feb-08
Jul-09
Nov-10
Date

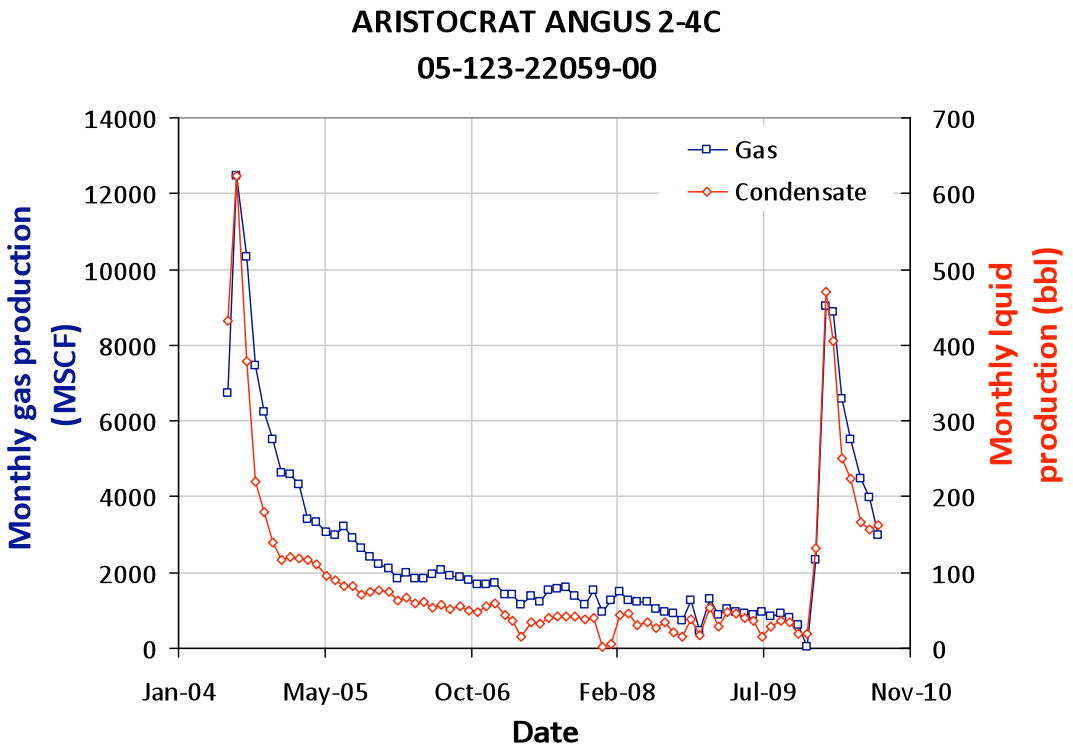
ARISTOCRAT ANGUS 2-4C
05-123-22059-00
Monthly gas production (MSCF)
Monthly liquid production (bbl)
Gas
Condensate
14000
12000
10000
8000
6000
4000
2000
0
700
600
500
400
300
200
100
0
Jan-04
May-05
Oct-06
Feb-08
Jul-09
Nov-10
Date

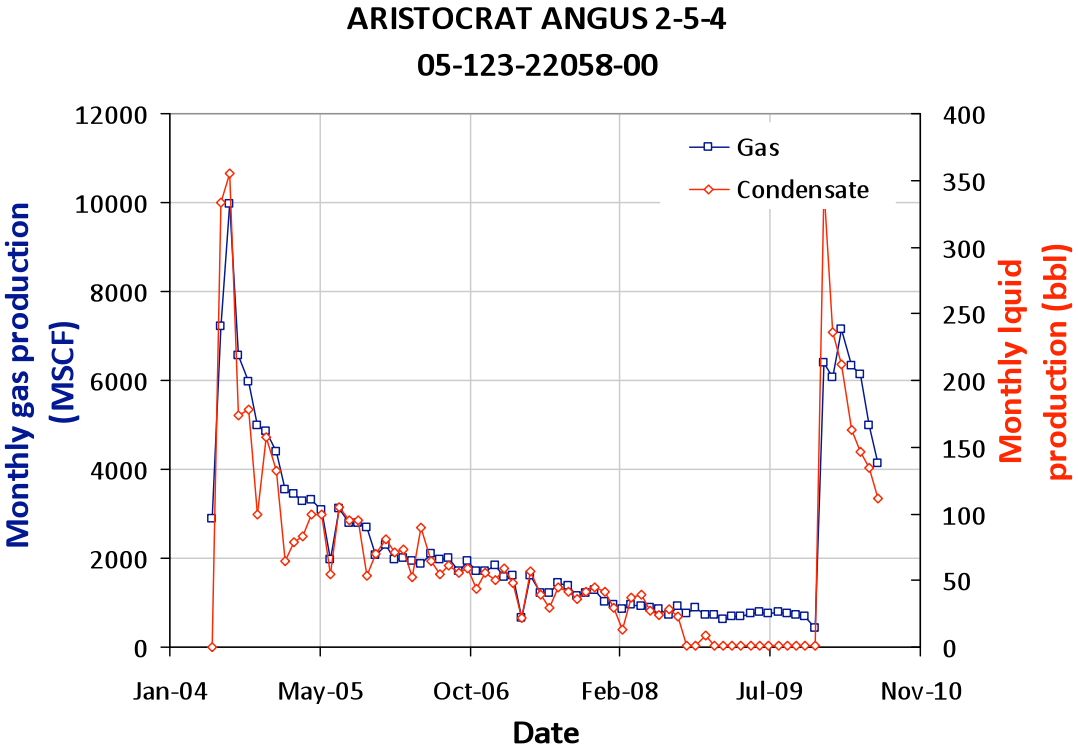
ARISTOCRAT ANGUS 2-5-4
05-123-22058-00
Monthly gas production (MSCF)
Monthly liquid production (bbl)
Gas
Condensate
12000
10000
8000
6000
4000
2000
0
400
350
300
250
200
150
100
50
0
Jan-04
May-05
Oct-06
Feb-08
Jul-09
Nov-10
Date

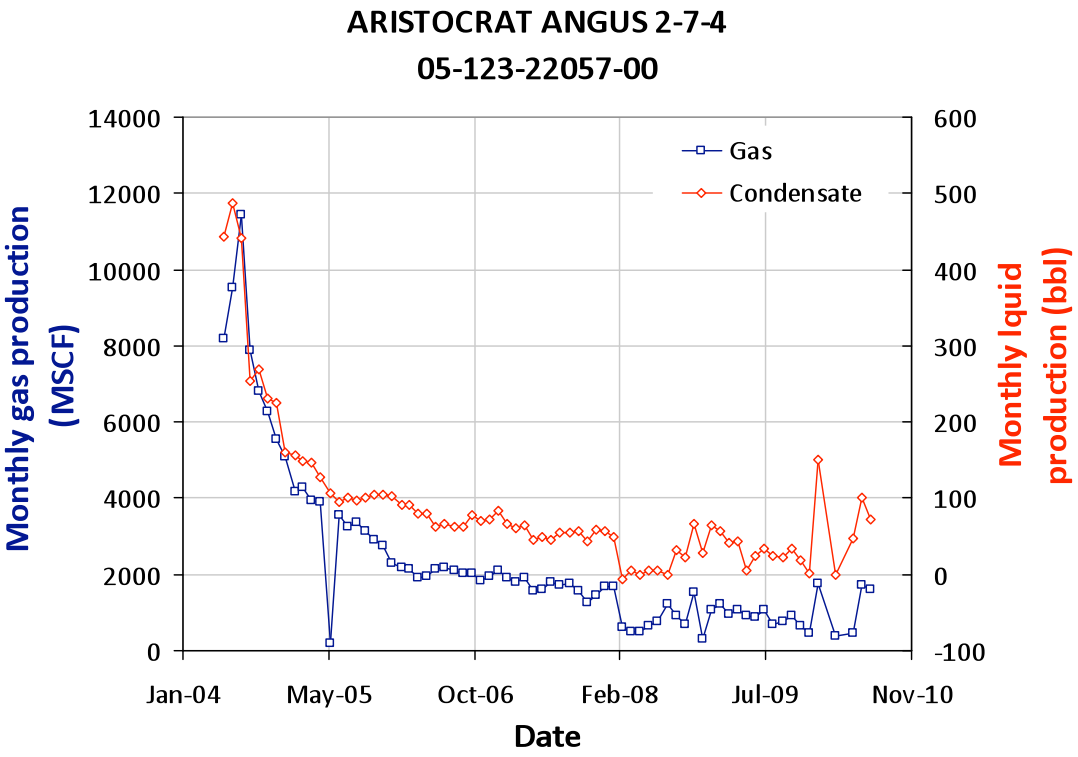
ARISTOCRAT ANGUS 2-7-4
05-123-22057-00
Monthly gas production (MSCF)
Monthly liquid production (bbl)
Gas
Condensate
14000
12000
10000
8000
6000
4000
2000
0
600
500
400
300
200
100
0
-100
Jan-04
May-05
Oct-06
Feb-08
Jul-09
Nov-10
Date

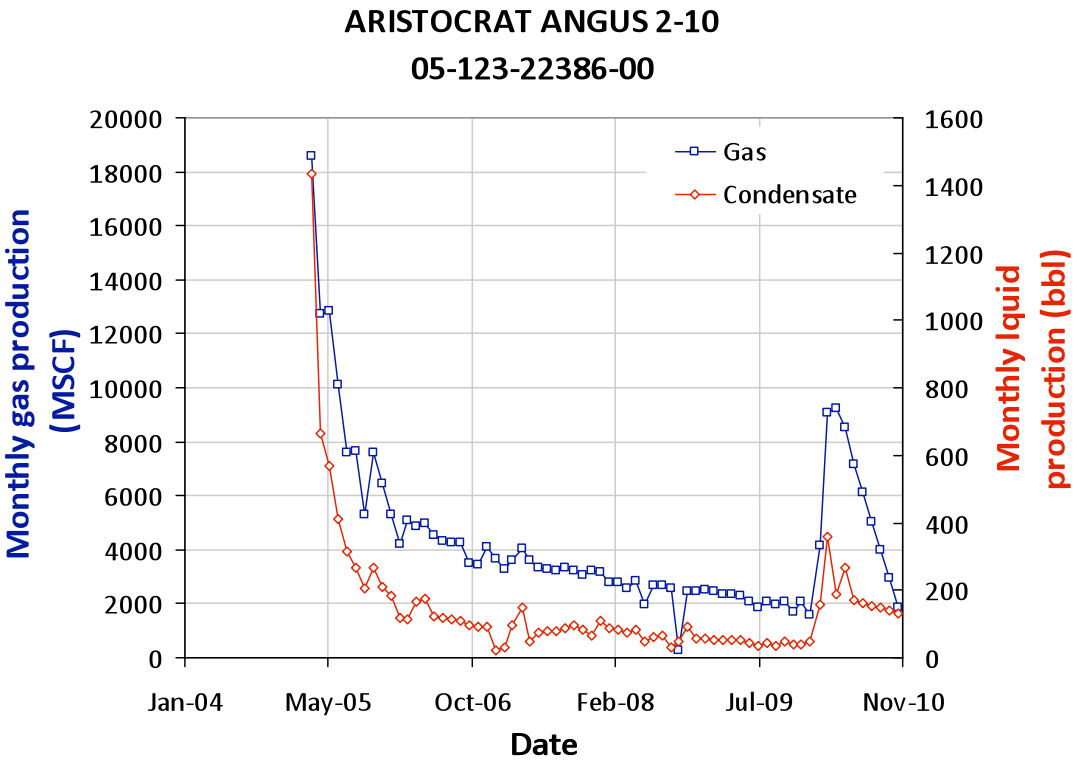
ARISTOCRAT ANGUS 2-10
05-123-22386-00
Monthly gas production (MSCF)
Monthly liquid production (bbl)
Gas
Condensate
20000
18000
16000
14000
12000
10000
8000
6000
4000
2000
0
1600
1400
1200
1000
800
600
400
200
0
Jan-04
May-05
Oct-06
Feb-08
Jul-09
Nov-10
Date

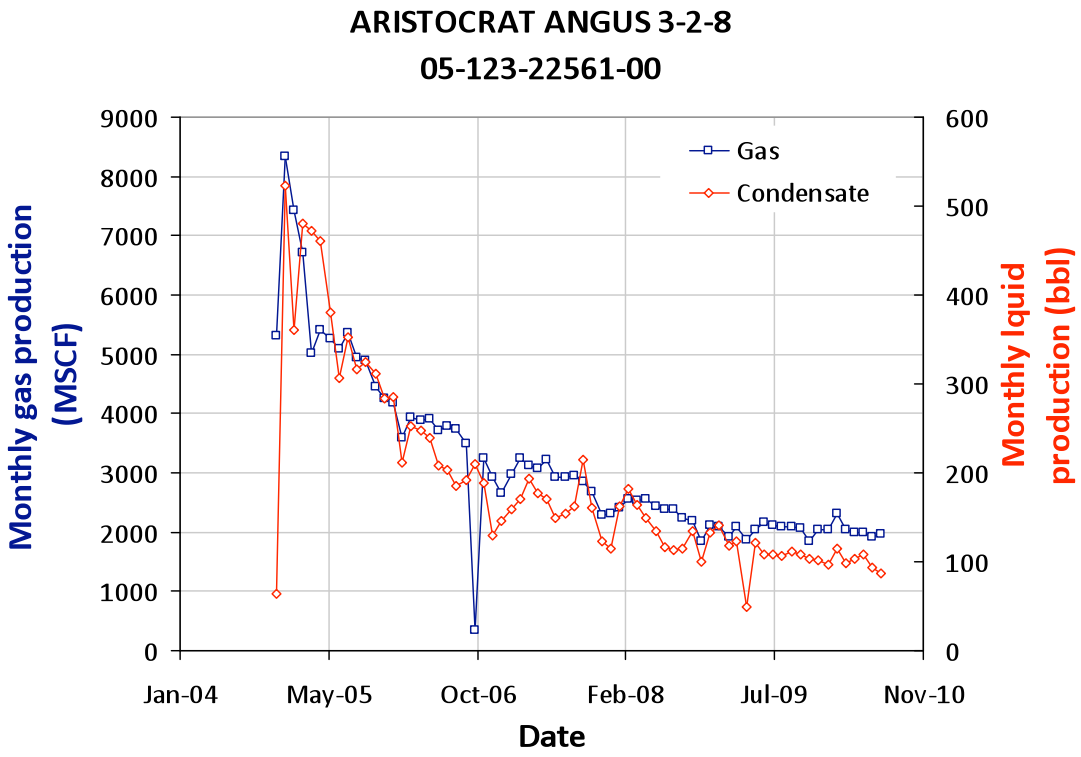
ARISTOCRAT ANGUS 3-2-8
05-123-22561-00
Monthly gas production (MSCF)
Monthly liquid production (bbl)
Gas
Condensate
9000
8000
7000
6000
5000
4000
3000
2000
1000
0
600
500
400
300
200
100
0
Jan-04
May-05
Oct-06
Feb-08
Jul-09
Nov-10
Date

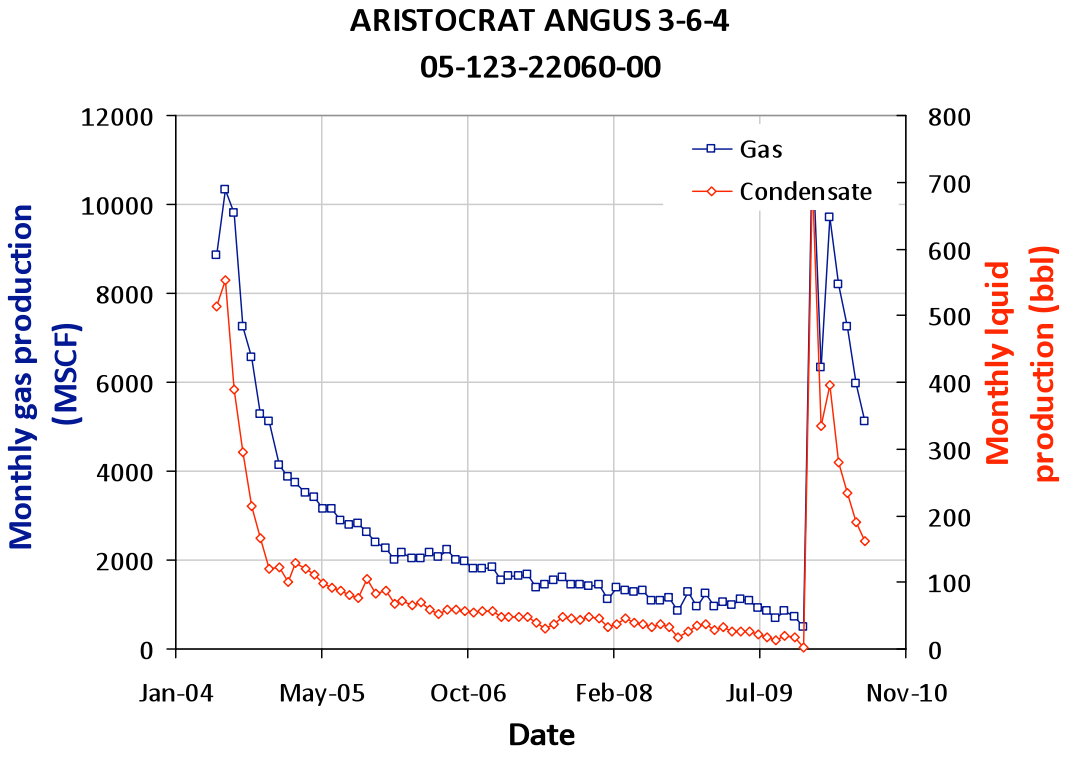
ARISTOCRAT ANGUS 3-6-4
05-123-22060-00
Monthly gas production (MSCF)
Monthly liquid production (bbl)
Gas
Condensate
12000
10000
8000
6000
4000
2000
0
800
700
600
500
400
300
200
100
0
Jan-04
May-05
Oct-06
Feb-08
Jul-09
Nov-10
Date

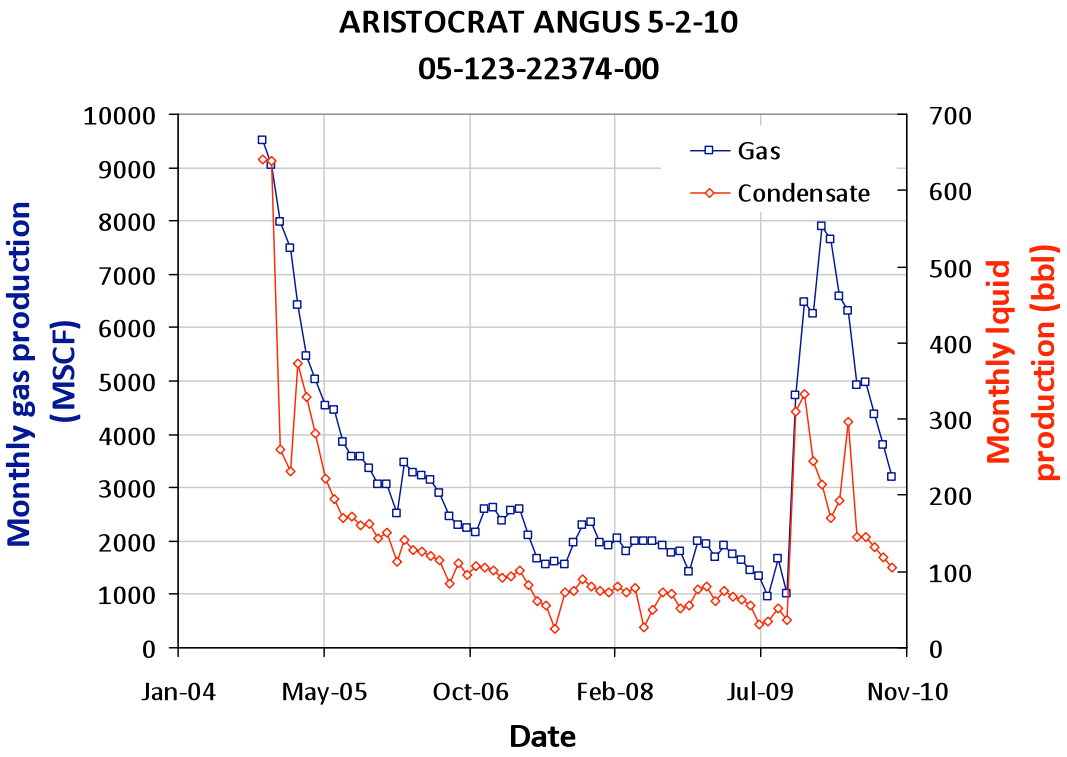
ARISTOCRAT ANGUS 5-2-10
05-123-22374-00
Monthly gas production (MSCF)
Monthly liquid production (bbl)
Gas
Condensate
10000
9000
8000
7000
6000
5000
4000
3000
2000
1000
0
700
600
500
400
300
200
100
0
Jan-04
May-05
Oct-06
Feb-08
Jul-09
Nov-10
Date

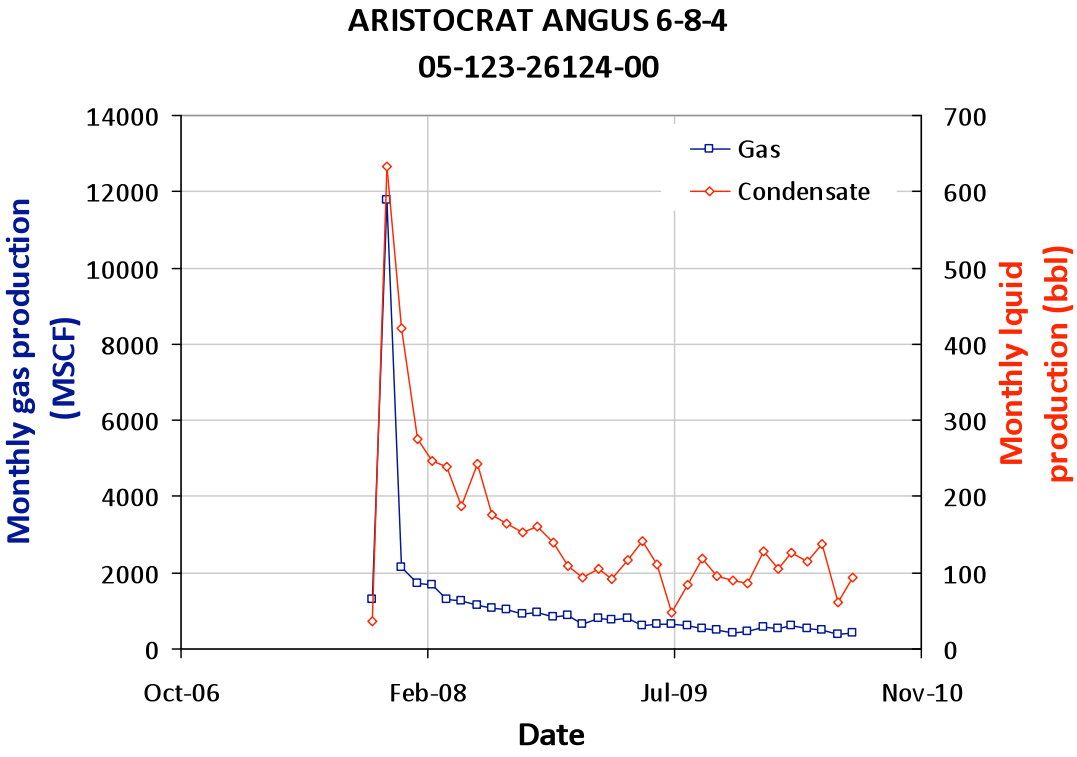
ARISTOCRAT ANGUS 6-8-4
05-123-26124-00
Monthly gas production (MSCF)
Monthly liquid production (bbl)
Gas
Condensate
14000
12000
10000
8000
6000
4000
2000
0
700
600
500
400
300
200
100
0
Oct-06
Feb-08
Jul-09
Nov-10
Date

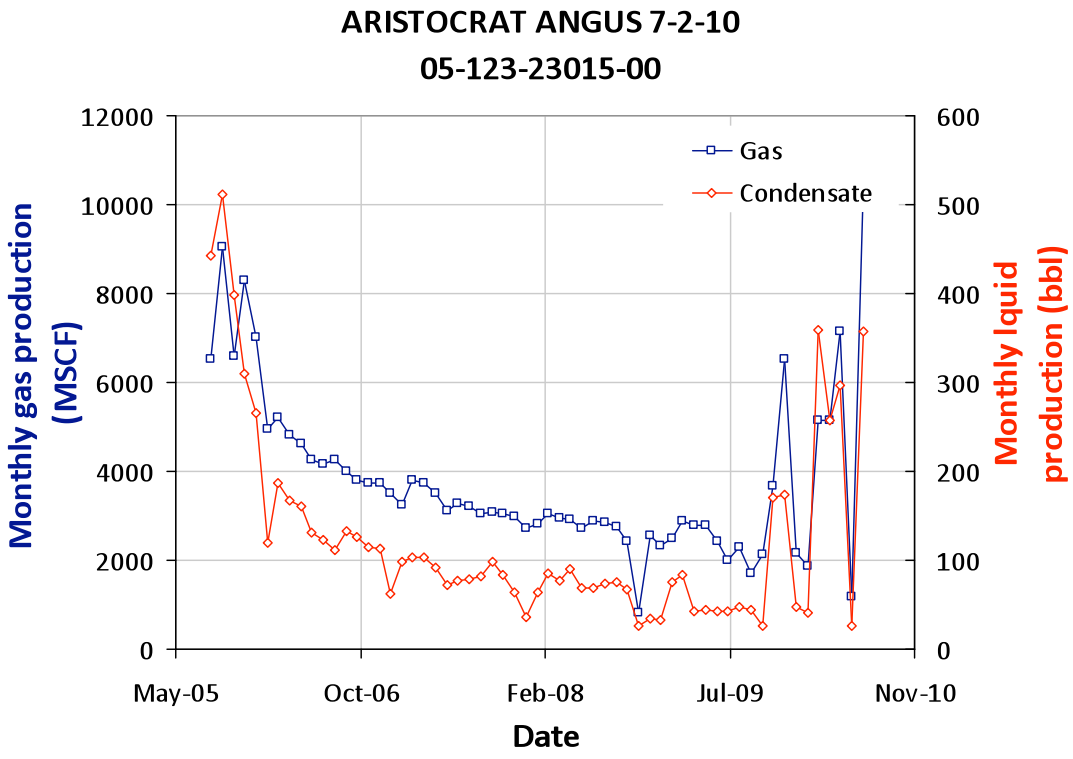
ARISTOCRAT ANGUS 7-2-10
05-123-23015-00
Monthly gas production (MSCF)
Monthly liquid production (bbl)
Gas
Condensate
12000
10000
8000
6000
4000
2000
0
600
500
400
300
200
100
0
May-05
Oct-06
Feb-08
Jul-09
Nov-10
Date

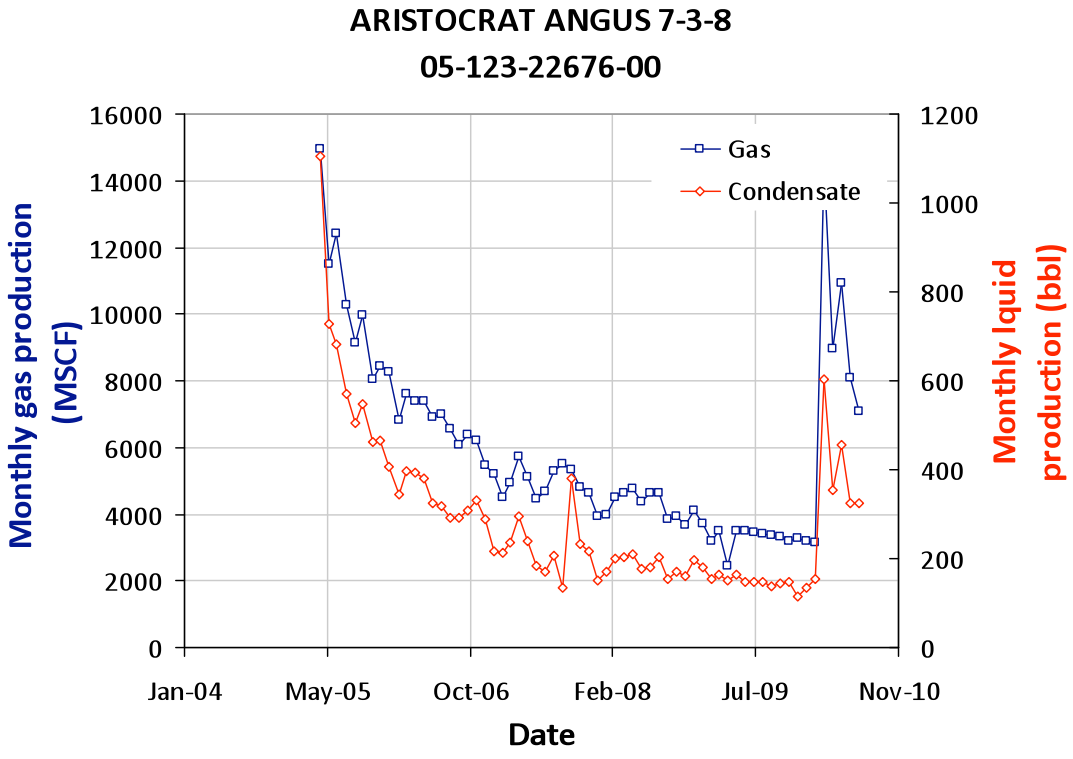
ARISTOCRAT ANGUS 7-3-8
05-123-22676-00
Monthly gas production (MSCF)
Monthly liquid production (bbl)
Gas
Condensate
16000
14000
12000
10000
8000
6000
4000
2000
0
1200
1000
800
600
400
200
0
Jan-04
May-05
Oct-06
Feb-08
Jul-09
Nov-10
Date

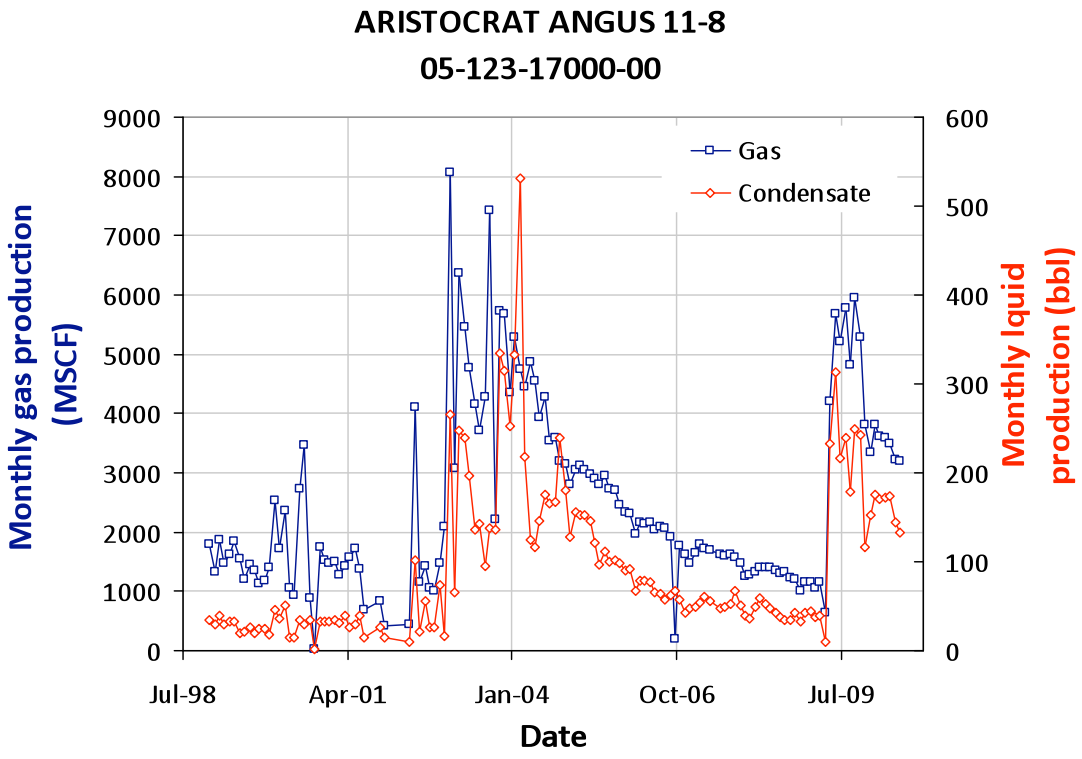
ARISTOCRAT ANGUS 11-8
05-123-17000-00
Monthly gas production (MSCF)
Monthly liquid production (bbl)
Gas
Condensate
9000
8000
7000
6000
5000
4000
3000
2000
1000
0
600
500
400
300
200
100
0
Jul-98
Apr-01
Jan-04
Oct-06
Jul-09
Date

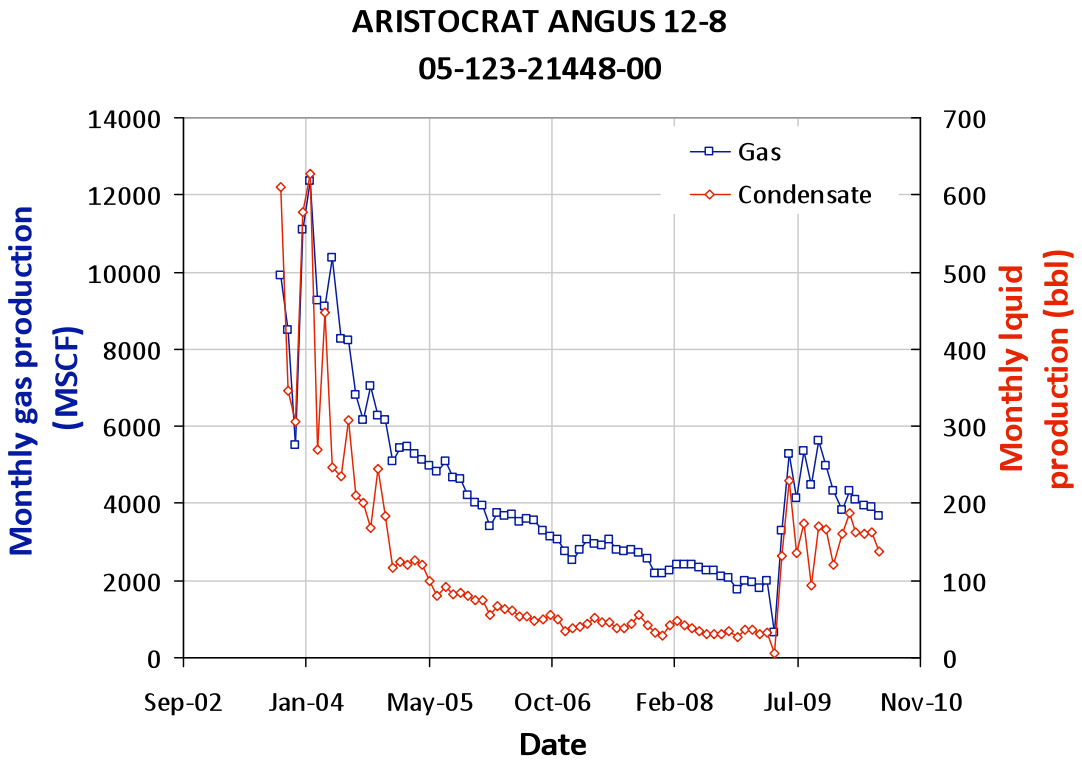
ARISTOCRAT ANGUS 12-8
05-123-21448-00
Monthly gas production (MSCF)
Monthly liquid production (bbl)
Gas
Condensate
14000
12000
10000
8000
6000
4000
2000
0
700
600
500
400
300
200
100
0
Sep-02
Jan-04
May-05
Oct-06
Feb-08
Jul-09
Nov-10
Date

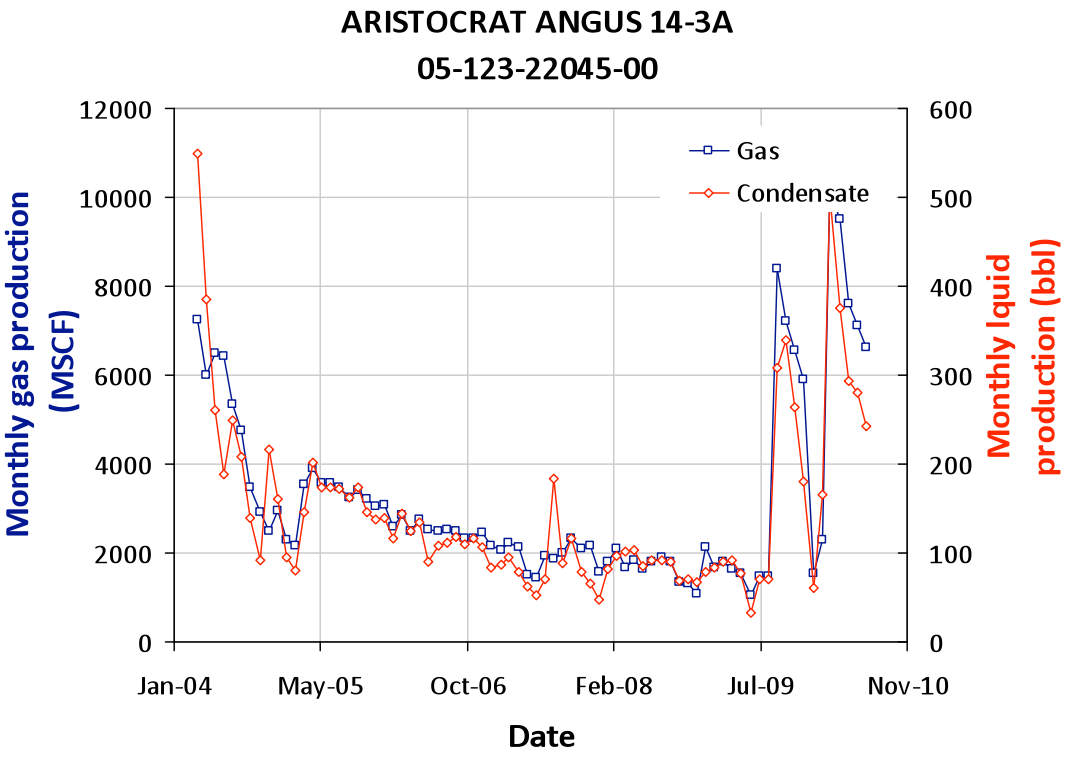
ARISTOCRAT ANGUS 14-3A
05-123-22045-00
Monthly gas production (MSCF)
Monthly liquid production (bbl)
Gas
Condensate
12000
10000
8000
6000
4000
2000
0
600
500
400
300
200
100
0
Jan-04
May-05
Oct-06
Feb-08
Jul-09
Nov-10
Date

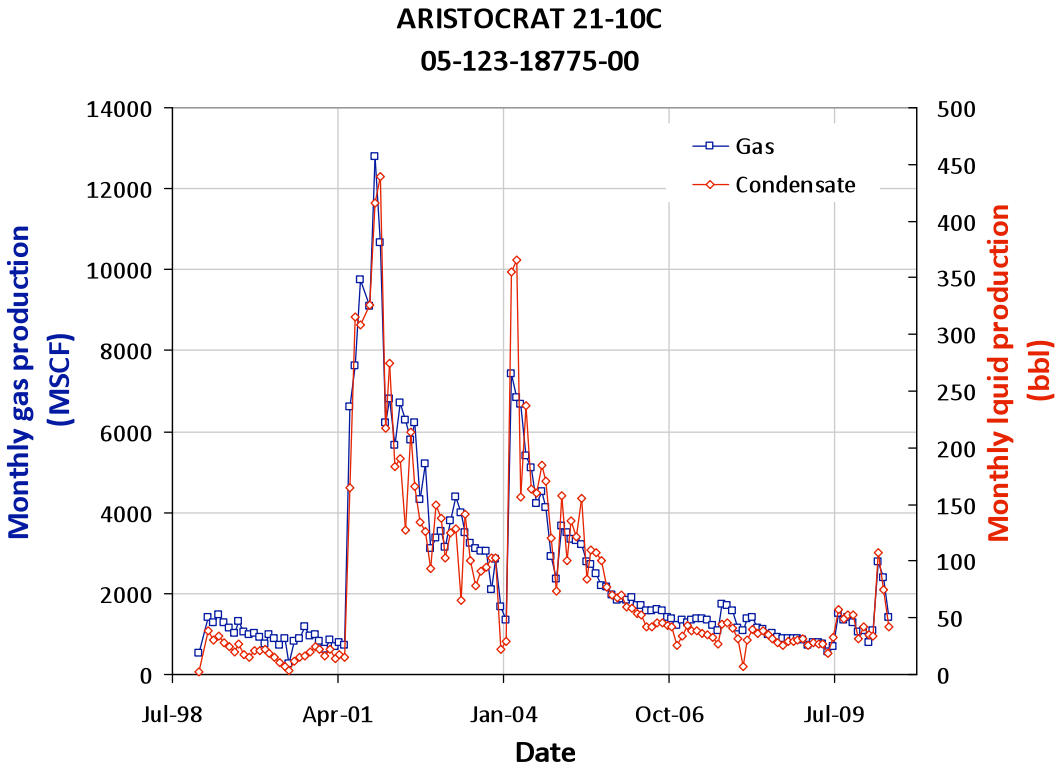
ARISTOCRAT 21-10C
05-123-18775-00
Monthly gas production (MSCF)
Monthly liquid production (bbl)
Gas
Condensate
14000
12000
10000
8000
6000
4000
2000
0
500
450
400
350
300
250
200
150
100
50
0
Jul-98
Apr-01
Jan-04
Oct-06
Jul-09
Date

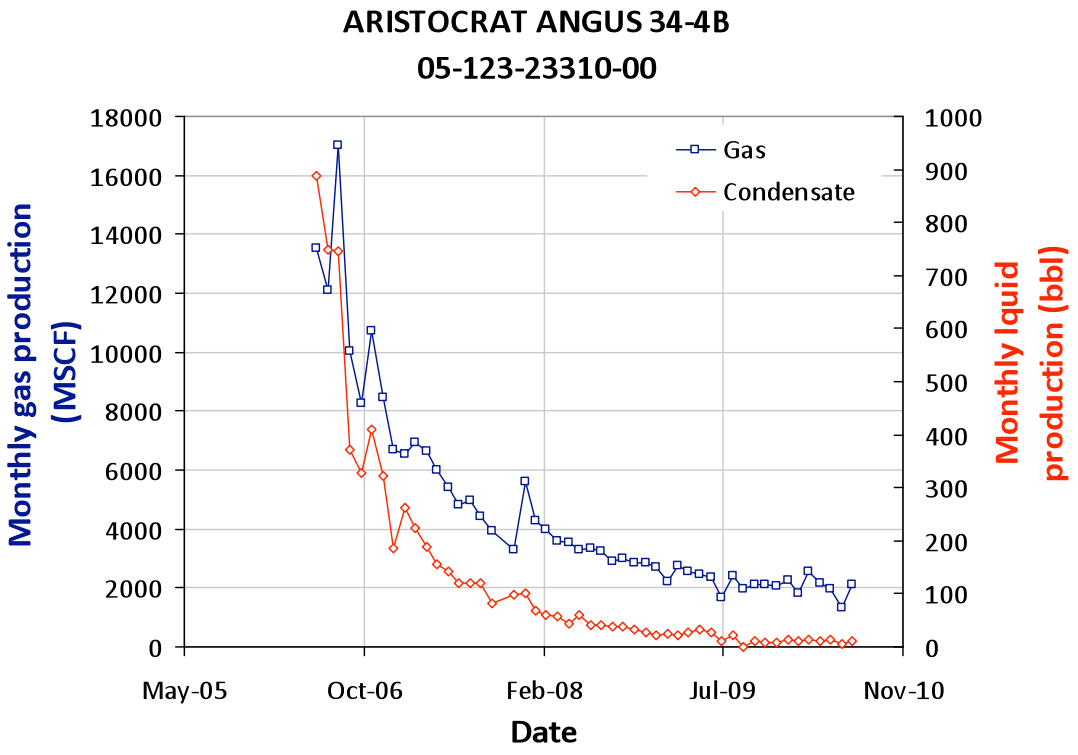
ARISTOCRAT ANGUS 34-4B
05-123-23310-00
Monthly gas production (MSCF)
Monthly liquid production (bbl)
Gas
Condensate
18000
16000
14000
12000
10000
8000
6000
4000
2000
0
1000
900
800
700
600
500
400
300
200
100
0
May-05
Oct-06
Feb-08
Jul-09
Nov-10
Date

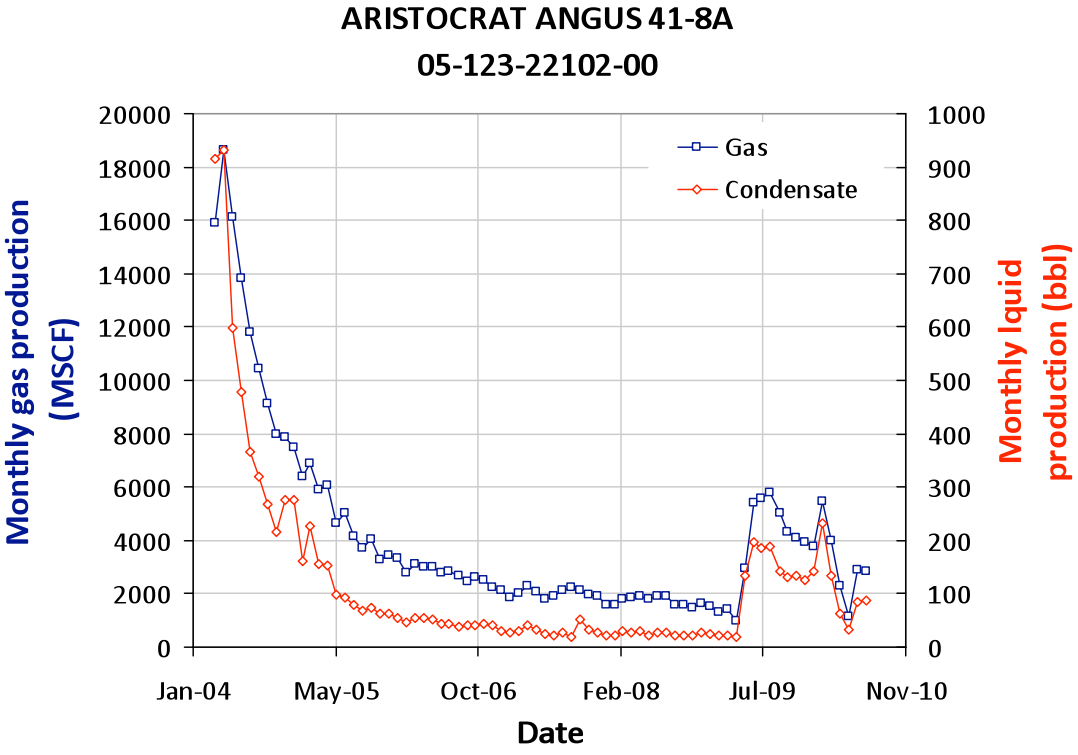
ARISTOCRAT ANGUS 41-8A
05-123-22102-00
Monthly gas production (MSCF)
Monthly liquid production (bbl)
Gas
Condensate
20000
18000
16000
14000
12000
10000
8000
6000
4000
2000
0
1000
900
800
700
600
500
400
300
200
100
0
Jan-04
May-05
Oct-06
Feb-08
Jul-09
Nov-10
Date

ARISTOCRAT ANGUS 42-10
05-123-16673-00

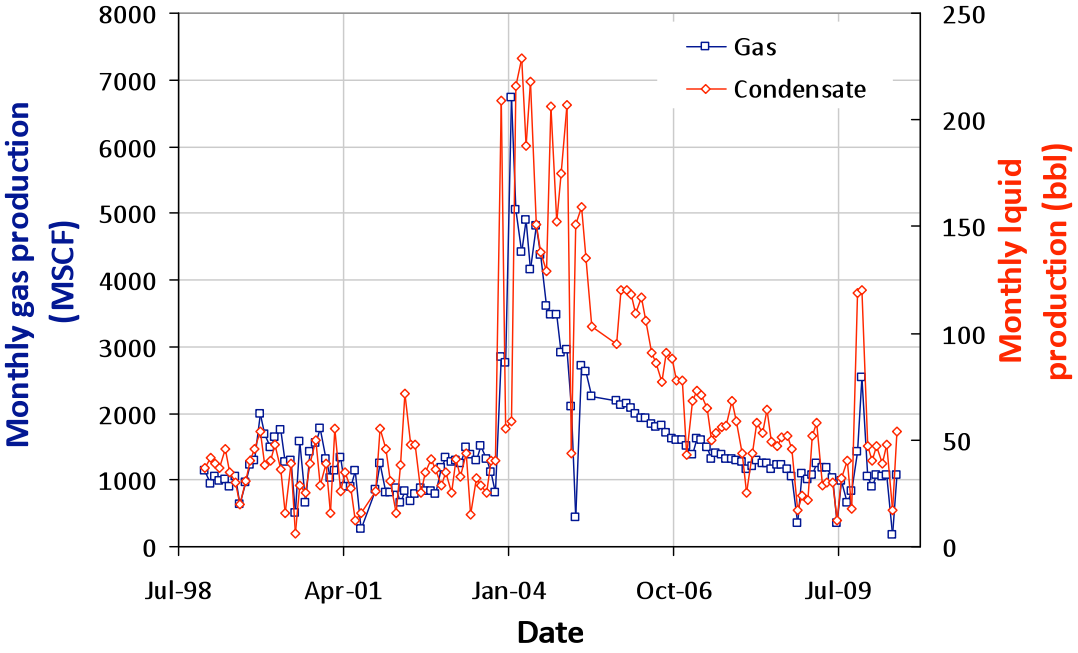

AUGUST 15-29
05-123-19167-00

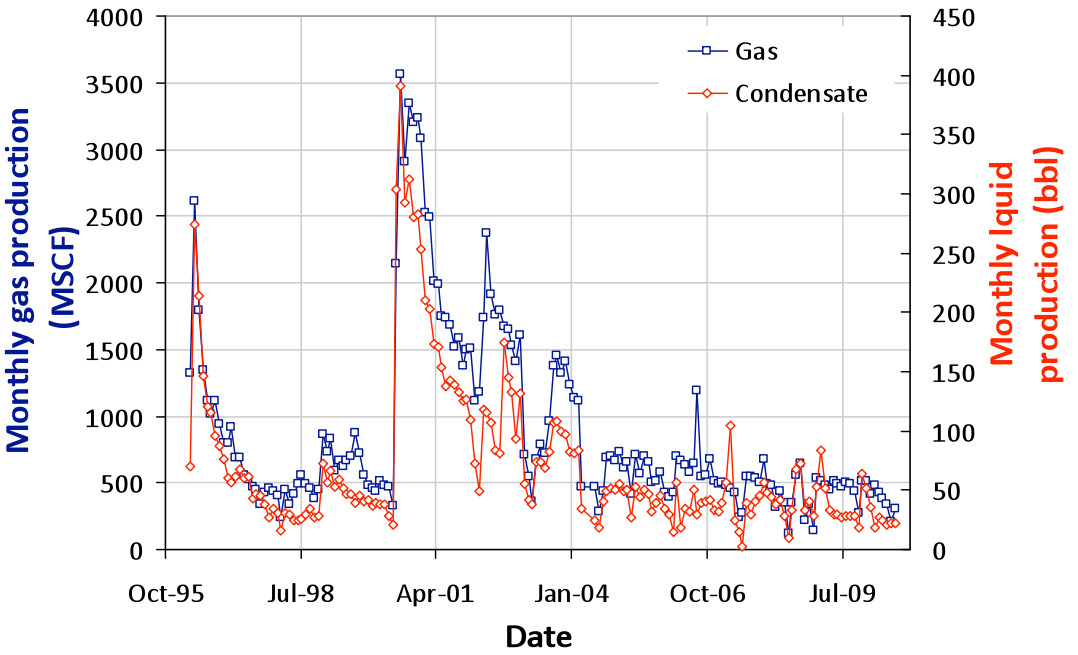

AUGUST 16-29
05-123-16100-00

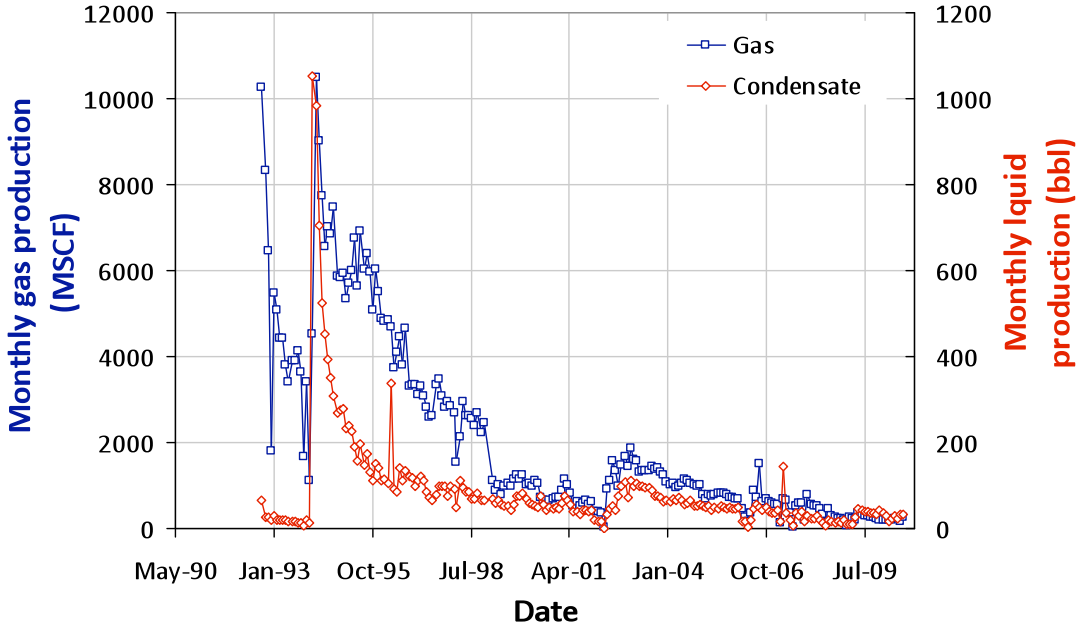

BB DRAW H 8-9
05-123-17039-00

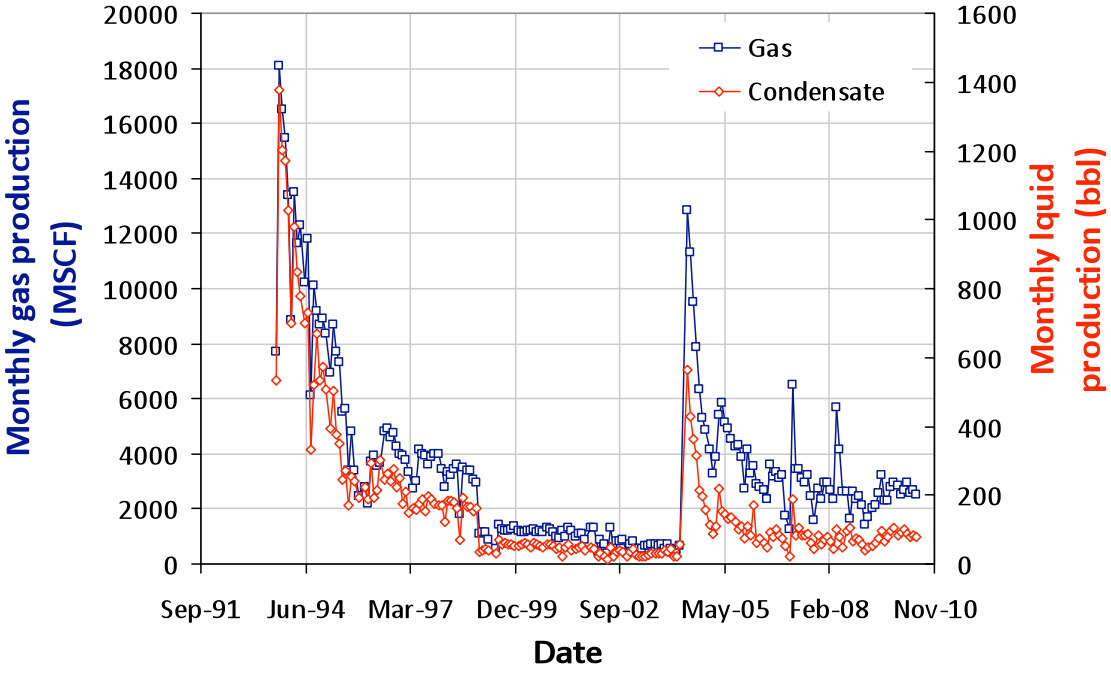

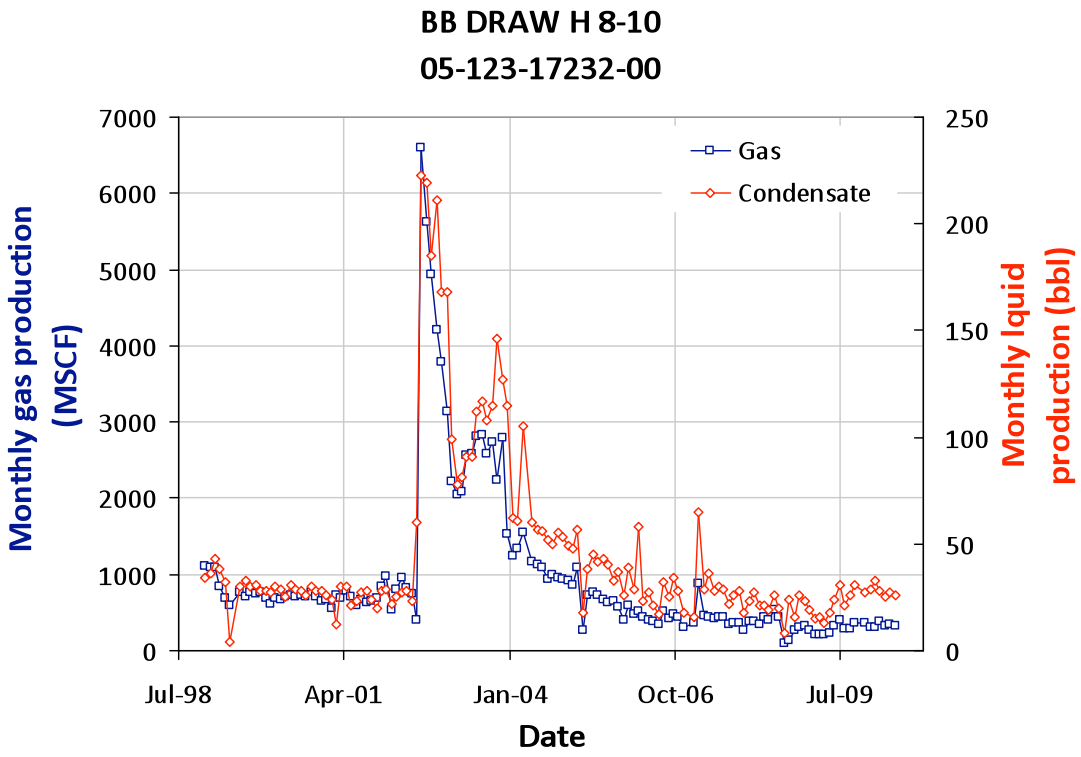
BB DRAW H 8-10
05-123-17232-00
Monthly gas production (MSCF)
Monthly liquid production (bbl)
Gas
Condensate
7000
6000
5000
4000
3000
2000
1000
0
250
200
150
100
50
0
Jul-98
Apr-01
Jan-04
Oct-06
Jul-09
Date

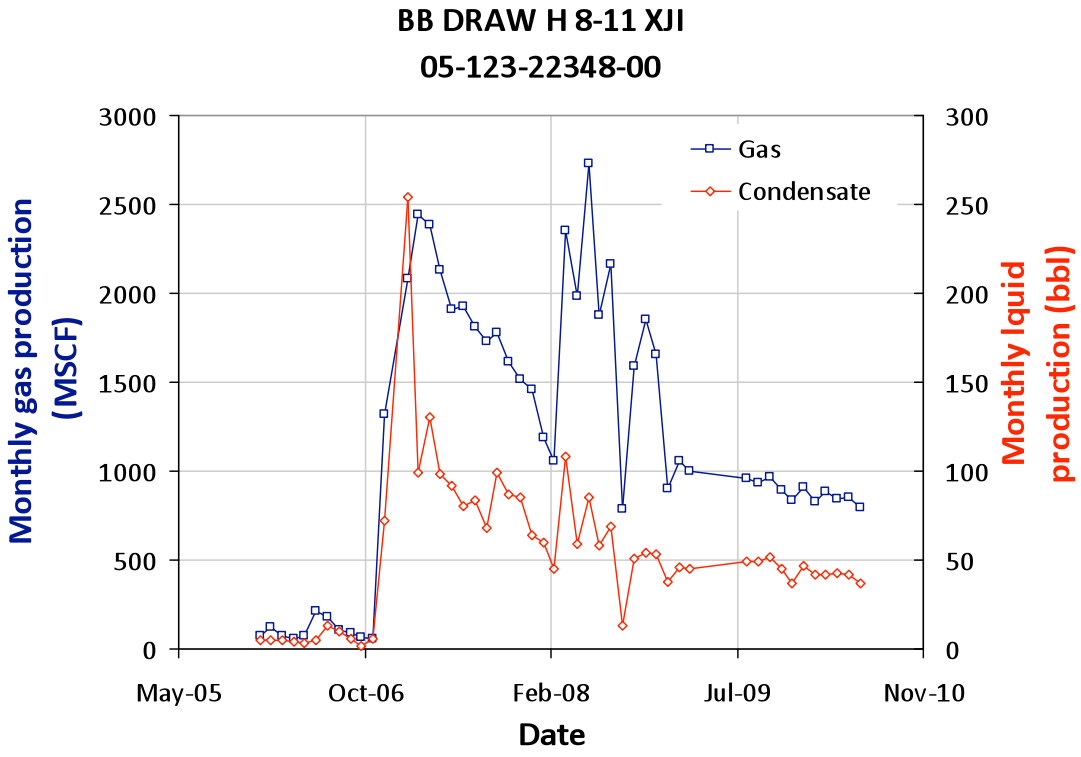
BB DRAW H 8-11 XJI
05-123-22348-00
Monthly gas production (MSCF)
Monthly liquid production (bbl)
Gas
Condensate
3000
2500
2000
1500
1000
500
0
300
250
200
150
100
50
0
May-05
Oct-06
Feb-08
Jul-09
Nov-10
Date

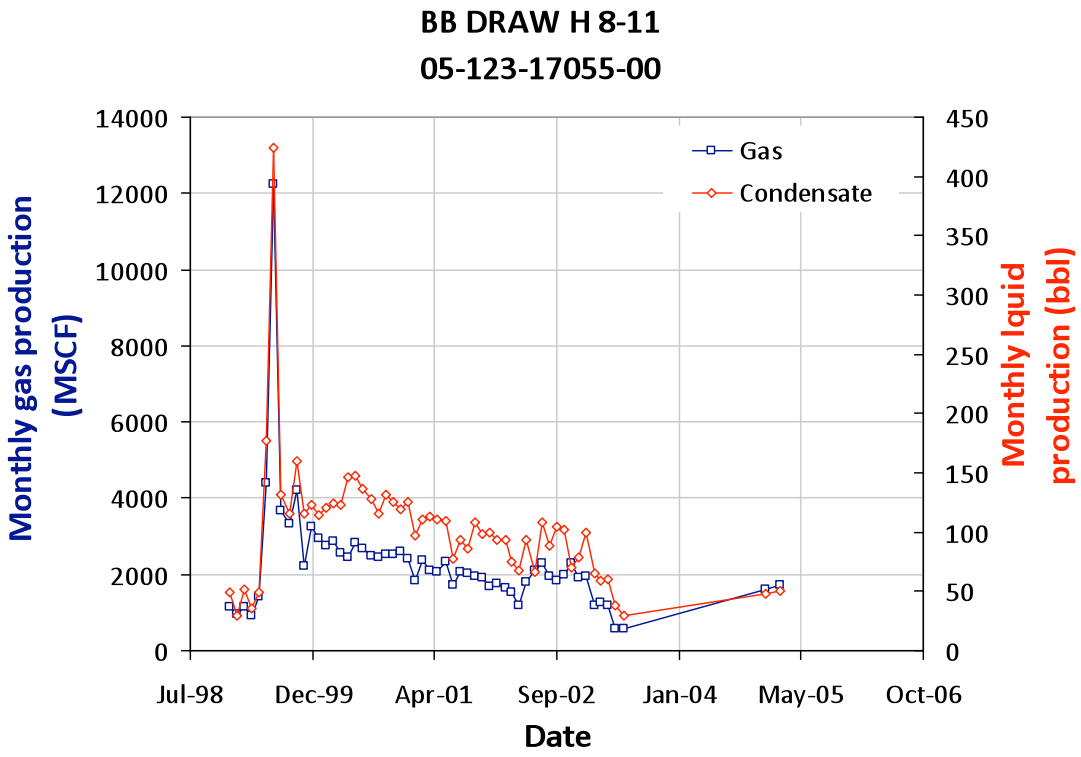
BB DRAW H 8-11
05-123-17055-00
Monthly gas production (MSCF)
Monthly liquid production (bbl)
Gas
Condensate
14000
12000
10000
8000
6000
4000
2000
0
450
400
350
300
250
200
150
100
50
0
Jul-98
Dec-99
Apr-01
Sep-02
Jan-04
May-05
Oct-06
Date

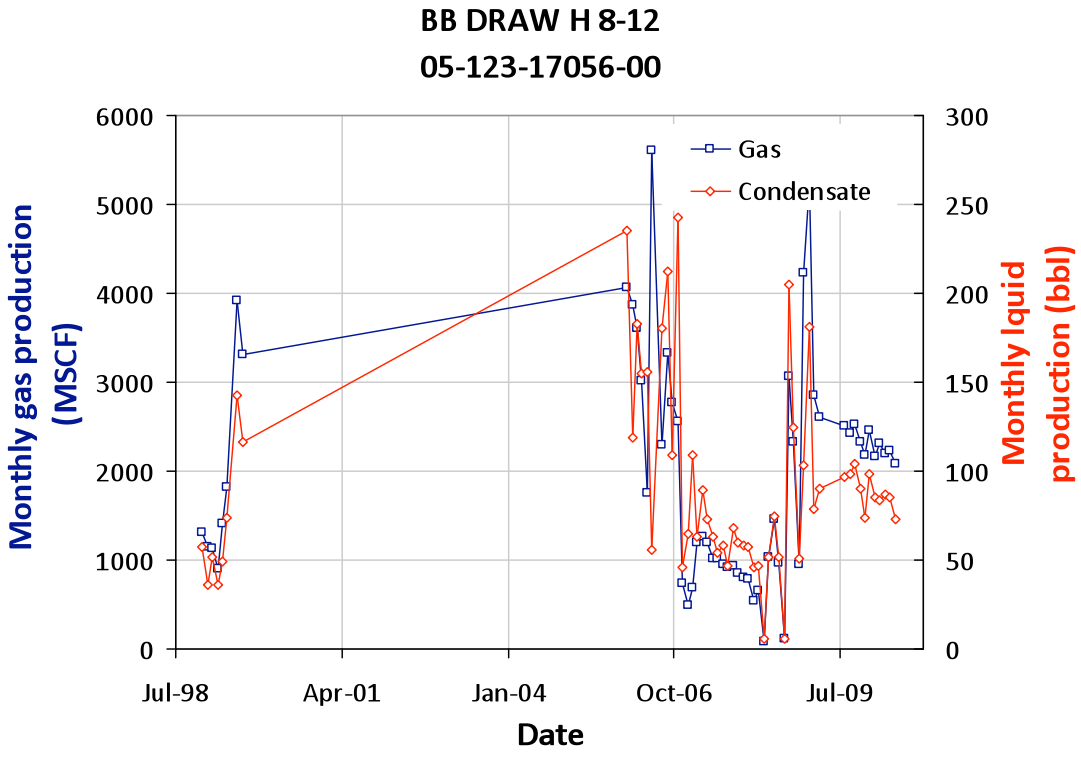
BB DRAW H 8-12
05-123-17056-00
Monthly gas production (MSCF)
Monthly liquid production (bbl)
Gas
Condensate
6000
5000
4000
3000
2000
1000
0
300
250
200
150
100
50
0
Jul-98
Apr-01
Jan-04
Oct-06
Jul-09
Date

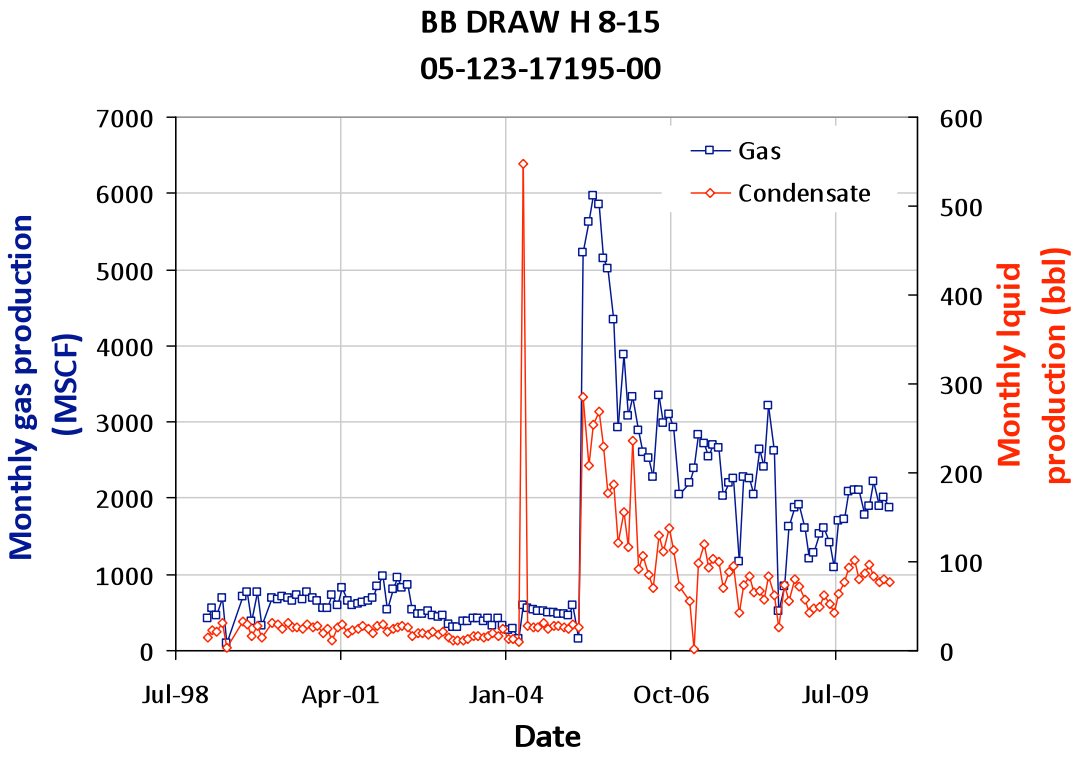
BB DRAW H 8-15
05-123-17195-00
Monthly gas production (MSCF)
Monthly liquid production (bbl)
Gas
Condensate
7000
6000
5000
4000
3000
2000
1000
0
600
500
400
300
200
100
0
Jul-98
Apr-01
Jan-04
Oct-06
Jul-09
Date

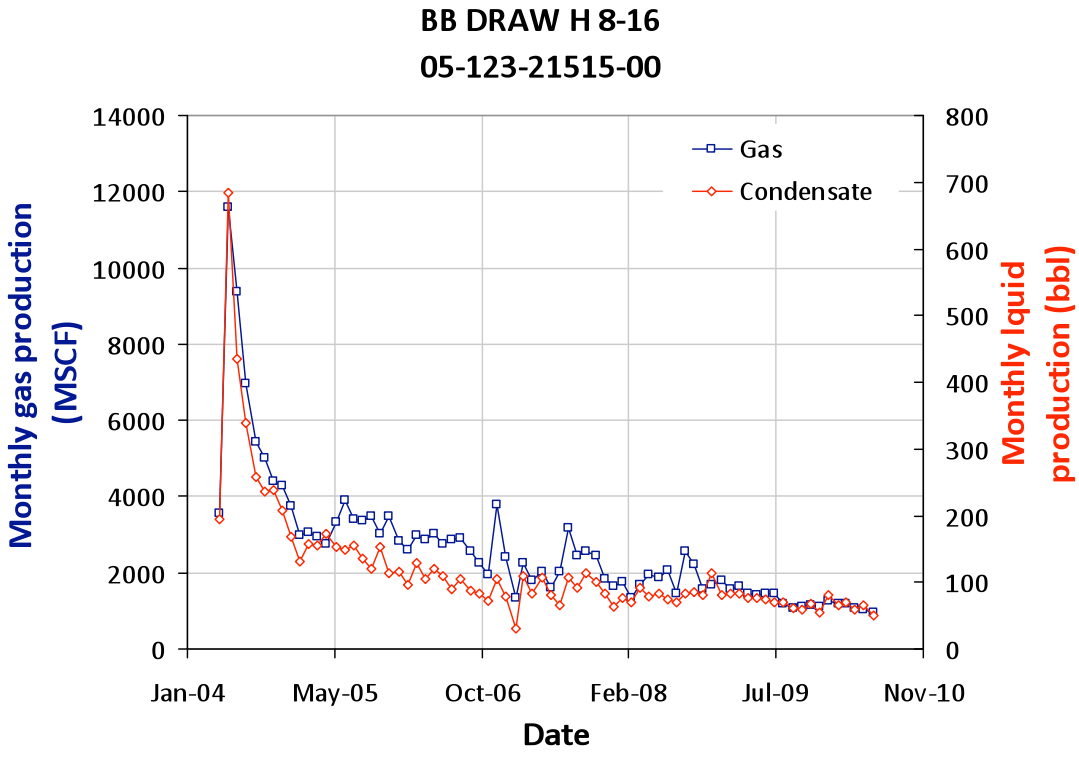
BB DRAW H 8-16
05-123-21515-00
Monthly gas production (MSCF)
Monthly liquid production (bbl)
Gas
Condensate
14000
12000
10000
8000
6000
4000
2000
0
800
700
600
500
400
300
200
100
0
Jan-04
May-05
Oct-06
Feb-08
Jul-09
Nov-10
Date

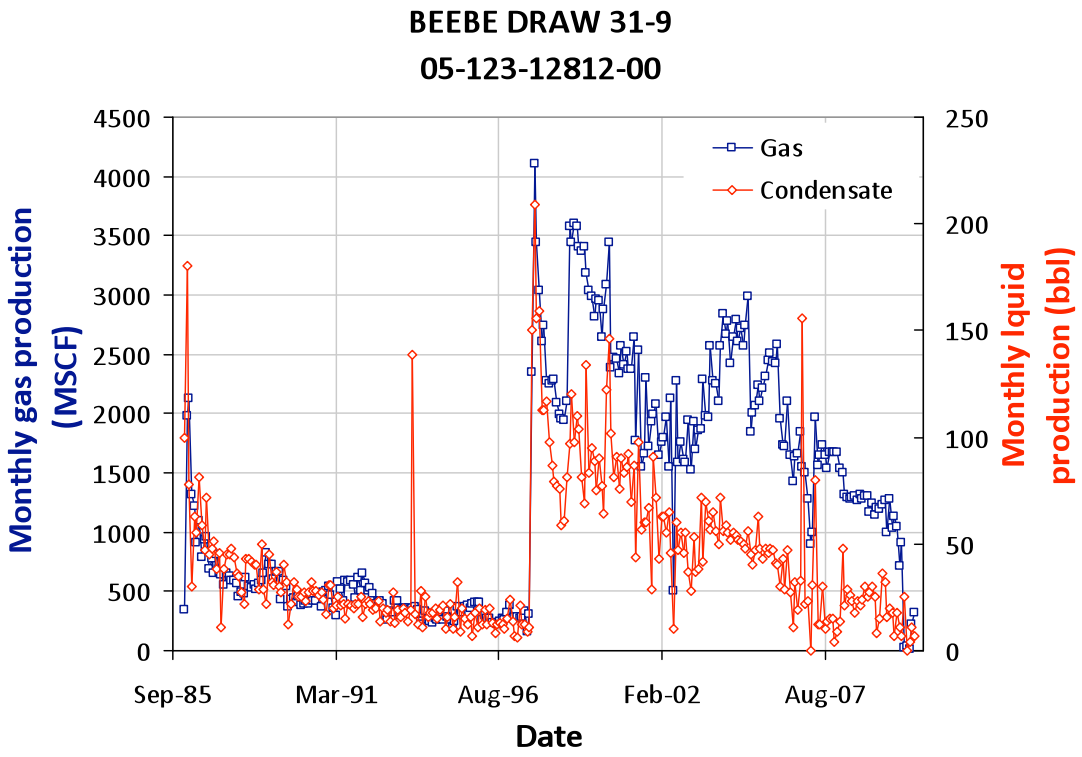
BEEBE DRAW 31-9
05-123-12812-00
Monthly gas production (MSCF)
Monthly liquid production (bbl)
Gas
Condensate
4500
4000
3500
3000
2500
2000
1500
1000
500
0
250
200
150
100
50
0
Sep-85
Mar-91
Aug-96
Feb-02
Aug-07
Date

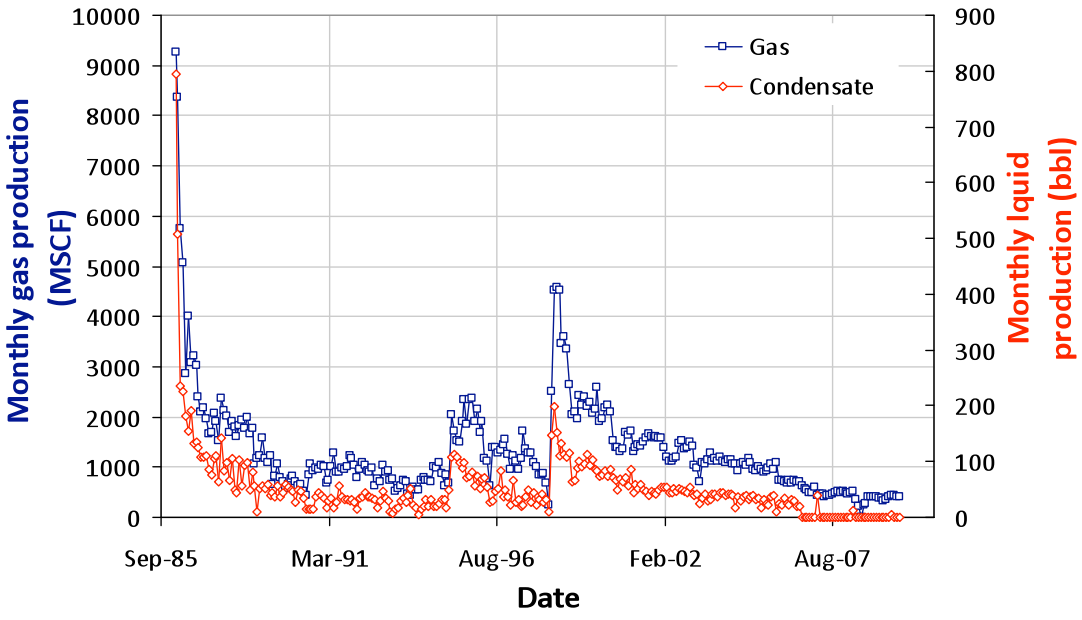
BEEBE DRAW UPRR 31-17
05-123-13008-00
Monthly gas production (MSCF)
Monthly liquid production (bbl)
Gas
Condensate
10000
9000
8000
7000
6000
5000
4000
3000
2000
1000
0
900
800
700
600
500
400
300
200
100
0
Sep-85
Mar-91
Aug-96
Feb-02
Aug-07
Date

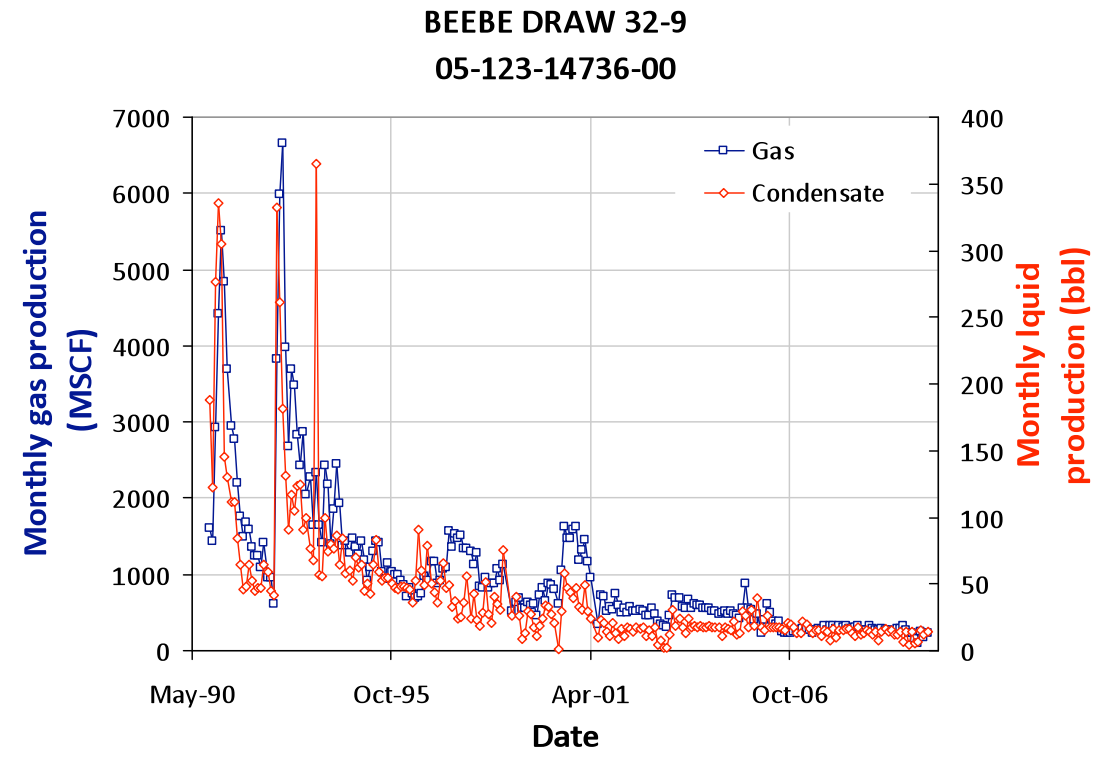
BEEBE DRAW 32-9
05-123-14736-00
Monthly gas production (MSCF)
Monthly liquid production (bbl)
Gas
Condensate
7000
6000
5000
4000
3000
2000
1000
0
400
350
300
250
200
150
100
50
0
May-90
Oct-95
Apr-01
Oct-06
Date

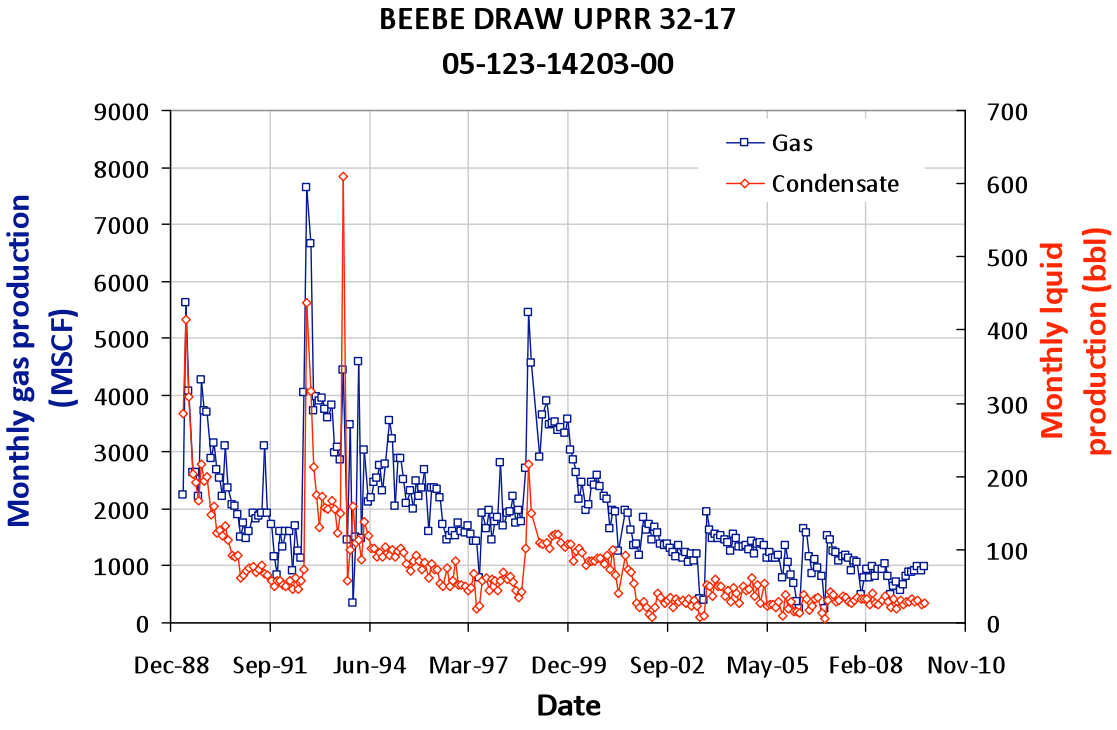
BEEBE DRAW UPRR 32-17
05-123-14203-00
Monthly gas production (MSCF)
Monthly liquid production (bbl)
Gas
Condensate
9000
8000
7000
6000
5000
4000
3000
2000
1000
0
700
600
500
400
300
200
100
0
Dec-88
Sep-91
Jun-94
Mar-97
Dec-99
Sep-02
May-05
Feb-08
Nov-10
Date

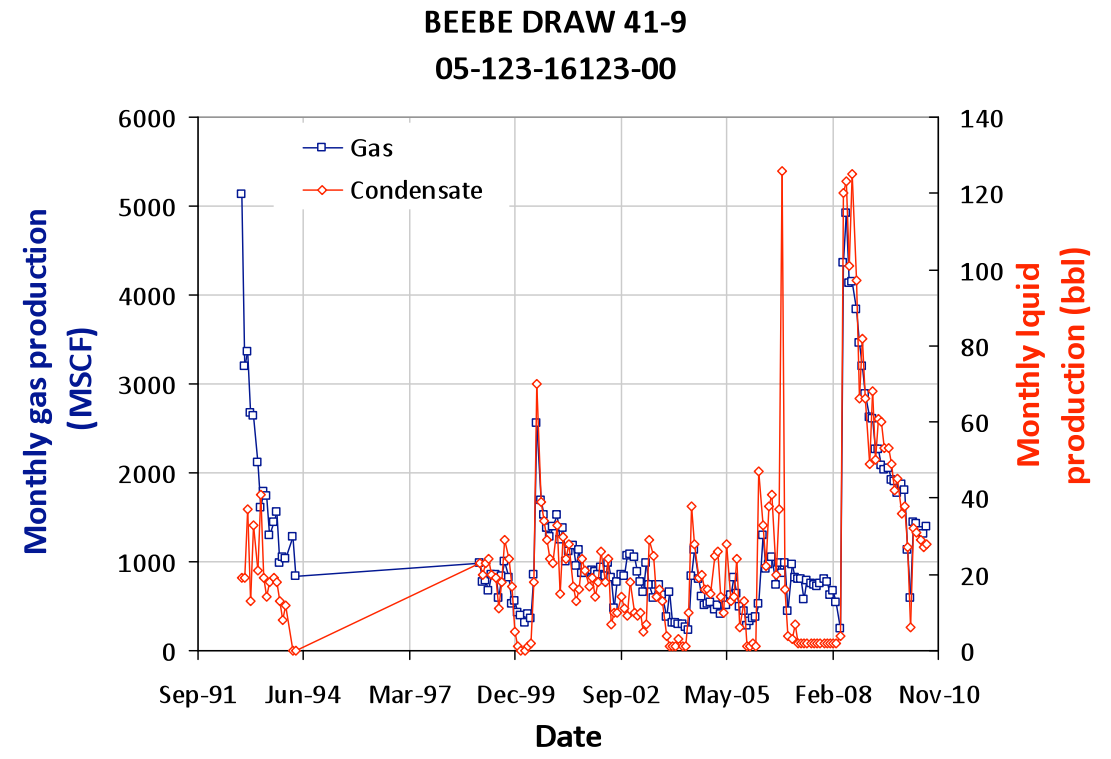
BEEBE DRAW 41-9
05-123-16123-00
Gas
Condensate
Monthly gas production (MSCF)
Monthly lquid production (bbl)
6000
5000
4000
3000
2000
1000
0
140
120
100
80
60
40
20
0
Sep-91
Jun-94
Mar-97
Dec-99
Sep-02
May-05
Feb-08
Nov-10
Date

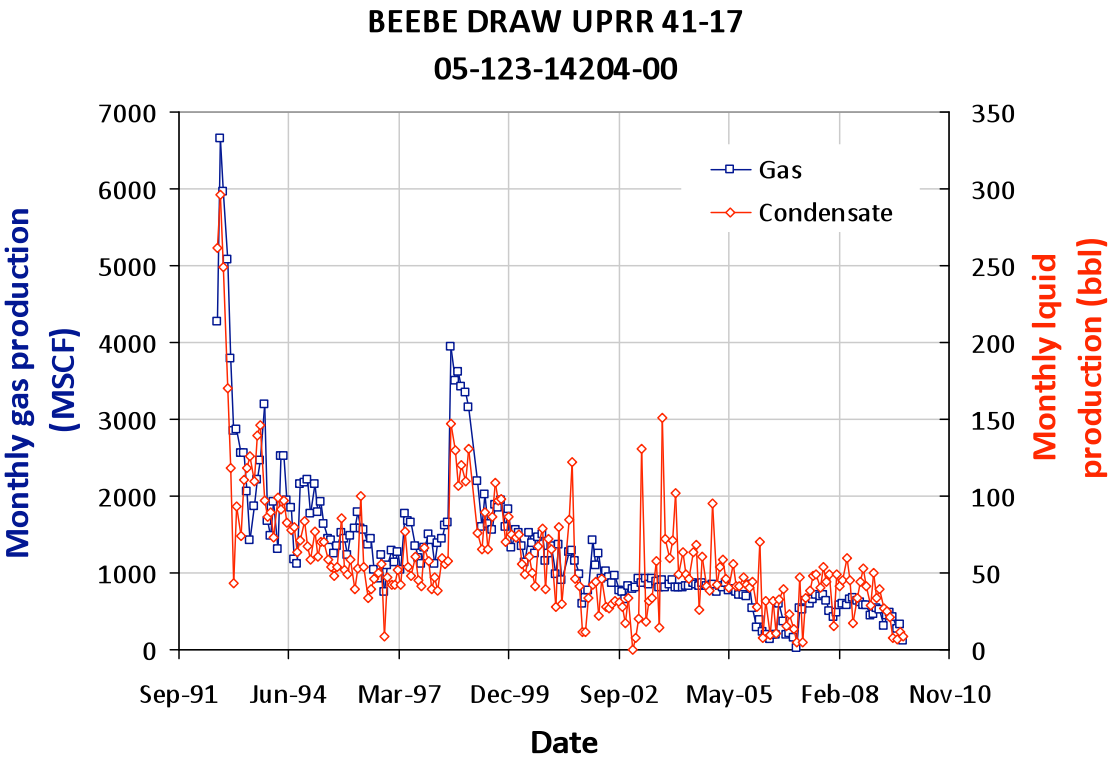
BEEBE DRAW UPRR 41-17
05-123-14204-00
Gas
Condensate
Monthly gas production (MSCF)
Monthly lquid production (bbl)
7000
6000
5000
4000
3000
2000
1000
0
350
300
250
200
150
100
50
0
Sep-91
Jun-94
Mar-97
Dec-99
Sep-02
May-05
Feb-08
Nov-10
Date

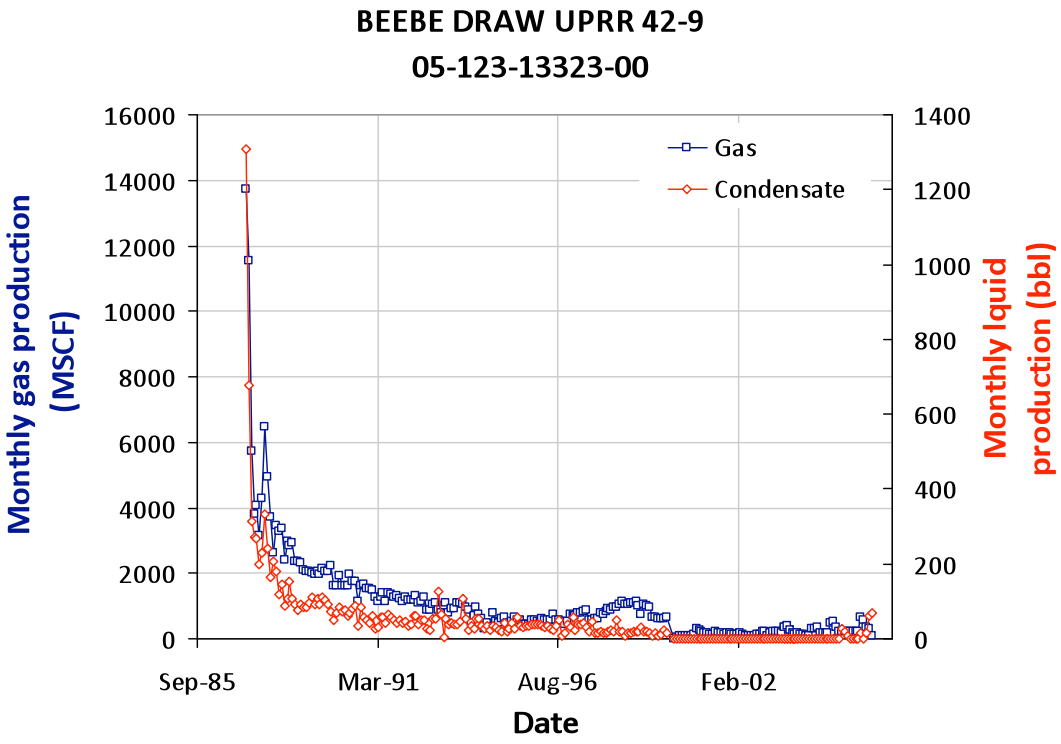
BEEBE DRAW UPRR 42-9
05-123-13323-00
Monthly gas production (MSCF)
Monthly liquid production (bbl)
Gas
Condensate
16000
14000
12000
10000
8000
6000
4000
2000
0
1400
1200
1000
800
600
400
200
0
Sep-85
Mar-91
Aug-96
Feb-02
Date

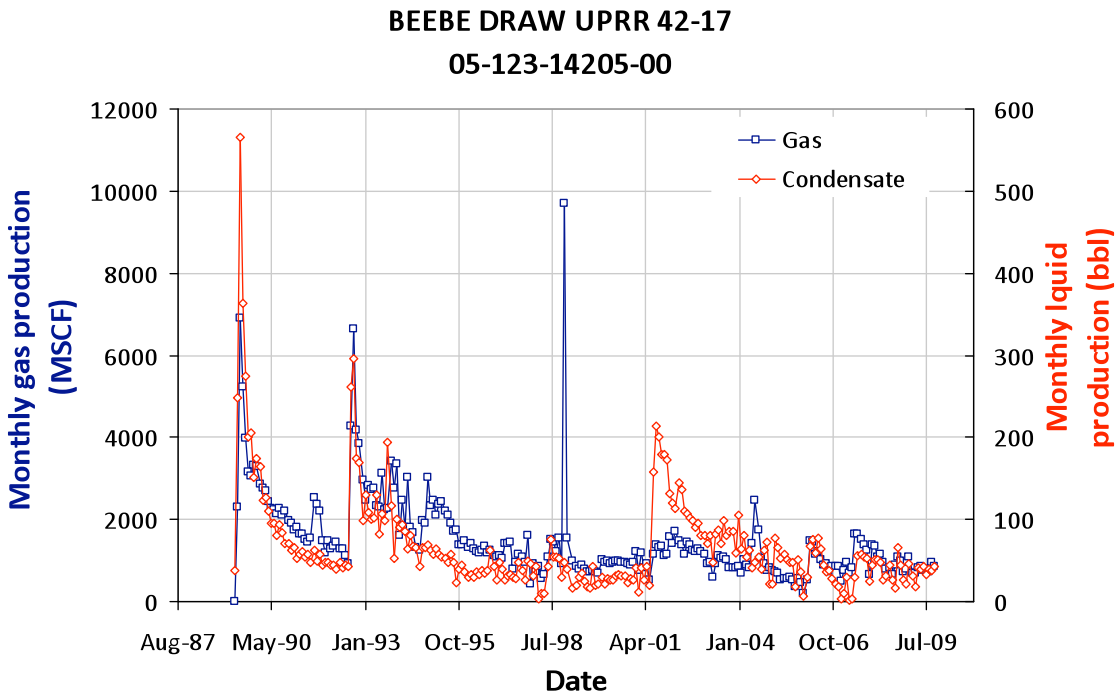
BEEBE DRAW UPRR 42-17
05-123-14205-00
Monthly gas production (MSCF)
Monthly liquid production (bbl)
Gas
Condensate
12000
10000
8000
6000
4000
2000
0
600
500
400
300
200
100
0
Aug-87
May-90
Jan-93
Oct-95
Jul-98
Apr-01
Jan-04
Oct-06
Jul-09
Date

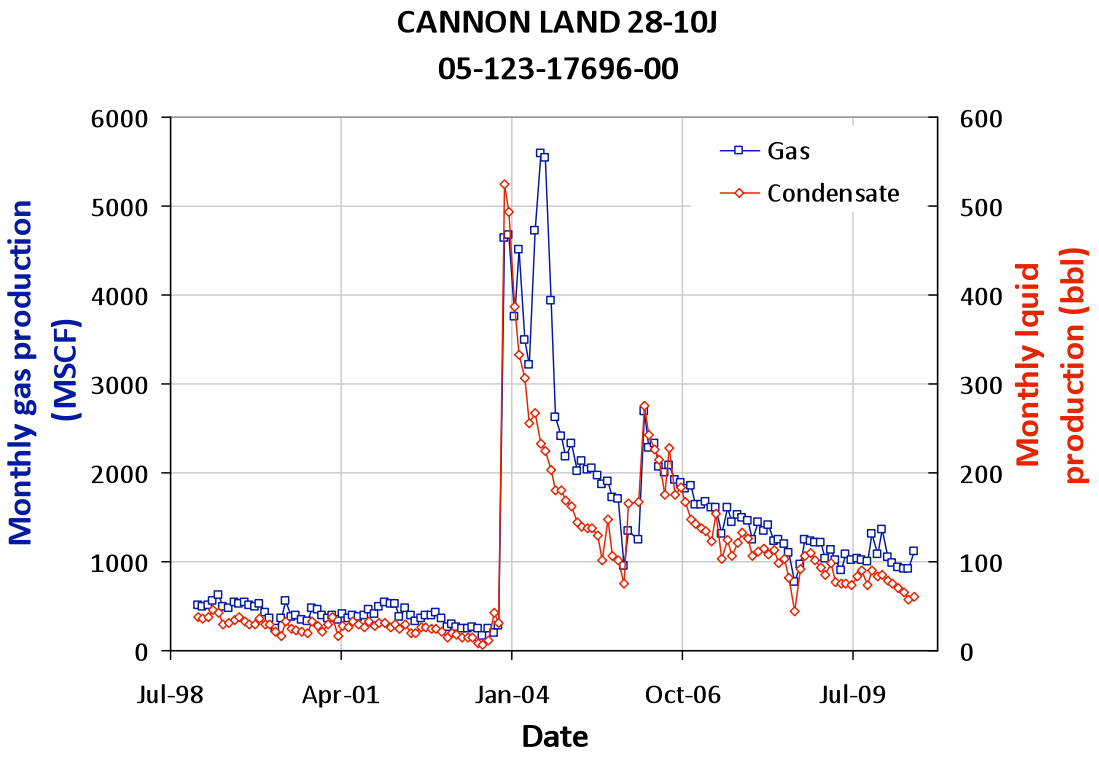
CANNON LAND 28-10J
05-123-17696-00
Monthly gas production (MSCF)
Monthly liquid production (bbl)
Gas
Condensate
6000
5000
4000
3000
2000
1000
0
600
500
400
300
200
100
0
Jul-98
Apr-01
Jan-04
Oct-06
Jul-09
Date

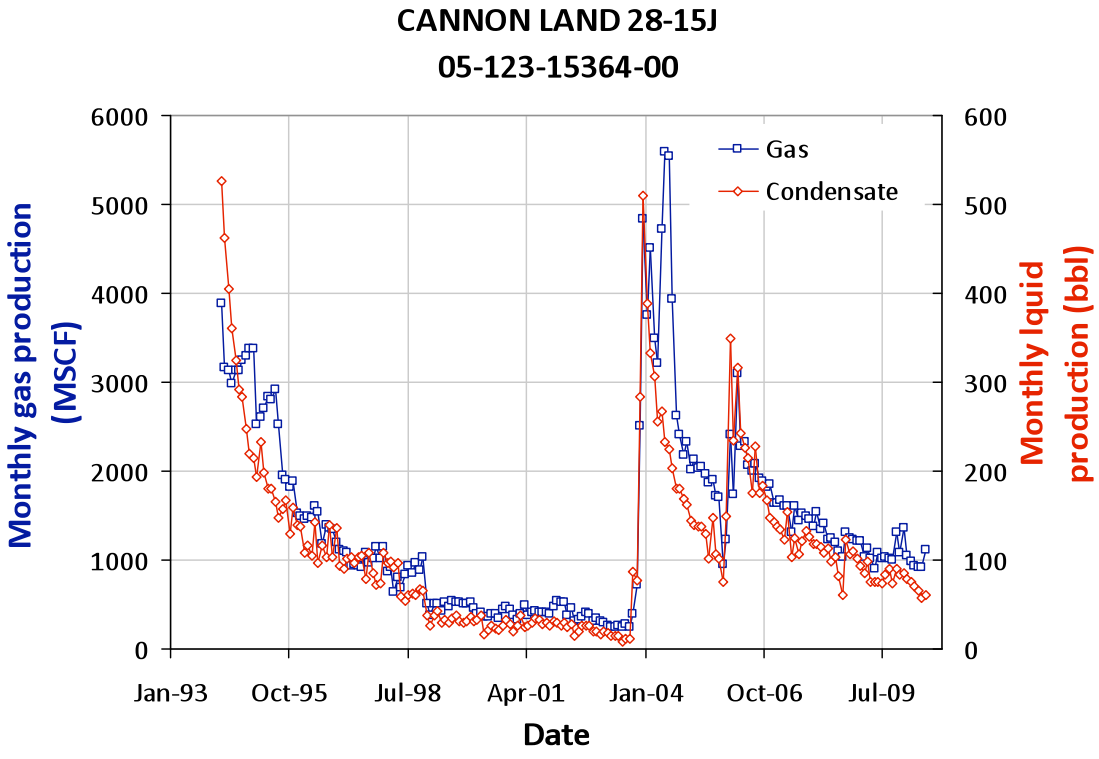
CANNON LAND 28-15J
05-123-15364-00
Monthly gas production (MSCF)
Monthly liquid production (bbl)
Gas
Condensate
6000
5000
4000
3000
2000
1000
0
600
500
400
300
200
100
0
Jan-93
Oct-95
Jul-98
Apr-01
Jan-04
Oct-06
Jul-09
Date

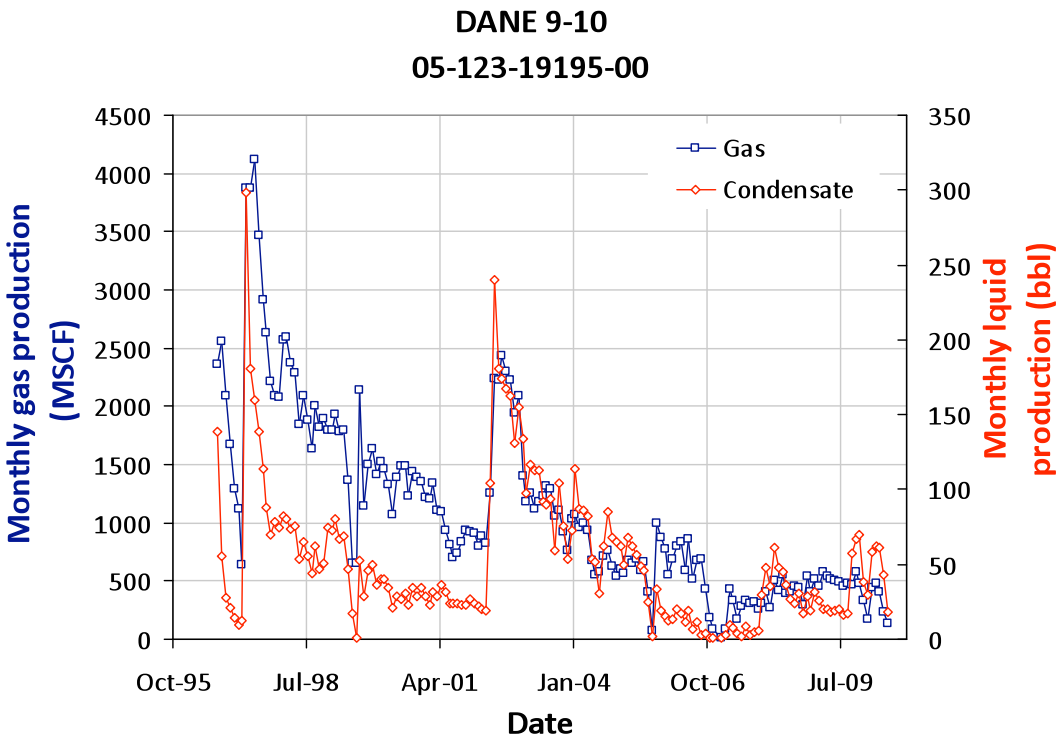
DANE 9-10
05-123-19195-00
Gas
Condensate
Monthly gas production (MSCF)
Monthly lquid production (bbl)
4500
4000
3500
3000
2500
2000
1500
1000
500
0
350
300
250
200
150
100
50
0
Oct-95
Jul-98
Apr-01
Jan-04
Oct-06
Jul-09
Date

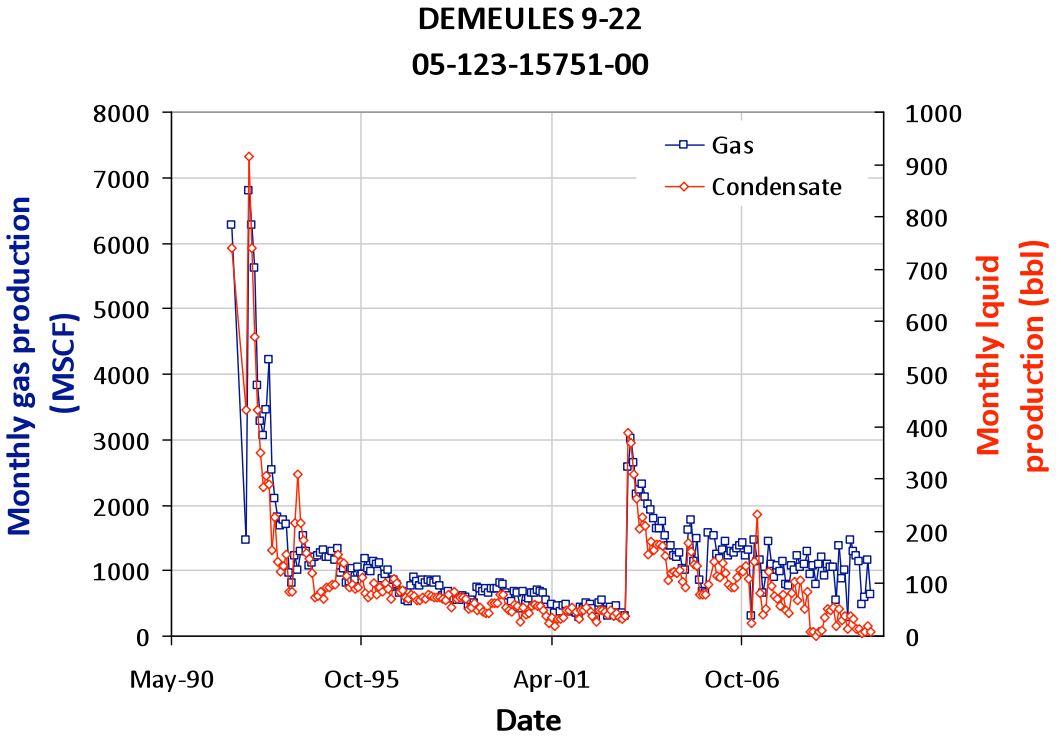
DEMEULES 9-22
05-123-15751-00
Gas
Condensate
Monthly gas production (MSCF)
Monthly lquid production (bbl)
8000
7000
6000
5000
4000
3000
2000
1000
0
1000
900
800
700
600
500
400
300
200
100
0
May-90
Oct-95
Apr-01
Oct-06
Date

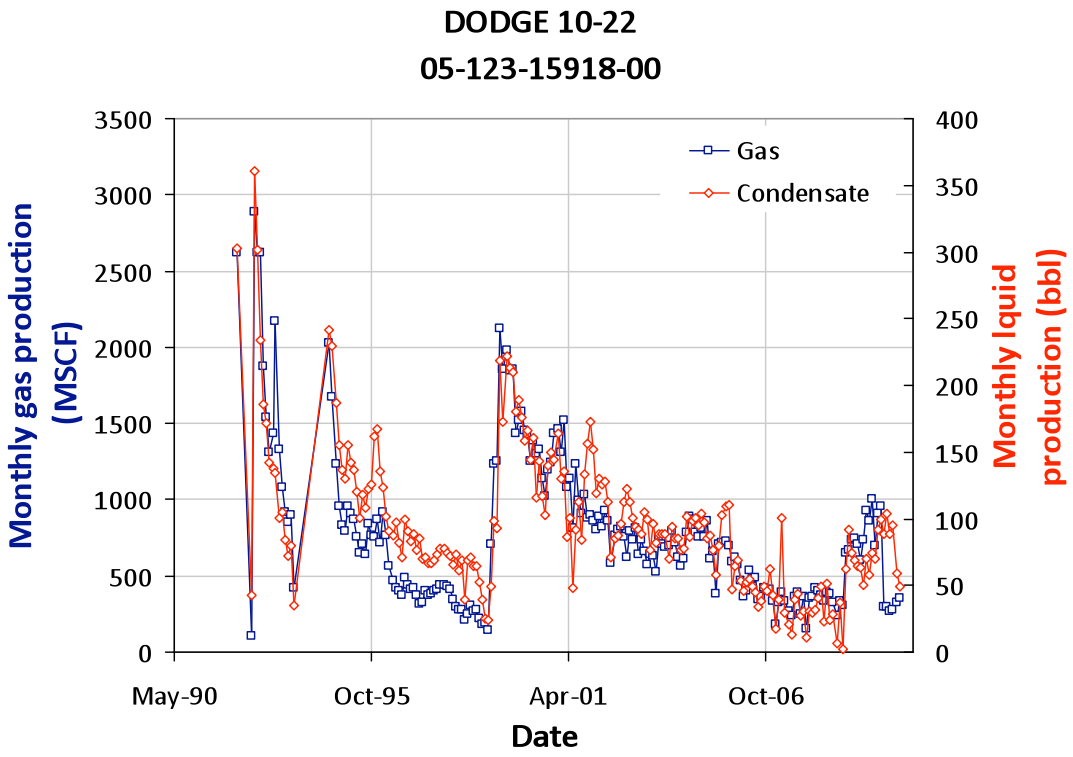
DODGE 10-22
05-123-15918-00
Monthly gas production (MSCF)
Monthly liquid production (bbl)
Gas
Condensate
3500
3000
2500
2000
1500
1000
500
0
400
350
300
250
200
150
100
50
0
May-90
Oct-95
Apr-01
Oct-06
Date

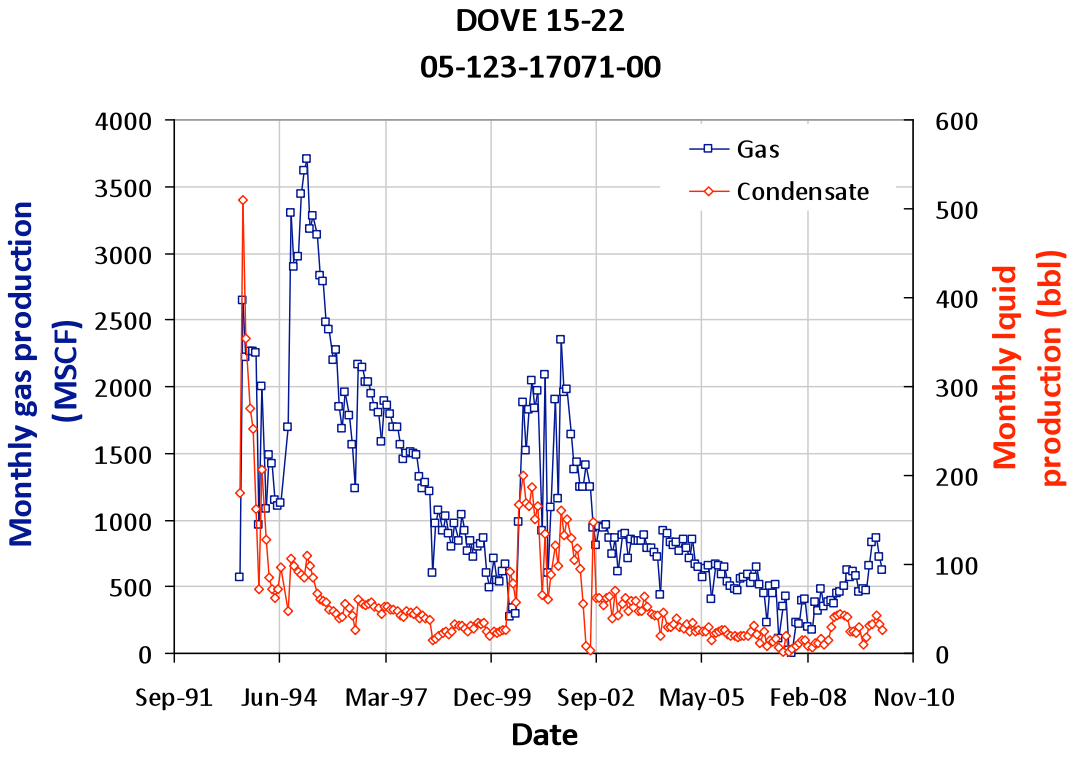
DOVE 15-22
05-123-17071-00
Monthly gas production (MSCF)
Monthly liquid production (bbl)
Gas
Condensate
4000
3500
3000
2500
2000
1500
1000
500
0
600
500
400
300
200
100
0
Sep-91
Jun-94
Mar-97
Dec-99
Sep-02
May-05
Feb-08
Nov-10
Date

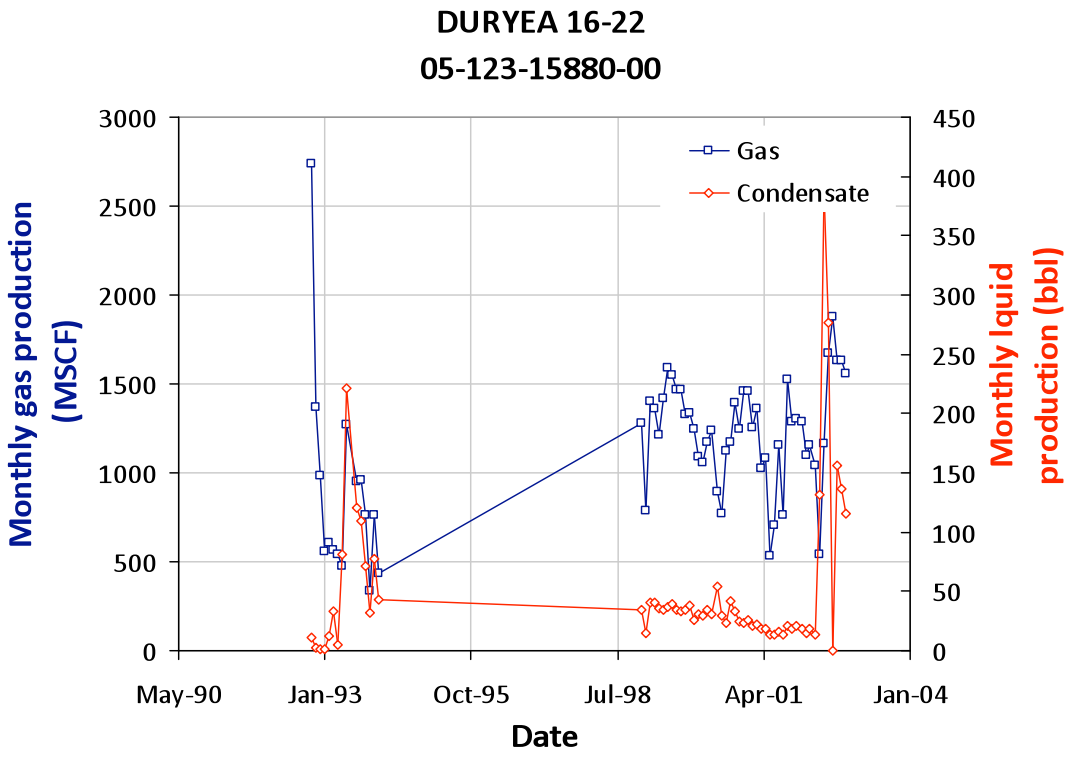
DURYEA 16-22
05-123-15880-00
Monthly gas production (MSCF)
Monthly lquid production (bbl)
Gas
Condensate
3000
2500
2000
1500
1000
500
0
450
400
350
300
250
200
150
100
50
0
May-90
Jan-93
Oct-95
Jul-98
Apr-01
Jan-04
Date

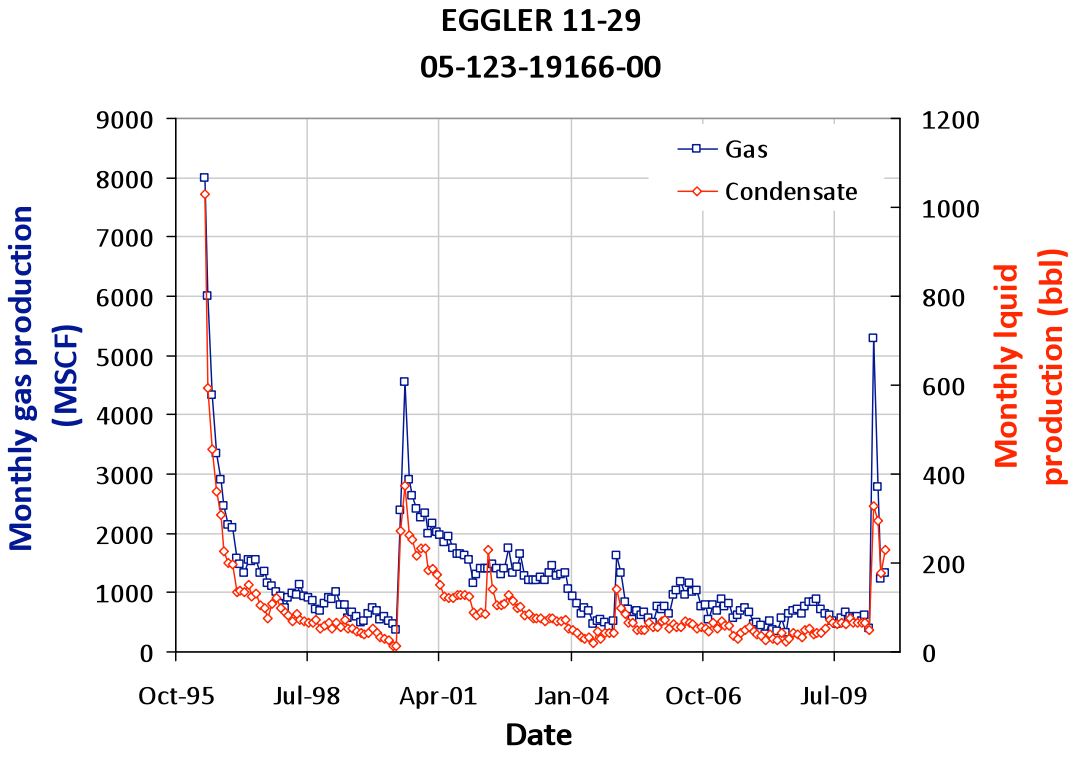
EGGLER 11-29
05-123-19166-00
Monthly gas production (MSCF)
Monthly lquid production (bbl)
Gas
Condensate
9000
8000
7000
6000
5000
4000
3000
2000
1000
0
1200
1000
800
600
400
200
0
Oct-95
Jul-98
Apr-01
Jan-04
Oct-06
Jul-09
Date

EGGLER 14-29

05-123-16101-00

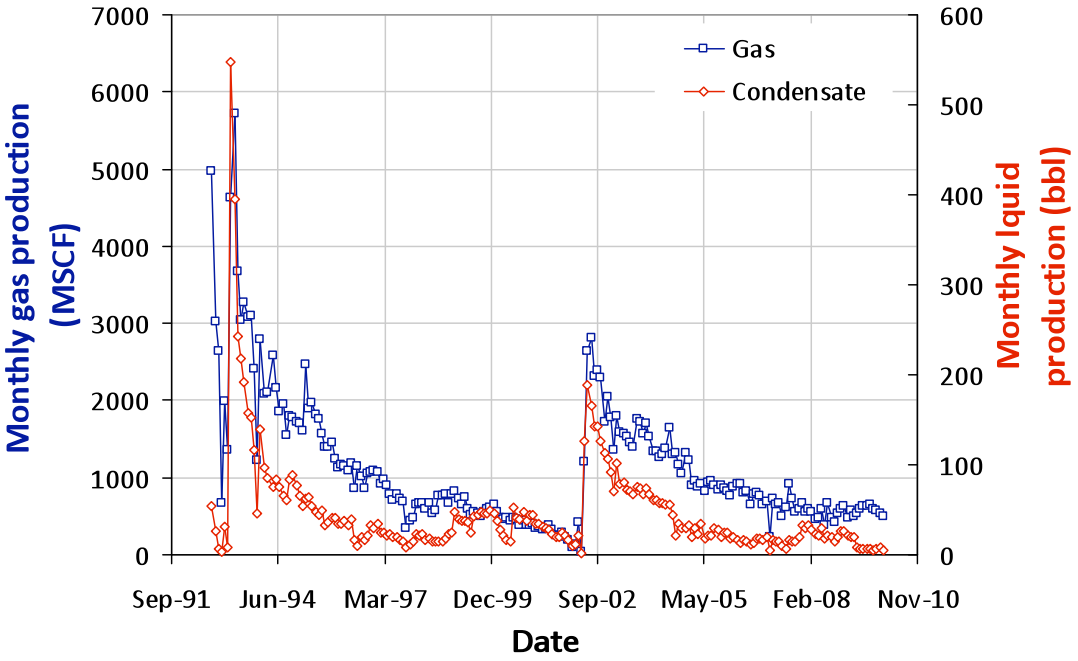

FEDERAL 12-10

05-123-17136-00

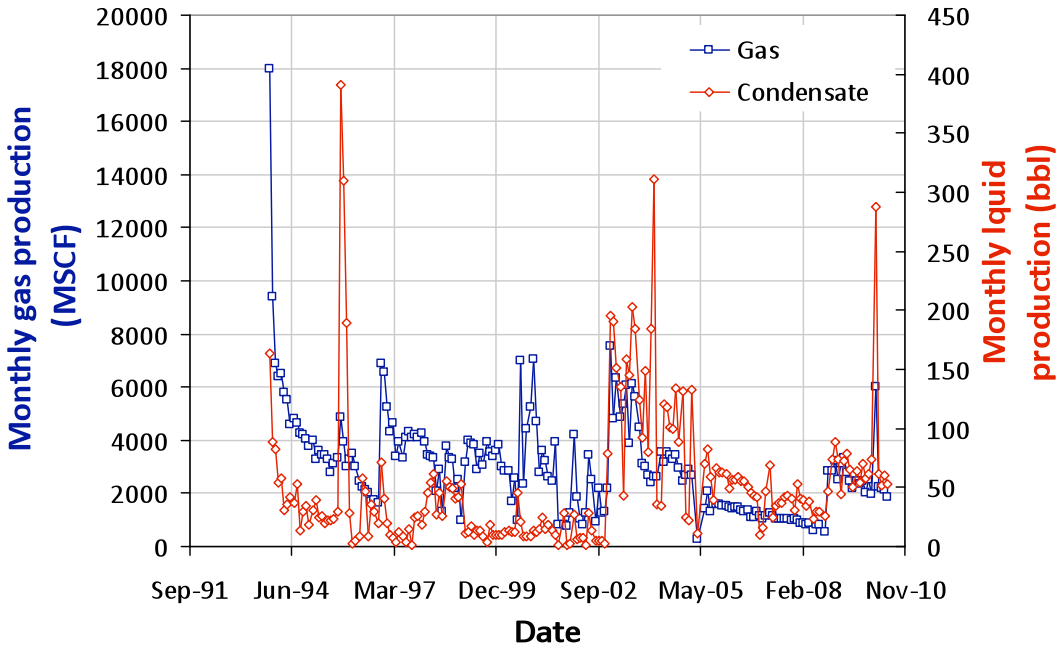

FEDERAL 32-10

05-123-17137-00

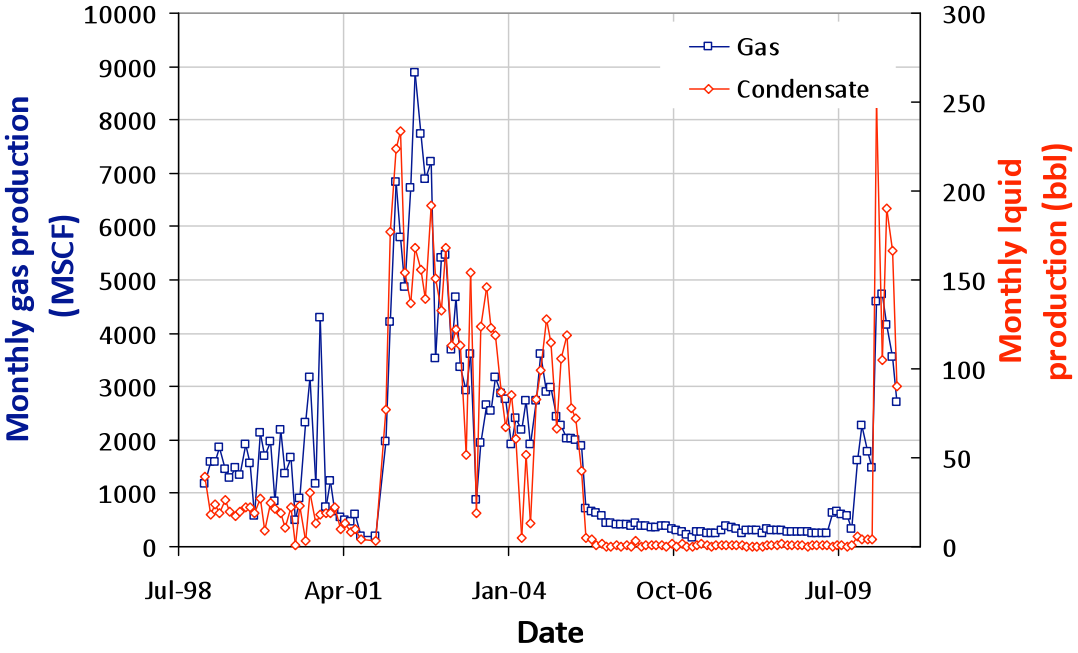

FRANK 1-21 C

05-123-12549-00

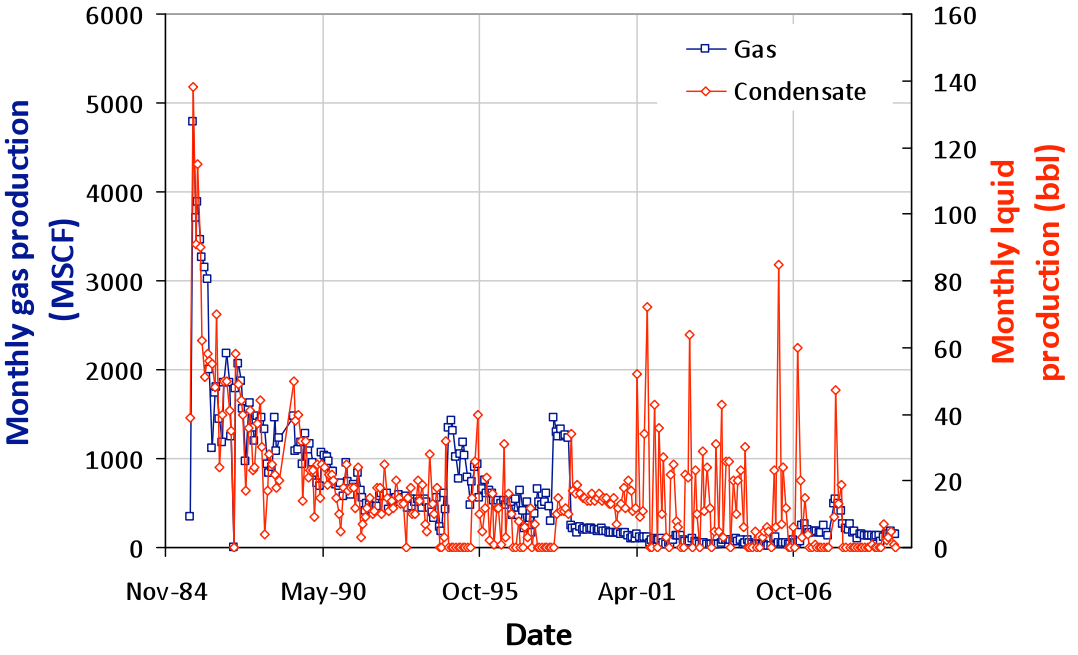

FRANK 21-10

05-123-15157-00

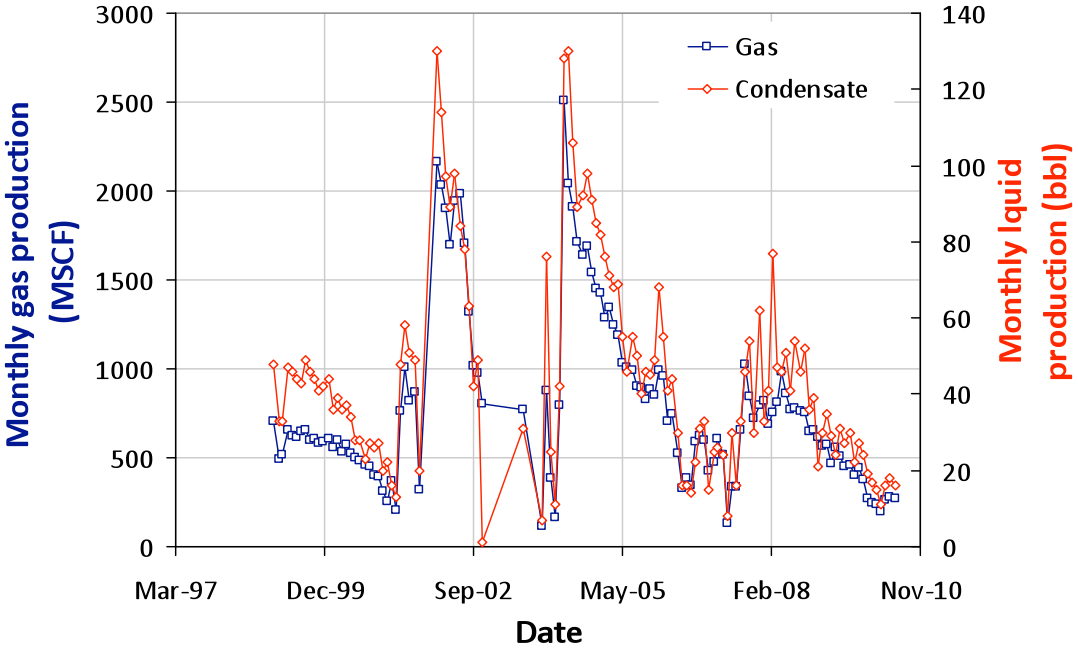

FRANK H 21-11

05-123-15158-00

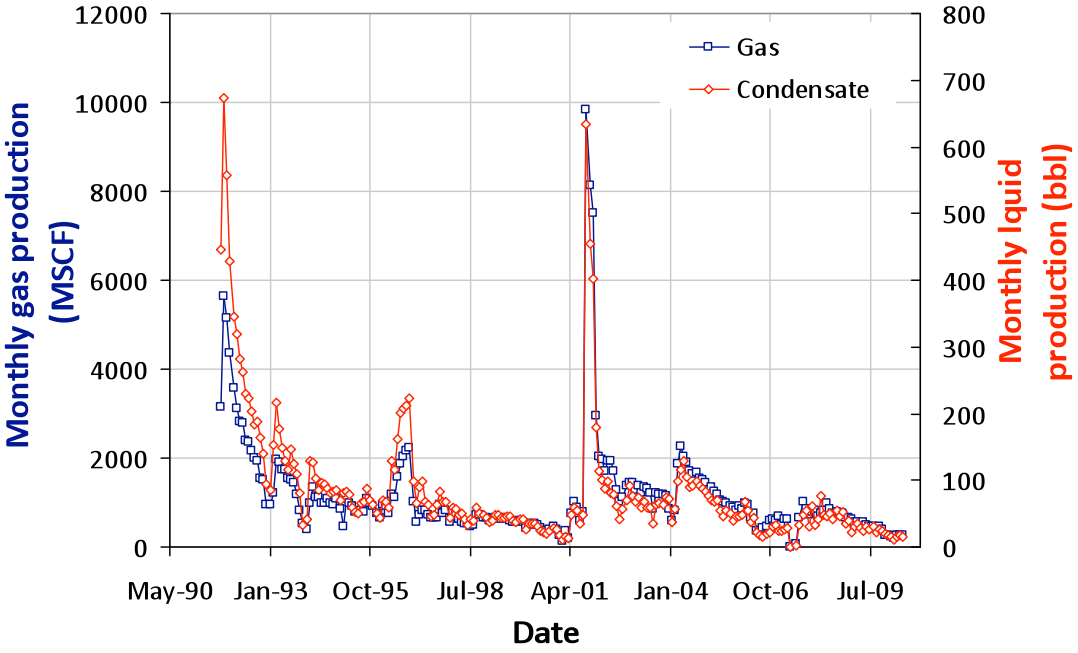

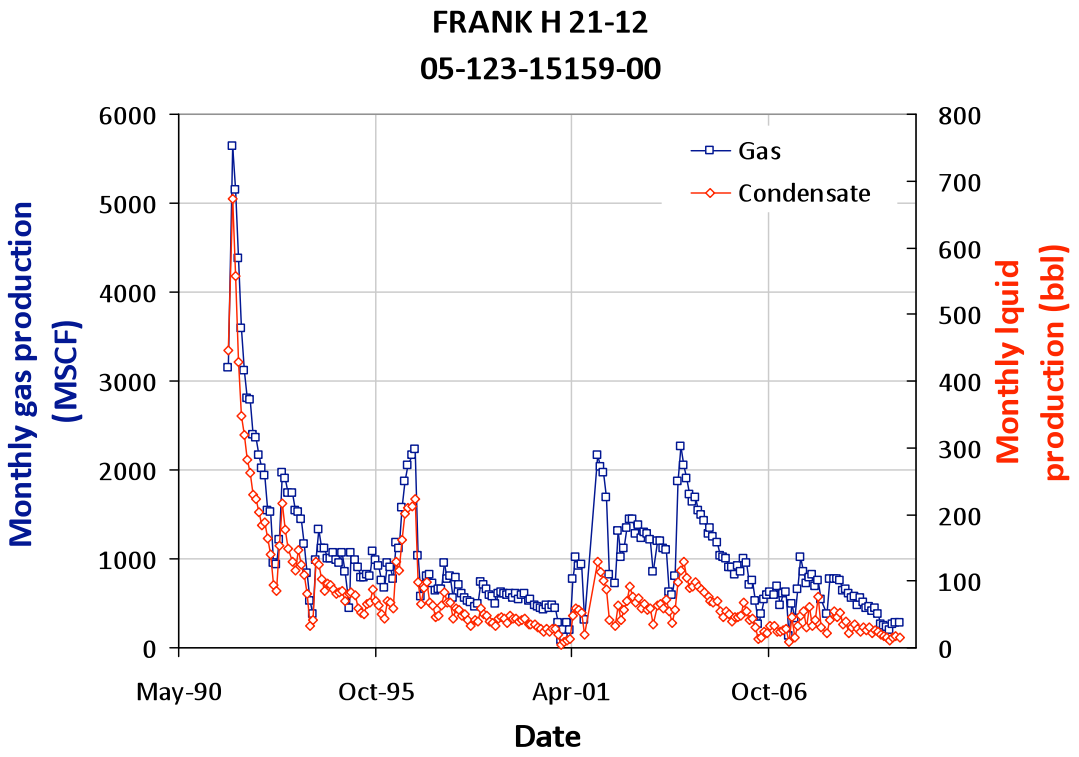
FRANK H 21-12
05-123-15159-00
Monthly gas production (MSCF)
Monthly liquid production (bbl)
Gas
Condensate
6000
5000
4000
3000
2000
1000
0
800
700
600
500
400
300
200
100
0
May-90
Oct-95
Apr-01
Oct-06
Date

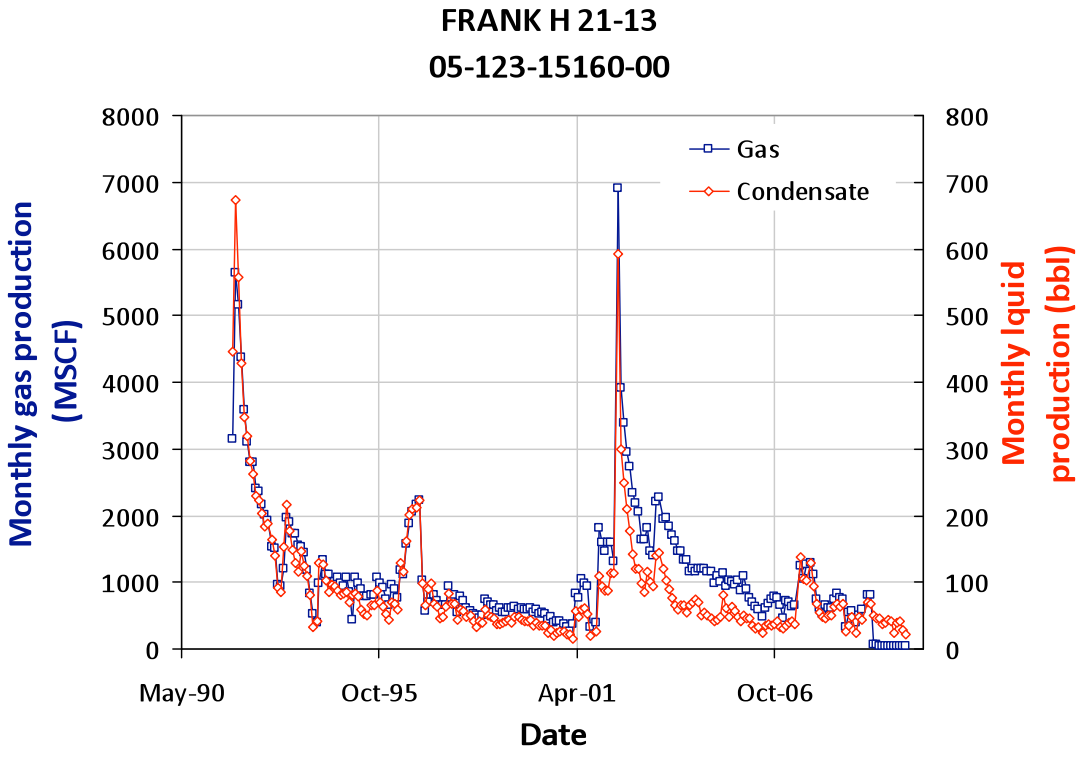
FRANK H 21-13
05-123-15160-00
Monthly gas production (MSCF)
Monthly liquid production (bbl)
Gas
Condensate
8000
7000
6000
5000
4000
3000
2000
1000
0
800
700
600
500
400
300
200
100
0
May-90
Oct-95
Apr-01
Oct-06
Date

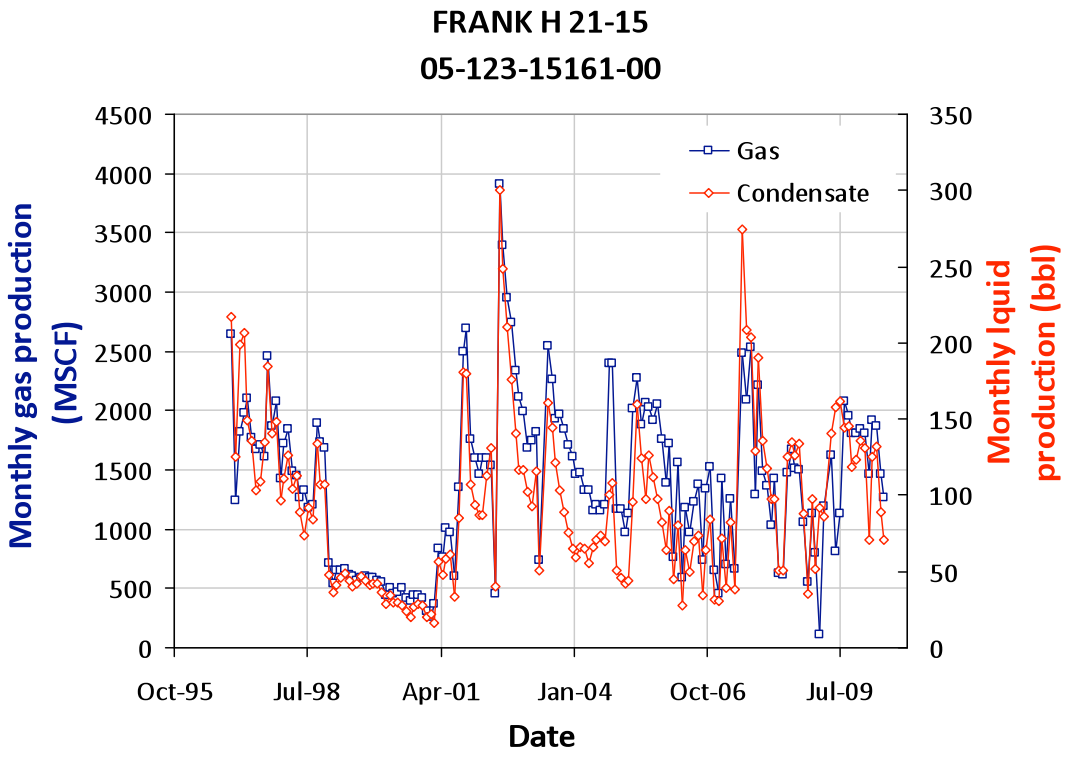
FRANK H 21-15
05-123-15161-00
Monthly gas production (MSCF)
Monthly liquid production (bbl)
Gas
Condensate
4500
4000
3500
3000
2500
2000
1500
1000
500
0
350
300
250
200
150
100
50
0
Oct-95
Jul-98
Apr-01
Jan-04
Oct-06
Jul-09
Date

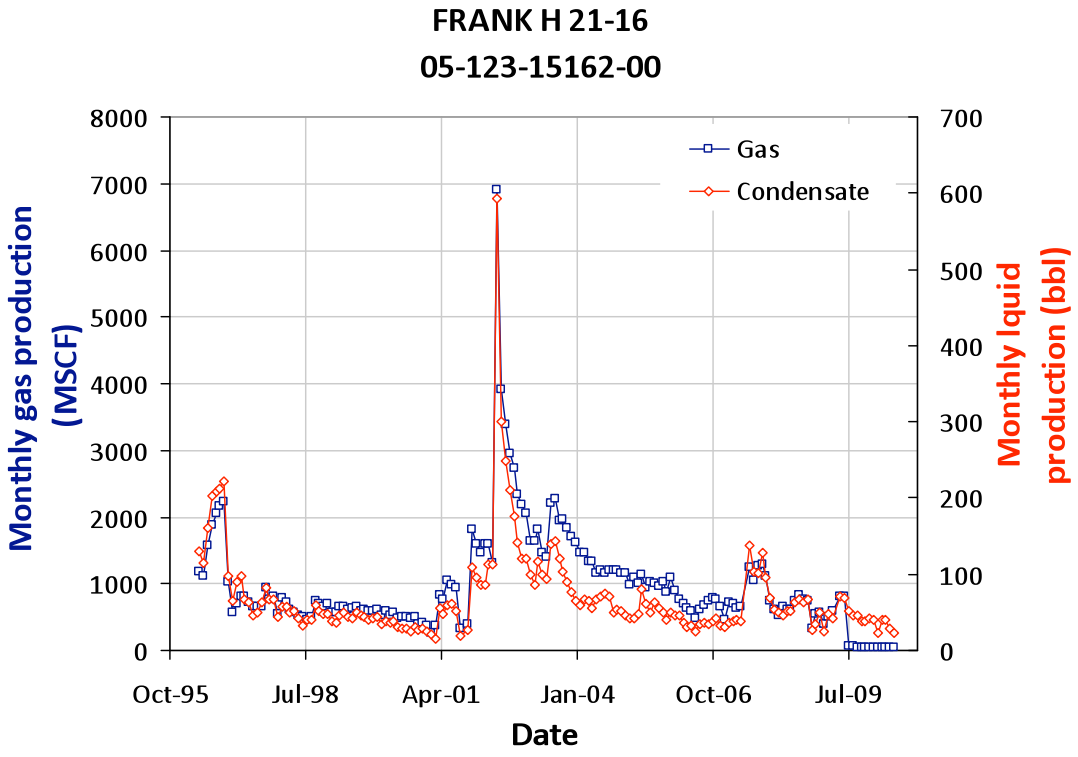
FRANK H 21-16
05-123-15162-00
Monthly gas production (MSCF)
Monthly liquid production (bbl)
Gas
Condensate
8000
7000
6000
5000
4000
3000
2000
1000
0
700
600
500
400
300
200
100
0
Oct-95
Jul-98
Apr-01
Jan-04
Oct-06
Jul-09
Date

FRANK 22-21

05-123-19874-00

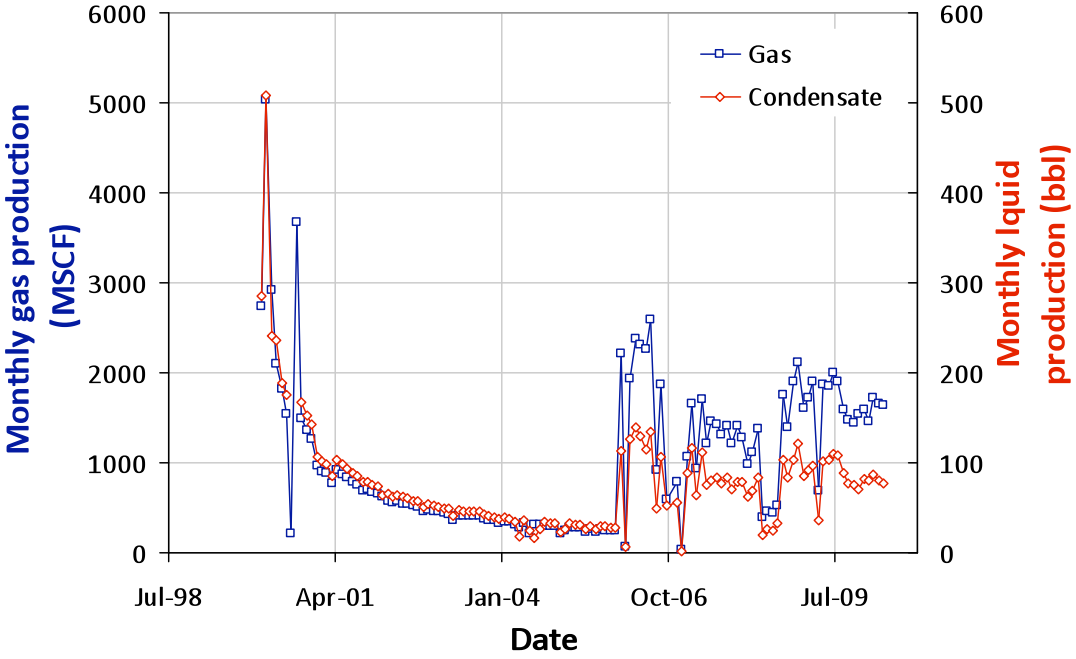

FRANK 22-25

05-123-21639-00

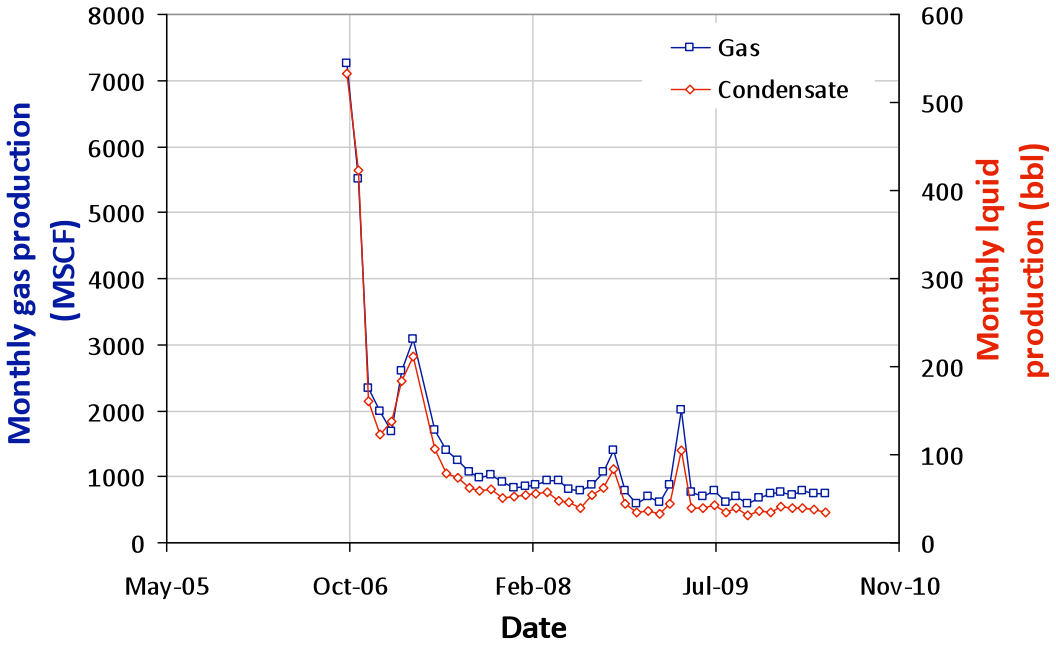

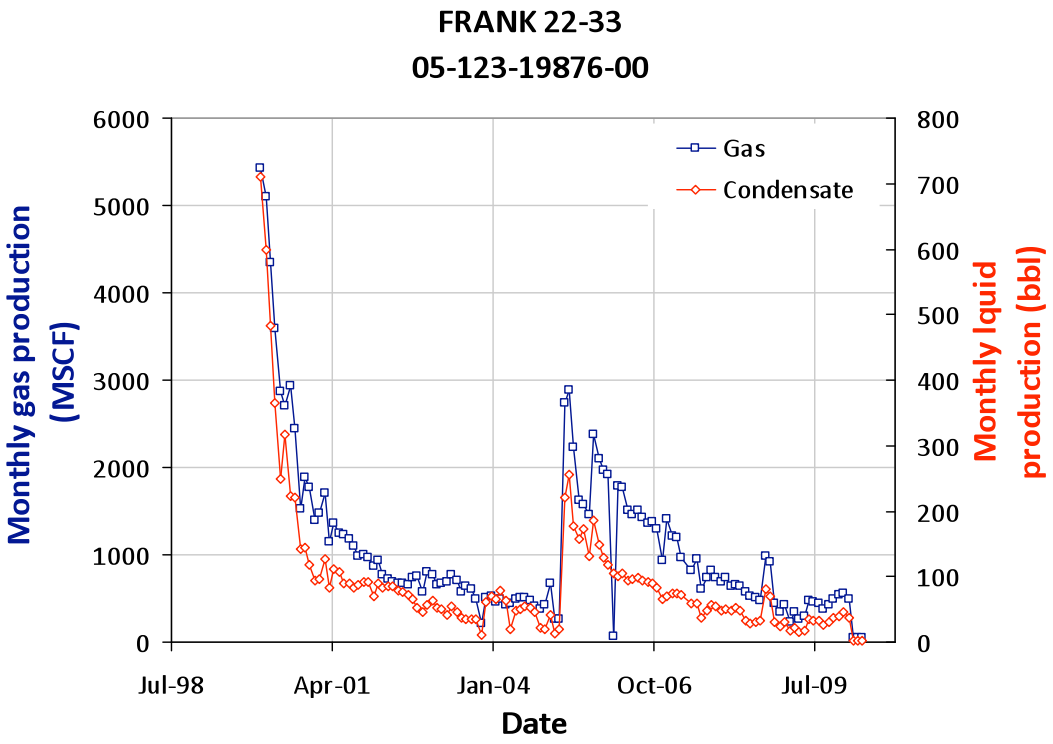
FRANK 22-33
05-123-19876-00
Gas
Condensate
Monthly gas production (MSCF)
Monthly liquid production (bbl)
6000
5000
4000
3000
2000
1000
0
800
700
600
500
400
300
200
100
0
Jul-98
Apr-01
Jan-04
Oct-06
Jul-09
Date

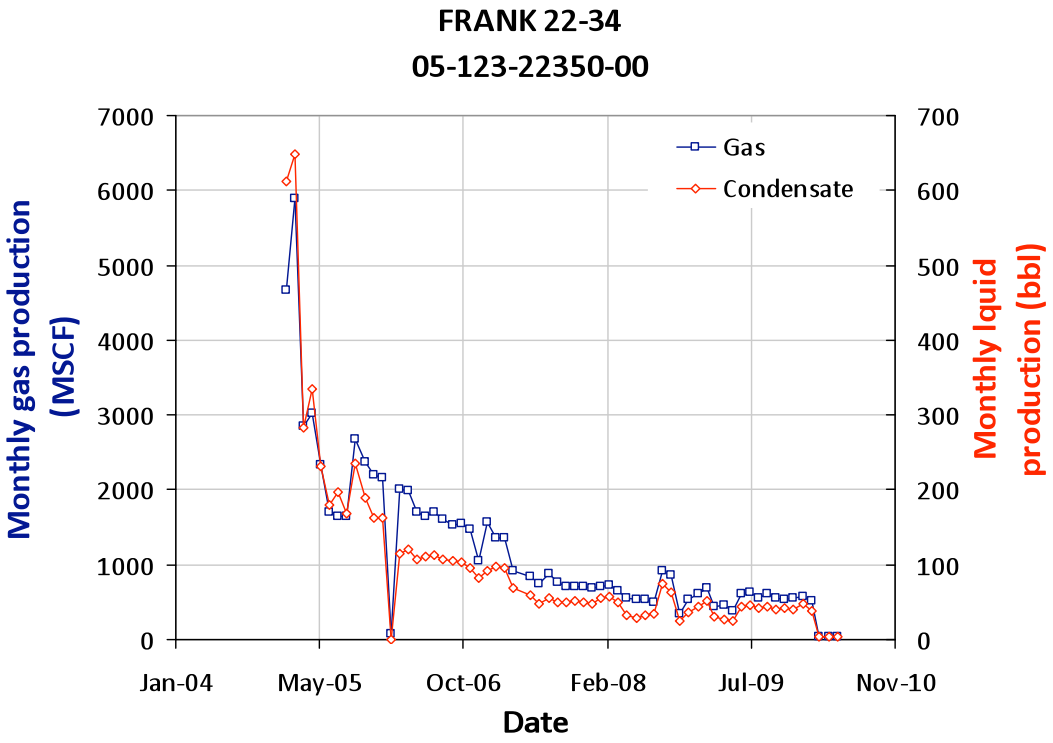
FRANK 22-34
05-123-22350-00
Gas
Condensate
Monthly gas production (MSCF)
Monthly liquid production (bbl)
7000
6000
5000
4000
3000
2000
1000
0
700
600
500
400
300
200
100
0
Jan-04
May-05
Oct-06
Feb-08
Jul-09
Nov-10
Date

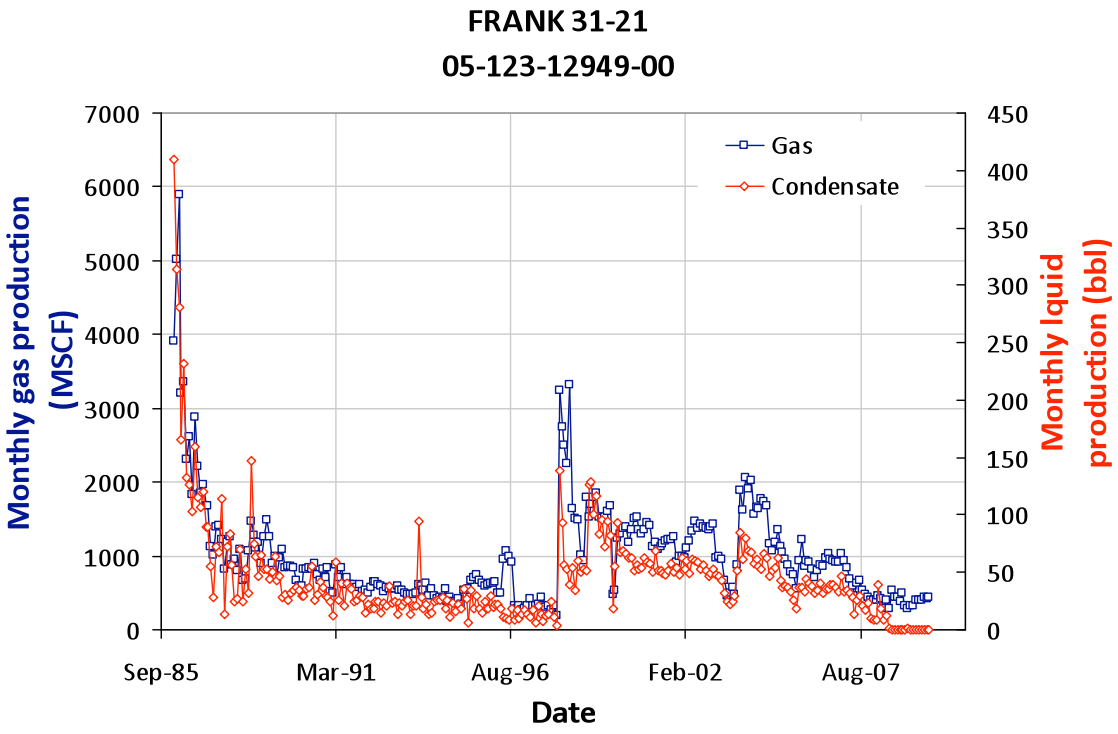
FRANK 31-21
05-123-12949-00
Monthly gas production (MSCF)
Monthly liquid production (bbl)
Gas
Condensate
7000
6000
5000
4000
3000
2000
1000
0
450
400
350
300
250
200
150
100
50
0
Sep-85
Mar-91
Aug-96
Feb-02
Aug-07
Date

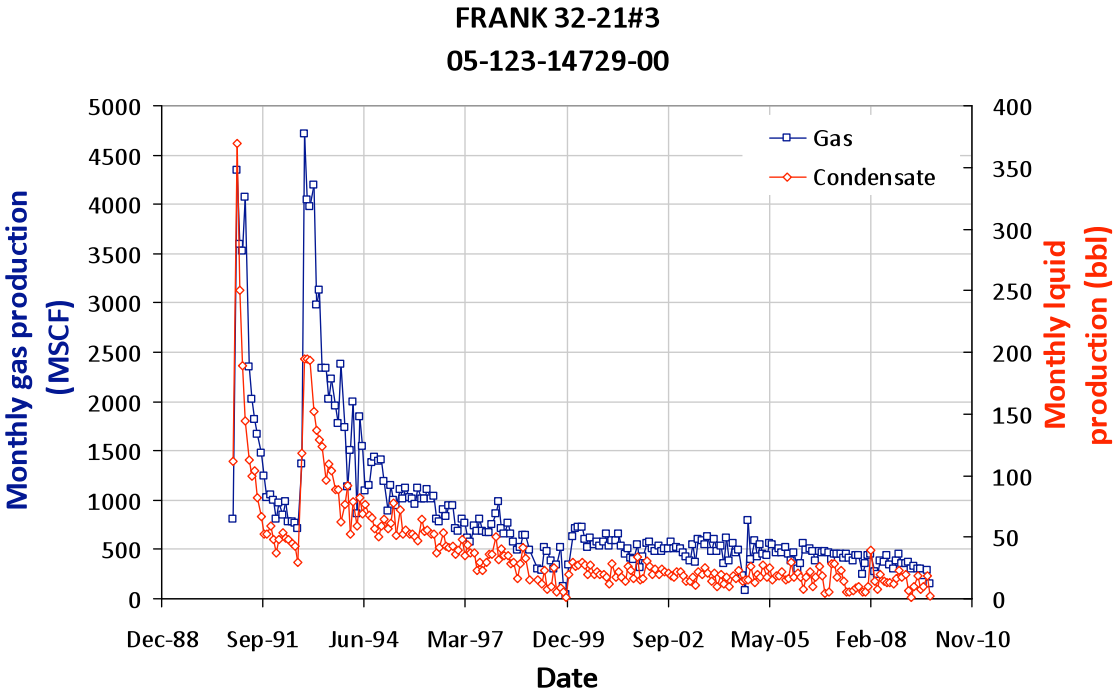
FRANK 32-21#3
05-123-14729-00
Monthly gas production (MSCF)
Monthly liquid production (bbl)
Gas
Condensate
5000
4500
4000
3500
3000
2500
2000
1500
1000
500
0
400
350
300
250
200
150
100
50
0
Dec-88
Sep-91
Jun-94
Mar-97
Dec-99
Sep-02
May-05
Feb-08
Nov-10
Date

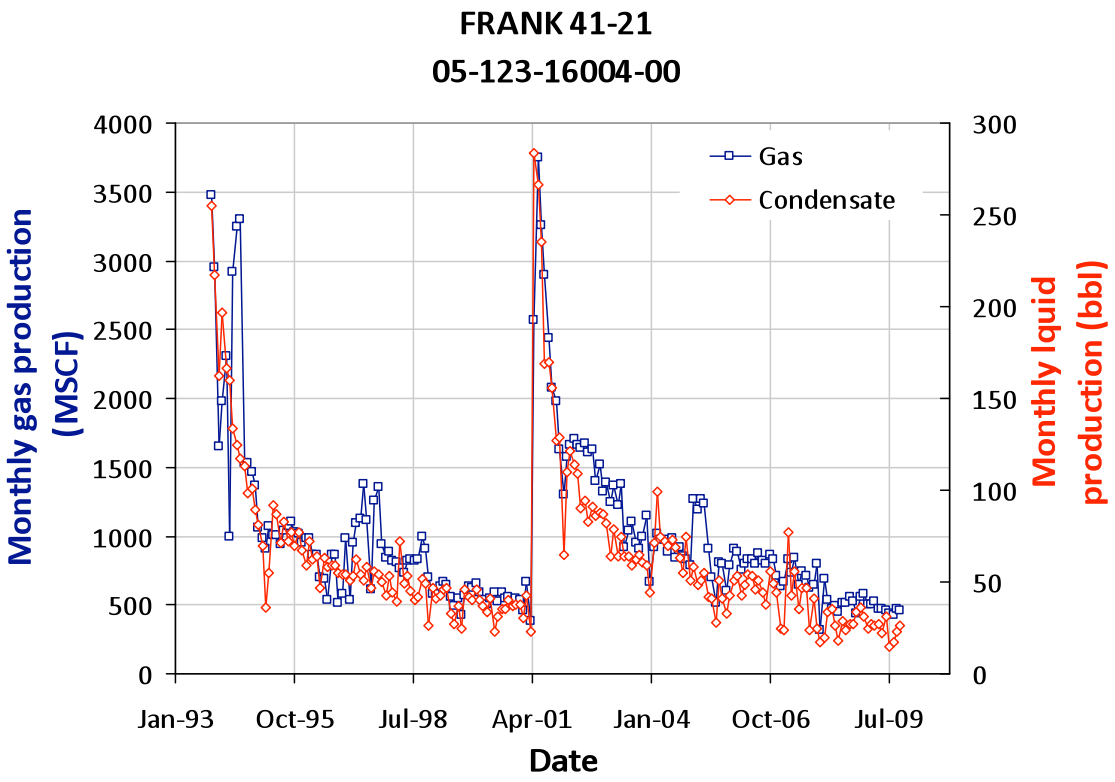
FRANK 41-21
05-123-16004-00
Monthly gas production (MSCF)
Monthly liquid production (bbl)
Gas
Condensate
4000
3500
3000
2500
2000
1500
1000
500
0
300
250
200
150
100
50
0
Jan-93
Oct-95
Jul-98
Apr-01
Jan-04
Oct-06
Jul-09
Date

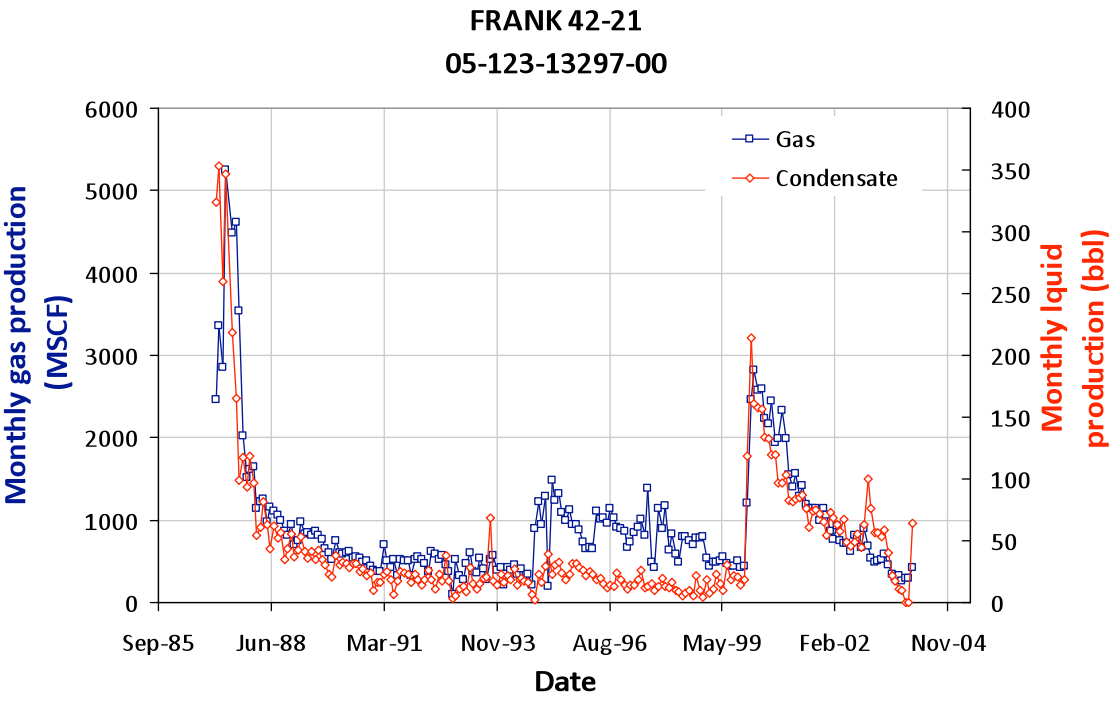
FRANK 42-21
05-123-13297-00
Monthly gas production (MSCF)
Monthly liquid production (bbl)
Gas
Condensate
6000
5000
4000
3000
2000
1000
0
400
350
300
250
200
150
100
50
0
Sep-85
Jun-88
Mar-91
Nov-93
Aug-96
May-99
Feb-02
Nov-04
Date

FRANK 43-21

05-123-15491-00

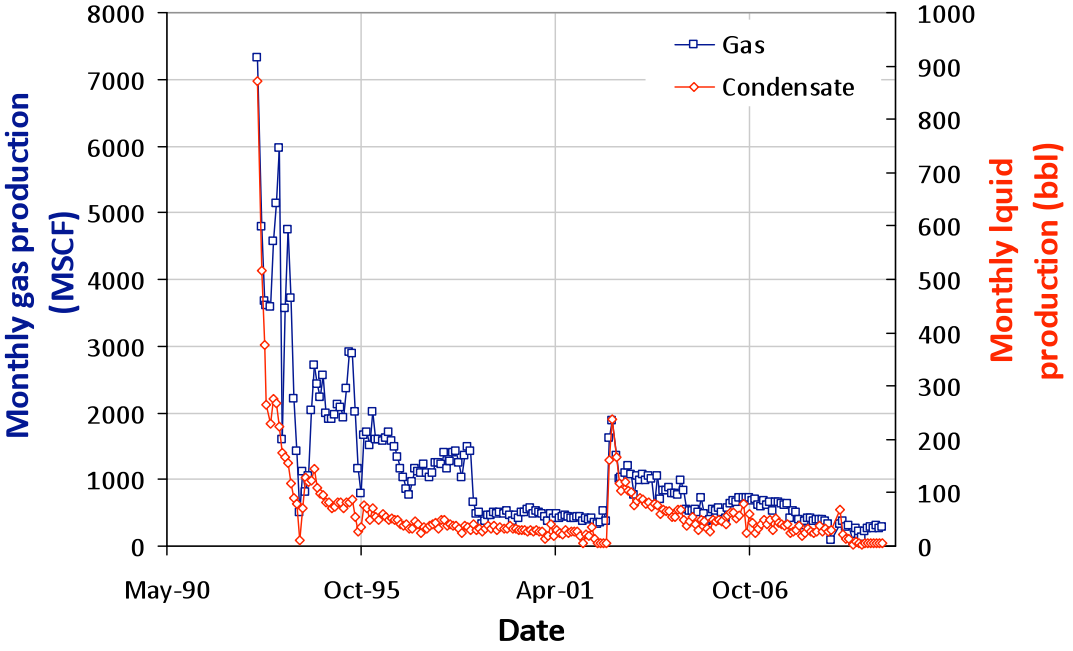

FRICO 1-22

05-123-18120-00

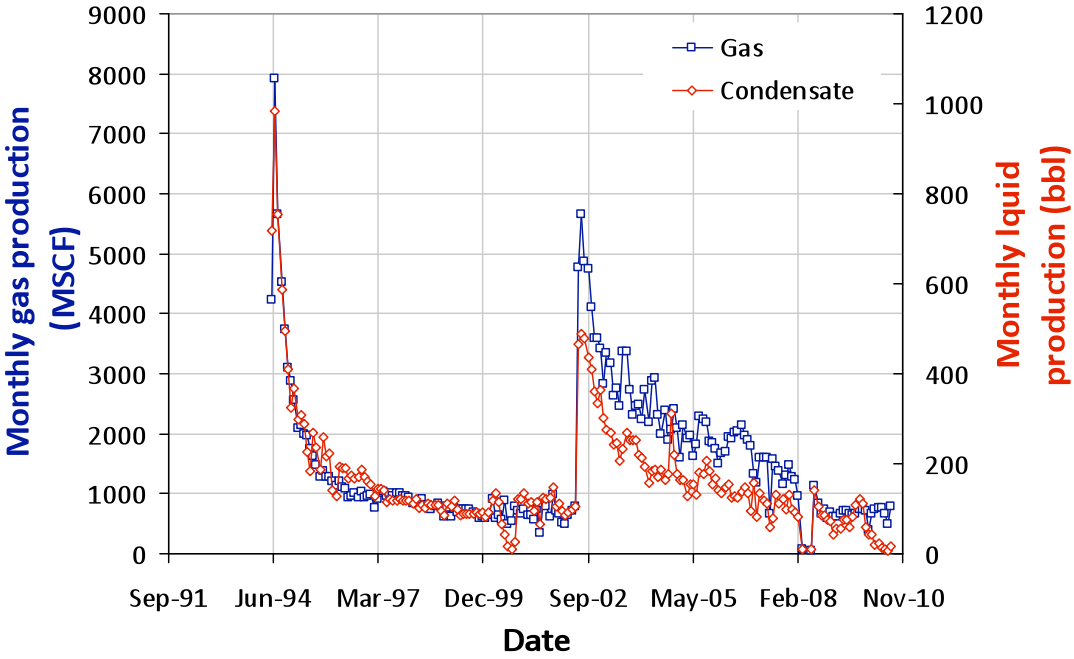

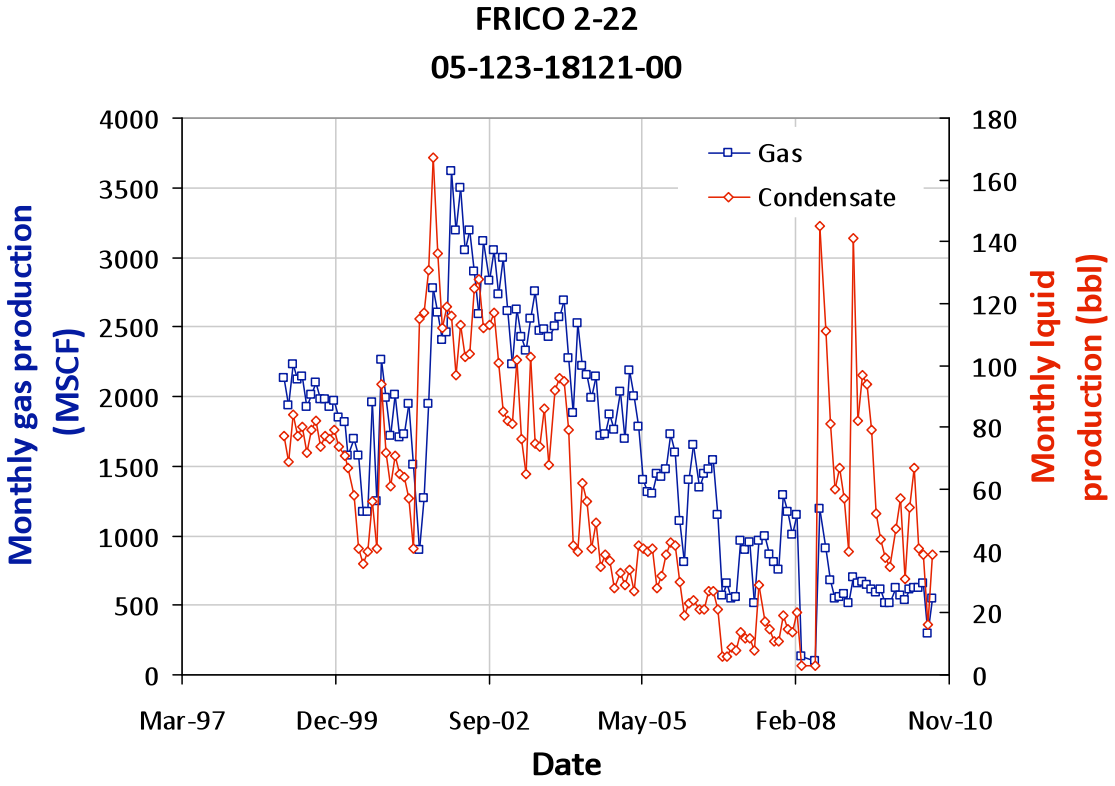
FRICO 2-22
05-123-18121-00
Monthly gas production (MSCF)
Monthly liquid production (bbl)
Gas
Condensate
4000
3500
3000
2500
2000
1500
1000
500
0
180
160
140
120
100
80
60
40
20
0
Mar-97
Dec-99
Sep-02
May-05
Feb-08
Nov-10
Date

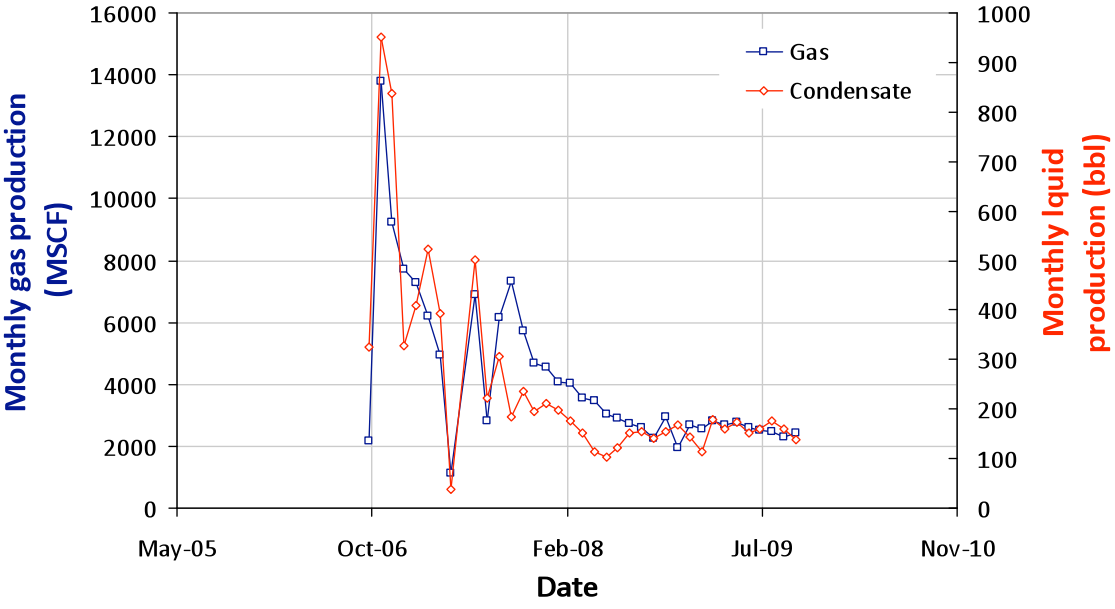
FRICO 5-15
05-123-24207-00
Monthly gas production (MSCF)
Monthly liquid production (bbl)
Gas
Condensate
16000
14000
12000
10000
8000
6000
4000
2000
0
1000
900
800
700
600
500
400
300
200
100
0
May-05
Oct-06
Feb-08
Jul-09
Nov-10
Date

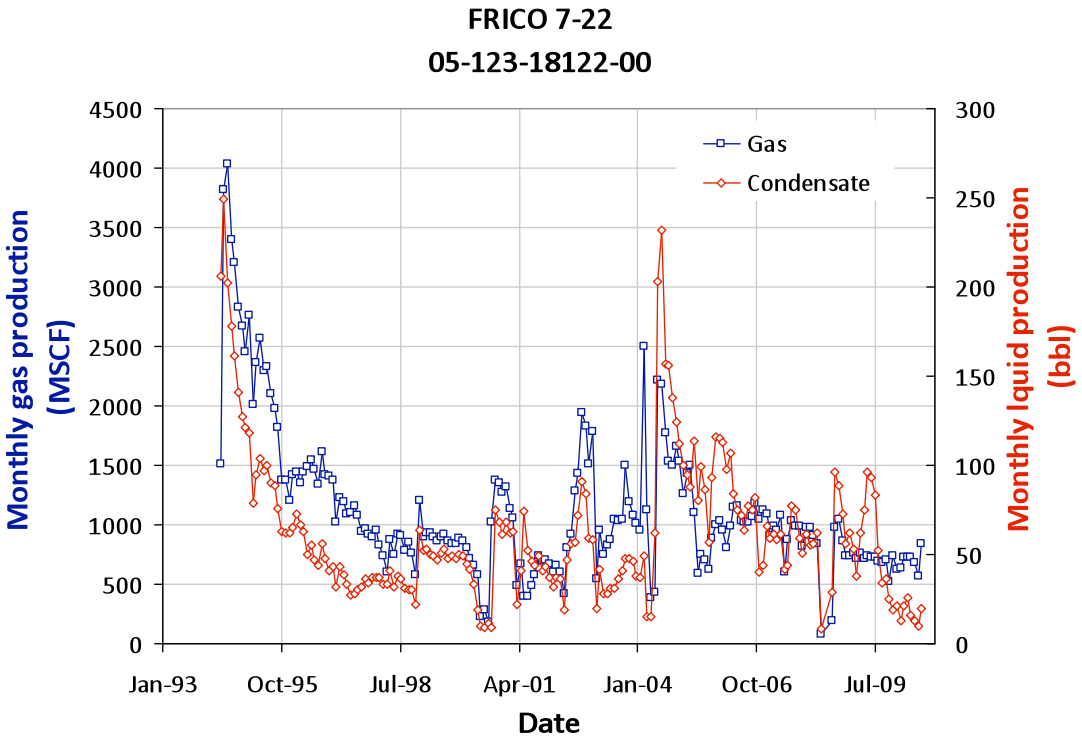
FRICO 7-22
05-123-18122-00
Monthly gas production (MSCF)
Monthly liquid production (bbl)
Gas
Condensate
4500
4000
3500
3000
2500
2000
1500
1000
500
0
300
250
200
150
100
50
0
Jan-93
Oct-95
Jul-98
Apr-01
Jan-04
Oct-06
Jul-09
Date

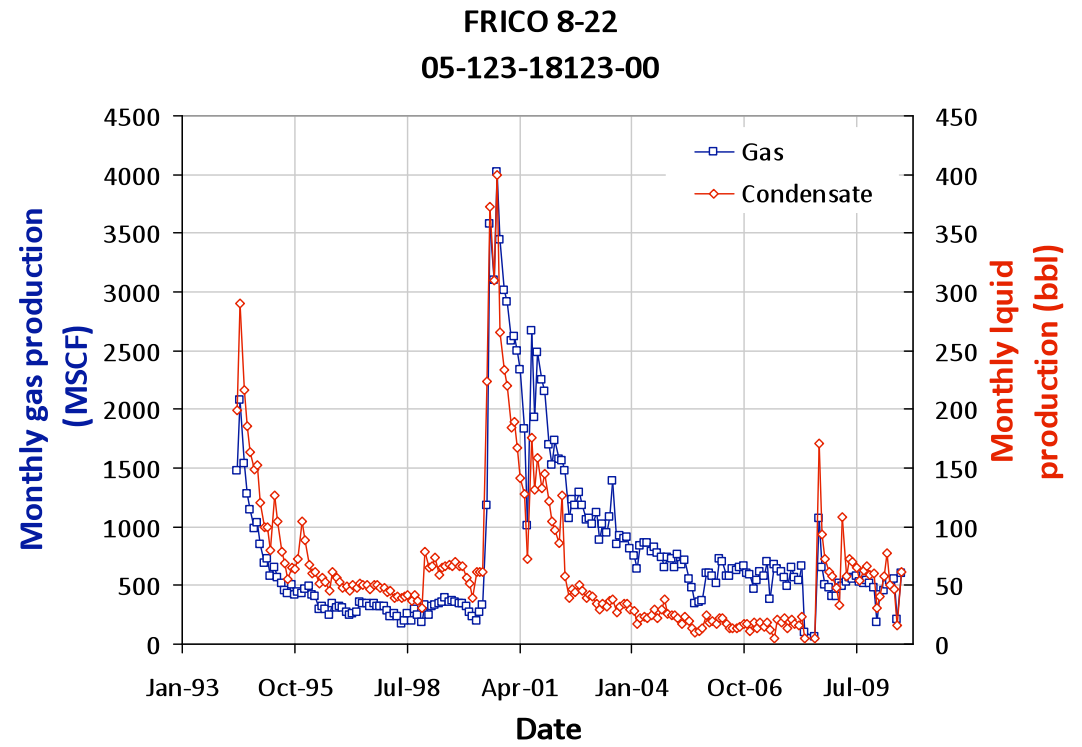
FRICO 8-22
05-123-18123-00
Monthly gas production (MSCF)
Monthly liquid production (bbl)
Gas
Condensate
4500
4000
3500
3000
2500
2000
1500
1000
500
0
450
400
350
300
250
200
150
100
50
0
Jan-93
Oct-95
Jul-98
Apr-01
Jan-04
Oct-06
Jul-09
Date

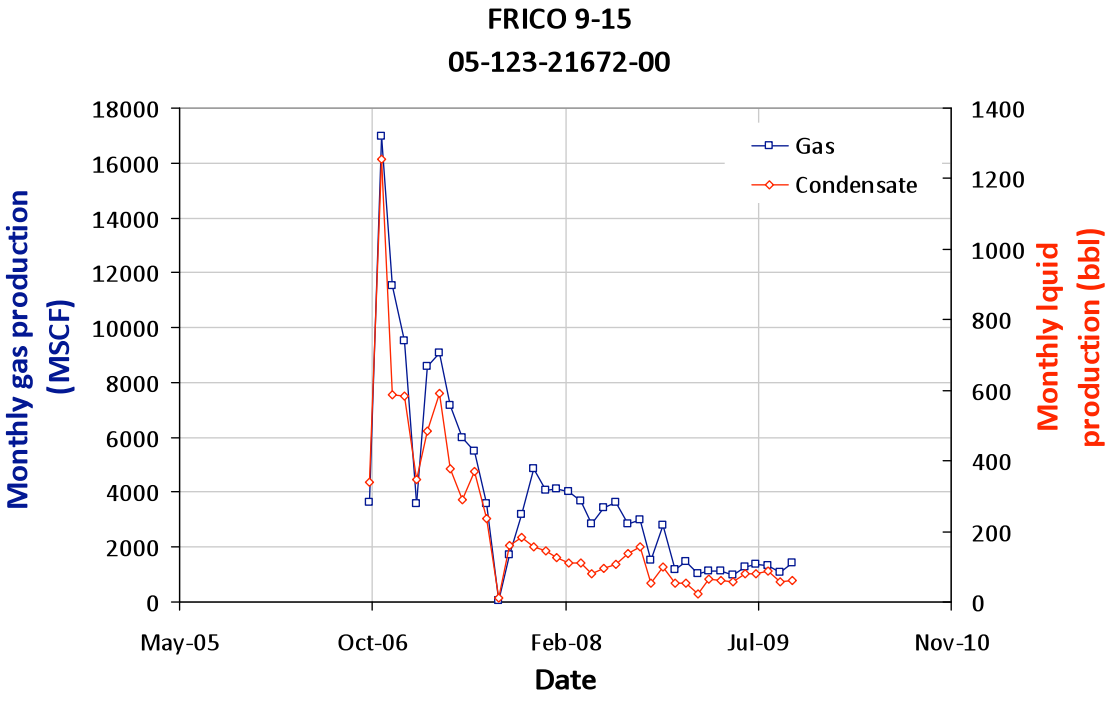
FRICO 9-15
05-123-21672-00
Monthly gas production (MSCF)
Monthly liquid production (bbl)
Gas
Condensate
18000
16000
14000
12000
10000
8000
6000
4000
2000
0
1400
1200
1000
800
600
400
200
0
May-05
Oct-06
Feb-08
Jul-09
Nov-10
Date

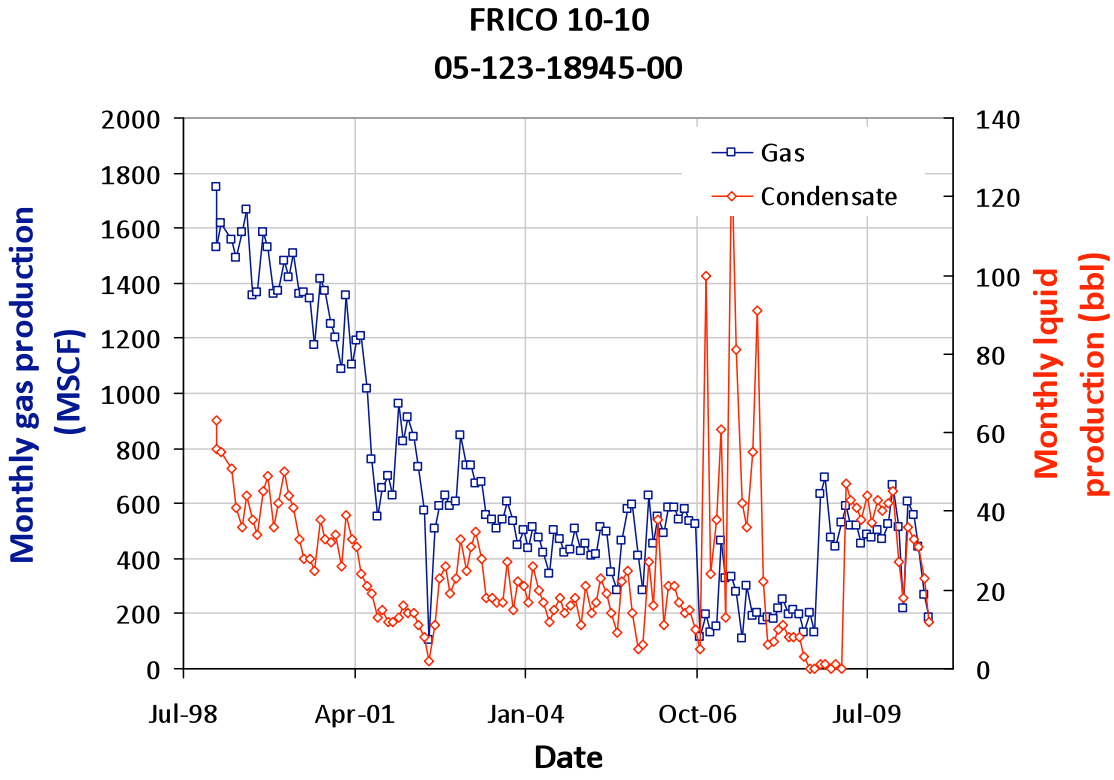
FRICO 10-10
05-123-18945-00
Monthly gas production (MSCF)
Monthly liquid production (bbl)
Gas
Condensate
2000
1800
1600
1400
1200
1000
800
600
400
200
0
140
120
100
80
60
40
20
0
Jul-98
Apr-01
Jan-04
Oct-06
Jul-09
Date

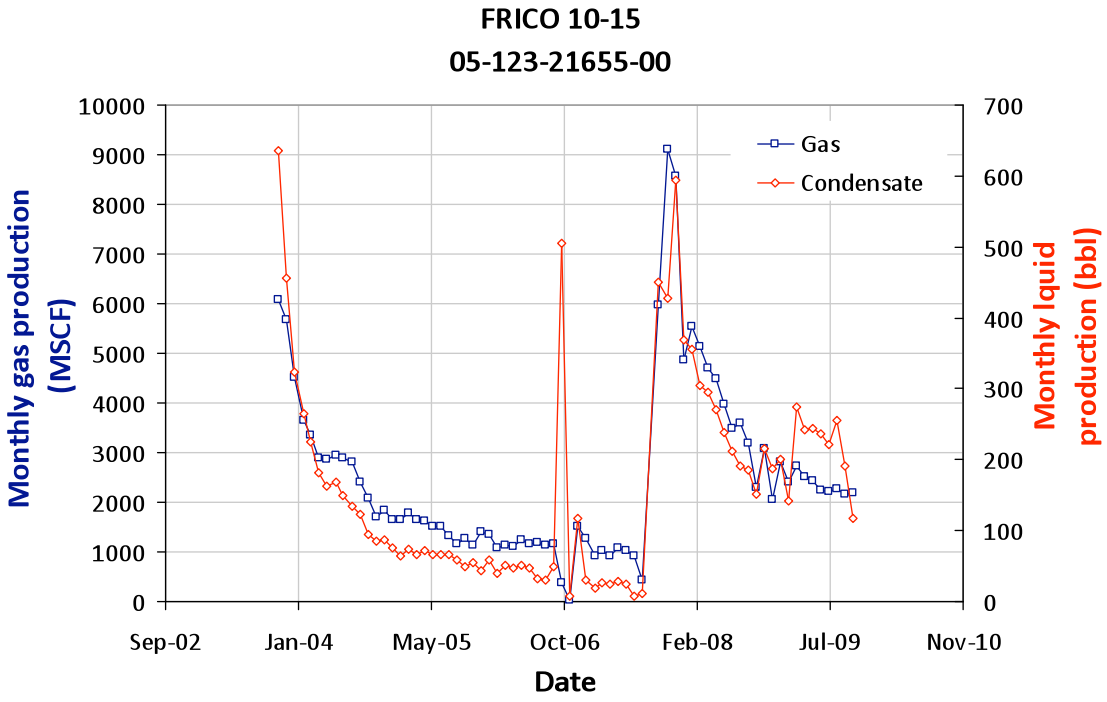
FRICO 10-15
05-123-21655-00
Monthly gas production (MSCF)
Monthly liquid production (bbl)
Gas
Condensate
10000
9000
8000
7000
6000
5000
4000
3000
2000
1000
0
700
600
500
400
300
200
100
0
Sep-02
Jan-04
May-05
Oct-06
Feb-08
Jul-09
Nov-10
Date

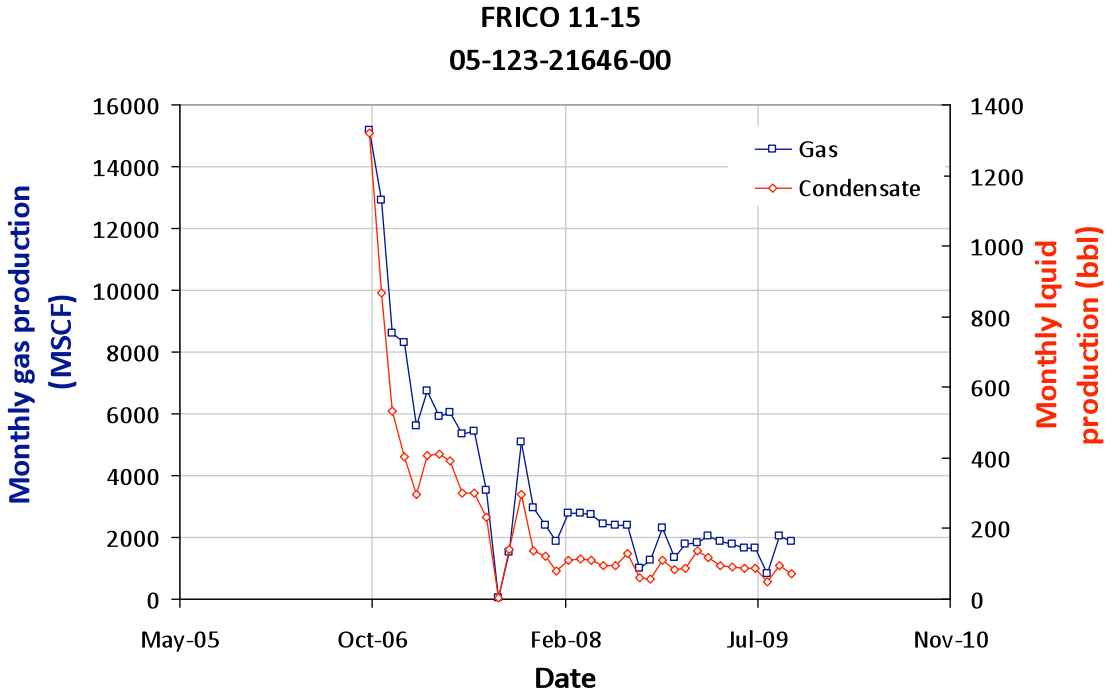
FRICO 11-15
05-123-21646-00
Monthly gas production (MSCF)
Monthly liquid production (bbl)
Gas
Condensate
16000
14000
12000
10000
8000
6000
4000
2000
0
1400
1200
1000
800
600
400
200
0
May-05
Oct-06
Feb-08
Jul-09
Nov-10
Date

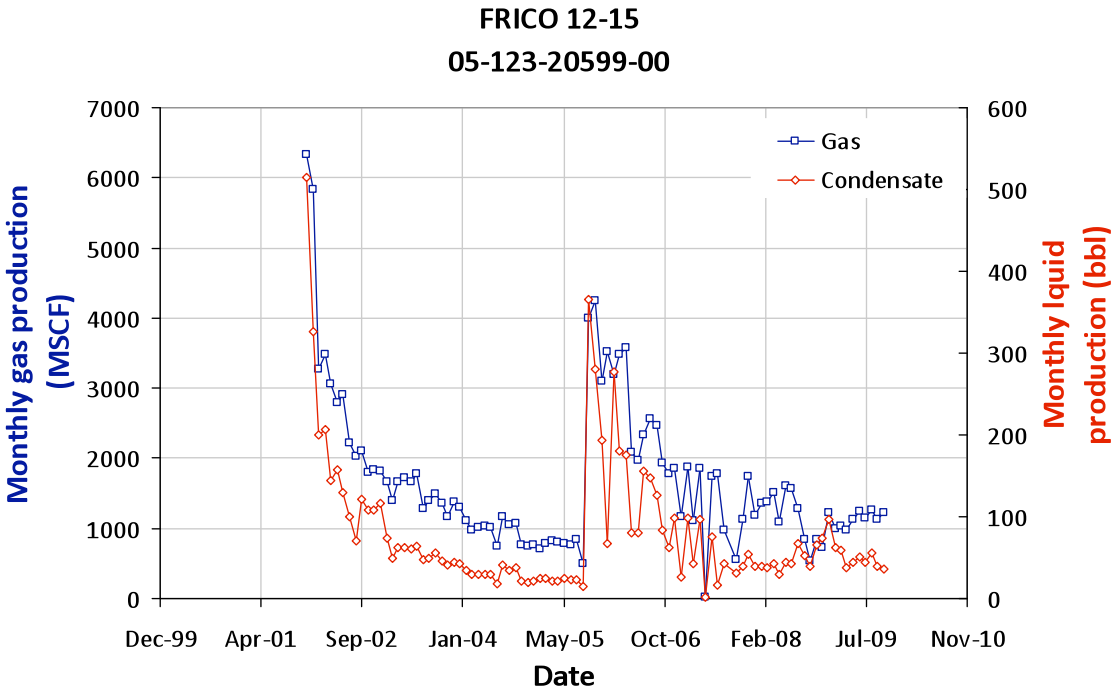
FRICO 12-15
05-123-20599-00
Monthly gas production (MSCF)
Monthly lquid production (bbl)
Gas
Condensate
7000
6000
5000
4000
3000
2000
1000
0
600
500
400
300
200
100
0
Dec-99
Apr-01
Sep-02
Jan-04
May-05
Oct-06
Feb-08
Jul-09
Nov-10
Date

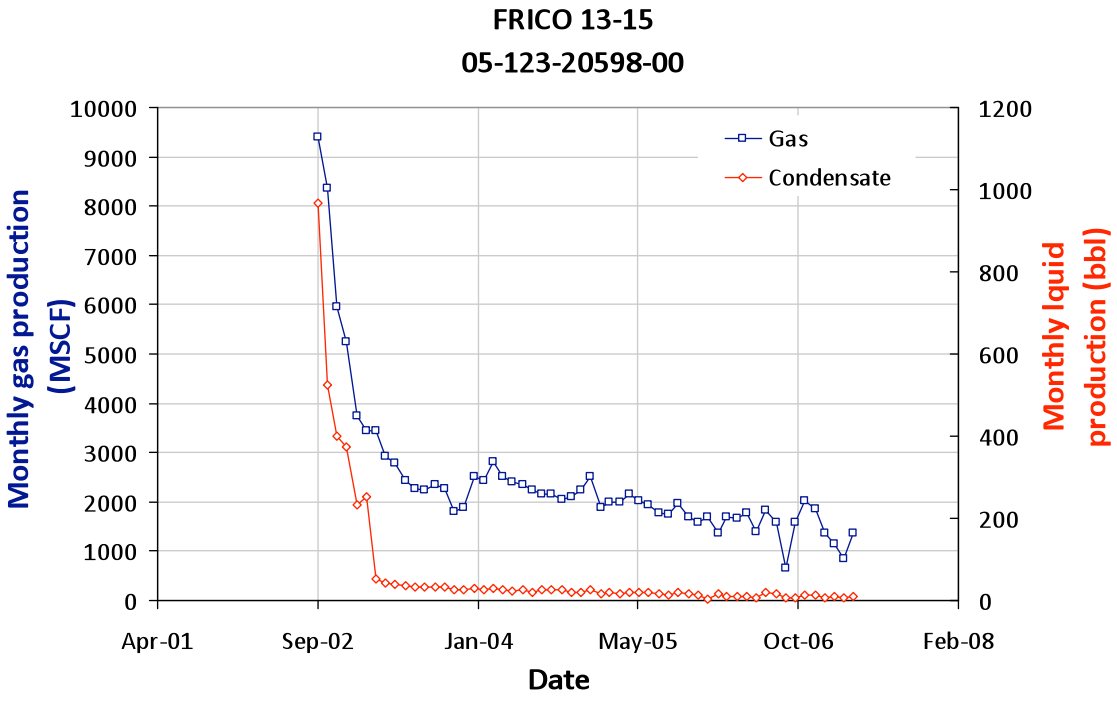
FRICO 13-15
05-123-20598-00
Monthly gas production (MSCF)
Monthly lquid production (bbl)
Gas
Condensate
10000
9000
8000
7000
6000
5000
4000
3000
2000
1000
0
1200
1000
800
600
400
200
0
Apr-01
Sep-02
Jan-04
May-05
Oct-06
Feb-08
Date

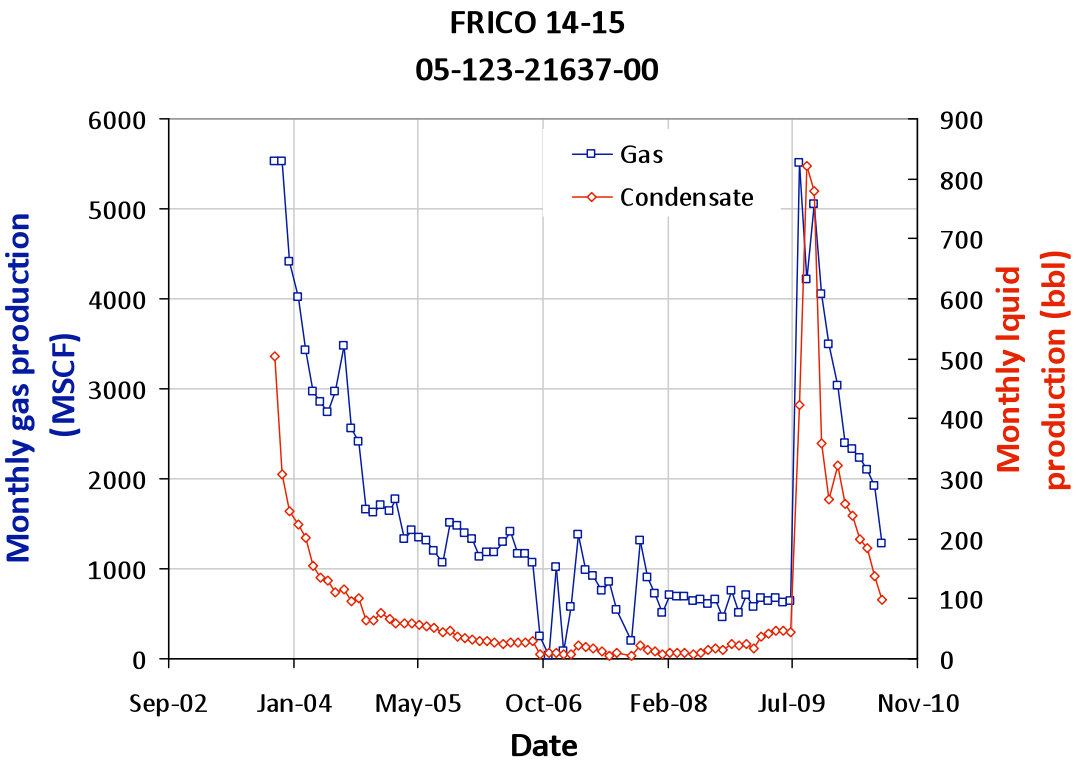
FRICO 14-15
05-123-21637-00
Monthly gas production (MSCF)
Monthly liquid production (bbl)
Gas
Condensate
6000
5000
4000
3000
2000
1000
0
900
800
700
600
500
400
300
200
100
0
Sep-02
Jan-04
May-05
Oct-06
Feb-08
Jul-09
Nov-10
Date

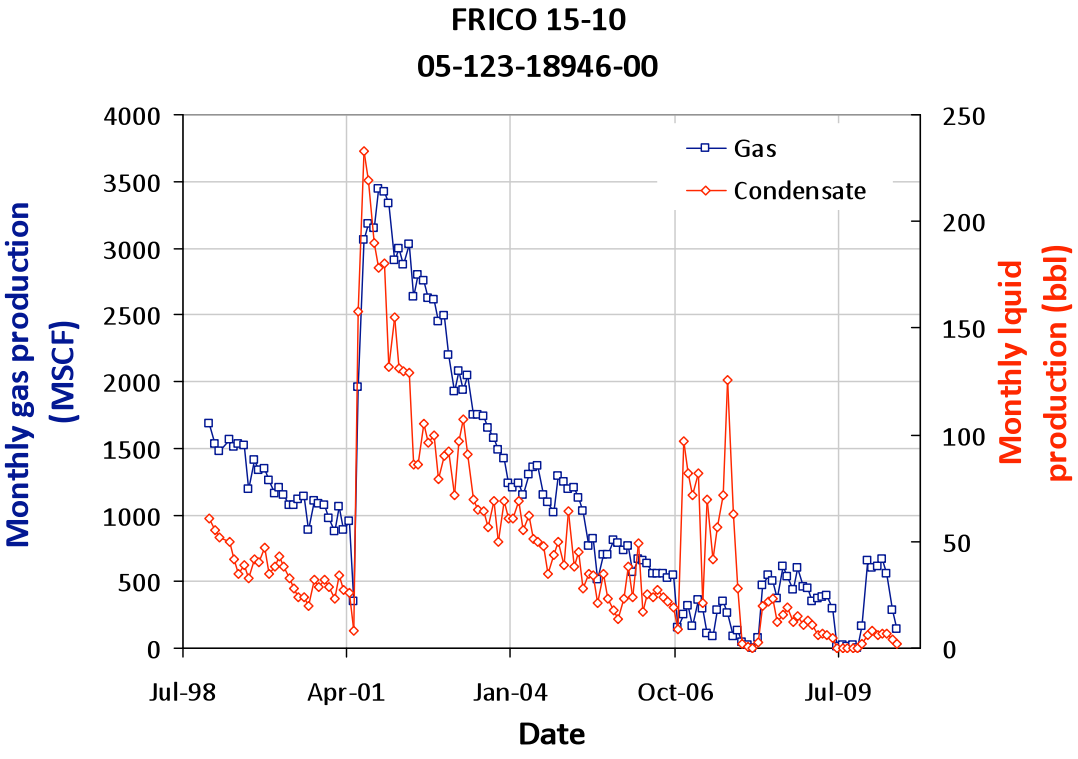
FRICO 15-10
05-123-18946-00
Monthly gas production (MSCF)
Monthly liquid production (bbl)
Gas
Condensate
4000
3500
3000
2500
2000
1500
1000
500
0
250
200
150
100
50
0
Jul-98
Apr-01
Jan-04
Oct-06
Jul-09
Date

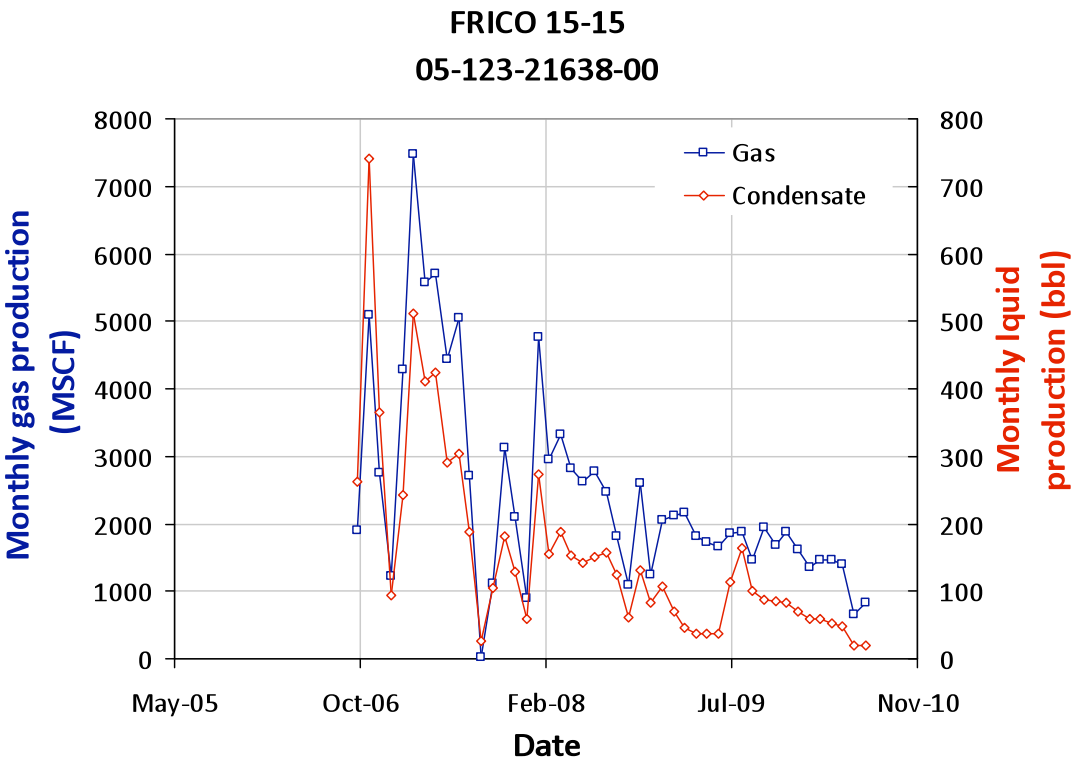
FRICO 15-15
05-123-21638-00
Monthly gas production (MSCF)
Monthly liquid production (bbl)
Gas
Condensate
8000
7000
6000
5000
4000
3000
2000
1000
0
800
700
600
500
400
300
200
100
0
May-05
Oct-06
Feb-08
Jul-09
Nov-10
Date

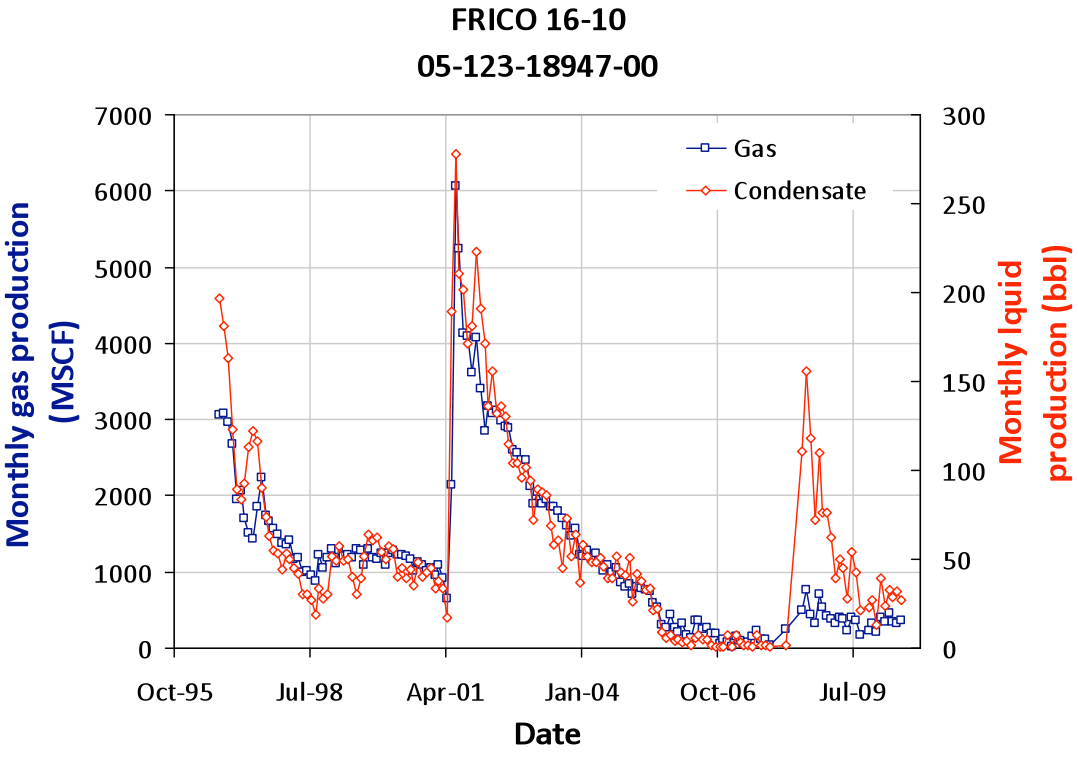
FRICO 16-10
05-123-18947-00
Monthly gas production (MSCF)
Monthly liquid production (bbl)
Gas
Condensate
7000
6000
5000
4000
3000
2000
1000
0
300
250
200
150
100
50
0
Oct-95
Jul-98
Apr-01
Jan-04
Oct-06
Jul-09
Date

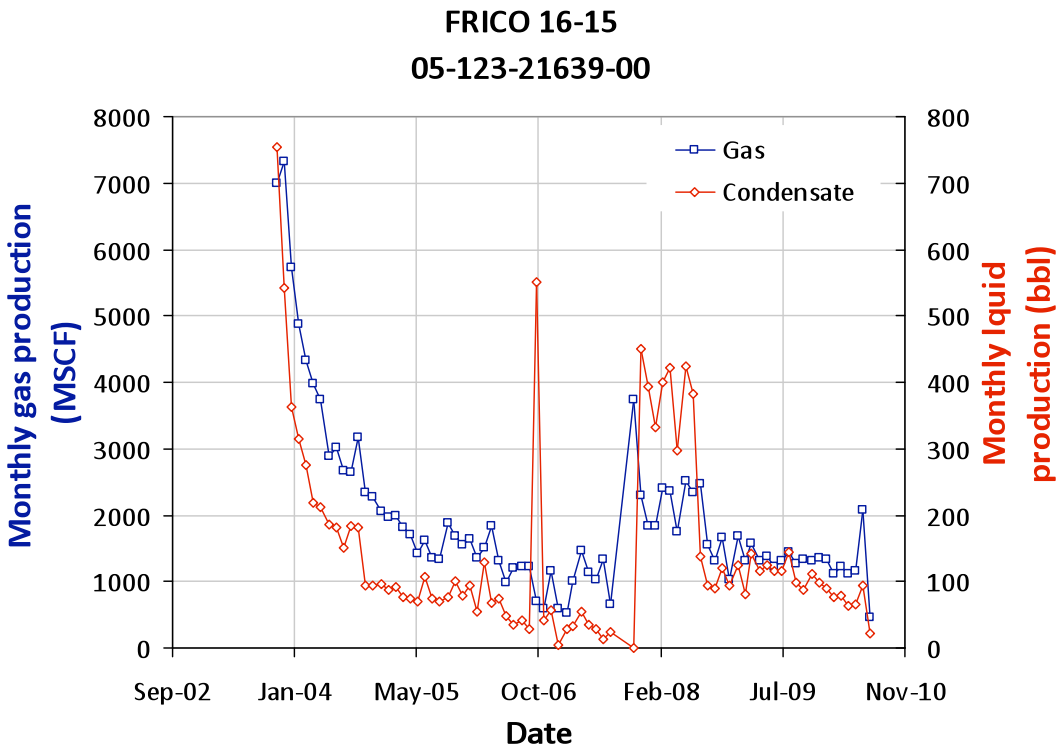
FRICO 16-15
05-123-21639-00
Monthly gas production (MSCF)
Monthly liquid production (bbl)
Gas
Condensate
8000
7000
6000
5000
4000
3000
2000
1000
0
800
700
600
500
400
300
200
100
0
Sep-02
Jan-04
May-05
Oct-06
Feb-08
Jul-09
Nov-10
Date

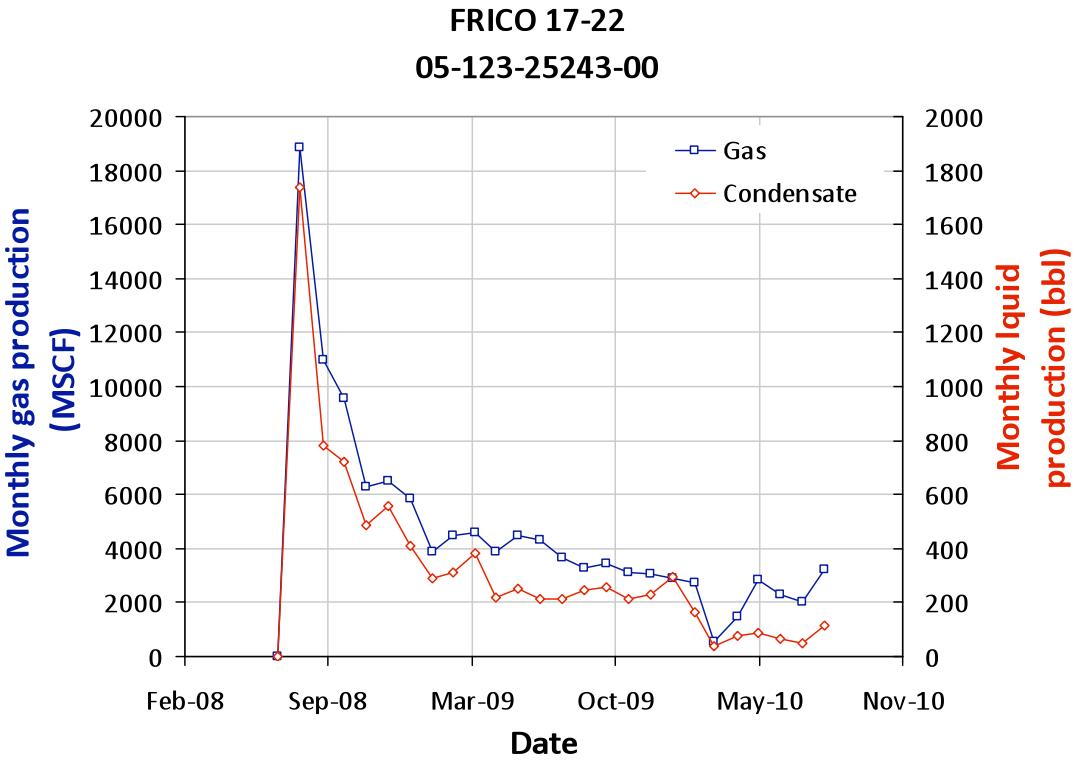
FRICO 17-22
05-123-25243-00
Monthly gas production (MSCF)
Monthly liquid production (bbl)
Gas
Condensate
20000
18000
16000
14000
12000
10000
8000
6000
4000
2000
0
2000
1800
1600
1400
1200
1000
800
600
400
200
0
Feb-08
Sep-08
Mar-09
Oct-09
May-10
Nov-10
Date

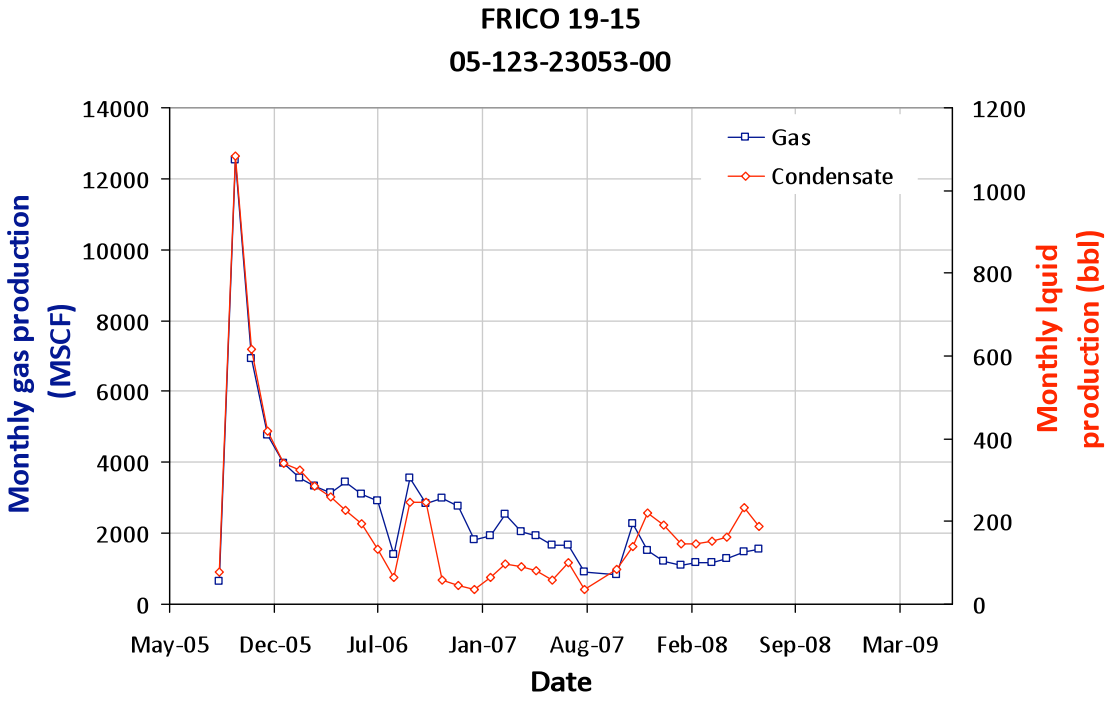
FRICO 19-15
05-123-23053-00
Monthly gas production (MSCF)
Monthly liquid production (bbl)
Gas
Condensate
14000
12000
10000
8000
6000
4000
2000
0
1200
1000
800
600
400
200
0
May-05
Dec-05
Jul-06
Jan-07
Aug-07
Feb-08
Sep-08
Mar-09
Date

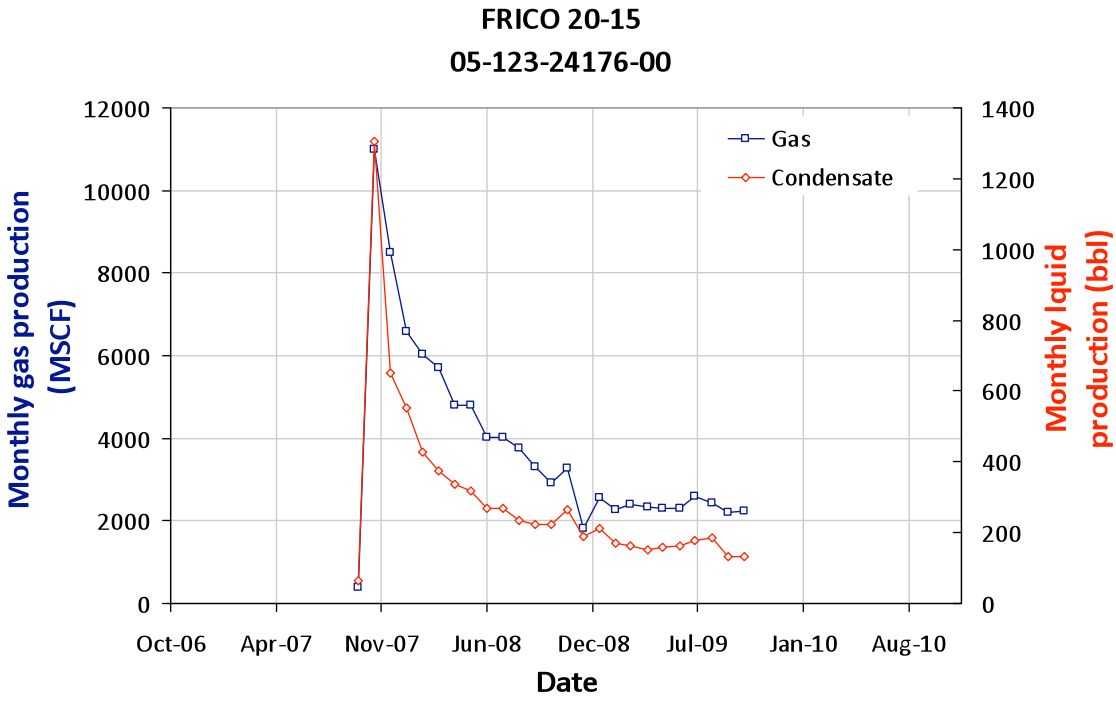
FRICO 20-15
05-123-24176-00
Monthly gas production (MSCF)
Monthly liquid production (bbl)
Gas
Condensate
12000
10000
8000
6000
4000
2000
0
1400
1200
1000
800
600
400
200
0
Oct-06
Apr-07
Nov-07
Jun-08
Dec-08
Jul-09
Jan-10
Aug-10
Date

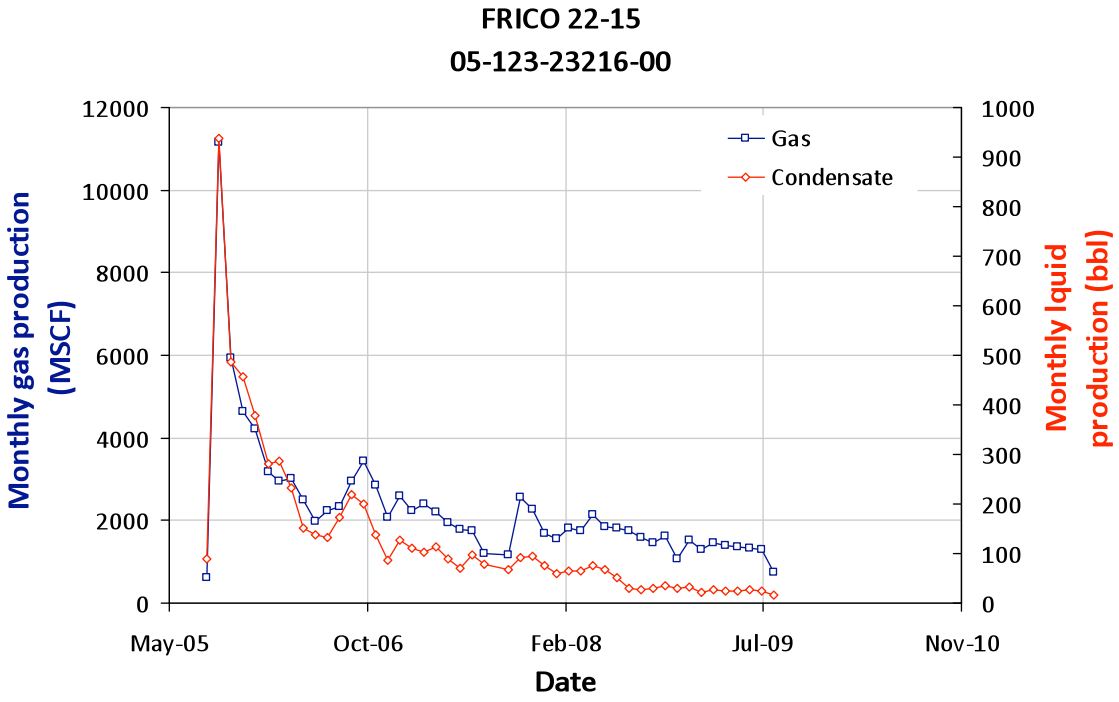
FRICO 22-15
05-123-23216-00
Monthly gas production (MSCF)
Monthly liquid production (bbl)
Gas
Condensate
12000
10000
8000
6000
4000
2000
0
1000
900
800
700
600
500
400
300
200
100
0
May-05
Oct-06
Feb-08
Jul-09
Nov-10
Date

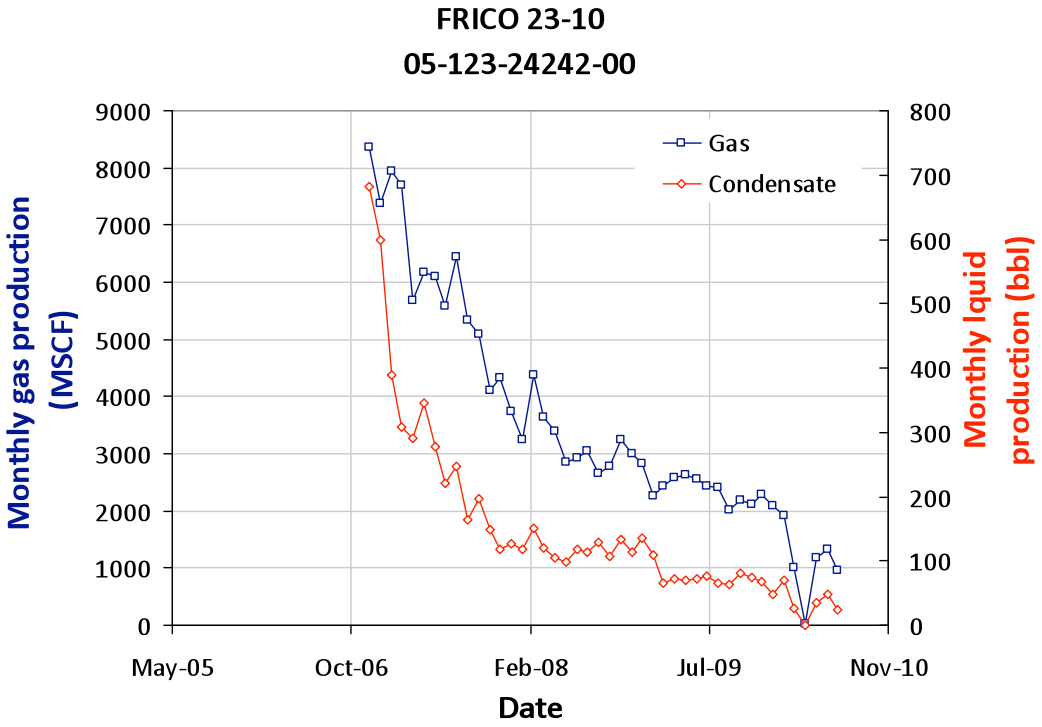
FRICO 23-10
05-123-24242-00
Monthly gas production (MSCF)
Monthly liquid production (bbl)
Gas
Condensate
9000
8000
7000
6000
5000
4000
3000
2000
1000
0
800
700
600
500
400
300
200
100
0
May-05
Oct-06
Feb-08
Jul-09
Nov-10
Date

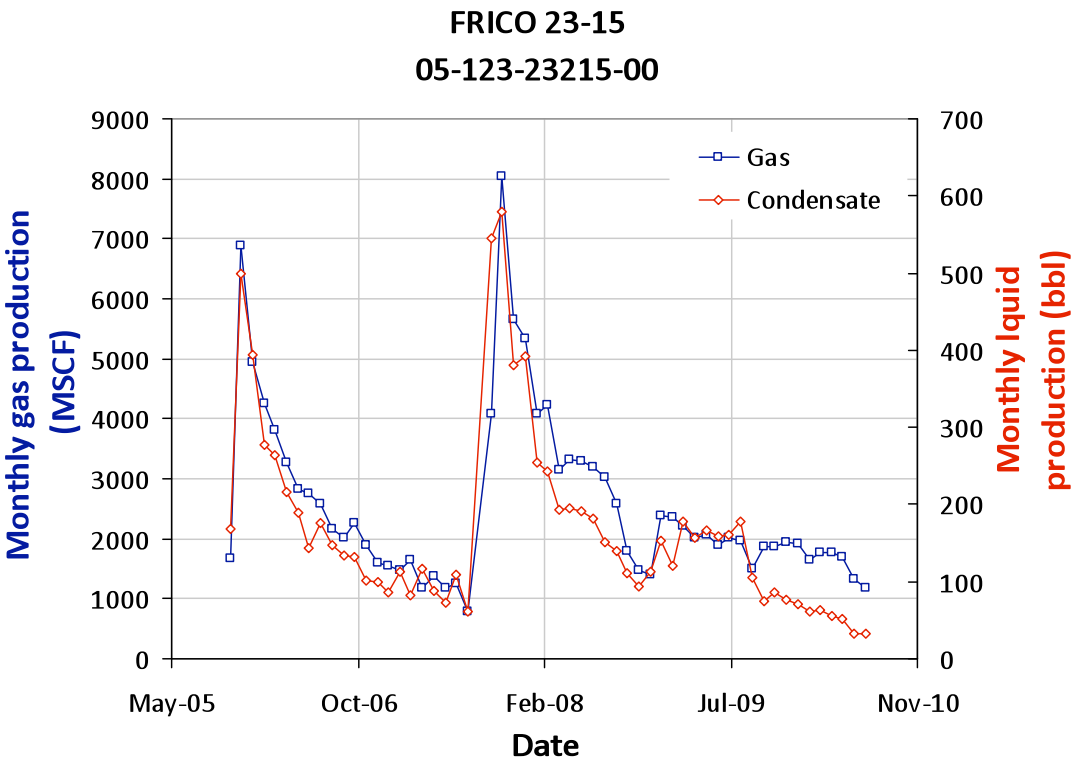
FRICO 23-15
05-123-23215-00
Monthly gas production (MSCF)
Monthly liquid production (bbl)
Gas
Condensate
9000
8000
7000
6000
5000
4000
3000
2000
1000
0
700
600
500
400
300
200
100
0
May-05
Oct-06
Feb-08
Jul-09
Nov-10
Date

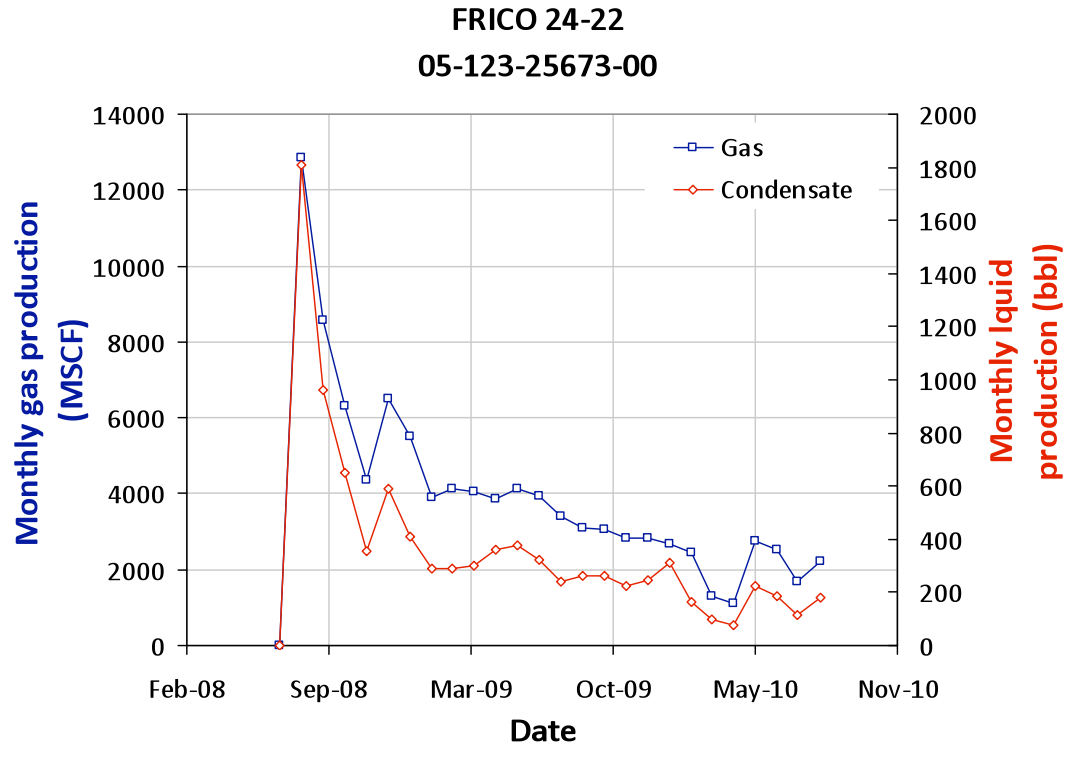
FRICO 24-22
05-123-25673-00
Monthly gas production (MSCF)
Monthly liquid production (bbl)
Gas
Condensate
14000
12000
10000
8000
6000
4000
2000
0
2000
1800
1600
1400
1200
1000
800
600
400
200
0
Feb-08
Sep-08
Mar-09
Oct-09
May-10
Nov-10
Date

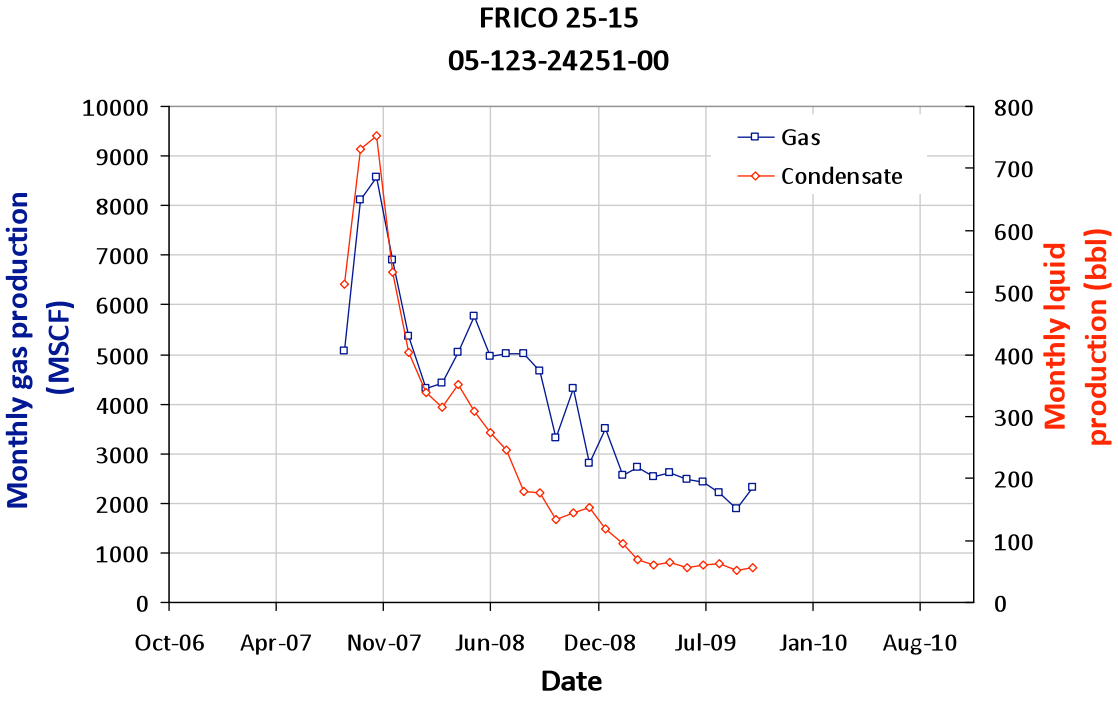
FRICO 25-15
05-123-24251-00
Monthly gas production (MSCF)
Monthly liquid production (bbl)
Gas
Condensate
10000
9000
8000
7000
6000
5000
4000
3000
2000
1000
0
800
700
600
500
400
300
200
100
0
Oct-06
Apr-07
Nov-07
Jun-08
Dec-08
Jul-09
Jan-10
Aug-10
Date

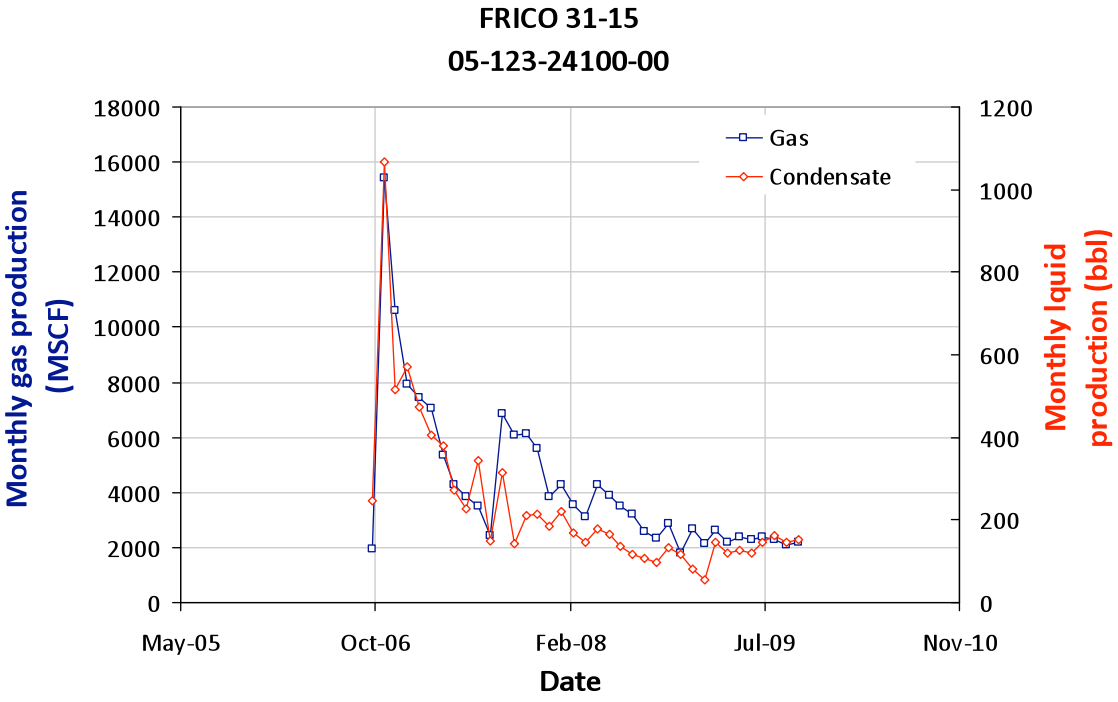
FRICO 31-15
05-123-24100-00
Monthly gas production (MSCF)
Monthly liquid production (bbl)
Gas
Condensate
18000
16000
14000
12000
10000
8000
6000
4000
2000
0
1200
1000
800
600
400
200
0
May-05
Oct-06
Feb-08
Jul-09
Nov-10
Date

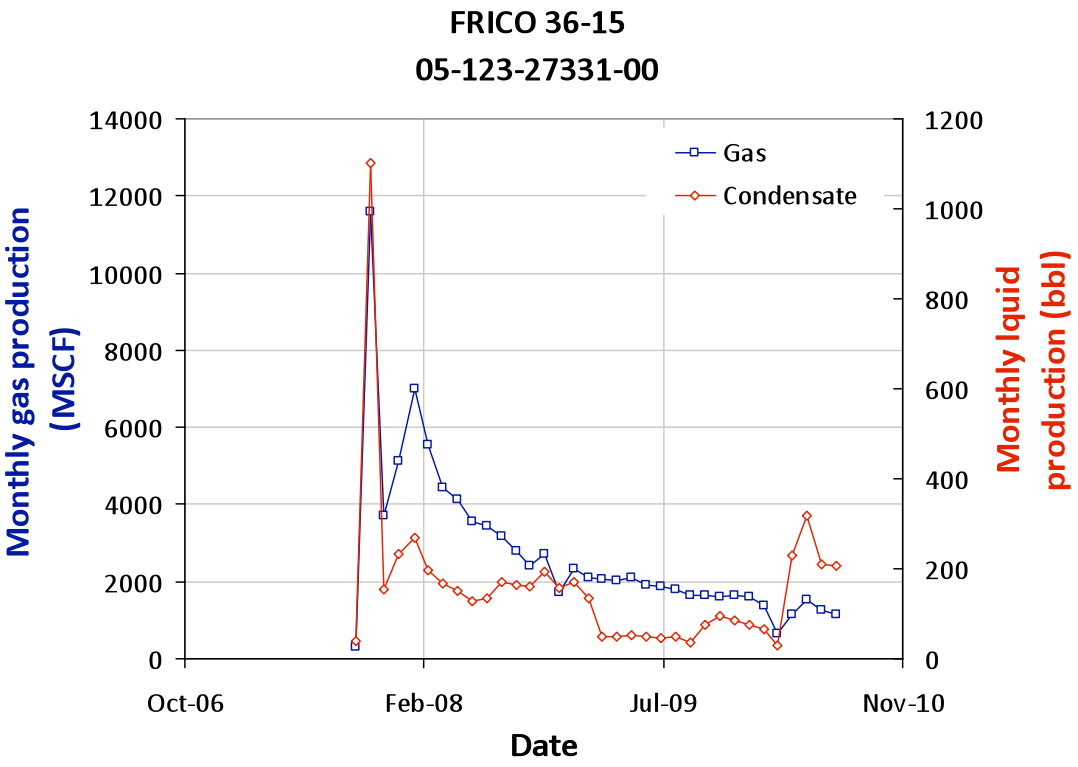
FRICO 36-15
05-123-27331-00
Gas
Condensate
Monthly gas production (MSCF)
Monthly liquid production (bbl)
14000
12000
10000
8000
6000
4000
2000
0
1200
1000
800
600
400
200
0
Oct-06
Feb-08
Jul-09
Nov-10
Date

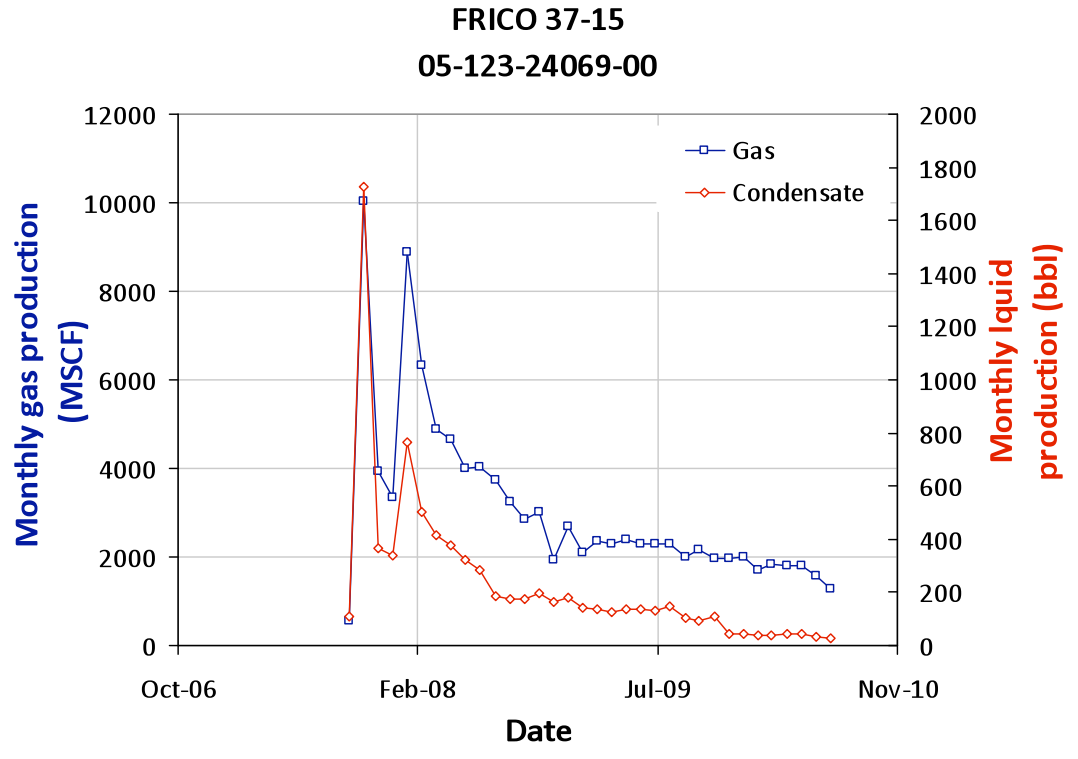
FRICO 37-15
05-123-24069-00
Gas
Condensate
Monthly gas production (MSCF)
Monthly liquid production (bbl)
12000
10000
8000
6000
4000
2000
0
2000
1800
1600
1400
1200
1000
800
600
400
200
0
Oct-06
Feb-08
Jul-09
Nov-10
Date

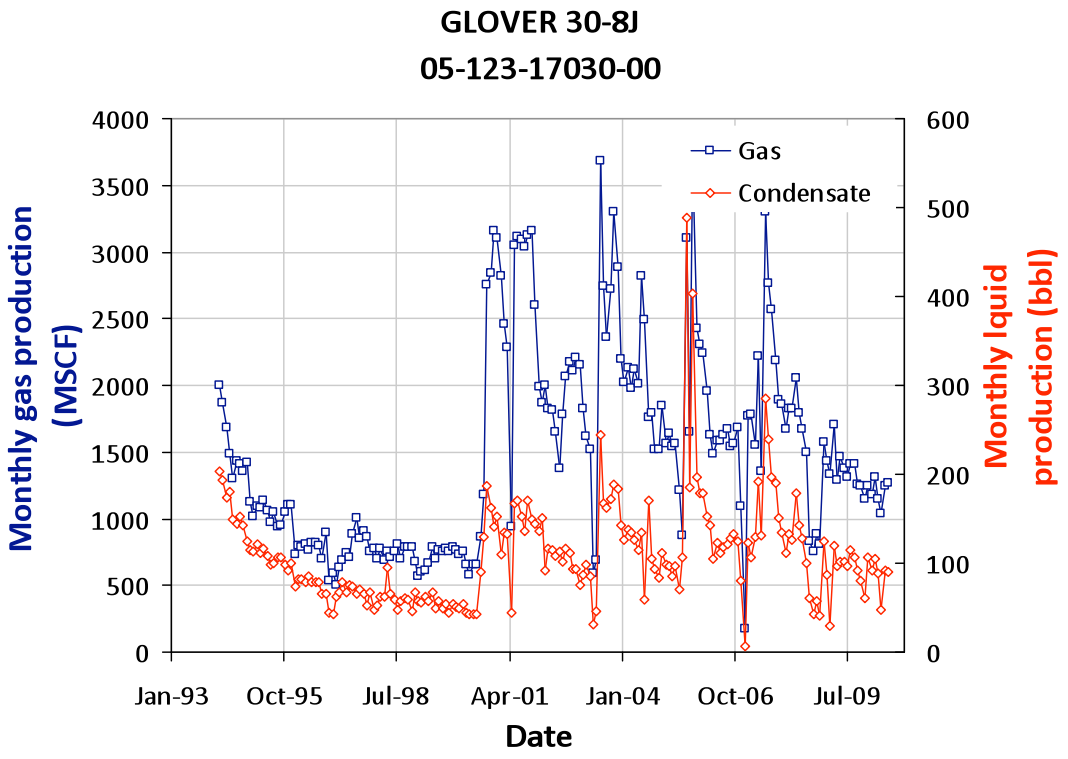
GLOVER 30-8J
05-123-17030-00
Gas
Condensate
Monthly gas production (MSCF)
Monthly liquid production (bbl)
4000
3500
3000
2500
2000
1500
1000
500
0
600
500
400
300
200
100
0
Jan-93
Oct-95
Jul-98
Apr-01
Jan-04
Oct-06
Jul-09
Date

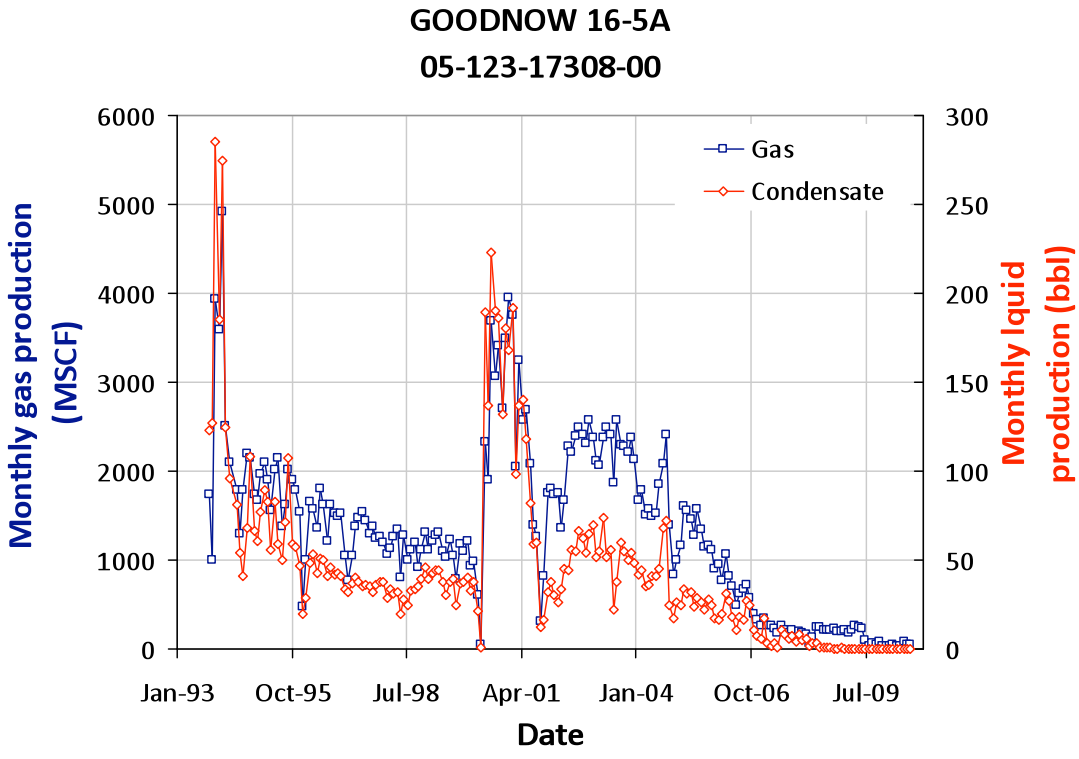
GOODNOW 16-5A
05-123-17308-00
Gas
Condensate
Monthly gas production (MSCF)
Monthly liquid production (bbl)
6000
5000
4000
3000
2000
1000
0
300
250
200
150
100
50
0
Jan-93
Oct-95
Jul-98
Apr-01
Jan-04
Oct-06
Jul-09
Date

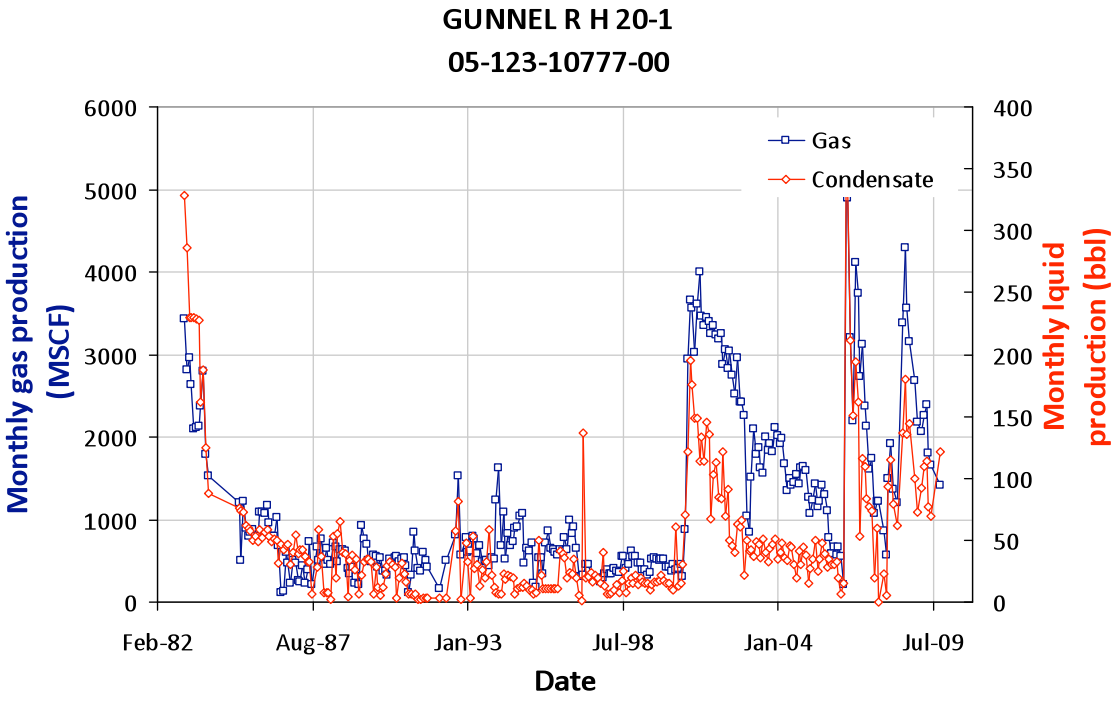
GUNNEL R H 20-1
05-123-10777-00
Monthly gas production (MSCF)
Monthly liquid production (bbl)
Gas
Condensate
6000
5000
4000
3000
2000
1000
0
400
350
300
250
200
150
100
50
0
Feb-82
Aug-87
Jan-93
Jul-98
Jan-04
Jul-09
Date

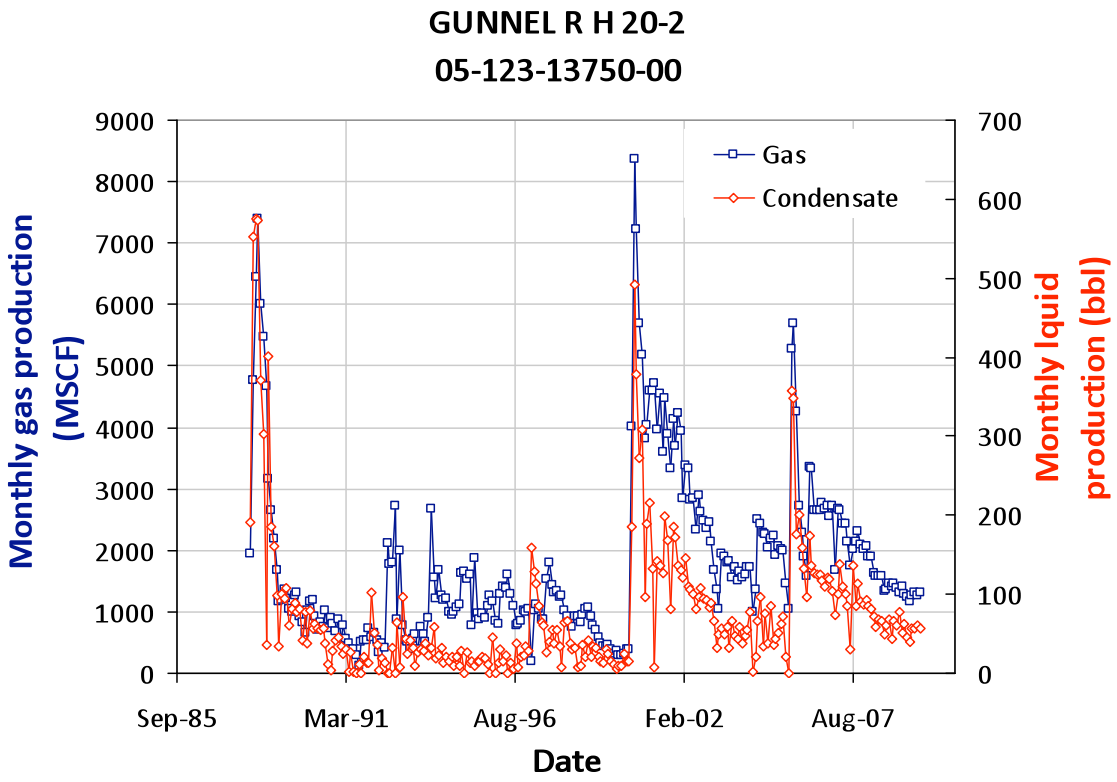
GUNNEL R H 20-2
05-123-13750-00
Monthly gas production (MSCF)
Monthly liquid production (bbl)
Gas
Condensate
9000
8000
7000
6000
5000
4000
3000
2000
1000
0
700
600
500
400
300
200
100
0
Sep-85
Mar-91
Aug-96
Feb-02
Aug-07
Date

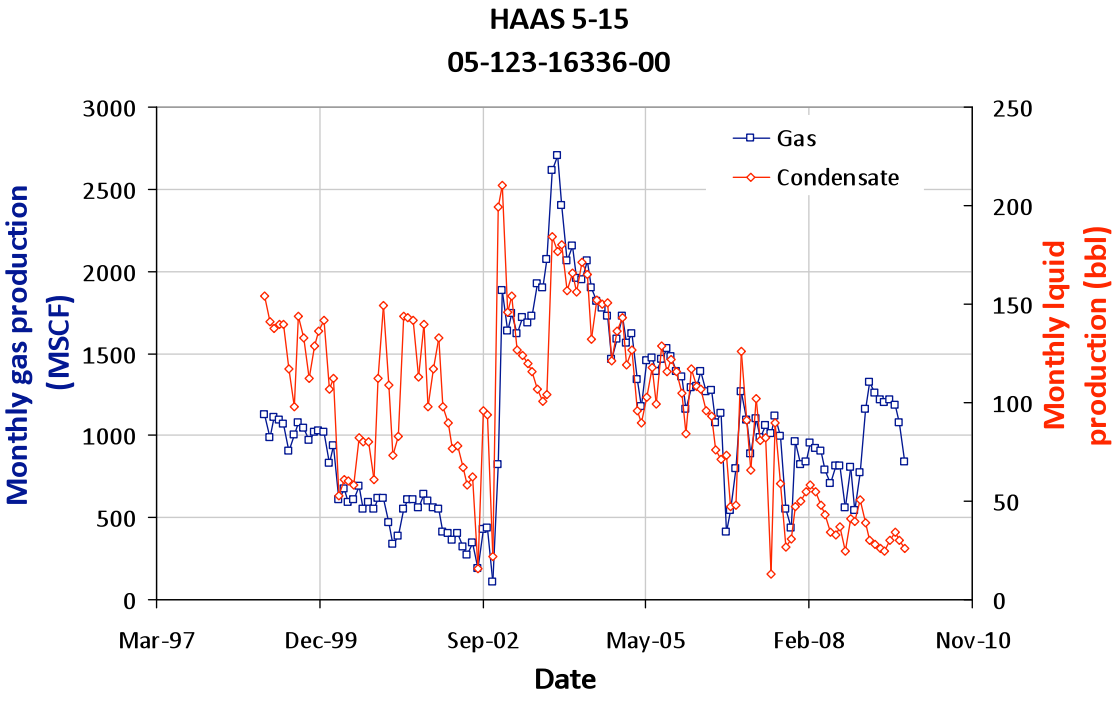
HAAS 5-15
05-123-16336-00
Monthly gas production (MSCF)
Monthly liquid production (bbl)
Gas
Condensate
3000
2500
2000
1500
1000
500
0
250
200
150
100
50
0
Mar-97
Dec-99
Sep-02
May-05
Feb-08
Nov-10
Date

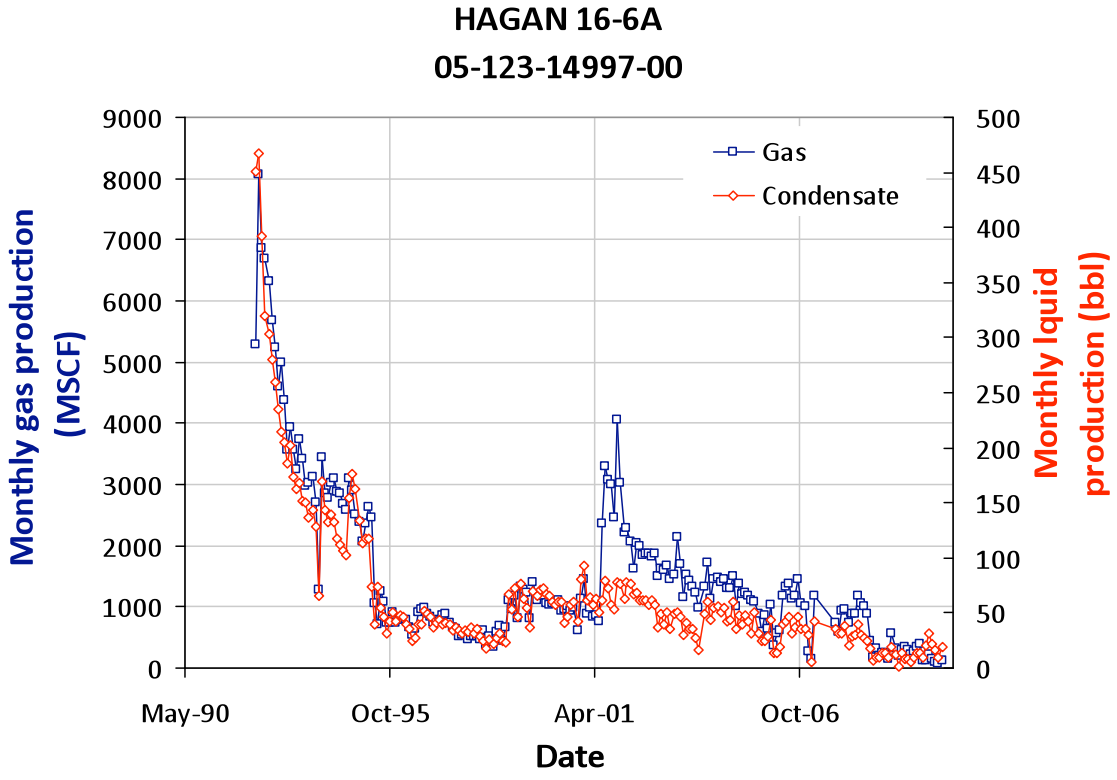
HAGAN 16-6A
05-123-14997-00
Monthly gas production (MSCF)
Monthly liquid production (bbl)
Gas
Condensate
9000
8000
7000
6000
5000
4000
3000
2000
1000
0
500
450
400
350
300
250
200
150
100
50
0
May-90
Oct-95
Apr-01
Oct-06
Date

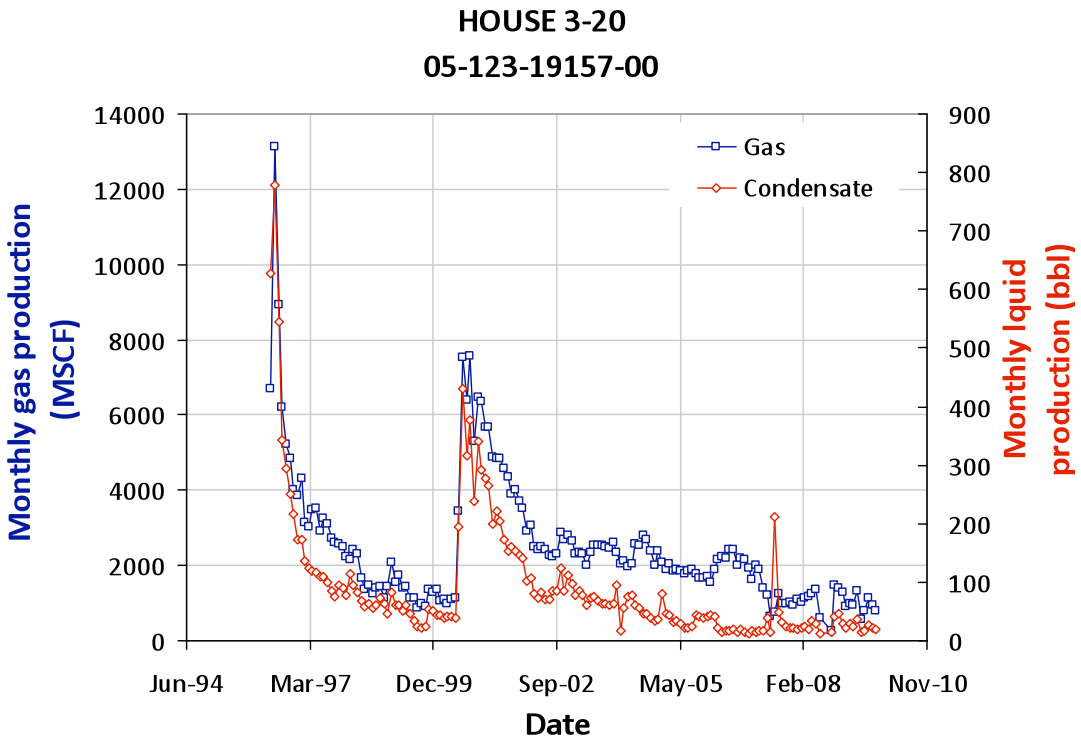
HOUSE 3-20
05-123-19157-00
Monthly gas production (MSCF)
Monthly liquid production (bbl)
Gas
Condensate
14000
12000
10000
8000
6000
4000
2000
0
900
800
700
600
500
400
300
200
100
0
Jun-94
Mar-97
Dec-99
Sep-02
May-05
Feb-08
Nov-10
Date

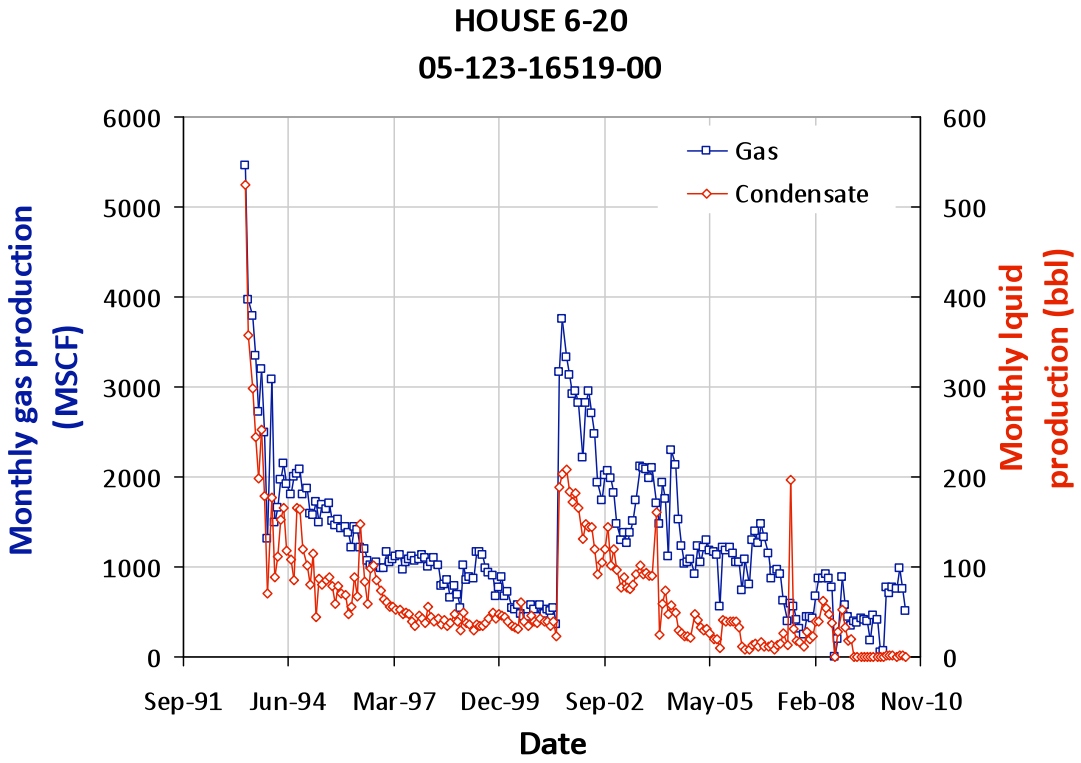
HOUSE 6-20
05-123-16519-00
Monthly gas production (MSCF)
Monthly liquid production (bbl)
Gas
Condensate
6000
5000
4000
3000
2000
1000
0
600
500
400
300
200
100
0
Sep-91
Jun-94
Mar-97
Dec-99
Sep-02
May-05
Feb-08
Nov-10
Date

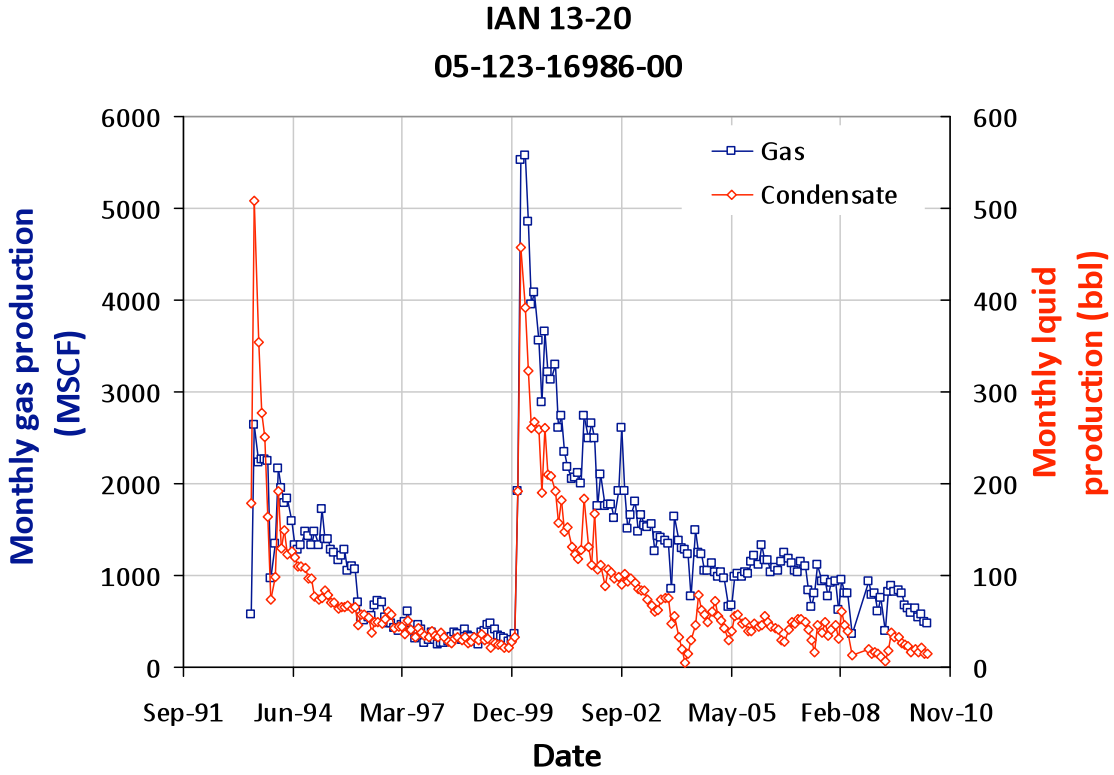
IAN 13-20
05-123-16986-00
Monthly gas production (MSCF)
Monthly liquid production (bbl)
Gas
Condensate
6000
5000
4000
3000
2000
1000
0
600
500
400
300
200
100
0
Sep-91
Jun-94
Mar-97
Dec-99
Sep-02
May-05
Feb-08
Nov-10
Date

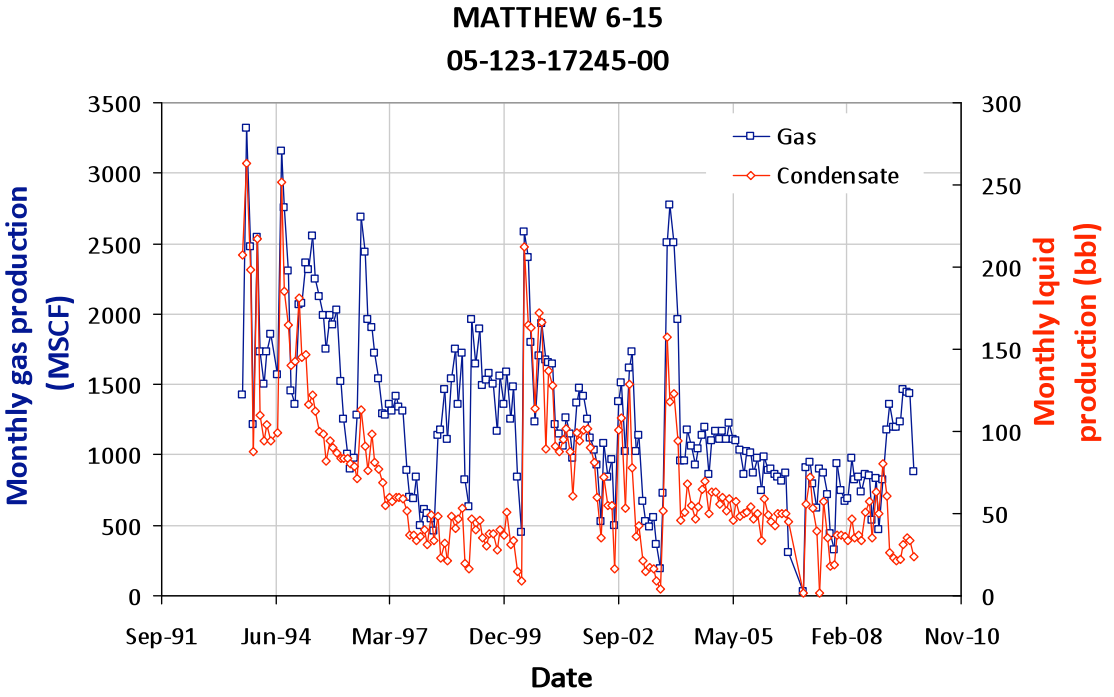
MATTHEW 6-15
05-123-17245-00
Monthly gas production (MSCF)
Monthly liquid production (bbl)
Gas
Condensate
3500
3000
2500
2000
1500
1000
500
0
300
250
200
150
100
50
0
Sep-91
Jun-94
Mar-97
Dec-99
Sep-02
May-05
Feb-08
Nov-10
Date

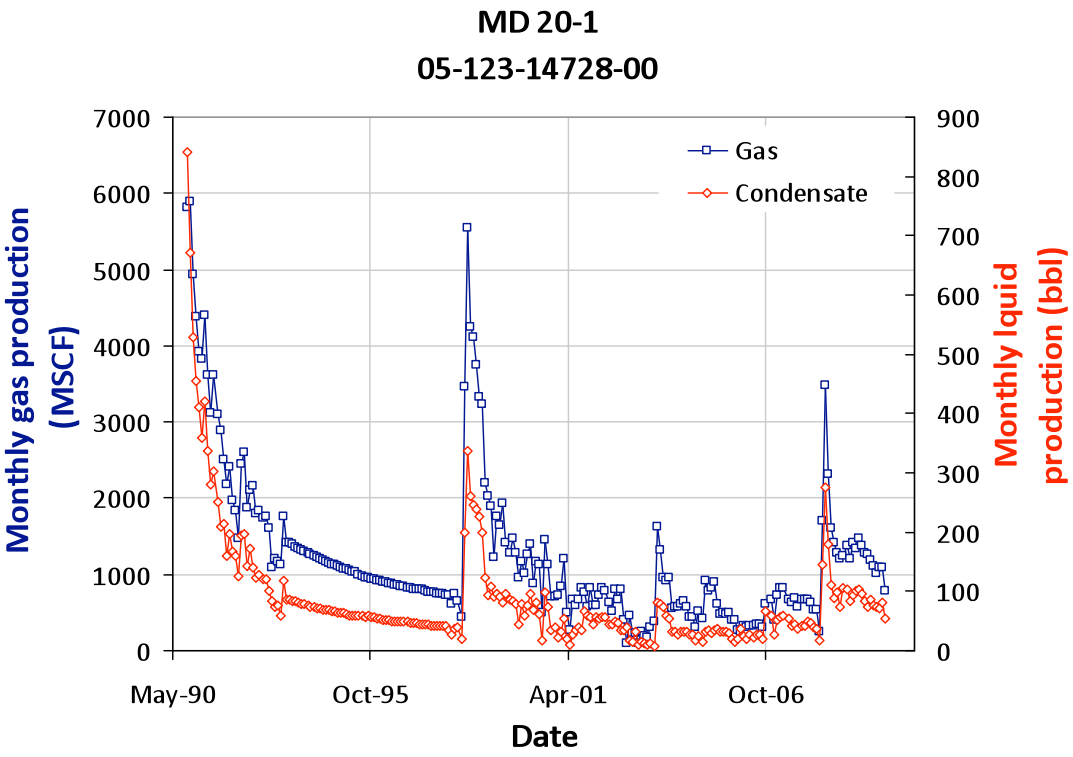
MD 20-1
05-123-14728-00
Monthly gas production (MSCF)
Monthly liquid production (bbl)
Gas
Condensate
7000
6000
5000
4000
3000
2000
1000
0
900
800
700
600
500
400
300
200
100
0
May-90
Oct-95
Apr-01
Oct-06
Date

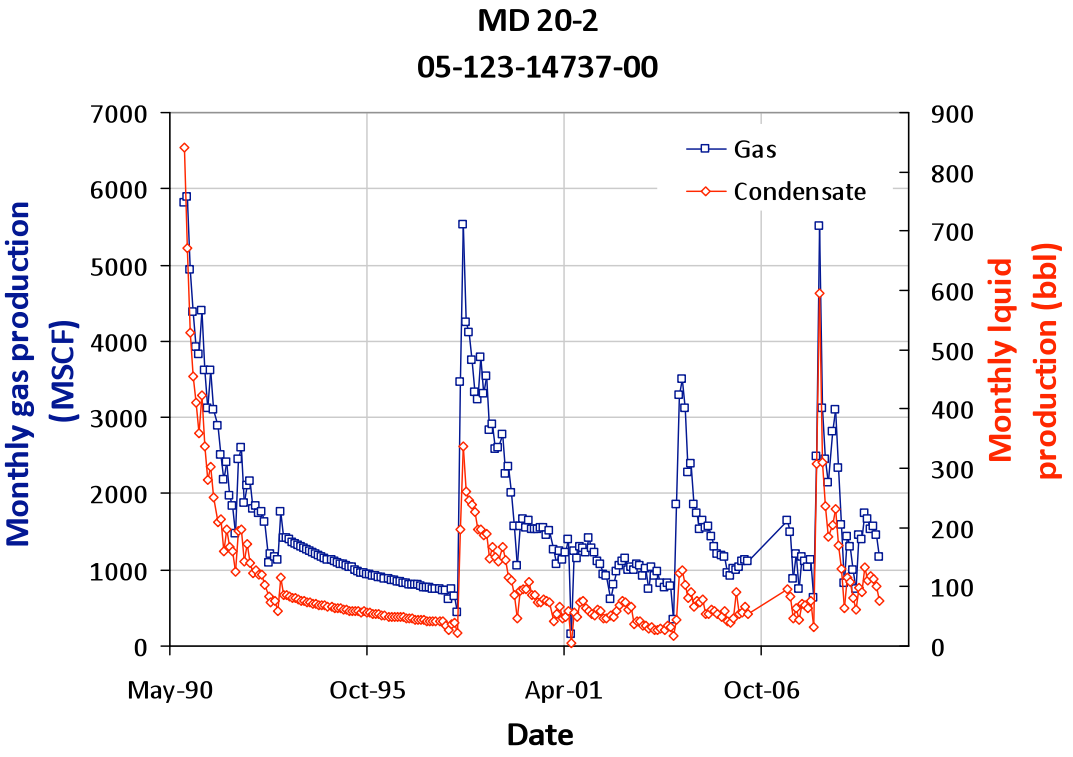
MD 20-2
05-123-14737-00
Monthly gas production (MSCF)
Monthly liquid production (bbl)
Gas
Condensate
7000
6000
5000
4000
3000
2000
1000
0
900
800
700
600
500
400
300
200
100
0
May-90
Oct-95
Apr-01
Oct-06
Date

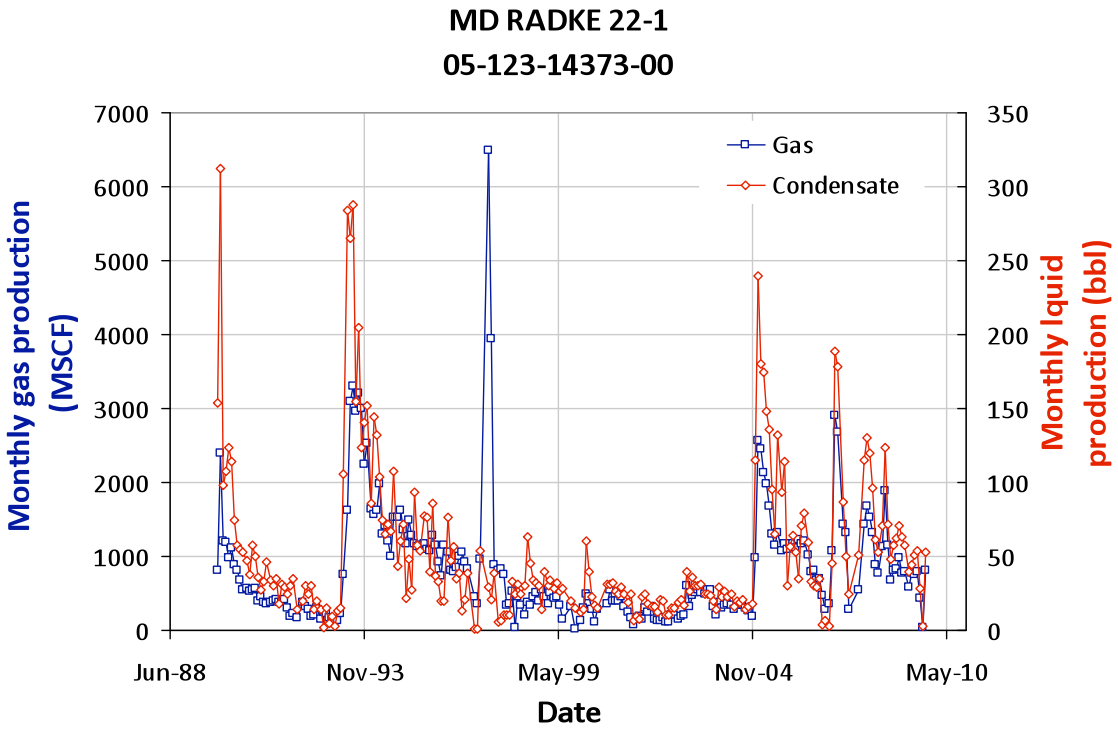
MD RADKE 22-1
05-123-14373-00
Monthly gas production (MSCF)
Monthly liquid production (bbl)
Gas
Condensate
7000
6000
5000
4000
3000
2000
1000
0
350
300
250
200
150
100
50
0
Jun-88
Nov-93
May-99
Nov-04
May-10
Date

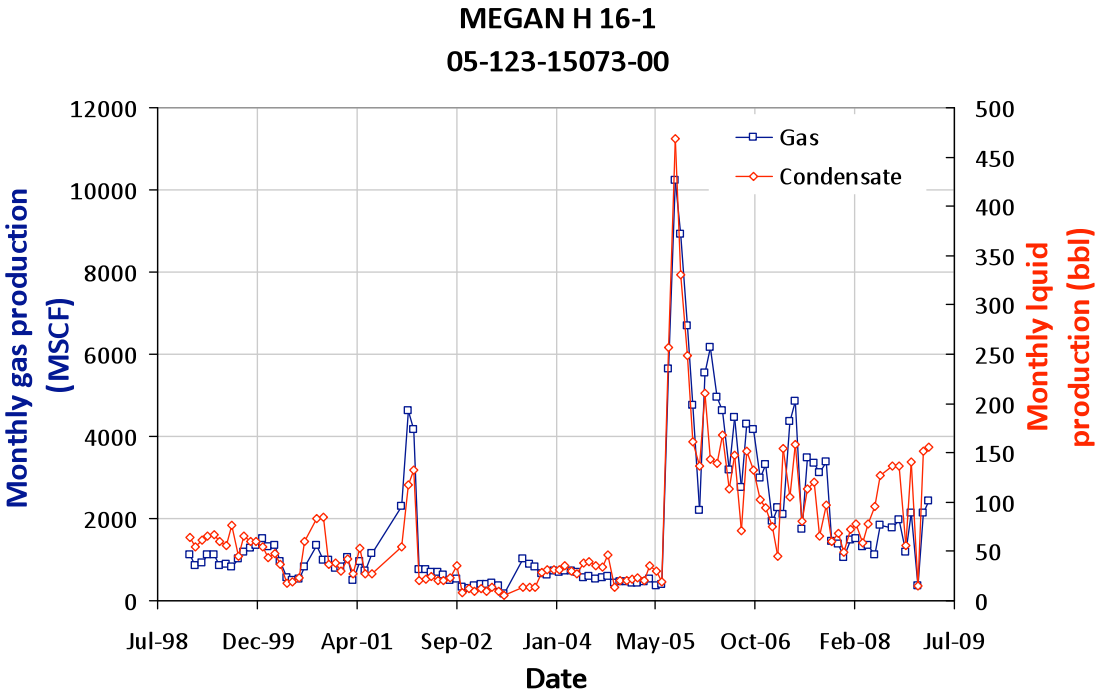
MEGAN H 16-1
05-123-15073-00
Monthly gas production (MSCF)
Monthly liquid production (bbl)
Gas
Condensate
12000
10000
8000
6000
4000
2000
0
500
450
400
350
300
250
200
150
100
50
0
Jul-98
Dec-99
Apr-01
Sep-02
Jan-04
May-05
Oct-06
Feb-08
Jul-09
Date

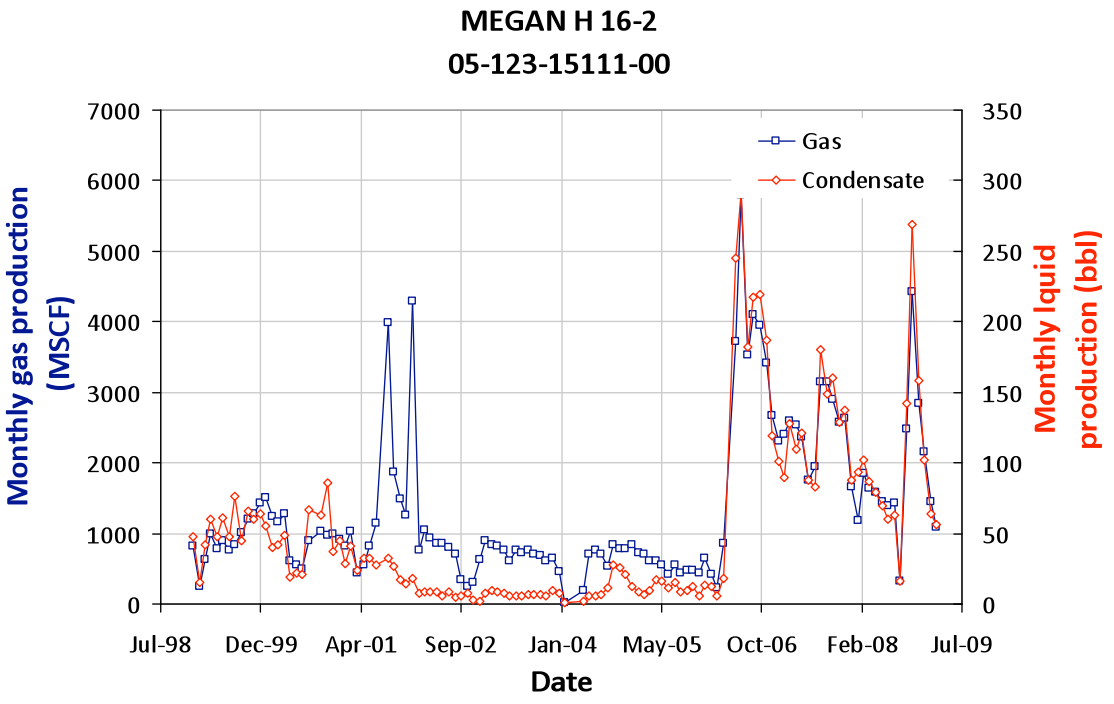
MEGAN H 16-2
05-123-15111-00
Monthly gas production (MSCF)
Monthly liquid production (bbl)
Gas
Condensate
7000
6000
5000
4000
3000
2000
1000
0
350
300
250
200
150
100
50
0
Jul-98
Dec-99
Apr-01
Sep-02
Jan-04
May-05
Oct-06
Feb-08
Jul-09
Date

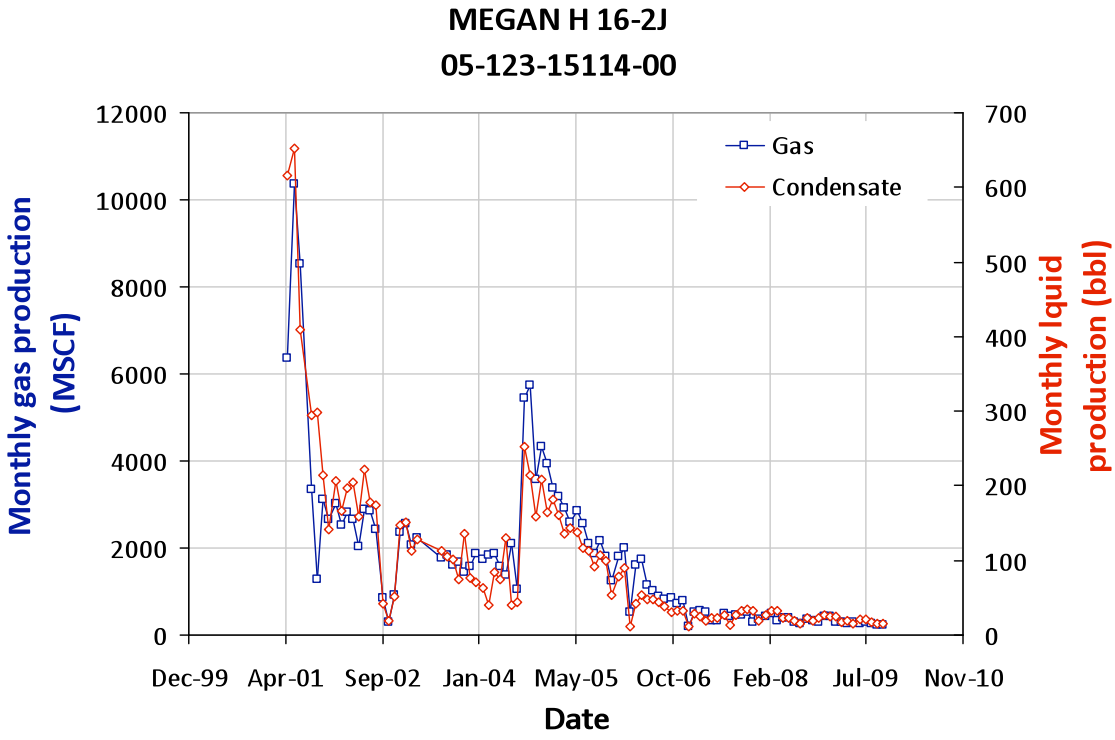
MEGAN H 16-2J
05-123-15114-00
Monthly gas production (MSCF)
Monthly liquid production (bbl)
Gas
Condensate
12000
10000
8000
6000
4000
2000
0
700
600
500
400
300
200
100
0
Dec-99
Apr-01
Sep-02
Jan-04
May-05
Oct-06
Feb-08
Jul-09
Nov-10
Date

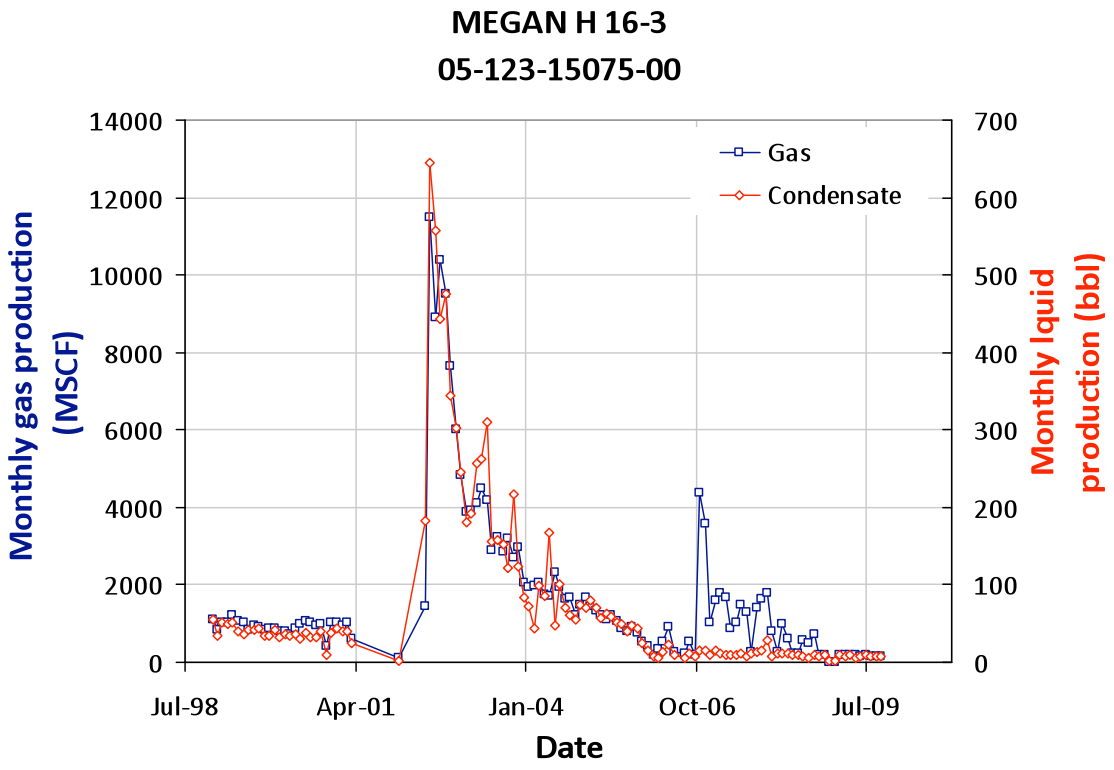
MEGAN H 16-3
05-123-15075-00
Monthly gas production (MSCF)
Monthly liquid production (bbl)
Gas
Condensate
14000
12000
10000
8000
6000
4000
2000
0
700
600
500
400
300
200
100
0
Jul-98
Apr-01
Jan-04
Oct-06
Jul-09
Date

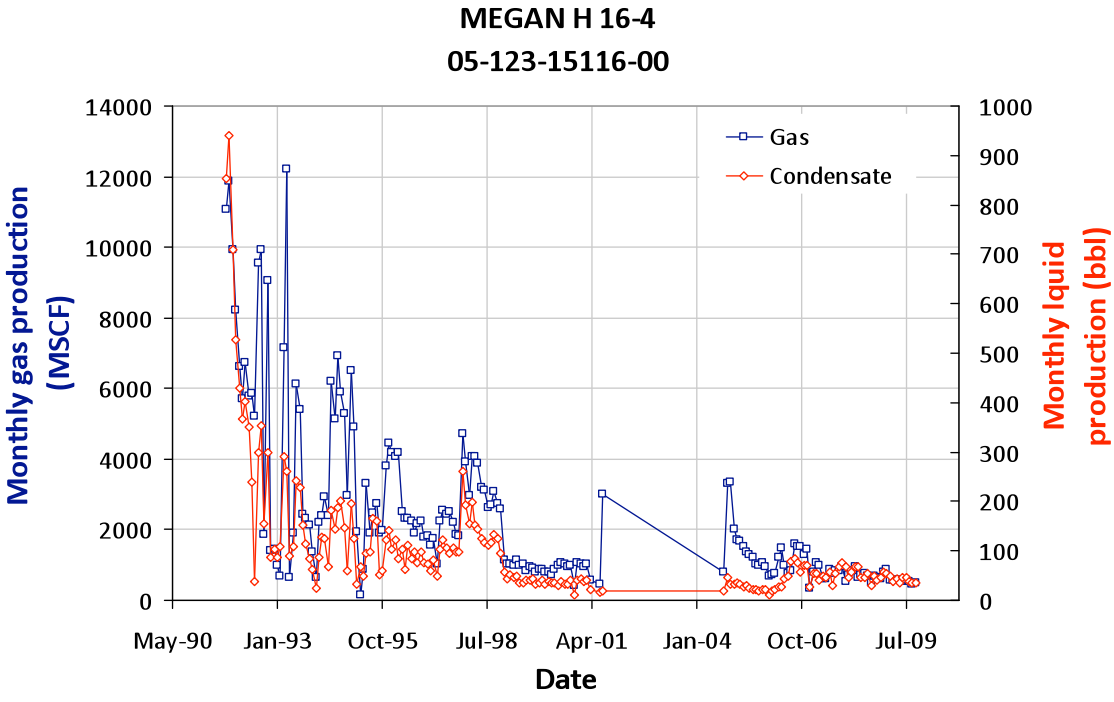
MEGAN H 16-4
05-123-15116-00
Monthly gas production (MSCF)
Monthly liquid production (bbl)
Gas
Condensate
14000
12000
10000
8000
6000
4000
2000
0
1000
900
800
700
600
500
400
300
200
100
0
May-90
Jan-93
Oct-95
Jul-98
Apr-01
Jan-04
Oct-06
Jul-09
Date

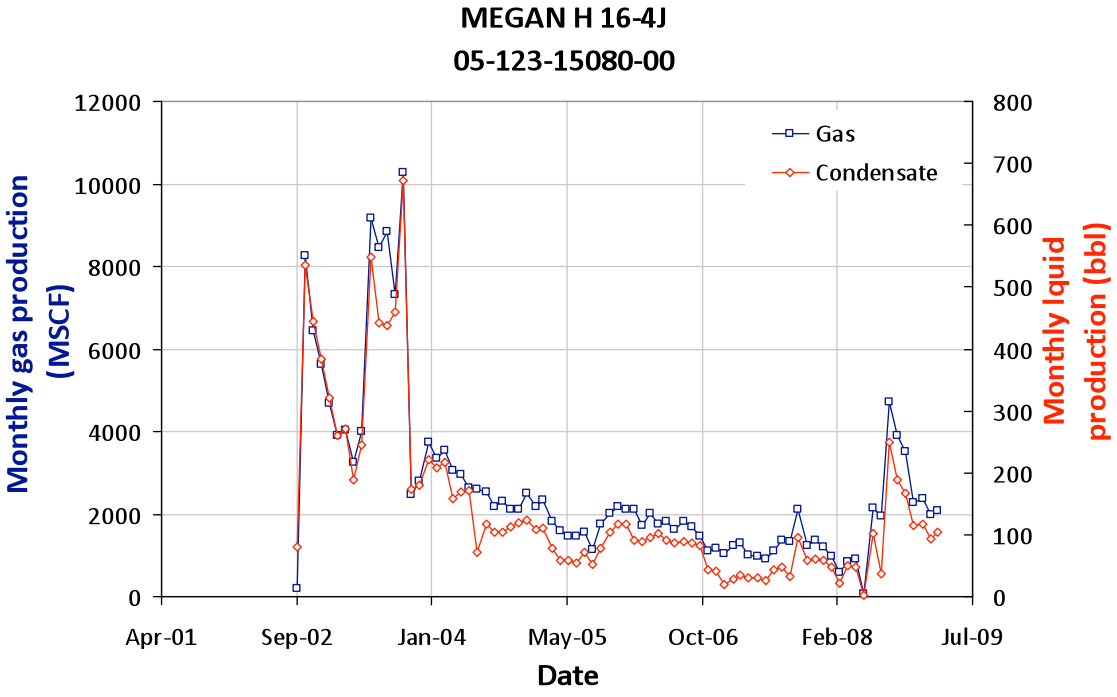
MEGAN H 16-4J
05-123-15080-00
Monthly gas production (MSCF)
Monthly liquid production (bbl)
Gas
Condensate
12000
10000
8000
6000
4000
2000
0
800
700
600
500
400
300
200
100
0
Apr-01
Sep-02
Jan-04
May-05
Oct-06
Feb-08
Jul-09
Date

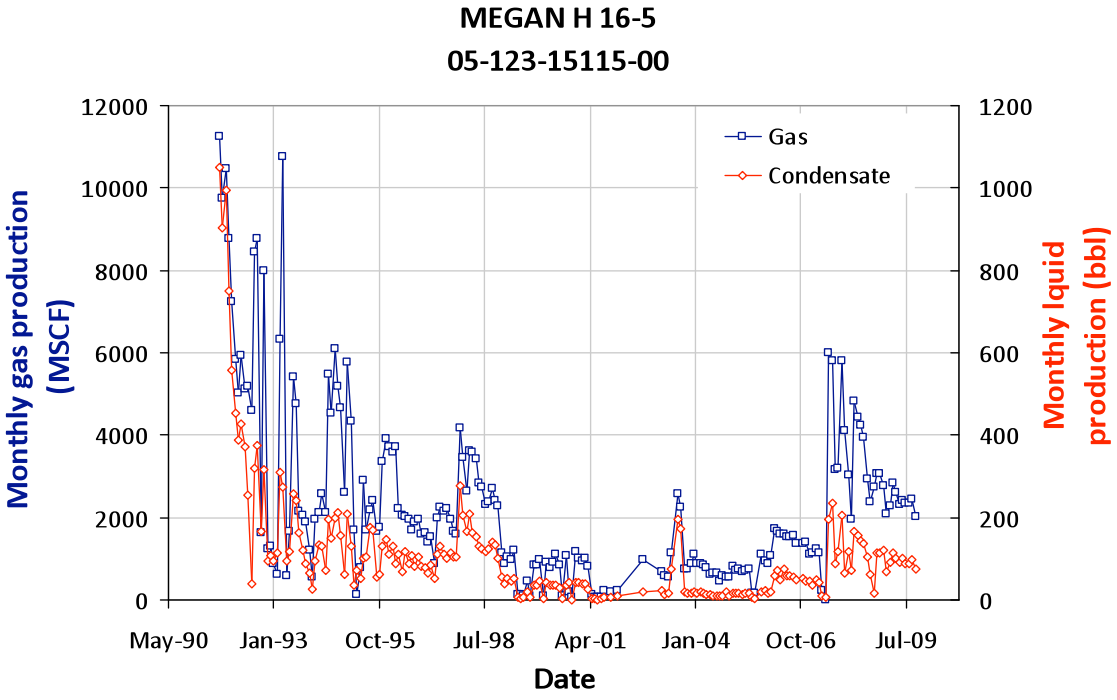
MEGAN H 16-5
05-123-15115-00
Monthly gas production (MSCF)
Monthly liquid production (bbl)
Gas
Condensate
12000
10000
8000
6000
4000
2000
0
1200
1000
800
600
400
200
0
May-90
Jan-93
Oct-95
Jul-98
Apr-01
Jan-04
Oct-06
Jul-09
Date

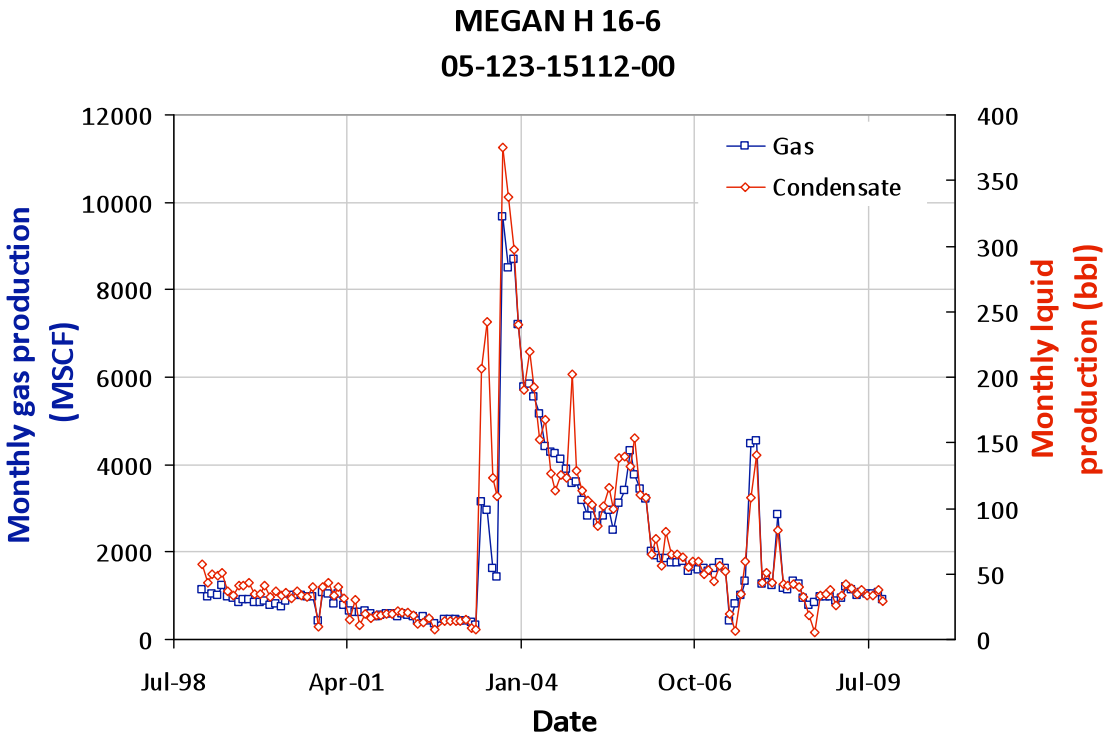
MEGAN H 16-6
05-123-15112-00
Monthly gas production (MSCF)
Monthly liquid production (bbl)
Gas
Condensate
12000
10000
8000
6000
4000
2000
0
400
350
300
250
200
150
100
50
0
Jul-98
Apr-01
Jan-04
Oct-06
Jul-09
Date

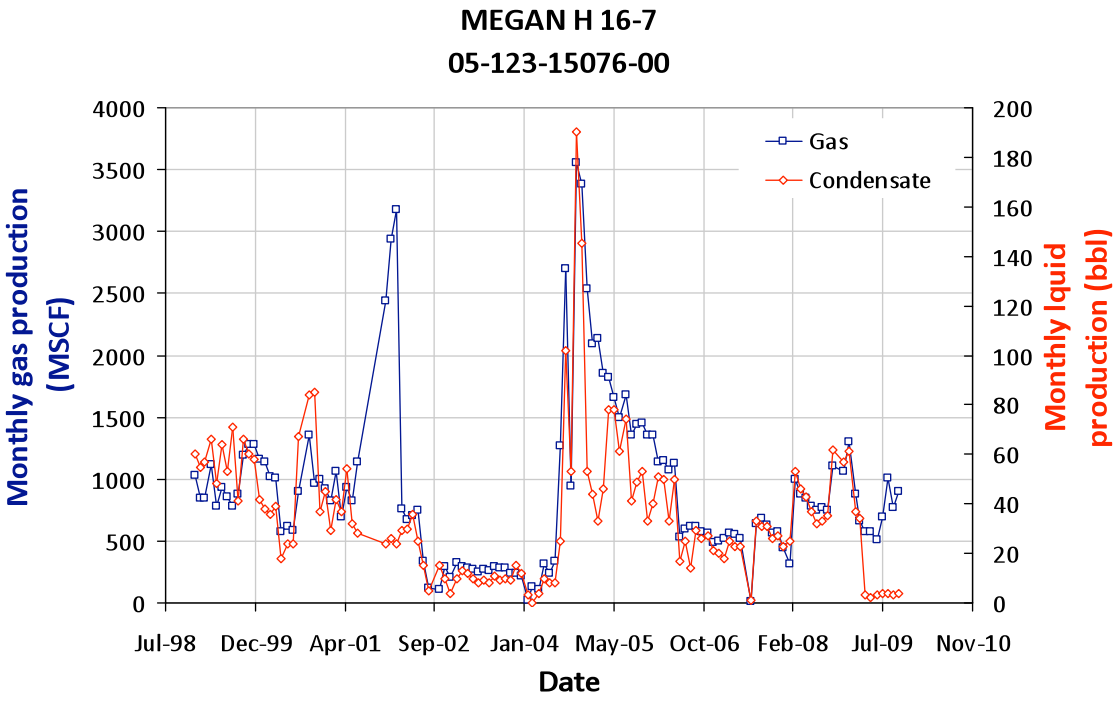
MEGAN H 16-7
05-123-15076-00
Monthly gas production (MSCF)
Monthly liquid production (bbl)
Gas
Condensate
4000
3500
3000
2500
2000
1500
1000
500
0
200
180
160
140
120
100
80
60
40
20
0
Jul-98
Dec-99
Apr-01
Sep-02
Jan-04
May-05
Oct-06
Feb-08
Jul-09
Nov-10
Date

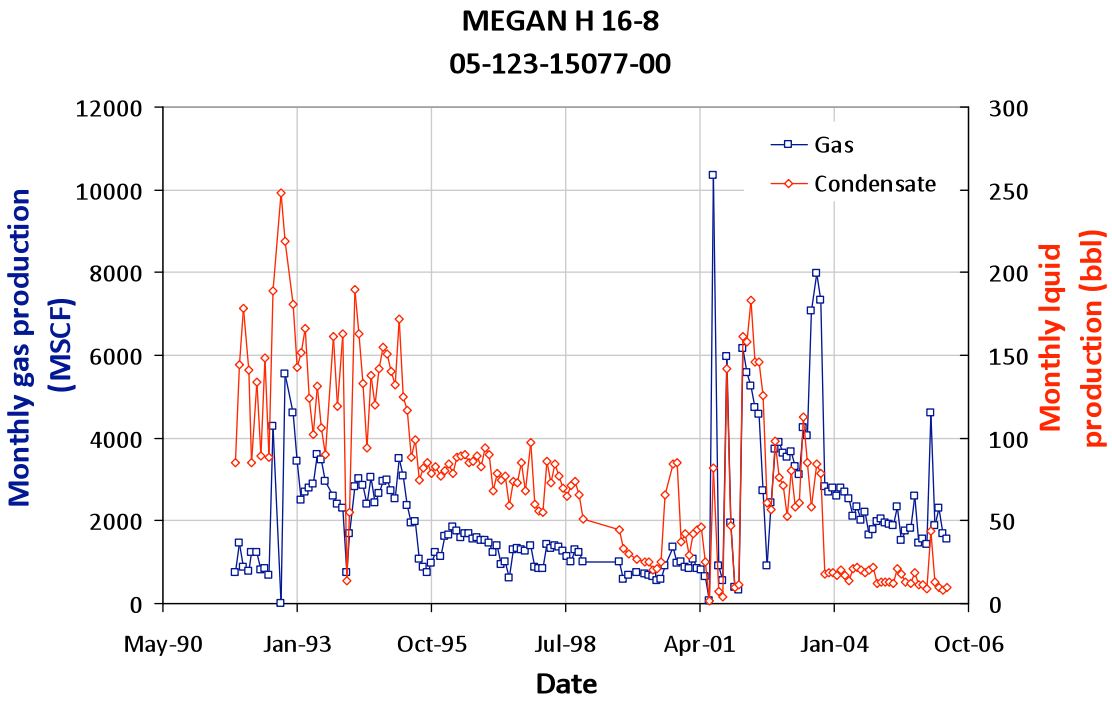
MEGAN H 16-8
05-123-15077-00
Monthly gas production (MSCF)
Monthly liquid production (bbl)
Gas
Condensate
12000
10000
8000
6000
4000
2000
0
300
250
200
150
100
50
0
May-90
Jan-93
Oct-95
Jul-98
Apr-01
Jan-04
Oct-06
Date

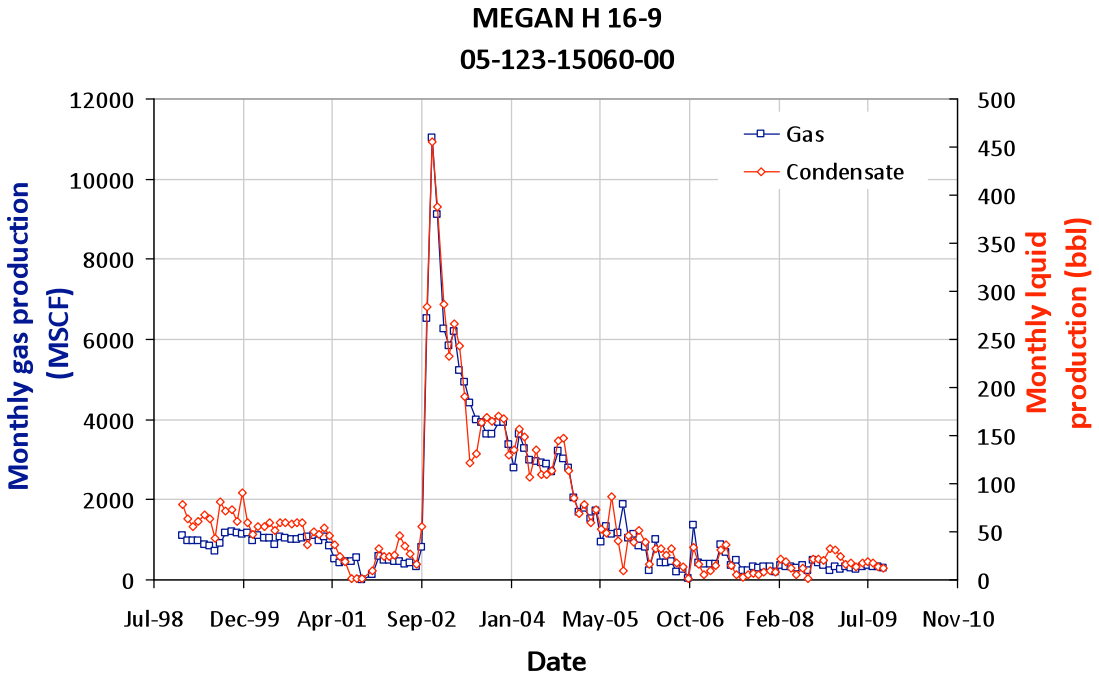
MEGAN H 16-9
05-123-15060-00
Monthly gas production (MSCF)
Monthly liquid production (bbl)
Gas
Condensate
12000
10000
8000
6000
4000
2000
0
500
450
400
350
300
250
200
150
100
50
0
Jul-98
Dec-99
Apr-01
Sep-02
Jan-04
May-05
Oct-06
Feb-08
Jul-09
Nov-10
Date

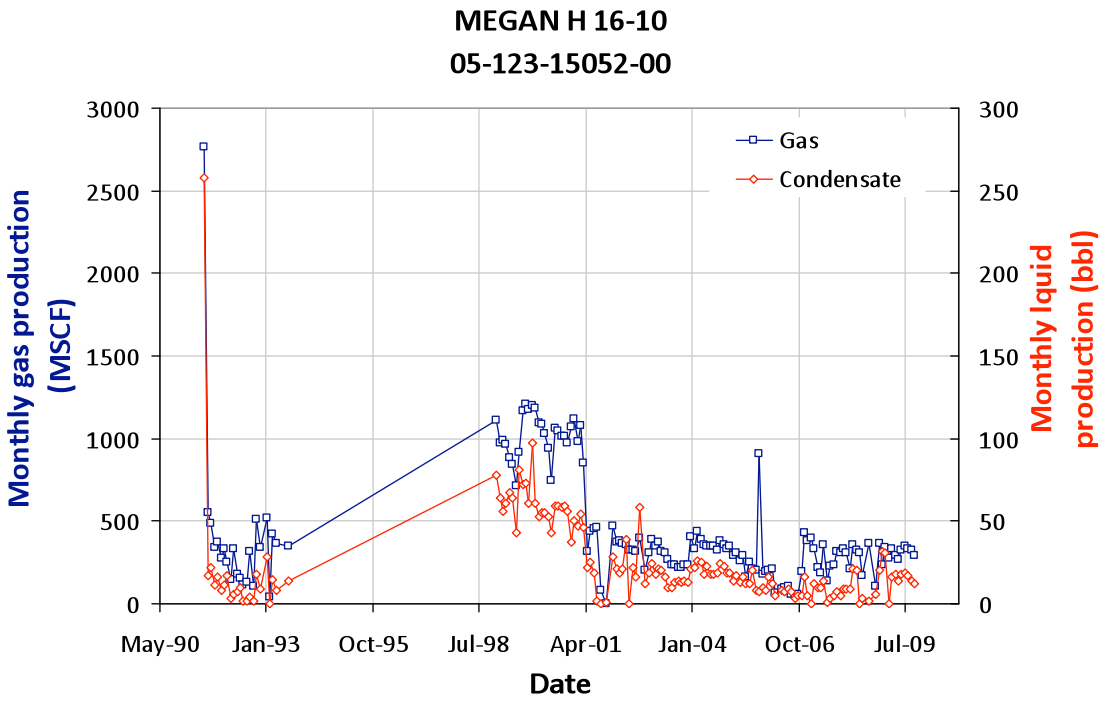
MEGAN H 16-10
05-123-15052-00
Monthly gas production (MSCF)
Monthly liquid production (bbl)
Gas
Condensate
3000
2500
2000
1500
1000
500
0
300
250
200
150
100
50
0
May-90
Jan-93
Oct-95
Jul-98
Apr-01
Jan-04
Oct-06
Jul-09
Date

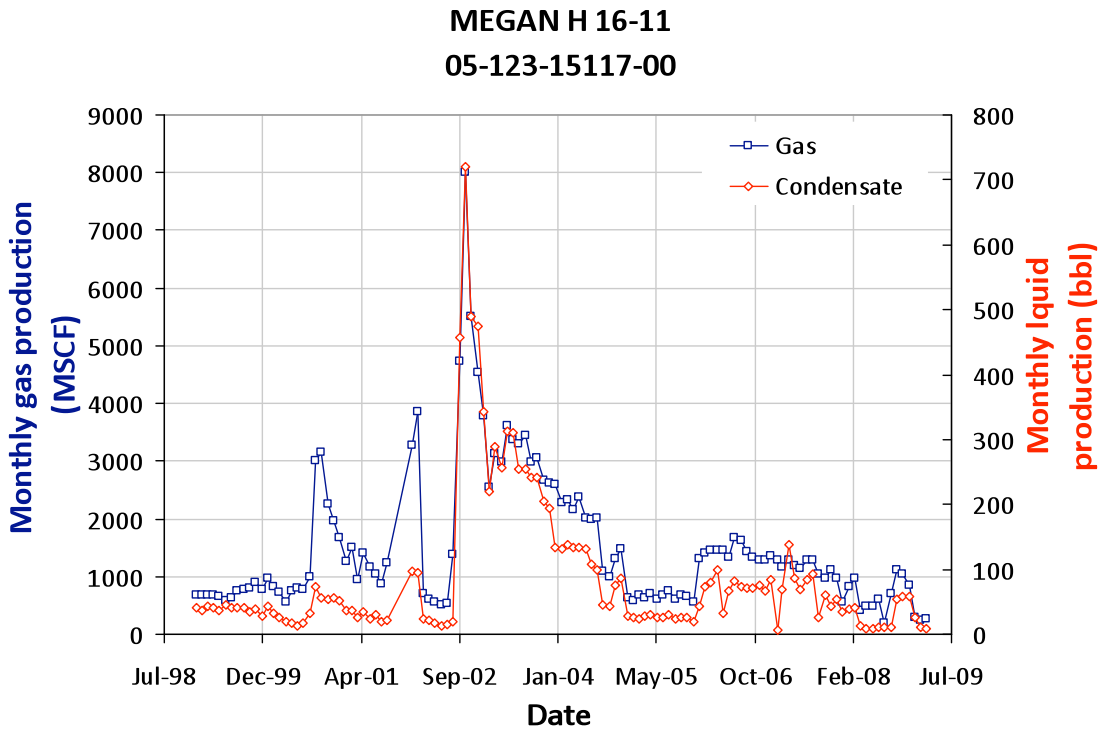
MEGAN H 16-11
05-123-15117-00
Monthly gas production (MSCF)
Monthly liquid production (bbl)
Gas
Condensate
9000
8000
7000
6000
5000
4000
3000
2000
1000
0
800
700
600
500
400
300
200
100
0
Jul-98
Dec-99
Apr-01
Sep-02
Jan-04
May-05
Oct-06
Feb-08
Jul-09
Date

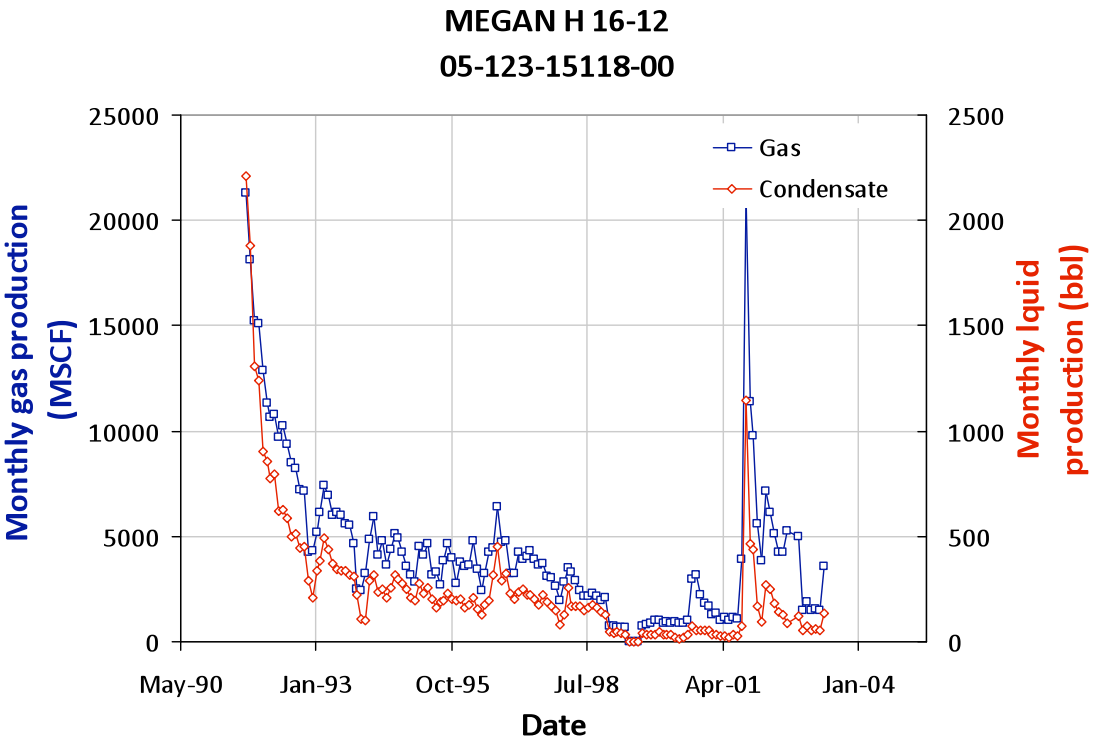
MEGAN H 16-12
05-123-15118-00
Monthly gas production (MSCF)
Monthly liquid production (bbl)
Gas
Condensate
25000
20000
15000
10000
5000
0
2500
2000
1500
1000
500
0
May-90
Jan-93
Oct-95
Jul-98
Apr-01
Jan-04
Date

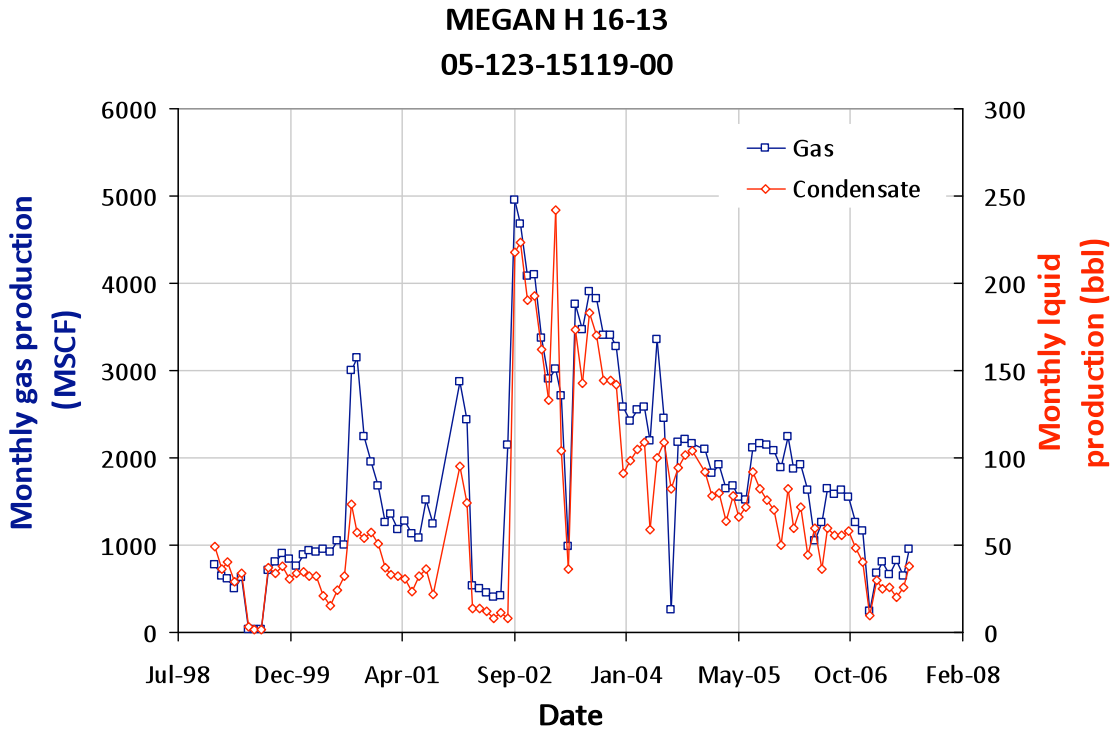
MEGAN H 16-13
05-123-15119-00
Monthly gas production (MSCF)
Monthly liquid production (bbl)
Gas
Condensate
6000
5000
4000
3000
2000
1000
0
300
250
200
150
100
50
0
Jul-98
Dec-99
Apr-01
Sep-02
Jan-04
May-05
Oct-06
Feb-08
Date

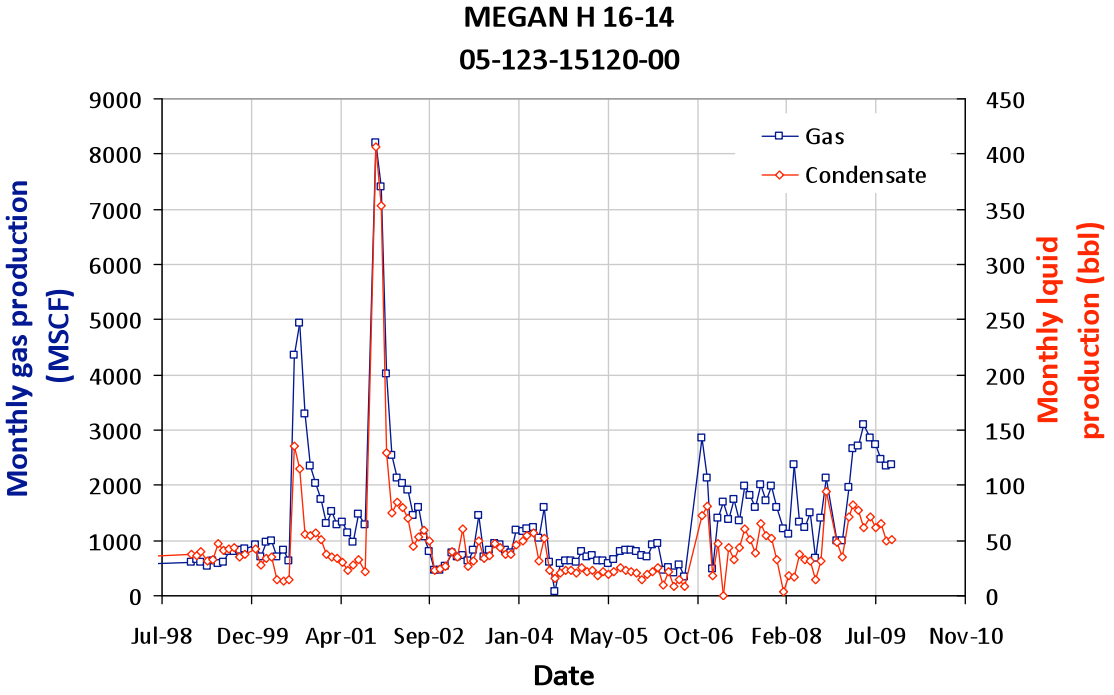
MEGAN H 16-14
05-123-15120-00
Monthly gas production (MSCF)
Monthly liquid production (bbl)
Gas
Condensate
9000
8000
7000
6000
5000
4000
3000
2000
1000
0
450
400
350
300
250
200
150
100
50
0
Jul-98
Dec-99
Apr-01
Sep-02
Jan-04
May-05
Oct-06
Feb-08
Jul-09
Nov-10
Date

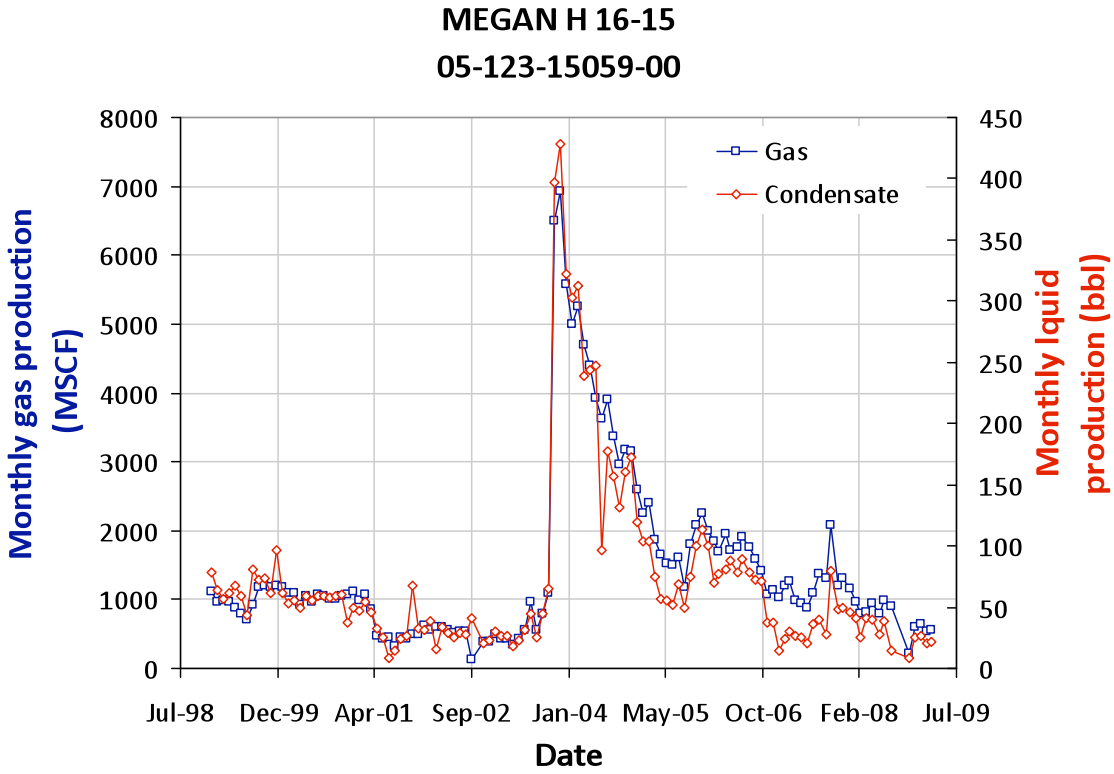
MEGAN H 16-15
05-123-15059-00
Monthly gas production (MSCF)
Monthly liquid production (bbl)
Gas
Condensate
8000
7000
6000
5000
4000
3000
2000
1000
0
450
400
350
300
250
200
150
100
50
0
Jul-98
Dec-99
Apr-01
Sep-02
Jan-04
May-05
Oct-06
Feb-08
Jul-09
Date

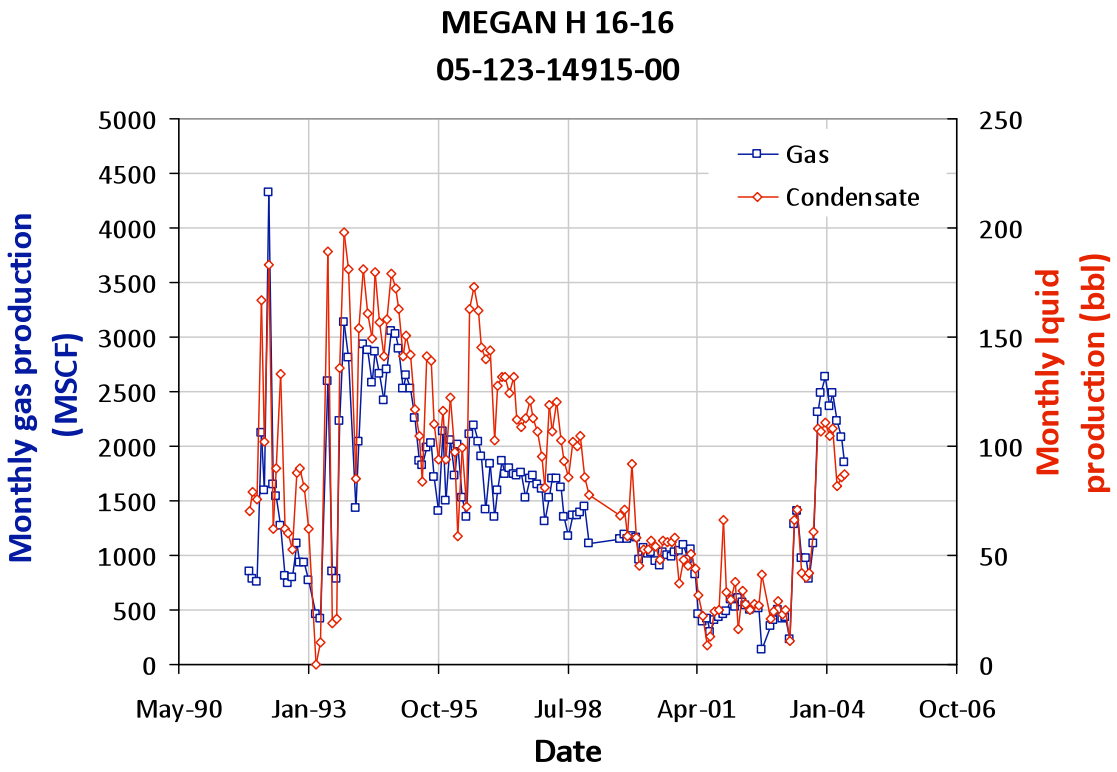
MEGAN H 16-16
05-123-14915-00
Monthly gas production (MSCF)
Monthly liquid production (bbl)
Gas
Condensate
5000
4500
4000
3500
3000
2500
2000
1500
1000
500
0
250
200
150
100
50
0
May-90
Jan-93
Oct-95
Jul-98
Apr-01
Jan-04
Oct-06
Date

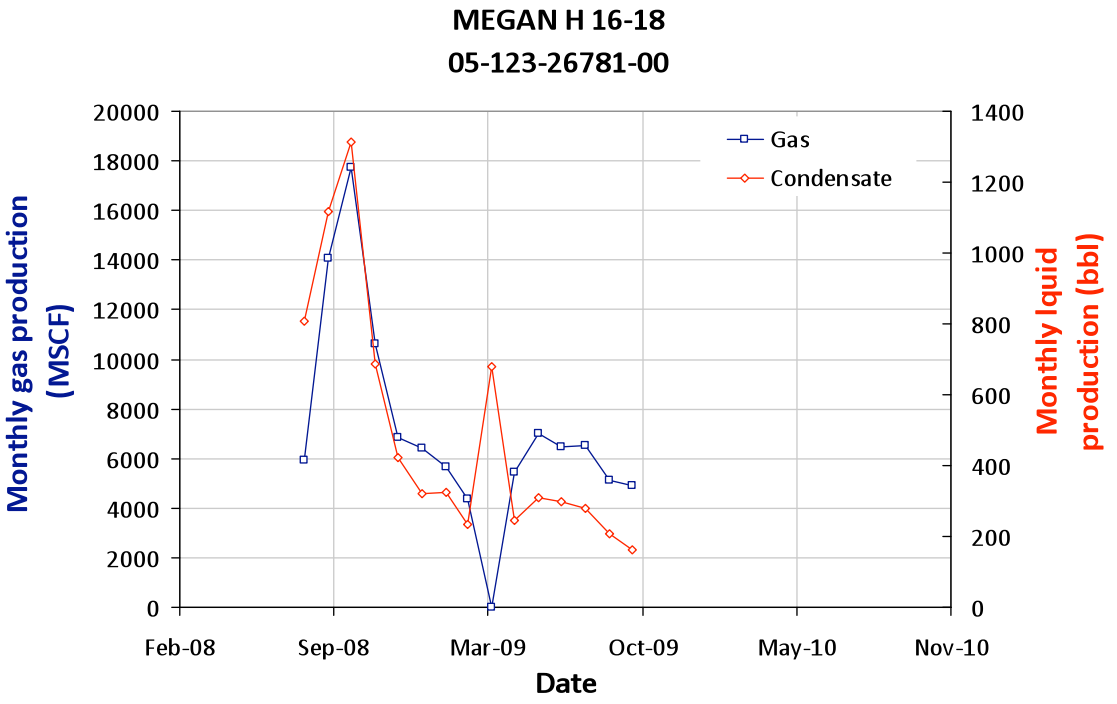
MEGAN H 16-18
05-123-26781-00
Monthly gas production (MSCF)
Monthly liquid production (bbl)
Gas
Condensate
20000
18000
16000
14000
12000
10000
8000
6000
4000
2000
0
1400
1200
1000
800
600
400
200
0
Feb-08
Sep-08
Mar-09
Oct-09
May-10
Nov-10
Date

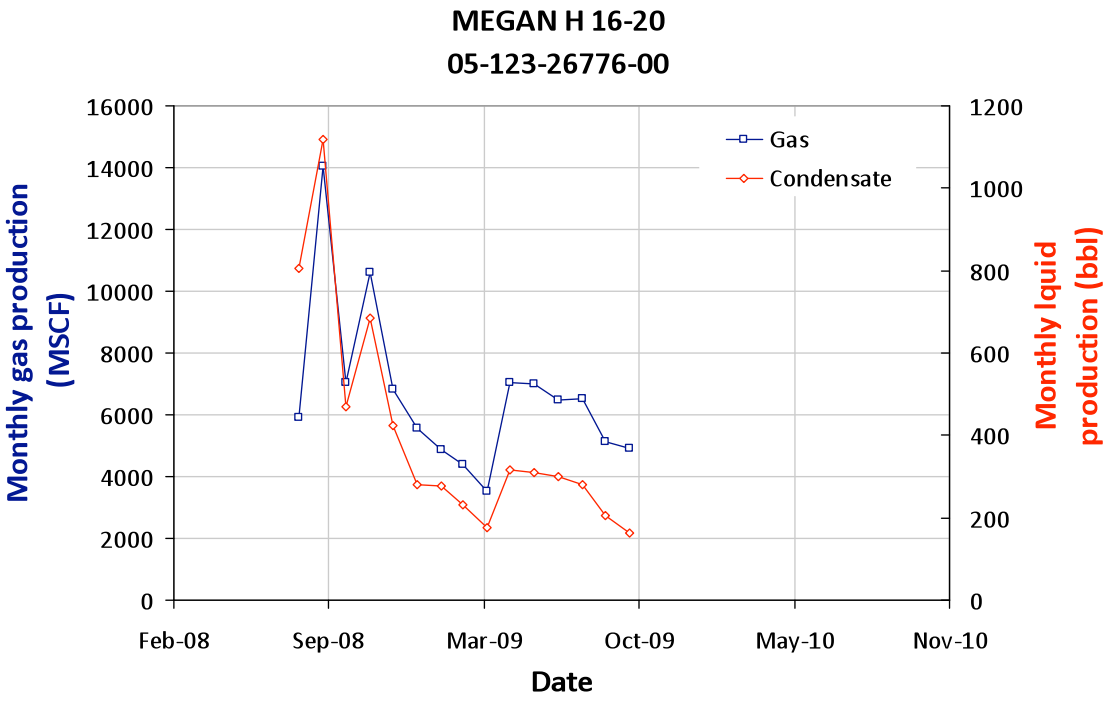
MEGAN H 16-20
05-123-26776-00
Monthly gas production (MSCF)
Monthly liquid production (bbl)
Gas
Condensate
16000
14000
12000
10000
8000
6000
4000
2000
0
1200
1000
800
600
400
200
0
Feb-08
Sep-08
Mar-09
Oct-09
May-10
Nov-10
Date

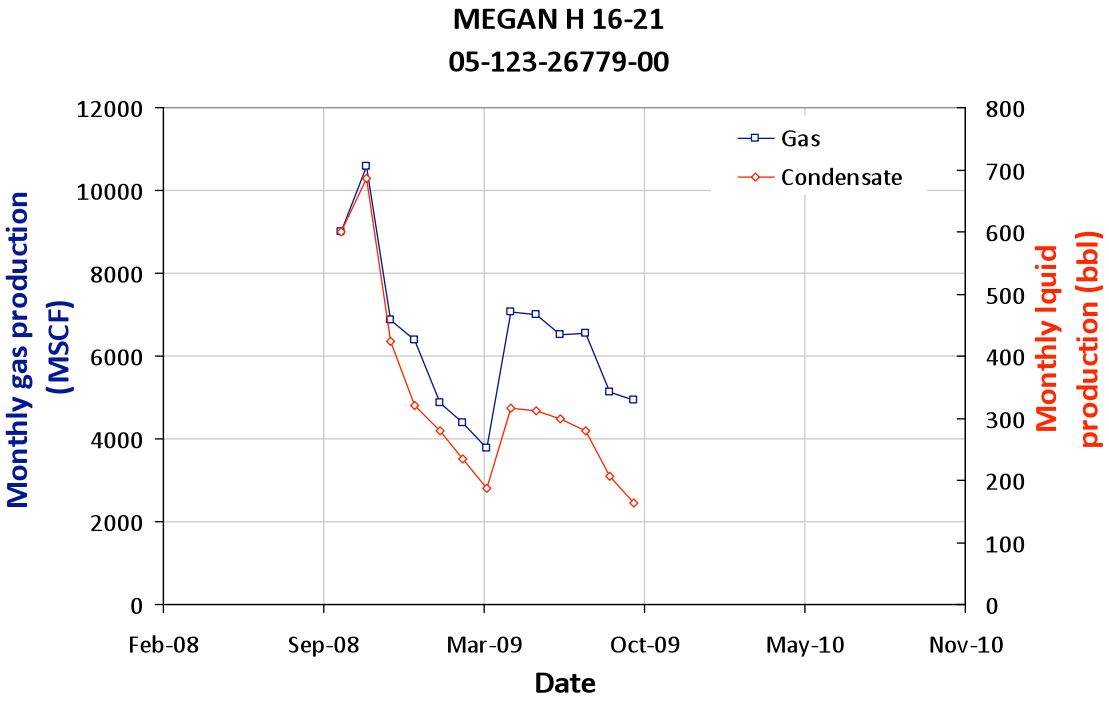
MEGAN H 16-21
05-123-26779-00
Monthly gas production (MSCF)
Monthly liquid production (bbl)
Gas
Condensate
12000
10000
8000
6000
4000
2000
0
800
700
600
500
400
300
200
100
0
Feb-08
Sep-08
Mar-09
Oct-09
May-10
Nov-10
Date

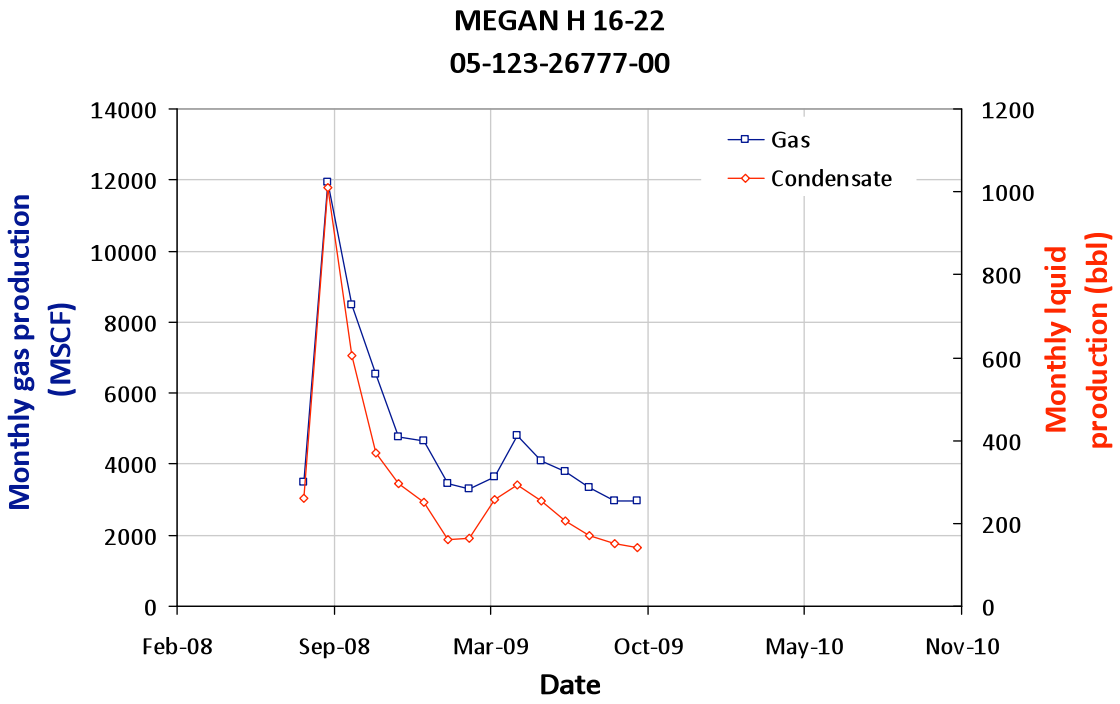
MEGAN H 16-22
05-123-26777-00
Monthly gas production (MSCF)
Monthly liquid production (bbl)
Gas
Condensate
14000
12000
10000
8000
6000
4000
2000
0
1200
1000
800
600
400
200
0
Feb-08
Sep-08
Mar-09
Oct-09
May-10
Nov-10
Date

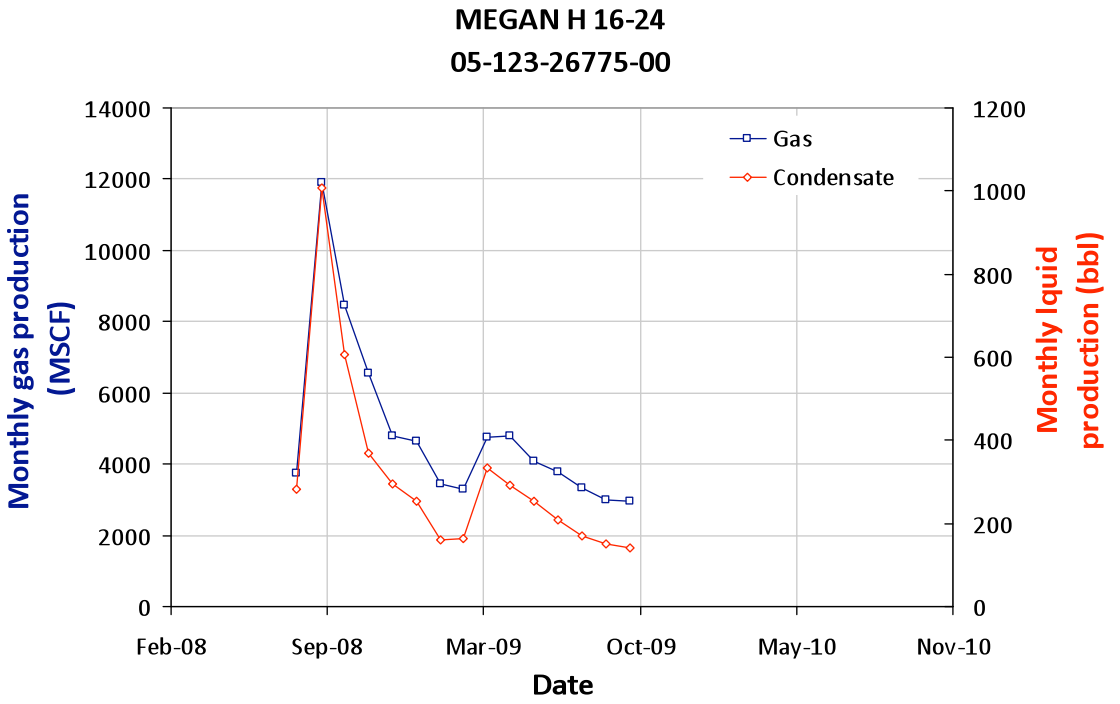
MEGAN H 16-24
05-123-26775-00
Monthly gas production (MSCF)
Monthly liquid production (bbl)
Gas
Condensate
14000
12000
10000
8000
6000
4000
2000
0
1200
1000
800
600
400
200
0
Feb-08
Sep-08
Mar-09
Oct-09
May-10
Nov-10
Date

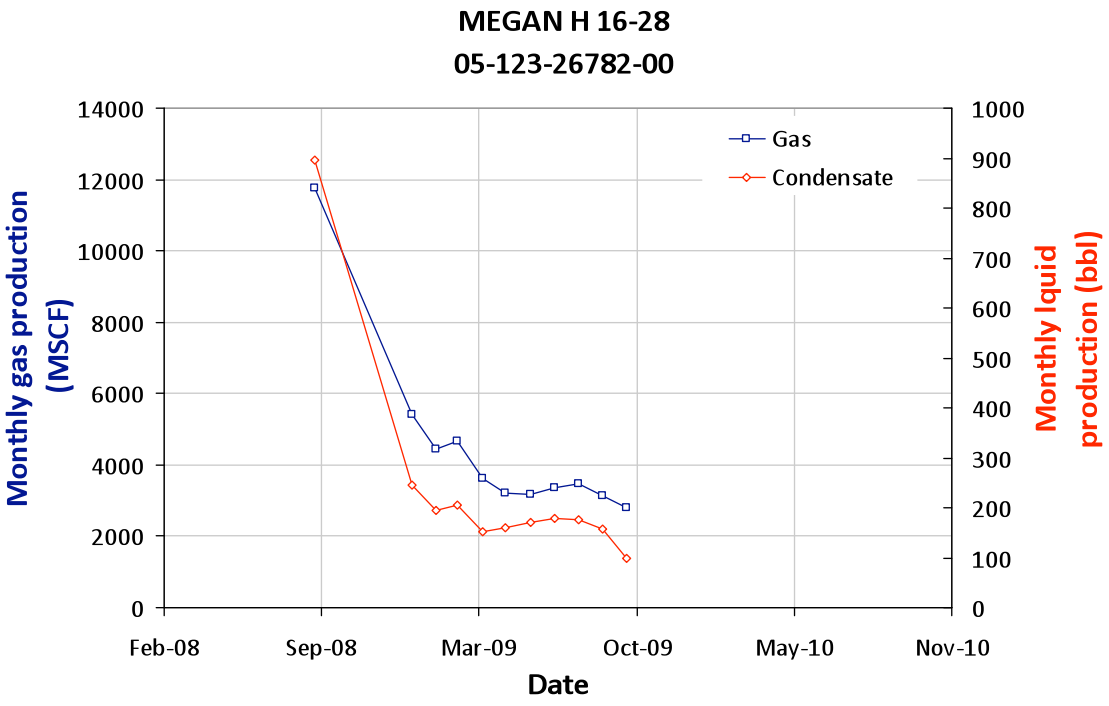
MEGAN H 16-28
05-123-26782-00
Monthly gas production (MSCF)
Monthly liquid production (bbl)
Gas
Condensate
14000
12000
10000
8000
6000
4000
2000
0
1000
900
800
700
600
500
400
300
200
100
0
Feb-08
Sep-08
Mar-09
Oct-09
May-10
Nov-10
Date

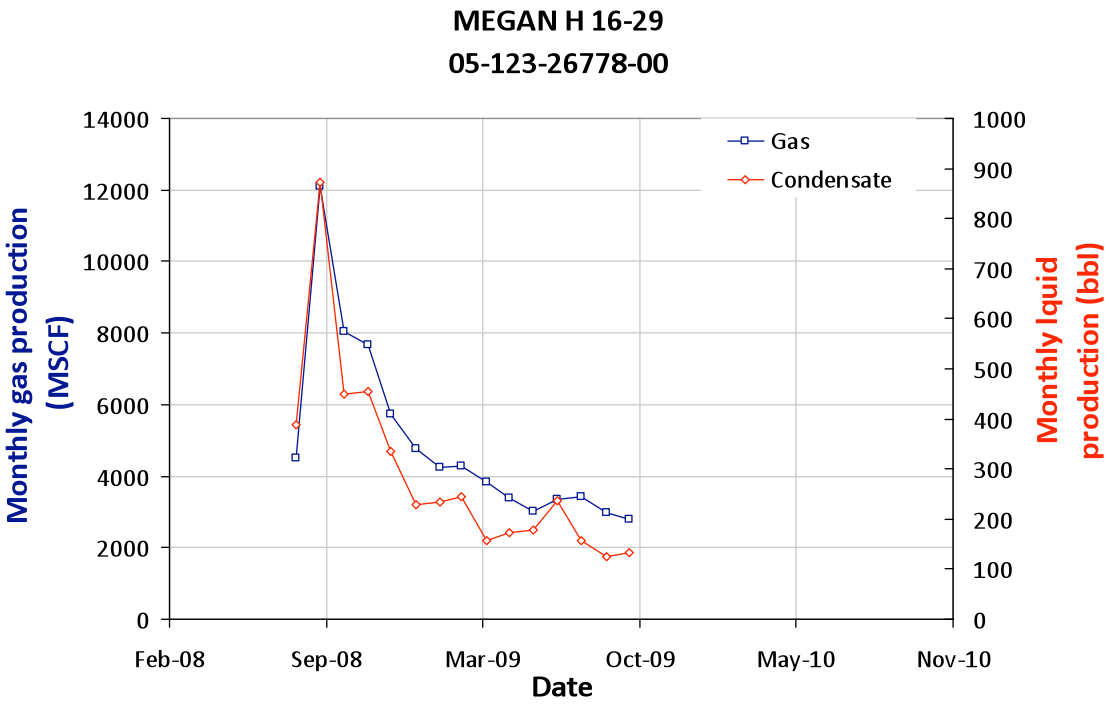
MEGAN H 16-29
05-123-26778-00
Monthly gas production (MSCF)
Monthly liquid production (bbl)
Gas
Condensate
14000
12000
10000
8000
6000
4000
2000
0
1000
900
800
700
600
500
400
300
200
100
0
Feb-08
Sep-08
Mar-09
Oct-09
May-10
Nov-10
Date

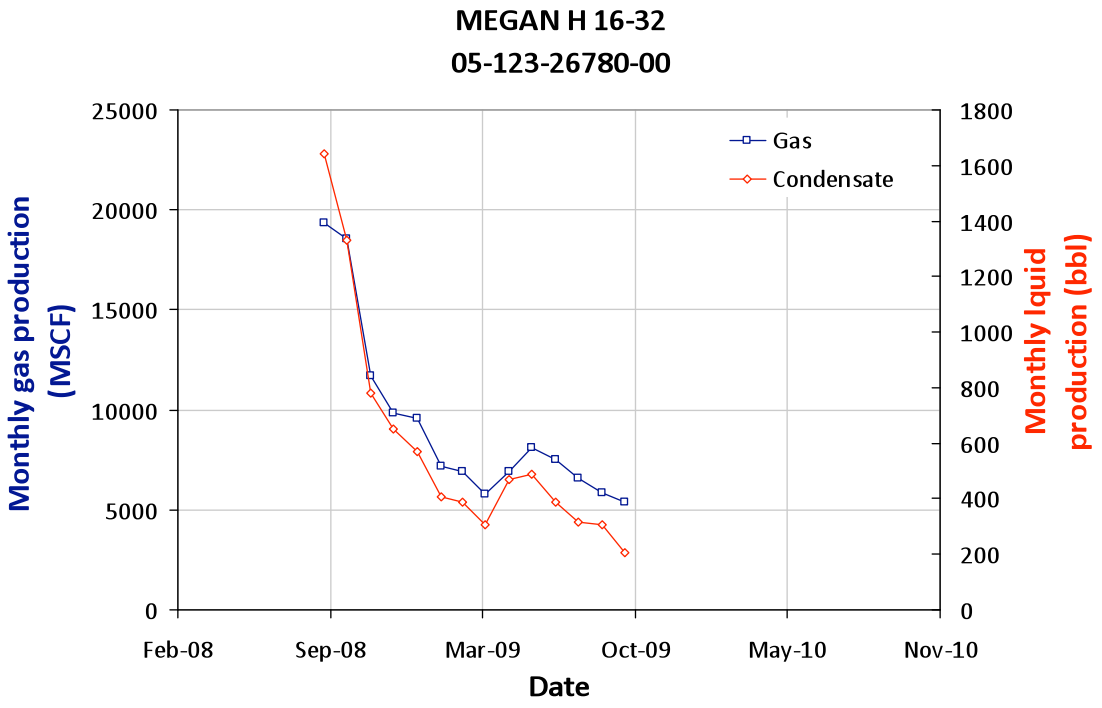
MEGAN H 16-32
05-123-26780-00
Monthly gas production (MSCF)
Monthly liquid production (bbl)
Gas
Condensate
25000
20000
15000
10000
5000
0
1800
1600
1400
1200
1000
800
600
400
200
0
Feb-08
Sep-08
Mar-09
Oct-09
May-10
Nov-10
Date

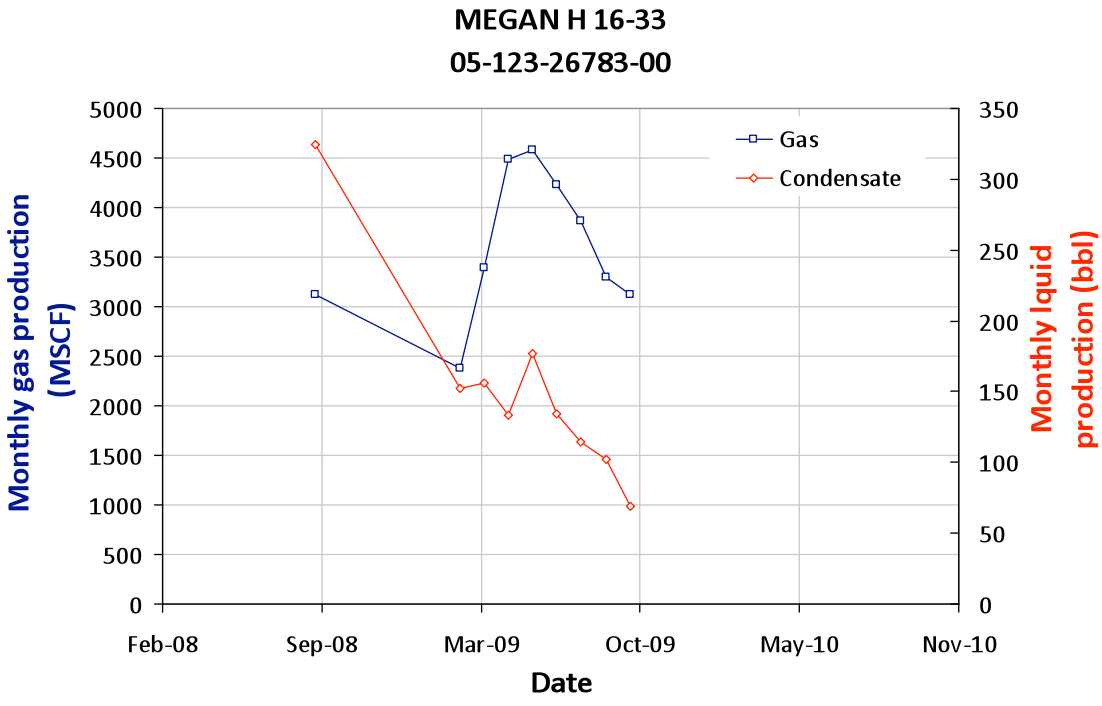
MEGAN H 16-33
05-123-26783-00
Monthly gas production (MSCF)
Monthly liquid production (bbl)
Gas
Condensate
5000
4500
4000
3500
3000
2500
2000
1500
1000
500
0
350
300
250
200
150
100
50
0
Feb-08
Sep-08
Mar-09
Oct-09
May-10
Nov-10
Date

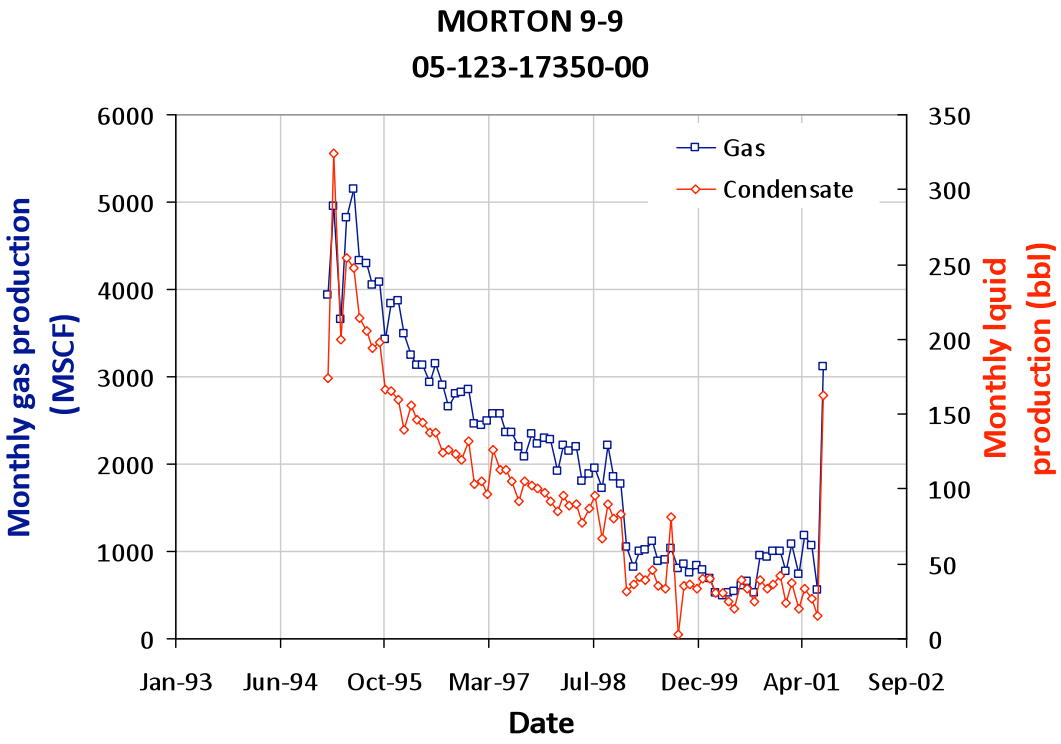
MORTON 9-9
05-123-17350-00
Gas
Condensate
Monthly gas production (MSCF)
Monthly liquid production (bbl)
6000
5000
4000
3000
2000
1000
0
350
300
250
200
150
100
50
0
Jan-93
Jun-94
Oct-95
Mar-97
Jul-98
Dec-99
Apr-01
Sep-02
Date

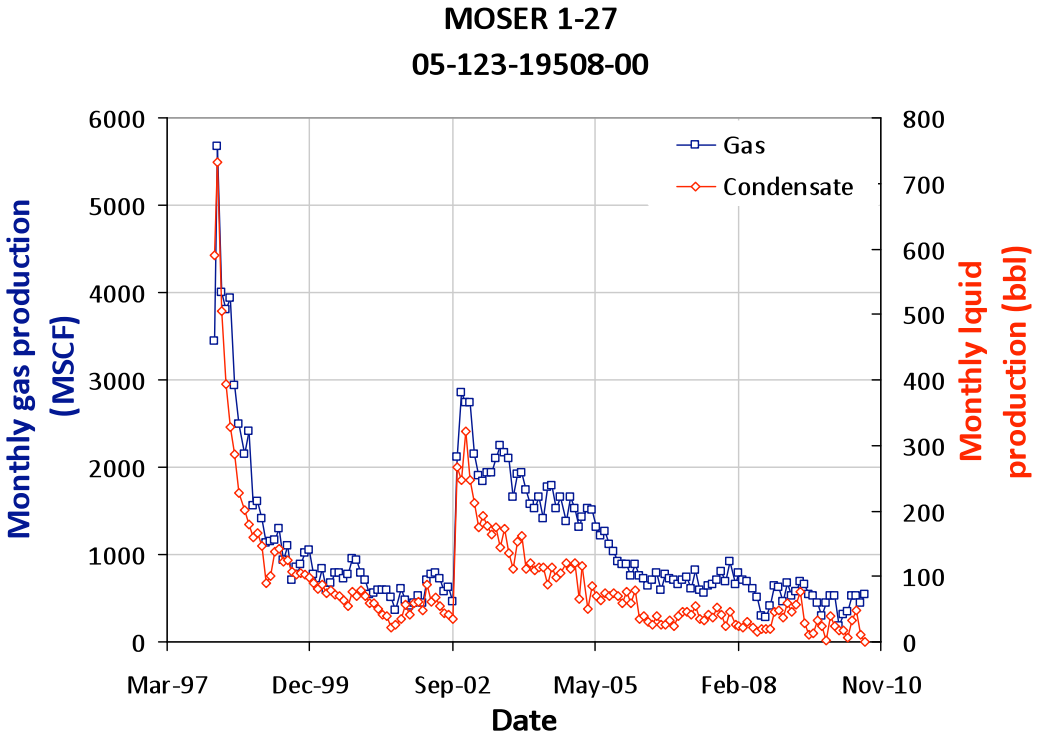
MOSER 1-27
05-123-19508-00
Gas
Condensate
Monthly gas production (MSCF)
Monthly liquid production (bbl)
6000
5000
4000
3000
2000
1000
0
800
700
600
500
400
300
200
100
0
Mar-97
Dec-99
Sep-02
May-05
Feb-08
Nov-10
Date

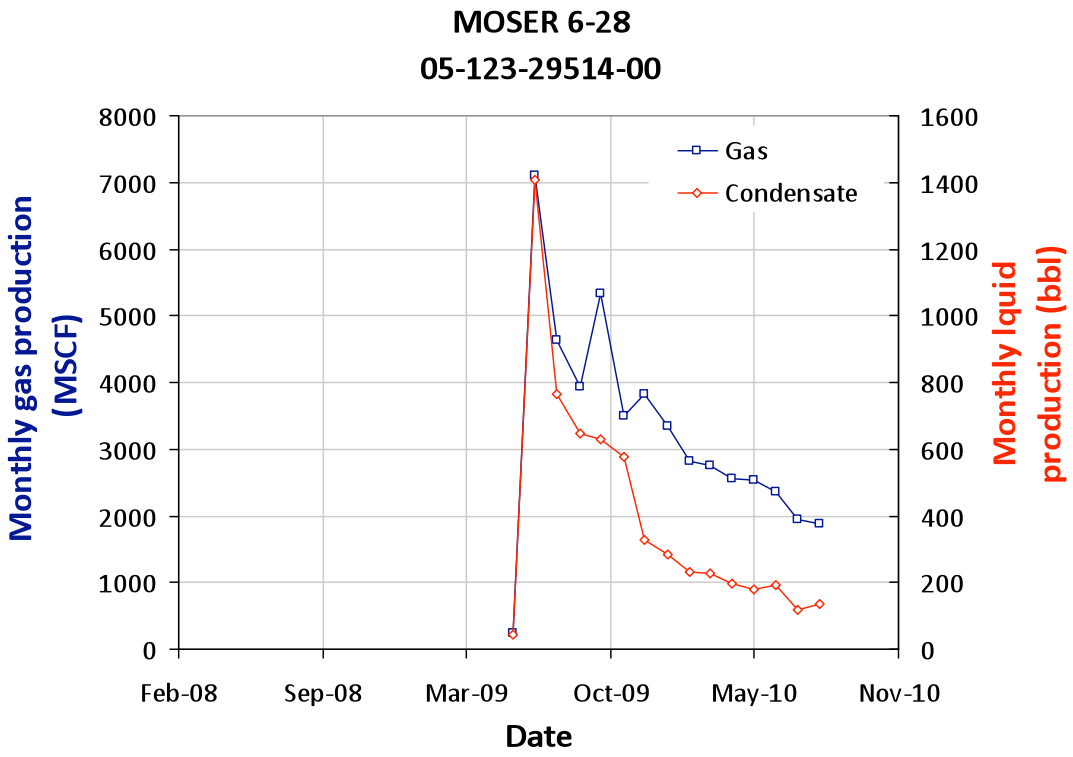
MOSER 6-28
05-123-29514-00
Monthly gas production (MSCF)
Monthly liquid production (bbl)
Gas
Condensate
8000
7000
6000
5000
4000
3000
2000
1000
0
1600
1400
1200
1000
800
600
400
200
0
Feb-08
Sep-08
Mar-09
Oct-09
May-10
Nov-10
Date

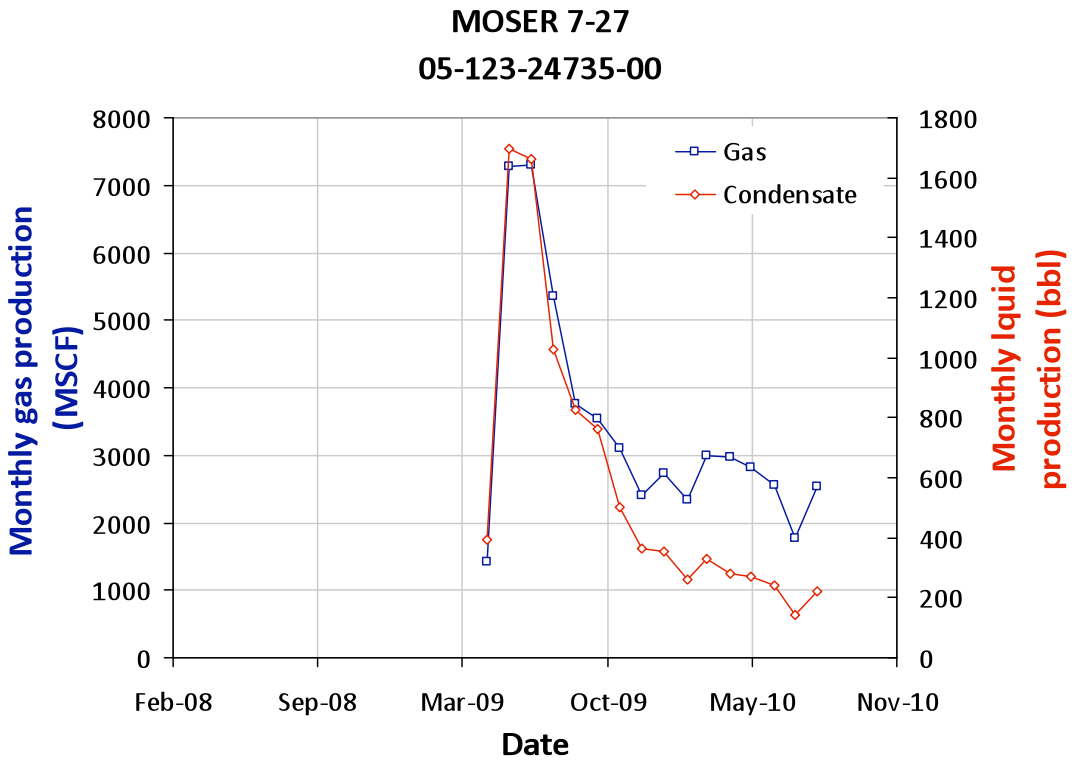
MOSER 7-27
05-123-24735-00
Monthly gas production (MSCF)
Monthly liquid production (bbl)
Gas
Condensate
8000
7000
6000
5000
4000
3000
2000
1000
0
1800
1600
1400
1200
1000
800
600
400
200
0
Feb-08
Sep-08
Mar-09
Oct-09
May-10
Nov-10
Date

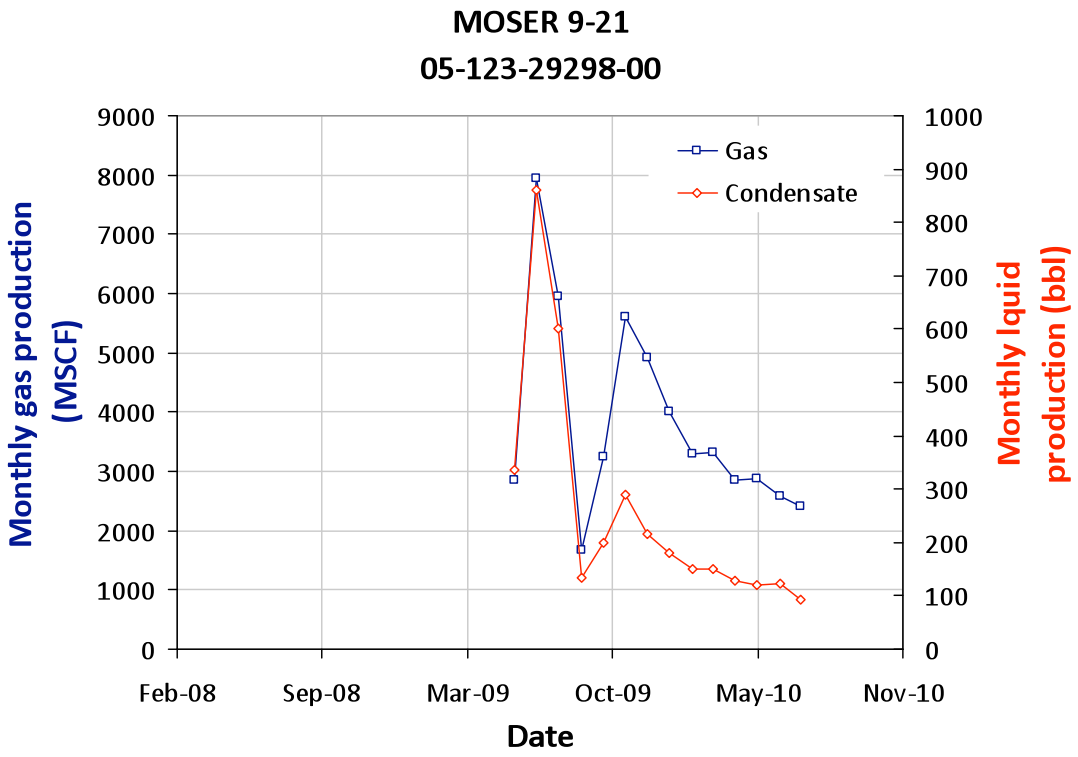
MOSER 9-21
05-123-29298-00
Monthly gas production (MSCF)
Monthly liquid production (bbl)
Gas
Condensate
9000
8000
7000
6000
5000
4000
3000
2000
1000
0
1000
900
800
700
600
500
400
300
200
100
0
Feb-08
Sep-08
Mar-09
Oct-09
May-10
Nov-10
Date

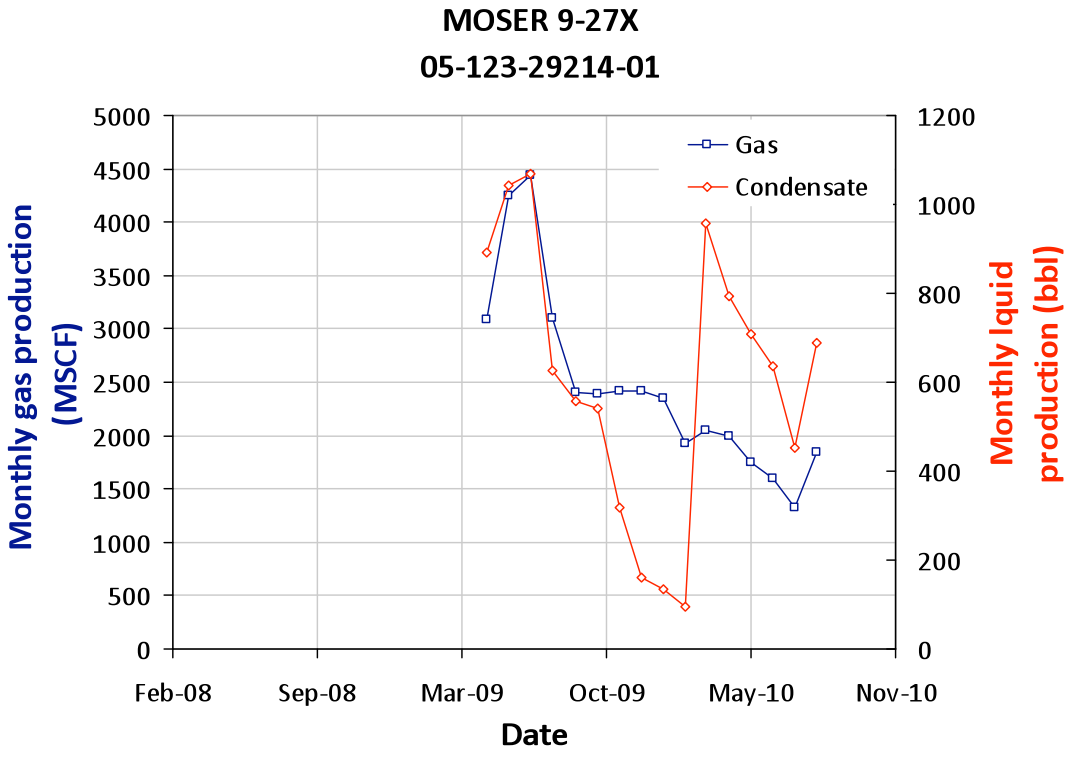
MOSER 9-27X
05-123-29214-01
Monthly gas production (MSCF)
Monthly liquid production (bbl)
Gas
Condensate
5000
4500
4000
3500
3000
2500
2000
1500
1000
500
0
1200
1000
800
600
400
200
0
Feb-08
Sep-08
Mar-09
Oct-09
May-10
Nov-10
Date

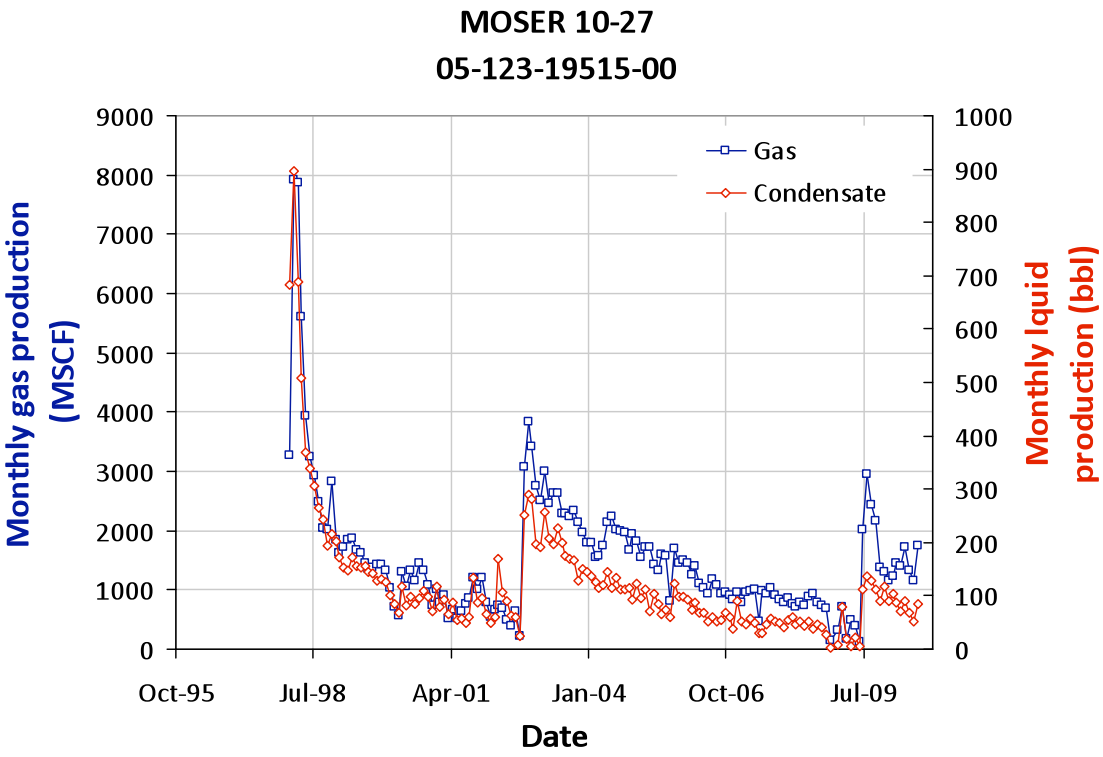
MOSER 10-27
05-123-19515-00
Monthly gas production (MSCF)
Monthly liquid production (bbl)
Gas
Condensate
9000
8000
7000
6000
5000
4000
3000
2000
1000
0
1000
900
800
700
600
500
400
300
200
100
0
Oct-95
Jul-98
Apr-01
Jan-04
Oct-06
Jul-09
Date

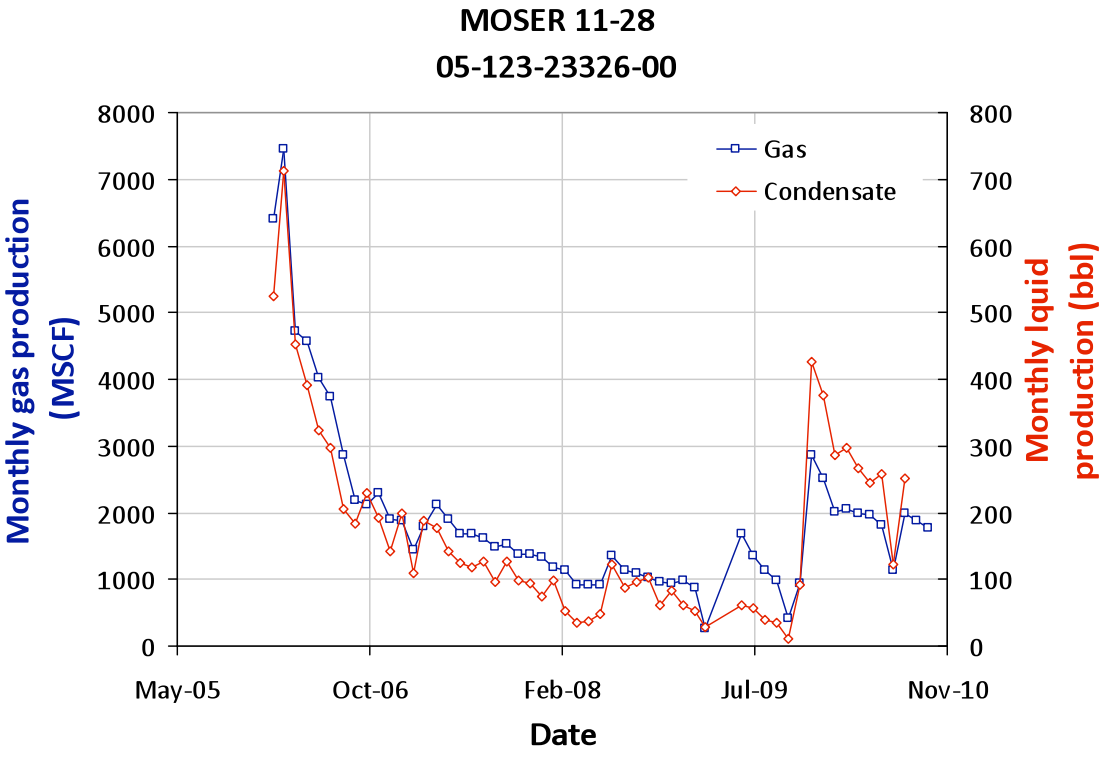
MOSER 11-28
05-123-23326-00
Monthly gas production (MSCF)
Monthly liquid production (bbl)
Gas
Condensate
8000
7000
6000
5000
4000
3000
2000
1000
0
800
700
600
500
400
300
200
100
0
May-05
Oct-06
Feb-08
Jul-09
Nov-10
Date

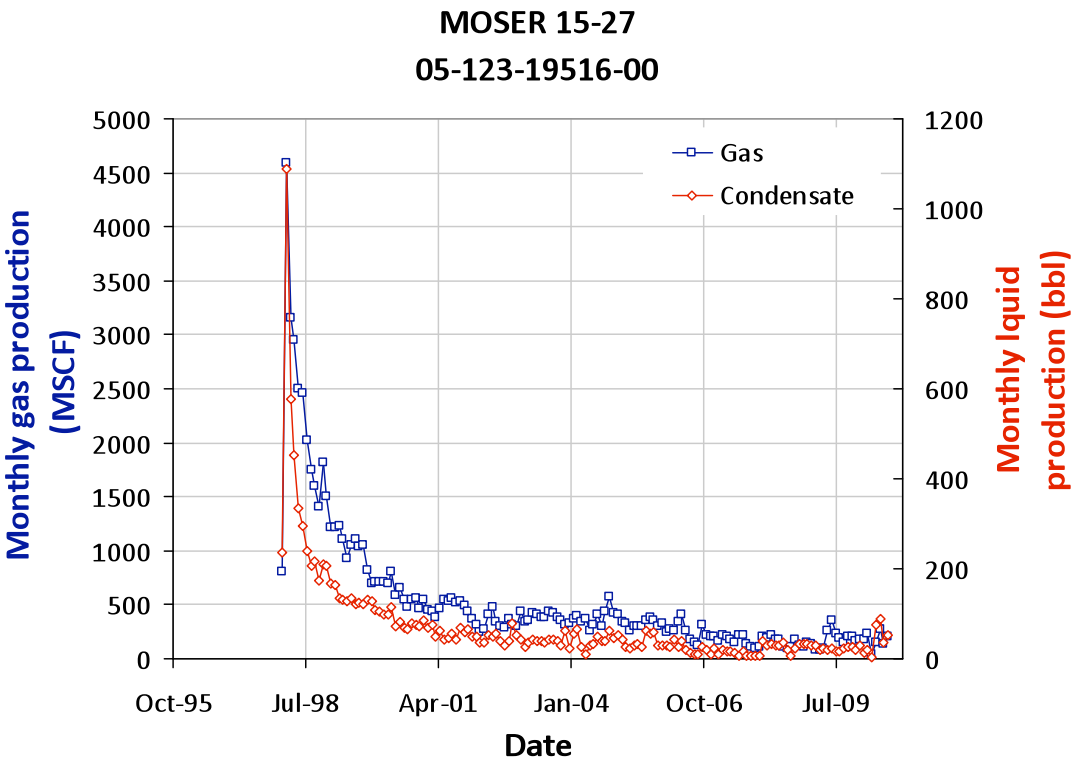
MOSER 15-27
05-123-19516-00
Monthly gas production (MSCF)
Monthly liquid production (bbl)
Gas
Condensate
5000
4500
4000
3500
3000
2500
2000
1500
1000
500
0
1200
1000
800
600
400
200
0
Oct-95
Jul-98
Apr-01
Jan-04
Oct-06
Jul-09
Date

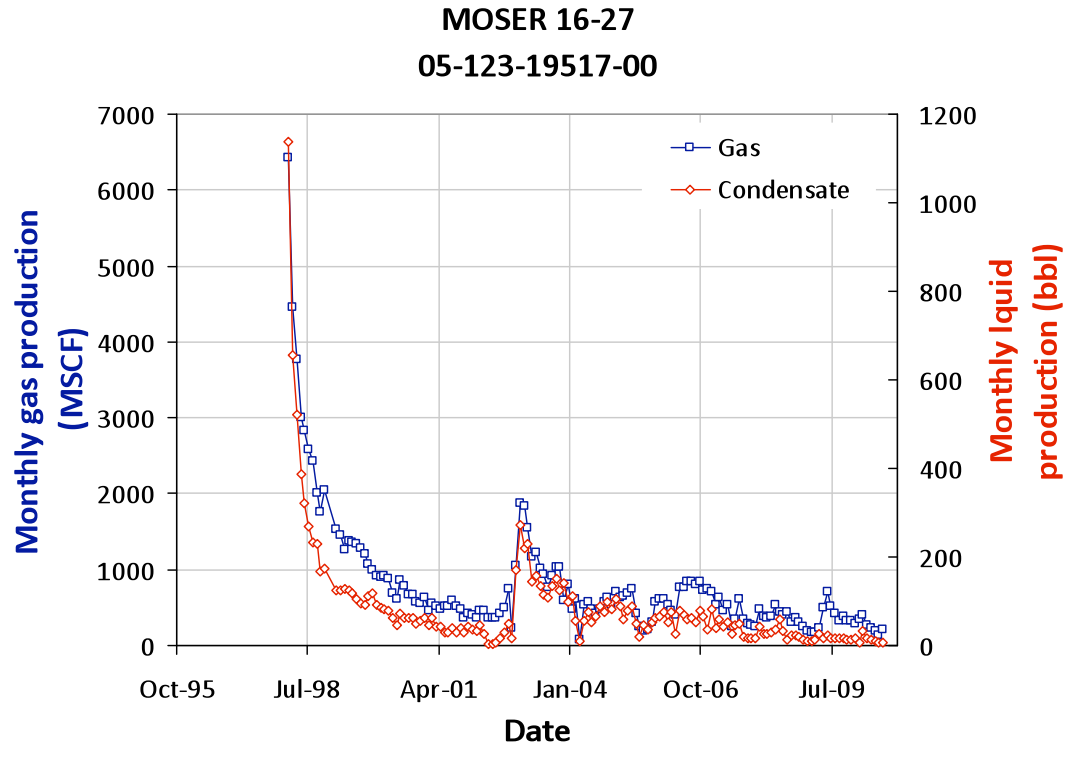
MOSER 16-27
05-123-19517-00
Monthly gas production (MSCF)
Monthly liquid production (bbl)
Gas
Condensate
7000
6000
5000
4000
3000
2000
1000
0
1200
1000
800
600
400
200
0
Oct-95
Jul-98
Apr-01
Jan-04
Oct-06
Jul-09
Date

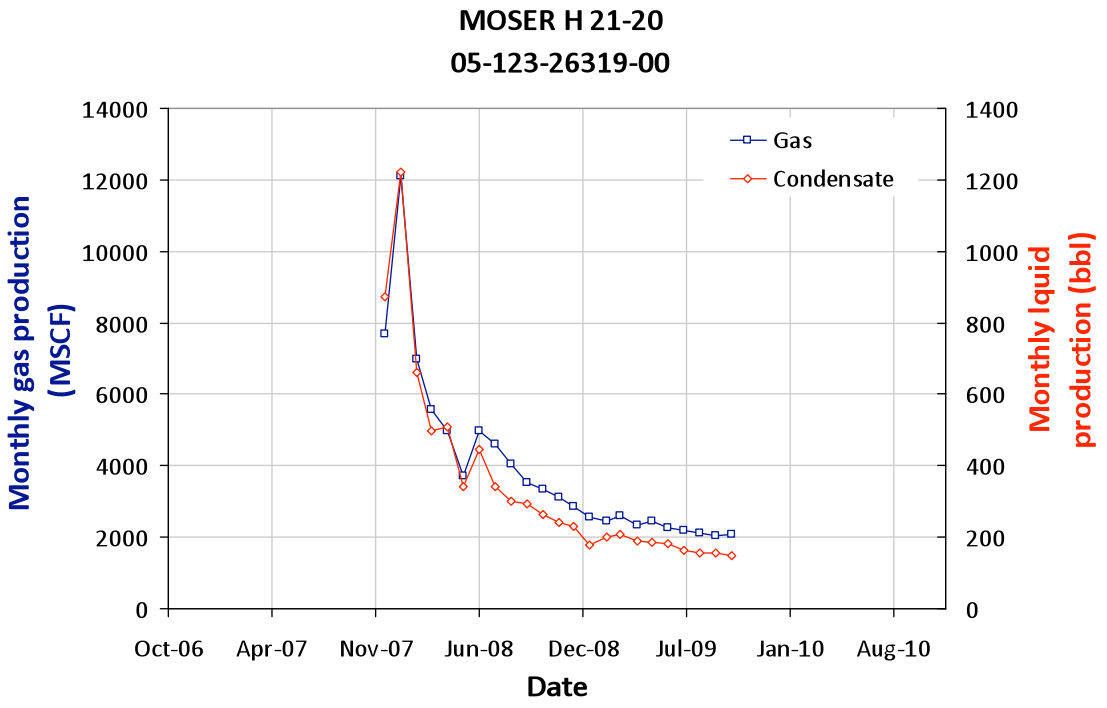
MOSER H 21-20
05-123-26319-00
Monthly gas production (MSCF)
Monthly liquid production (bbl)
Gas
Condensate
14000
12000
10000
8000
6000
4000
2000
0
1400
1200
1000
800
600
400
200
0
Oct-06
Apr-07
Nov-07
Jun-08
Dec-08
Jul-09
Jan-10
Aug-10
Date

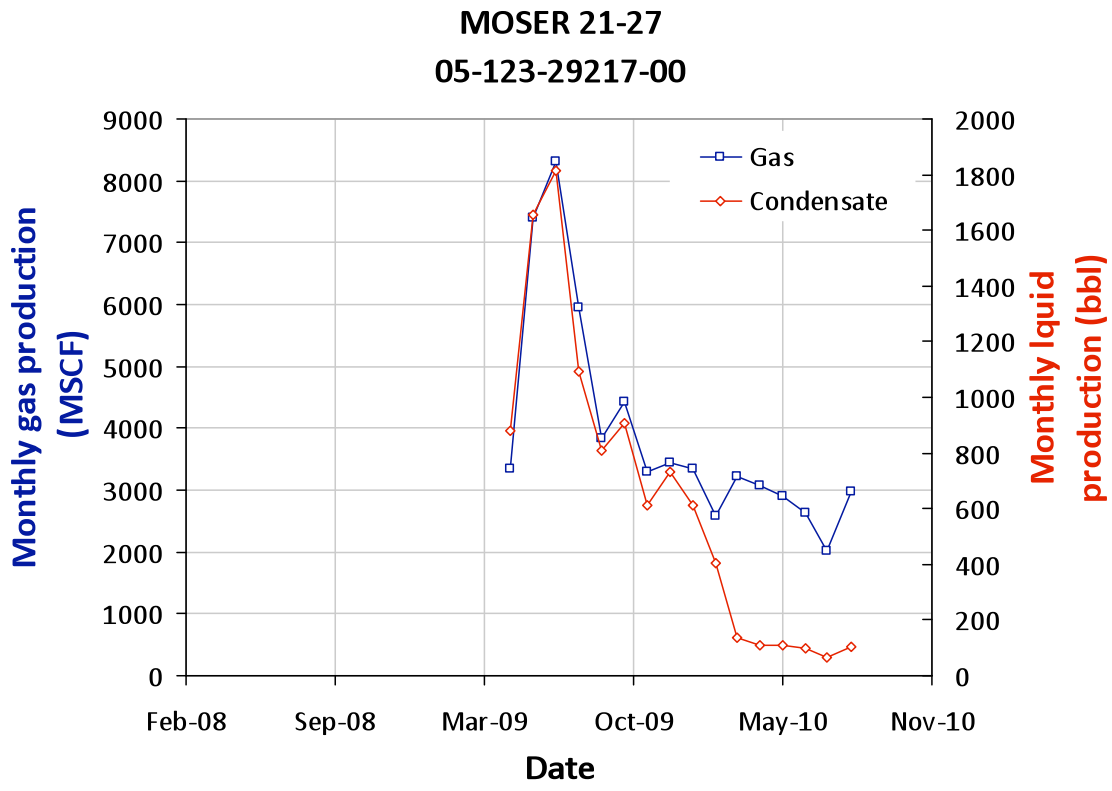
MOSER 21-27
05-123-29217-00
Monthly gas production (MSCF)
Monthly liquid production (bbl)
Gas
Condensate
9000
8000
7000
6000
5000
4000
3000
2000
1000
0
2000
1800
1600
1400
1200
1000
800
600
400
200
0
Feb-08
Sep-08
Mar-09
Oct-09
May-10
Nov-10
Date

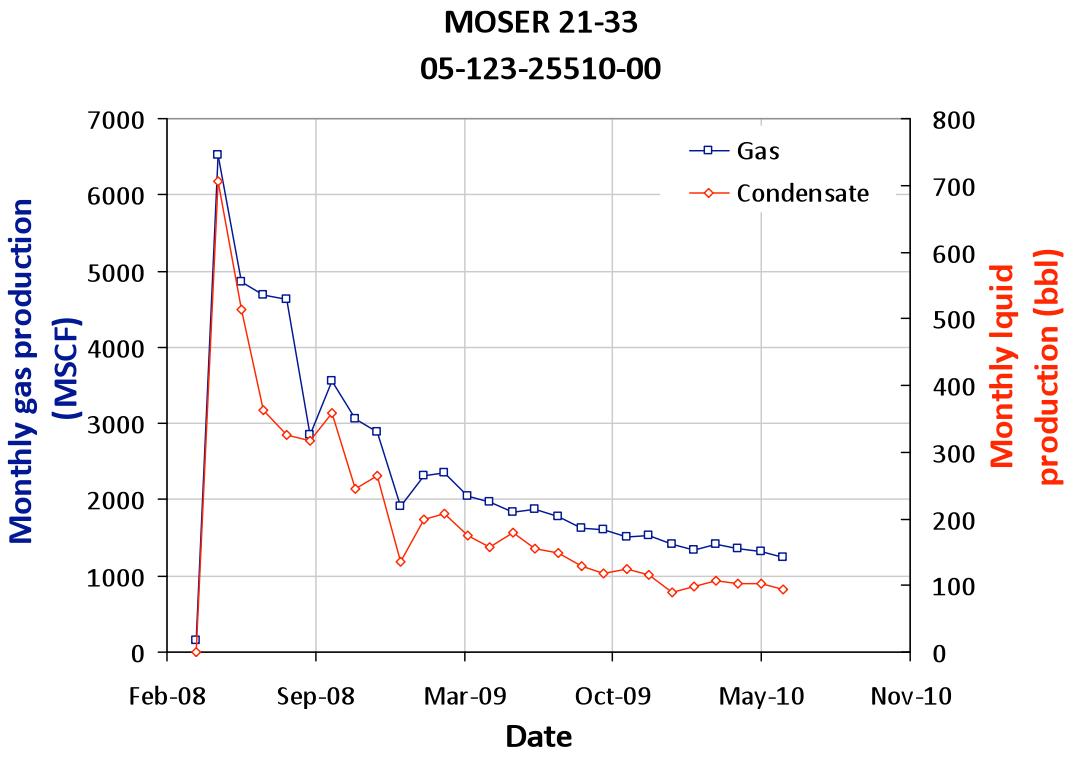
MOSER 21-33
05-123-25510-00
Monthly gas production (MSCF)
Monthly liquid production (bbl)
Gas
Condensate
7000
6000
5000
4000
3000
2000
1000
0
800
700
600
500
400
300
200
100
0
Feb-08
Sep-08
Mar-09
Oct-09
May-10
Nov-10
Date

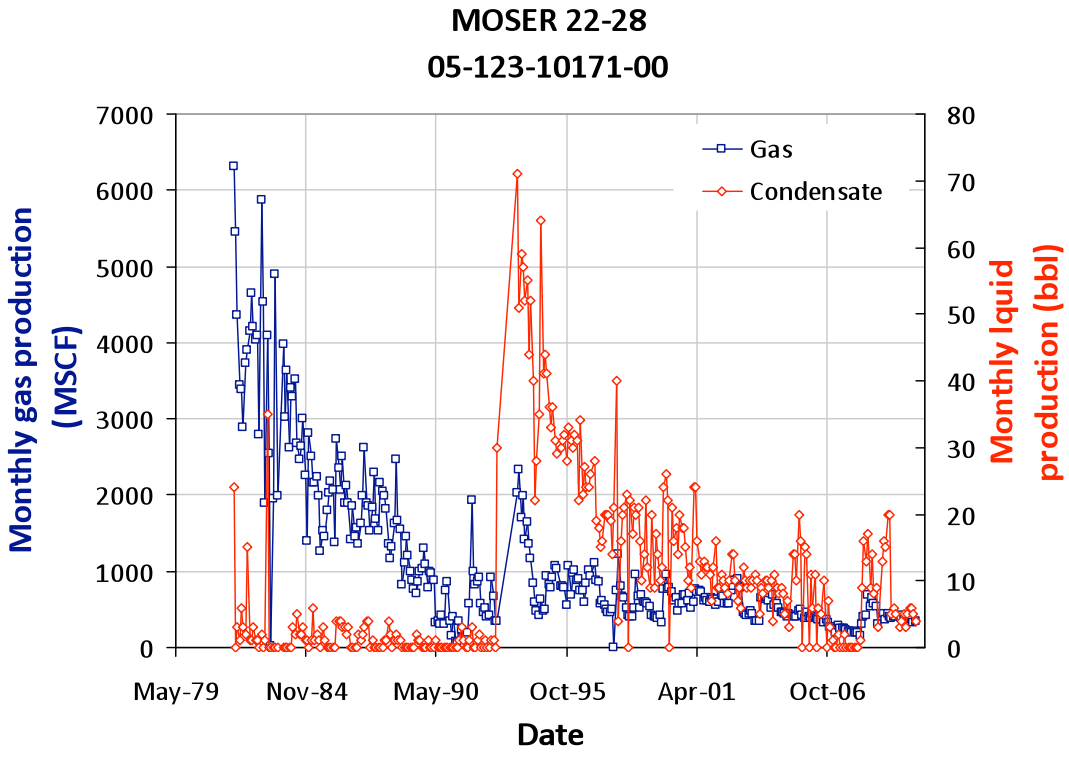
MOSER 22-28
05-123-10171-00
Monthly gas production (MSCF)
Monthly liquid production (bbl)
Gas
Condensate
7000
6000
5000
4000
3000
2000
1000
0
80
70
60
50
40
30
20
10
0
May-79
Nov-84
May-90
Oct-95
Apr-01
Oct-06
Date

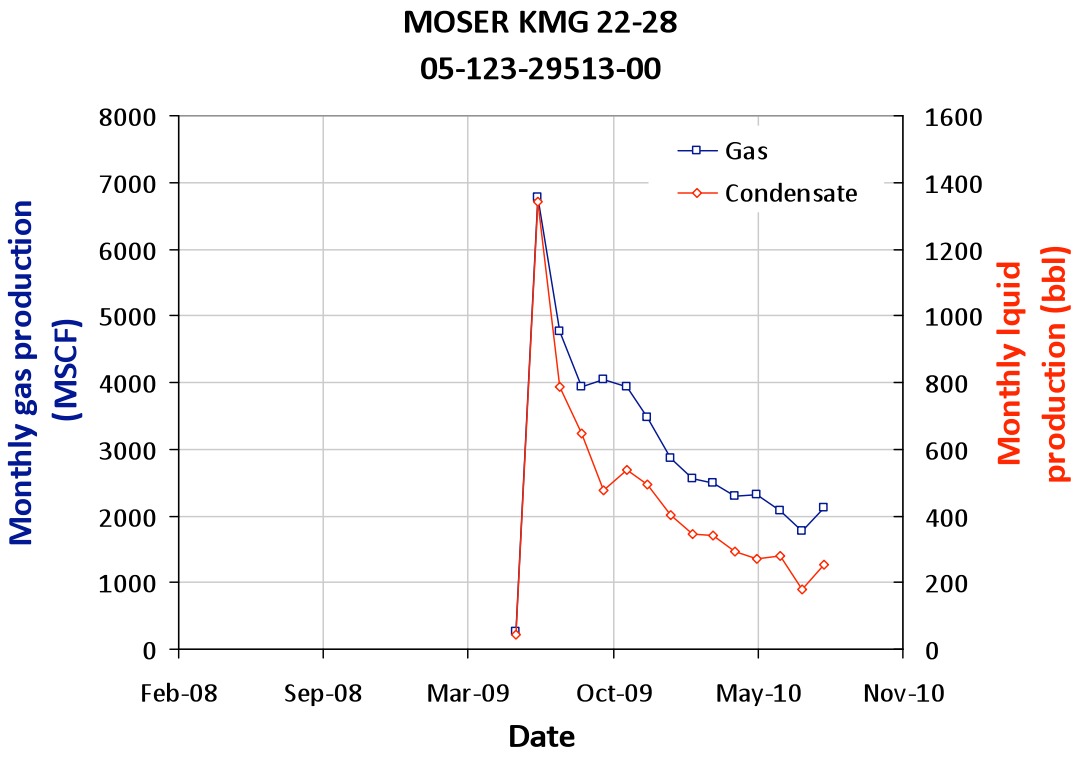
MOSER KMG 22-28
05-123-29513-00
Monthly gas production (MSCF)
Monthly liquid production (bbl)
Gas
Condensate
8000
7000
6000
5000
4000
3000
2000
1000
0
1600
1400
1200
1000
800
600
400
200
0
Feb-08
Sep-08
Mar-09
Oct-09
May-10
Nov-10
Date

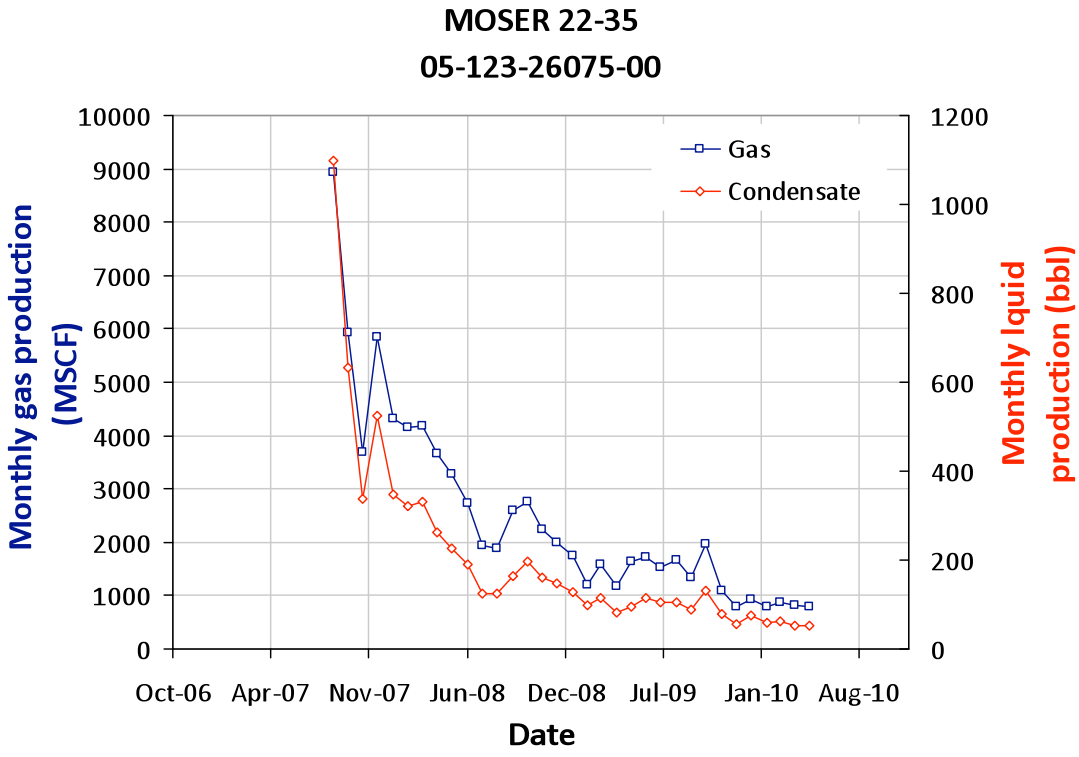
MOSER 22-35
05-123-26075-00
Monthly gas production (MSCF)
Monthly liquid production (bbl)
Gas
Condensate
10000
9000
8000
7000
6000
5000
4000
3000
2000
1000
0
1200
1000
800
600
400
200
0
Oct-06
Apr-07
Nov-07
Jun-08
Dec-08
Jul-09
Jan-10
Aug-10
Date

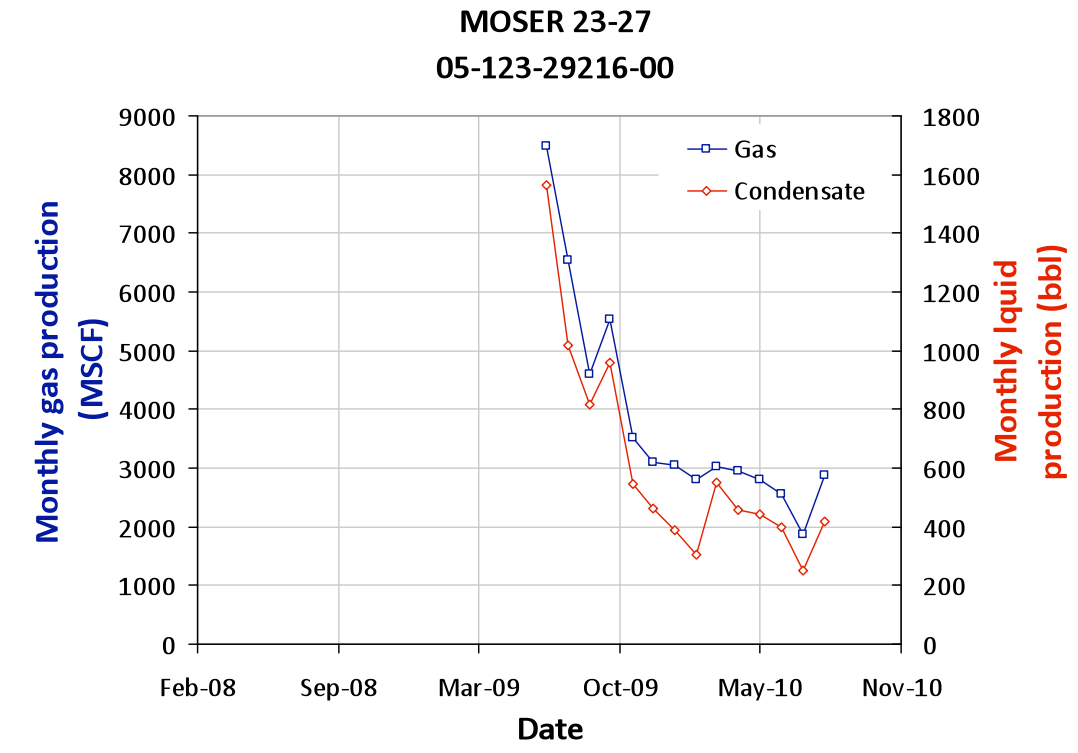
MOSER 23-27
05-123-29216-00
Monthly gas production (MSCF)
Monthly liquid production (bbl)
Gas
Condensate
9000
8000
7000
6000
5000
4000
3000
2000
1000
0
1800
1600
1400
1200
1000
800
600
400
200
0
Feb-08
Sep-08
Mar-09
Oct-09
May-10
Nov-10
Date

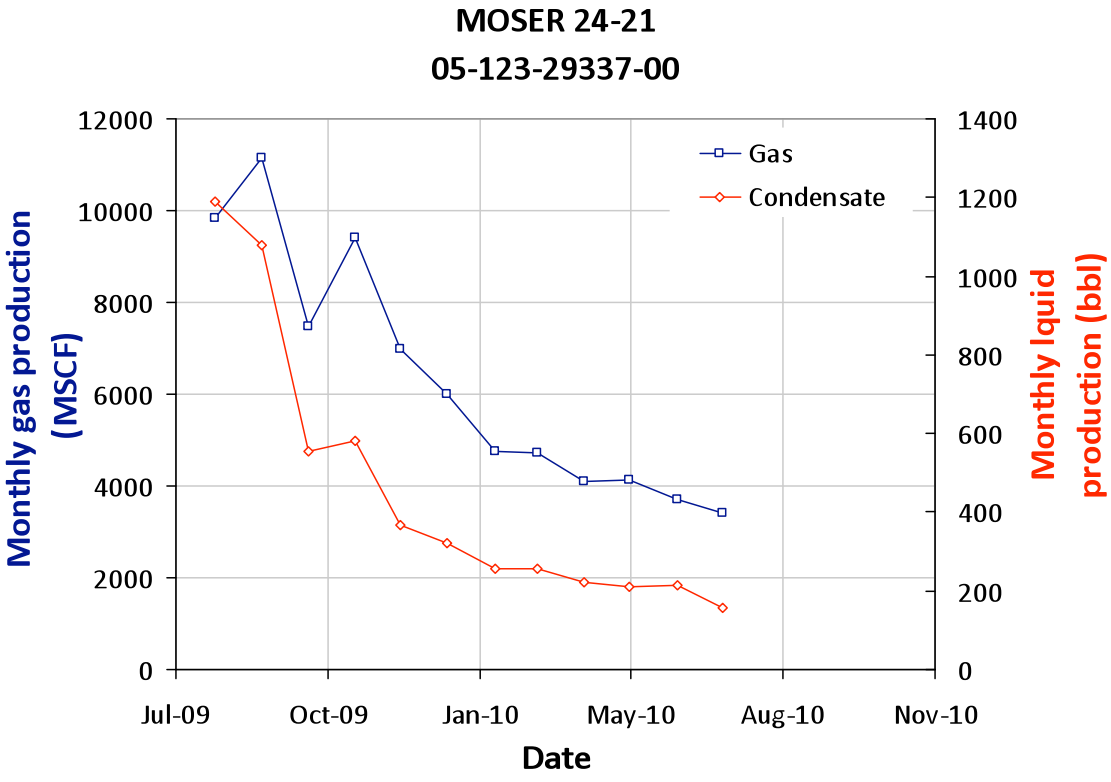
MOSER 24-21
05-123-29337-00
Monthly gas production (MSCF)
Monthly liquid production (bbl)
Gas
Condensate
12000
10000
8000
6000
4000
2000
0
1400
1200
1000
800
600
400
200
0
Jul-09
Oct-09
Jan-10
May-10
Aug-10
Nov-10
Date

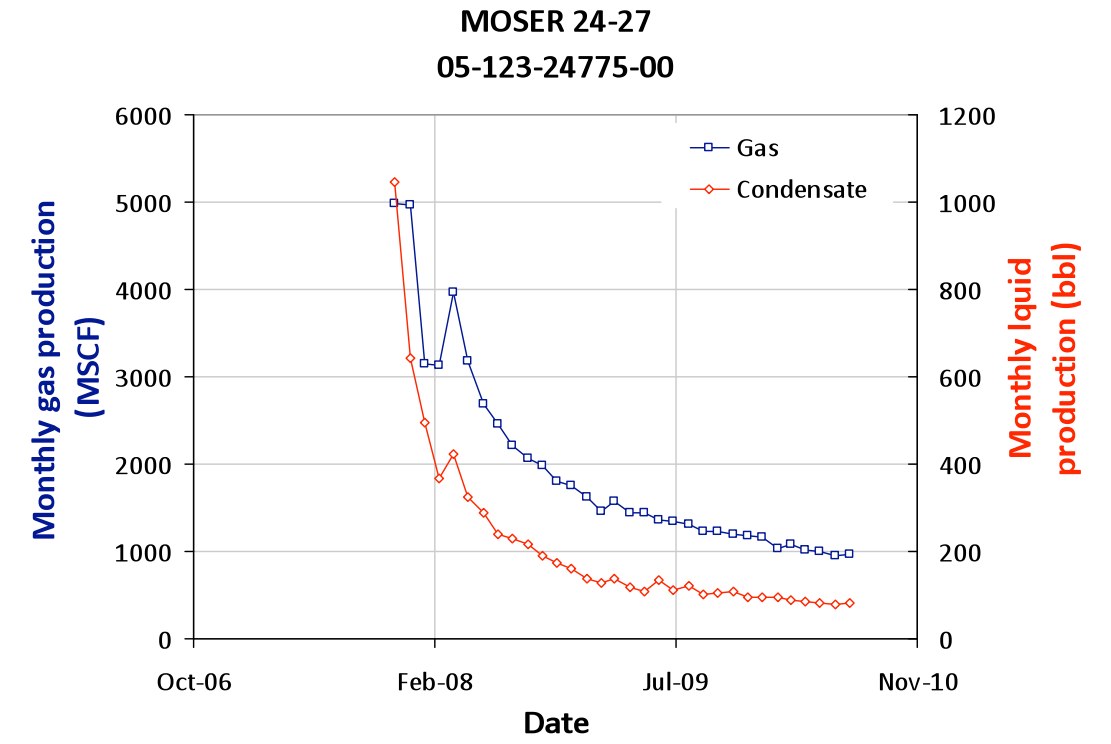
MOSER 24-27
05-123-24775-00
Monthly gas production (MSCF)
Monthly liquid production (bbl)
Gas
Condensate
6000
5000
4000
3000
2000
1000
0
1200
1000
800
600
400
200
0
Oct-06
Feb-08
Jul-09
Nov-10
Date

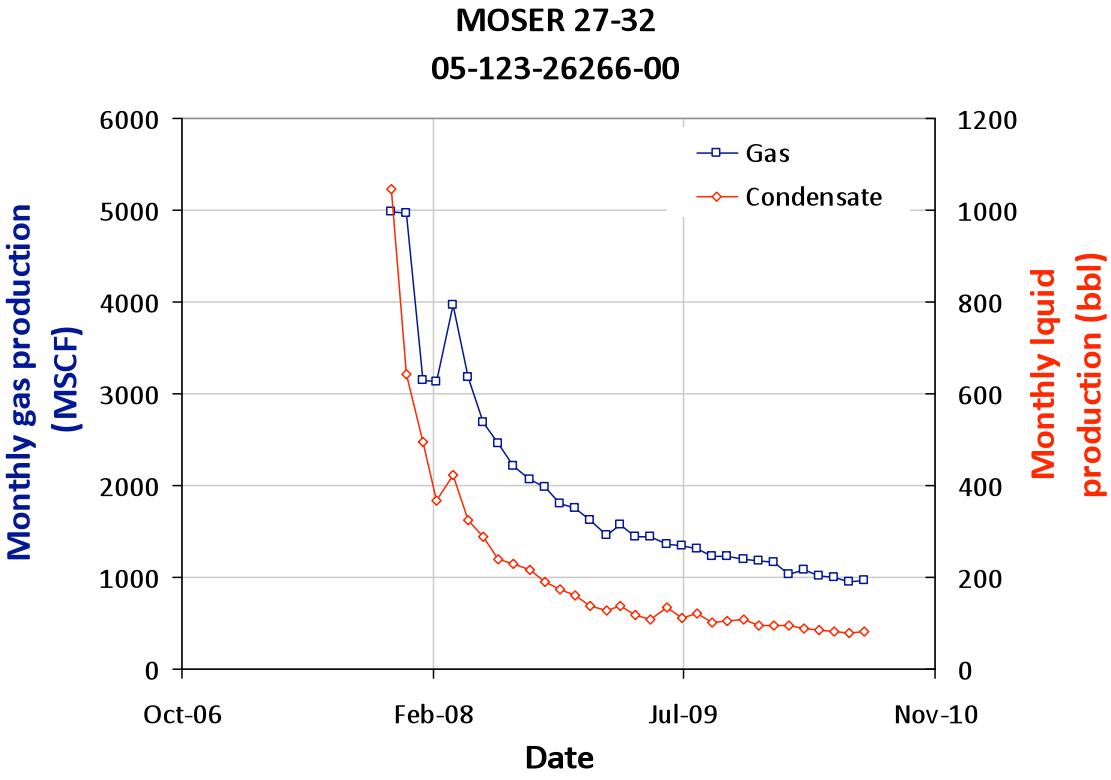
MOSER 27-32
05-123-26266-00
Monthly gas production (MSCF)
Monthly liquid production (bbl)
Gas
Condensate
6000
5000
4000
3000
2000
1000
0
1200
1000
800
600
400
200
0
Oct-06
Feb-08
Jul-09
Nov-10
Date

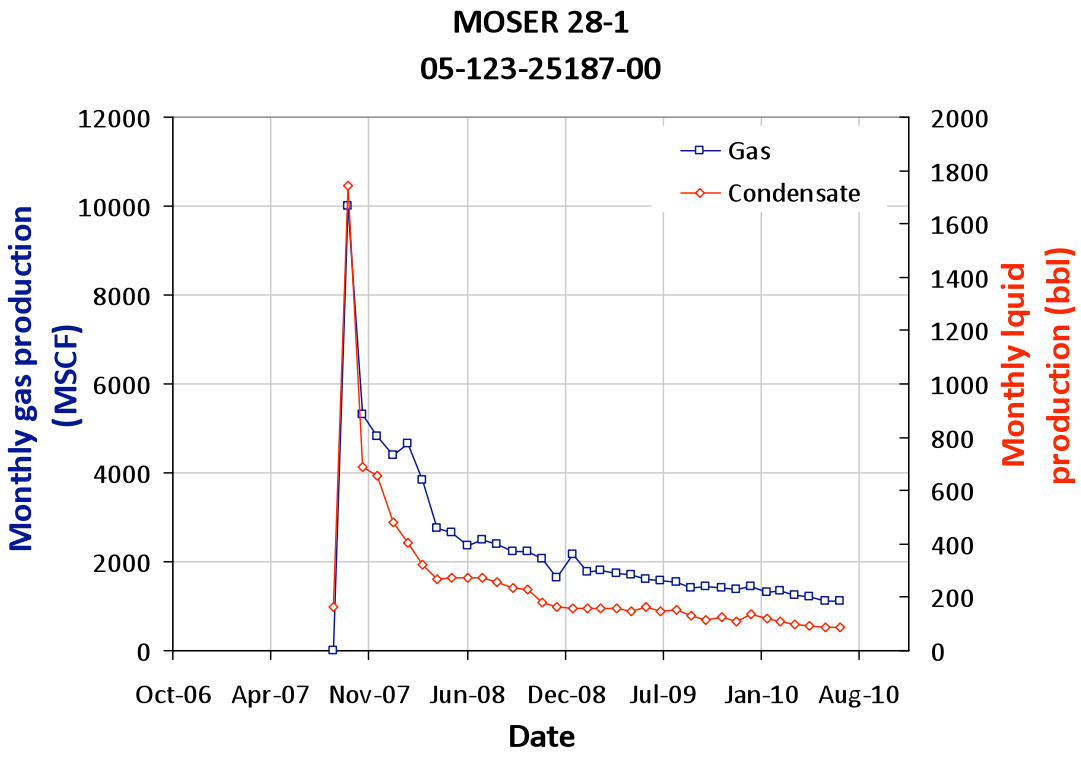
MOSER 28-1
05-123-25187-00
Gas
Condensate
Monthly gas production (MSCF)
Monthly liquid production (bbl)
12000
10000
8000
6000
4000
2000
0
2000
1800
1600
1400
1200
1000
800
600
400
200
0
Oct-06
Apr-07
Nov-07
Jun-08
Dec-08
Jul-09
Jan-10
Aug-10
Date

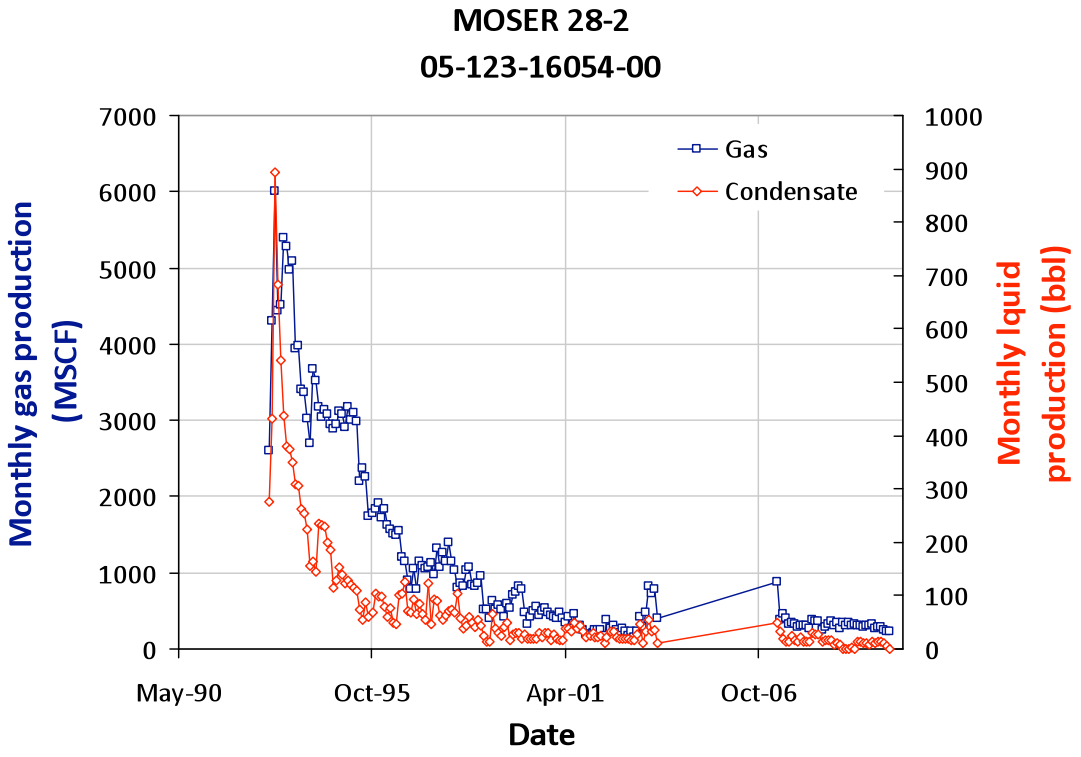
MOSER 28-2
05-123-16054-00
Gas
Condensate
Monthly gas production (MSCF)
Monthly liquid production (bbl)
7000
6000
5000
4000
3000
2000
1000
0
1000
900
800
700
600
500
400
300
200
100
0
May-90
Oct-95
Apr-01
Oct-06
Date

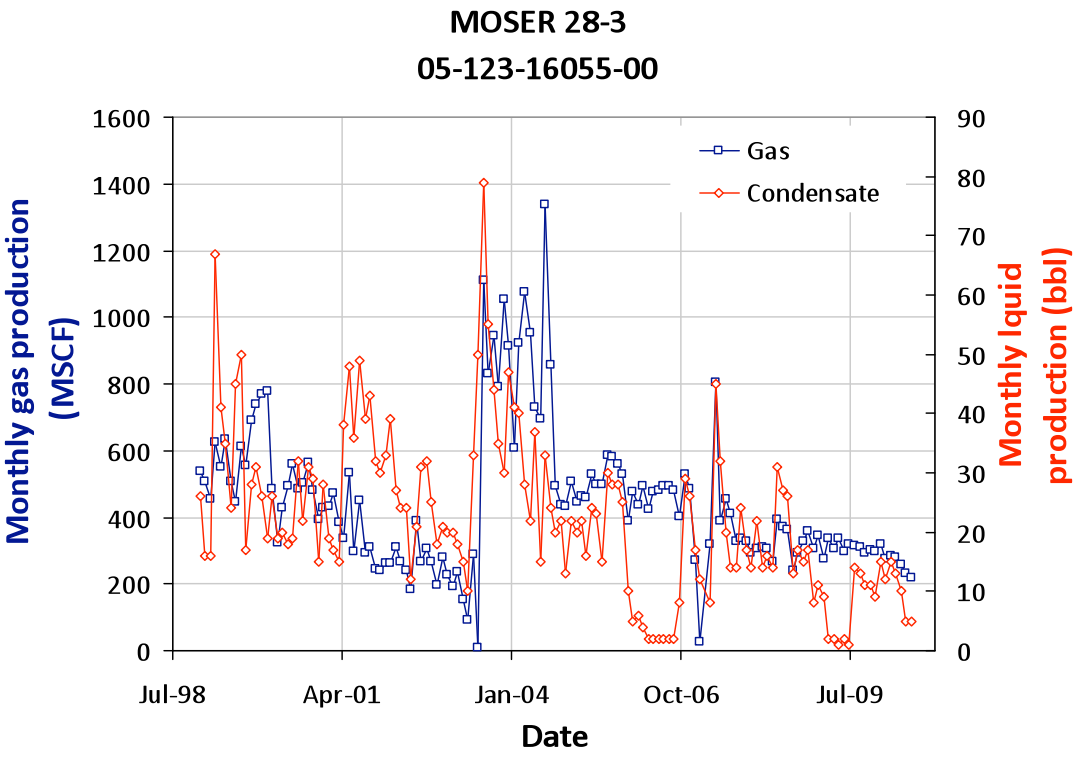
MOSER 28-3
05-123-16055-00
Monthly gas production (MSCF)
Monthly liquid production (bbl)
Gas
Condensate
1600
1400
1200
1000
800
600
400
200
0
90
80
70
60
50
40
30
20
10
0
Jul-98
Apr-01
Jan-04
Oct-06
Jul-09
Date

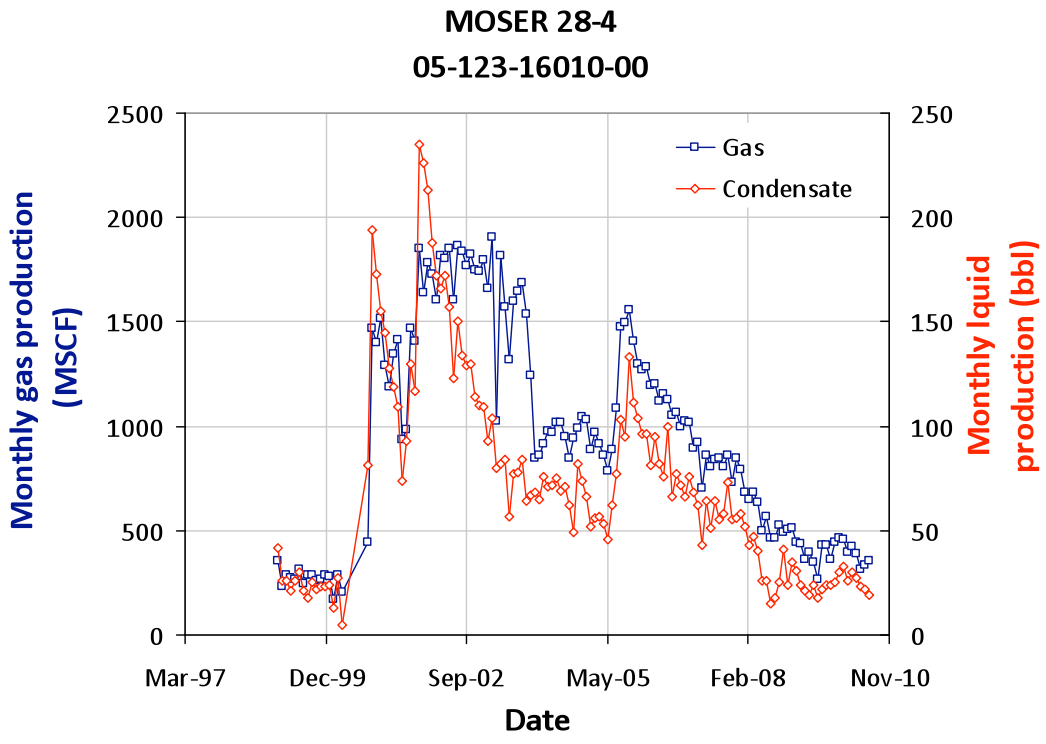
MOSER 28-4
05-123-16010-00
Monthly gas production (MSCF)
Monthly liquid production (bbl)
Gas
Condensate
2500
2000
1500
1000
500
0
250
200
150
100
50
0
Mar-97
Dec-99
Sep-02
May-05
Feb-08
Nov-10
Date

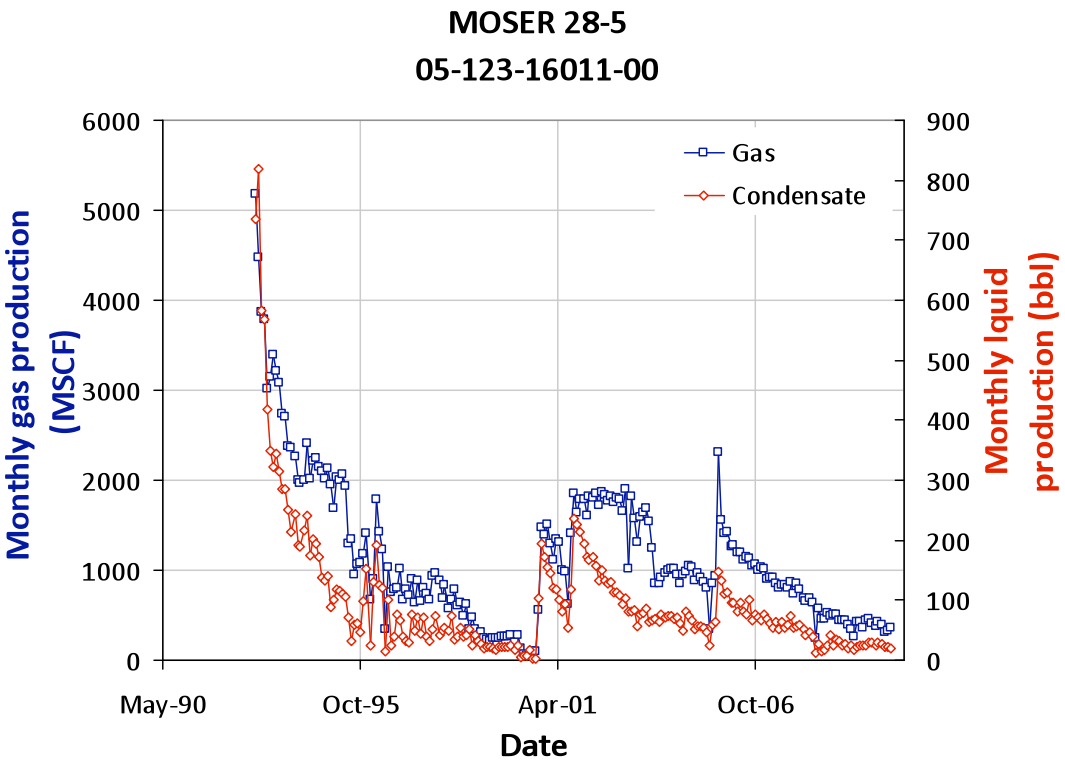
MOSER 28-5
05-123-16011-00
Gas
Condensate
Monthly gas production (MSCF)
Monthly liquid production (bbl)
6000
5000
4000
3000
2000
1000
0
900
800
700
600
500
400
300
200
100
0
May-90
Oct-95
Apr-01
Oct-06
Date

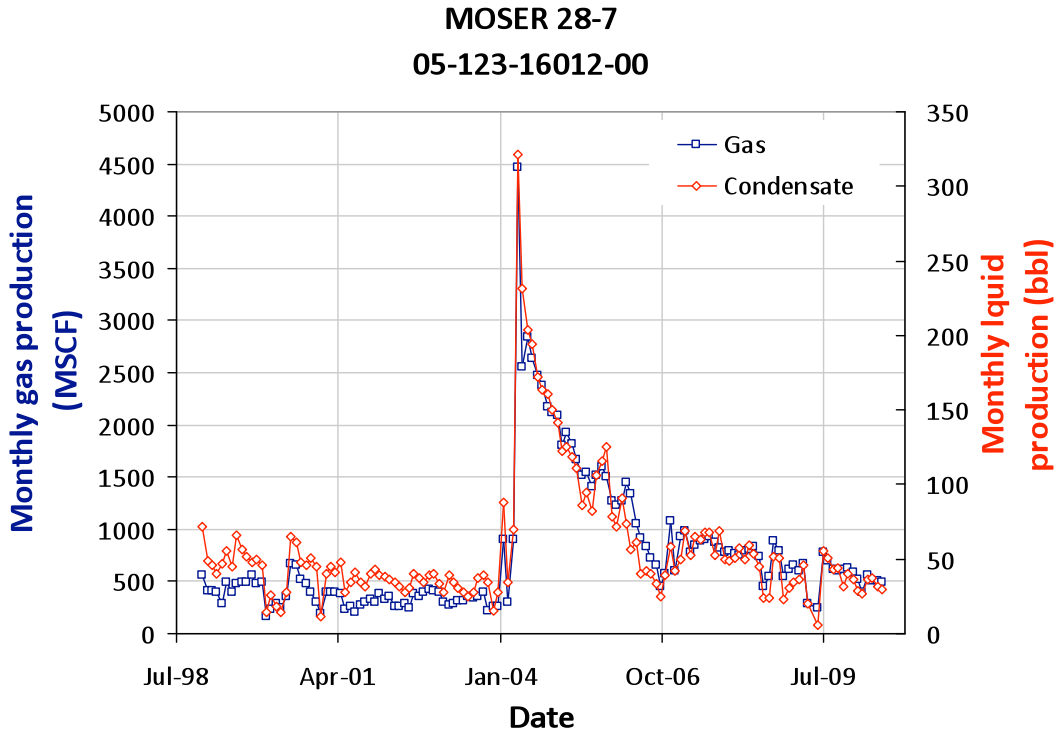
MOSER 28-7
05-123-16012-00
Gas
Condensate
Monthly gas production (MSCF)
Monthly liquid production (bbl)
5000
4500
4000
3500
3000
2500
2000
1500
1000
500
0
350
300
250
200
150
100
50
0
Jul-98
Apr-01
Jan-04
Oct-06
Jul-09
Date

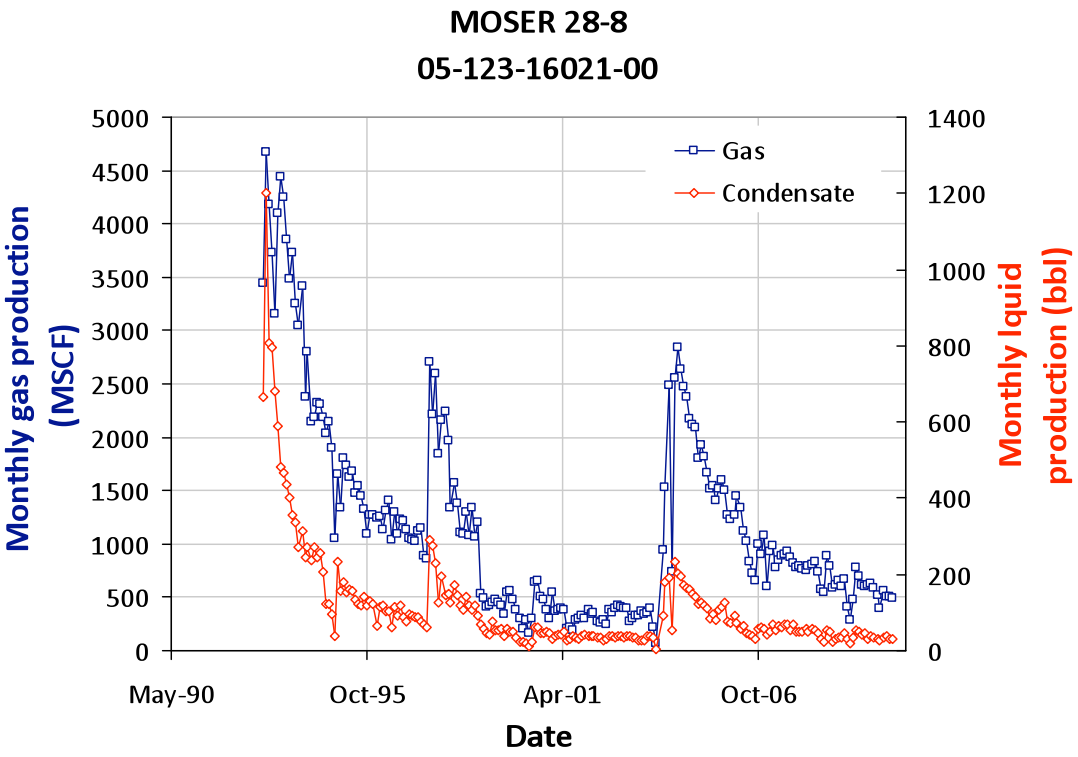
MOSER 28-8
05-123-16021-00
Monthly gas production (MSCF)
Monthly liquid production (bbl)
Gas
Condensate
5000
4500
4000
3500
3000
2500
2000
1500
1000
500
0
1400
1200
1000
800
600
400
200
0
May-90
Oct-95
Apr-01
Oct-06
Date

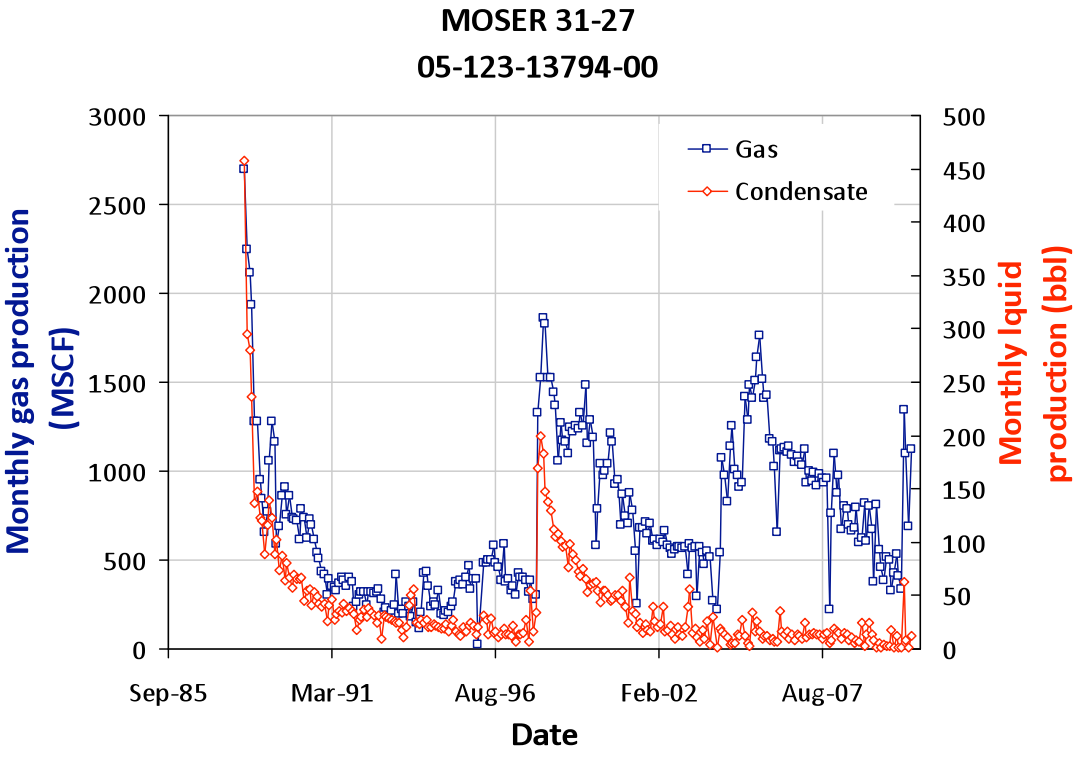
MOSER 31-27
05-123-13794-00
Monthly gas production (MSCF)
Monthly liquid production (bbl)
Gas
Condensate
3000
2500
2000
1500
1000
500
0
500
450
400
350
300
250
200
150
100
50
0
Sep-85
Mar-91
Aug-96
Feb-02
Aug-07
Date

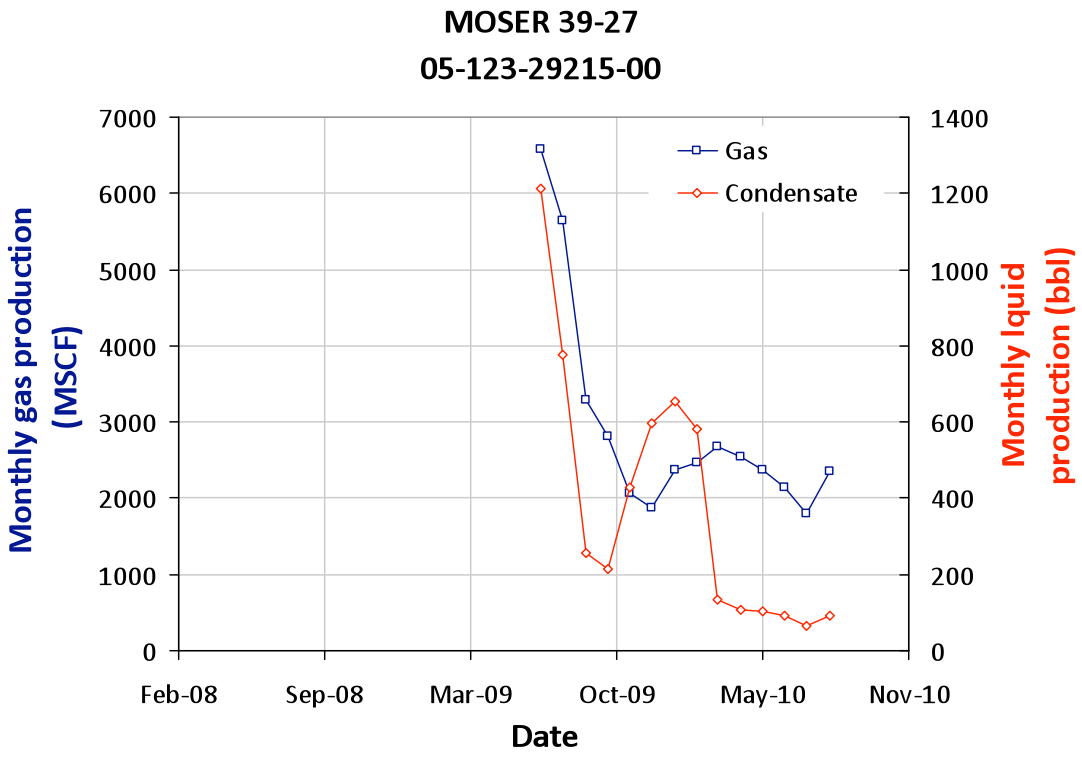
MOSER 39-27
05-123-29215-00
Monthly gas production (MSCF)
Monthly liquid production (bbl)
Gas
Condensate
7000
6000
5000
4000
3000
2000
1000
0
1400
1200
1000
800
600
400
200
0
Feb-08
Sep-08
Mar-09
Oct-09
May-10
Nov-10
Date

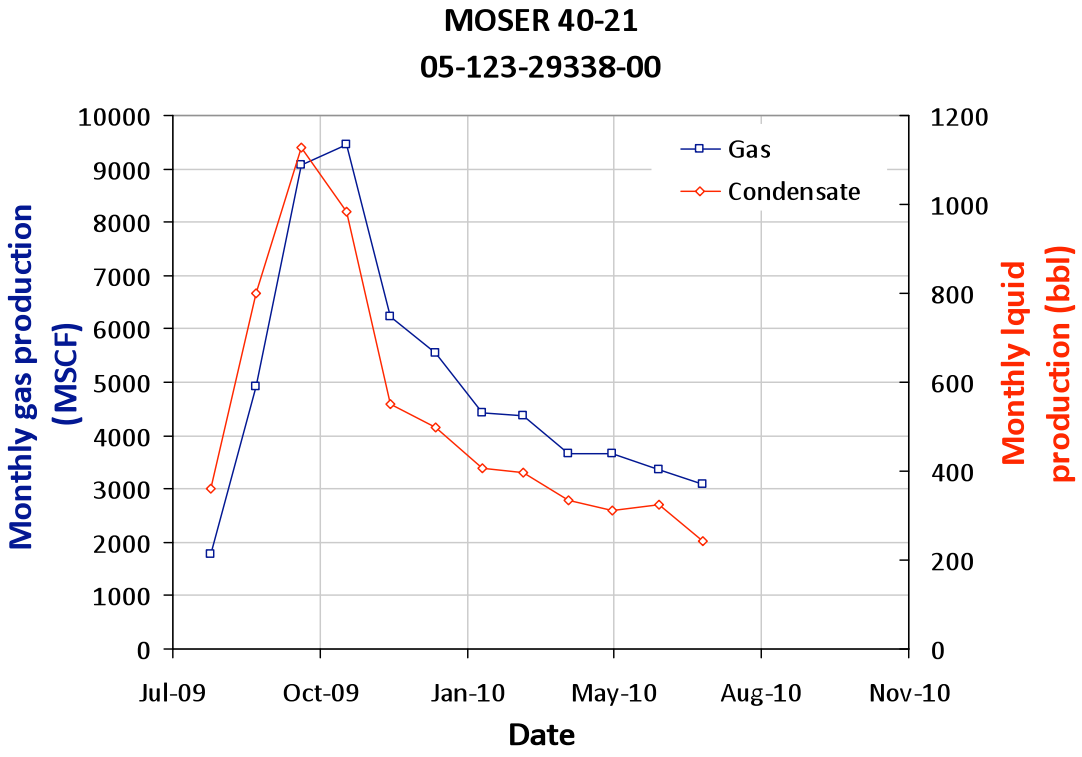
MOSER 40-21
05-123-29338-00
Monthly gas production (MSCF)
Monthly liquid production (bbl)
Gas
Condensate
10000
9000
8000
7000
6000
5000
4000
3000
2000
1000
0
1200
1000
800
600
400
200
0
Jul-09
Oct-09
Jan-10
May-10
Aug-10
Nov-10
Date

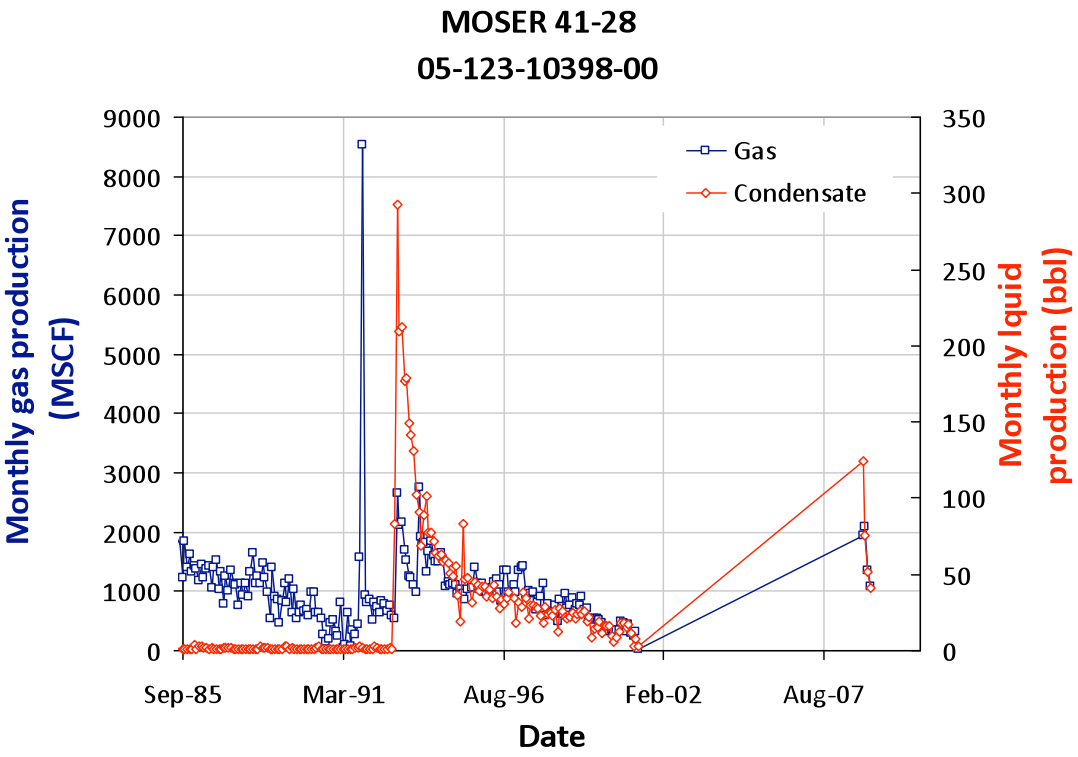
MOSER 41-28
05-123-10398-00
Monthly gas production (MSCF)
Monthly liquid production (bbl)
Gas
Condensate
9000
8000
7000
6000
5000
4000
3000
2000
1000
0
350
300
250
200
150
100
50
0
Sep-85
Mar-91
Aug-96
Feb-02
Aug-07
Date

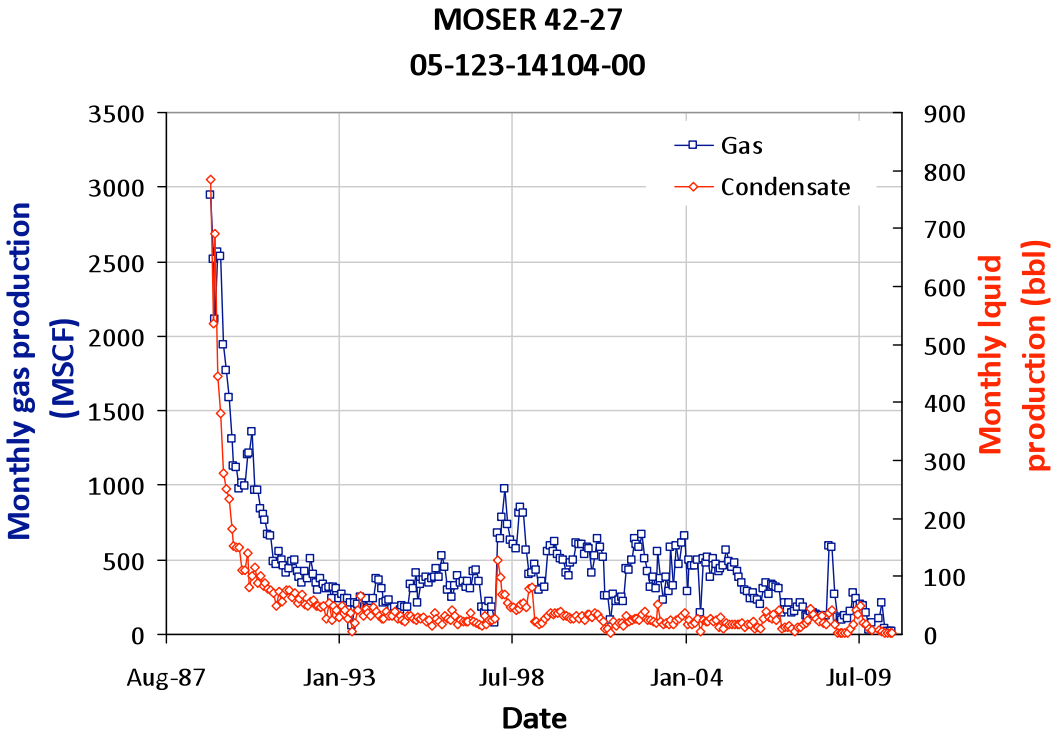
MOSER 42-27
05-123-14104-00
Monthly gas production (MSCF)
Monthly liquid production (bbl)
Gas
Condensate
3500
3000
2500
2000
1500
1000
500
0
900
800
700
600
500
400
300
200
100
0
Aug-87
Jan-93
Jul-98
Jan-04
Jul-09
Date

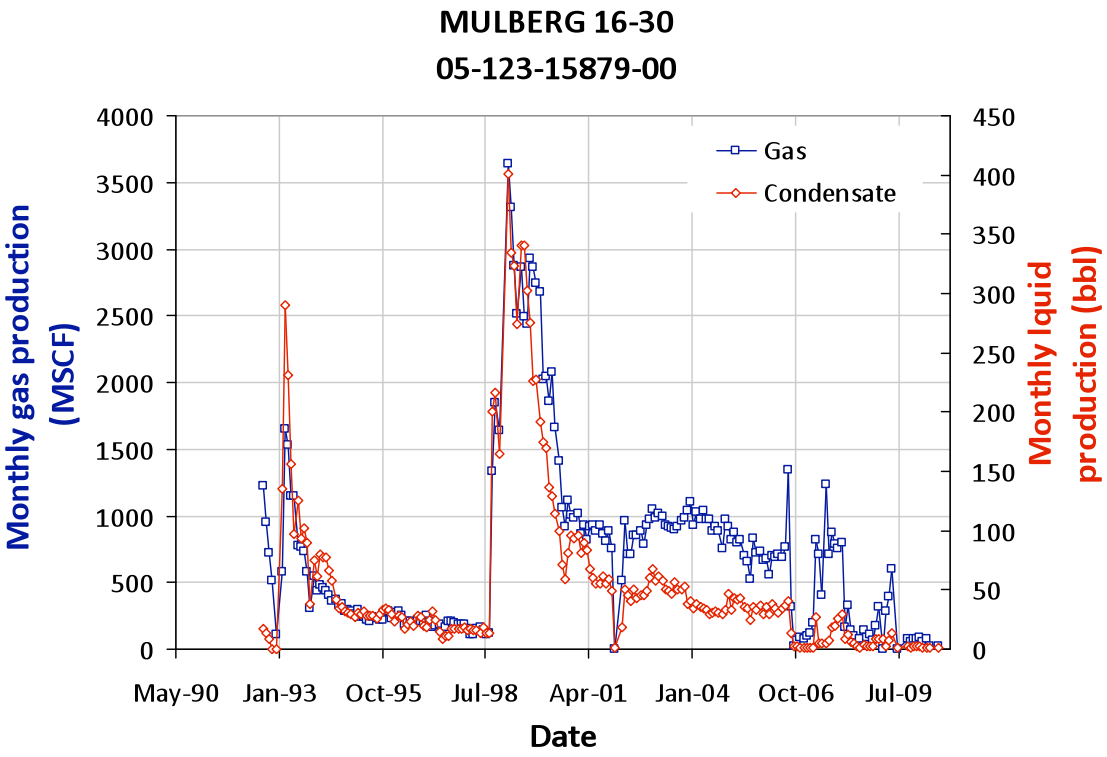
MULBERG 16-30
05-123-15879-00
Monthly gas production (MSCF)
Monthly liquid production (bbl)
Gas
Condensate
4000
3500
3000
2500
2000
1500
1000
500
0
450
400
350
300
250
200
150
100
50
0
May-90
Jan-93
Oct-95
Jul-98
Apr-01
Jan-04
Oct-06
Jul-09
Date

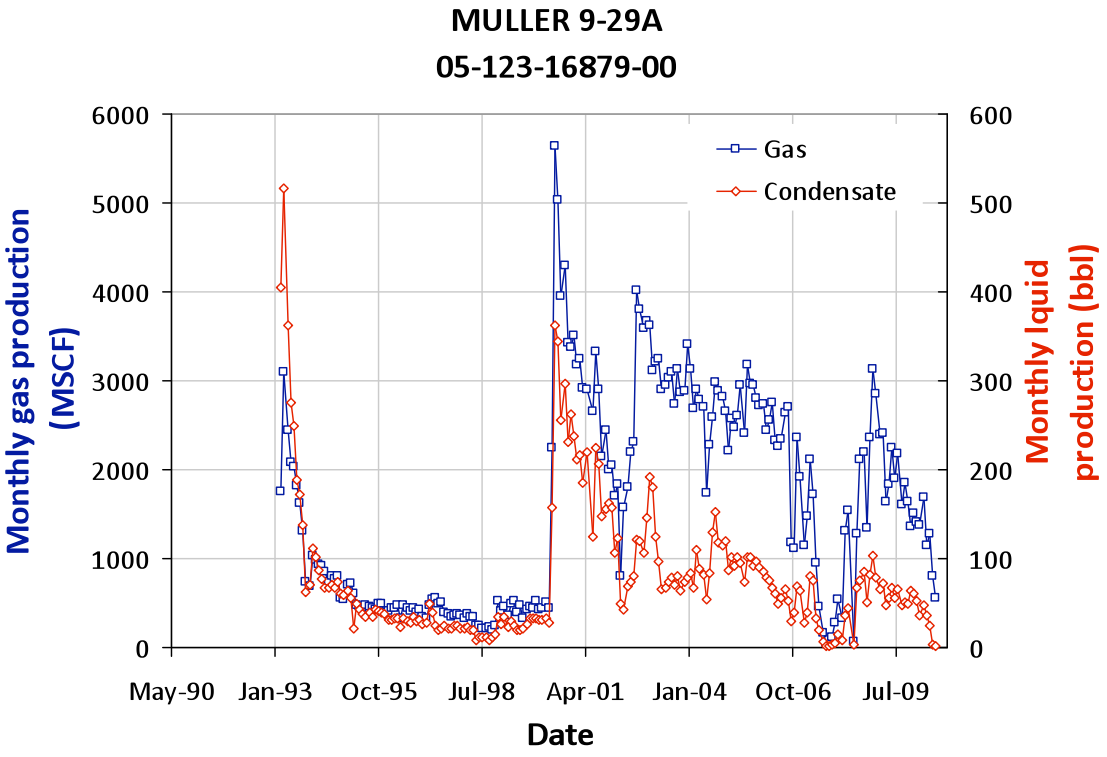
MULLER 9-29A
05-123-16879-00
Monthly gas production (MSCF)
Monthly liquid production (bbl)
Gas
Condensate
6000
5000
4000
3000
2000
1000
0
600
500
400
300
200
100
0
May-90
Jan-93
Oct-95
Jul-98
Apr-01
Jan-04
Oct-06
Jul-09
Date

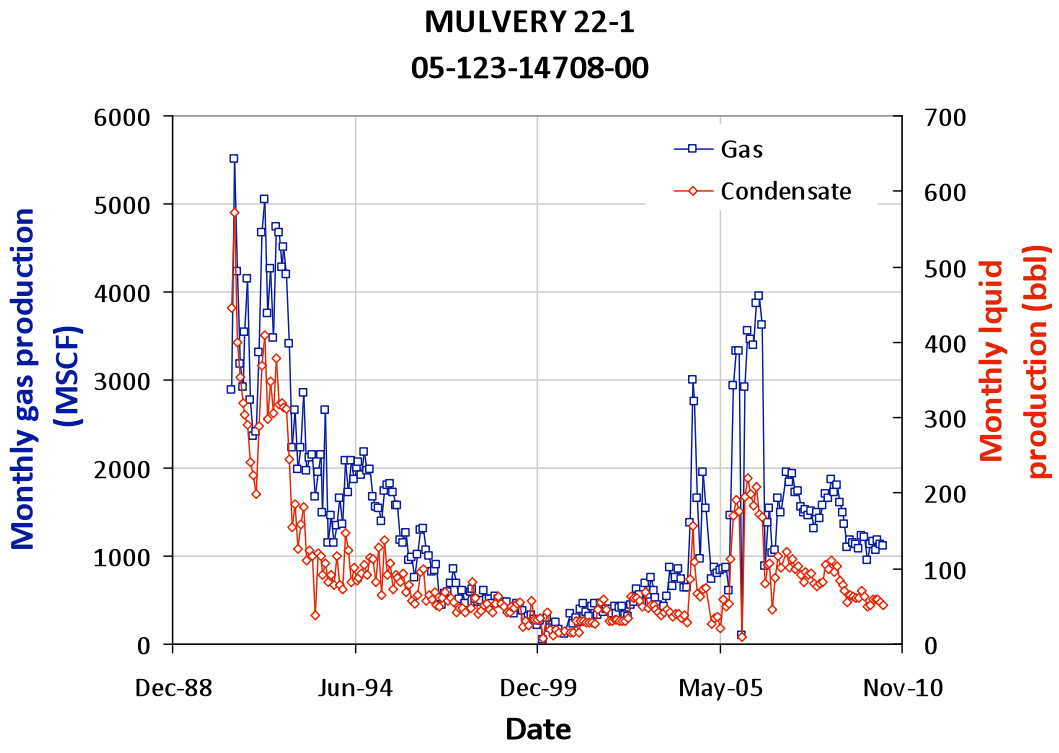
MULVERY 22-1
05-123-14708-00
Gas
Condensate
Monthly gas production (MSCF)
Monthly liquid production (bbl)
6000
5000
4000
3000
2000
1000
0
700
600
500
400
300
200
100
0
Dec-88
Jun-94
Dec-99
May-05
Nov-10
Date

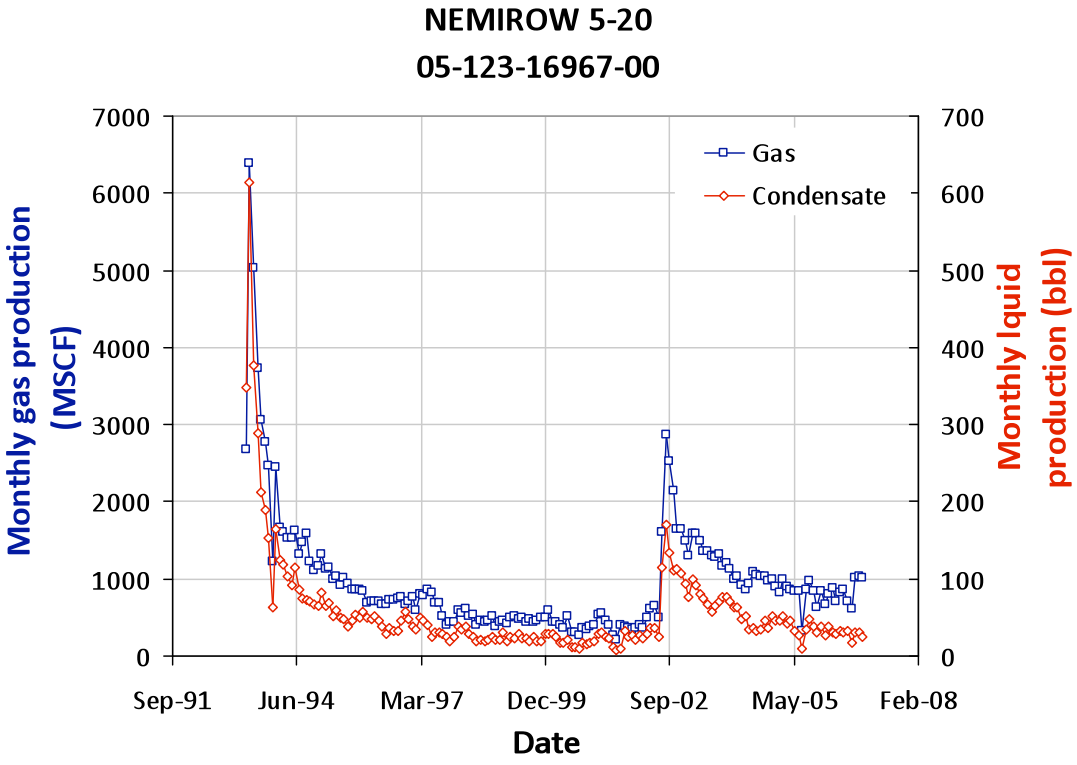
NEMIROW 5-20
05-123-16967-00
Gas
Condensate
Monthly gas production (MSCF)
Monthly liquid production (bbl)
7000
6000
5000
4000
3000
2000
1000
0
700
600
500
400
300
200
100
0
Sep-91
Jun-94
Mar-97
Dec-99
Sep-02
May-05
Feb-08
Date

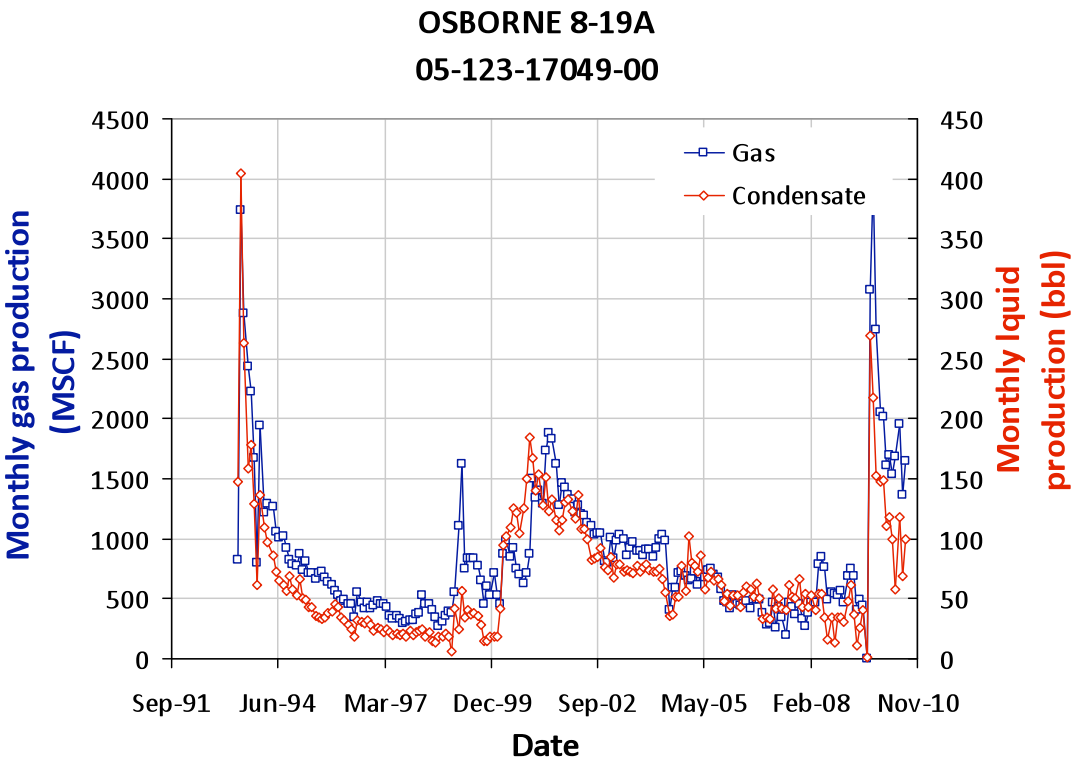
OSBORNE 8-19A
05-123-17049-00
Monthly gas production (MSCF)
Monthly liquid production (bbl)
Gas
Condensate
4500
4000
3500
3000
2500
2000
1500
1000
500
0
450
400
350
300
250
200
150
100
50
0
Sep-91
Jun-94
Mar-97
Dec-99
Sep-02
May-05
Feb-08
Nov-10
Date

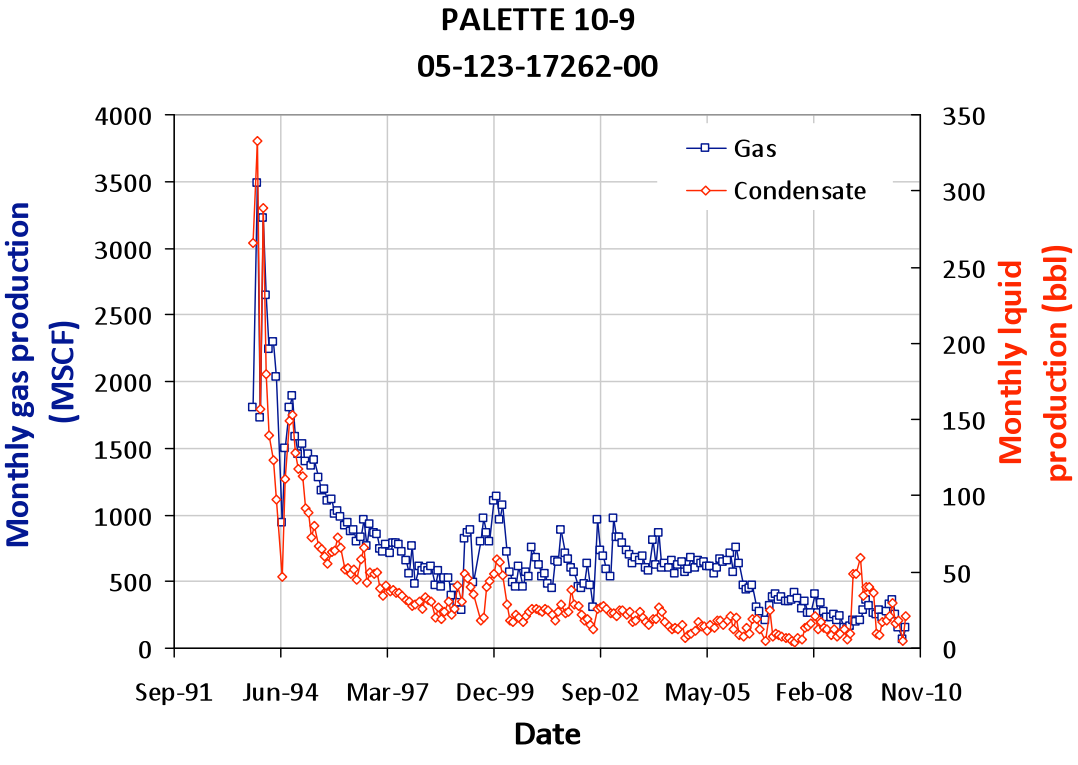
PALETTE 10-9
05-123-17262-00
Monthly gas production (MSCF)
Monthly liquid production (bbl)
Gas
Condensate
4000
3500
3000
2500
2000
1500
1000
500
0
350
300
250
200
150
100
50
0
Sep-91
Jun-94
Mar-97
Dec-99
Sep-02
May-05
Feb-08
Nov-10
Date

PANTALEO 10-29A

05-123-16880-00

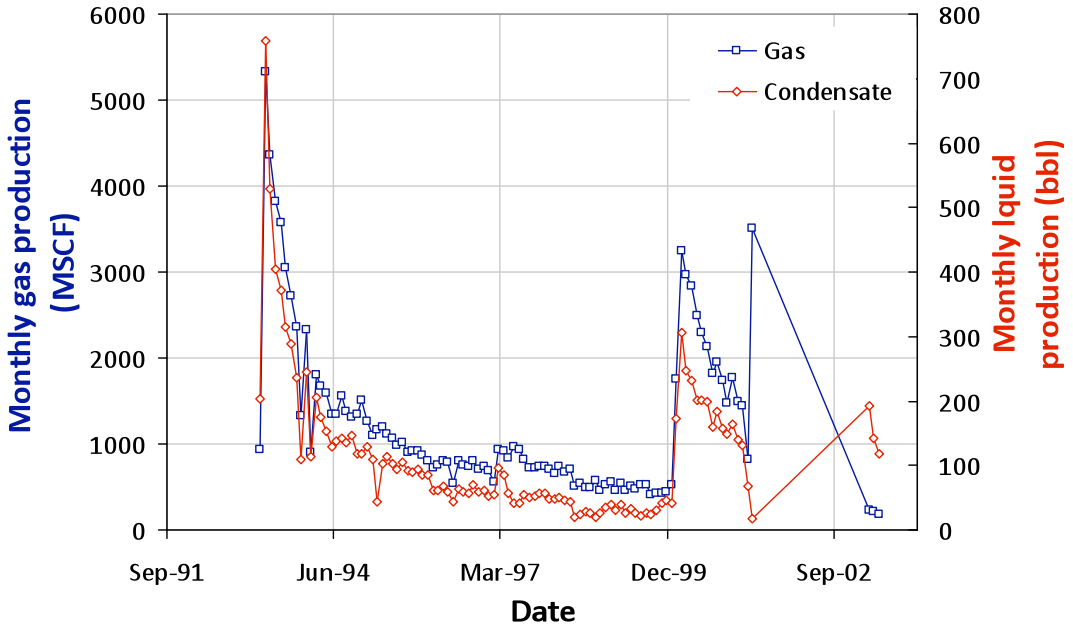

PARAS 9-30

05-123-16951-00

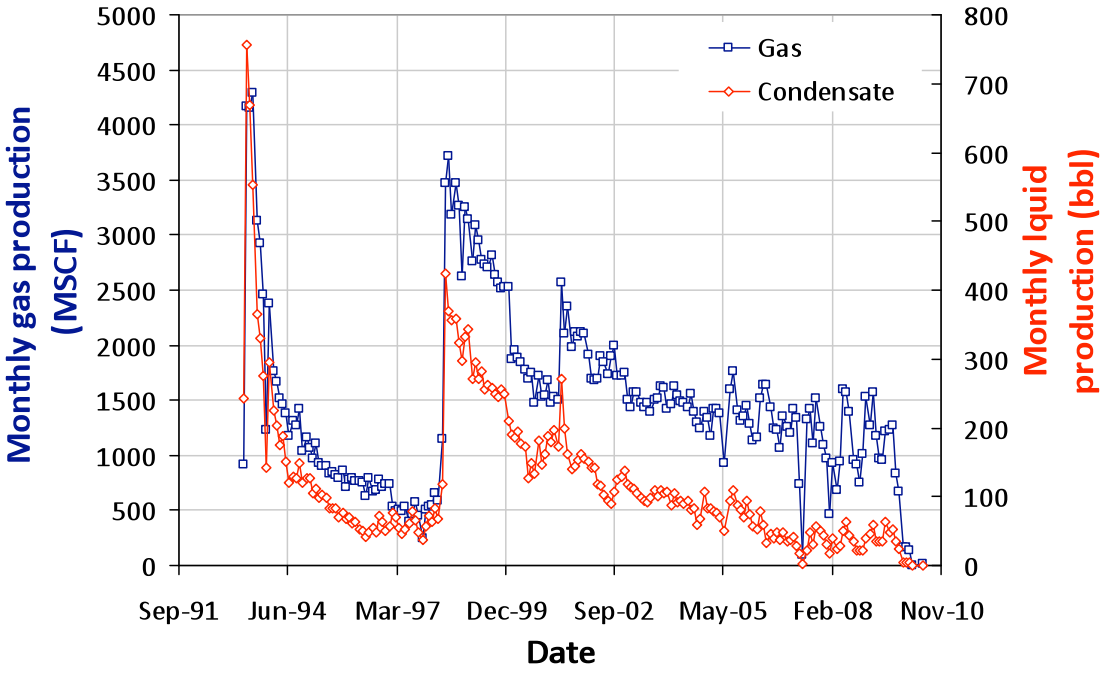

PETERSON 12-29

05-123-16881-00

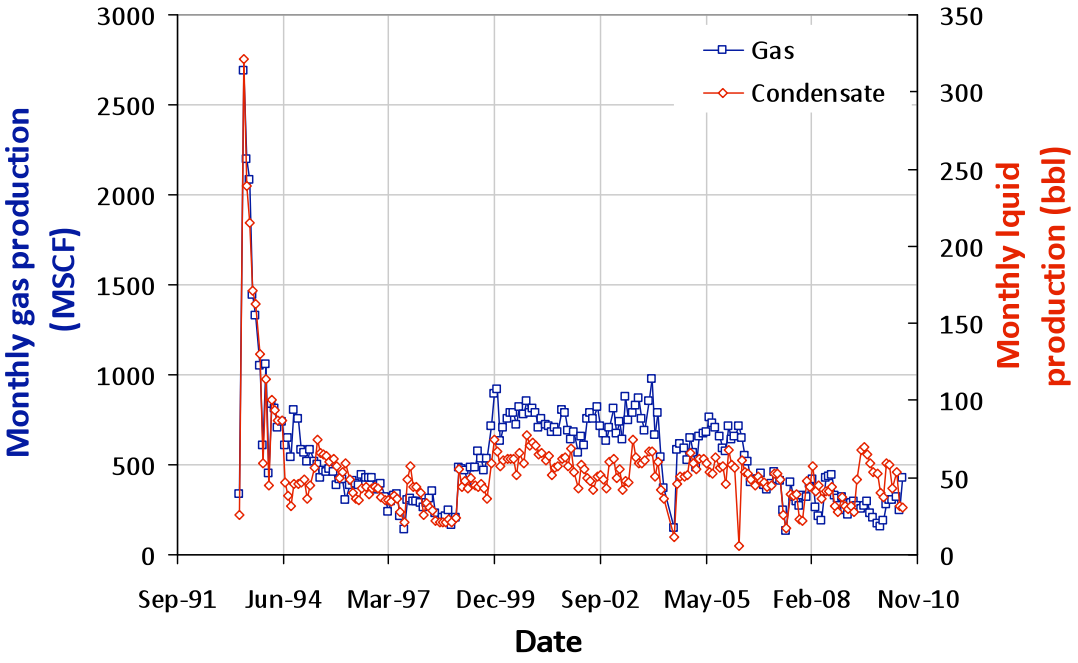

PICKRELL 13-5A

05-123-17305-00

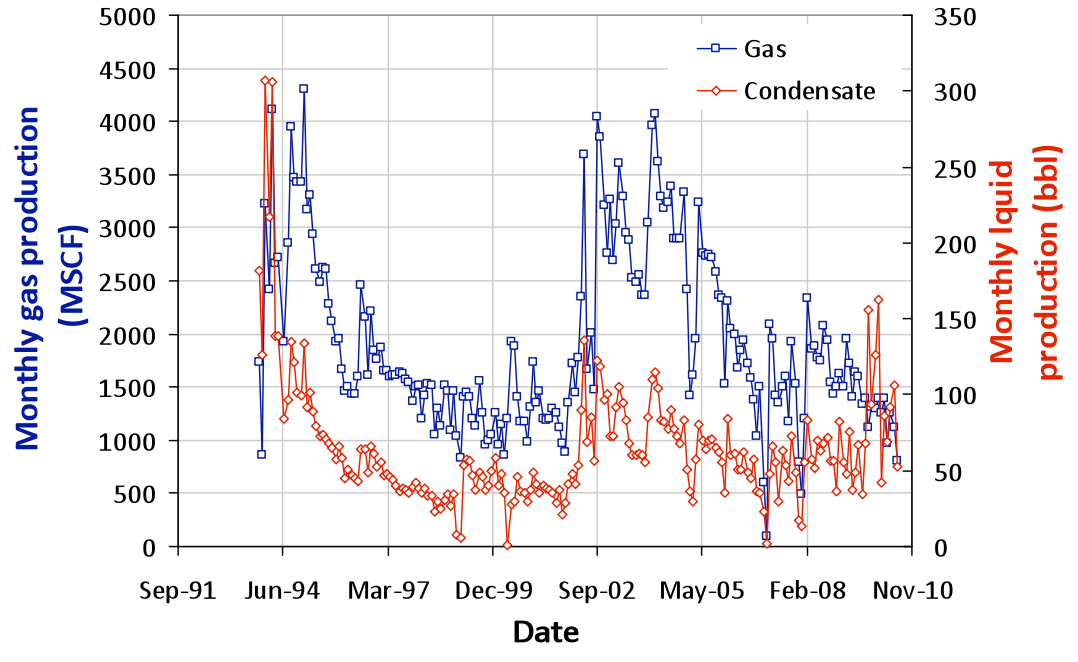

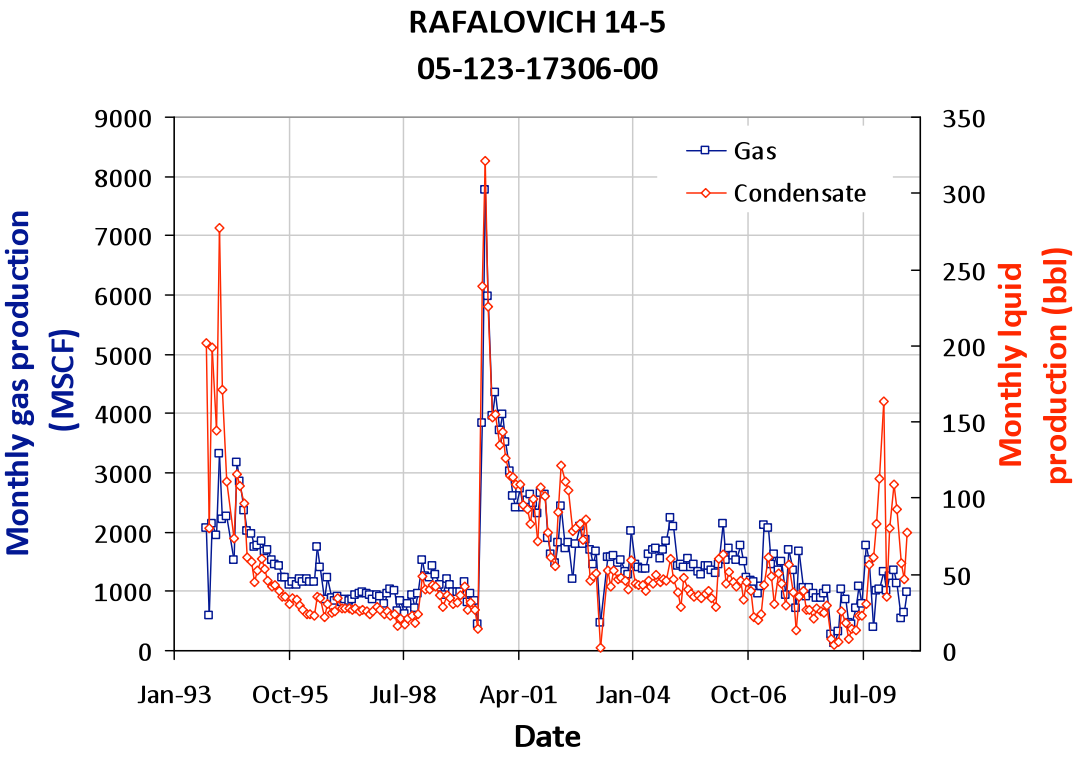
RAFALOVICH 14-5
05-123-17306-00
Monthly gas production (MSCF)
Monthly liquid production (bbl)
Gas
Condensate
9000
8000
7000
6000
5000
4000
3000
2000
1000
0
350
300
250
200
150
100
50
0
Jan-93
Oct-95
Jul-98
Apr-01
Jan-04
Oct-06
Jul-09
Date

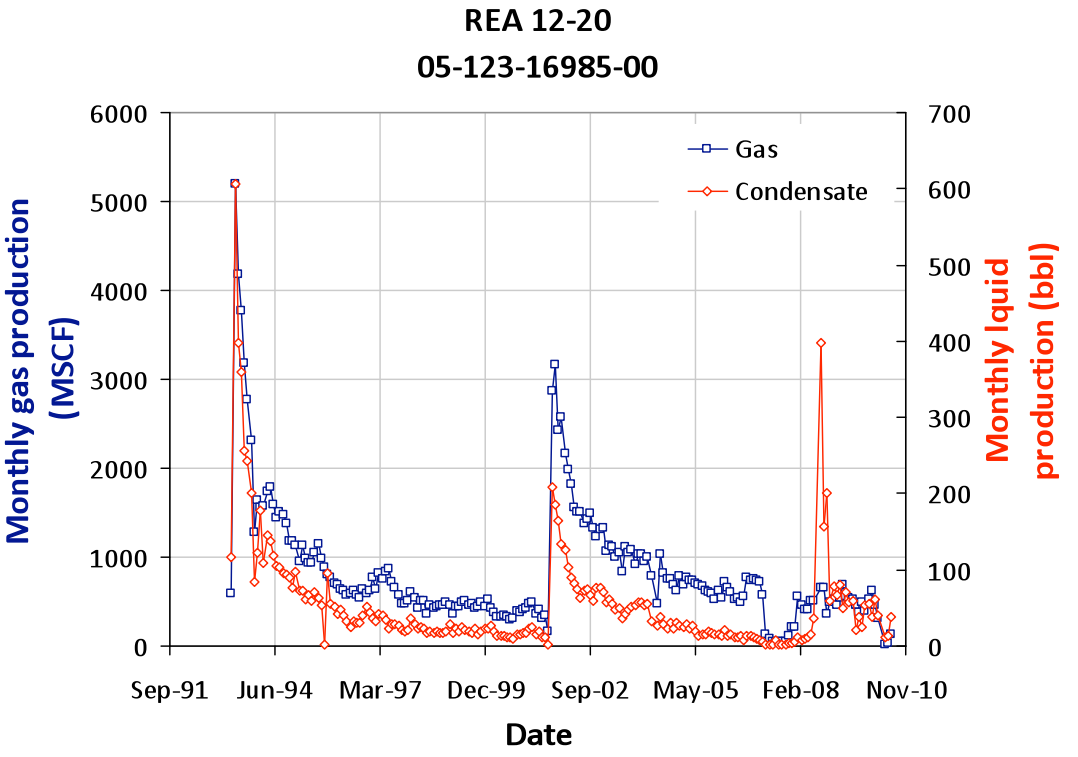
REA 12-20
05-123-16985-00
Monthly gas production (MSCF)
Monthly liquid production (bbl)
Gas
Condensate
6000
5000
4000
3000
2000
1000
0
700
600
500
400
300
200
100
0
Sep-91
Jun-94
Mar-97
Dec-99
Sep-02
May-05
Feb-08
Nov-10
Date

REAM 15-5
05-123-17307-00

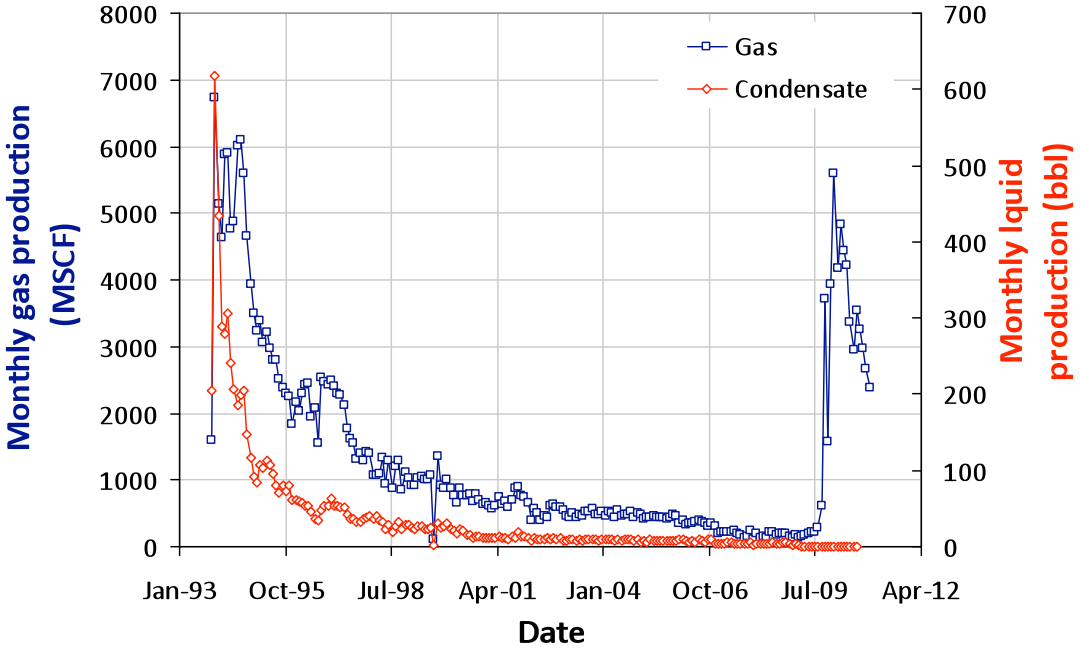

REI 1-9
05-123-23318-00

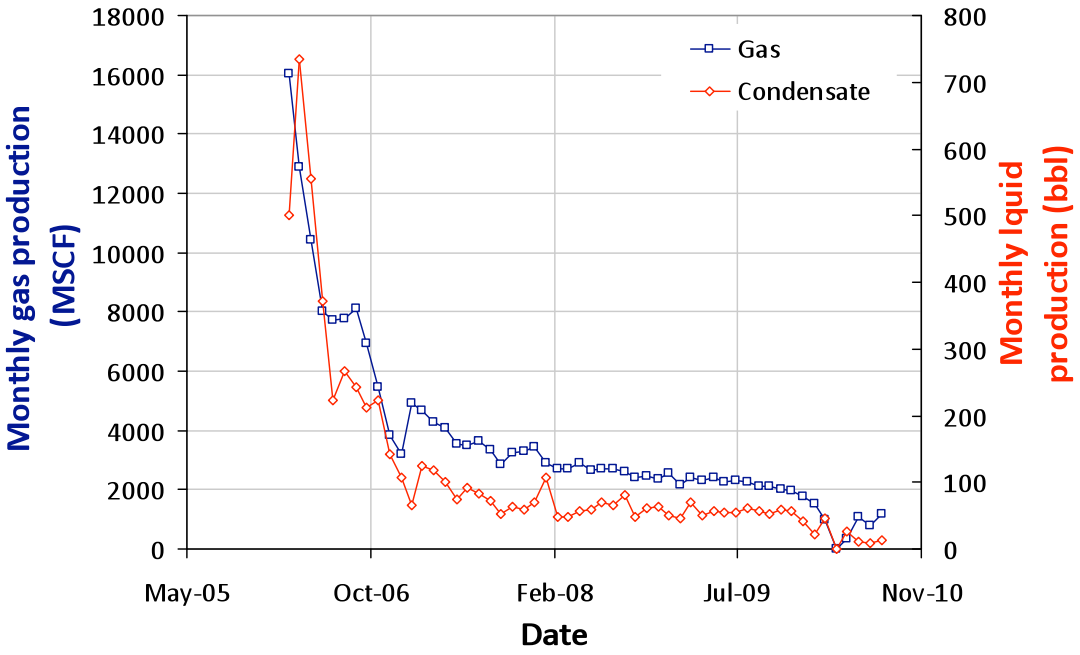

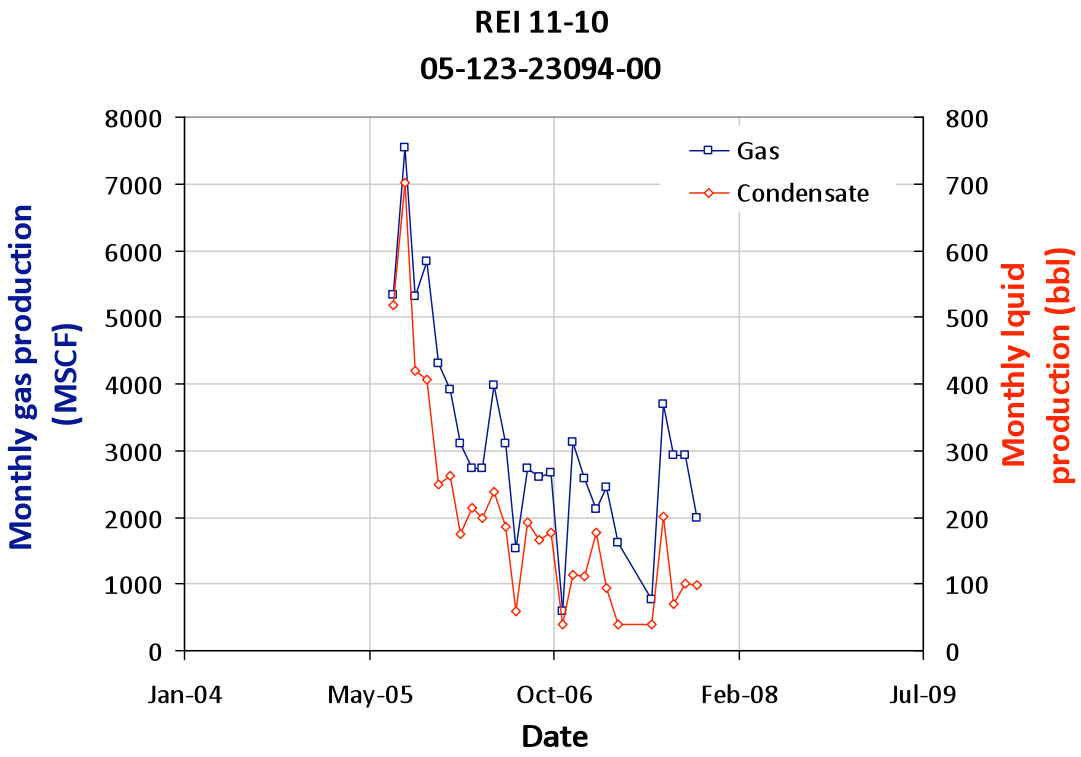
REI 11-10
05-123-23094-00
Monthly gas production (MSCF)
Monthly liquid production (bbl)
Gas
Condensate
8000
7000
6000
5000
4000
3000
2000
1000
0
800
700
600
500
400
300
200
100
0
Jan-04
May-05
Oct-06
Feb-08
Jul-09
Date

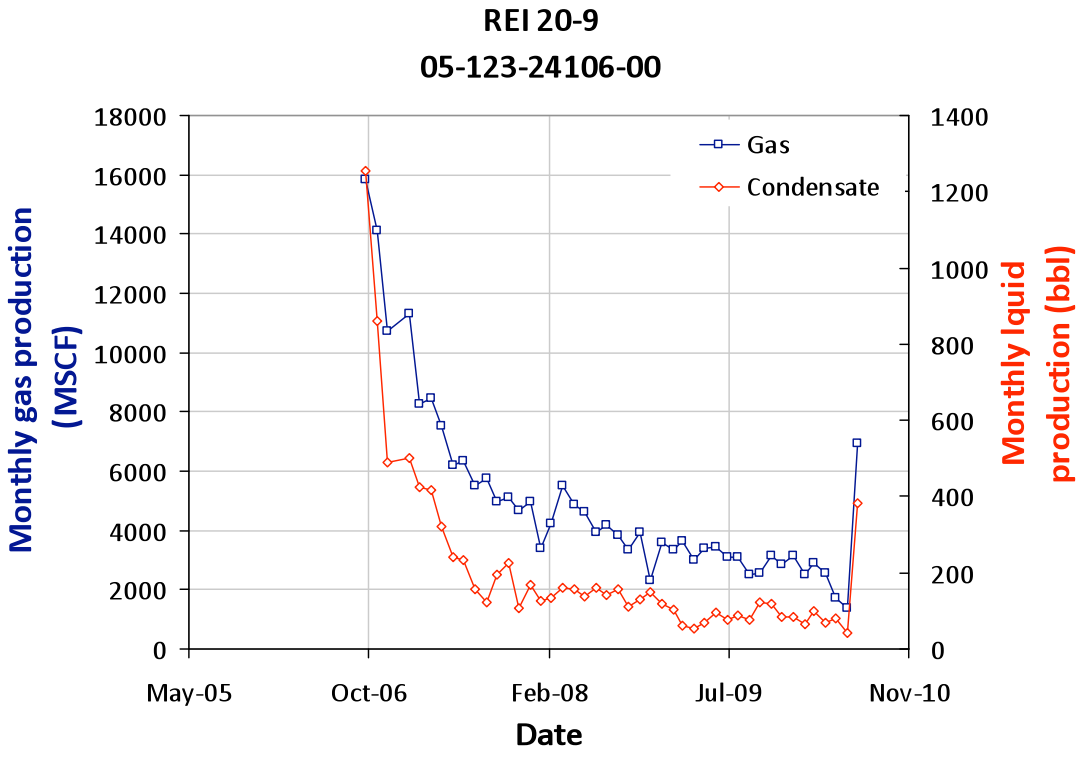
REI 20-9
05-123-24106-00
Monthly gas production (MSCF)
Monthly liquid production (bbl)
Gas
Condensate
18000
16000
14000
12000
10000
8000
6000
4000
2000
0
1400
1200
1000
800
600
400
200
0
May-05
Oct-06
Feb-08
Jul-09
Nov-10
Date

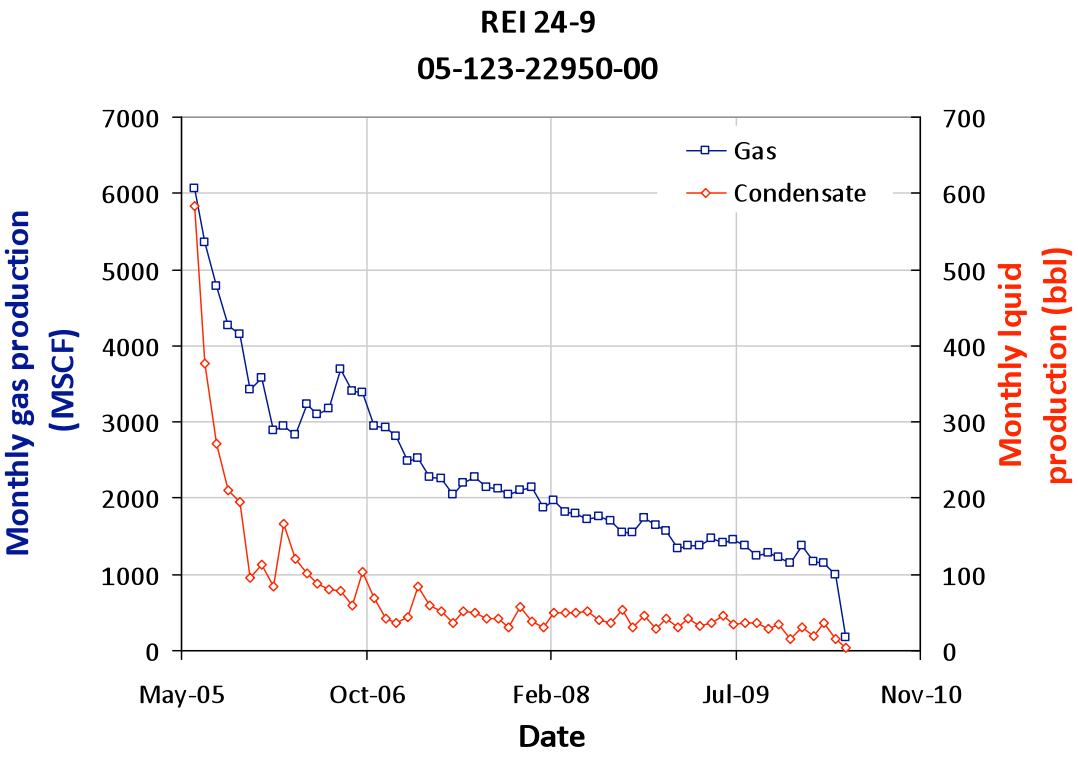
REI 24-9
05-123-22950-00
Monthly gas production (MSCF)
Monthly liquid production (bbl)
Gas
Condensate
7000
6000
5000
4000
3000
2000
1000
0
700
600
500
400
300
200
100
0
May-05
Oct-06
Feb-08
Jul-09
Nov-10
Date

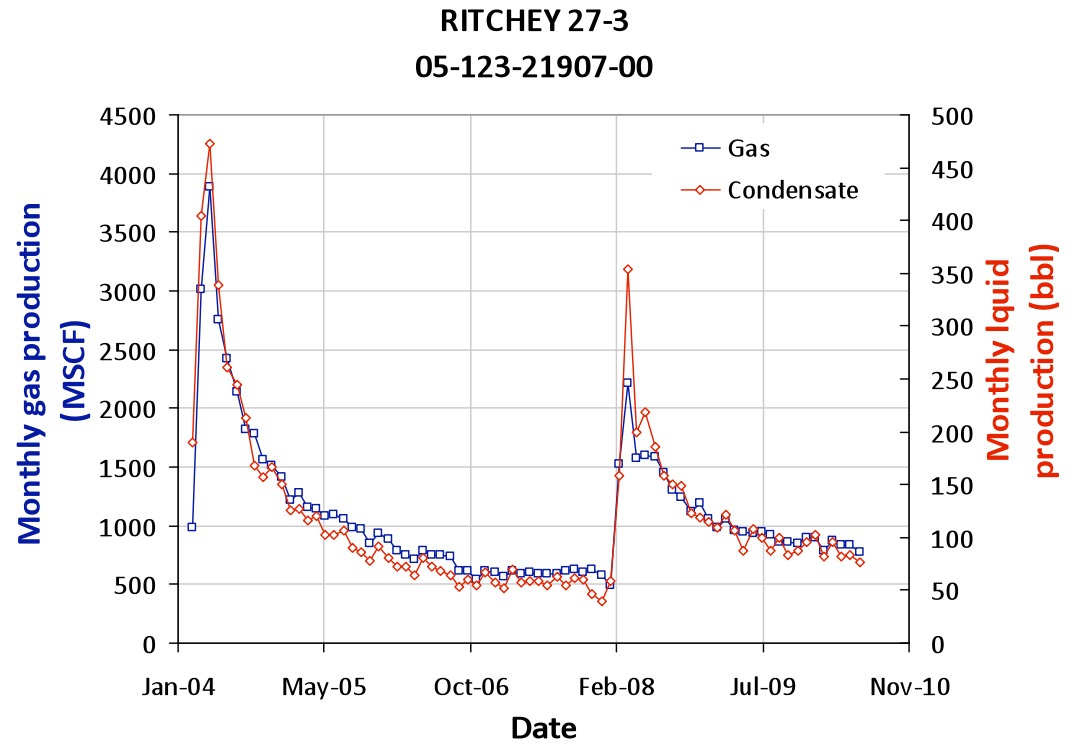
RITCHEY 27-3
05-123-21907-00
Monthly gas production (MSCF)
Monthly liquid production (bbl)
Gas
Condensate
4500
4000
3500
3000
2500
2000
1500
1000
500
0
500
450
400
350
300
250
200
150
100
50
0
Jan-04
May-05
Oct-06
Feb-08
Jul-09
Nov-10
Date

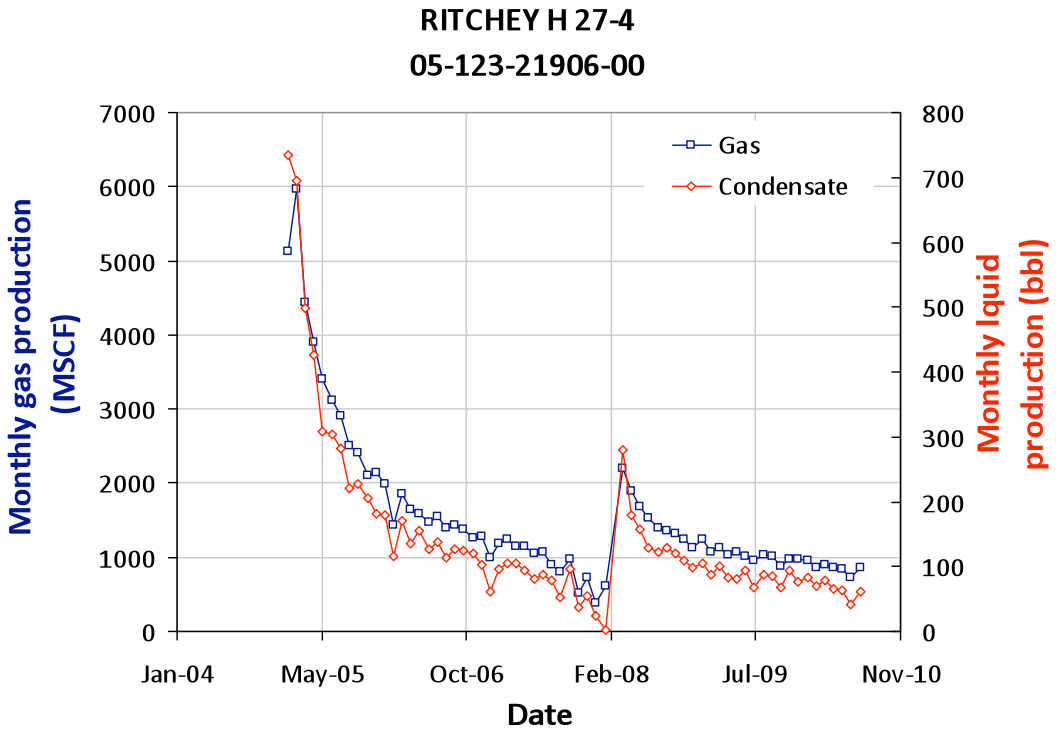
RITCHEY H 27-4
05-123-21906-00
Monthly gas production (MSCF)
Monthly liquid production (bbl)
Gas
Condensate
7000
6000
5000
4000
3000
2000
1000
0
800
700
600
500
400
300
200
100
0
Jan-04
May-05
Oct-06
Feb-08
Jul-09
Nov-10
Date

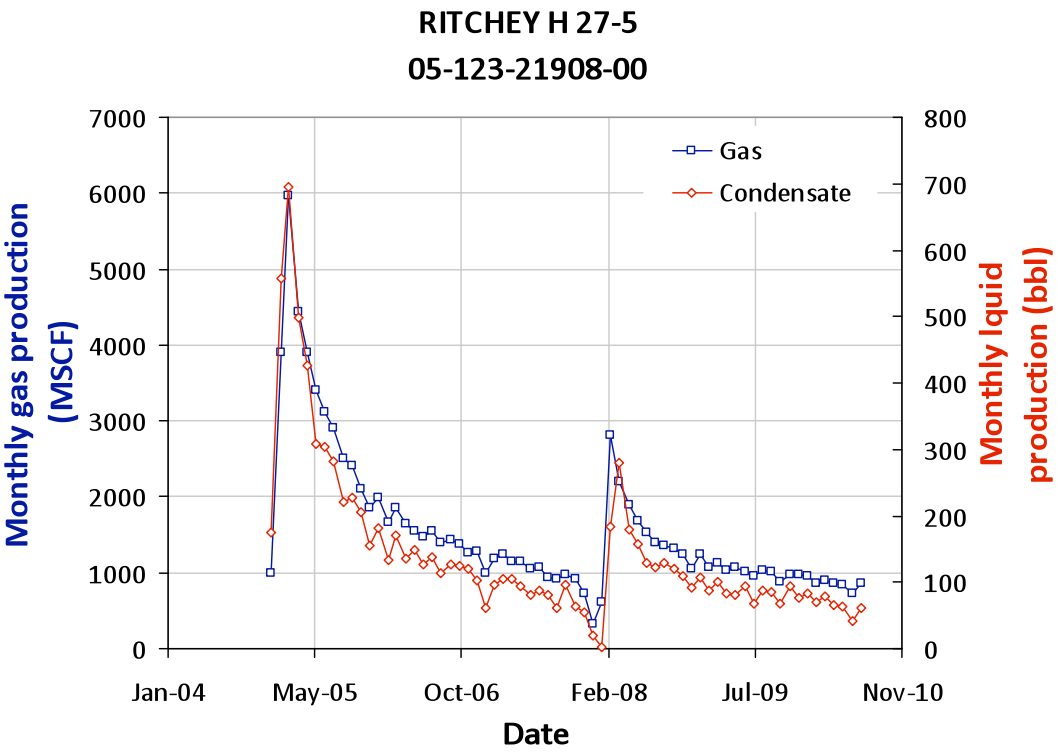
RITCHEY H 27-5
05-123-21908-00
Monthly gas production (MSCF)
Monthly liquid production (bbl)
Gas
Condensate
7000
6000
5000
4000
3000
2000
1000
0
800
700
600
500
400
300
200
100
0
Jan-04
May-05
Oct-06
Feb-08
Jul-09
Nov-10
Date

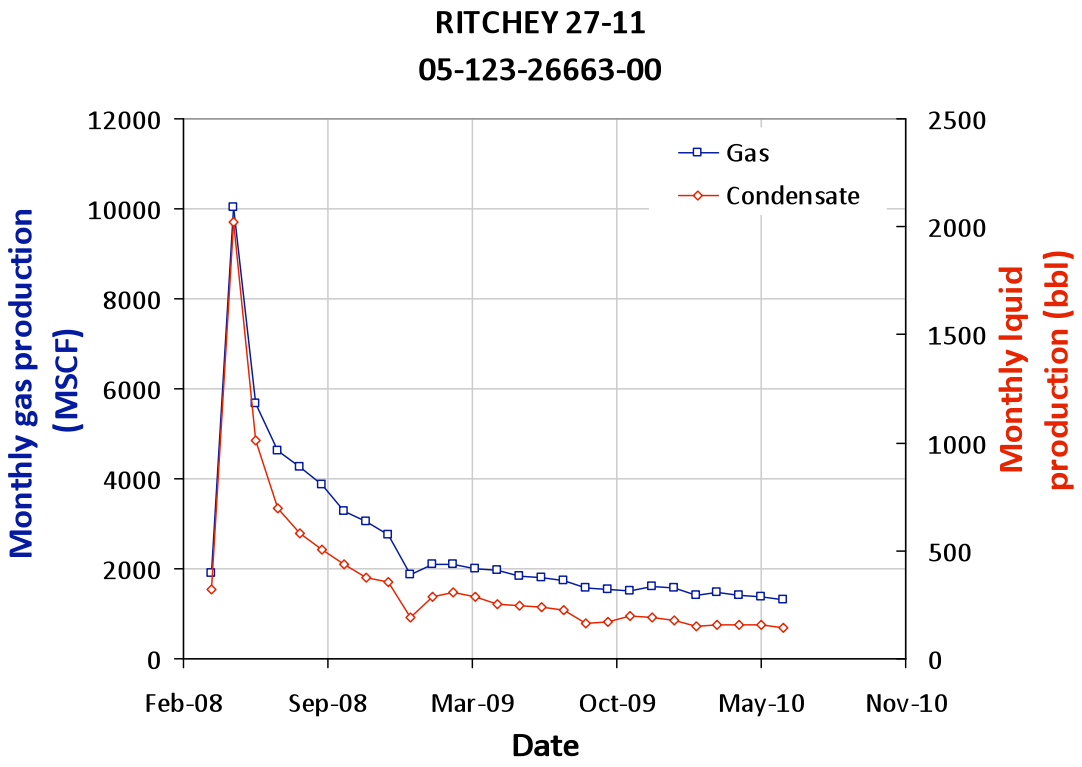
RITCHEY 27-11
05-123-26663-00
Monthly gas production (MSCF)
Monthly liquid production (bbl)
Gas
Condensate
12000
10000
8000
6000
4000
2000
0
2500
2000
1500
1000
500
0
Feb-08
Sep-08
Mar-09
Oct-09
May-10
Nov-10
Date

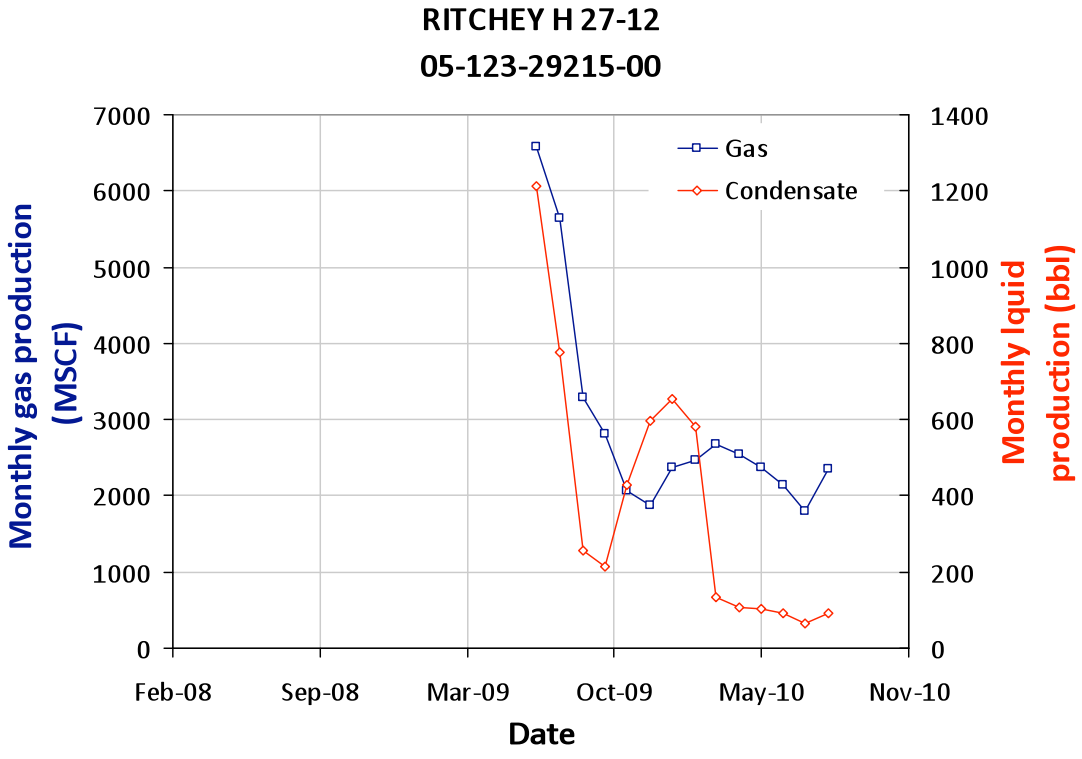
RITCHEY H 27-12
05-123-29215-00
Monthly gas production (MSCF)
Monthly liquid production (bbl)
Gas
Condensate
7000
6000
5000
4000
3000
2000
1000
0
1400
1200
1000
800
600
400
200
0
Feb-08
Sep-08
Mar-09
Oct-09
May-10
Nov-10
Date

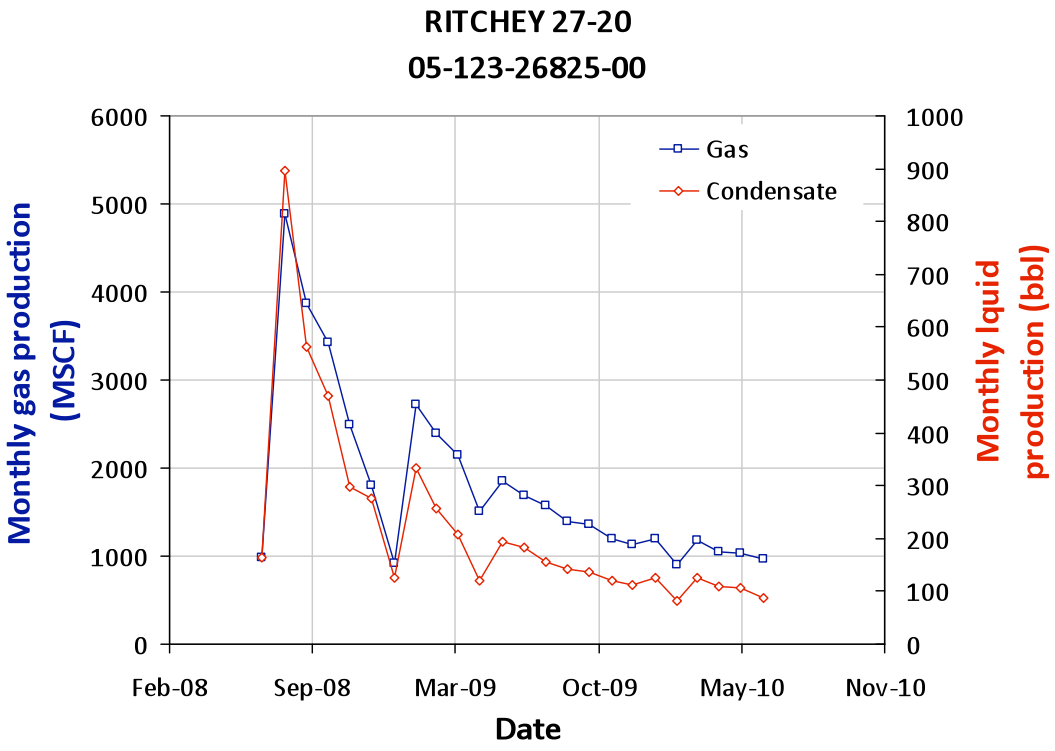
RITCHEY 27-20
05-123-26825-00
Monthly gas production (MSCF)
Monthly liquid production (bbl)
Gas
Condensate
6000
5000
4000
3000
2000
1000
0
1000
900
800
700
600
500
400
300
200
100
0
Feb-08
Sep-08
Mar-09
Oct-09
May-10
Nov-10
Date

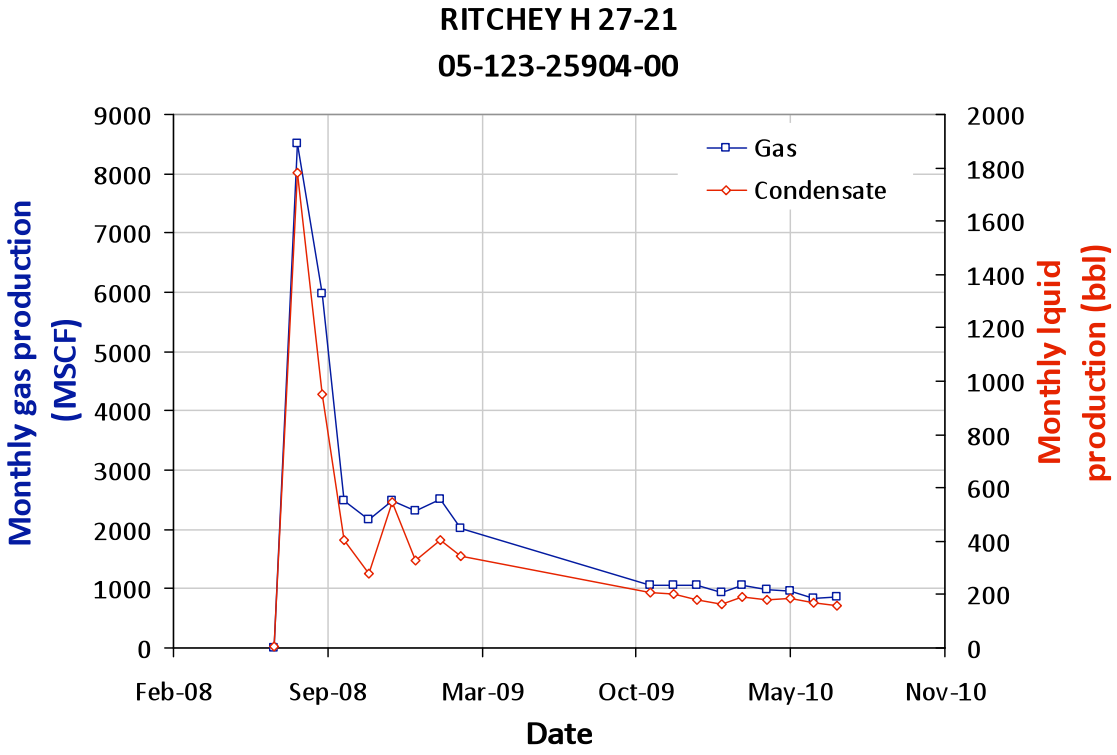
RITCHEY H 27-21
05-123-25904-00
Monthly gas production (MSCF)
Monthly liquid production (bbl)
Gas
Condensate
9000
8000
7000
6000
5000
4000
3000
2000
1000
0
2000
1800
1600
1400
1200
1000
800
600
400
200
0
Feb-08
Sep-08
Mar-09
Oct-09
May-10
Nov-10
Date

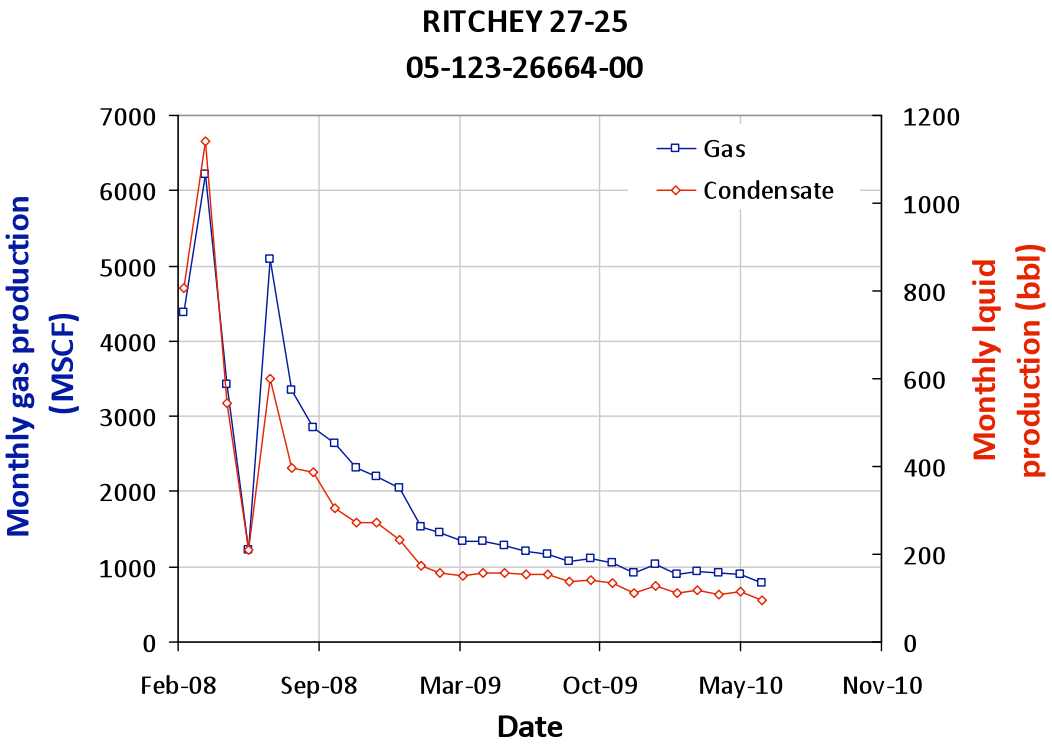
RITCHEY 27-25
05-123-26664-00
Monthly gas production (MSCF)
Monthly lquid production (bbl)
Gas
Condensate
7000
6000
5000
4000
3000
2000
1000
0
1200
1000
800
600
400
200
0
Feb-08
Sep-08
Mar-09
Oct-09
May-10
Nov-10
Date

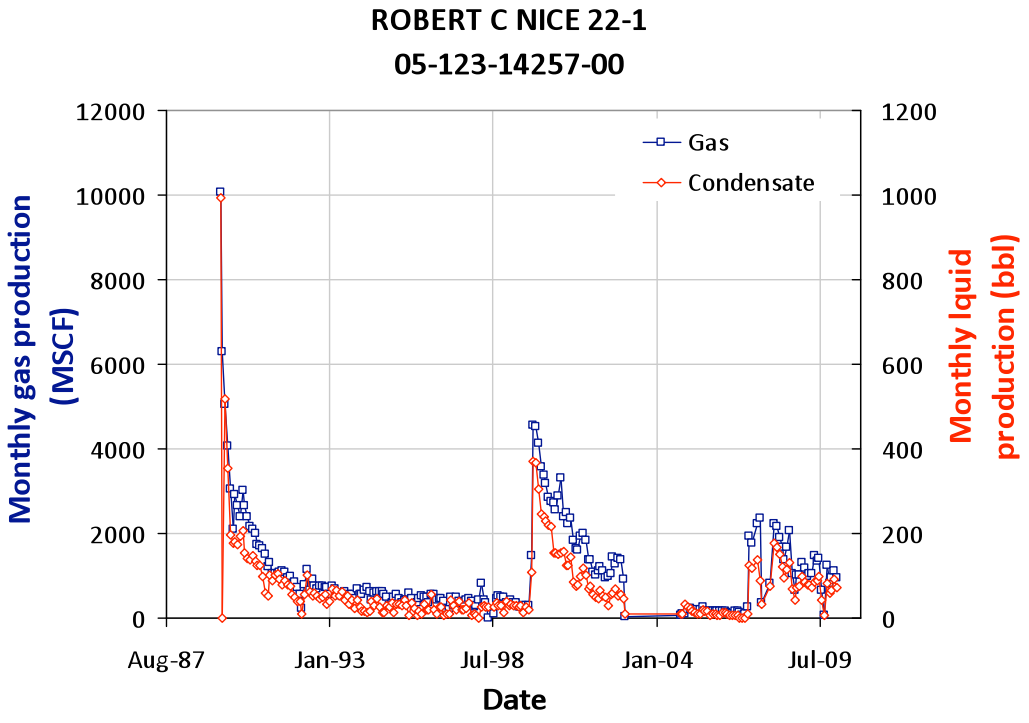
ROBERT C NICE 22-1
05-123-14257-00
Monthly gas production (MSCF)
Monthly lquid production (bbl)
Gas
Condensate
12000
10000
8000
6000
4000
2000
0
1200
1000
800
600
400
200
0
Aug-87
Jan-93
Jul-98
Jan-04
Jul-09
Date

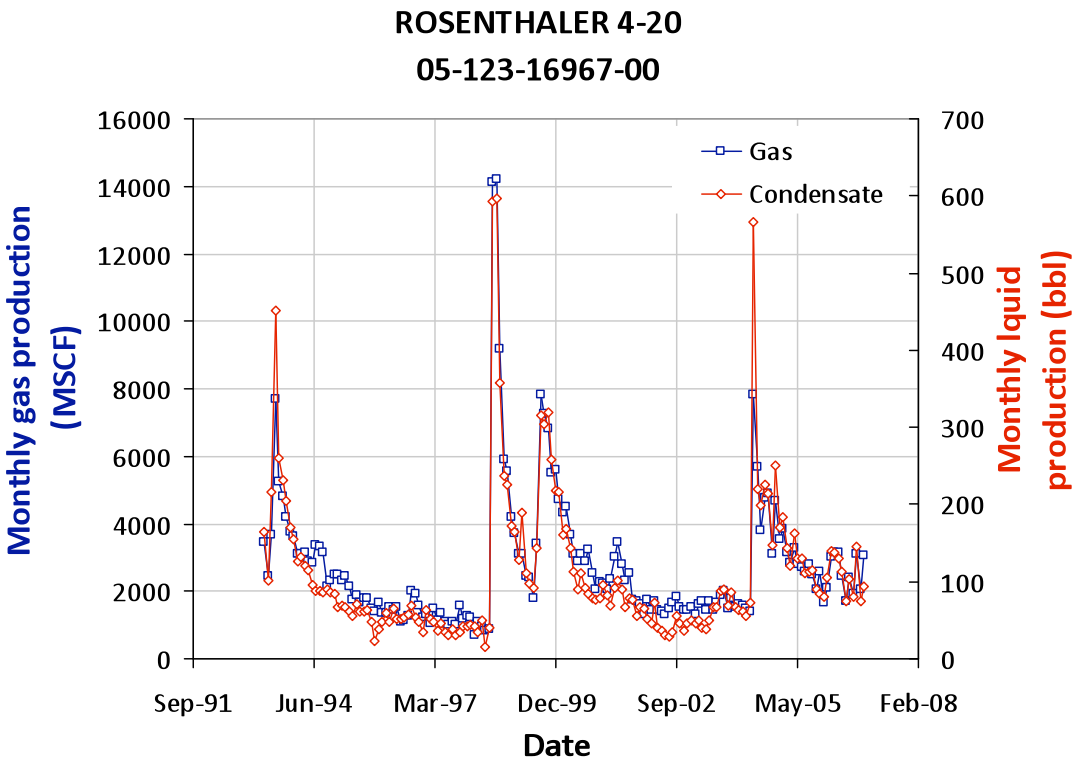
ROSENTHALER 4-20
05-123-16967-00
Monthly gas production (MSCF)
Monthly liquid production (bbl)
Gas
Condensate
16000
14000
12000
10000
8000
6000
4000
2000
0
700
600
500
400
300
200
100
0
Sep-91
Jun-94
Mar-97
Dec-99
Sep-02
May-05
Feb-08
Date

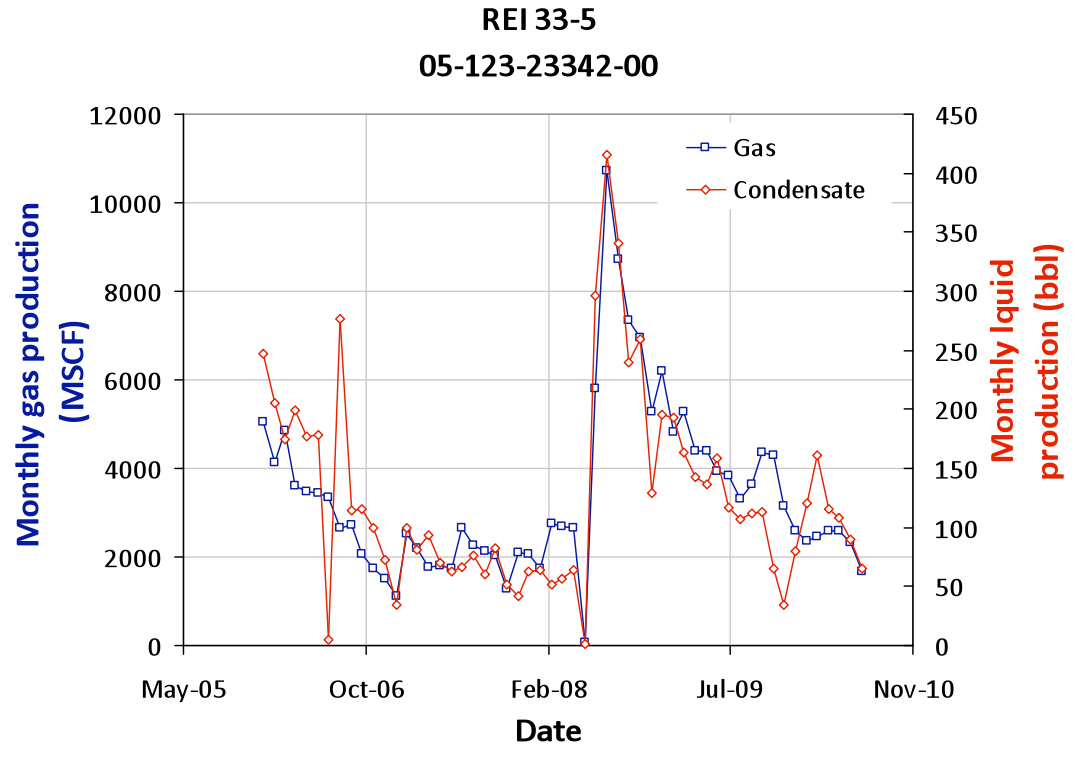
REI 33-5
05-123-23342-00
Monthly gas production (MSCF)
Monthly liquid production (bbl)
Gas
Condensate
12000
10000
8000
6000
4000
2000
0
450
400
350
300
250
200
150
100
50
0
May-05
Oct-06
Feb-08
Jul-09
Nov-10
Date

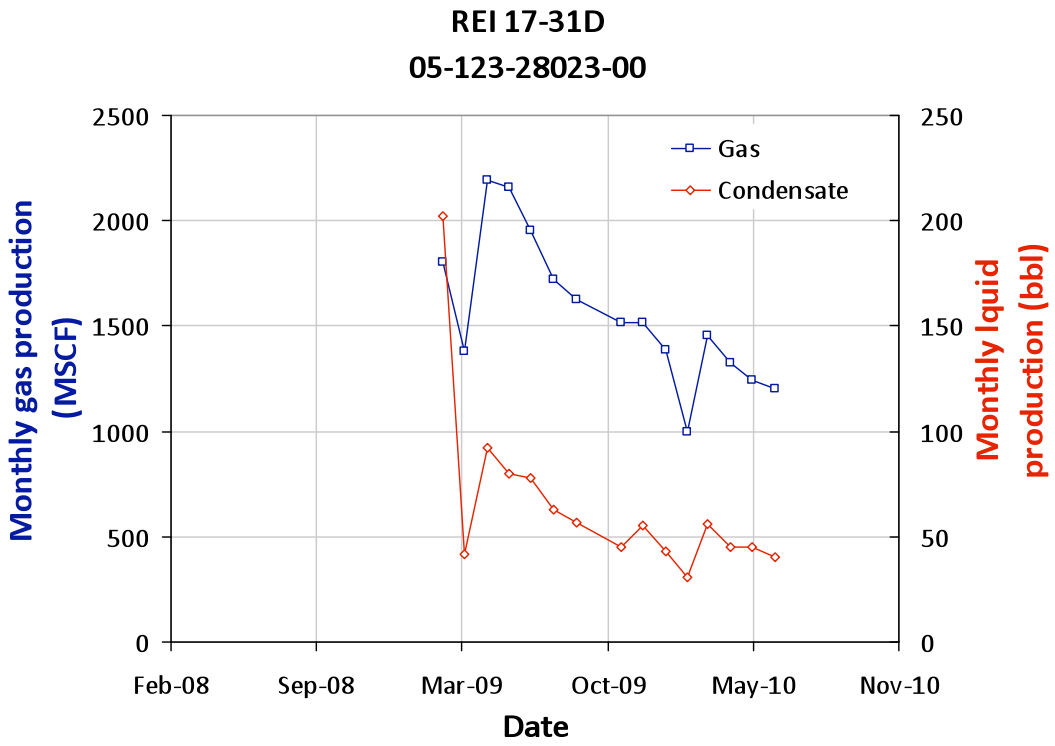
REI 17-31D
05-123-28023-00
Monthly gas production (MSCF)
Monthly liquid production (bbl)
Gas
Condensate
2500
2000
1500
1000
500
0
250
200
150
100
50
0
Feb-08
Sep-08
Mar-09
Oct-09
May-10
Nov-10
Date

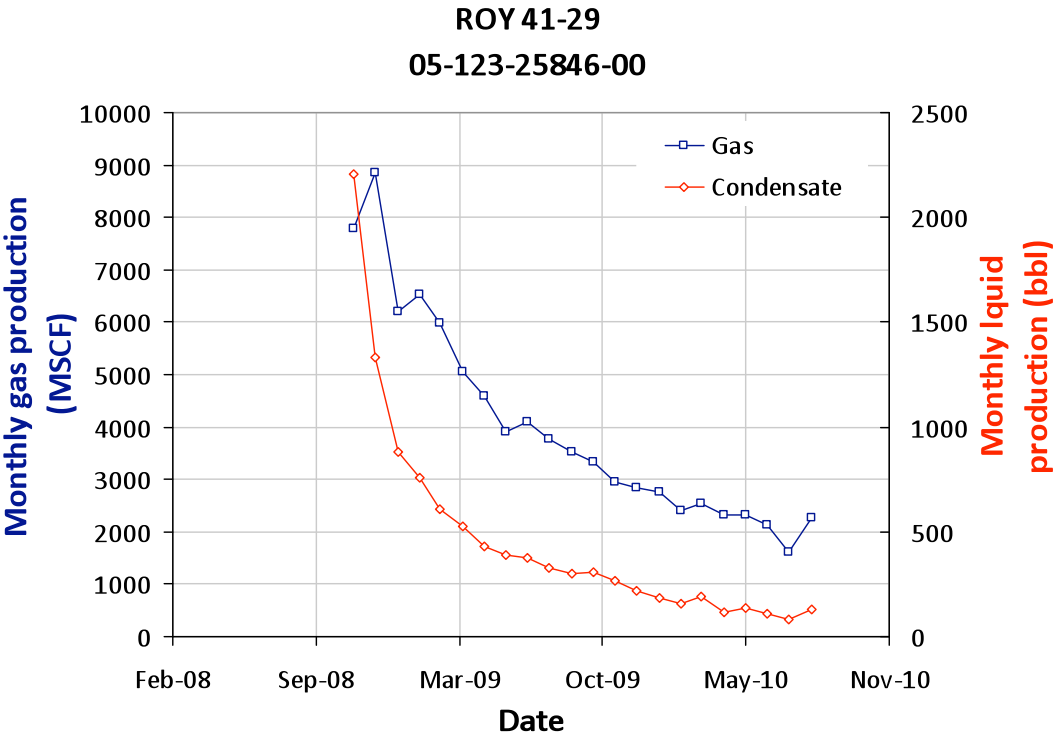
ROY 41-29
05-123-25846-00
Monthly gas production (MSCF)
Monthly liquid production (bbl)
Gas
Condensate
10000
9000
8000
7000
6000
5000
4000
3000
2000
1000
0
2500
2000
1500
1000
500
0
Feb-08
Sep-08
Mar-09
Oct-09
May-10
Nov-10
Date

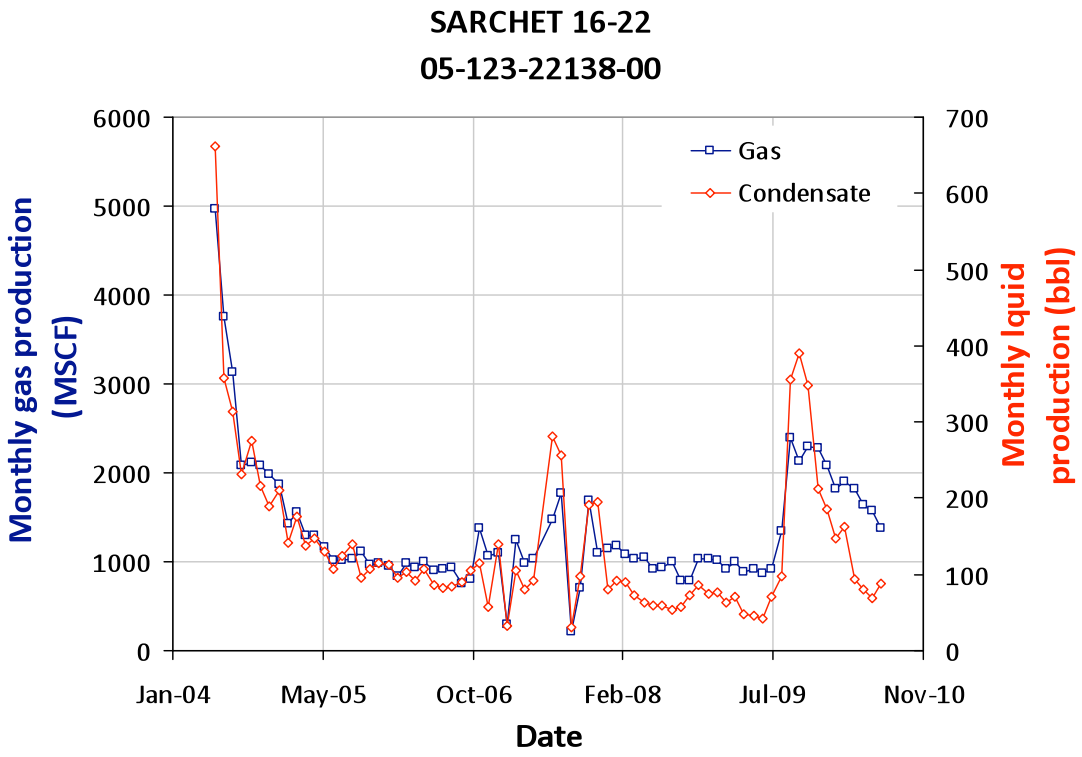
SARCHET 16-22
05-123-22138-00
Monthly gas production (MSCF)
Monthly liquid production (bbl)
Gas
Condensate
6000
5000
4000
3000
2000
1000
0
700
600
500
400
300
200
100
0
Jan-04
May-05
Oct-06
Feb-08
Jul-09
Nov-10
Date

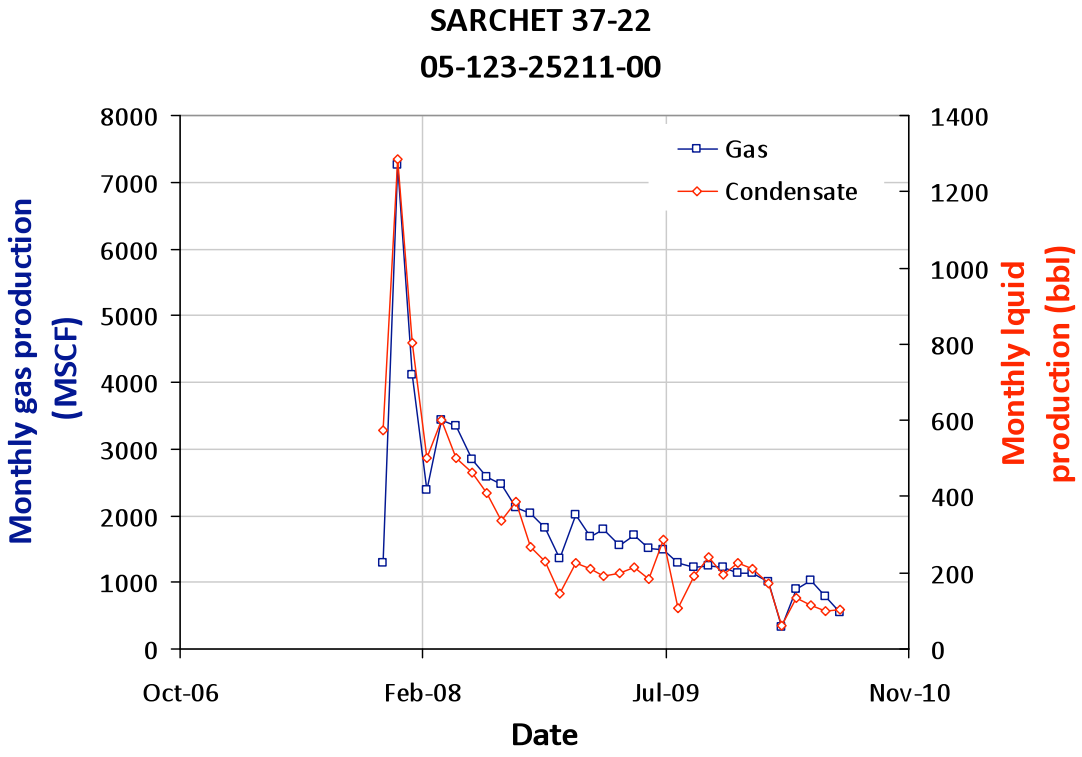
SARCHET 37-22
05-123-25211-00
Monthly gas production (MSCF)
Monthly liquid production (bbl)
Gas
Condensate
8000
7000
6000
5000
4000
3000
2000
1000
0
1400
1200
1000
800
600
400
200
0
Oct-06
Feb-08
Jul-09
Nov-10
Date

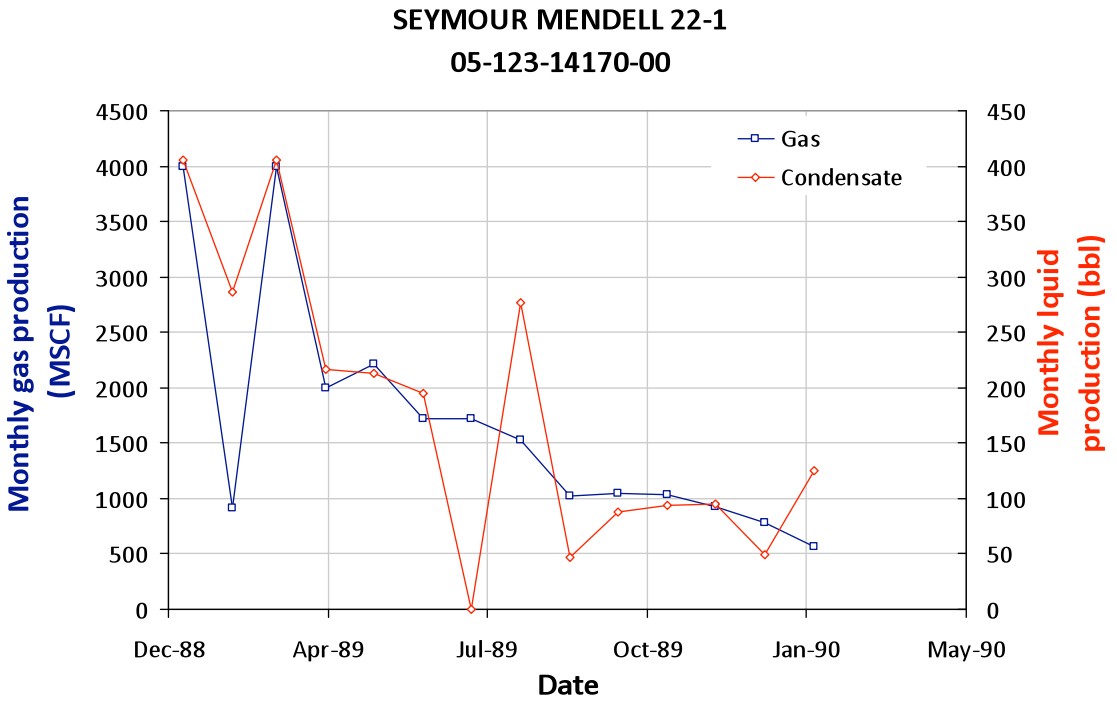
SEYMOUR MENDELL 22-1
05-123-14170-00
Monthly gas production (MSCF)
Monthly liquid production (bbl)
Gas
Condensate
4500
4000
3500
3000
2500
2000
1500
1000
500
0
450
400
350
300
250
200
150
100
50
0
Dec-88
Apr-89
Jul-89
Oct-89
Jan-90
May-90
Date

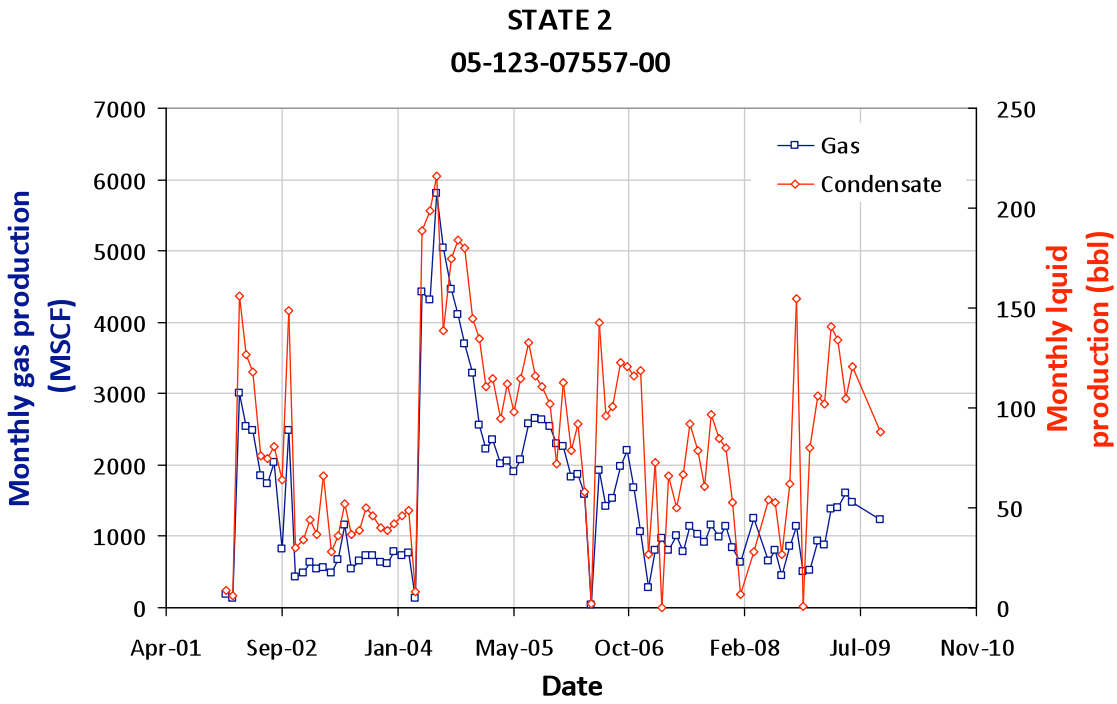
STATE 2
05-123-07557-00
Monthly gas production (MSCF)
Monthly liquid production (bbl)
Gas
Condensate
7000
6000
5000
4000
3000
2000
1000
0
250
200
150
100
50
0
Apr-01
Sep-02
Jan-04
May-05
Oct-06
Feb-08
Jul-09
Nov-10
Date

STATE 23
05-123-07670-00

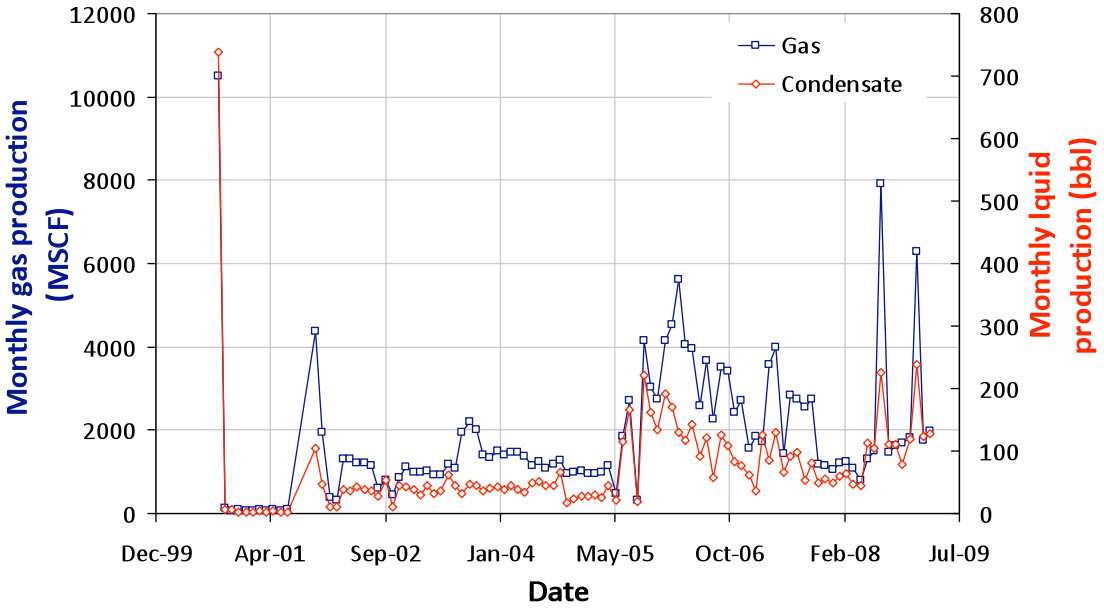

THORSON 9-27
05-123-16431-00

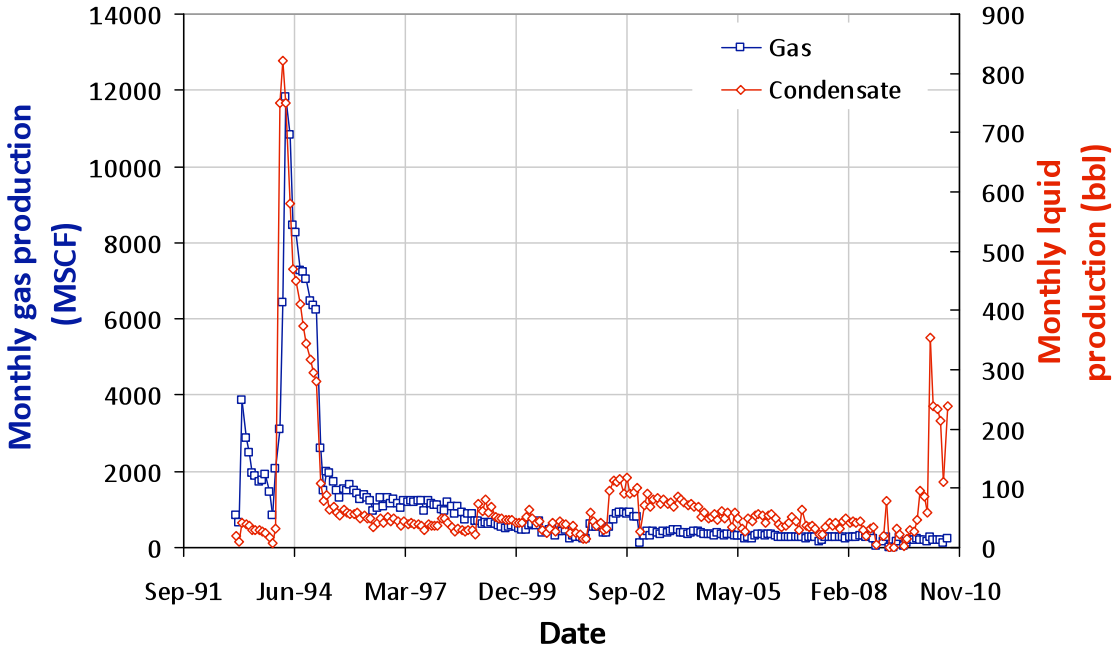

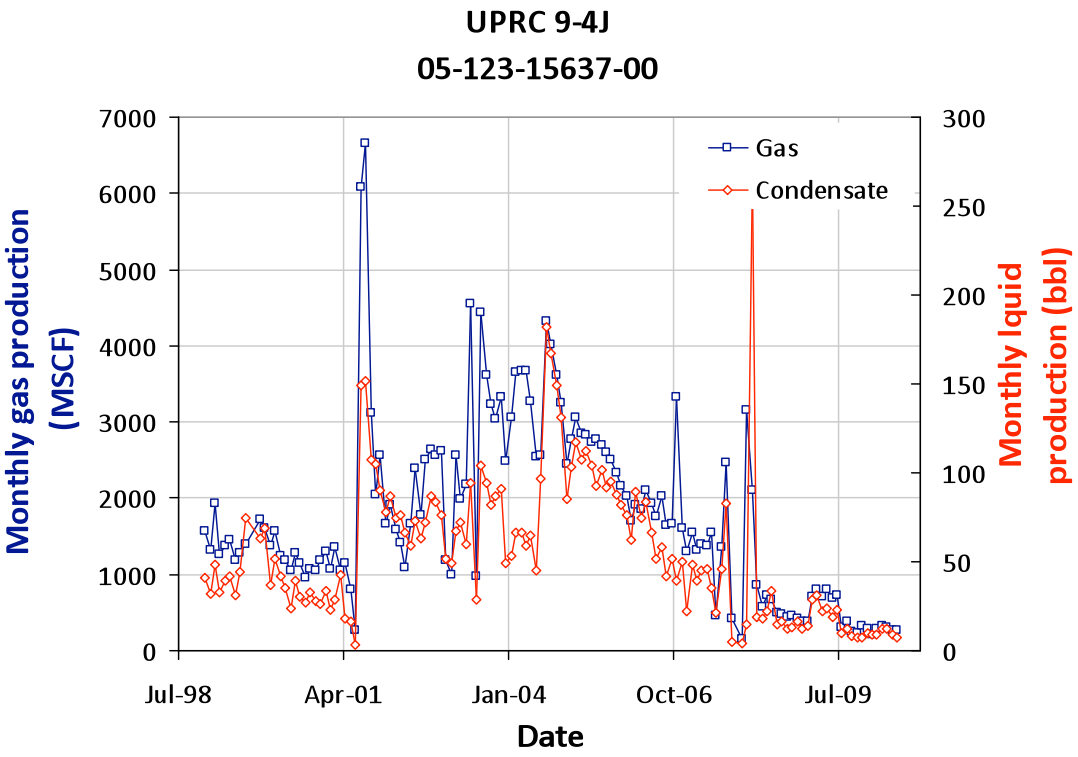
UPRC 9-4J
05-123-15637-00
Monthly gas production (MSCF)
Monthly liquid production (bbl)
Gas
Condensate
7000
6000
5000
4000
3000
2000
1000
0
300
250
200
150
100
50
0
Jul-98
Apr-01
Jan-04
Oct-06
Jul-09
Date

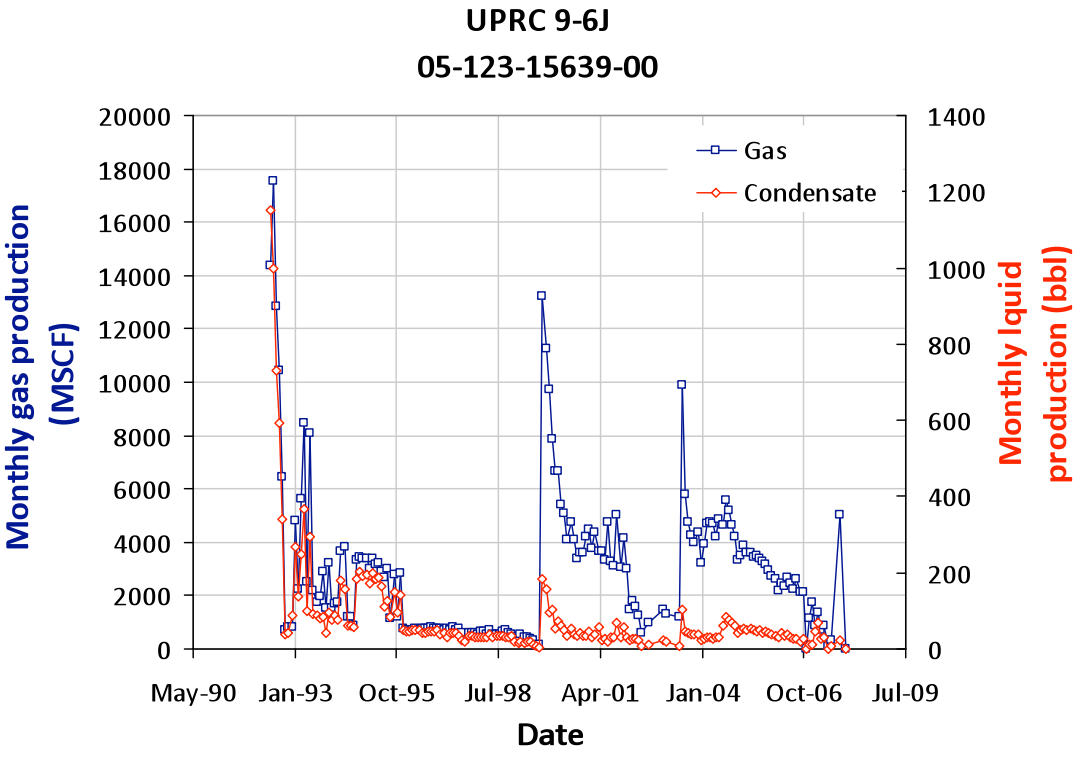
UPRC 9-6J
05-123-15639-00
Monthly gas production (MSCF)
Monthly liquid production (bbl)
Gas
Condensate
20000
18000
16000
14000
12000
10000
8000
6000
4000
2000
0
1400
1200
1000
800
600
400
200
0
May-90
Jan-93
Oct-95
Jul-98
Apr-01
Jan-04
Oct-06
Jul-09
Date

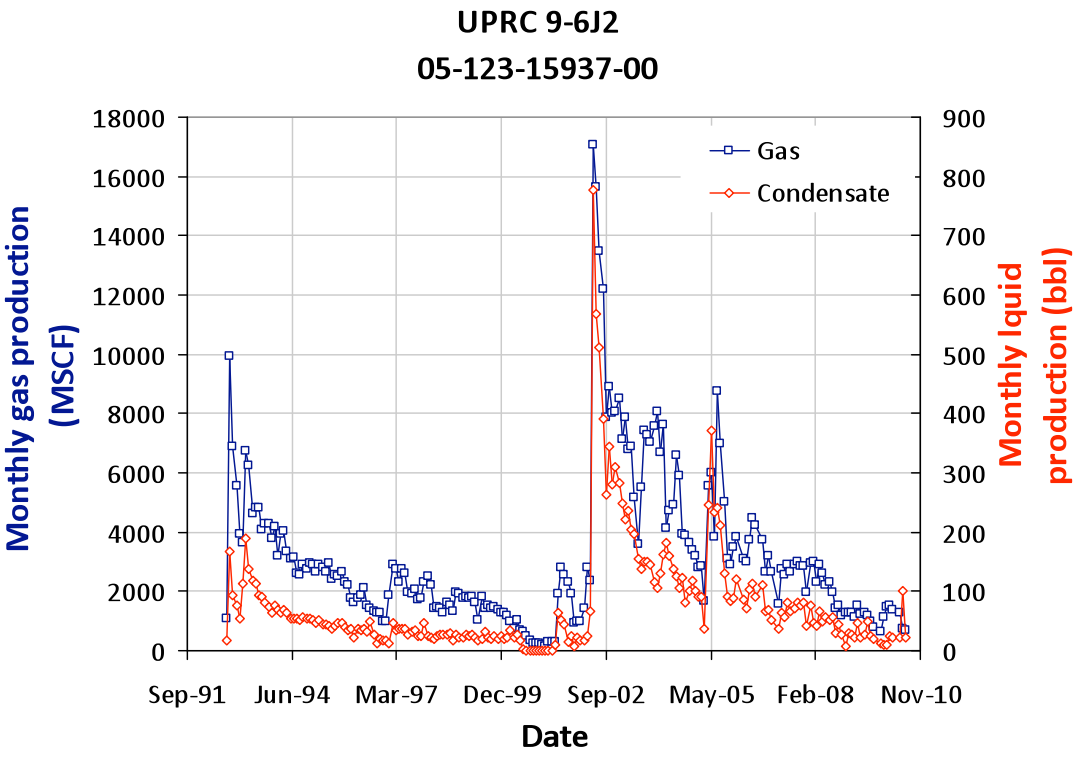
UPRC 9-6J2
05-123-15937-00
Monthly gas production (MSCF)
Monthly liquid production (bbl)
Gas
Condensate
18000
16000
14000
12000
10000
8000
6000
4000
2000
0
900
800
700
600
500
400
300
200
100
0
Sep-91
Jun-94
Mar-97
Dec-99
Sep-02
May-05
Feb-08
Nov-10
Date

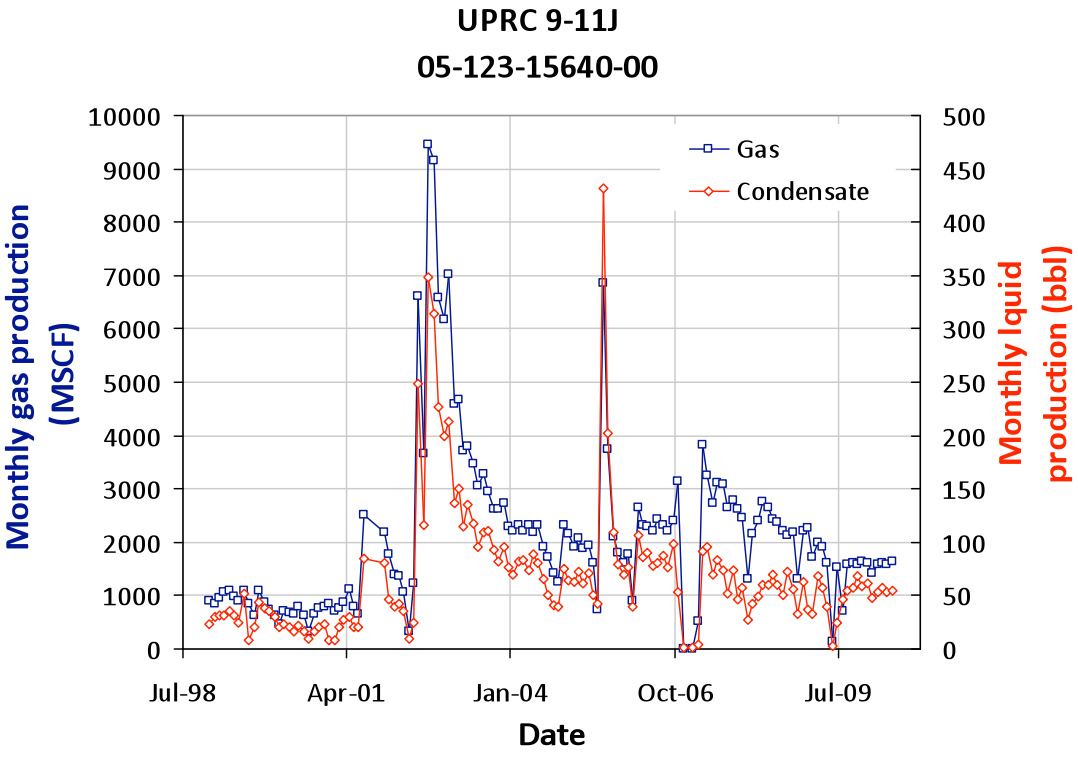
UPRC 9-11J
05-123-15640-00
Monthly gas production (MSCF)
Monthly liquid production (bbl)
Gas
Condensate
10000
9000
8000
7000
6000
5000
4000
3000
2000
1000
0
500
450
400
350
300
250
200
150
100
50
0
Jul-98
Apr-01
Jan-04
Oct-06
Jul-09
Date

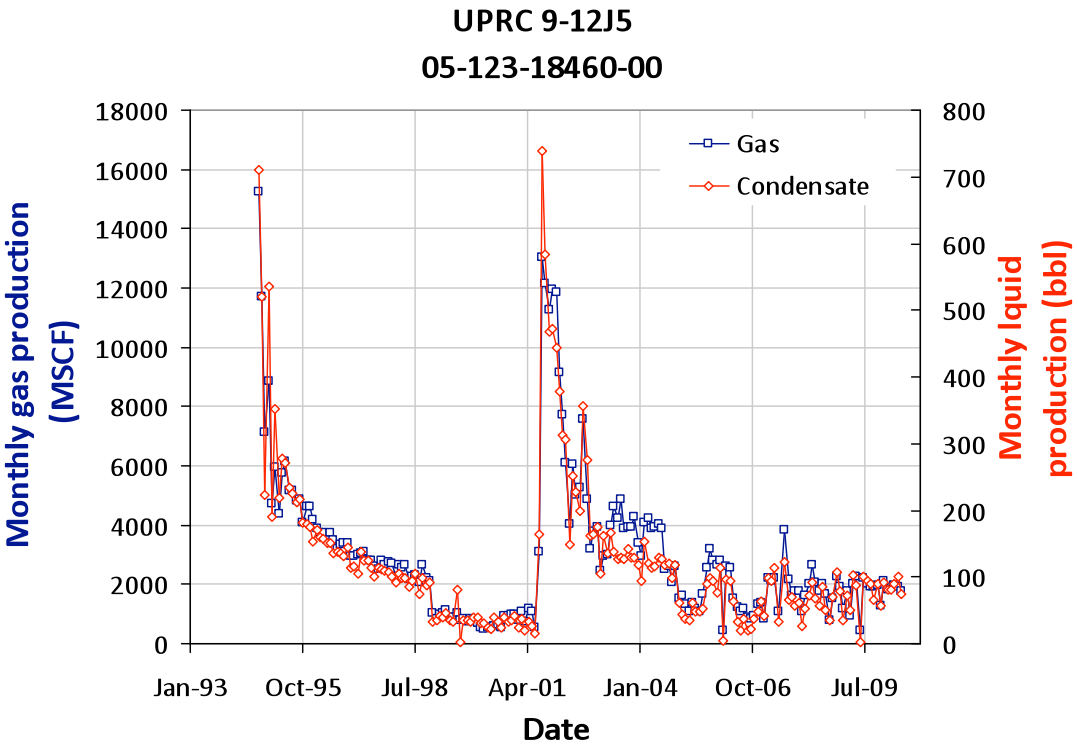
UPRC 9-12J5
05-123-18460-00
Monthly gas production (MSCF)
Monthly liquid production (bbl)
Gas
Condensate
18000
16000
14000
12000
10000
8000
6000
4000
2000
0
800
700
600
500
400
300
200
100
0
Jan-93
Oct-95
Jul-98
Apr-01
Jan-04
Oct-06
Jul-09
Date

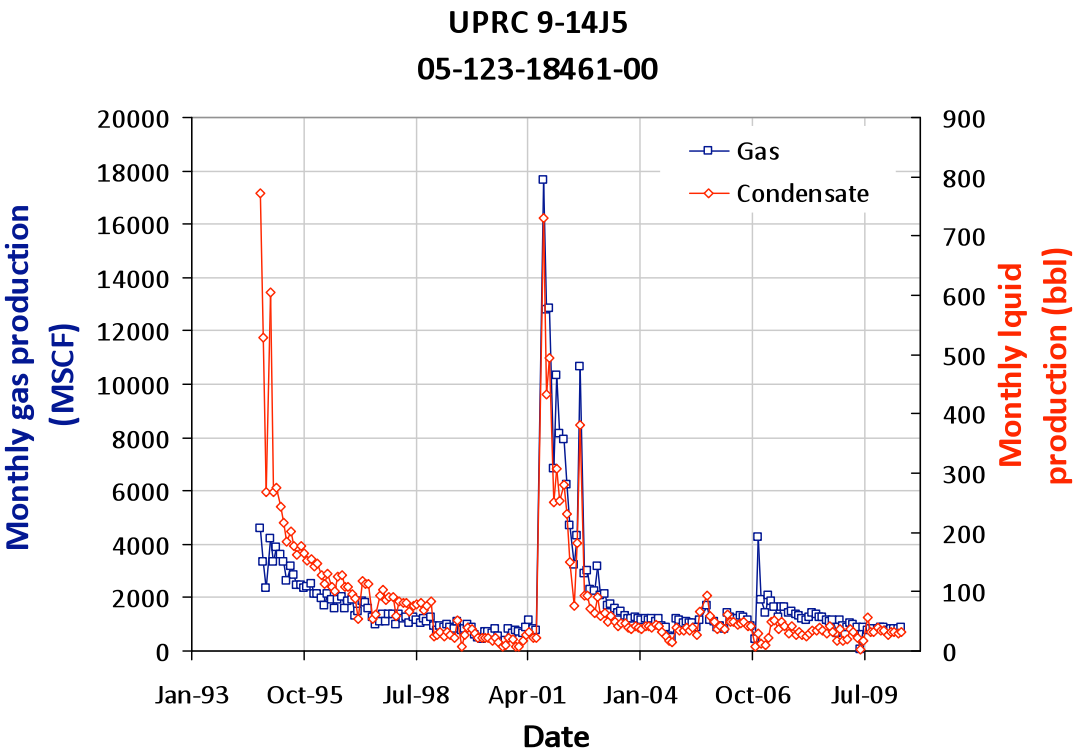
UPRC 9-14J5
05-123-18461-00
Monthly gas production (MSCF)
Monthly liquid production (bbl)
Gas
Condensate
20000
18000
16000
14000
12000
10000
8000
6000
4000
2000
0
900
800
700
600
500
400
300
200
100
0
Jan-93
Oct-95
Jul-98
Apr-01
Jan-04
Oct-06
Jul-09
Date

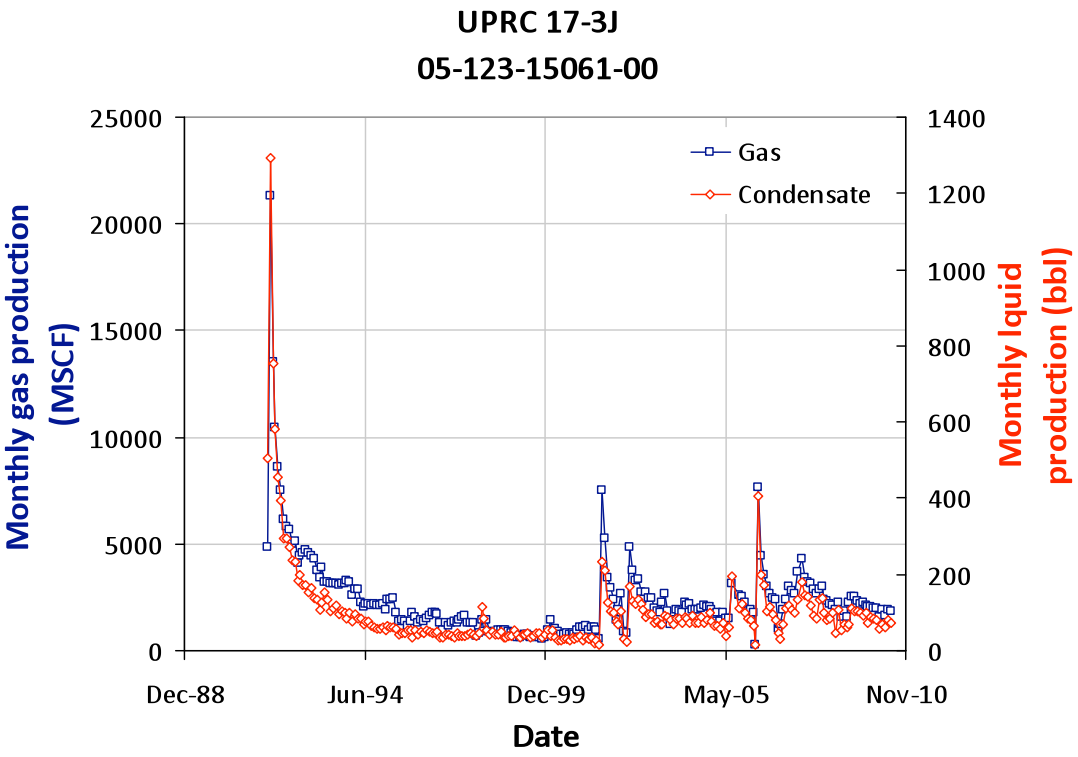
UPRC 17-3J
05-123-15061-00
Monthly gas production (MSCF)
Monthly liquid production (bbl)
Gas
Condensate
25000
20000
15000
10000
5000
0
1400
1200
1000
800
600
400
200
0
Dec-88
Jun-94
Dec-99
May-05
Nov-10
Date

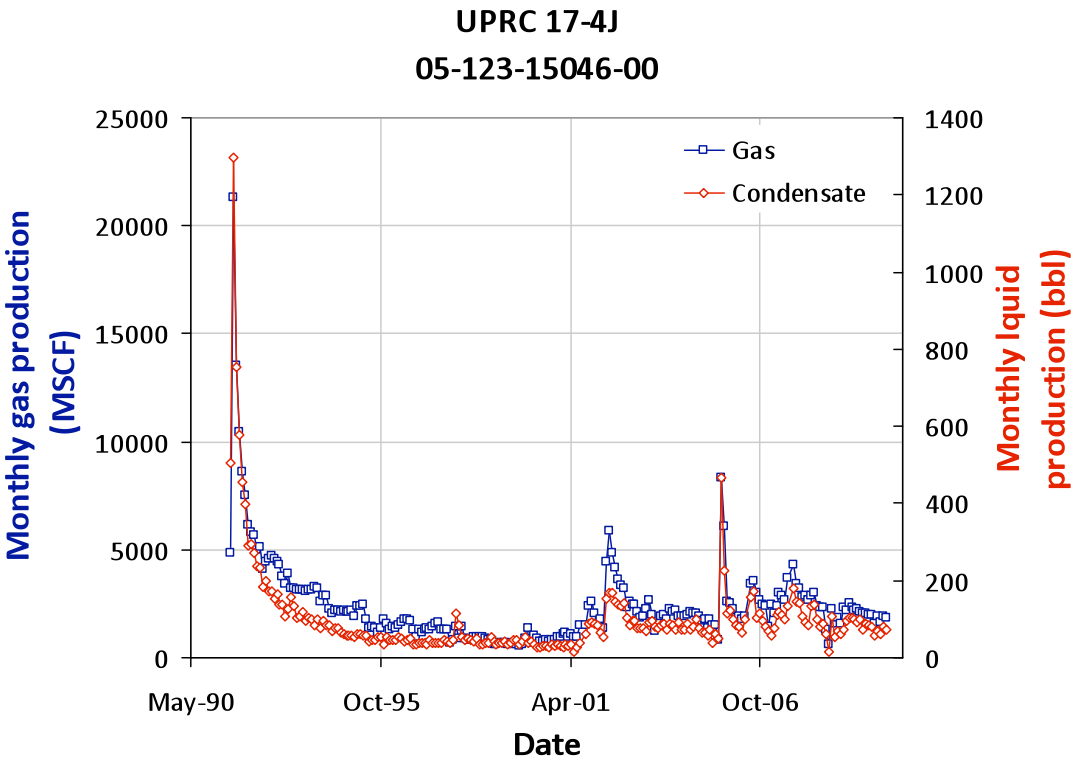
UPRC 17-4J
05-123-15046-00
Monthly gas production (MSCF)
Monthly liquid production (bbl)
Gas
Condensate
25000
20000
15000
10000
5000
0
1400
1200
1000
800
600
400
200
0
May-90
Oct-95
Apr-01
Oct-06
Date

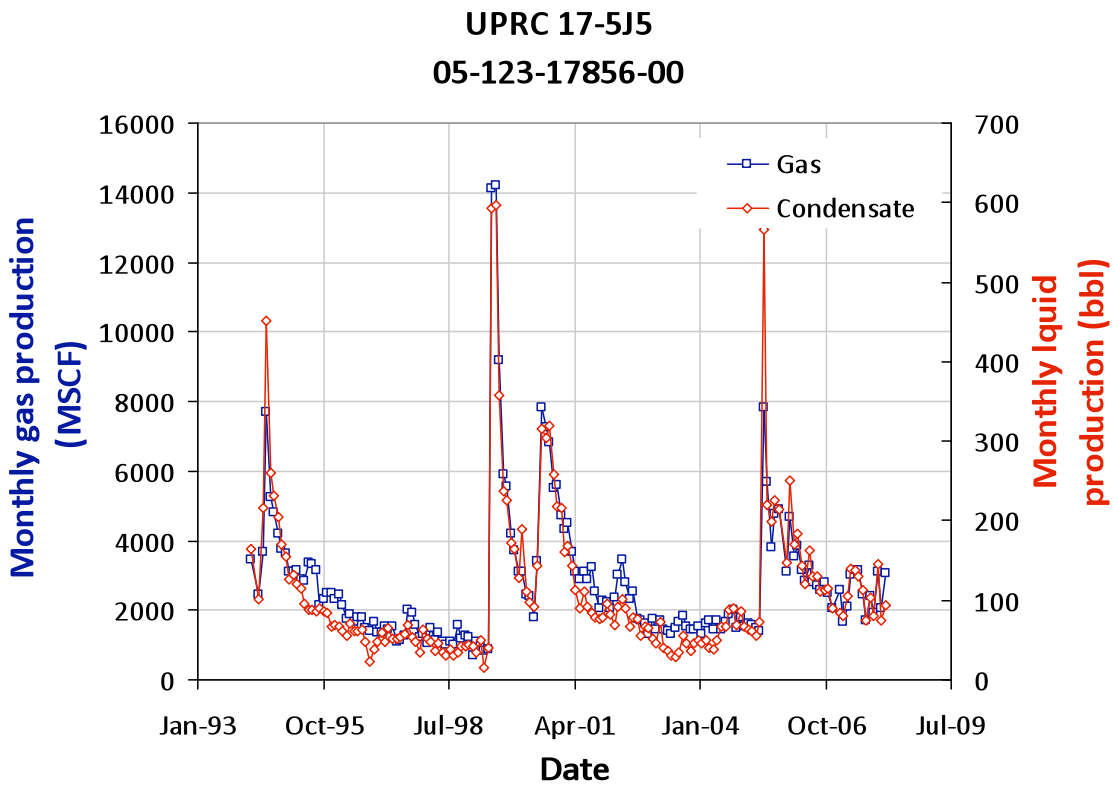
UPRC 17-5J5
05-123-17856-00
Monthly gas production (MSCF)
Monthly liquid production (bbl)
Gas
Condensate
16000
14000
12000
10000
8000
6000
4000
2000
0
700
600
500
400
300
200
100
0
Jan-93
Oct-95
Jul-98
Apr-01
Jan-04
Oct-06
Jul-09
Date

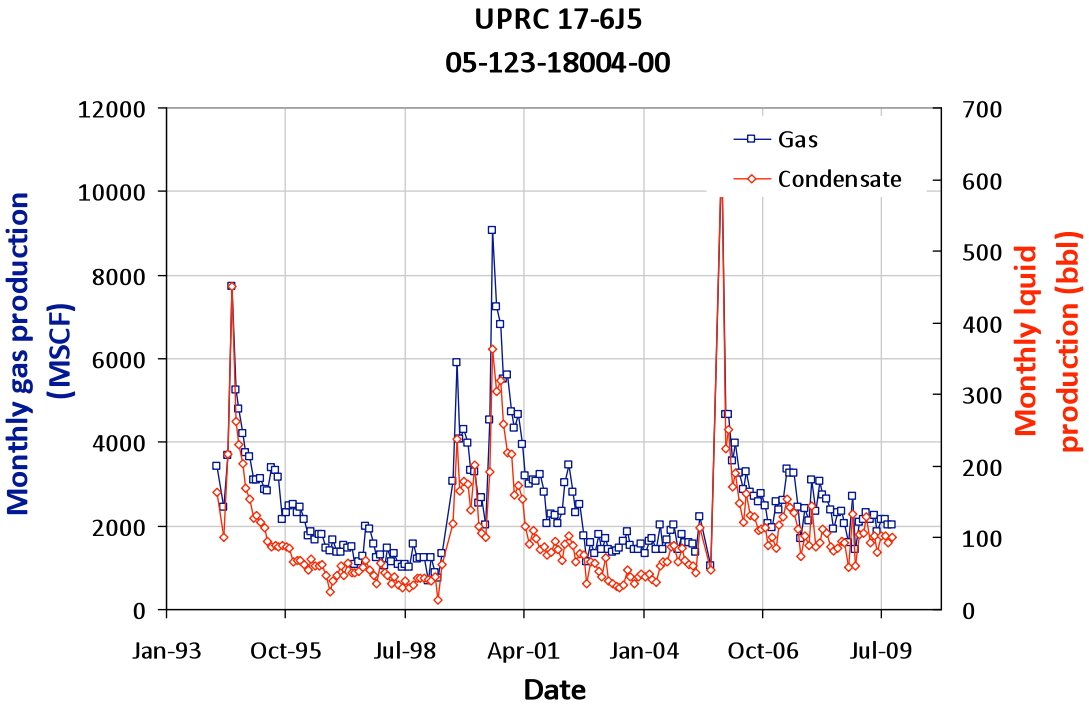
UPRC 17-6J5
05-123-18004-00
Monthly gas production (MSCF)
Monthly liquid production (bbl)
Gas
Condensate
12000
10000
8000
6000
4000
2000
0
700
600
500
400
300
200
100
0
Jan-93
Oct-95
Jul-98
Apr-01
Jan-04
Oct-06
Jul-09
Date

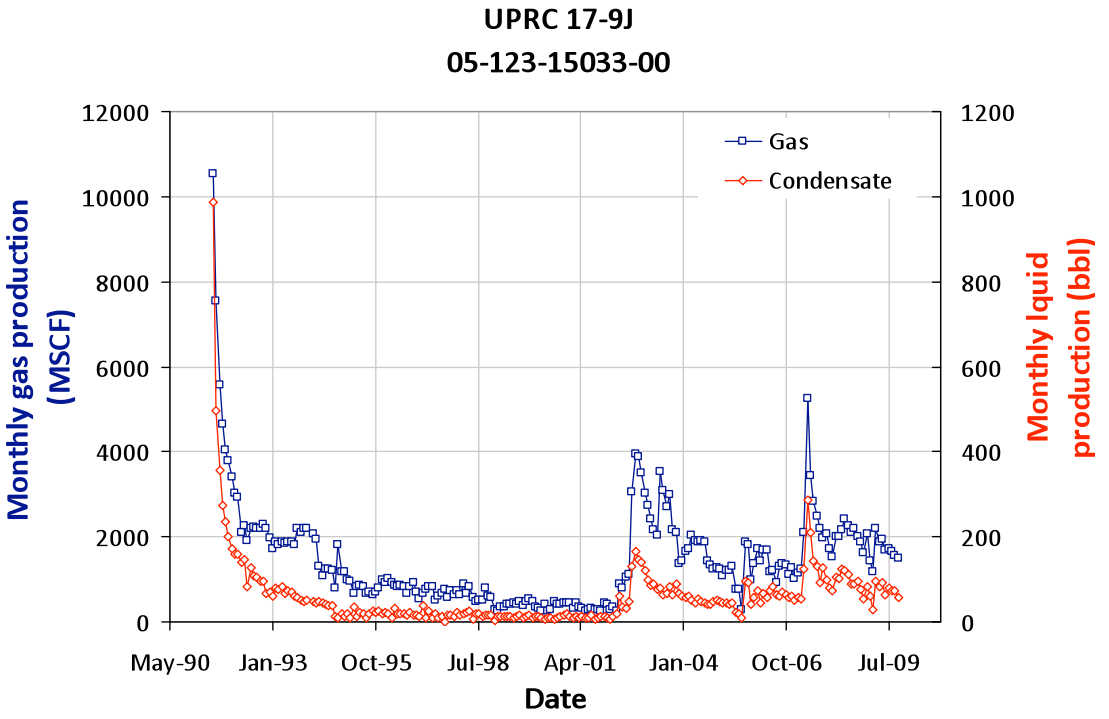
UPRC 17-9J
05-123-15033-00
Monthly gas production (MSCF)
Monthly liquid production (bbl)
Gas
Condensate
12000
10000
8000
6000
4000
2000
0
1200
1000
800
600
400
200
0
May-90
Jan-93
Oct-95
Jul-98
Apr-01
Jan-04
Oct-06
Jul-09
Date

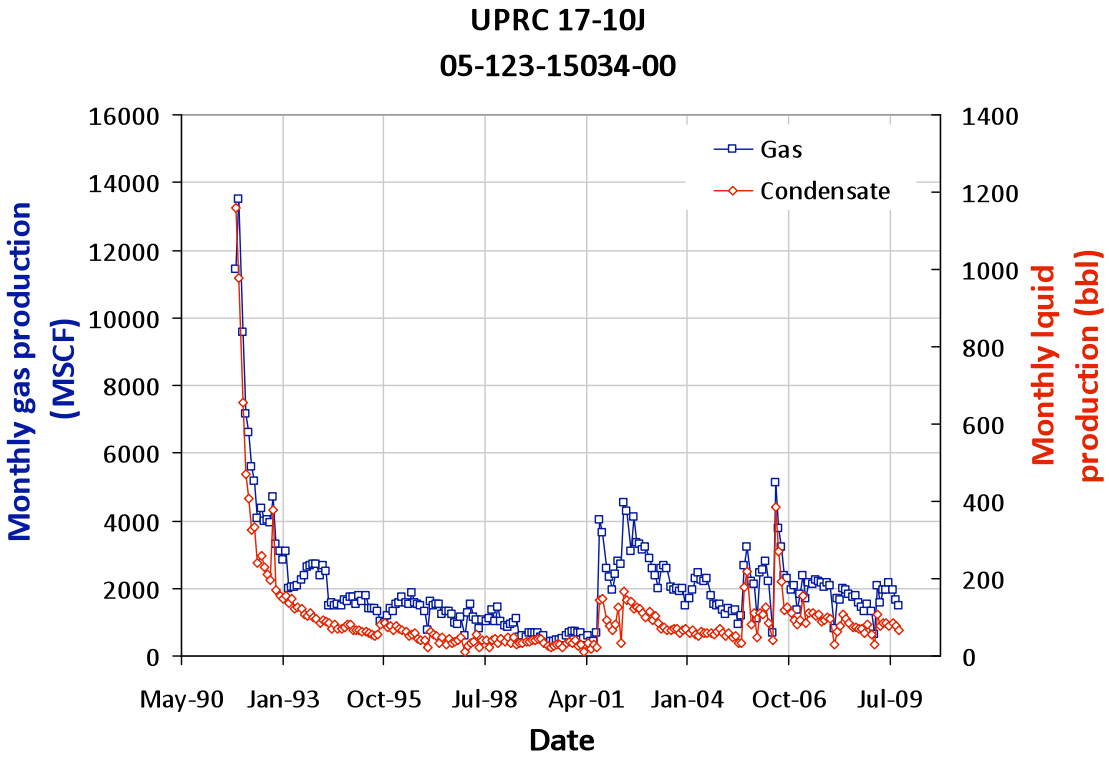
UPRC 17-10J
05-123-15034-00
Monthly gas production (MSCF)
Monthly liquid production (bbl)
Gas
Condensate
16000
14000
12000
10000
8000
6000
4000
2000
0
1400
1200
1000
800
600
400
200
0
May-90
Jan-93
Oct-95
Jul-98
Apr-01
Jan-04
Oct-06
Jul-09
Date

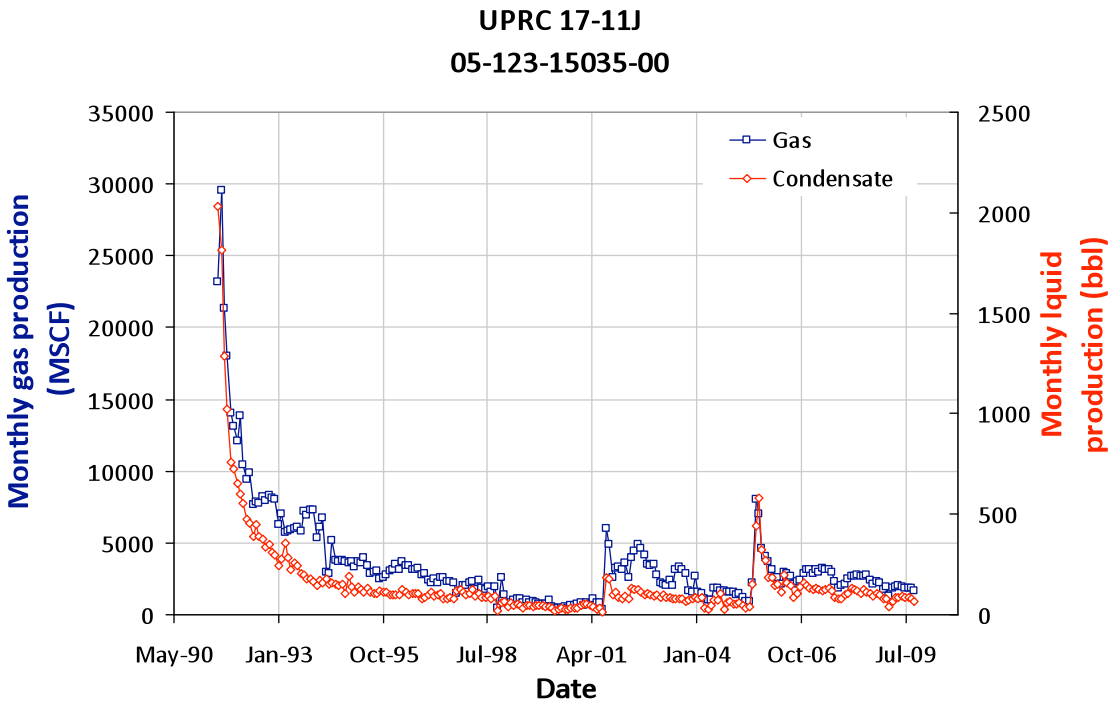
UPRC 17-11J
05-123-15035-00
Monthly gas production (MSCF)
Monthly liquid production (bbl)
Gas
Condensate
35000
30000
25000
20000
15000
10000
5000
0
2500
2000
1500
1000
500
0
May-90
Jan-93
Oct-95
Jul-98
Apr-01
Jan-04
Oct-06
Jul-09
Date

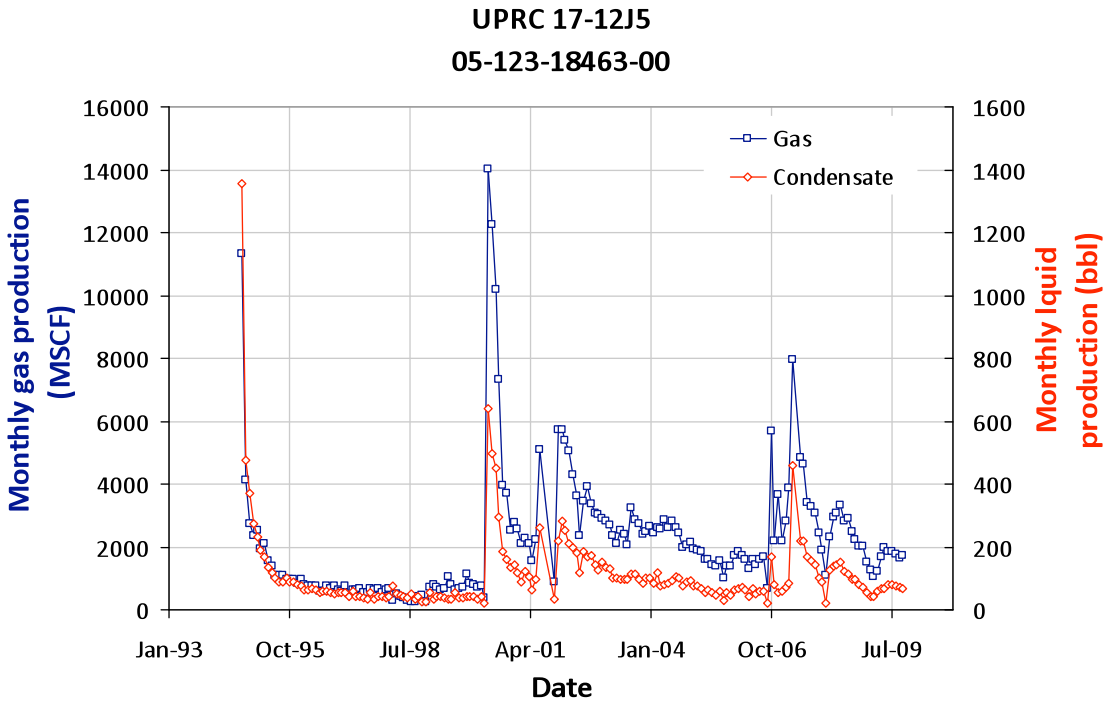
UPRC 17-12J5
05-123-18463-00
Monthly gas production (MSCF)
Monthly liquid production (bbl)
Gas
Condensate
16000
14000
12000
10000
8000
6000
4000
2000
0
1600
1400
1200
1000
800
600
400
200
0
Jan-93
Oct-95
Jul-98
Apr-01
Jan-04
Oct-06
Jul-09
Date

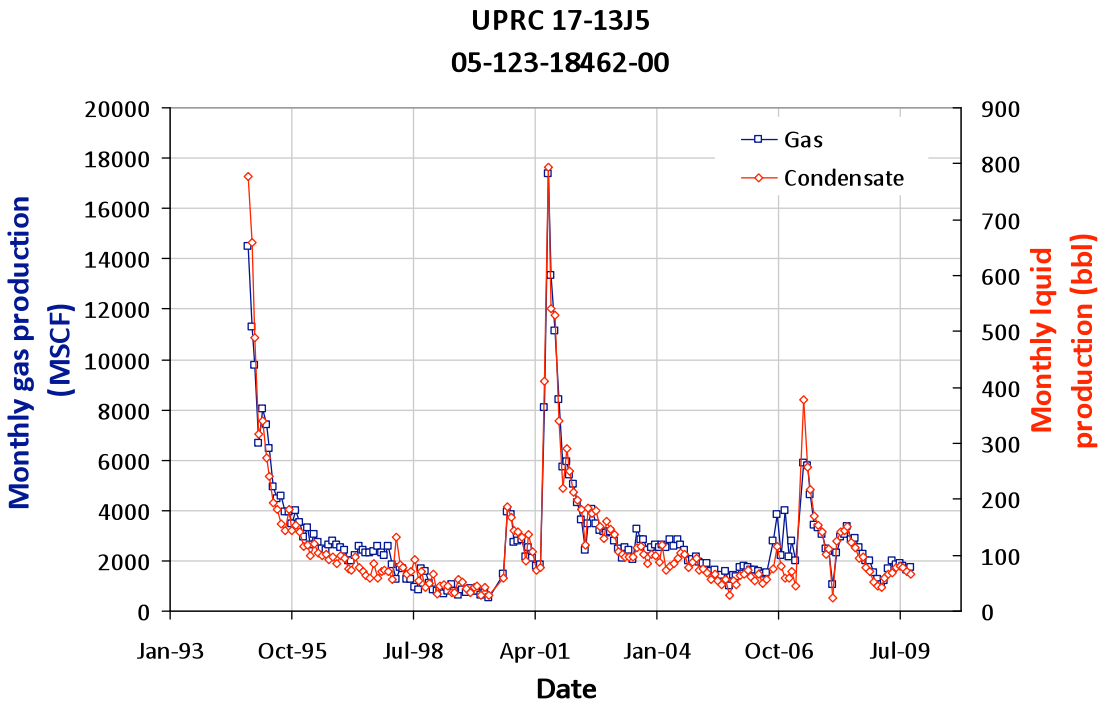
UPRC 17-13J5
05-123-18462-00
Monthly gas production (MSCF)
Monthly liquid production (bbl)
Gas
Condensate
20000
18000
16000
14000
12000
10000
8000
6000
4000
2000
0
900
800
700
600
500
400
300
200
100
0
Jan-93
Oct-95
Jul-98
Apr-01
Jan-04
Oct-06
Jul-09
Date

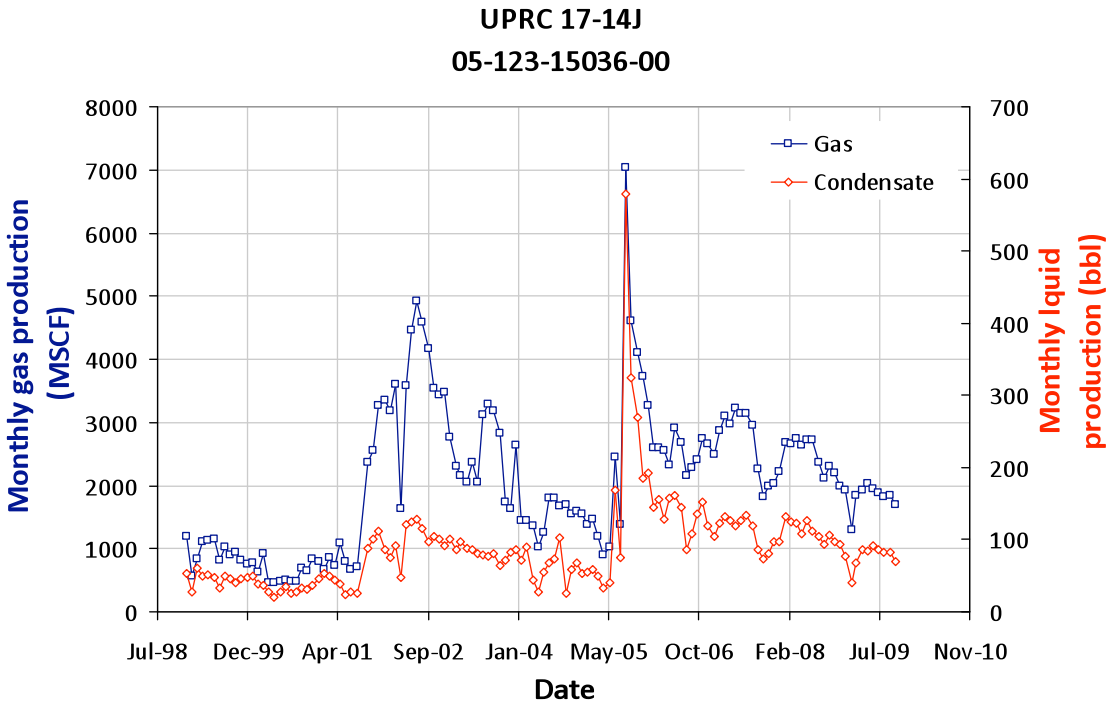
UPRC 17-14J
05-123-15036-00
Monthly gas production (MSCF)
Monthly liquid production (bbl)
Gas
Condensate
8000
7000
6000
5000
4000
3000
2000
1000
0
700
600
500
400
300
200
100
0
Jul-98
Dec-99
Apr-01
Sep-02
Jan-04
May-05
Oct-06
Feb-08
Jul-09
Nov-10
Date

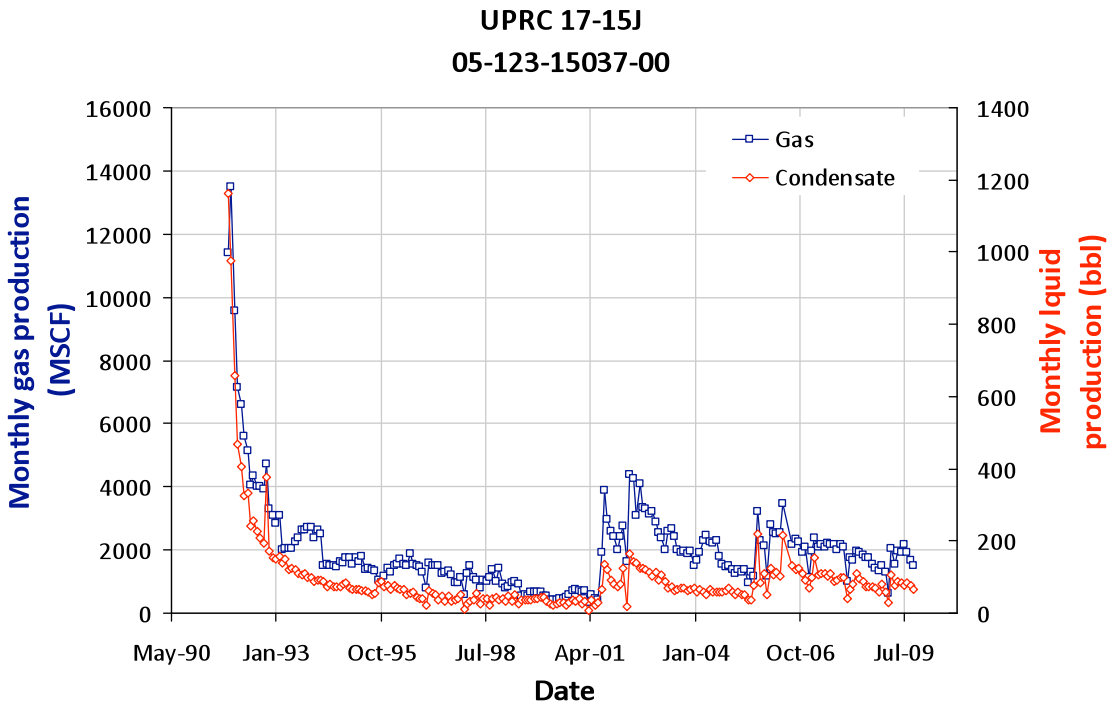
UPRC 17-15J
05-123-15037-00
Monthly gas production (MSCF)
Monthly liquid production (bbl)
Gas
Condensate
16000
14000
12000
10000
8000
6000
4000
2000
0
1400
1200
1000
800
600
400
200
0
May-90
Jan-93
Oct-95
Jul-98
Apr-01
Jan-04
Oct-06
Jul-09
Date

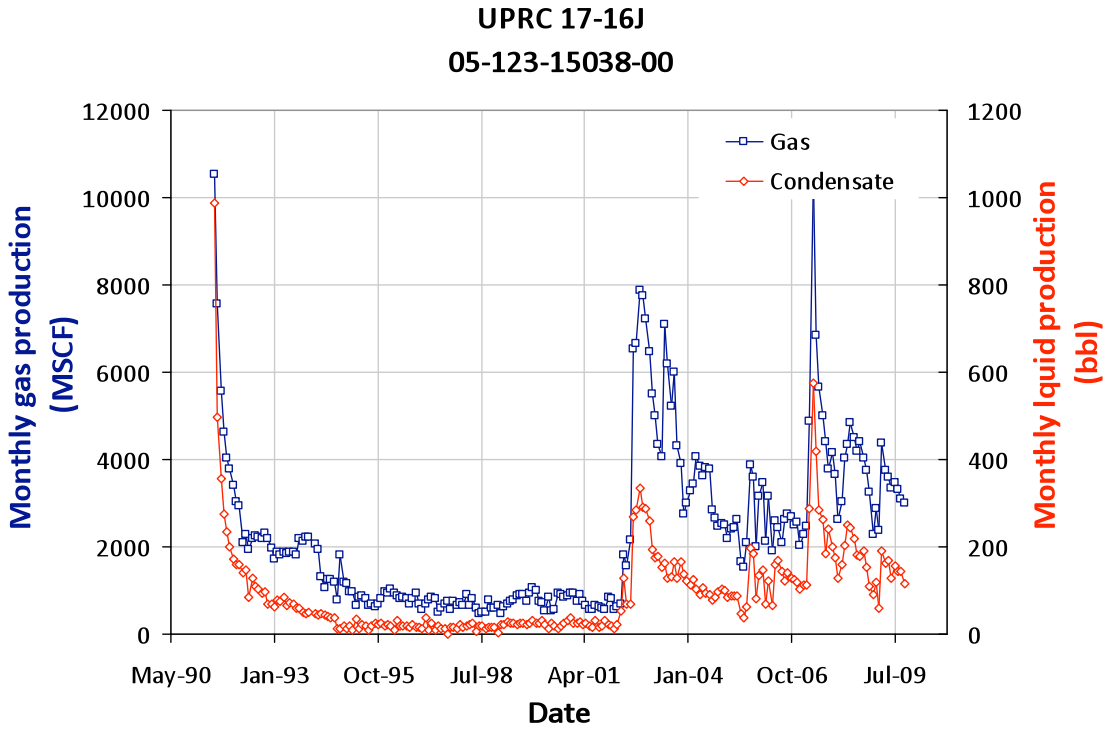
UPRC 17-16J
05-123-15038-00
Monthly gas production (MSCF)
Monthly liquid production (bbl)
Gas
Condensate
12000
10000
8000
6000
4000
2000
0
1200
1000
800
600
400
200
0
May-90
Jan-93
Oct-95
Jul-98
Apr-01
Jan-04
Oct-06
Jul-09
Date

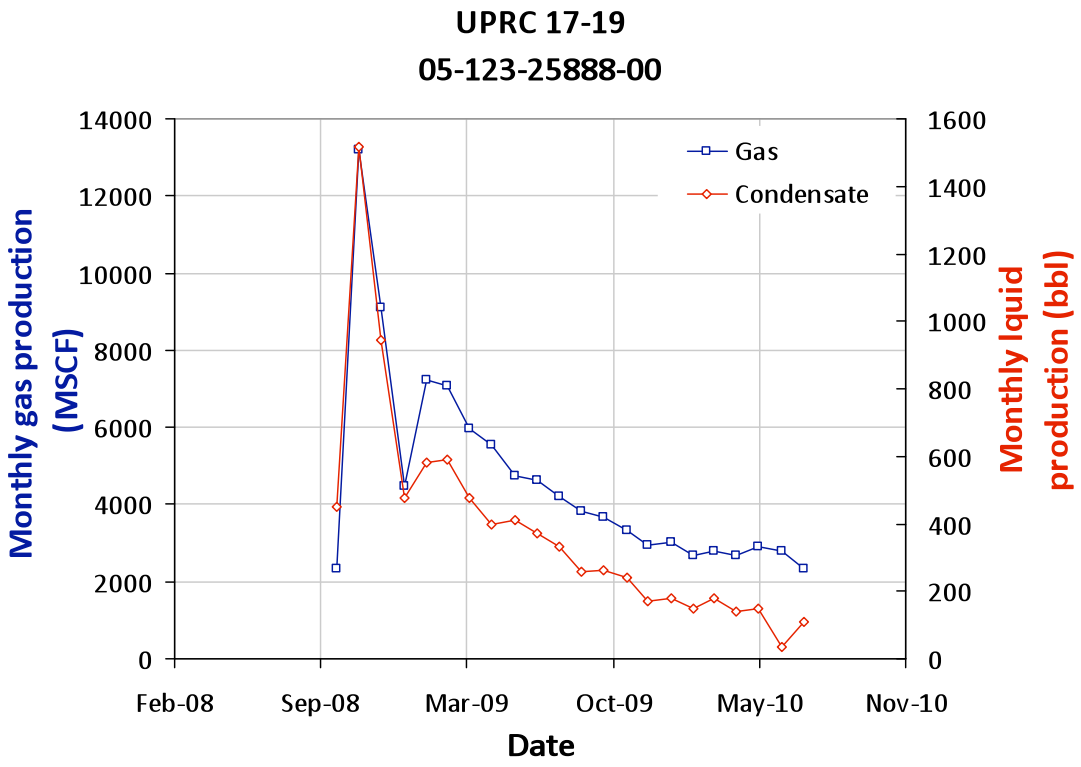
UPRC 17-19
05-123-25888-00
Monthly gas production (MSCF)
Monthly liquid production (bbl)
Gas
Condensate
14000
12000
10000
8000
6000
4000
2000
0
1600
1400
1200
1000
800
600
400
200
0
Feb-08
Sep-08
Mar-09
Oct-09
May-10
Nov-10
Date

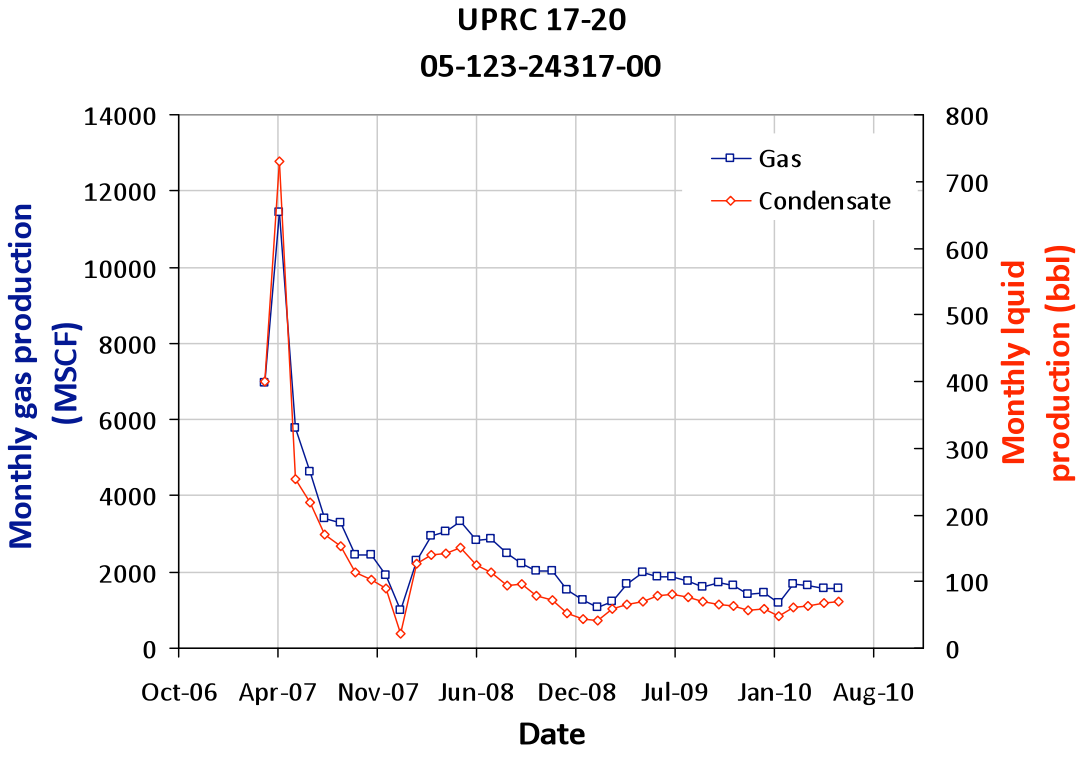
UPRC 17-20
05-123-24317-00
Monthly gas production (MSCF)
Monthly liquid production (bbl)
Gas
Condensate
14000
12000
10000
8000
6000
4000
2000
0
800
700
600
500
400
300
200
100
0
Oct-06
Apr-07
Nov-07
Jun-08
Dec-08
Jul-09
Jan-10
Aug-10
Date

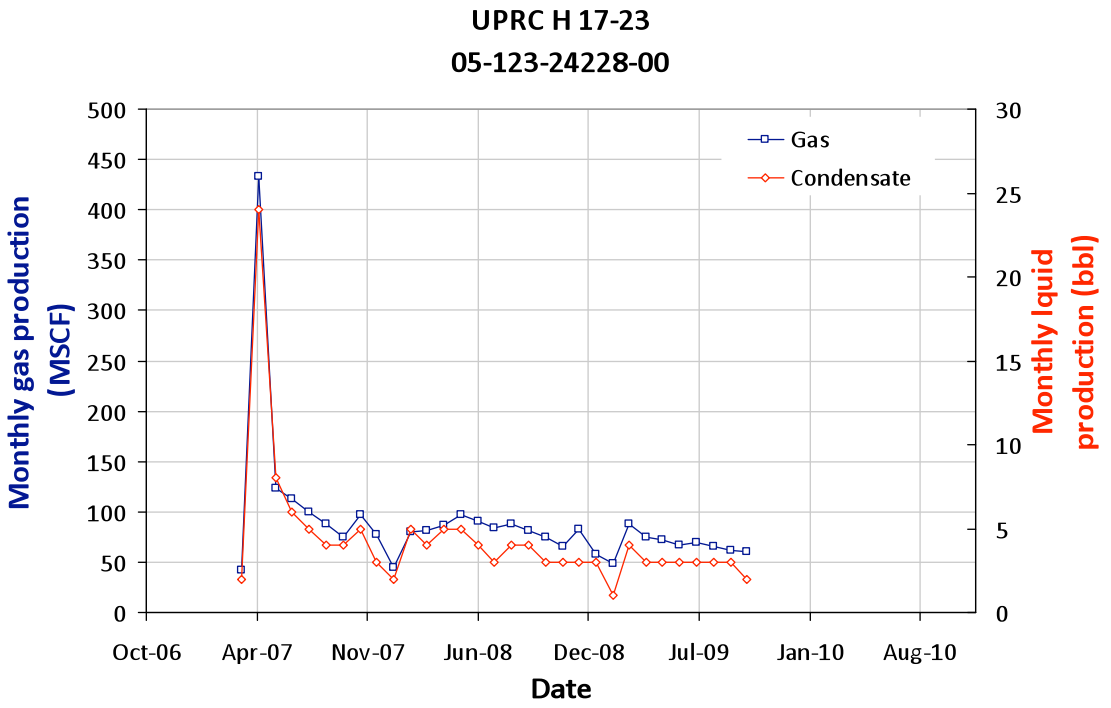
UPRC H 17-23
05-123-24228-00
Monthly gas production (MSCF)
Monthly liquid production (bbl)
Gas
Condensate
500
450
400
350
300
250
200
150
100
50
0
30
25
20
15
10
5
0
Oct-06
Apr-07
Nov-07
Jun-08
Dec-08
Jul-09
Jan-10
Aug-10
Date

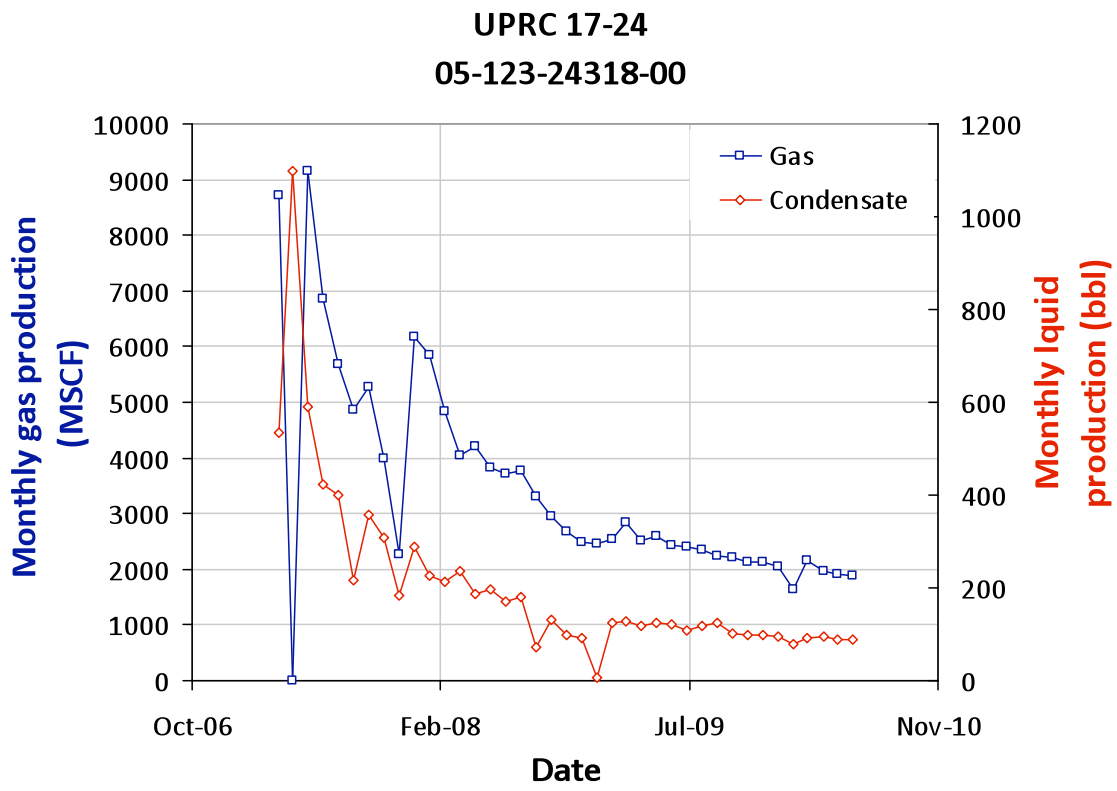
UPRC 17-24
05-123-24318-00
Monthly gas production (MSCF)
Monthly liquid production (bbl)
Gas
Condensate
10000
9000
8000
7000
6000
5000
4000
3000
2000
1000
0
1200
1000
800
600
400
200
0
Oct-06
Feb-08
Jul-09
Nov-10
Date

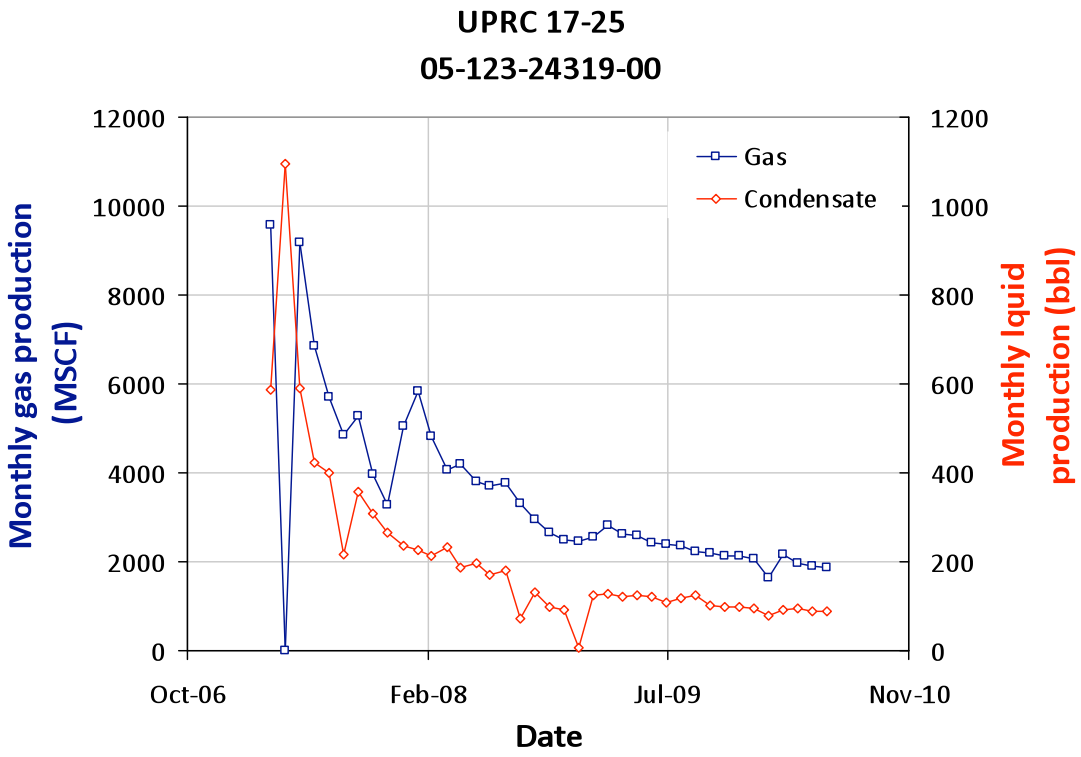
UPRC 17-25
05-123-24319-00
Monthly gas production (MSCF)
Monthly liquid production (bbl)
Gas
Condensate
12000
10000
8000
6000
4000
2000
0
1200
1000
800
600
400
200
0
Oct-06
Feb-08
Jul-09
Nov-10
Date

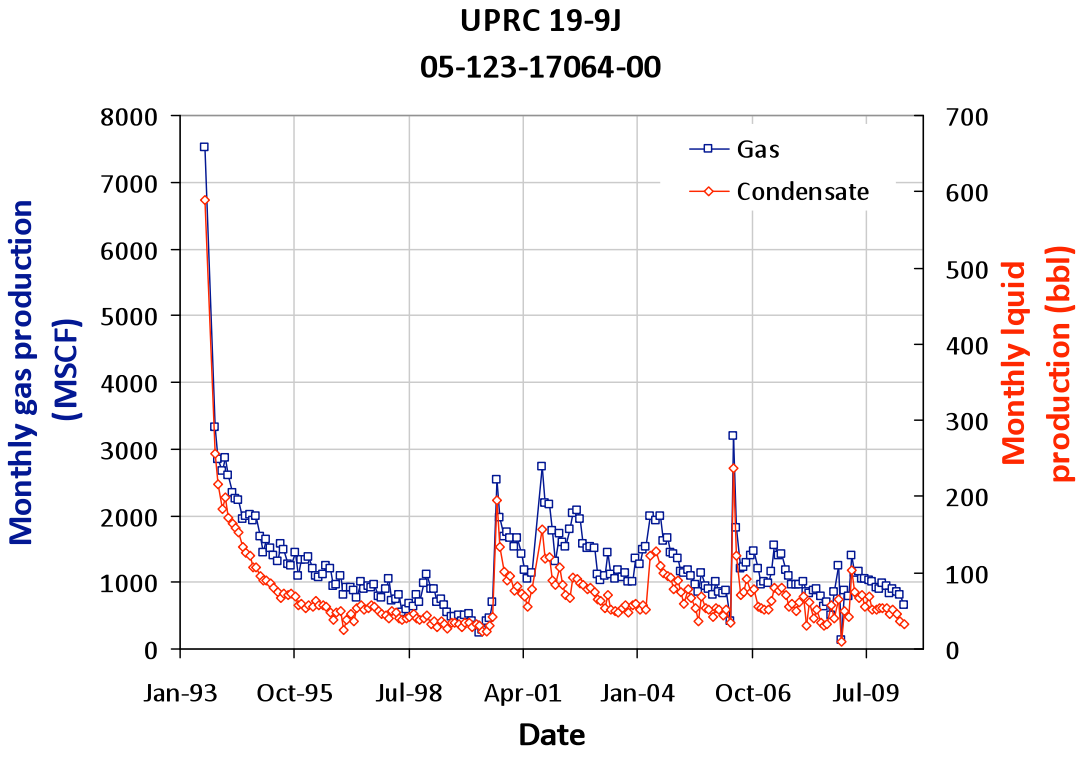
UPRC 19-9J
05-123-17064-00
Monthly gas production (MSCF)
Monthly liquid production (bbl)
Gas
Condensate
8000
7000
6000
5000
4000
3000
2000
1000
0
700
600
500
400
300
200
100
0
Jan-93
Oct-95
Jul-98
Apr-01
Jan-04
Oct-06
Jul-09
Date

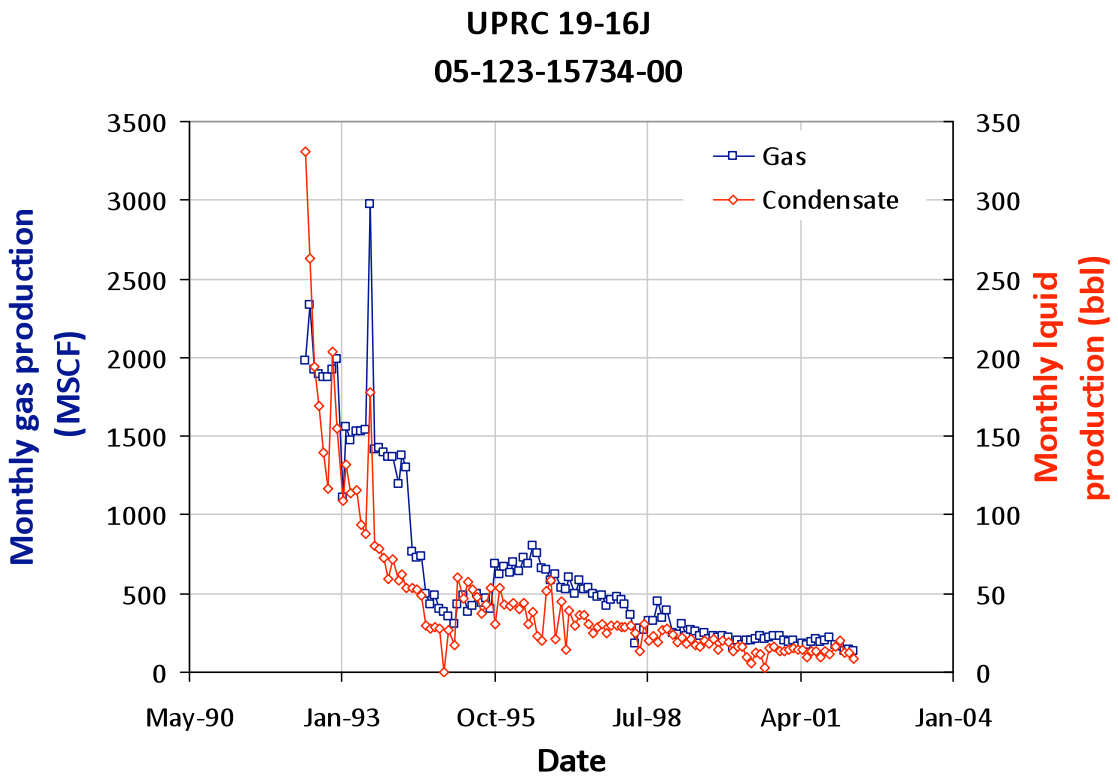
UPRC 19-16J
05-123-15734-00
Monthly gas production (MSCF)
Monthly liquid production (bbl)
Gas
Condensate
3500
3000
2500
2000
1500
1000
500
0
350
300
250
200
150
100
50
0
May-90
Jan-93
Oct-95
Jul-98
Apr-01
Jan-04
Date

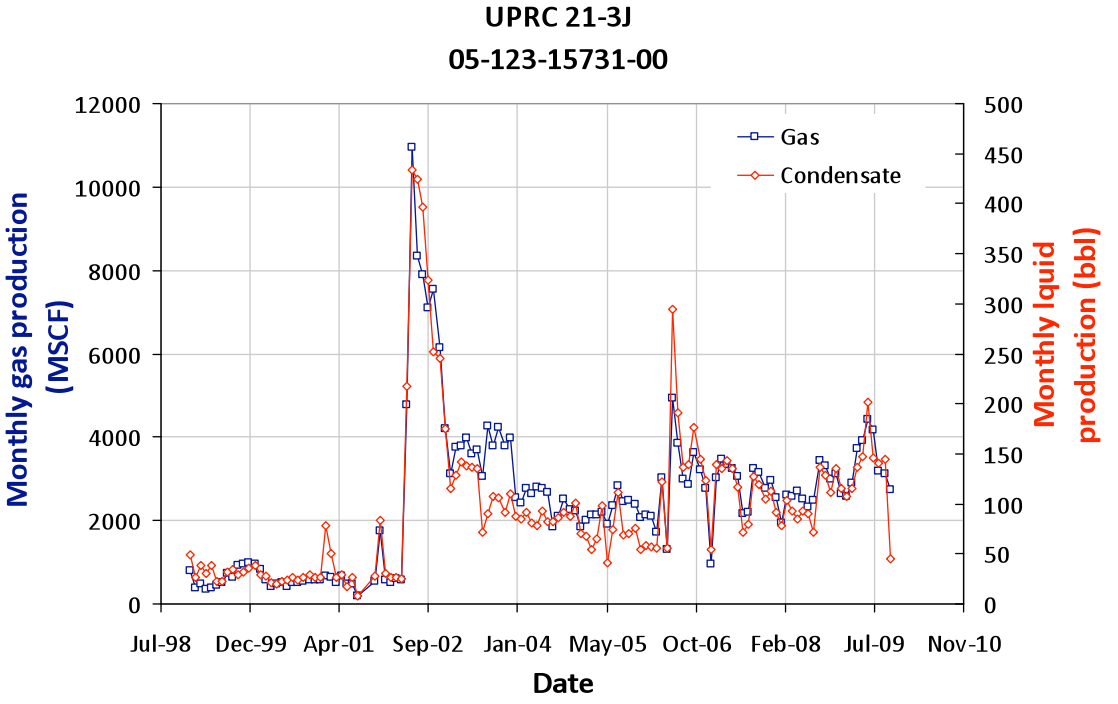
UPRC 21-3J
05-123-15731-00
Monthly gas production (MSCF)
Monthly liquid production (bbl)
Gas
Condensate
12000
10000
8000
6000
4000
2000
0
500
450
400
350
300
250
200
150
100
50
0
Jul-98
Dec-99
Apr-01
Sep-02
Jan-04
May-05
Oct-06
Feb-08
Jul-09
Nov-10
Date

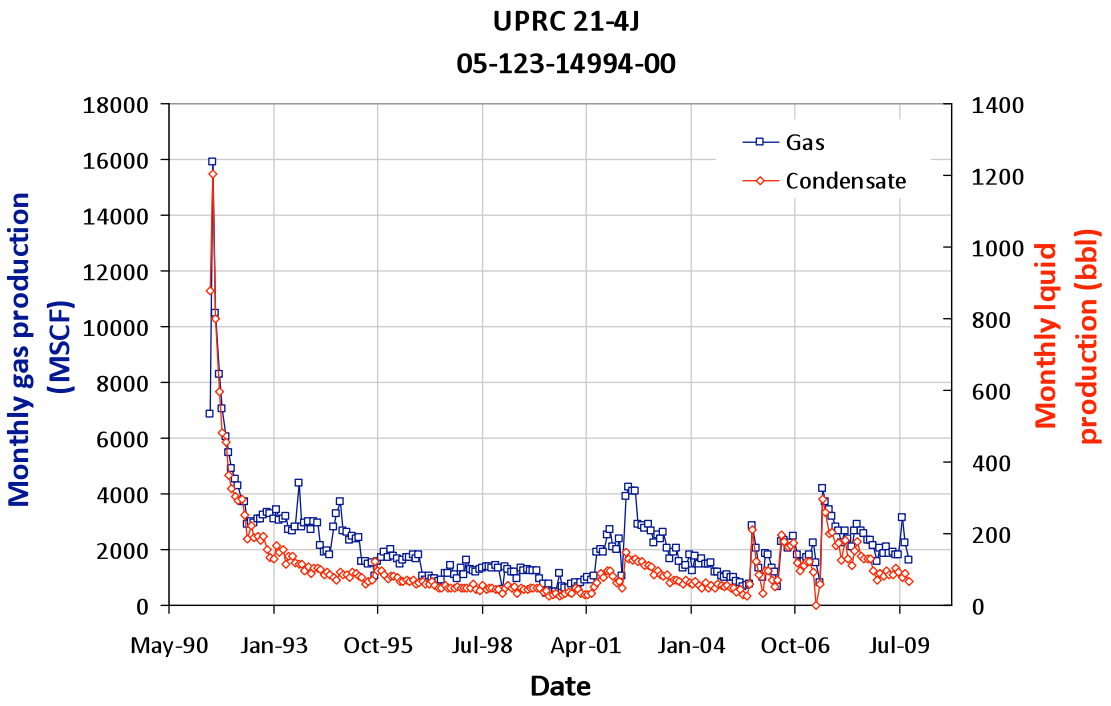
UPRC 21-4J
05-123-14994-00
Monthly gas production (MSCF)
Monthly liquid production (bbl)
Gas
Condensate
18000
16000
14000
12000
10000
8000
6000
4000
2000
0
1400
1200
1000
800
600
400
200
0
May-90
Jan-93
Oct-95
Jul-98
Apr-01
Jan-04
Oct-06
Jul-09
Date

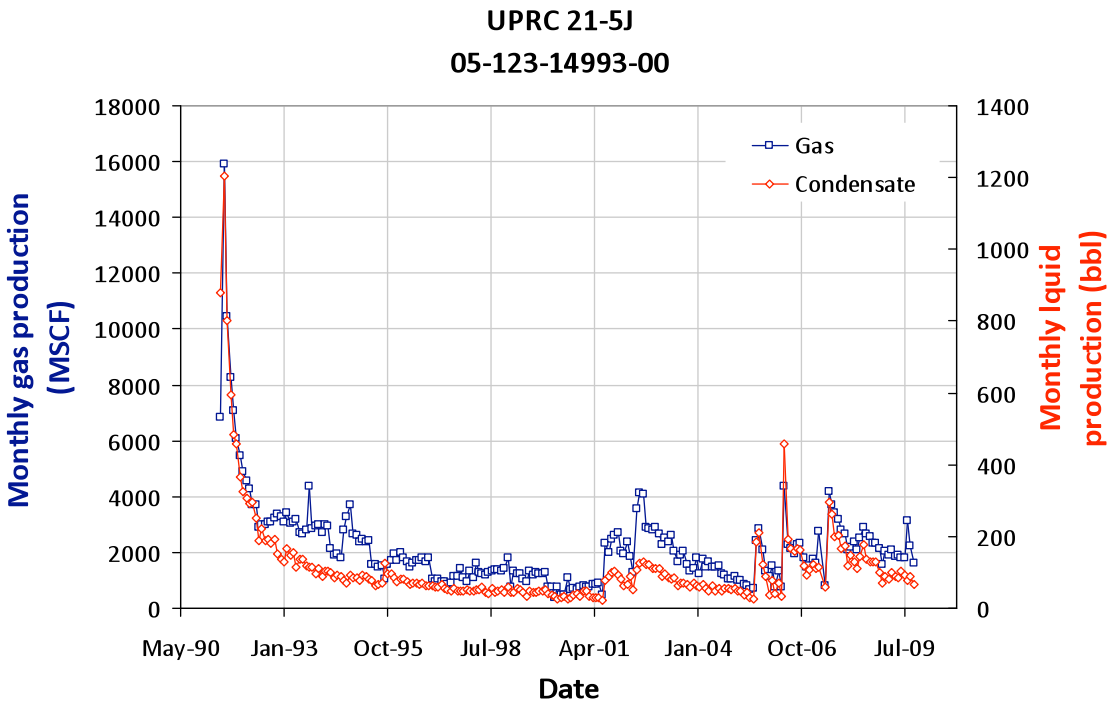
UPRC 21-5J
05-123-14993-00
Monthly gas production (MSCF)
Monthly liquid production (bbl)
Gas
Condensate
18000
16000
14000
12000
10000
8000
6000
4000
2000
0
1400
1200
1000
800
600
400
200
0
May-90
Jan-93
Oct-95
Jul-98
Apr-01
Jan-04
Oct-06
Jul-09
Date

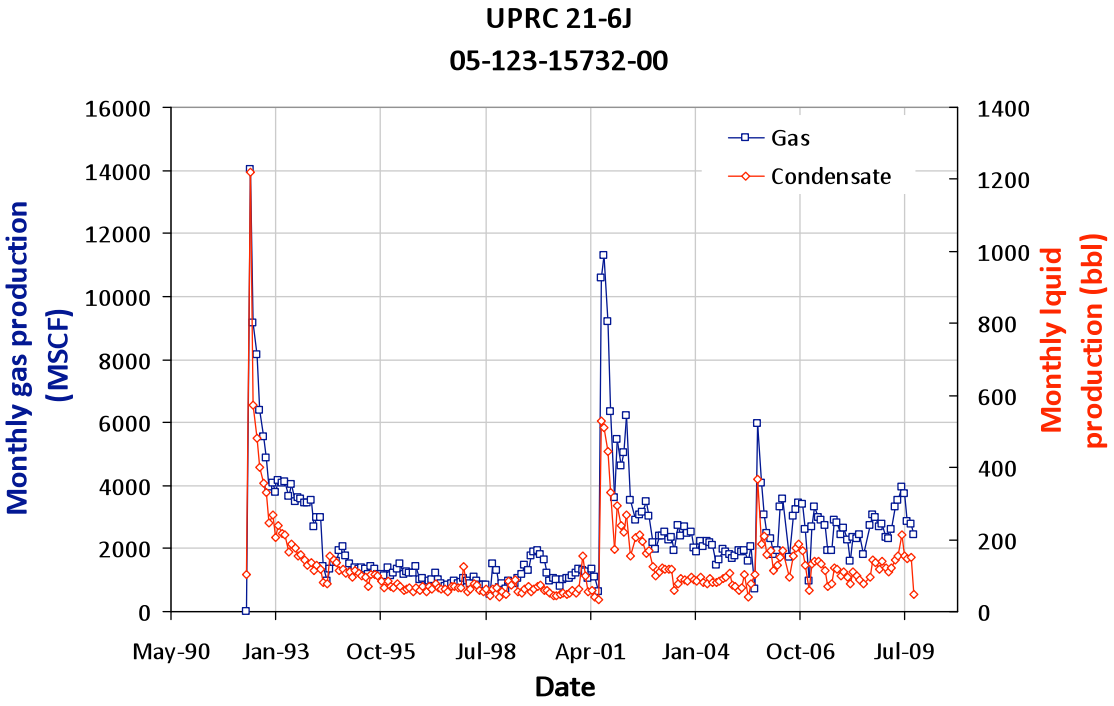
UPRC 21-6J
05-123-15732-00
Monthly gas production (MSCF)
Monthly liquid production (bbl)
Gas
Condensate
16000
14000
12000
10000
8000
6000
4000
2000
0
1400
1200
1000
800
600
400
200
0
May-90
Jan-93
Oct-95
Jul-98
Apr-01
Jan-04
Oct-06
Jul-09
Date

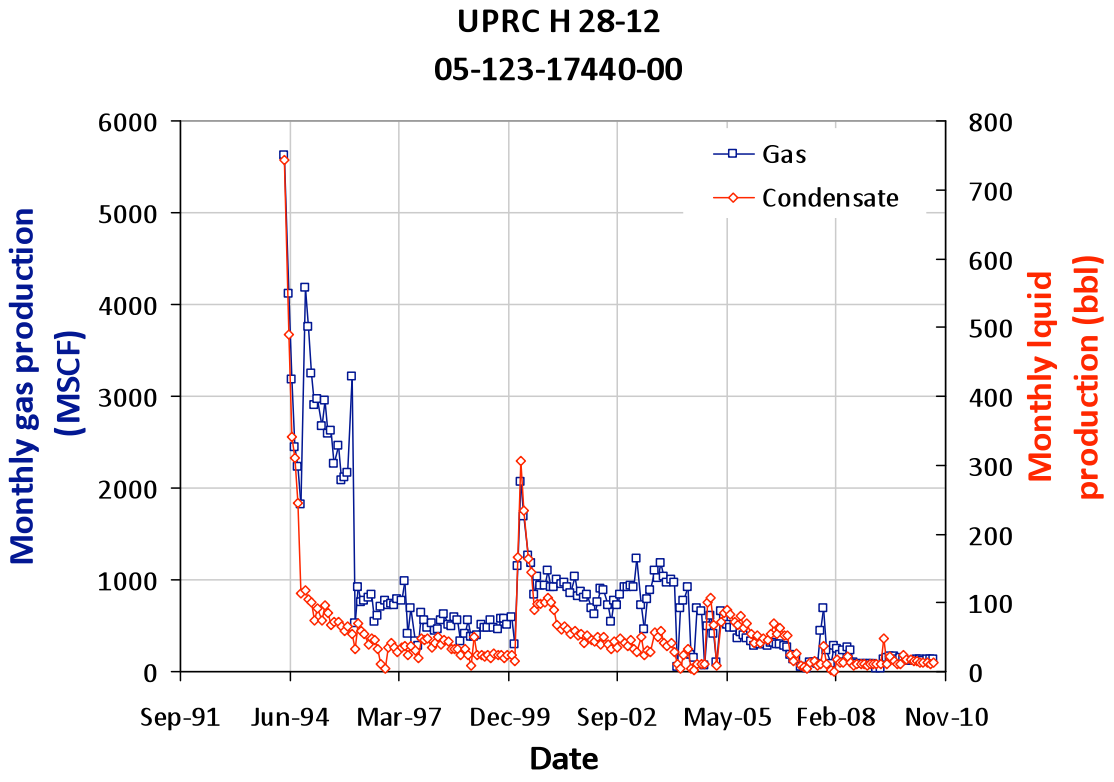
UPRC H 28-12
05-123-17440-00
Monthly gas production (MSCF)
Monthly liquid production (bbl)
Gas
Condensate
6000
5000
4000
3000
2000
1000
0
800
700
600
500
400
300
200
100
0
Sep-91
Jun-94
Mar-97
Dec-99
Sep-02
May-05
Feb-08
Nov-10
Date

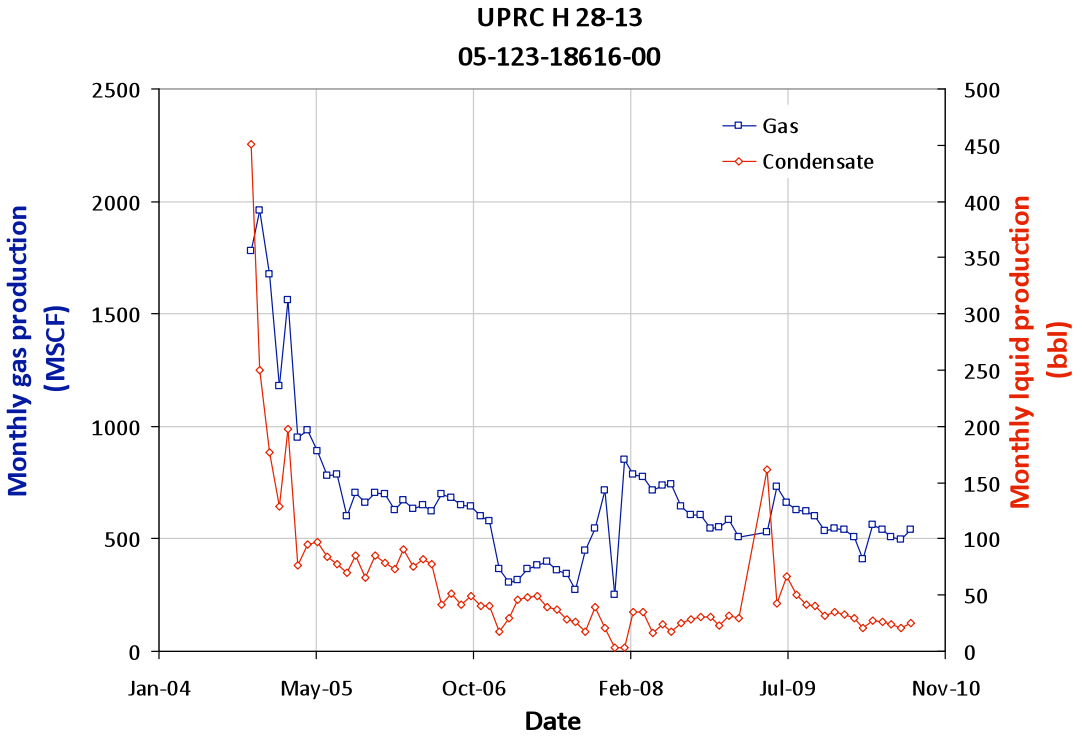
UPRC H 28-13
05-123-18616-00
Monthly gas production (MSCF)
Monthly liquid production (bbl)
Gas
Condensate
2500
2000
1500
1000
500
0
500
450
400
350
300
250
200
150
100
50
0
Jan-04
May-05
Oct-06
Feb-08
Jul-09
Nov-10
Date

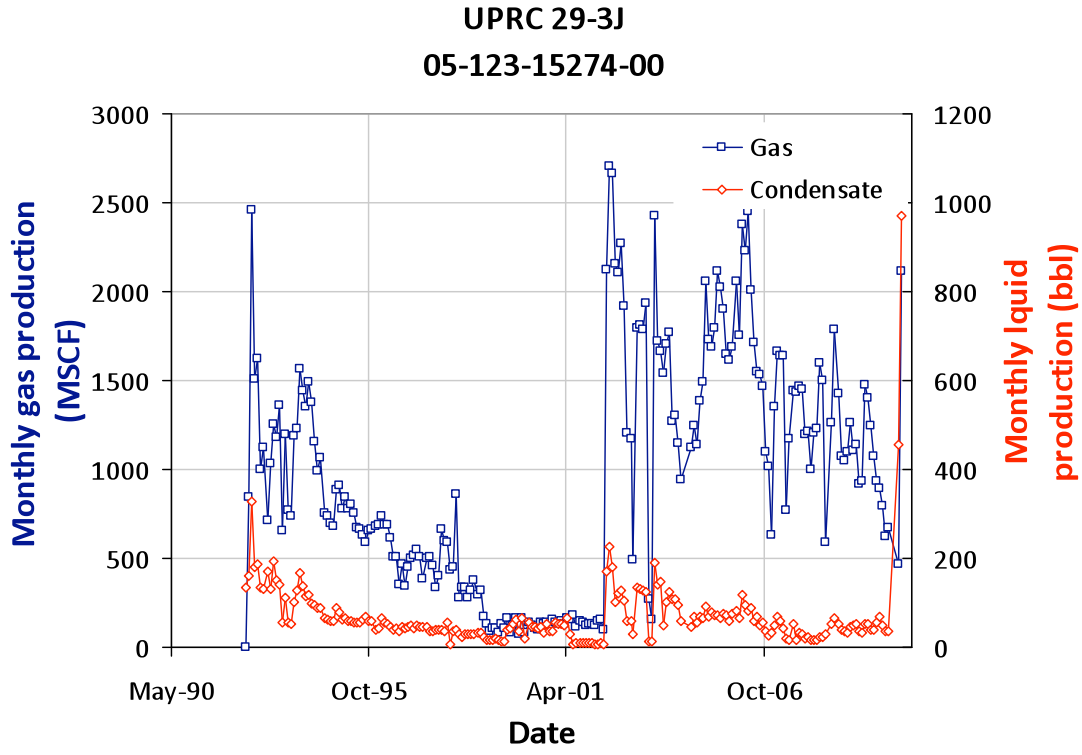
UPRC 29-3J
05-123-15274-00
Monthly gas production (MSCF)
Monthly liquid production (bbl)
Gas
Condensate
3000
2500
2000
1500
1000
500
0
1200
1000
800
600
400
200
0
May-90
Oct-95
Apr-01
Oct-06
Date

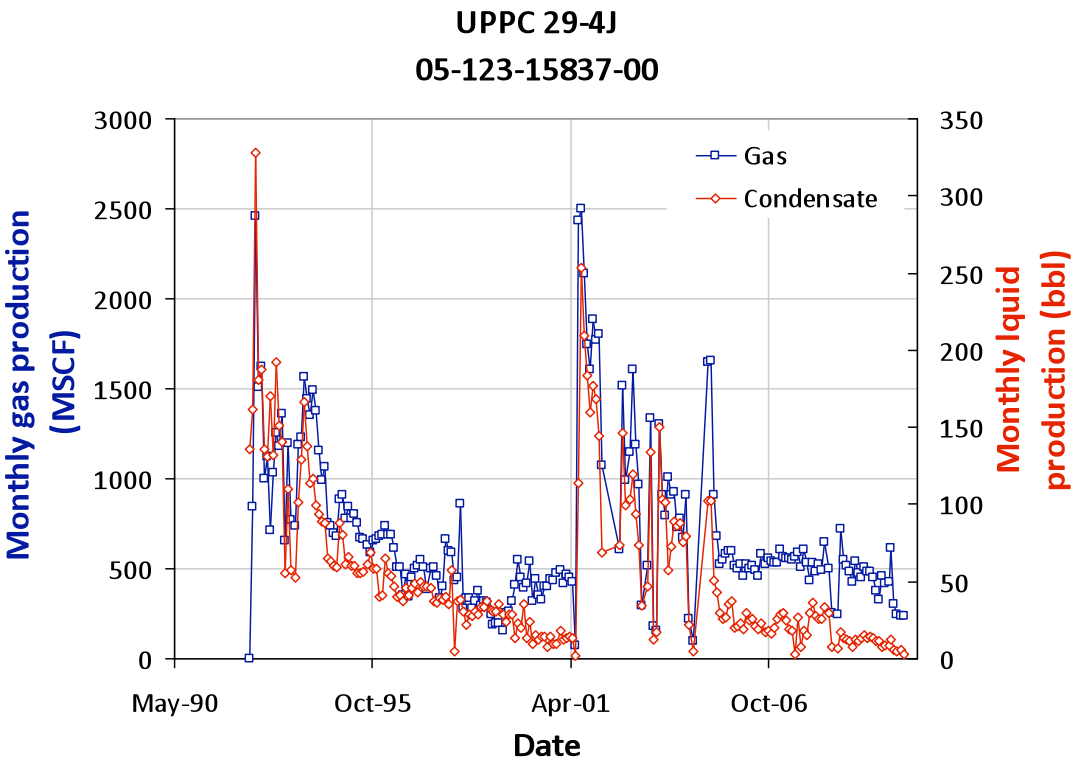
UPPC 29-4J
05-123-15837-00
Monthly gas production (MSCF)
Monthly liquid production (bbl)
Gas
Condensate
3000
2500
2000
1500
1000
500
0
350
300
250
200
150
100
50
0
May-90
Oct-95
Apr-01
Oct-06
Date

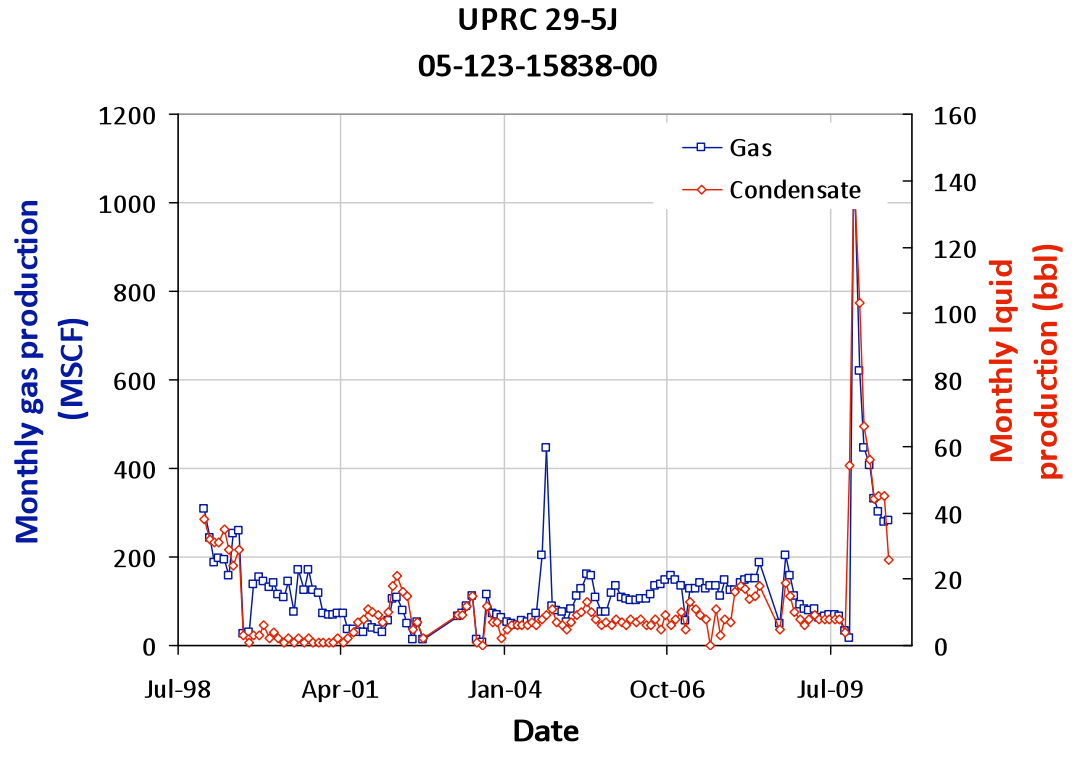
UPRC 29-5J
05-123-15838-00
Monthly gas production (MSCF)
Monthly liquid production (bbl)
Gas
Condensate
1200
1000
800
600
400
200
0
160
140
120
100
80
60
40
20
0
Jul-98
Apr-01
Jan-04
Oct-06
Jul-09
Date

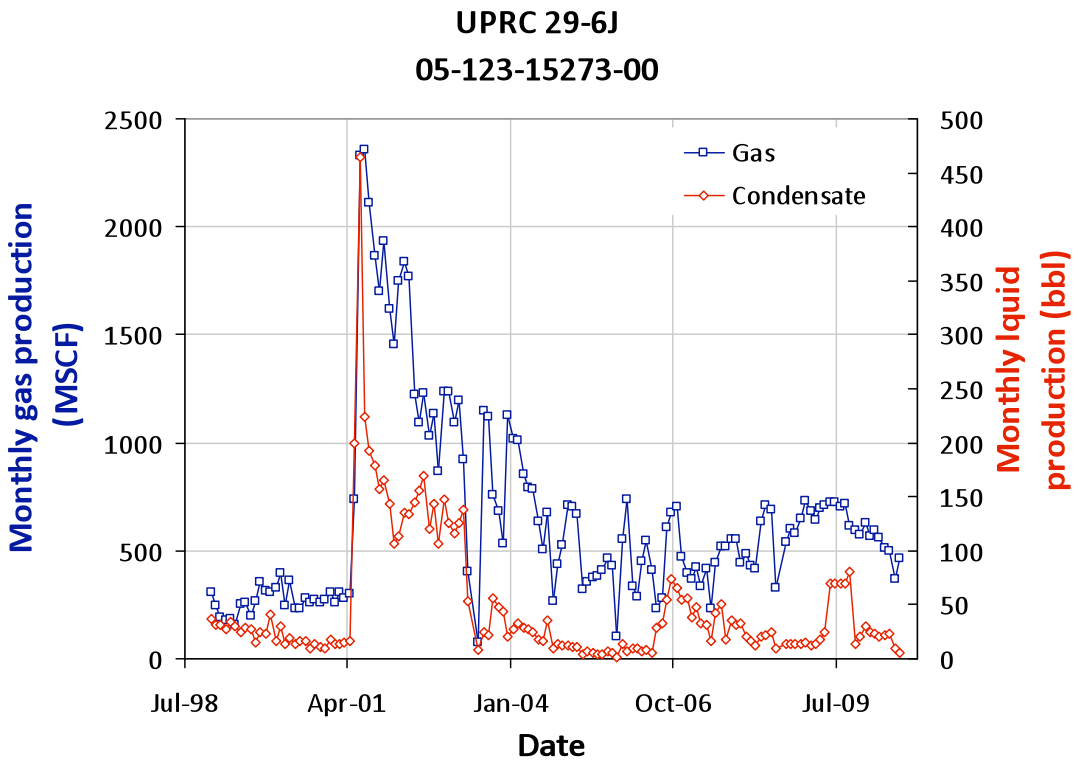
UPRC 29-6J
05-123-15273-00
Gas
Condensate
Monthly gas production (MSCF)
Monthly liquid production (bbl)
2500
2000
1500
1000
500
0
500
450
400
350
300
250
200
150
100
50
0
Jul-98
Apr-01
Jan-04
Oct-06
Jul-09
Date

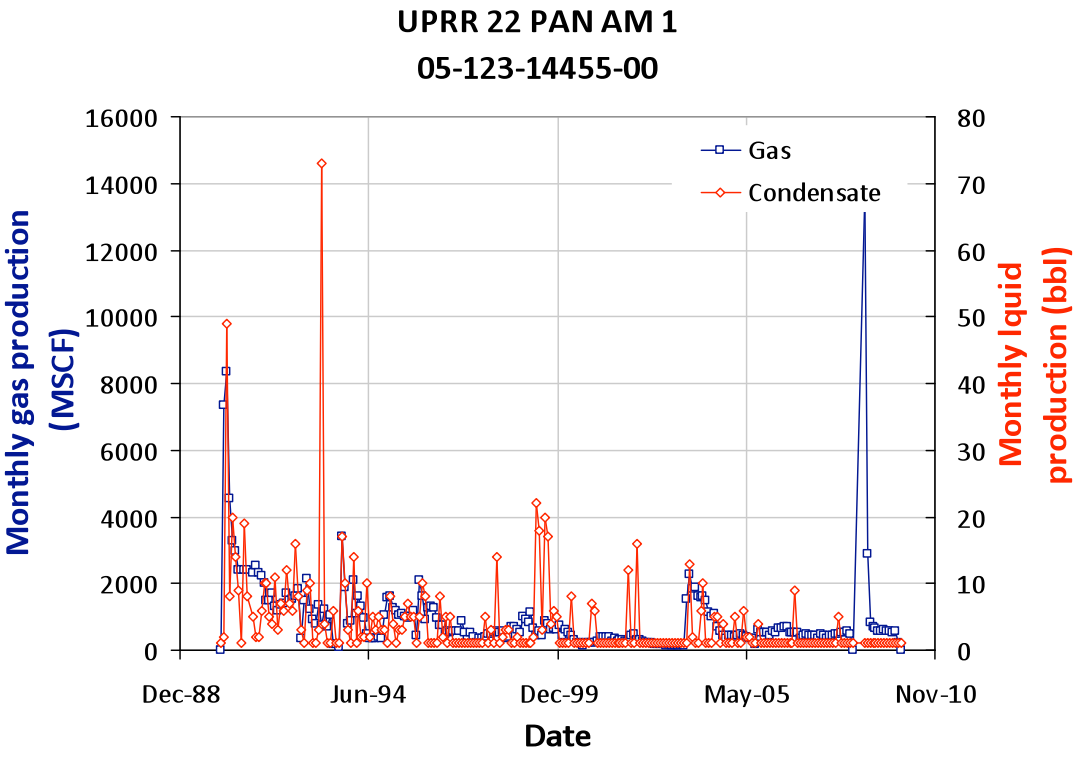
UPRR 22 PAN AM 1
05-123-14455-00
Gas
Condensate
Monthly gas production (MSCF)
Monthly liquid production (bbl)
16000
14000
12000
10000
8000
6000
4000
2000
0
80
70
60
50
40
30
20
10
0
Dec-88
Jun-94
Dec-99
May-05
Nov-10
Date

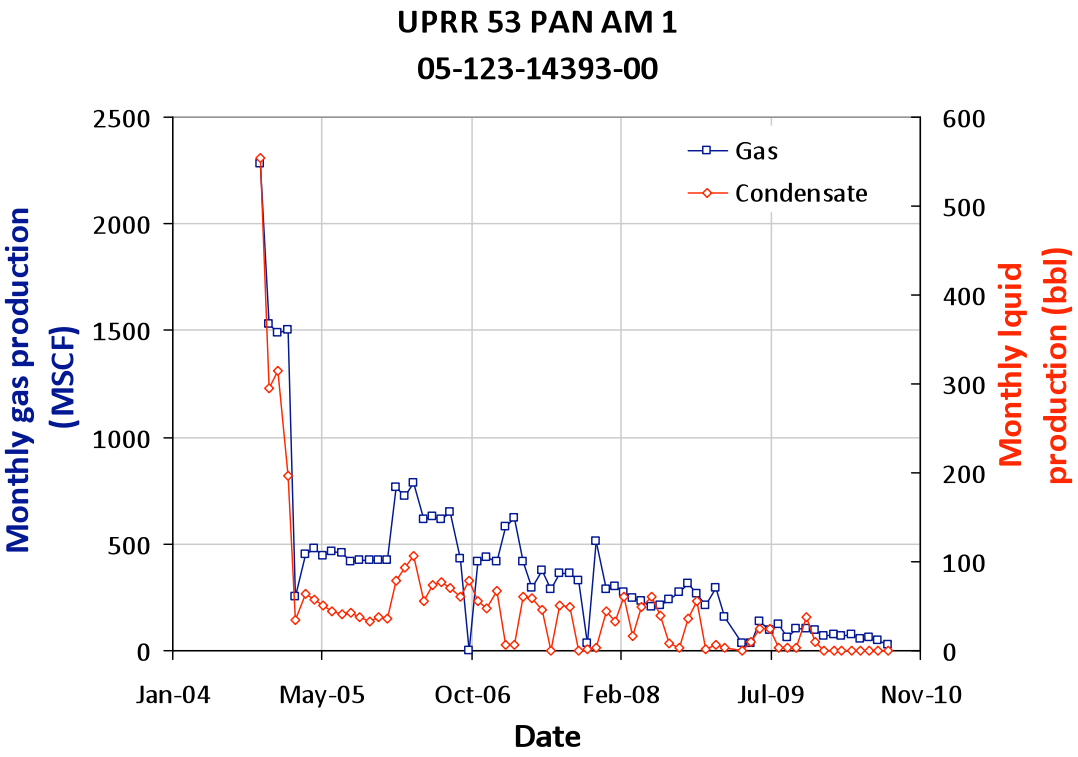
UPRR 53 PAN AM 1
05-123-14393-00
Monthly gas production (MSCF)
Monthly liquid production (bbl)
Gas
Condensate
2500
2000
1500
1000
500
0
600
500
400
300
200
100
0
Jan-04
May-05
Oct-06
Feb-08
Jul-09
Nov-10
Date

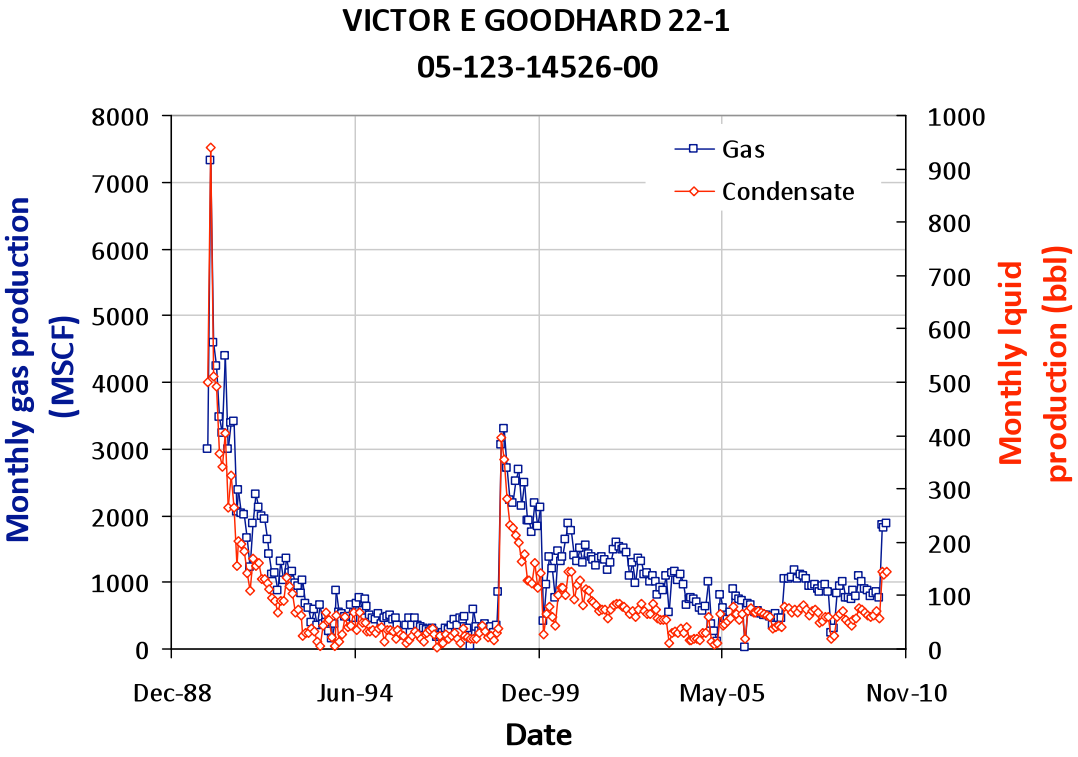
VICTOR E GOODHARD 22-1
05-123-14526-00
Monthly gas production (MSCF)
Monthly liquid production (bbl)
Gas
Condensate
8000
7000
6000
5000
4000
3000
2000
1000
0
1000
900
800
700
600
500
400
300
200
100
0
Dec-88
Jun-94
Dec-99
May-05
Nov-10
Date

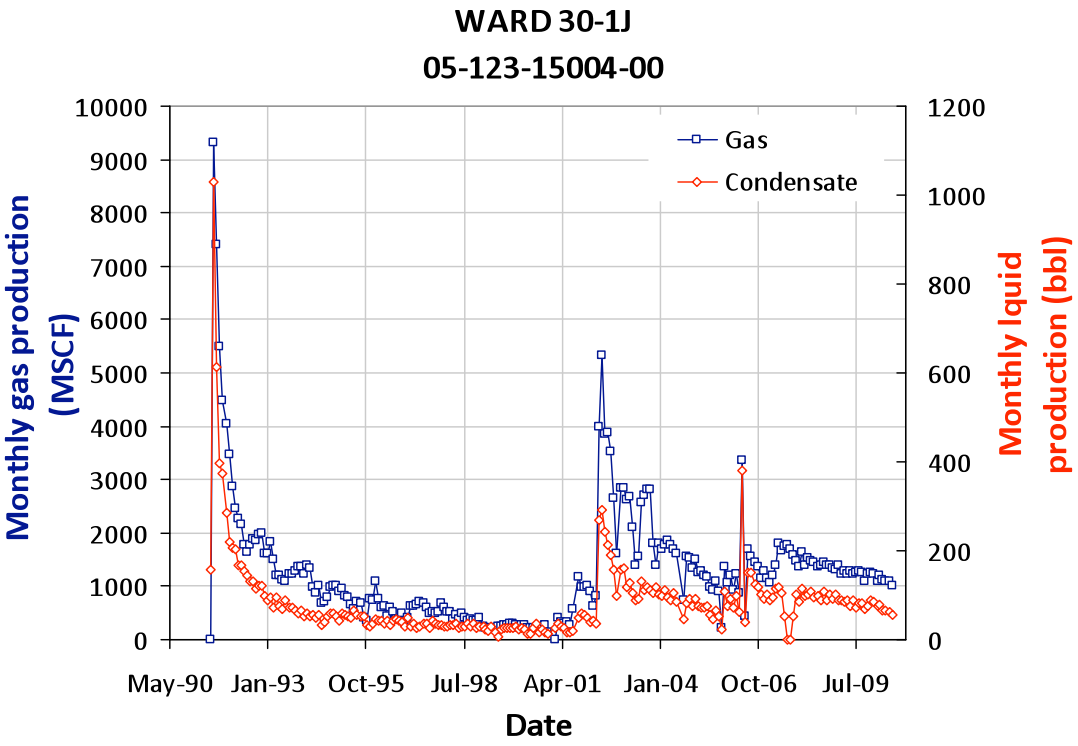
WARD 30-1J
05-123-15004-00
Gas
Condensate
Monthly gas production (MSCF)
Monthly liquid production (bbl)
10000
9000
8000
7000
6000
5000
4000
3000
2000
1000
0
1200
1000
800
600
400
200
0
May-90
Jan-93
Oct-95
Jul-98
Apr-01
Jan-04
Oct-06
Jul-09
Date

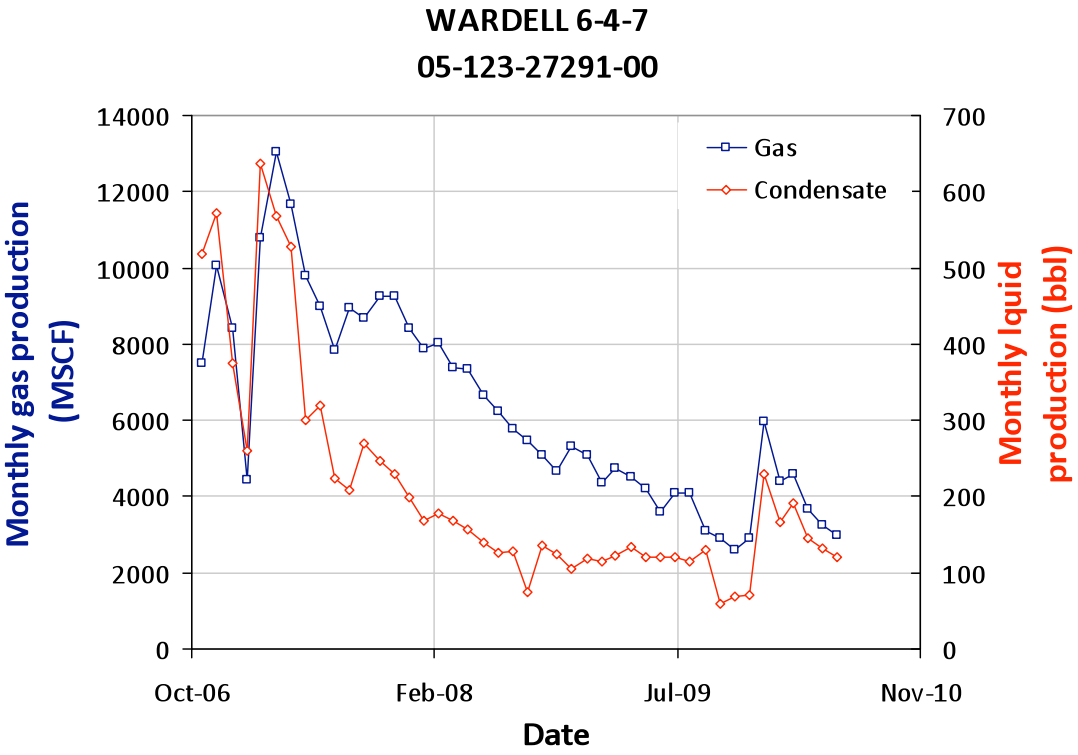
WARDELL 6-4-7
05-123-27291-00
Gas
Condensate
Monthly gas production (MSCF)
Monthly liquid production (bbl)
14000
12000
10000
8000
6000
4000
2000
0
700
600
500
400
300
200
100
0
Oct-06
Feb-08
Jul-09
Nov-10
Date

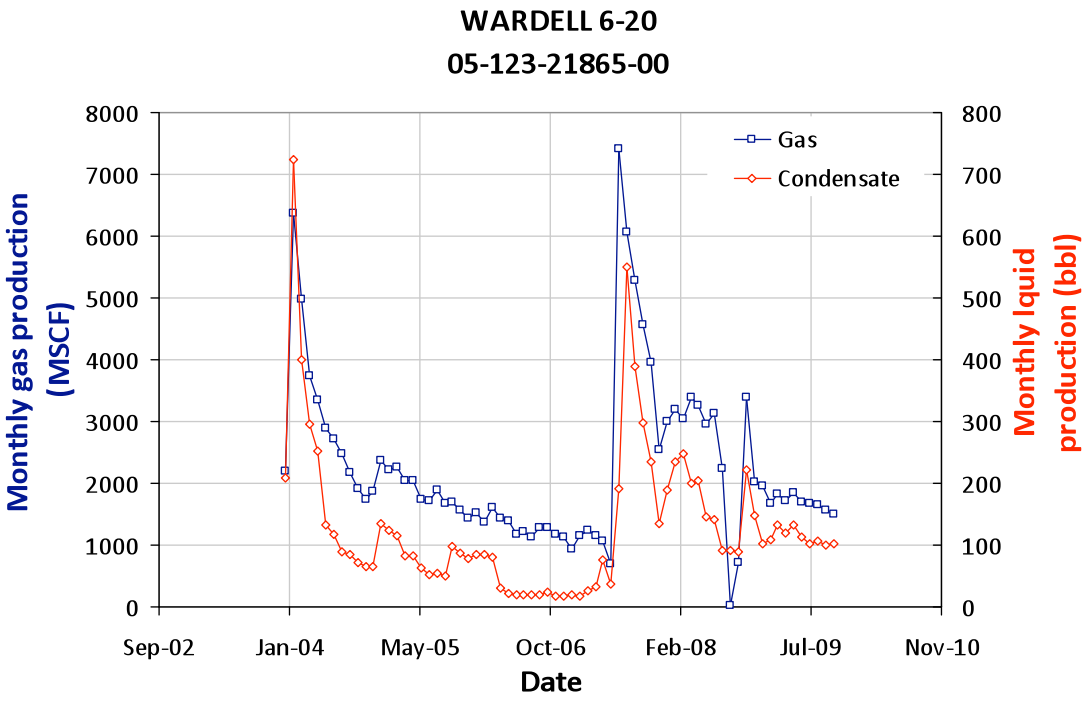
WARDELL 6-20
05-123-21865-00
Monthly gas production (MSCF)
Monthly liquid production (bbl)
Gas
Condensate
8000
7000
6000
5000
4000
3000
2000
1000
0
800
700
600
500
400
300
200
100
0
Sep-02
Jan-04
May-05
Oct-06
Feb-08
Jul-09
Nov-10
Date

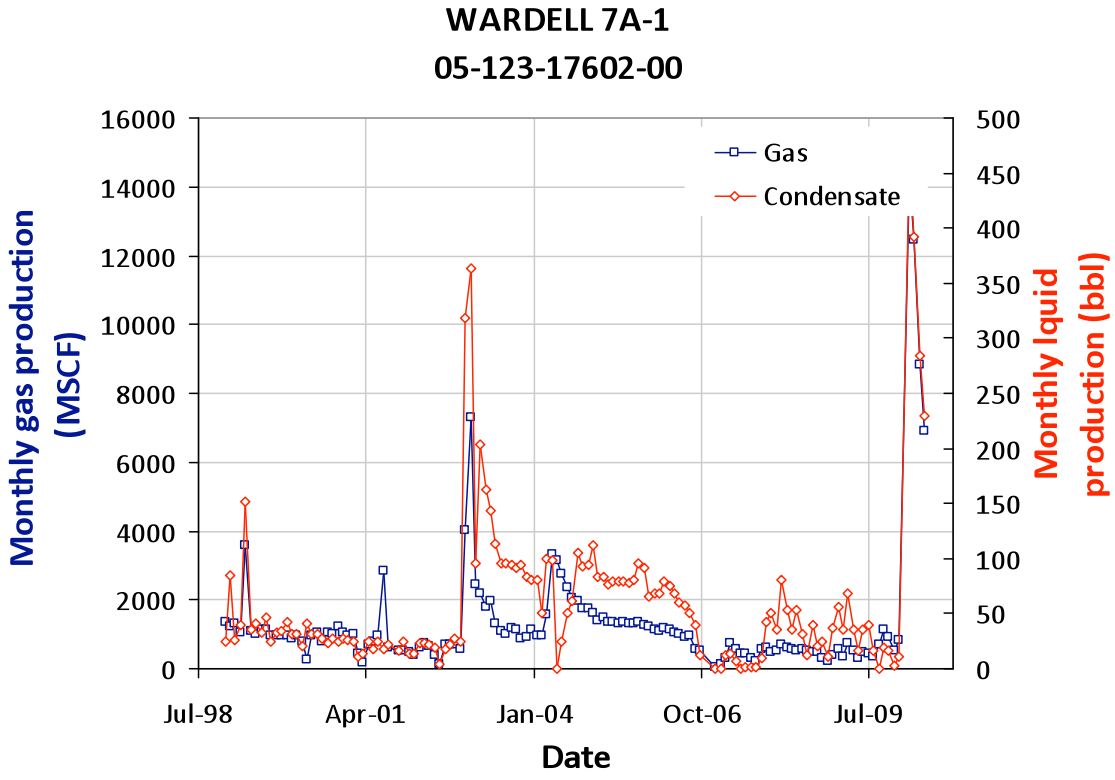
WARDELL 7A-1
05-123-17602-00
Monthly gas production (MSCF)
Monthly liquid production (bbl)
Gas
Condensate
16000
14000
12000
10000
8000
6000
4000
2000
0
500
450
400
350
300
250
200
150
100
50
0
Jul-98
Apr-01
Jan-04
Oct-06
Jul-09
Date

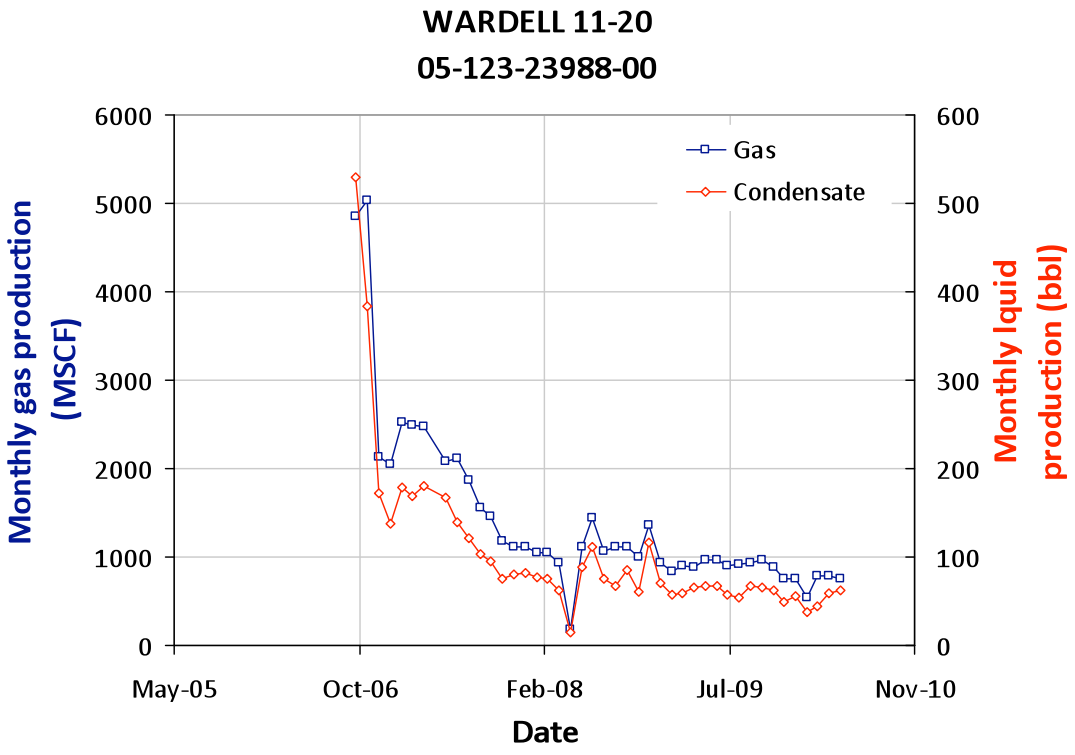
WARDELL 11-20
05-123-23988-00
Monthly gas production (MSCF)
Monthly liquid production (bbl)
Gas
Condensate
6000
5000
4000
3000
2000
1000
0
600
500
400
300
200
100
0
May-05
Oct-06
Feb-08
Jul-09
Nov-10
Date

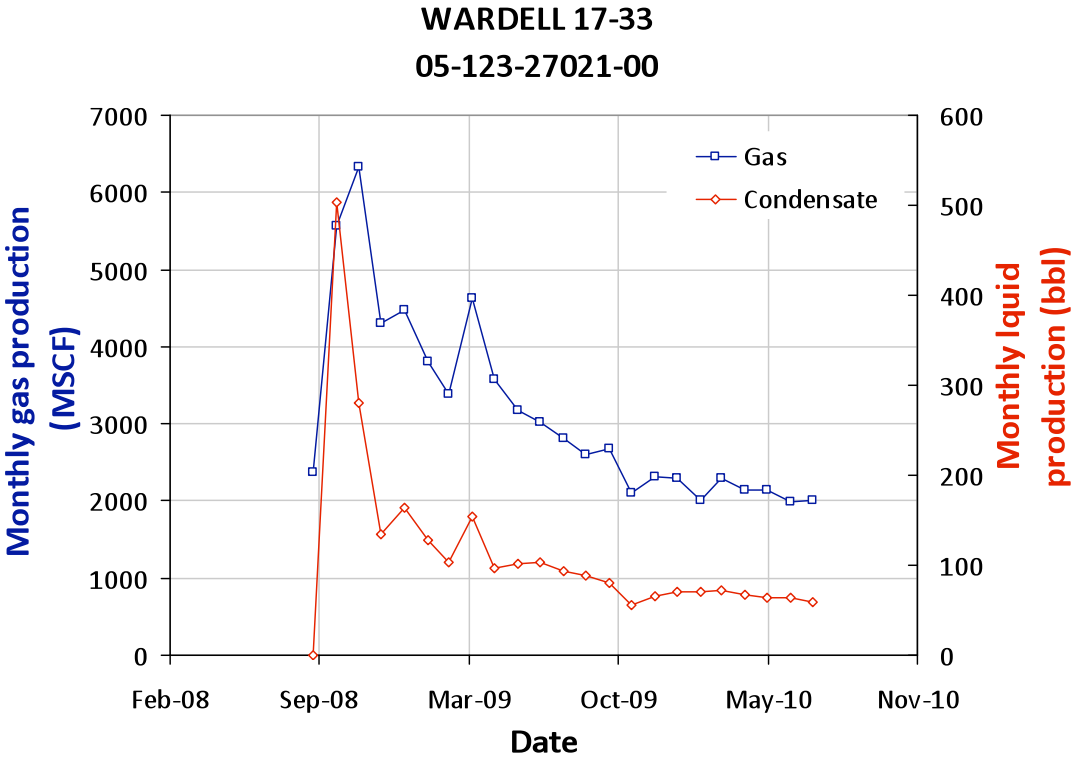
WARDELL 17-33
05-123-27021-00
Monthly gas production (MSCF)
Monthly liquid production (bbl)
Gas
Condensate
7000
6000
5000
4000
3000
2000
1000
0
600
500
400
300
200
100
0
Feb-08
Sep-08
Mar-09
Oct-09
May-10
Nov-10
Date

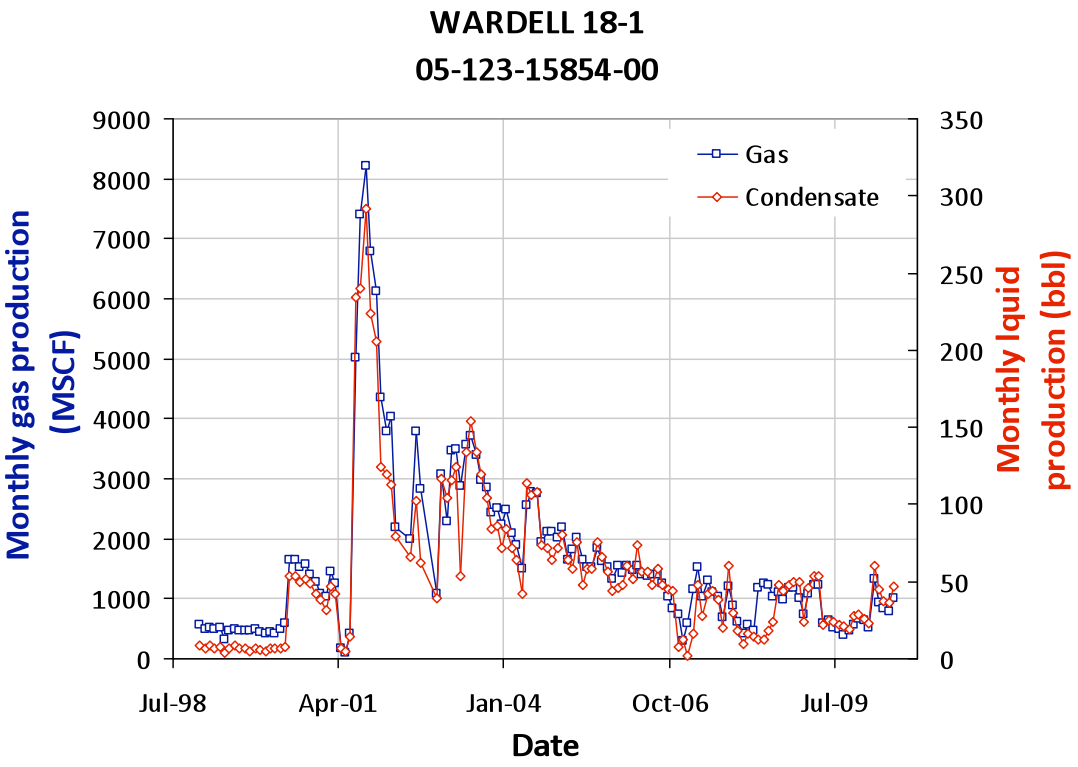
WARDELL 18-1
05-123-15854-00
Monthly gas production (MSCF)
Monthly lquid production (bbl)
Gas
Condensate
9000
8000
7000
6000
5000
4000
3000
2000
1000
0
350
300
250
200
150
100
50
0
Jul-98
Apr-01
Jan-04
Oct-06
Jul-09
Date

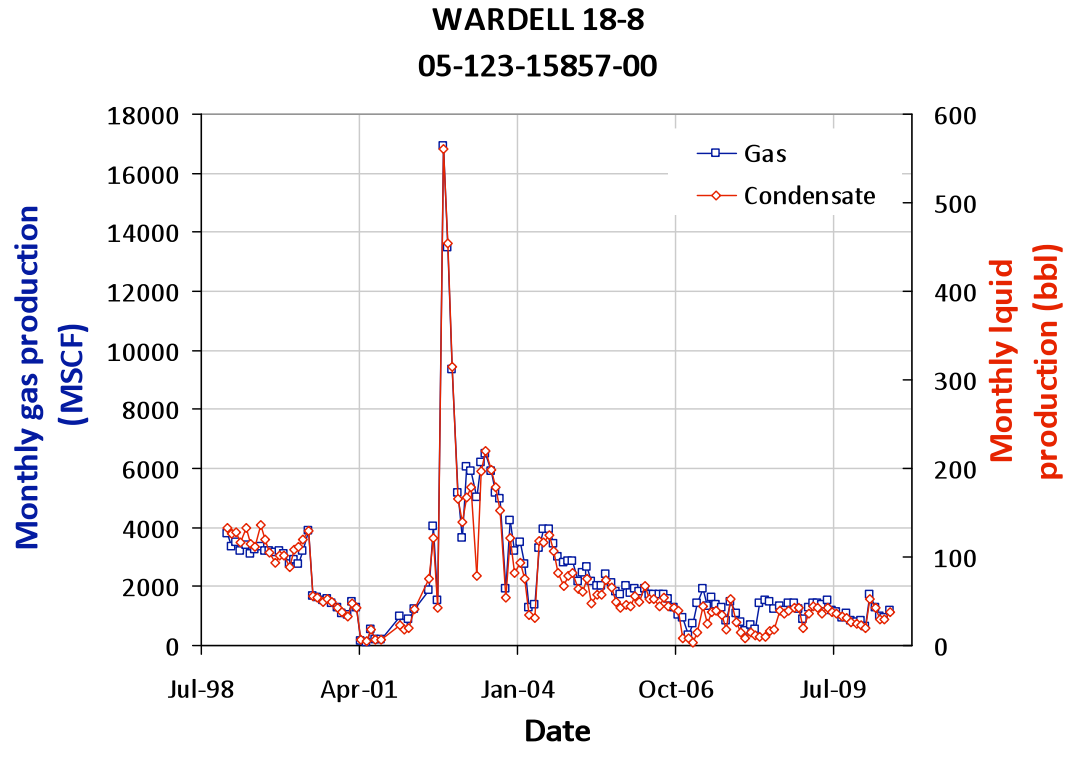
WARDELL 18-8
05-123-15857-00
Monthly gas production (MSCF)
Monthly lquid production (bbl)
Gas
Condensate
18000
16000
14000
12000
10000
8000
6000
4000
2000
0
600
500
400
300
200
100
0
Jul-98
Apr-01
Jan-04
Oct-06
Jul-09
Date

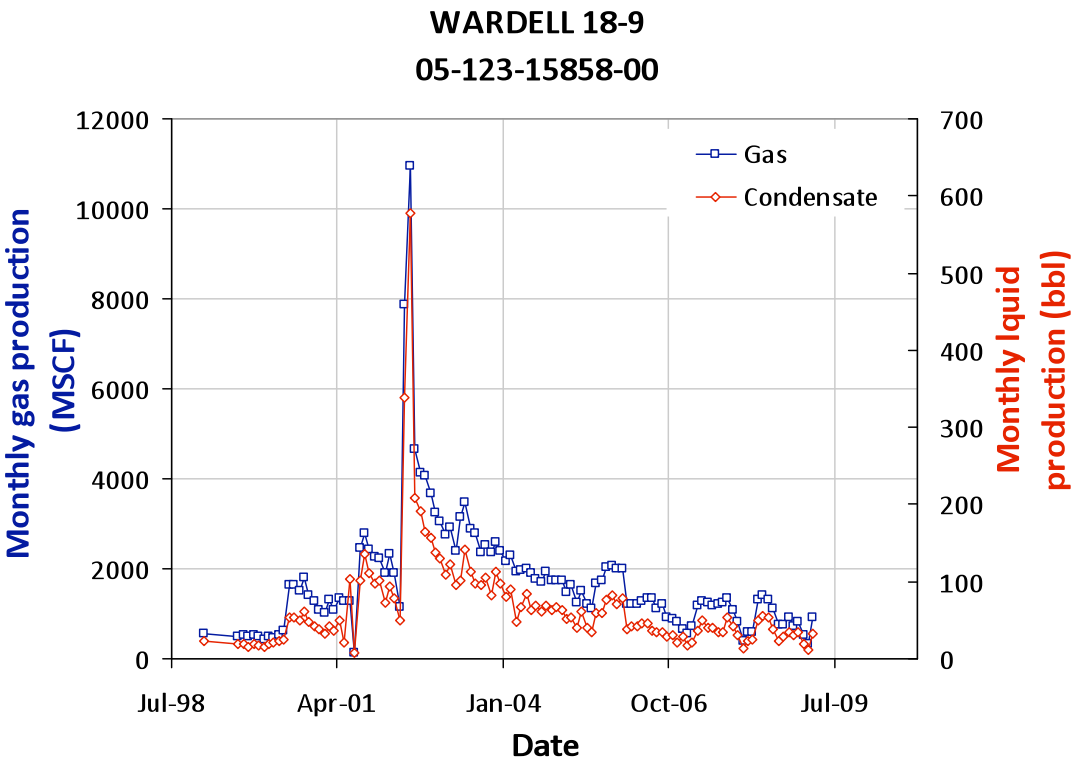
WARDELL 18-9
05-123-15858-00
Monthly gas production (MSCF)
Monthly lquid production (bbl)
Gas
Condensate
12000
10000
8000
6000
4000
2000
0
700
600
500
400
300
200
100
0
Jul-98
Apr-01
Jan-04
Oct-06
Jul-09
Date

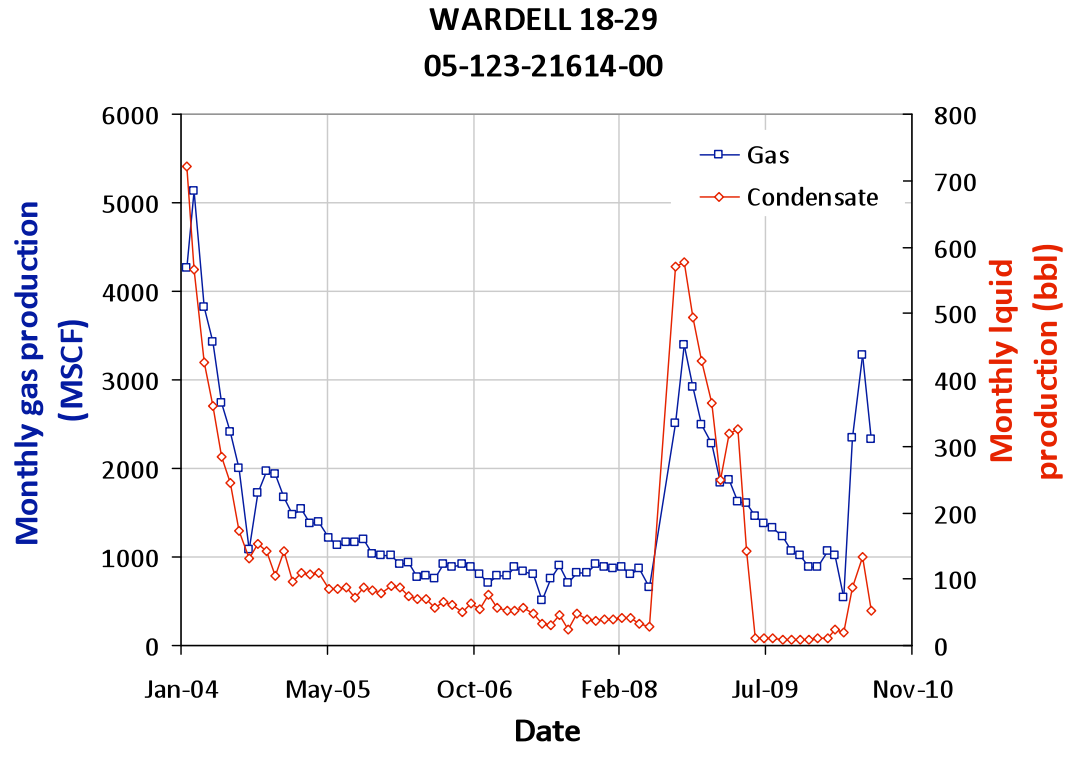
WARDELL 18-29
05-123-21614-00
Monthly gas production (MSCF)
Monthly lquid production (bbl)
Gas
Condensate
6000
5000
4000
3000
2000
1000
0
800
700
600
500
400
300
200
100
0
Jan-04
May-05
Oct-06
Feb-08
Jul-09
Nov-10
Date

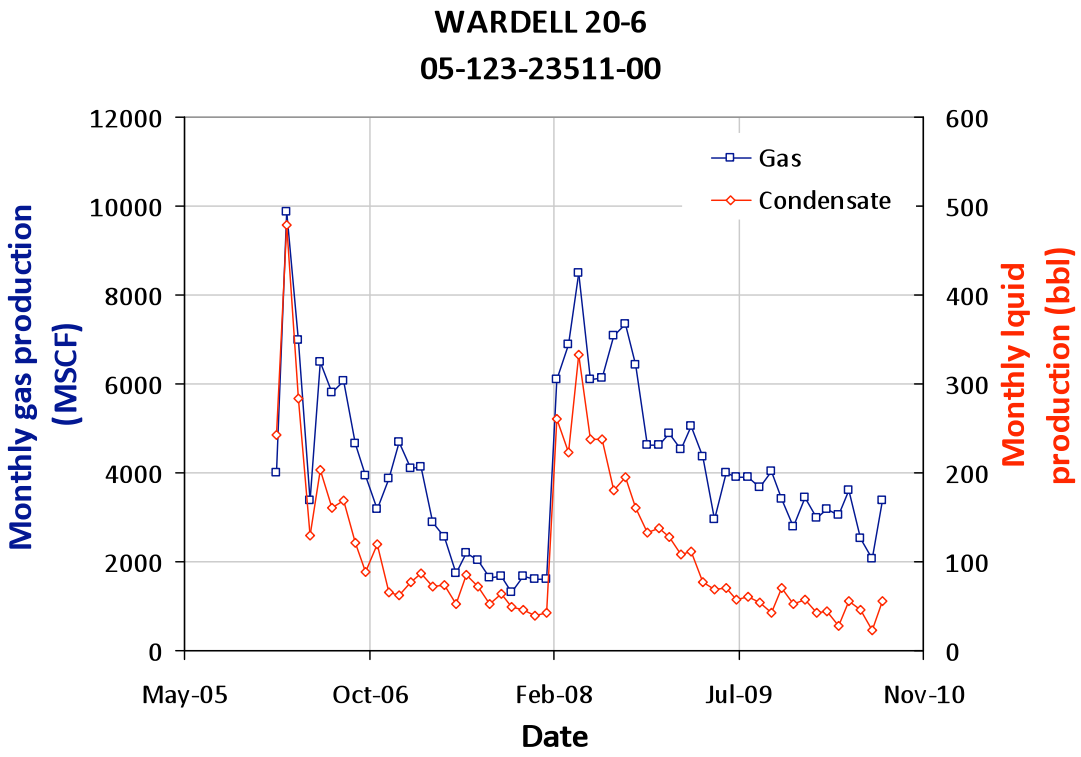
WARDELL 20-6
05-123-23511-00
Monthly gas production (MSCF)
Monthly liquid production (bbl)
Gas
Condensate
12000
10000
8000
6000
4000
2000
0
600
500
400
300
200
100
0
May-05
Oct-06
Feb-08
Jul-09
Nov-10
Date

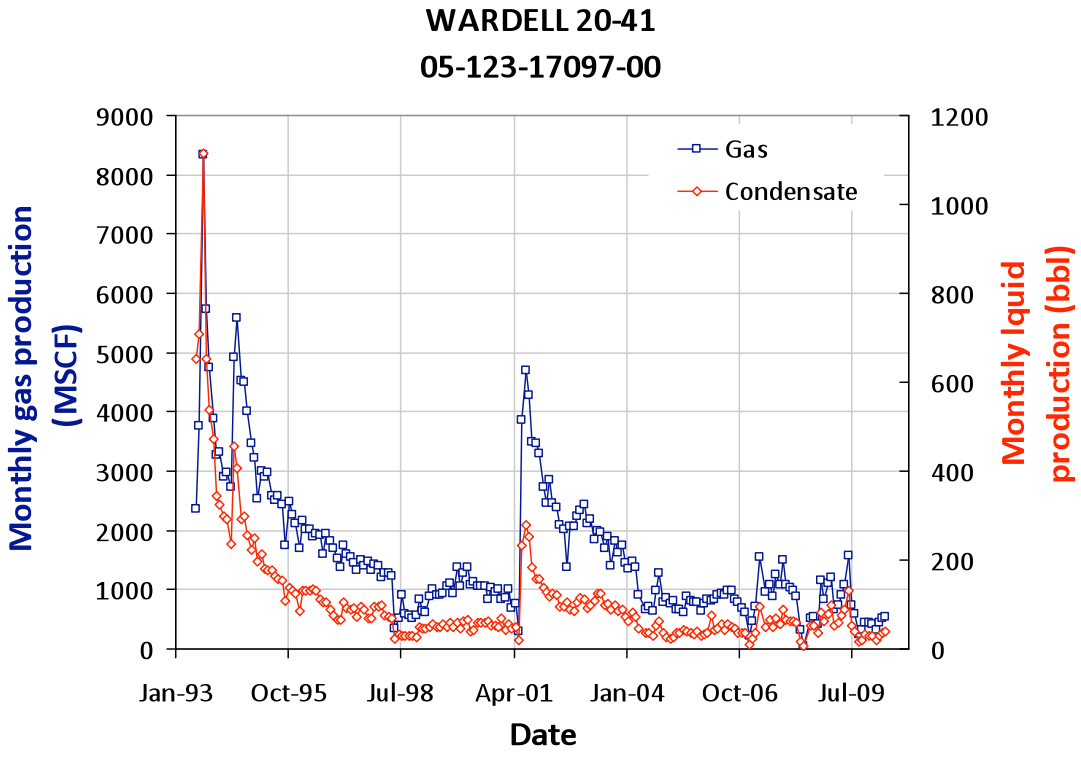
WARDELL 20-41
05-123-17097-00
Monthly gas production (MSCF)
Monthly liquid production (bbl)
Gas
Condensate
9000
8000
7000
6000
5000
4000
3000
2000
1000
0
1200
1000
800
600
400
200
0
Jan-93
Oct-95
Jul-98
Apr-01
Jan-04
Oct-06
Jul-09
Date

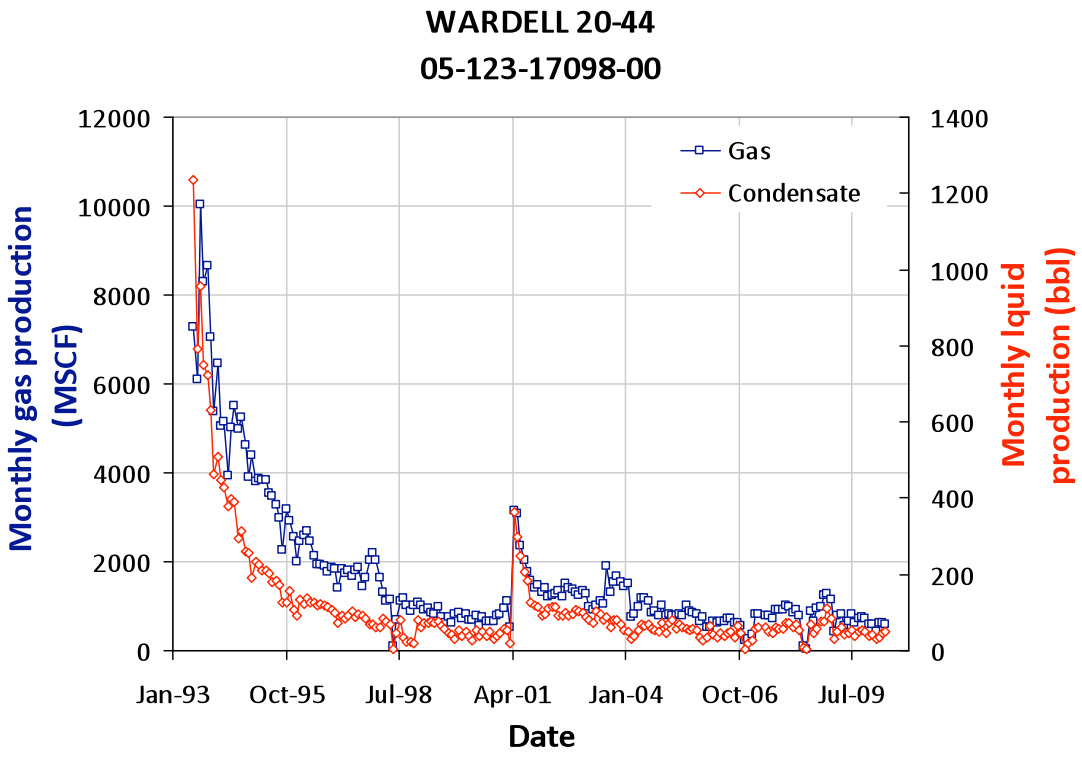
WARDELL 20-44
05-123-17098-00
Monthly gas production (MSCF)
Monthly liquid production (bbl)
Gas
Condensate
12000
10000
8000
6000
4000
2000
0
1400
1200
1000
800
600
400
200
0
Jan-93
Oct-95
Jul-98
Apr-01
Jan-04
Oct-06
Jul-09
Date

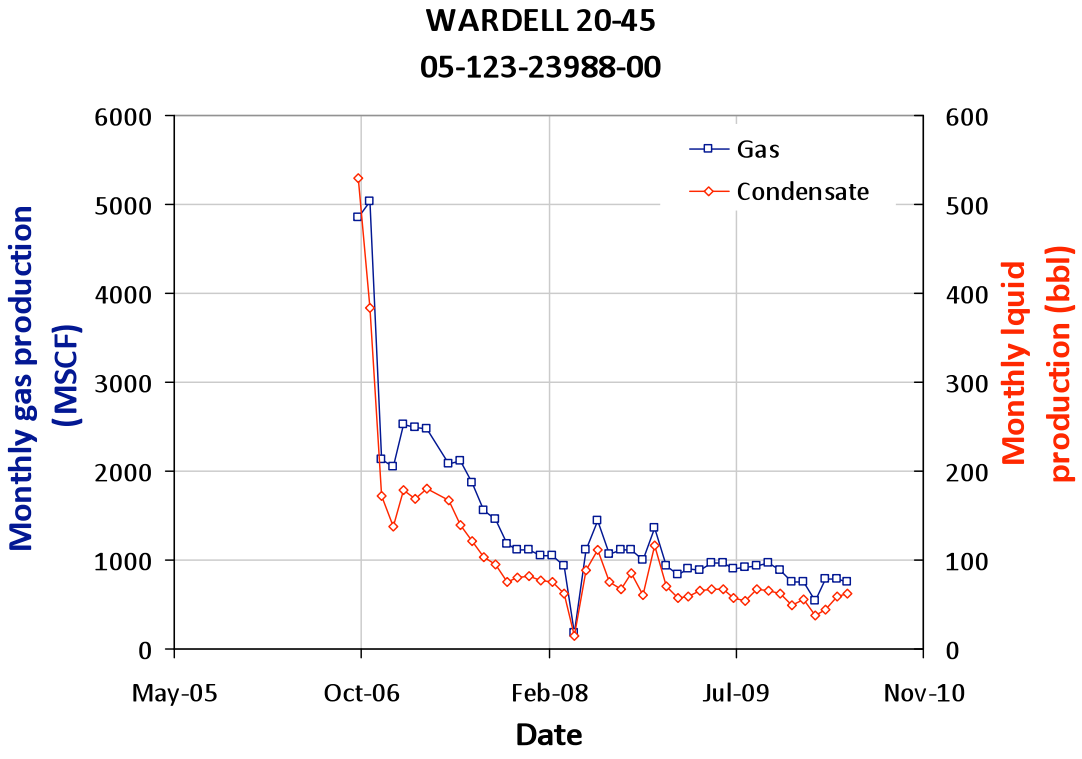
WARDELL 20-45
05-123-23988-00
Monthly gas production (MSCF)
Monthly liquid production (bbl)
Gas
Condensate
6000
5000
4000
3000
2000
1000
0
600
500
400
300
200
100
0
May-05
Oct-06
Feb-08
Jul-09
Nov-10
Date

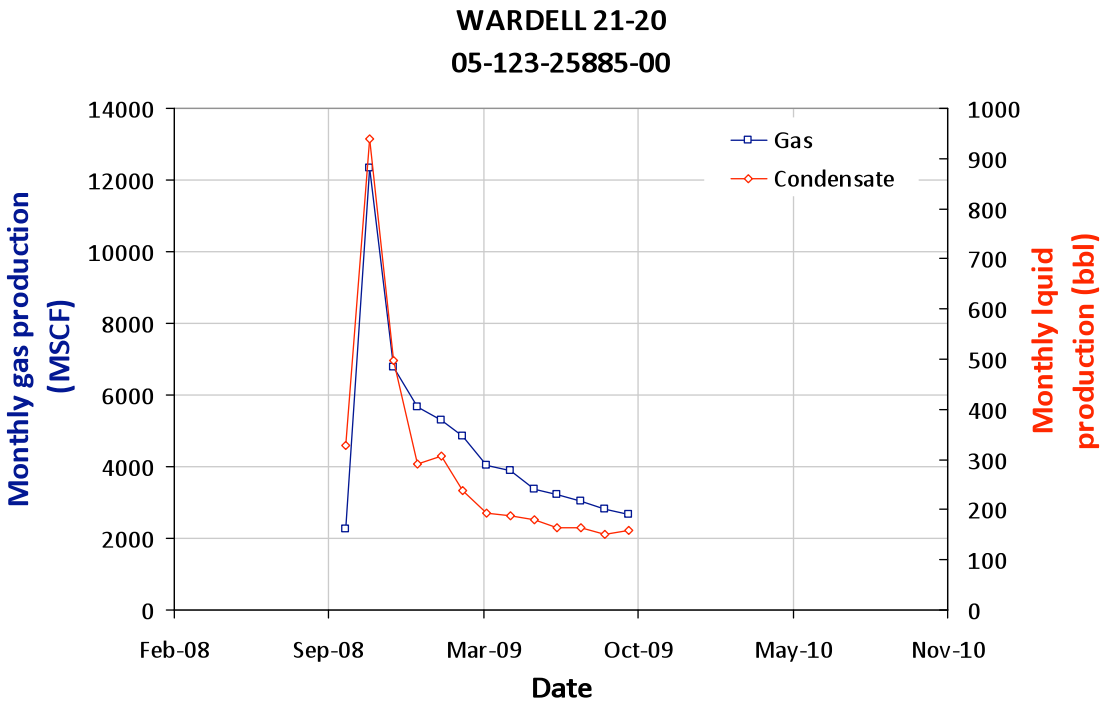
WARDELL 21-20
05-123-25885-00
Monthly gas production (MSCF)
Monthly lquid production (bbl)
Gas
Condensate
14000
12000
10000
8000
6000
4000
2000
0
1000
900
800
700
600
500
400
300
200
100
0
Feb-08
Sep-08
Mar-09
Oct-09
May-10
Nov-10
Date

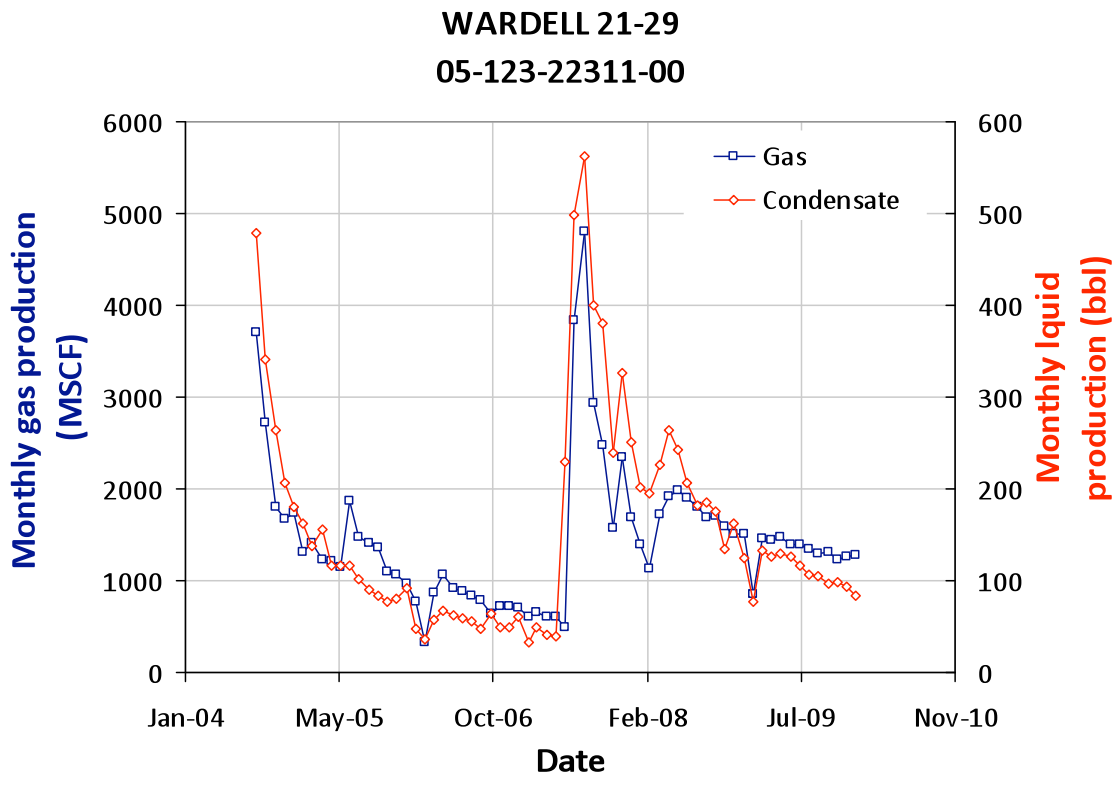
WARDELL 21-29
05-123-22311-00
Monthly gas production (MSCF)
Monthly lquid production (bbl)
Gas
Condensate
6000
5000
4000
3000
2000
1000
0
600
500
400
300
200
100
0
Jan-04
May-05
Oct-06
Feb-08
Jul-09
Nov-10
Date

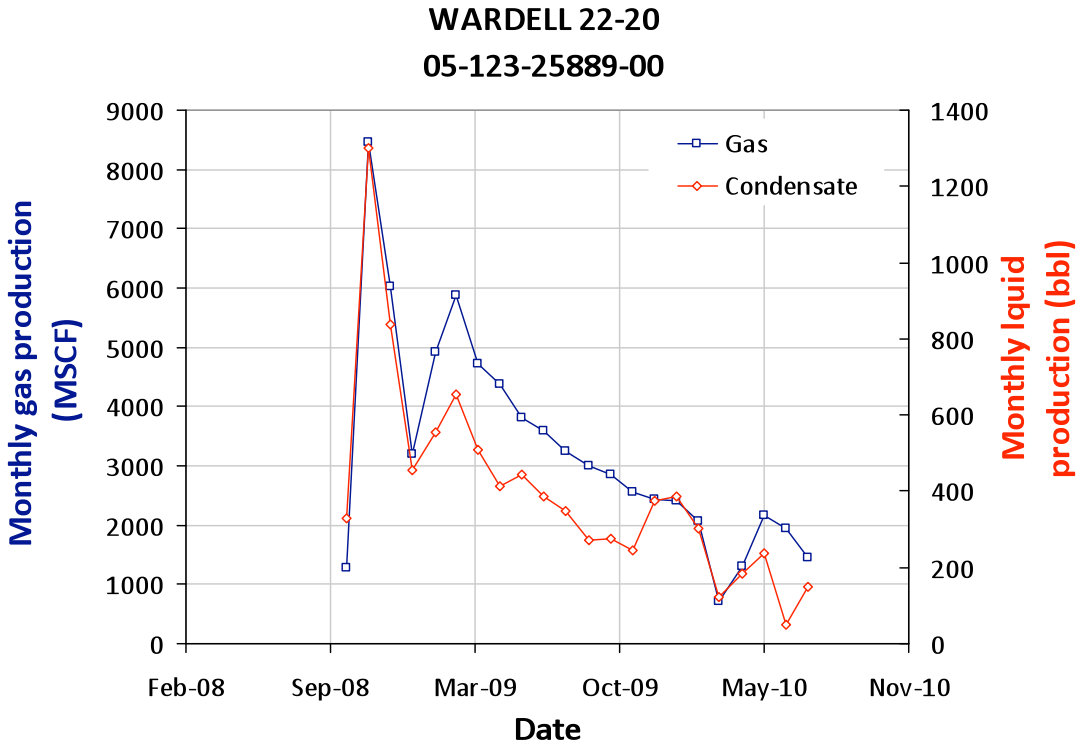
WARDELL 22-20
05-123-25889-00
Monthly gas production (MSCF)
Monthly liquid production (bbl)
Gas
Condensate
9000
8000
7000
6000
5000
4000
3000
2000
1000
0
1400
1200
1000
800
600
400
200
0
Feb-08
Sep-08
Mar-09
Oct-09
May-10
Nov-10
Date

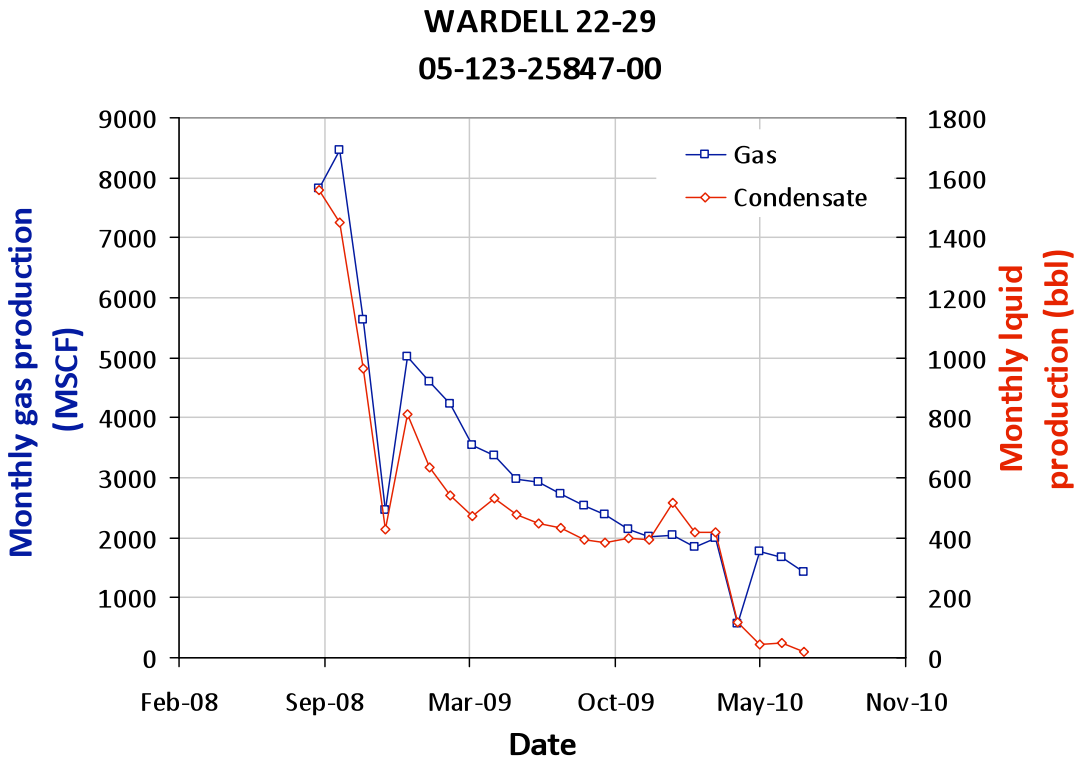
WARDELL 22-29
05-123-25847-00
Monthly gas production (MSCF)
Monthly liquid production (bbl)
Gas
Condensate
9000
8000
7000
6000
5000
4000
3000
2000
1000
0
1800
1600
1400
1200
1000
800
600
400
200
0
Feb-08
Sep-08
Mar-09
Oct-09
May-10
Nov-10
Date

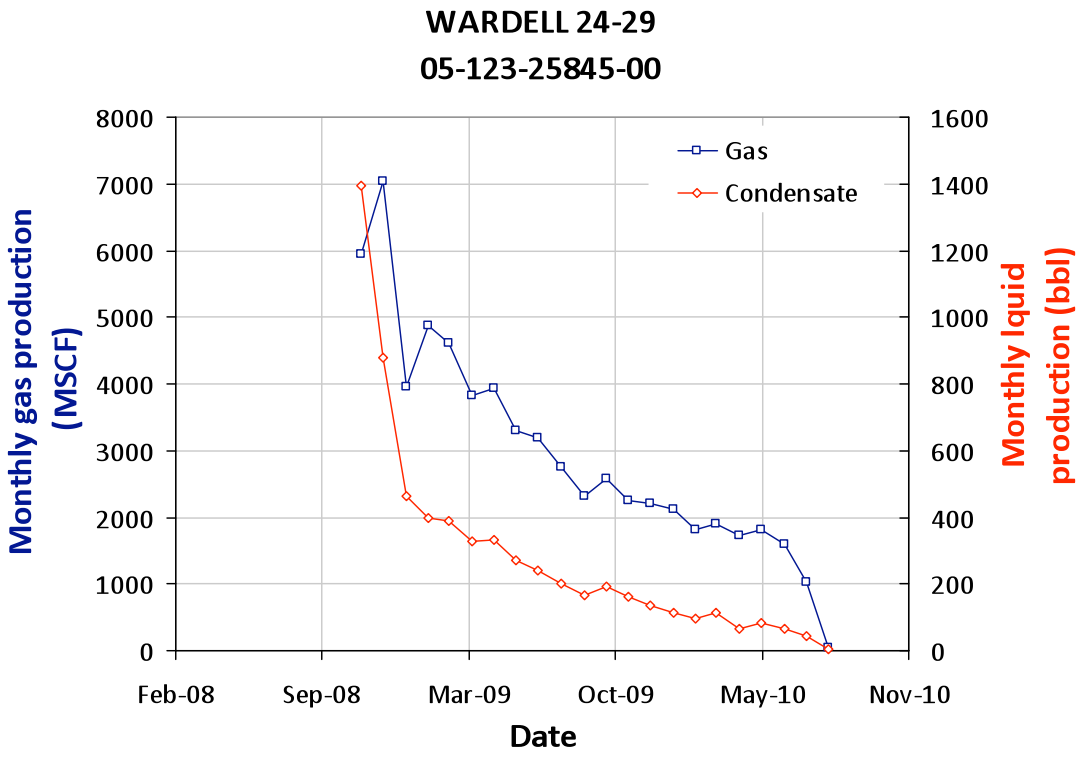
WARDELL 24-29
05-123-25845-00
Monthly gas production (MSCF)
Monthly liquid production (bbl)
Gas
Condensate
8000
7000
6000
5000
4000
3000
2000
1000
0
1600
1400
1200
1000
800
600
400
200
0
Feb-08
Sep-08
Mar-09
Oct-09
May-10
Nov-10
Date

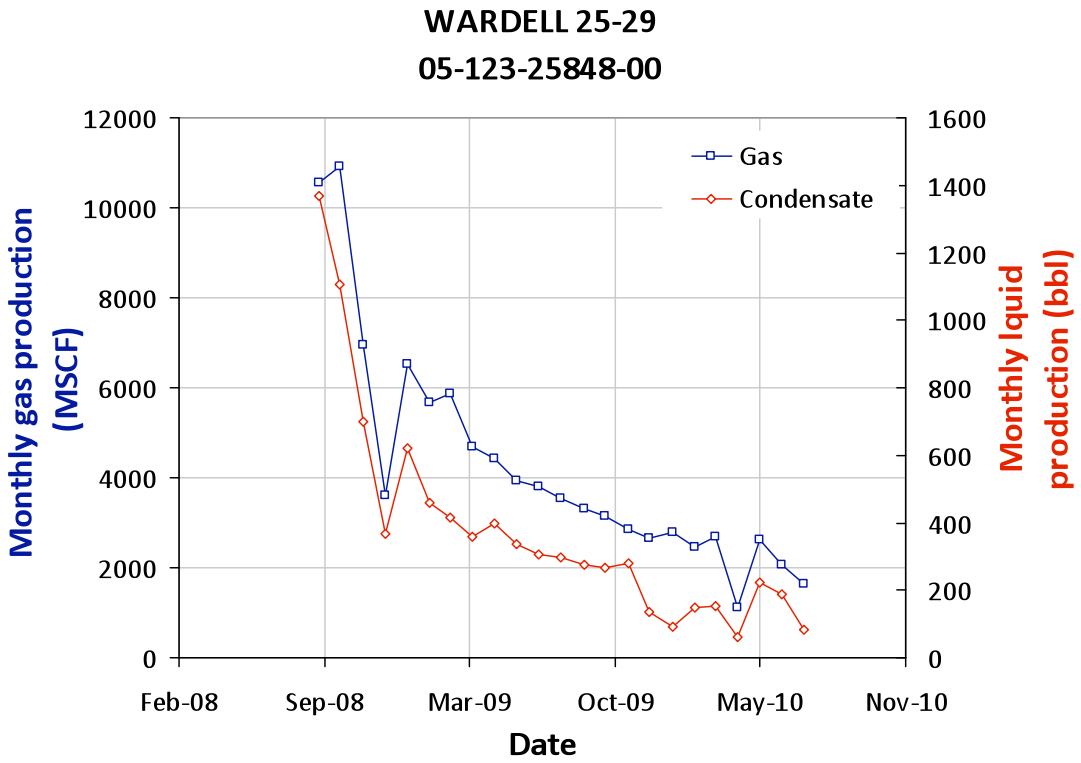
WARDELL 25-29
05-123-25848-00
Monthly gas production (MSCF)
Monthly liquid production (bbl)
Gas
Condensate
12000
10000
8000
6000
4000
2000
0
1600
1400
1200
1000
800
600
400
200
0
Feb-08
Sep-08
Mar-09
Oct-09
May-10
Nov-10
Date

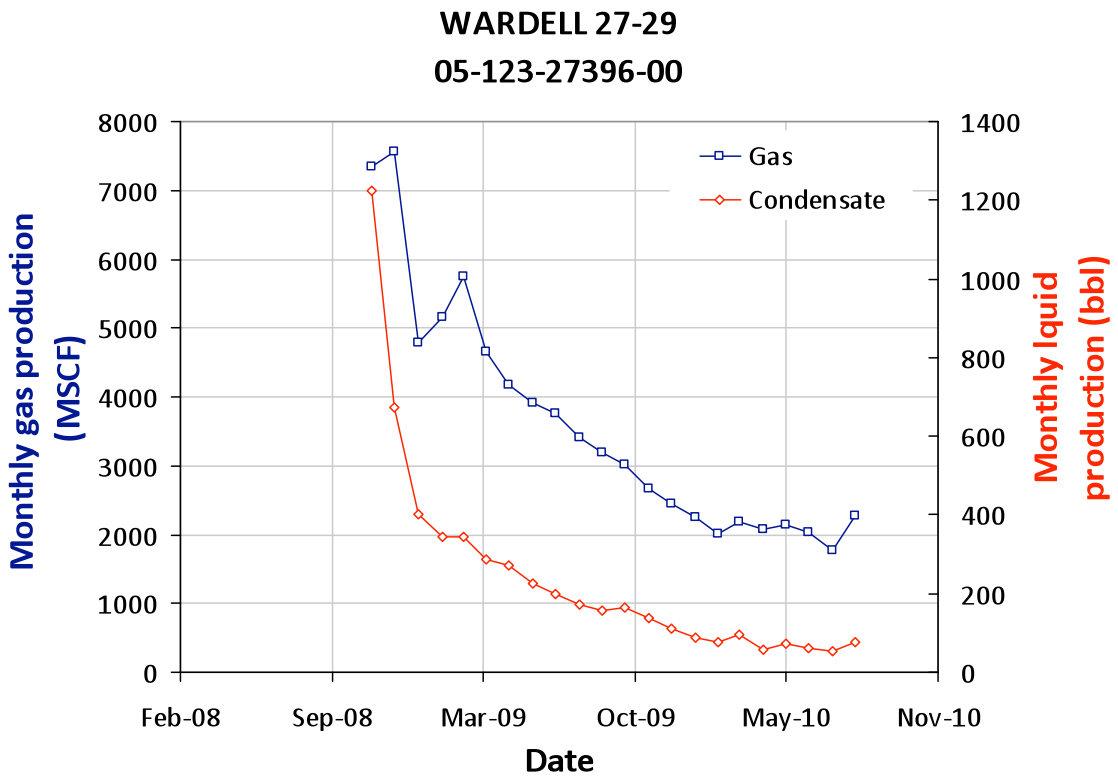
WARDELL 27-29
05-123-27396-00
Monthly gas production (MSCF)
Monthly liquid production (bbl)
Gas
Condensate
8000
7000
6000
5000
4000
3000
2000
1000
0
1400
1200
1000
800
600
400
200
0
Feb-08
Sep-08
Mar-09
Oct-09
May-10
Nov-10
Date

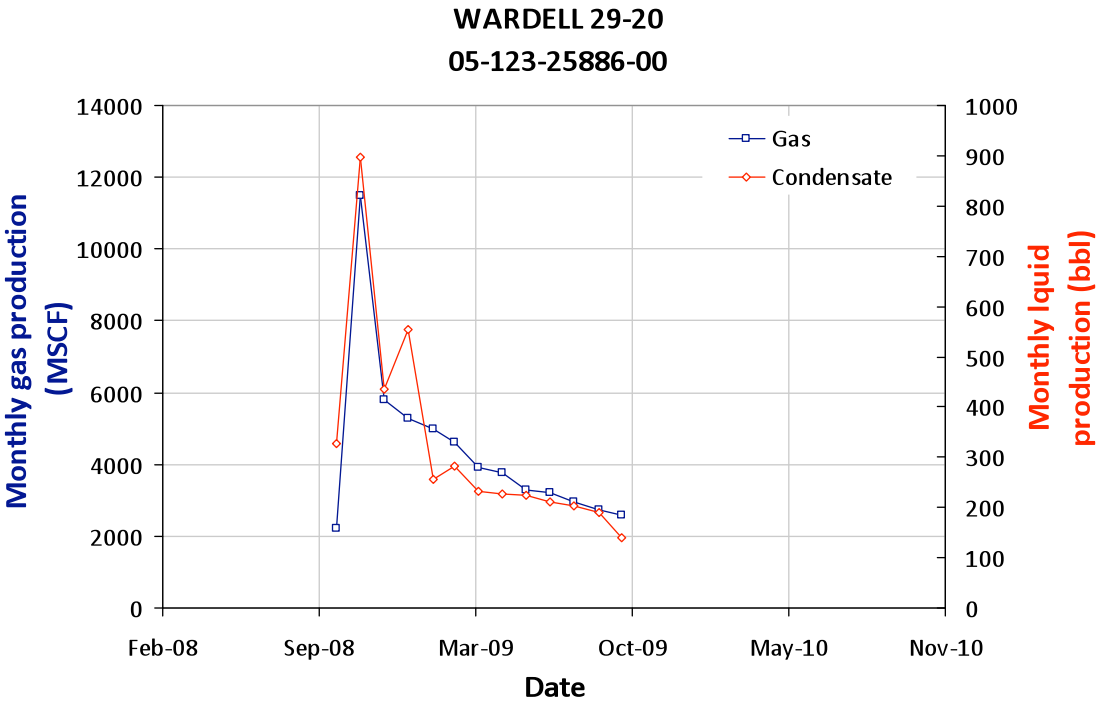
WARDELL 29-20
05-123-25886-00
Monthly gas production (MSCF)
Monthly liquid production (bbl)
Gas
Condensate
14000
12000
10000
8000
6000
4000
2000
0
1000
900
800
700
600
500
400
300
200
100
0
Feb-08
Sep-08
Mar-09
Oct-09
May-10
Nov-10
Date

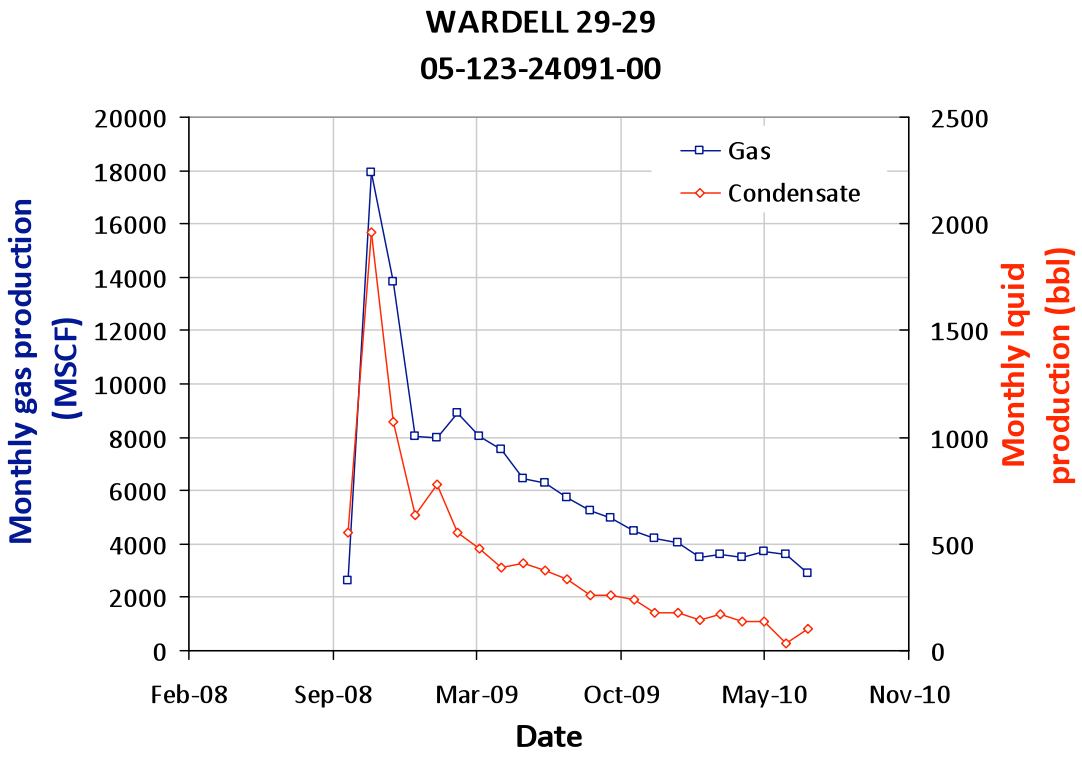
WARDELL 29-29
05-123-24091-00
Monthly gas production (MSCF)
Monthly liquid production (bbl)
Gas
Condensate
20000
18000
16000
14000
12000
10000
8000
6000
4000
2000
0
2500
2000
1500
1000
500
0
Feb-08
Sep-08
Mar-09
Oct-09
May-10
Nov-10
Date

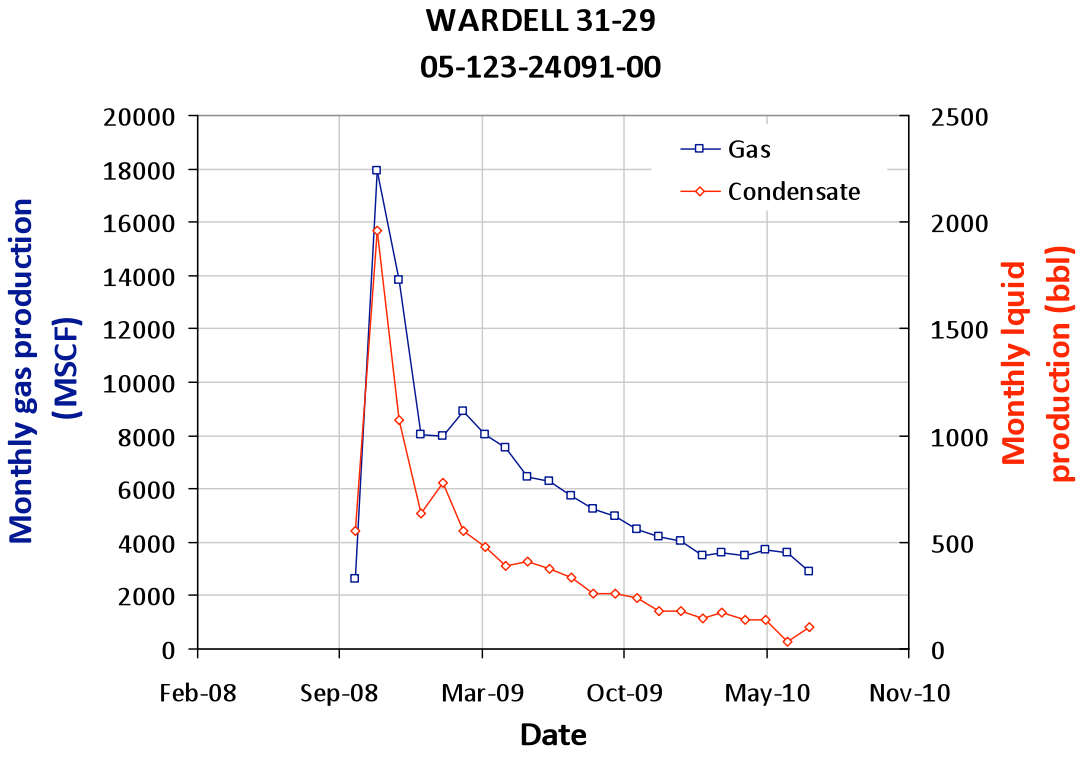
WARDELL 31-29
05-123-24091-00
Monthly gas production (MSCF)
Monthly liquid production (bbl)
Gas
Condensate
20000
18000
16000
14000
12000
10000
8000
6000
4000
2000
0
2500
2000
1500
1000
500
0
Feb-08
Sep-08
Mar-09
Oct-09
May-10
Nov-10
Date

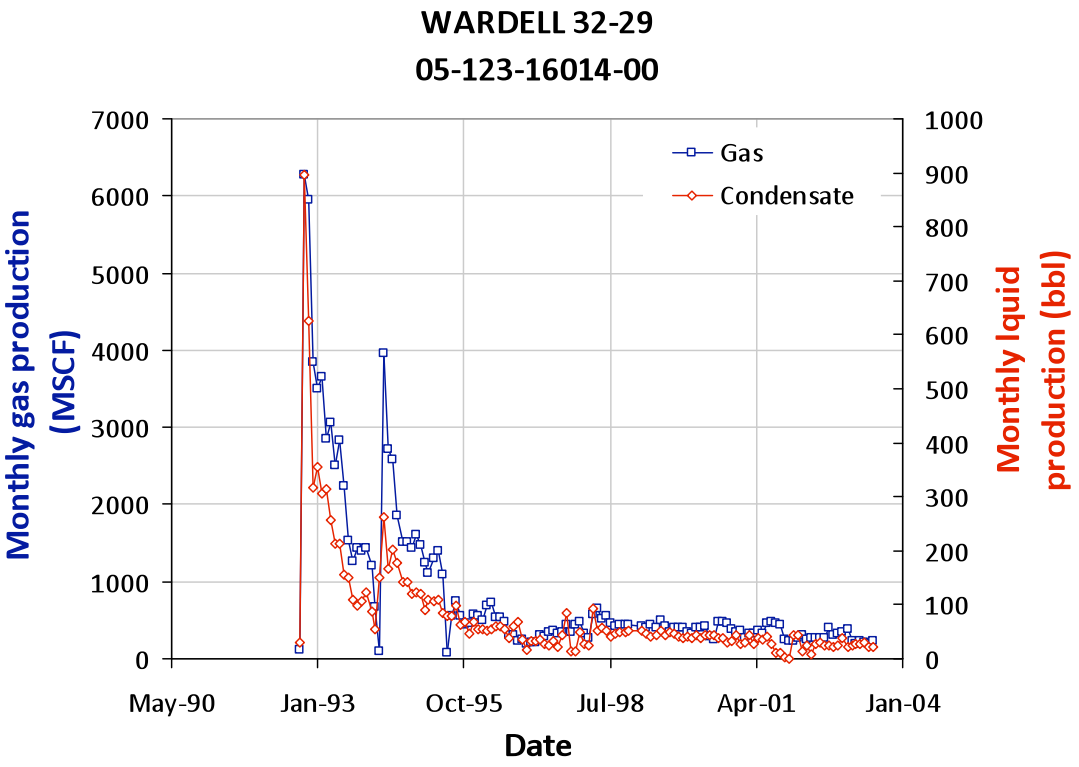
WARDELL 32-29
05-123-16014-00
Monthly gas production (MSCF)
Monthly liquid production (bbl)
Gas
Condensate
7000
6000
5000
4000
3000
2000
1000
0
1000
900
800
700
600
500
400
300
200
100
0
May-90
Jan-93
Oct-95
Jul-98
Apr-01
Jan-04
Date

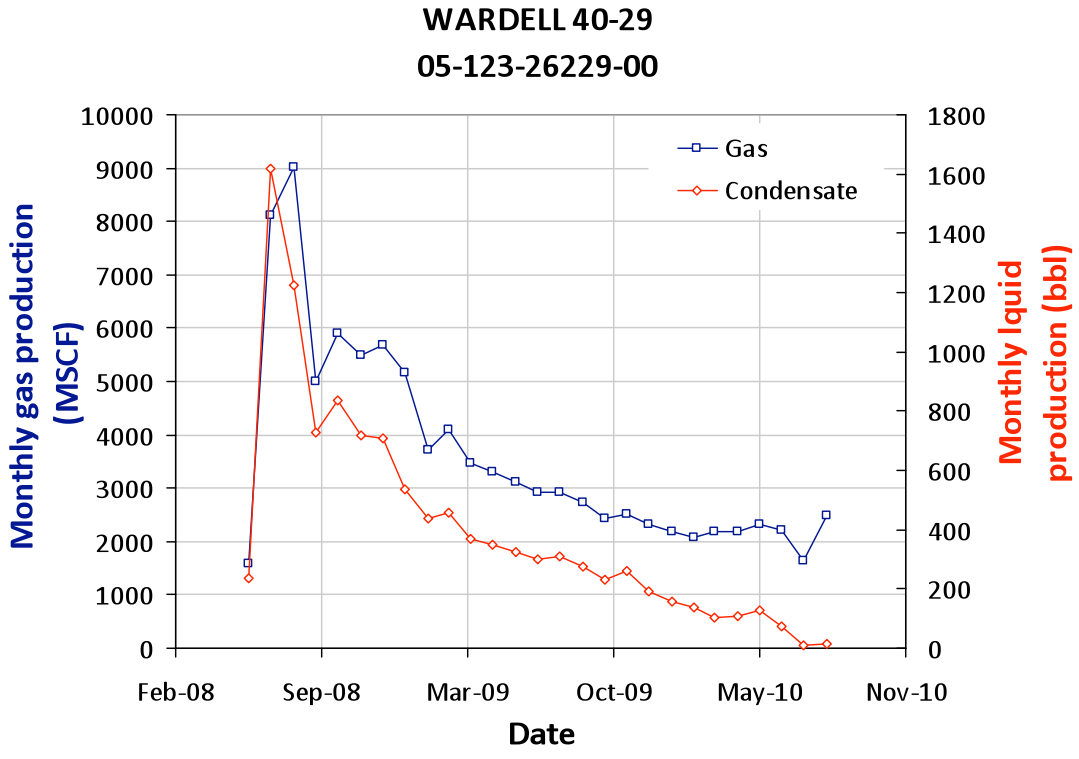
WARDELL 40-29
05-123-26229-00
Monthly gas production (MSCF)
Monthly liquid production (bbl)
Gas
Condensate
10000
9000
8000
7000
6000
5000
4000
3000
2000
1000
0
1800
1600
1400
1200
1000
800
600
400
200
0
Feb-08
Sep-08
Mar-09
Oct-09
May-10
Nov-10
Date

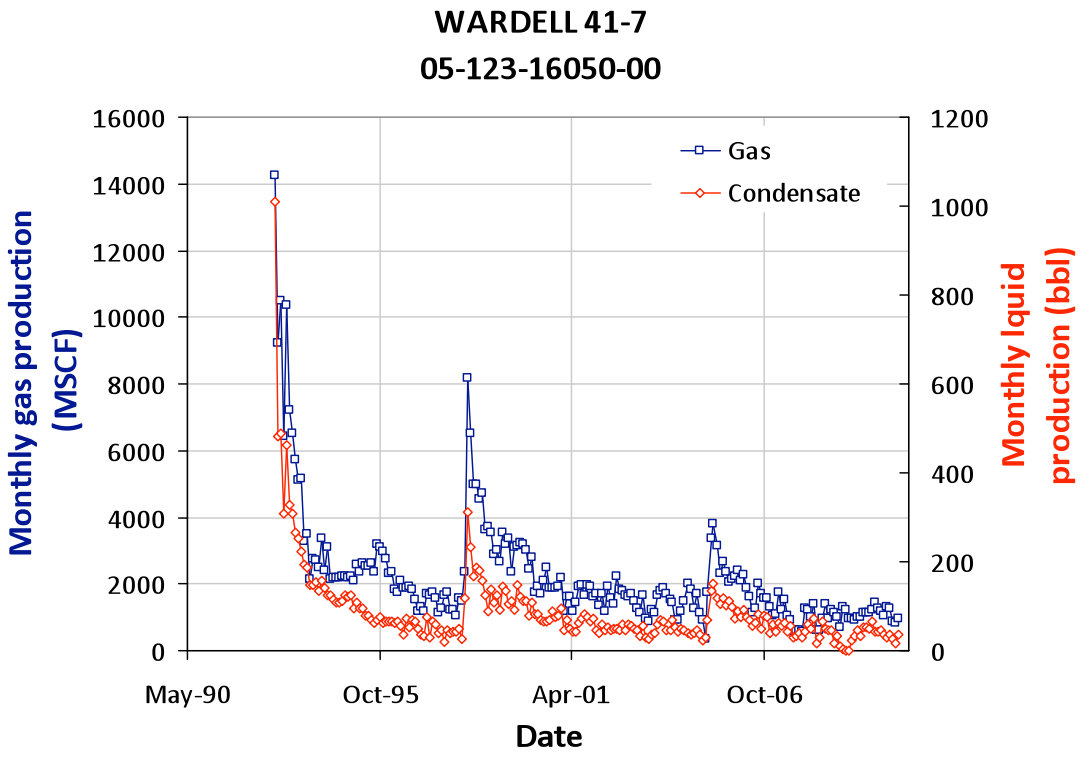
WARDELL 41-7
05-123-16050-00
Monthly gas production (MSCF)
Monthly liquid production (bbl)
Gas
Condensate
16000
14000
12000
10000
8000
6000
4000
2000
0
1200
1000
800
600
400
200
0
May-90
Oct-95
Apr-01
Oct-06
Date

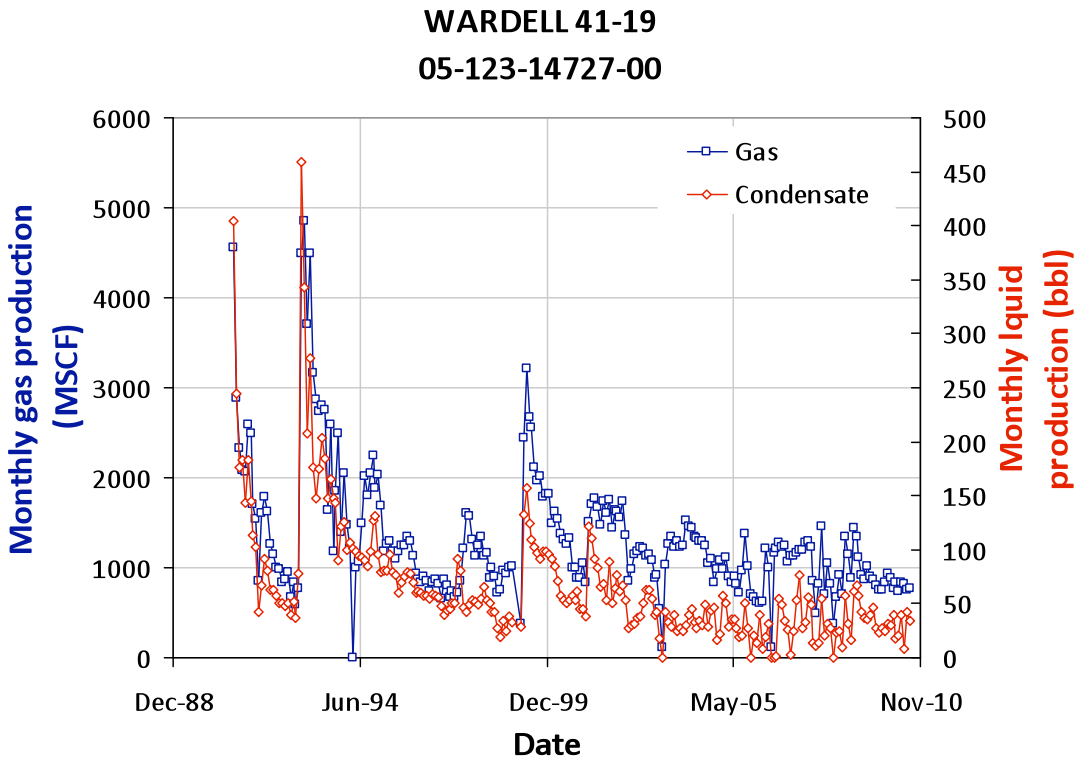
WARDELL 41-19
05-123-14727-00
Monthly gas production (MSCF)
Monthly liquid production (bbl)
Gas
Condensate
6000
5000
4000
3000
2000
1000
0
500
450
400
350
300
250
200
150
100
50
0
Dec-88
Jun-94
Dec-99
May-05
Nov-10
Date

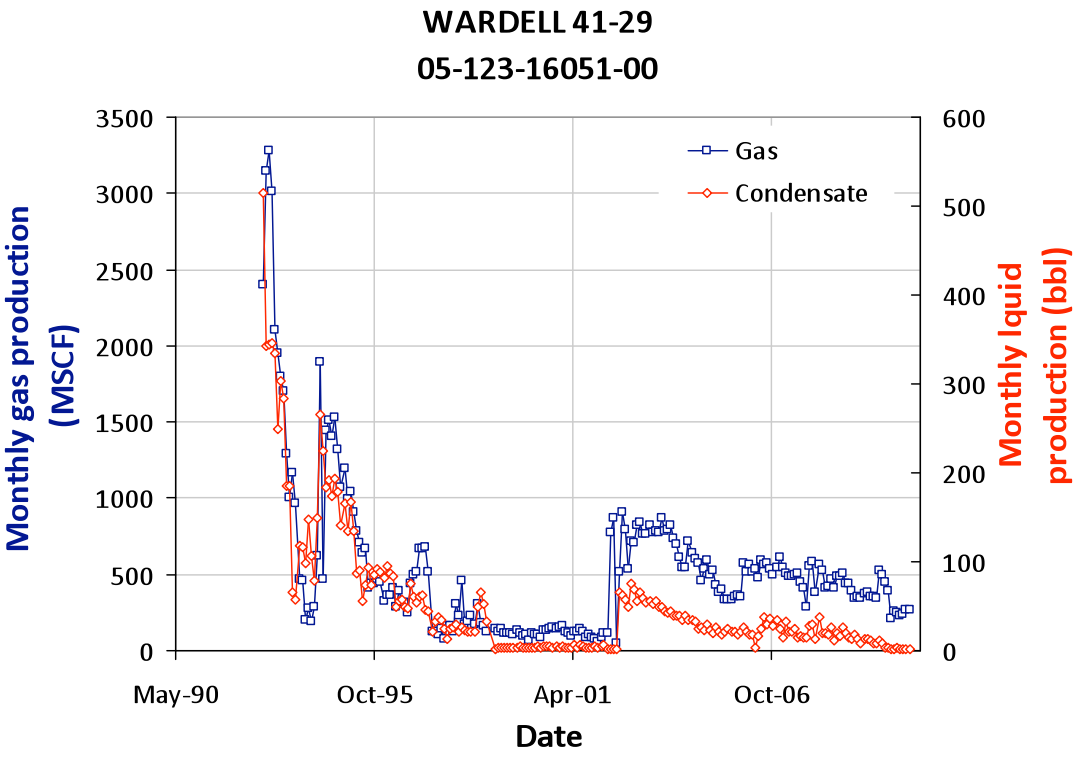
WARDELL 41-29
05-123-16051-00
Monthly gas production (MSCF)
Monthly liquid production (bbl)
Gas
Condensate
3500
3000
2500
2000
1500
1000
500
0
600
500
400
300
200
100
0
May-90
Oct-95
Apr-01
Oct-06
Date

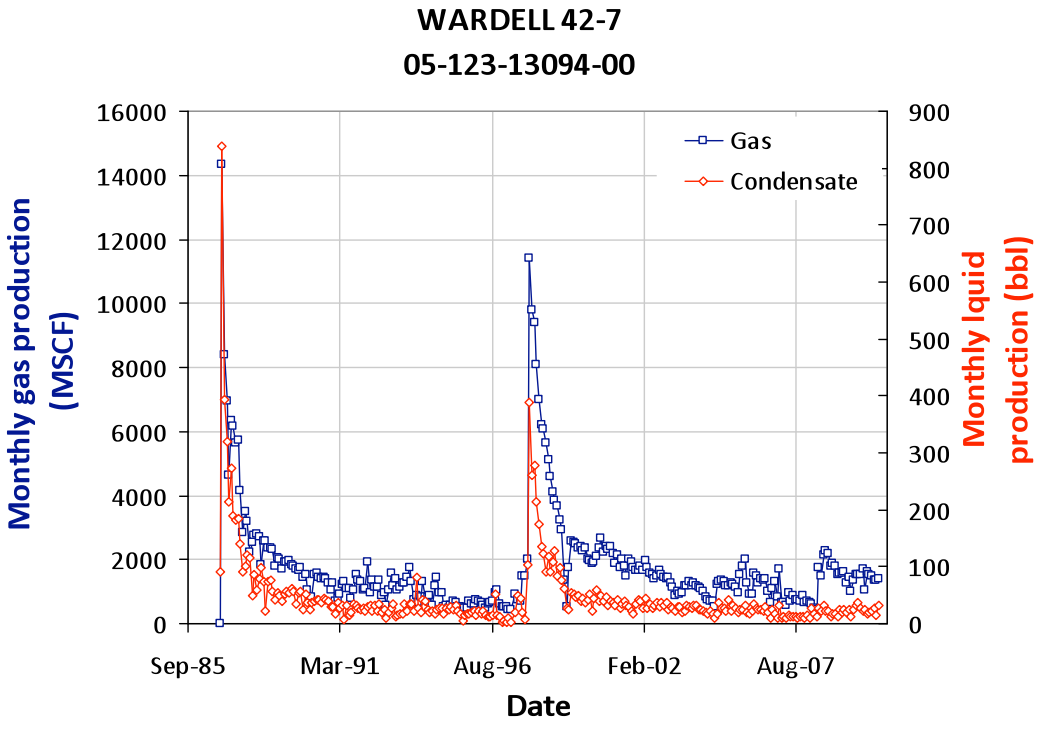
WARDELL 42-7
05-123-13094-00
Monthly gas production (MSCF)
Monthly liquid production (bbl)
Gas
Condensate
16000
14000
12000
10000
8000
6000
4000
2000
0
900
800
700
600
500
400
300
200
100
0
Sep-85
Mar-91
Aug-96
Feb-02
Aug-07
Date

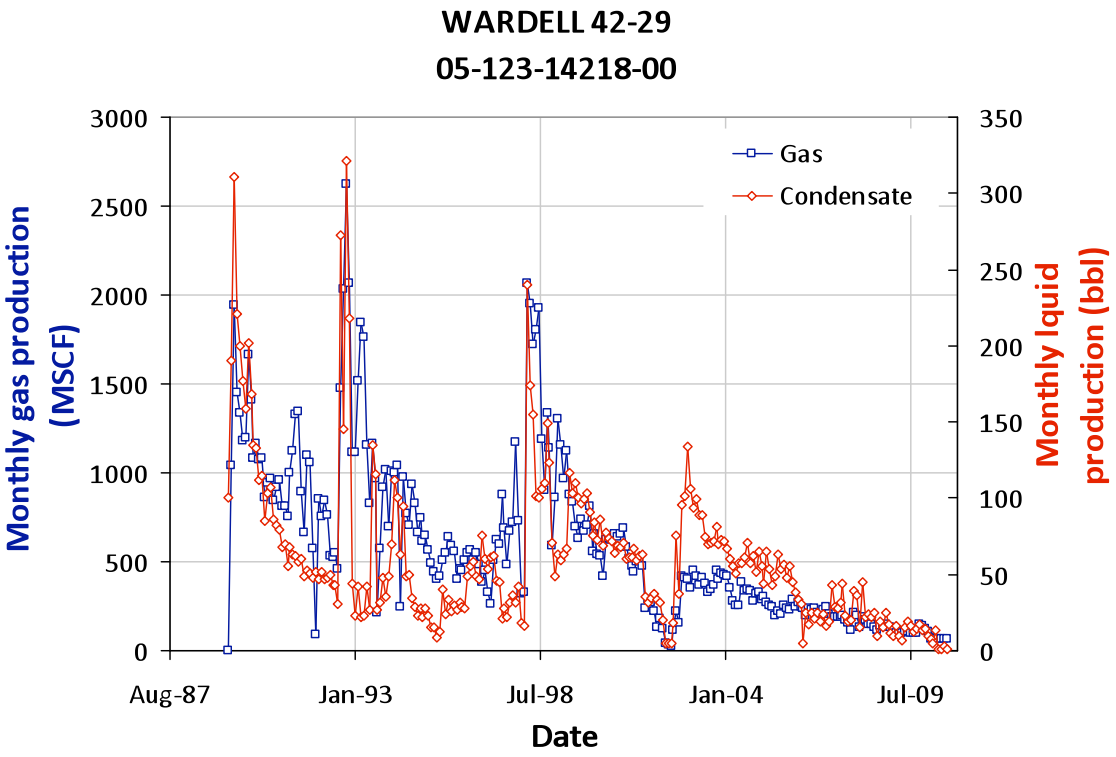
WARDELL 42-29
05-123-14218-00
Monthly gas production (MSCF)
Monthly liquid production (bbl)
Gas
Condensate
3000
2500
2000
1500
1000
500
0
350
300
250
200
150
100
50
0
Aug-87
Jan-93
Jul-98
Jan-04
Jul-09
Date

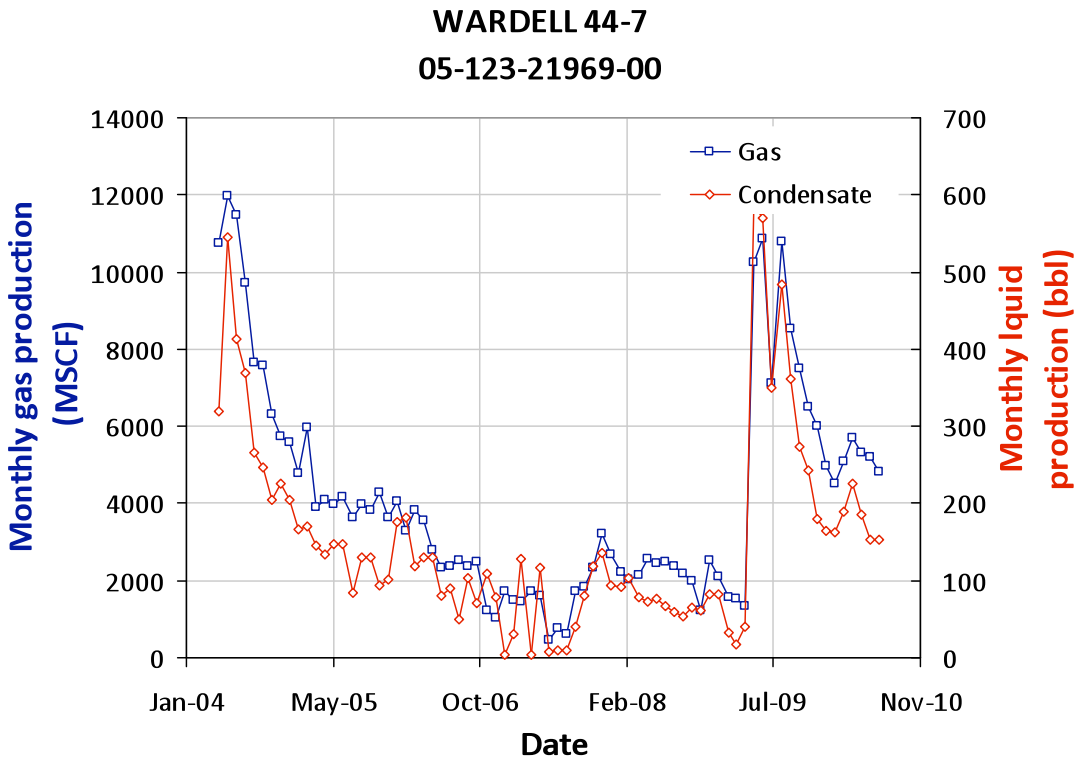
WARDELL 44-7
05-123-21969-00
Monthly gas production (MSCF)
Monthly liquid production (bbl)
Gas
Condensate
14000
12000
10000
8000
6000
4000
2000
0
700
600
500
400
300
200
100
0
Jan-04
May-05
Oct-06
Feb-08
Jul-09
Nov-10
Date

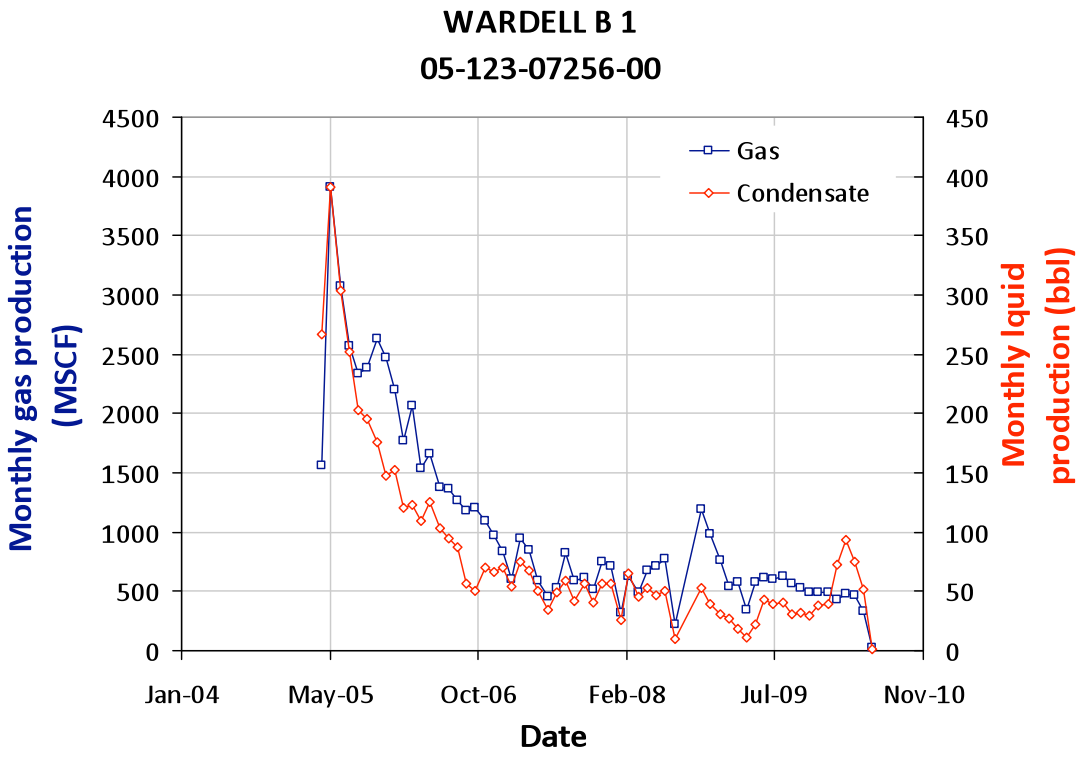
WARDELL B 1
05-123-07256-00
Monthly gas production (MSCF)
Monthly liquid production (bbl)
Gas
Condensate
4500
4000
3500
3000
2500
2000
1500
1000
500
0
450
400
350
300
250
200
150
100
50
0
Jan-04
May-05
Oct-06
Feb-08
Jul-09
Nov-10
Date

C.2. PRODUCTION DATA OF SELECTED REFRACTURED WELLS

Well	Prod. Time IF (months)	Cum. Prod. IF (Mscf)	Cum. Prod. IF (Bbl)	Q_{1month} IF (Mscf)	Q_{1month} IF (Bbl)
BB DRAW H 8-15	72	39163	2118	416	14
UPRC 29-6J	30	8038	700	309	37
MOSER H 28-4	18	4333	392	352	42
WARDELL H 18-1	31	22612	601	572	9
WARDELL H 18-9	34	42007	1664	548	23
MOSER H 28-3	55	21707	1476	538	26
CANNON LAND 28-10J	59	23325	1546	511	38
MEGAN H 16-11	41	46930	1461	670	42
MOSER 28-7	64	23424	2473	564	72
FRANK H 21-10	50	39807	2190	709	48
UPRC 9-11J	38	34983	1099	910	23
MEGAN H 16-13	40	43027	1296	781	49
MEGAN H 16-2	84	70536	1903	818	48
BB DRAW H 8-10	42	29759	1138	1117	34
ARISTOCRAT ANGUS 42-10	57	62856	1945	1136	37
MEGAN H 16-3	29	25344	1035	1114	56
MEGAN H 16-1	72	61157	2654	1103	64
MEGAN H 16-6	52	37301	1420	1151	57
UPRC 17-14J	32	24003	1203	1185	53
MEGAN H 16-9	44	34579	1944	1111	78
MEGAN H 16-15	57	42634	2488	1111	78
ARISTOCRAT 21-10C	29	26561	540	1399	38
FRANK H 21-16	65	47645	3904	1184	130
ARISTOCRAT ANGUS 11-8	41	59516	1229	1791	39
HSR-FRICO 15-10	29	33470	985	1685	61

BEEBE DRAW 41-9	96	74283	621	2554	19
BEEBE DRAW 31-9	140	66894	3854	2124	180
GLOVER 30-8J	77	66917	6114	2003	203
HSR-MULBERG 16-30	72	26008	3063	1645	290
WARDELL 42-29	40	37717	3818	1942	311
HSR-FRICO 8-22	73	32110	5245	2079	290
STATE 2	28	28413	1576	3007	156
FRANK H 21-15	56	57691	4158	2649	217
MOSER H 41-28	131	198016	288	4076	5
HSR-AUGUST 15-29	50	33706	2875	2613	274
HSR-FRICO 16-10	56	76140	3265	3078	197
MD RADKE 22-1	42	20221	1860	2393	312
UPRC 29-4J	109	70796	6479	2456	328
UPRC 29-3J	120	65582	7130	2456	328
HSR-RAFALOVICH 14-5	78	98173	3626	3314	202
WARDELL H 18-8	40	82103	2833	3811	133
HSR-PETERSON 12-29	68	36941	4066	2691	321
UPRC 9-4J	65	163634	4429	4156	128
HSR-DANE 9-10	67	110461	3489	4113	139
STATE 23	58	64498	2395	4371	104
HSR-DODGE 10-22	70	53882	7616	2887	361
GUNNELL R H 20-1	189	134317	7077	3431	328
MEGAN H 16-16	127	179609	11297	4324	183
MOSER H 31-27	117	57642	5429	2696	458
HSR-FRICO 7-22	96	117607	5542	4032	249
HSR-IAN 13-20	80	67929	5973	2640	509
HSR-DOVE 15-22	86	136890	5936	2640	510
HSR-PICKRELL 13-5A	96	166402	5753	4304	307
HSR-OSBORNE 8-19A	90	67457	4975	3743	405

HSR-MULLER 9-29A	87	53176	4952	3091	516
WARDELL 41-29	19	24824	3777	3283	514
REI 33-5	30	71669	2858	5033	247
FRANK 32-21	23	36921	2099	4340	369
HSR-GOODNOW 16-5A	78	115145	4343	4924	285
RITCHEY H 27-3	48	51131	5392	3885	473
MEGAN H 16-8	105	173321	9692	5540	248
CANNON LAND 28-15J	116	120982	10094	3891	527
FRANK 42-21	92	79197	4267	5255	353
BEEBE DRAW 32-9	22	46661	2318	5506	336
WARDELL 41-19	76	109943	6791	4858	459
MOSER 42-27	109	58989	8139	2942	784
FRANK 22-21	71	50415	5015	5040	508
BEEBE DRAW UPRR 32-17	114	274065	11920	5621	414
FRANK 31-21	145	127340	6258	5895	409
BEEBE DRAW UPRR 41-17	70	130558	5305	6656	296
FRICO 14-15	68	93089	3660	5520	505
HSR-HOUSE 6-20	98	124536	7568	5464	524
UPRR 22 PAN AM 1	161	147058	781	8362	49
BEEBE DRAW UPRR 42-17	105	174304	5721	6919	296
HSR-PARAS 9-30	60	67894	7959	4296	757
HSR-REA 12-20	100	86710	6001	5202	607
SARCHET 16-22	61	73516	7422	4965	661
MULVERY 22-1	161	208542	15765	5502	572
HSR-EGGLER 14-29	114	132044	5779	5727	547
HSR FRICO 12-15	46	72778	3260	6325	515
WARDELL 18-29	53	68168	5647	5124	722

FRANK H 21-12	115	127632	11733	5638	673
FRANK H 21-13	115	129862	11907	5638	673
FRANK H 21-11	120	131833	11984	5638	673
FRANK 22-33	62	69371	6405	5432	710
HSR-REAM 15-5	190	224212	7193	6101	617
FRICO 23-15	22	54550	3863	6873	499
HSR-PANTALEO 10-29A	82	89186	8355	5320	758
FRICO 10-15	46	80237	4735	6094	635
MOSER H 1-27	56	65960	6802	5666	732
HSR-NEMIROW 5-20	110	96142	6037	6384	613
MOORE H 28-12	70	86679	4693	5619	744
MOSER H 28-5	94	118334	11050	5183	819
FRANK 41-21	96	109896	7243	7142	493
RITCHEY H 27-5	38	68427	6594	5959	695
RITCHEY H 27-4	37	66210	6293	5959	734
UPRC 17-5J5	62	129154	5008	7713	451
HSR-ROSENTHALER 4-20	62	129154	5008	7713	451
UPRC 17-6J5	62	129400	5031	7714	451
ARISTOCRAT ANGUS 14-3A	65	166686	7873	7239	549
WARDELL 6-20	42	79588	4054	6368	723
GUNNELL R H 20-2	148	175072	7925	7386	576
HSR-HAGAN 16-6A	111	197789	10189	8074	467
MD 20-1	92	142658	10587	5887	842
MD 20-2	92	142666	10866	5887	842
UPRC 19-9J	81	95931	5627	7516	590
MEGAN H 16-4J	70	184597	10134	8275	535
WARDELL 32-29	19	45668	4474	6265	895

MOSER 11-28	43	79407	6236	7448	712
HSR-DEMEULES 9-22	133	138905	14315	6283	914
FRICO 16-15	46	93877	5814	7332	755
MOSER 28-8	133	164383	18129	4668	1202
ARISTOCRAT ANGUS 2-5-4	67	135411	3891	9974	355
FRANK 43-21	119	161524	8012	7320	872
WARDELL 20-6	25	89343	2796	9869	479
VICTOR E GOODHARD 22-1	105	104526	9245	7323	940
HSR-MOSER 16-27	55	60544	6222	6419	1139
HSR-MOSER 10-27	56	89966	9014	7918	896
ARISTOCRAT ANGUS 5-2-10	60	168664	7306	9507	640
HSR-FRICO 1-22	96	111949	15719	7912	982
BEEBE DRAW UPRR 31-17	147	201942	8716	9260	795
HSR-EGGLER 11-29	49	64372	5855	7995	1029
ARISTOCRAT ANGUS 1-8	67	286923	7422	10850	564
MEGAN H 16-2J	36	87787	5608	10377	652
WARDELL 20-41	95	180514	13780	8346	1104
HSR FRICO 13-15	56	130334	3314	9394	967
WARDELL 44-7	60	201239	7143	11978	545
WARD 30-1J	128	126056	9124	9322	1028
ROBERT C NICE 22-1	124	112669	7450	10068	992
ARISTOCRAT ANGUS 12-8	67	283163	7585	12372	611
ARISTOCRAT ANGUS 2-4C	66	147571	4790	12465	624
UPRC H 17-9J	130	151134	6003	10539	988
UPRC H 17-16J	130	165932	6470	10539	998
HSR-AUGUST 16-29	113	362378	13504	10262	1052
WARDELL 20-44	93	223381	15311	10026	1236
MEGAN H 16-5	173	365416	18619	11250	1050
HSR HOUSE 3-20	50	129168	5910	13137	779

UPRC 17-15J	117	217238	11398	11420	1161
FEDERAL 12-10	36	144737	2020	17999	164
UPRC 17-13J5	77	177197	8858	14501	777
WARDELL UPRR 42-7	130	211053	6856	14333	838
UPRC 17-12J5	67	63434	5624	11329	1356
UPRC 9-12J5	82	223294	9526	15257	710
UPRC 9-3J	156	337336	12260	12917	1131
WARDELL 41-7	66	191720	8268	14242	1010
UPRC 17-10J	118	218208	11437	13494	1161
ARISTOCRAT ANGUS 1-6-4	67	207564	7328	15650	832
UPRC 21-3J	118	198625	12026	14045	1219
UPRC 21-6J	111	212340	12760	14045	1219
UPRC 21-4J	122	269589	14137	15888	1205
UPRC 21-5J	122	269380	14111	15888	1205
BB DRAW H 8-9	125	429683	25373	18072	1376
UPRC 17-3J	122	283726	11959	21312	1294
UPRC 17-4J	129	296797	12445	21313	1295
MEGAN H 16-12	120	486817	30658	21276	2209
UPRC 9-14J5	102	284904	13905	27834	1130
UPRC 17-11J	122	503577	22897	29568	2034

Well	F_{Co} $Q_{1theory}$ = 36190 Mscf	Q_{1month} RF (Mscf)	Q_{1month} RF (Bbl)	RF_{Co} $Q_{1theory}$ = 36190 Mscf
BB DRAW H 8-15	0.013815971	5962	285	0.211992263
UPRC 29-6J	0.014672561	2354	465	0.142138712
MOSER H 28-4	0.016689693	1866	194	0.083724786
WARDELL H 18-1	0.017297596	5019	234	0.177479967
WARDELL H 18-9	0.018955513	10948	578	0.398342083
MOSER H 28-3	0.019176568	1336	79	0.050013816
CANNON LAND 28-10J	0.020420006	4638	524	0.215031777
MEGAN H 16-11	0.025476651	8011	720	0.340729483
MOSER 28-7	0.027521415	4463	321	0.176540481
FRANK H 21-10	0.027549047	2511	130	0.090936723
UPRC 9-11J	0.028958276	9467	348	0.319287096
MEGAN H 16-13	0.029704338	4957	223	0.173943078
MEGAN H 16-2	0.030560928	3714	245	0.14324399
BB DRAW H 8-10	0.036501796	6600	223	0.21934236
ARISTOCRAT ANGUS 42-10	0.037524178	6737	229	0.224122686
MEGAN H 16-3	0.040066317	11488	645	0.424371373
MEGAN H 16-1	0.041088699	10239	469	0.360679746
MEGAN H 16-6	0.04125449	9671	375	0.329400387
UPRC 17-14J	0.04153081	4927	128	0.157363913
MEGAN H 16-9	0.043630837	11018	455	0.379883946
MEGAN H 16-15	0.043630837	6924	428	0.262282398
ARISTOCRAT 21-10C	0.04495717	12797	439	0.426388505
FRANK H 21-16	0.054269135	6902	593	0.289030119
ARISTOCRAT ANGUS 11-8	0.055954684	8066	266	0.266979829
HSR-FRICO 15-10	0.056673114	3442	233	0.133738602
BEEBE DRAW 41-9	0.073722023	4910	125	0.156396795
BEEBE DRAW 31-9	0.088532744	4103	209	0.148024316

GLOVER 30-8J	0.089002487	3160	187	0.118319978
HSR-MULBERG 16-30	0.093534125	11413	401	0.381845814
WARDELL 42-29	0.105222437	2622	273	0.117712075
HSR-FRICO 8-22	0.105526389	4023	400	0.177479967
STATE 2	0.108952749	5800	216	0.196076264
FRANK H 21-15	0.109173805	2501	181	0.099115778
MOSER H 41-28	0.113456756	2660	293	0.122077922
HSR-AUGUST 15-29	0.117629179	3561	312	0.150124344
HSR-FRICO 16-10	0.117712075	6055	278	0.213401492
MD RADKE 22-1	0.117850235	3196	288	0.136059685
UPRC 29-4J	0.122243714	2497	253	0.110942249
UPRC 29-3J	0.122243714	2708	225	0.112130423
HSR-RAFALOVICH 14-5	0.125062172	7766	321	0.267808787
WARDELL H 18-8	0.127355623	16908	561	0.560210003
HSR-PETERSON 12-29	0.127576679	914	79	0.038353136
UPRC 9-4J	0.136059685	6655	152	0.209090909
HSR-DANE 9-10	0.13669522	2430	240	0.106935618
STATE 23	0.138021553	4159	222	0.151726996
HSR-DODGE 10-22	0.139624206	2123	222	0.095468361
GUNNELL R H 20-1	0.149184858	3651	195	0.133213595
MEGAN H 16-16	0.149820392	2639	111	0.09132357
MOSER H 31-27	0.150428295	1858	200	0.08449848
HSR-FRICO 7-22	0.152694114	1945	91	0.068831169
HSR-IAN 13-20	0.157336281	5568	458	0.229787234
HSR-DOVE 15-22	0.157502072	2044	200	0.089638022
HSR-PICKRELL 13-5A	0.169825919	3685	136	0.124371373
HSR-OSBORNE 8-19A	0.170571981	1877	185	0.082536612
HSR-MULLER 9-29A	0.170958828	5644	362	0.215971263
WARDELL 41-29	0.175932578	1897	265	0.096352584

REI 33-5	0.180022106	10733	415	0.365377176
FRANK 32-21	0.181099751	4708	194	0.162254767
HSR-GOODNOW 16-5A	0.183310307	3696	223	0.139099199
RITCHEY H 27-3	0.18576955	2211	354	0.119784471
MEGAN H 16-8	0.194197292	10335	183	0.315915999
CANNON LAND 28-15J	0.194888091	4833	510	0.218098922
FRANK 42-21	0.203730312	1490	39	0.047637469
BEEBE DRAW 32-9	0.207847472	6662	332	0.239126831
WARDELL 41-19	0.210334347	3220	157	0.115004145
MOSER 42-27	0.211273833	980	127	0.048134844
FRANK 22-21	0.223487151	2371	139	0.088560376
BEEBE DRAW UPRR 32-17	0.223956894	5458	216	0.18662614
FRANK 31-21	0.230699088	3543	139	0.120945012
BEEBE DRAW UPRR 41-17	0.232992539	3942	147	0.133296491
FRICO 14-15	0.236253109	5506	821	0.288256424
HSR-HOUSE 6-20	0.237855761	3747	204	0.137358386
UPRR 22 PAN AM 1	0.239182095	2288	13	0.065377176
BEEBE DRAW UPRR 42-17	0.24025974	1572	213	0.078751036
HSR-PARAS 9-30	0.244211108	3715	425	0.17311412
HSR-REA 12-20	0.2443769	3171	209	0.122271346
SARCHET 16-22	0.246780879	2396	390	0.13086488
MULVERY 22-1	0.246863775	2992	157	0.108704062
HSR-EGGLER 14-29	0.24893617	2804	189	0.10881459
HSR FRICO 12-15	0.260154739	4238	365	0.177618127
WARDELL 18-29	0.261287649	3394	577	0.189444598
FRANK H 21-12	0.267366676	2168	130	0.081458967
FRANK H 21-13	0.267366676	6902	593	0.289030119

FRANK H 21-11	0.267366676	9821	633	0.376319425
FRANK 22-33	0.267808787	2882	255	0.12191213
HSR-REAM 15-5	0.270875933	5600	0	0.154738878
FRICO 23-15	0.272644377	8031	579	0.317905499
HSR-PANTALEO 10-29A	0.272672009	3239	307	0.1403979
FRICO 10-15	0.273666759	9099	594	0.349903288
MOSER H 1-27	0.277922078	2860	266	0.123127936
HSR-NEMIROW 5-20	0.278032606	2865	171	0.107515888
MOORE H 28-12	0.278612876	2065	307	0.107957999
MOSER H 28-5	0.278999724	1853	235	0.090163028
FRANK 41-21	0.27908262	3751	284	0.150732246
RITCHEY H 27-5	0.279883946	2819	279	0.124150318
RITCHEY H 27-4	0.28634982	2209	279	0.107294833
UPRC 17-5J5	0.287897209	14206	596	0.491351202
HSR-ROSENTHALER 4-20	0.287897209	14206	596	0.491351202
UPRC 17-6J5	0.287924841	5896	238	0.202376347
ARISTOCRAT ANGUS 14-3A	0.291047251	8384	339	0.287869577
WARDELL 6-20	0.295827577	7423	551	0.296463111
GUNNELL R H 20-2	0.299585521	8358	492	0.31251727
HSR-HAGAN 16-6A	0.300525007	3295	79	0.104144791
MD 20-1	0.302265819	5537	338	0.209035645
MD 20-2	0.302265819	5536	337	0.208842222
UPRC 19-9J	0.305498757	2530	196	0.102403979
MEGAN H 16-4J	0.31735286	4729	250	0.17211937
WARDELL 32-29	0.321497651	3954	263	0.152859906
MOSER 11-28	0.323846366	2859	427	0.14979276
HSR-DEMEULES 9-22	0.325145068	3025	387	0.147747997
FRICO 16-15	0.327770102	3742	451	0.178170765

MOSER 28-8	0.328267477	2835	235	0.117297596
ARISTOCRAT ANGUS 2-5-4	0.334457032	6397	344	0.233793866
FRANK 43-21	0.346836143	1884	239	0.091682785
WARDELL 20-6	0.352113844	8507	332	0.290107765
VICTOR E GOODHARD 22-1	0.358192871	3298	396	0.156783642
HSR-MOSER 16-27	0.366206134	1865	273	0.096794695
HSR-MOSER 10-27	0.367339044	3839	290	0.154158607
ARISTOCRAT ANGUS 5-2-10	0.368803537	6475	333	0.234125449
HSR-FRICO 1-22	0.381431335	5661	490	0.237662338
BEEBE DRAW UPRR 31-17	0.387676154	4527	198	0.157916552
HSR-EGGLER 11-29	0.391516994	4555	373	0.187703786
ARISTOCRAT ANGUS 1-8	0.39331307	5844	250	0.202928986
MEGAN H 16-2J	0.394832827	5731	253	0.200303951
WARDELL 20-41	0.41365018	4687	278	0.175600995
HSR FRICO 13-15	0.419894999	11011	1082	0.48364189
WARDELL 44-7	0.42133186	10254	588	0.380823432
WARD 30-1J	0.42801879	5317	292	0.195330202
ROBERT C NICE 22-1	0.442663719	4552	370	0.187123515
ARISTOCRAT ANGUS 12-8	0.443161094	5276	229	0.183752418
ARISTOCRAT ANGUS 2-4C	0.447886156	9020	471	0.327327991
UPRC H 17-9J	0.455015198	3932	167	0.136336004
UPRC H 17-16J	0.456673114	7865	335	0.272865432
HSR-AUGUST 16-29	0.457971815	1870	110	0.069908815
WARDELL 20-44	0.481956342	3138	362	0.146725615
MEGAN H 16-5	0.484940591	5987	235	0.204393479
HSR HOUSE 3-20	0.492152528	7546	430	0.27980105
UPRC 17-15J	0.508040895	4381	163	0.14807958
FEDERAL 12-10	0.524537165	6884	71	0.2019895
UPRC 17-13J5	0.529510915	17383	793	0.611798839

WARDELL UPRR 42-7	0.534982039	11396	389	0.379386571
UPRC 17-12J5	0.537855761	14006	639	0.492953855
UPRC 9-12J5	0.539292622	13045	738	0.482812932
UPRC 9-3J	0.544432164	3662	178	0.130699088
WARDELL 41-7	0.560983697	8190	311	0.277866814
UPRC 17-10J	0.565349544	4527	168	0.152942802
ARISTOCRAT ANGUS 1-6-4	0.570378558	8824	522	0.330367505
UPRC 21-3J	0.59019066	10945	434	0.374385189
UPRC 21-6J	0.59019066	10590	528	0.380160265
UPRC 21-4J	0.638795247	4259	148	0.142221608
UPRC 21-5J	0.638795247	4118	127	0.13484388
BB DRAW H 8-9	0.727493783	12823	564	0.447830893
UPRC 17-3J	0.803426361	7481	235	0.245675601
UPRC 17-4J	0.803619784	5893	170	0.191019619
MEGAN H 16-12	0.954130975	21174	1146	0.775075988
UPRC 9-14J5	0.956452059	17649	730	0.608704062
UPRC 17-11J	1.154241503	5960	184	0.195192042

Well	ΔEUR (BBLe)	R_{dep}	D_{iD}
BB DRAW H 8-15	31843.43	0.11033	0.00237
UPRC 29-6J	14235.37	0.03449	0.14730
MOSER H 28-4	25366.77	0.07050	0.04370
WARDELL H 18-1	32344.99	0.04785	0.06169
WARDELL H 18-9	23334.41	0.02620	0.04563
MOSER H 28-3	4472.70	0.07405	0.16138
CANNON LAND 28-10J	17854.43	0.04013	0.02638
MEGAN H 16-11	23570.35	0.07255	0.02911
MOSER 28-7	14591.93	0.06403	0.10412
FRANK H 21-10	12302.30	0.08109	0.13870
UPRC 9-11J	19150.85	0.14377	0.00233
MEGAN H 16-13	28714.16	0.11119	0.00227
MEGAN H 16-2	17568.45	0.06536	0.08638
BB DRAW H 8-10	11137.44	0.05133	0.07987
ARISTOCRAT ANGUS 42-10	22033.83	0.00870	0.01975
MEGAN H 16-3	22066.47	0.06340	0.03346
MEGAN H 16-1	24562.76	0.04312	0.05156
MEGAN H 16-6	38271.92	0.06257	0.04489
UPRC 17-14J	23453.33	0.11914	0.06792
MEGAN H 16-9	23157.28	0.04890	0.07055
MEGAN H 16-15	19696.44	0.07684	0.07076
ARISTOCRAT 21-10C	33004.85	0.03412	0.06626
FRANK H 21-16	16727.24	0.05888	0.05190
ARISTOCRAT ANGUS 11-8	27913.91	0.09481	0.06943
HSR-FRICO 15-10	19921.40	0.08267	0.06968
BEEBE DRAW 41-9	10835.84	0.14497	0.16540
BEEBE DRAW 31-9	11230.55	0.04394	0.23272

GLOVER 30-8J	14346.28	0.01534	0.09118
HSR-MULBERG 16-30	27522.67	0.01067	0.06881
WARDELL 42-29	9107.33	0.03143	0.11652
HSR-FRICO 8-22	18994.75	0.05934	0.20773
STATE 2	13196.57	0.16302	0.19015
FRANK H 21-15	18270.06	0.05067	0.11509
MOSER H 41-28	18333.12	0.00493	0.12416
HSR-AUGUST 15-29	16715.13	0.04559	0.22903
HSR-FRICO 16-10	11132.36	0.06930	0.11972
MD RADKE 22-1	17595.15	0.02329	0.32197
UPRC 29-4J	8142.89	0.02840	0.20359
UPRC 29-3J	11926.06	0.03494	0.20359
HSR-RAFALOVICH 14-5	20769.85	0.02359	0.11327
WARDELL H 18-8	31385.96	0.04879	0.01549
HSR-PETERSON 12-29	11115.12	0.02720	0.26829
UPRC 9-4J	17048.44	0.05068	0.01883
HSR-DANE 9-10	5104.74	0.08973	0.15104
STATE 23	14669.49	0.08601	0.45302
HSR-DODGE 10-22	16794.45	0.04048	0.13002
GUNNELL R H 20-1	22746.08	0.06200	0.16021
MEGAN H 16-16	10891.37	0.04201	0.37295
MOSER H 31-27	11197.80	0.01195	0.18128
HSR-FRICO 7-22	2833.85	0.07291	0.11146
HSR-IAN 13-20	29096.62	0.02527	0.07057
HSR-DOVE 15-22	9695.25	0.02303	0.11720
HSR-PICKRELL 13-5A	21032.73	0.05361	0.11165
HSR-OSBORNE 8-19A	14827.75	0.02661	0.24132
HSR-MULLER 9-29A	16582.81	0.07386	0.22691
WARDELL 41-29	8318.59	0.01993	0.23402

REI 33-5	17761.81	0.20770	0.10867
FRANK 32-21	14819.06	0.01714	0.15812
HSR-GOODNOW 16-5A	16465.83	0.01934	0.18009
RITCHEY H 27-3	6327.39	0.03931	0.21880
MEGAN H 16-8	31632.00	0.02374	0.18435
CANNON LAND 28-15J	17333.68	0.01302	0.20462
FRANK 42-21	10055.64	0.03188	0.26204
BEEBE DRAW 32-9	18717.32	0.01736	0.23042
WARDELL 41-19	13081.84	0.02511	0.21082
MOSER 42-27	9972.13	0.00832	0.10181
FRANK 22-21	8963.98	0.05683	0.36266
BEEBE DRAW UPRR 32-17	15089.43	0.02554	0.14773
FRANK 31-21	18201.14	0.04981	0.27931
BEEBE DRAW UPRR 41-17	11532.32	0.06472	0.27256
FRICO 14-15	9535.39	0.42193	0.10946
HSR-HOUSE 6-20	14416.66	0.03516	0.24046
UPRR 22 PAN AM 1	5900.07	0.03802	0.33592
BEEBE DRAW UPRR 42-17	5504.78	0.10682	0.24663
HSR-PARAS 9-30	29528.90	0.01237	0.12286
HSR-REA 12-20	9824.18	0.04438	0.23907
SARCHET 16-22	4756.58	0.10521	0.20735
MULVERY 22-1	23084.83	0.03383	0.17635
HSR-EGGLER 14-29	12805.60	0.02706	0.23815
HSR FRICO 12-15	10050.13	0.08073	0.22049
WARDELL 18-29	7197.55	0.08328	0.25200
FRANK H 21-12	9922.13	0.06198	0.12742
FRANK H 21-13	20891.39	0.02225	0.12755

FRANK H 21-11	23592.59	0.01946	0.12755
FRANK 22-33	8261.50	0.04563	0.15827
HSR-REAM 15-5	13393.27	0.06538	0.18397
FRICO 23-15	15341.10	0.19599	0.19873
HSR-PANTALEO 10-29A	8327.20	0.04535	0.21722
FRICO 10-15	20686.38	0.33516	0.11571
MOSER H 1-27	15123.66	0.02195	0.23023
HSR-NEMIROW 5-20	11267.78	0.03671	0.29469
MOORE H 28-12	6978.92	0.03329	0.21338
MOSER H 28-5	4454.19	0.04528	0.14759
FRANK 41-21	12342.68	0.03993	0.16909
RITCHEY H 27-5	6638.95	0.04356	0.21337
RITCHEY H 27-4	6362.08	0.05846	0.21361
UPRC 17-5J5	28500.13	0.05216	0.12852
HSR-ROSENTHALER 4-20	27956.57	0.02282	0.12852
UPRC 17-6J5	11901.02	0.08624	0.26737
ARISTOCRAT ANGUS 14-3A	12340.28	0.07391	0.20422
WARDELL 6-20	14945.44	0.04784	0.26879
GUNNELL R H 20-2	26374.51	0.03292	0.25204
HSR-HAGAN 16-6A	11481.62	0.05582	0.09316
MD 20-1	16703.93	0.02227	0.15873
MD 20-2	21042.31	0.01106	0.15874
UPRC 19-9J	16227.29	0.02404	0.33907
MEGAN H 16-4J	4719.17	0.10817	0.23073
WARDELL 32-29	15305.02	0.01819	0.31917
MOSER 11-28	6077.61	0.06396	0.27466
HSR-DEMEULES 9-22	10078.23	0.04187	0.15882
FRICO 16-15	9626.78	0.17406	0.18168

MOSER 28-8	13202.06	0.02640	0.06151
ARISTOCRAT ANGUS 2-5-4	8060.42	0.23603	0.27394
FRANK 43-21	5501.23	0.05307	0.21726
WARDELL 20-6	22624.81	0.20683	0.22706
VICTOR E GOODHARD 22-1	24301.76	0.02932	0.20306
HSR-MOSER 16-27	12252.23	0.01625	0.22431
HSR-MOSER 10-27	17788.21	0.02858	0.31903
ARISTOCRAT ANGUS 5-2-10	13587.83	0.08052	0.11691
HSR-FRICO 1-22	30403.83	0.01861	0.26443
BEEBE DRAW UPRR 31-17	14304.23	0.04350	0.23106
HSR-EGGLER 11-29	21283.25	0.02797	0.34125
ARISTOCRAT ANGUS 1-8	15461.04	0.29670	0.09201
MEGAN H 16-2J	7589.64	0.17256	0.43017
WARDELL 20-41	11507.12	0.05452	0.27506
HSR FRICO 13-15	12586.17	0.18537	0.25292
WARDELL 44-7	21967.59	0.07779	0.13884
WARD 30-1J	18678.22	0.02605	0.27183
ROBERT C NICE 22-1	16524.04	0.07156	0.32704
ARISTOCRAT ANGUS 12-8	12838.32	0.28516	0.12163
ARISTOCRAT ANGUS 2-4C	9452.95	0.23967	0.26061
UPRC H 17-9J	16350.78	0.07796	0.29726
UPRC H 17-16J	26490.71	0.05266	0.29726
HSR-AUGUST 16-29	7683.26	0.03631	0.27911
WARDELL 20-44	14039.37	0.02346	0.19528
MEGAN H 16-5	19082.67	0.17553	0.21950
HSR HOUSE 3-20	22552.35	0.02123	0.30045
UPRC 17-15J	12762.67	0.05176	0.24542
FEDERAL 12-10	30842.02	0.00518	0.33740
UPRC 17-13J5	25778.71	0.13597	0.19365

WARDELL UPRR 42-7	30628.55	0.01389	0.21869
UPRC 17-12J5	27068.94	0.12905	0.24808
UPRC 9-12J5	28629.84	0.05646	0.27416
UPRC 9-3J	11002.19	0.10148	0.17063
WARDELL 41-7	21602.95	0.04200	0.21220
UPRC 17-10J	20001.89	0.09786	0.24538
ARISTOCRAT ANGUS 1-6-4	12695.04	0.22649	0.21586
UPRC 21-3J	25339.44	0.07685	0.28586
UPRC 21-6J	22945.87	0.08204	0.28586
UPRC 21-4J	15667.63	0.06265	0.27992
UPRC 21-5J	15477.92	0.06536	0.28006
BB DRAW H 8-9	26459.86	0.03824	0.14715
UPRC 17-3J	16864.32	0.08619	0.33819
UPRC 17-4J	15574.19	0.06641	0.33819
MEGAN H 16-12	29764.18	0.04312	0.14123
UPRC 9-14J5	32410.78	0.04171	0.30696
UPRC 17-11J	14334.99	0.33559	0.40235

C.3. COMPLETION DATA OF SELECTED REFRACTURED WELLS

Well	Weight 20/40 IF (Mlbs)	Volume Water IF (MGal)	Weight 20/40 RF (Mlbs)	Volume Water RF (MGal)
BB DRAW H 8-15	300	103.32	246.04	133.207
UPRC 29-6J			261.06	120.666
MOSER H 28-4	250	82.273	200	131.628
WARDELL H 18-1	201	67	245.82	134.442
WARDELL H 18-9	200	69.375	246.38	131.595
MOSER H 28-3	250	80	246.28	134.032
CANNON LAND 28-10J			190.2	49.009
MEGAN H 16-11	200	70.014	246.04	131.041
MOSER 28-7	225	79.417	245.62	132.132
FRANK H 21-10	200	69.82	245.12	124.218
UPRC 9-11J			250.5	85.306
MEGAN H 16-13	210	71	245.84	130.934
MEGAN H 16-2	200	72.97	246.72	129.192
BB DRAW H 8-10	300	104.496	245.86	130.704
MEGAN H 16-3	200	70.41	245.94	131.998
MEGAN H 16-1	200	71.1	247.04	129.46
MEGAN H 16-6	200	70.4	245.88	130.49
UPRC 17-14J	169	71.4	246.98	130.451
MEGAN H 16-9	200	70.583	246.02	131.856
MEGAN H 16-15			180.74	66.54
FRANK H 21-16	200	70.04	246.02	131.701
HSR-FRICO 15-10			260.64	124.202
BEEBE DRAW 41-9			264.56	121.241
BEEBE DRAW 31-9			260.26	129.78
GLOVER 30-8J	190	64	245.9	129.402

HSR-MULBERG 16-30			261.66	129.444
WARDELL 42-29			260	135.03
HSR-FRICO 8-22			261.28	123.388
STATE 2			272.9	131.796
FRANK H 21-15	131	58	246.3	135.24
HSR-AUGUST 15-29			261.06	119.7
HSR-FRICO 16-10			262.02	122.976
UPRC 29-4J			261.903	119.668
UPRC 29-3J			263	119.784
HSR-RAFALOVICH 14-5			262.08	117.39
UPRC 9-4J	250.5	80.36	245.66	135.366
HSR-DANE 9-10			253.8	118.578
STATE 23	272	129.19	245.5	135.7184
HSR-DODGE 10-22			263.48	127.134
GUNNELL R H 20-1	97		215	126.924
MEGAN H 16-16	204	71	246.18	132.867
MOSER H 31-27			260.4	124.992
HSR-FRICO 7-22			261.34	121.769
HSR-IAN 13-20			263.2	118.027
HSR-DOVE 15-22			261	124.731
HSR-PICKRELL 13-5A			210	108.89
HSR-OSBORNE 8-19A			261.08	117.756
HSR-MULLER 9-29A			261.04	119.742
WARDELL 41-29			261.04	118.566
HSR-GOODNOW 16-5A			261.08	125.202
CANNON LAND 28-15J	198	50.781	249.72	133.404
FRANK 42-21			262.76	123.45
WARDELL 41-19			249.22	122.294
MOSER 42-27			260	123.06

BEEBE DRAW UPRR 32-17			260.9	133.14
FRANK 31-21			260.1	136.584
BEEBE DRAW UPRR 41-17			260.4	137.56
HSR-HOUSE 6-20			230	113.914
UPRR 22 PAN AM 1			261.3	120.391
BEEBE DRAW UPRR 42-17			261.62	118.776
HSR-PARAS 9-30			260	136.122
HSR-REA 12-20			172.57	110.478
SARCHET 16-22			203.92	248.675
HSR-EGGLER 14-29			263.28	112.098
HSR FRICO 12-15			116.84	172.554
WARDELL 18-29			250.1	176.939
FRANK H 21-13	143.5	68.6	222.3	127.386
FRANK H 21-11	200	70.768	245.66	134.786
HSR-PANTALEO 10-29A			260.84	121.628
FRICO 10-15			250.54	169.987
MOSER H 1-27			261.52	121.481
HSR-NEMIROW 5-20			261.08	120.561
MOORE H 28-12			261.6	119.742
MOSER H 28-5	190	64	246.86	131.208
FRANK 41-21			262.68	121.548
UPRC 17-5J5	416	93	249.9	136.71
HSR-ROSENTHALER 4-20			261.18	119.813
UPRC 17-6J5	420	101.178	245.78	134.526
WARDELL 6-20			200.76	233.99
GUNNELL R H 20-2	289.5	93.45	247.92	131.754
HSR-HAGAN 16-6A			261.06	122.808

UPRC 19-9J	416	120.221	245.8	141.036
HSR-DEMEULES 9-22			262.64	125.768
FRICO 16-15			201.7	249.56
MOSER 28-8	250	82.235	245.5	128.443
FRANK 43-21			261.86	119.397
HSR-MOSER 16-27			261.52	119.112
HSR-MOSER 10-27			261.4	117.894
BEEBE DRAW UPRR 31-17			234.563	164.808
HSR-EGGLER 11-29			261.72	141.162
MEGAN H 16-2J	270.26	130.03	246.28	132.777
WARD 30-1J	250.5	80.77	246.26	131.648
UPRC H 17-9J	250.5	79	245.78	130.967
UPRC H 17-16J	250.5	80	245.62	132.701
HSR-AUGUST 16-29			262.86	121.716
HSR HOUSE 3-20			261.62	119.868
UPRC 17-15J	190	67	248.48	133.296
UPRC 17-13J5	435	106.167	247.38	132.616
WARDELL UPRR 42-7			262.44	131.67
UPRC 17-12J5	420	96.625	246.24	135.87
UPRC 9-12J5	416.72	106.26	247.76	130.89
UPRC 9-3J	158	112.81	245.58	129.58
WARDELL 41-7			260	136.059
UPRC 17-10J	192.7	67	245.52	130.988
UPRC 21-3J	190	63.966	246.02	130.974
UPRC 21-6J	190	64.364	246.08	132.972
UPRC 21-4J	252	80	245.72	130.471
UPRC 21-5J	160	66.83	249.4	130.604
BB DRAW H 8-9	300	98.364	245.66	129.1151836
UPRC 17-3J	263.9	82.992	246.24	131.964

UPRC 17-4J	134.19	69.594	246	132.273
MEGAN H 16-12	205	71	247.14	124.614
UPRC 9-14J5	418	109.2	246.66	132.408
UPRC 17-11J	250.5	79.986	247.24	134.369

Glossary

$\alpha = 1\text{-}K/K_s$ = Biot's stress coefficient

β = dimensionless shear modulus ratio

B_g = average gas formation volume factor, res ft^3/SCF

$c = \varkappa/S$ = diffusivity coefficient, $(m^2.s^{-1})$

c_{fl} = fluid compressibility, psi^{-1} (Pa^{-1})

c_t = total compressibility, psi^{-1} (Pa^{-1})

δ_{ij} = Kronecker's delta

D_i = initial production decline, $month^{-1}$

D_{iD} = fracture decline number

E = Young's modulus, psi (Pa)

E_b = Young's modulus of the bounding layers, psi (Pa)

E_p = Young's modulus of the pay zone, psi (Pa)

ε_{ij} = strain tensor

η = poroelastic coefficient

F_{CD} = dimensionless fracture conductivity

F_{Co} = fracture completion number

γ = dimensionless fracture height ratio

G_b = bounding layer shear modulus, psi (Pa)

G_{pi} = cumulative production of neighbor well i, MSCF (m^3)

G_r = pay zone shear modulus, psi (Pa)

h = formation thickness, ft (m)

h_f = fracture half-height, ft (m)

h_p = pay zone half-thickness, ft (m)

k = intrinsic permeability, md (m^2)

k_f = fracture permeability, md (m^2)

K = dry bulk modulus, psi (Pa)

K_u = undrained bulk modulus, psi (Pa)

$\varkappa = k/\mu$ = mobility coefficient, ($m^2.Pa^{-1}.s^{-1}$)

$K_{fl} = 1/c_{fl}$ = reservoir fluid bulk modulus, psi (Pa)

K_s = grain bulk modulus, psi (Pa)

λ = dimensionless L_f'/ L_f ratio

L_f = initial fracture half-length, ft (m)

L_f' = distance to isotropic point, ft (m)

m(p) = real-gas pseudopressure, ($Pa.s^{-1}$)

M = Biot modulus, psi (Pa)

μ = fluid viscosity, cp (Pa.s)

m_s = proppant mass, lbm (kg)

n = number of neighbor wells

ν = Poisson's ratio

ν_b = Poisson's ratio in the bounding layers

ν_p = Poisson's ratio in the pay zone

p = pore pressure, psi (Pa)

$p^* = |p_R - p_{wb}|$ = characteristic pore pressure, psi (Pa)

p_c = closure stress, psi (Pa)

p_D = dimensionless pressure

q_i = fluid discharge vector, bbl/day ($m^3.s^{-1}$)

ϕ = formation porosity

ϕ_f = fracture porosity

Π = dimensionless stress deviator

Π_{mech} = mechanical stress reorientation number

$p_{net} = p_C - \sigma_{hmin}$ = net closure stress, psi (Pa)

Π_{poro} = poroelastic stress reorientation number

P_0 = far-field mean stress, psi (Pa)

p_R = initial reservoir pressure, psi (Pa)

p_{wf} = wellbore pressure, psi (Pa)

q = production rate, MSCF/D ($m^3.s^{-1}$)

Q_{1month} = cumulative well production after 1 month, MSCF (m^3)

q_D = dimensionless flow rate

$q_{sc}(t)$ = wellbore flow rate at standard conditions, MSCF/D ($m^3.s^{-1}$)

R_{Dep} = reservoir depletion number

ρ = density of the porous material, $lbm.ft^{-3}$ ($kg.m^{-3}$)

ρ_s = fluid density, $lbm.ft^{-3}$ ($kg.m^{-3}$)

ρ_s = proppant density, $lbm.ft^{-3}$ ($kg.m^{-3}$)

r_i = distance between neighbor well i and well of interest, ft (m)

s_5^o = distance between fracture and end of 5-degree stress reorientation region, ft (m)

s_{10}^o = distance between fracture and end of 10-degree stress reorientation region, ft (m)

s_{90}^o = distance between fracture and isotropic point (=L_f'), ft (m)

σ^* = characteristic stress, psi (Pa)

σ_{ij} = stress tensor, psi (Pa)

σ_{hmax} = maximum horizontal in-situ stress, psi (Pa)

σ_{hmin} = minimum horizontal in-situ stress, psi (Pa)

$\Delta\sigma_h$ = in-situ horizontal stress contrast, psi (Pa)

σ_V = vertical in-situ stress, psi (Pa)

S_0 = far-field stress deviator, psi (Pa)

S_w = formation water saturation

t = time, hours (s)

T = tensile strength, psi (Pa)

T = reservoir temperature, K (ºR)

t_{DLf} = dimensionless time

τ = dimensionless time

t_{IF} = production time of the initial fracture, (months)

u_i = displacement vector, ft (m)

w_f = fracture width, ft (m)

w_0 = maximum fracture width, ft (m)

Z = gas deviation factor

ζ = variation of fluid content

References

Barba, R.E. 2009. A Novel Approach to Identifying Refracturing Candidates and Executing Refracture Treatments in Multiple Zone Reservoirs. Paper SPE 125008 presented at the 2009 SPE Annual Technical Conference and Exhibition, New Orleans, Louisiana, 4-7 October. DOI: 10.2118/125008-MS.

Berchenko, I. and Detournay, E. 1997. Deviation of Hydraulic Fractures through Poroelastic Stress Changes Induced by Fluid Injection and Pumping. *Int. J. Rock Mech. Min. Sci.* **34** (6): 1009-1019.

Biot, M.A. 1955. Theory of Elasticity and Consolidation for a Porous Anisotropic Solid. *J. Appl. Phys.* **26** (1955): 182-185.

Britt, L.K., Smith, M.B., Haddad, Z., Lawrence, P., Chipperfield, S., and Hellman, T. 2006. Water-Fracs: We Do Need Proppant After All. Paper SPE 102227 presented at the 2006 SPE Annual Technical Conference and Exhibition, San Antonio, Texas, 24-27 September. DOI: 10.2118/102227-MS.

Bunger, A.P., Zhang, X., and Jeffrey, R.G. 2011. Parameters Effecting the Interaction among Closely Spaced Hydraulic Fractures. Paper SPE 140426 presented at the SPE Hydraulic Fracturing Technology Conference, The Woodlands, Texas, 24-26 January. DOI: 10.2118/140426-MS.

Cheng, Y. 2009. Boundary Element Analysis of the Stress Distribution around Multiple Fractures: Implications for the Spacing of Perforation Clusters of Hydraulically Fractured Horizontal Wells. Paper SPE 125769 presented at the SPE Eastern Regional Meeting, Charleston, West Virginia, 23-25 September. DOI: 10.2118/125769-MS.

Cipolla, C.L. 2009. Modeling Production and Evaluating Fracture Performance in Unconventional Gas Reservoirs. *J. Pet Tech* **61** (9): 84-90. SPE-118536-MS. DOI: 10.2118/118536-MS.

Cipolla, C.L., Lolon, E.P., Mayerhofer, M.J., and Warpinski, N.R. 2009. Fracture Design Considerations in Horizontal Wells Drilled in Unconventional Gas Reservoirs. Paper SPE 119366 presented at the SPE Hydraulic Fracturing Technology Conference, The Woodlands, Texas, 19-21 January. DOI: 10.2118/119366-MS.

Daneshy, A. 2011. Hydraulic Fracturing of Horizontal Wells: Issues and Insights. Paper SPE 140134 presented at the SPE Hydraulic Fracturing Technology Conference, The Woodlands, Texas, 24-26 January. DOI: 10.2118/140134-MS.

Detournay, E. and Cheng, A.H.-D. 1993. Fundamentals of Poroelasticity. Chapter 5 in Comprehensive Rock Engineering: Principles, Practice and Projects, Pergamon Press, pp. 113-171.

Dozier, G., Elbel, J., Fielder, E., Hoover, R., Lemp, S., Reeves, S., Siebrits, E., Wisler, D., and Wolhart, S. 2003. Refracturing Works. *Oilfield Review*: 38-53.

Elbel, J.L. and Mack, M.G. 1993. Refracturing: Observations and Theories. Paper SPE 25464 presented at the SPE Production Operations Symposium, Oklahoma City, Oklahoma, 21-23 March. DOI: 10.2118/25464-MS.

Fisher, M.K., Heinze, J.R., Harris, C.D., Davidson, B.M., Wright, C.A., and Dunn, K.P. 2004. Optimizing Horizontal Completion Techniques in the Barnett Shale Using Microseismic Fracture Mapping. Paper SPE 90051 presented at the 2004 SPE Annual Technical Conference and Exhibition, Houston, Texas, 26-29 September. DOI: 10.2118/90051-MS.

Fisher, M.K., Wright, C.A., Davidson, B.M., Goodwin, A.K., Fielder, E.O., Buckler, W.S., and Steinsberger, N.P. 2002. Integrated Fracture Mapping Technologies to Optimize Stimulations in the Barnett Shale. Paper SPE 77441 presented at the 2002 SPE Annual Technical Conference and Exhibition, San Antonio, Texas, September 29-October 2. DOI: 10.2118/77441-MS.

FLAC3D. 2011. Theory and Background. Itasca Consulting Group, Inc.

Gadde, P.B., Liu, Y., Norman, J., Bonnecaze, R., and Sharma, M.M. 2004. Modeling Proppant Settling in Water-Fracs. Paper SPE 89875 presented at the 2004 SPE Annual Technical Conference and Exhibition, Houston, Texas, 26-29 September. DOI: 10.2118/89875-MS.

Gas Technology Institute. 1996. Assessment of Technology Barriers and Potential Benefits of Restimulation R&D for Natural Gas Wells. GRI-96/0267.

Guppy, K.H., Cinco-Ley, H., Ramey Jr., H.J. 1981. Effect of Non-Darcy Flow on the Constant-Pressure Production of Fractured Wells. *SPE Journal* **21** (3): 390-400. SPE-9344-PA. DOI: 10.2118/9344-PA.

Holditch, S.A. 2006. Tight Gas Sands. *J. Pet Tech* **58** (6): 86-93. SPE-103356-MS. DOI: 10.2118/103356-MS.

Ketter, A.A., Heinze, J.R., Daniels, J.L., and Waters, G. 2008. A Field Study in Optimizing Completion Strategies for Fracture Initiation in Barnett Shale Horizontal Wells. *SPE Prod & Oper* **23** (3): 373-378. DOI: 10.2118/103232-PA.

King, G.E., Haile, L., Shuss, J., and Dobkins, T.A. 2008. Increasing Fracture Path Complexity and Controlling Downward Fracture Growth in the Barnett Shale. Paper SPE 119896 presented at the SPE Shale Gas Production Conference, Fort Worth, Texas, 16-18 November. DOI: 10.2118/119896-MS.

King, G.E. 2010. Thirty Years of Gas Shale Fracturing: What Have We Learned? Paper SPE 133456 presented at the 2010 SPE Annual Technical Conference and Exhibition, Florence, Italy, 19-22 September. DOI: 10.2118/133456-MS.

Le Calvez, J.H., Klem, R.C., Bennett, L., Erwemi, A., Craven, M. and Palacio, J.C. 2007. Real-Time Microseismic Monitoring of Hydraulic Fracture Treatments: A Tool to Improve Completion and Reservoir Management. Paper SPE 106159 at the SPE Hydraulic Fracturing Technology Conference, College Station, Texas, 29-31 January. DOI: 10.2118/106159-MS.

Li, P. 2008. Theoretical Study on Reorientation Mechanism of Hydraulic Fractures. SPE-105724-MS. DOI: 10.2118/105724-MS.

Li, P. and Song, Z. 2006. Study on Reorientation Mechanism of Refracturing in Ordos Basin - A Case Study: Chang 6 Formation, Yanchang Group, Triassic System in Wangyao Section of Ansai Oil Field. Paper SPE 104260 presented at the SPE International Oil & Gas Conference and Exhibition held in Beijing, China, 5-7 December. DOI: 10.2118/104260-MS.

Liu, Y., Gadde, P.B., and Sharma, M.M. 2007. Proppant Placement Using Reverse-Hybrid Fracs. *SPE Prod & Oper* **22** (3): 348-356. DOI: 10.2118/99580-PA.

Liu, H., Lan, Z., Zhang, G., Hou, F., He, X., and Liu, X. 2008. Evaluation of Refracture Reorientation in Both Laboratory and Field Scales. Paper SPE 112445 presented at the SPE International Symposium and Exhibition on Formation Damage Control, Lafayette, Louisiana, 13-15 February. DOI: 10.2118/112445-MS.

Lolon, E.P., Cipolla, C.L., Weijers, L. Hesketh, R.E., and Grigg M.W. 2009. Evaluating Horizontal Well Placement and Hydraulic Fracture Spacing/Conductivity in the Bakken Formation, North Dakota. Paper SPE 124905 presented at the 2009 SPE Annual Technical Conference and Exhibition, New Orleans, Louisiana, 4-7 October. DOI: 10.2118/124905-MS.

Maxwell, S.C., Urbancic, T.I., Steinsberger, N., and Zinno, R. 2002. Microseismic Imaging of Hydraulic Fracture Complexity in the Barnett Shale. Paper SPE 77440 presented at the 2002 SPE Annual Technical Conference and Exhibition, San Antonio, Texas, September 29-October 2. DOI: 10.2118/77440-MS.

Maxwell, S.C., Waltman, C.K., Warpinski, N.R., Mayerhofer, M.J., and Boroumand, N. 2009. Imaging Seismic Deformation Induced by Hydraulic Fracture Complexity. *SPE Res Eval & Eng* **12** (1): 48-52. SPE-102801-PA. DOI: 10.2118/102801-PA.

Mayerhofer, M.J., Lolon, E.P., Warpinski, N.R., Cipolla, C.L., Walser, D., and Rightmire, C.M. 2010. What is Stimulated Reservoir Volume? *SPE Prod & Oper* **25** (1): 89-98. SPE-119890-PA. DOI: 10.2118/119890-PA.

Mayerhofer, M.J., Lolon, E.P., Youngblood, J.E., and Heinze, J.R. 2006. Integration of Microseismic Fracture Mapping Results with Numerical Fracture Network Production Modeling in the Barnett Shale. Paper SPE 102103 presented at the

2006 SPE Annual Technical Conference and Exhibition, San Antonio, Texas, 24-27 September. DOI: 10.2118/102103-MS.

McDaniel, B.W. 2010. Horizontal Wells with Multi-Stage Fracs Provide Better Economics for Many Lower Permeability Reservoirs. Paper SPE 133427 presented at the SPE Asia Pacific Oil and Gas Conference and Exhibition, Brisbane, Queensland, Australia, 18-20 October. DOI: 10.2118/133427-MS.

Minner, W.A., Wright, C.A., Stanley, G.R., de Pater, C.J., Gorham, T.L., Eckerfield, L.D., and Hejl, K.A. 2002. Waterflood and Production-Induced stress Changes Dramatically Affect Hydraulic Fracture Behavior in Lost Hills Infill Wells. Paper SPE 77536 presented at the 2002 SPE Annual Technical Conference and Exhibition, San Antonio, Texas, 29 September-2 October. DOI: 10.2118/77536-MS.

Mohaghegh, S. and Reeves, S.R. 2000. Development of an Intelligent Systems Approach for Restimulation Candidate Selection. Paper SPE 59767 presented at the SPE/CERI Gas Technology Symposium, Calgary, Alberta, Canada, 3-5 April. DOI: 10.2118/59767-MS.

Moore, L.P. and Ramakrishnan, H. 2006. Restimulation: Candidate Selection Methodologies and Treatment Optimization. Paper SPE 102681 presented at the 2006 SPE Annual Technical Conference and Exhibition, San Antonio, Texas, 24-27 September. DOI: 10.2118/102681-MS.

Mutalik, P.N. and Gibson, B. 2008. Case History of Sequential and Simultaneous Fracturing of the Barnett Shale in Parker County. Paper SPE 116124 presented at the 2008 SPE Annual Technical Conference and Exhibition, Denver, Colorado, 21-24 September. DOI: 10.2118/116124-MS.

Oberwinkler, C., Ruthammer, G., Zangl, G., and Economides, M.J. 2004. New Tools for Fracture Design Optimization. Paper SPE 86467 presented at the SPE International Symposium and Exhibition on Formation Damage Control, Lafayette, Louisiana, 18-20 February. DOI: 10.2118/86467-MS.

Olsen, T.N., Bratton, T.R., and Thiercelin, M.J. 2009. Quantifying Proppant Transport for Complex Fractures in Unconventional Formations. Paper SPE 119300 presented at the SPE Hydraulic Fracturing Technology Conference, The Woodlands, Texas, 19-21 January. DOI: 10.2118/119300-MS.

Olson, J.E. 2008. Multi-fracture Propagation Modeling: Application to Hydraulic Fracturing in Shales and Tight Gas Sands. Paper ARMA 08-327 presented at the 42nd US Rock Mechanics Symposium, San Francisco, California, June 29-July 2.

Olson, J.E. and Dahi-Taleghani, A. 2009. Modeling Simultaneous Growth of Multiple Hydraulic Fractures and Their Interaction With Natural Fractures. Paper SPE 119739 presented at the SPE Hydraulic Fracturing Technology Conference, The Woodlands, Texas, 19-21 January. DOI: 10.2118/119739-MS.

Palisch, T.T., Vincent M.C., and Handren, P.J. 2008. Slickwater Fracturing – Food for Thought. Paper SPE 115766 presented at the 2008 SPE Annual Technical Conference and Exhibition, Denver, Colorado, 21-24 September. DOI: 10.2118/115766-MS.

Palmer, I.D. 1993. Induced Stress due to Hydraulic Fracture in Coalbed Methane Wells. Paper SPE 25861 presented at the SPE Rocky Mountain Regional Reservoirs Symposium, Denver, Colorado, 12-14 April. DOI: 10.2118/25861-MS.

Reeves, S.R. 2001. Natural Gas Production Enhancement via Restimulation. GRI-01/0144.

Reeves, S.R., Bastian, P.A., Spivey, J.P., Flumerfelt, R.W., Mohaghegh, S., and Koperna, G.J. 2000. Benchmarking of Restimulation Candidate Selection Techniques in Layered Tight Gas Sand Formations Using Reservoir Simulation. Paper SPE 63096 presented at the 2000 SPE Annual Technical Conference and Exhibition, Dallas, Texas, 1-4 October. DOI: 10.2118/63096-MS.

Reeves, S.R., Hill, D.G., Timer, R.L., Bastian, P.A., Conway, M.W., and Mohaghegh, S. 1999. Restimulation of Tight Gas Sand Wells in the Rocky Mountain Region. Paper SPE 55627 presented at the SPE Rocky Mountain Regional Meeting, Gillette, Wyoming, 15-18 May. DOI: 10.2118/55627-MS.

Roussel, N.P. and Sharma, M.M. 2010. Quantifying Transient Effects in Altered-Stress Refracturing of Vertical Wells. *SPE Journal* **15** (3): 770-782. SPE-119522-PA. DOI: 10.2118/119522-PA.
Presented at the 2009 SPE Hydraulic Fracturing Technology Conference, The Woodlands, Texas, 19-21 January.

Roussel, N.P. and Sharma, M.M. 2011. Optimizing Fracture Spacing and Sequencing in Horizontal-Well Fracturing. *SPE Prod & Oper* **26** (2): 173-184. SPE-127986-PA. DOI: 10.2118/127986-PA.
Presented at the 2010 SPE International Symposium and Exhibition on Formation Damage Control, Lafayette, Louisiana, 10-12 February.

Roussel, N.P. and Sharma, M.M. 2010. Role of Stress Reorientation in the Success of Refracture Treatments in Tight Gas Sands. Paper SPE 134491 presented at the 2010 SPE Annual Technical Conference and Exhibition, Florence, Italy, 19-22 September. DOI: 10.2118/134491-MS.

Roussel, N.P. and Sharma, M.M. 2011. Selecting Candidate Wells for Refracturing Using Production Data. Paper SPE 146103 to be presented at the 2011 SPE Annual Technical Conference and Exhibition, Denver, Colorado, 30 October-2 November. DOI: 10.2118/146103-MS.

Roussel, N.P. and Sharma, M.M. 2011. Strategies to Minimize Frac Spacing and Stimulate Natural Fractures in Horizontal Completions. Paper SPE 146104 to be

presented at the 2011 SPE Annual Technical Conference and Exhibition, Denver, Colorado, 30 October-2 November. DOI: 10.2118/146104-MS.

Roussel, N.P. and Sharma, M.M. 2011. Method for Determining Spacing of Hydraulic Fractures in a Rock Formation. US Provisional Application No. 61/501,003.

Sharma, M.M., Gadde, P.B., Sullivan, R., Sigal, R., Fielder, R., Copeland, D., Griffin, L. and Weijers, L. 2004.Slick Water and Hybrid Fracs in the Bossier: Some Lessons Learnt. Paper SPE 89876 presented at the 2004 SPE Annual Technical Conference and Exhibition, Houston, Texas, 26-29 September. DOI: 10.2118/89876-MS.

Siebrits, E. and Elbel, J.L. 1998. Parameters Affecting Azimuth and Length of a Secondary Fracture during a Refracture Treatment. Paper SPE 48928 presented at the 1998 SPE Annual Technical Conference and Exhibition, New Orleans, Louisiana, 27-30 September. DOI: 10.2118/48928-MS.

Siebrits, E., Elbel, J.L., and Hoover, R.S. 2000. Refracture Reorientation Enhances Gas Production in Barnett Shale Tight Gas Wells. Paper SPE 63030 presented at the 2000 SPE Annual Technical Conference and Exhibition, Dallas, Texas, 1-4 October. DOI: 10.2118/63030-MS.

Singh, V., Roussel, N.P., and Sharma, M.M. 2008. Stress Reorientation around Horizontal Wells. Paper SPE 116092 presented at the 2008 SPE Annual Technical Conference and Exhibition, Denver, Colorado, 21-24 September. DOI: 10.2118/116092-MS.

Sneddon, I.N. 1946. The Distribution of Stress in the Neighborhood of a Crack in an Elastic Solid. *Proceedings, Royal Society of London* **A-187**: 229-260.

Sneddon, I.N. and Elliot, H.A. 1946. The Opening of a Griffith Crack Under Internal Pressure. *Quart. Appl. Math.* **4** (3): 362-367.

Soliman, M.Y. and Boonen, P. 1997. Review of Fractured Horizontal Wells Technology. Paper SPE 36289 presented at the SPE Asia Pacific Oil and Gas Conference Exhibition, Kuala Lumpur, Malaysia, 14-18 April. DOI: 10.2118/36289-MS.

Soliman, M.Y., East, L., and Adams, D. 2008. GeoMechanics Aspects of Multiple Fracturing of Horizontal and Vertical Wells. *SPE Drill & Compl* **23** (3): 217-228. SPE-86992-PA. DOI: 10.2118/86992-PA.

Soliman, M.Y., East, L., and Augustine, J. 2010. Fracturing Design Aimed at Enhancing Fracture Complexity. Paper SPE 130043 presented at the SPE EUROPEC/EAGE Annual Conference and Exhibition, 14-17 June, Barcelona, Spain. DOI: 10.2118/130043-MS.

U.S. Energy Information Administration. 2011. Annual Energy Outlook 2011 with Projections to 2035. DOE/EIA-0383.

U.S. Energy Information Administration. 2011. World Shale Gas Resources: and Initial Assessment of 14 Regions Outside the United States.

Vermylen, J.P. and Zoback, M.D. 2011. Hydraulic Fracturing, Microseismic Magnitudes, and Stress Evolution in the Barnett Shale, Texas, USA. Paper SPE 140507 presented at the SPE Hydraulic Fracturing Technology Conference, The Woodlands, Texas, 24-26 January. DOI: 10.2118/140507-MS.

Vincent, M.C. 2010. Refracs – Why do they Work, and Why do they Fail in 100 Published Field Studies? Paper SPE 134330 presented at the 2010 SPE Annual Technical Conference and Exhibition, Florence, Italy, 19-22 September. DOI: 10.2118/134330-MS.

Walsh, M.P. and Lake, L.W. 2003. A Generalized Approach to Primary Hydrocarbon Recovery. Handbook of Petroleum Exploration and Production Series, Elsevier, Amsterdam, The Netherlands.

Warpinski, N.R. and Branagan, P.T. 1989. Altered Stress Fracturing. *J. Pet Tech* **41** (9): 990-997. SPE-17533-PA. DOI: 10.2118/17533-PA.

Warpinski, N.R., Mayerhofer, M.J., Vincent, M.C., Cipolla, C.L., and Lolon, E.P. 2008. Stimulating Unconventional Reservoirs: Maximizing Network Growth While Optimizing Fracture Conductivity. Paper SPE 114173 presented at the SPE Unconventional Reservoir Conference, Keystone, Colorado, 10-12 February. DOI: 10.2118/114173-MS.

Waters, G., Dean, B., Downie, R., Kerrihard, K., Austbo, L., and McPherson, B. 2009. Simultaneous Hydraulic Fracturing of Adjacent Wells in the Woodford Shale. Paper SPE 119635 presented at the SPE Hydraulic Fracturing Technology Conference, The Woodlands, Texas, 19-21 January. DOI: 10.2118/119635-MS.

Weng, X. and Siebrits, E. 2007. Effect of Production-Induced Stress Field on Refracture Propagation and Pressure Response. Paper SPE 106043 at the SPE Hydraulic Fracturing Technology Conference, College Station, Texas, 29-31 January. DOI: 10.2118/106043-MS.

Weng, X., Kresse, O., Cohen, C., Wu, R. and Gu, H. 2011. Modeling of Hydraulic Fracture Network Propagation in a Naturally Fractured Formation. Paper SPE 140253 presented at the SPE Hydraulic Fracturing Technology Conference, The Woodlands, Texas, 24-26 January. DOI: 10.2118/140253-MS.

Wolhart, S., Zoll, M., McIntosh, G., and Weijers, L. 2007. Surface Tiltmeter Mapping Shows Hydraulic Fracture Reorientation in the Codell Formation Wattenberg Field, Colorado. Paper SPE 110034 presented at the 2007 SPE Annual Technical Conference and Exhibition, Anaheim, California, 11-14 November. DOI: 10.2118/110034-MS.

Wright, C.A. and Conant, R.A. 1995. Hydraulic Fracture Orientation and Production / Injection induced Reservoir Stress Changes in Diatomite Waterfloods. Paper SPE

29625 presented at the SPE Western Regional Meeting, Bakersfield, California, 8-10 March. DOI: 10.2118/29625-MS.

Wright, C.A. and Conant, R.A. 1995. Hydraulic Fracture Reorientation in Primary and Secondary Recovery for Low-Permeability Reservoirs. Paper SPE 30484 presented at the 1995 SPE Annual Technical Conference and Exhibition, Dallas, Texas, 22-25 October. DOI: 10.2118/30484-MS.

Wright, C.A., Stewart, D.W., and Emanuele, M.A. 1994. Reorientation of Propped Refracture Treatments in the Lost Hills Field. Paper SPE 27896 presented at the SPE Western Regional Meeting, Long Beach, California, 23-25 March. DOI: 10.2118/27896-MS.

Zhai, Z. and Sharma, M.M. 2007. Estimating Fracture Reorientation due to Long Term Fluid Injection/Production. Paper SPE 106387 presented at the SPE Production and Operations Symposium, Oklahoma City, Oklahoma, 31 March-3 April. DOI: 10.2118/106387-MS.

The format used in references is recommended by the Society of Petroleum Engineers (2011)

Vita

Nicolas P. Roussel graduated with a PhD in Petroleum and Geosystems Engineering at The University of Texas at Austin. He has authored 1 patent and over 10 publications, including 4 peer-reviewed journal articles. His research has been focusing on the physical modeling of stress reorientation and its application to the optimization of horizontal completions in unconventional reservoirs and restimulation operations in vertical wells. Previous work also includes modeling of the multiphase flow behavior of fluid suspensions, including fracturing fluids and fiber-reinforced polymers. Roussel holds an MS degree in mechanical engineering from the Georgia Institute of Technology in Atlanta, Georgia and a diplôme d'ingénieur from Arts et Métiers ParisTech in Paris, France. He is a member of the Society of Petroleum Engineers, Phi Kappa Phi honor society, and founded in 2008 the Petroleum Graduate Student Association at The University of Texas at Austin of which he was president for two years.

Permanent address (or email): nroussel@utexas.edu

This dissertation was typed by Nicolas P. Roussel.